

POLITECNICO DI TORINO

Master degree in Aerospace Engineering



**Politecnico
di Torino**



Master thesis

Numerical simulating and analytical modelling the wake behind vertical axis wind turbines: a verification analysis

Relators:

Prof. Carlos Simão Ferreira

Prof. Gaetano Iuso

Co-relator:

PhD. Ming Huang

Candidate:

Davide Monni S263303

Academic year 2020-2021

Numerical simulating and analytical modelling the wake behind vertical axis wind turbines: a verification analysis

by

Monni Davide

to obtain the Master degree in Aerospace Engineering
at Politecnico di Torino,
to be defended publicly on Monday July 12, 2021.

Student number: S263303
Project duration: October 1, 2020 – July 12, 2021
Thesis committee: Prof. Carlos Simão Ferreira, TU Delft, supervisor
Prof. Gaetano Iuso, Politecnico di Torino, supervisor
PhD. Ming Huang, TU Delft, co-relator



**Politecnico
di Torino**



*To my family,
Turin, July 2021*

The will to act

Abstract

Vertical axis wind turbines (VAWTs) have been demonstrated to possibly be more efficient than traditional turbines, especially in wind farm deployment, where the wake-turbine interaction is intensive and the wake aerodynamics should be accurately modelled. Tools to analyse VAWTs are still studied and improved, especially analytical wake models which are widely used by companies when studying a wind farm layout thanks to their low computational cost. Similar models are capable of providing the most relevant parameters when considering a wind farm: velocity deficit and wake's width, using a limited number of input parameters. Nevertheless, they are often based on neglecting relevant aspects, on incorrect assumptions and derivation and most of the times are horizontal axis wind turbines (HAWTs) wake models simply transposed to VAWTs. Therefore they are considered inaccurate. The purpose of this thesis is to investigate such methods, defining their validity range as well as their limitations, shedding light on possible improvements and corrections.

Two existing analytical wake models are investigated: one based on a top-hat distribution for the velocity deficit and the other on a Gaussian distribution, they were both developed in a Python environment based on free-access library `py-wake`. The models were supported by two different equations for the wake decay constant, widely used for HAWTs: the Niayifar law and the Abkar law. Using field and high fidelity data, original versions of the selected wake models for HAWTs were validated. Several tests were then run for VAWT case and models were then compared against experimental and high fidelity simulation data in the literature, covering different conditions by changing the aspect ratio (AR) from 0.25 to 2 as well as thrust coefficient (C_T) from 0.3 up to 0.8. The range of validity of these analytical tools was then analysed.

Numerical simulations based on the actuator line theory coupled with unsteady RANS equations were introduced as a higher fidelity data source for comparison, to better understand the effects of Reynolds number (Re) and turbulence. Such model, coupled with the $k-\epsilon$ turbulence model, was already developed as a library for the open-source software OpenFOAM. It was firstly validated against experimental and literature data that covered conditions ranging from low Reynolds number ($\approx 10^5$) to high Re ($\approx 10^7$), to study the Reynolds number effect on the modelling. Effect of environmental turbulence intensity on wake recovery was qualitatively analysed with values ranging from extremely low (1%) to high (8%) turbulence intensity (I). Results obtained from the numerical simulations were then compared with analytical wake models predictions for the different scales and Reynolds' numbers.

Existing analytical wake models for VAWTs were found being accurate especially when dealing with the far wake region and in high turbulence intensity environment. The Gaussian model supported by Abkar's law showed the best agreement with a deviation from high fidelity data for the maximum velocity deficit ranging from less than 1% up to 8% when different C_T and AR were tested. Using instead Niayifar's law the difference increases up to 30% in the far wake. When the near wake was considered, the error for the Gaussian models increased up to 60% if Abkar's law is considered and up to 55% when using Niayifar's one. In similar cases averaged velocities calculated showed slightly better agreement with high fidelity data. A peak in the difference between maximum deficit calculated by Gaussian models was observed ranging from 50% to 40% in low turbulence intensity conditions when considering the near and far wake respectively. Top-hat models instead showed better agreement in extreme conditions, when high aspect ratios and low turbulence intensities are experienced, showing 40% deviation less than Gaussian models in the near wake for the average velocity deficit. The agreement showed by top-hat models with high fidelity data in the far wake region was found to depend on the law used for the wake decay constant. Overall the one based on Niayifar law displayed better results, providing 12% average deviation less in both high and low turbulent conditions.

Additional analysis of the numerical results showed that wake's structures at different Reynolds' number were qualitatively similar. Vortical structures were found to be present in each of the cases analysed but with different intensity: for high Reynolds' number the intensity of edge vortices was one order of magnitude lower than the smallest case. Similarly the turbulence effect on the wake was investigated and was found to be strictly related to the Reynolds number experienced, leading to different shape and deficit values: in the low Re case without turbulence, crossflow extension of the wake almost doubled, while it was found to be reduced by less

than 10% in the high Re case along spanwise direction.

The detailed analysis of wake models for VAWTs leads to significant considerations about their validity and their limitations. When considering far wake regions and high turbulence conditions, wake models are capable of providing accurate results. In contrast, the models perform poorly in the near wake, as well as in low turbulence condition. The latter is mainly because that the existing formulation of wake decay/expansion is derived based on the field data for HAWTs, where the ambient turbulence level is higher, and the turbine induced wake structure is totally different. The second main limitation is related to the inability to replicate wake deflection, something that only wake models for yawed HAWTs has kept into account. Therefore, in conclusion, it is important to improve the models in the future by introducing expressions for the wake decay constant based on VAWT real aerodynamics and modelling wake's centre displacement.

Acknowledgements

This thesis is the conclusion of a long journey that lasted almost six years. Even with all the effort I have always put into the studio, I have never faced before such a detailed, difficult and complete work that put me so hard to the test. I can say that I am extremely proud of the final result and of what I have learned in all these years that does not make in vain all the sacrifices I have stood along the way.

I am very grateful to Professor Iuso who gave me the opportunity to undertake this project with TU Delft, it would not have been possible without him. A huge thank you to Professor Carlos Ferreira, who met me in a desperate situation with no way out and gave me the opportunity to continue working on a project that I loved from the very first moment without having to give it up. Special thanks to Ming, it has been an amazing 9 months run and without your help I would still be at the very beginning. Thank you not only for all that I have learned thanks to you but also for having endured and encouraged me to give the best of myself during all these months, always ready to listen to me and help me at any time. It is a pity that we have never met and known in person, but I trust that one day, sooner or later, we will have that opportunity. Thanks also goes to Professor Scarano with whom I had the pleasure of working for several months.

To my family, if I got this far it was mainly because of you. Thank you for teaching me the values of hard work, commitment and giving me the wonderful opportunity of studying in another city, knowing the world and growing. Thank you for always supporting me regardless of the situation, encouraging me to give my best, advising me in my choices but especially enduring my nature, especially during the last year. I hope to make you half as proud as I am of you.

Mary, they have been 6 (+1) amazing years. We met as kids, many years have passed and many things have changed but you are still here. Without your continuous and constant support, without your dedication in listening to me, I would not have come a long way. Thank you for putting up with me as well as with the distance that separated us. I will never forget that you have always waited for me. Always ready to give me your opinion, to advise me at any time, you have always been *a light to me in dark places, when all other lights went out*. I am the luckiest person in the world to have you by my side every single day.

Last but not least, thanks to all those who have accompanied me in these 6 years, both to those who stayed until the end, and to those who remained behind. I would not be the same person without you. A special thanks, however, goes to Edoardo and Andrea, you were much more than just university colleagues but rather brothers in arms and special friends. I will always carry you in my heart. Thanks also to all those I had the pleasure to meet at Collegio and with whom I have bonded, with those more and less, I will remember with pleasure this second home and especially the fantastic year on the ground floor.

* * *

Questa tesi è il coronamento di un lungo percorso durato quasi sei anni. Pur con tutto l'impegno che ho sempre messo nello studio, non avevo mai affrontato un lavoro così dettagliato, approfondito e completo e che mi mettesse così duramente alla prova. Posso dire di essere estremamente fiero del risultato finale e di quello che ho imparato in tutti questi anni, il ché non rende vani tutti i sacrifici fatti, talvolta dolorosi.

Un sentito ringraziamento va al professor Iuso che mi ha dato la possibilità di intraprendere questo progetto con TU Delft, senza di lei non sarebbe stato possibile. Un enorme grazie al professor Carlos Ferreira, che mi ha incontrato in una situazione disperata e senza via di uscita e mi ha concesso l'opportunità di continuare a lavorare a un progetto che ho adorato fin dal primo istante senza doverlo abbandonare. Un grazie speciale a Ming, sono stati 9 mesi fantastici e senza il tuo aiuto sarei ancora all'inizio. Grazie non solo per tutto quello che ho imparato per merito tuo ma anche per avermi sopportato e spronato in tutti questi mesi a dare il meglio di me stesso, sempre pronto ad ascoltarmi e aiutarmi in qualsiasi momento. E' un peccato non poterci mai essere incontrati e conosciuti di persona, ma confido che un giorno, prima o poi, ne avremo l'occasione. Un grazie va anche al professor Scarano con cui ho avuto il piacere di lavorare per svariati mesi. Alla mia famiglia, se sono arrivato fin qua è stato principalmente per merito vostro. Grazie per avermi insegnato i valori del lavoro duro, dell'impegno e di avermi regalato questa splendida possibilità di studiare in un'altra città, di conoscere il mondo e di crescere. Grazie di avermi sempre sostenuto a prescindere dalla

situazione, spronandomi a dare il meglio di me, consigliandomi nelle scelte ma specialmente sopportando il mio carattere, specie durante l'ultimo anno. Spero di rendervi fieri almeno la metà di quanto io sono fiero di voi.

Mary, sono stati 6 (+1) anni fantastici. Ci siamo conosciuti da ragazzini, sono passati tanti anni e tante cose sono cambiate: tu sei sempre rimasta. Senza il tuo supporto continuo e costante, senza la tua dedizione nell'ascoltarmi non avrei fatto molta strada. Grazie di aver sopportato me e specialmente la distanza che ci separava. Non mi dimenticherò il fatto che tu mi abbia sempre aspettato. Sempre pronta a darmi il tuo parere, a consigliarmi in ogni momento, sei sempre stata *una luce nei luoghi oscuri, quando ogni altra luce si era spenta*. Sono la persona più fortunata del mondo ad averti al mio fianco ogni singolo giorno.

Ultimi ma non meno importanti, grazie a tutti coloro che mi hanno accompagnato in questi 6 anni, sia a chi è rimasto fino alla fine, sia a chi è rimasto indietro. Non sarei la stessa persona senza di voi. Un ringraziamento speciale però va ad Edoardo e Andrea, siete stati molto più che semplici compagni di università quanto piuttosto dei fratelli al fronte e dei fantastici amici. Un grazie anche a tutti coloro che ho avuto il piacere di conoscere in Collegio e con cui ho legato, chi più chi meno, ricorderò con piacere questa seconda casa e specialmente il fantastico anno al piano zero.

Contents

Abstract	iii
Acknowledgements	v
List of Figures	xi
List of Tables	xvii
Nomenclature	xix
1 Introduction	1
1.1 Context analysis and problem statement	1
1.2 Research objective and research questions	2
1.3 Methodology	3
1.4 Thesis outline	4
2 Literature study	7
2.1 Introduction to VAWTs	7
2.1.1 VAWTs classification	7
2.1.2 Comparison with HAWTs	9
2.1.3 Working principles and relevant parameters	10
2.2 Aerodynamics of VAWTs	14
2.2.1 Blade scale	14
2.2.2 Turbine scale	19
2.2.3 Wake scale	20
2.3 Turbine modelling: from HAWT to VAWT	24
2.3.1 Turbine modelling for HAWTs	24
2.3.2 Turbine modeling for VAWTs	26
2.4 Analytical wake models for HAWT	33
2.4.1 Jensen model	33
2.4.2 Larsen model	34
2.4.3 Ainslie model	34
2.4.4 Frandsen model	35
2.4.5 Fuga method	35
2.4.6 BPA model	35
2.4.7 Updates and additions to the BPA model	36
2.4.8 BPA yawed model	37
2.5 Wake modeling for VAWTs	40
2.5.1 Analytical wake models for VAWTs	40
2.5.2 Vortex models	44
2.5.3 RANS models	44
3 Methods	47
3.1 Numerical simulation of the wake of VAWTs	47
3.1.1 URANS equations	47
3.1.2 Actuator line model for VAWTs	57
3.2 Analytical wake modelling	71
3.2.1 Wake model for HAWTs	71
3.2.2 Wake model for VAWTs	77

4	Validation and cases analysis	83
4.1	Benchmarks and simulations set-up	83
4.1.1	Numerical simulations cases analysed	83
4.1.2	Set-up of analytical wake models for HAWTs	95
4.1.3	Analytical wake models cases analysed for VAWTs	95
4.2	Verification of the models and simulations	99
4.2.1	Validation of the numerical simulations	99
4.2.2	Validation of analytical wake models for HAWTs from py-wake	105
4.2.3	Verification of self-similarity hypothesis for VAWT far wake	110
4.2.4	Validation of the code structure for VAWT wake models	112
5	The Reynolds' number effect on VAWT wake	115
5.1	Wake similarity under different Reynolds numbers	115
5.2	Conclusions	119
6	The turbulence effect	121
6.1	Ambient turbulence effect on wake recovery	121
6.2	Conclusions	124
7	The range of validity of existing wake models	127
7.1	Comparison against numerical simulations	127
7.1.1	Comparison for low Re case	127
7.1.2	Comparison for medium Re case	134
7.1.3	Comparison for high Re case	139
7.2	Comparison against literature data	144
7.2.1	Comparison with Abkar & Dabiri [3] - Thrust coefficient effects	144
7.2.2	Comparison with Tescione et al. [110] - Low turbulence intensity effect	150
7.2.3	Comparison with Shamsoddin et al. [97] - Aspect ratio effect	153
7.3	Conclusions of the chapter	159
8	Final remarks	163
8.1	Conclusions	163
8.2	Model improvements	164
A	General knowledge about wind energy	167
A.1	Origins and overview	167
A.1.1	Global context's influence	167
A.1.2	Renewable resources and wind turbines	167
A.1.3	Historical references	170
A.1.4	Wind turbines' usage across the world	173
A.1.5	All that glitters ain't gold: disadvantages and environmental issues	180
B	Derivation and deep analysis of turbine models and wake models	183
B.1	Turbine modeling for HAWTs	183
B.1.1	Blade element momentum theory - BEM	183
B.1.2	Actuator line model for HAWTs	184
B.1.3	Actuator surface model for HAWTs	184
B.2	Turbine modeling for VAWTs	185
B.2.1	Actuator cylinder	185
B.3	Wake modelling for HAWTs	186
B.3.1	Analytical wake models for HAWTs	186
B.4	Wake modelling for VAWTs	191
B.4.1	Analytical wake models for VAWTs	191
B.4.2	Blade resolved methods for VAWTs - LES equations	194
C	Wake models code scripts analysis	197
C.1	Wake models scripts structure	197
C.1.1	Input definition	197
C.1.2	2D Arrays calculation	198
C.1.3	3D Arrays calculation	204

C.2	Wake models scripts validation against literature data	208
C.2.1	Validation of the code structure	208
C.2.2	Validation against literature data.	211
D	Additional data and results collection	215
D.1	Debugging and verification of code scripts	215
D.2	Maximum and mean velocity deficit along crossflow direction in Shamsoddin et al. [97]	217
D.3	Velocity profiles in the Reynolds' number effect analysis	218
D.4	Velocity profiles in different turbulent conditions.	219
	Bibliography	221

List of Figures

2.1	Éole turbine [17]	8
2.2	Anew-B1 turbine [50]	8
2.3	Different types of VAWTs, image from [91]	9
2.4	Comparison of the power coefficients for different turbines, image from [32]	11
2.5	Main components of a H-VAWT (left) and a Phi-shaped (or troposkien) VAWT (right)	11
2.6	Schematic of velocity triangles in VAWTs	12
2.7	Schematic of the angles used when discussing VAWTs	12
2.8	Denomination of the flow regions when a positive (left) and negative (right) rotational velocity Ω is observed	12
2.9	Brief recap of the main phenomena that characterize the different scales in VAWT's aerodynamics	14
2.10	Normalized instantaneous vorticity magnitude from the study by Posa et al. [87]. The results have been obtained by a LES simulation for TSR = 1.35 (left) and TSR=2.21 (right)	16
2.11	Visualization of the vorticity magnitude generated by a VAWT's blade. The tip vortices are visible near the edges of the blade. Image from [13]	17
2.12	Location of the tip vortices during turbine's rotation and their different motion. The image is from [110]	18
2.13	Visualization of how the TSR affects the blockage exerted on the flow (top) by a high-solidity turbine and the amount of reversed flow (bottom). Image from [90]	19
2.14	Images from [89] which allow to understand both how wake's centre is deflected moving downstream (top) as well as the CVPs generated at the edges of the turbine and how they evolve (bottom).	22
2.15	Work flow of the 3D actuator surface method. Image from [100]	25
2.16	Cross-section airfoil element, image from [104]	26
2.17	Schematic of single streamtube model from [41]	27
2.18	Schematic of multiple streamtube model from [41]	28
2.19	Schematic of double multiple streamtube model from [41]	28
2.20	Actuator surface model blade discretization, forces and vectors, image from [62]	29
2.21	Cross-section airfoil element for a VAWT, image from [66]	30
2.22	Loads distribution for radial and tangential forces along the cylinder, image from [16]	31
2.23	Control volume used in Jensen's model with the related symbols used in the equation: V is the speed in the wake, r is its radius, r_0 the wake radius at rotor position, V_a the velocity just behind the rotor and V_∞ the freestream speed [43]	33
2.24	Geometry of the wake and flow field distribution in the Lam & Peng model [51]	40
2.25	Schematic of how the blade and the vortex structures are replicated in a vortex model	44
3.1	Difference in the mean value for a steady and unsteady state condition	49
3.2	Schematic of the pimple algorithm	56
3.3	How the blades are divided into elements and how the lines are divided	58
3.4	Schematic of the calculation loop when coupling RANS and actuator line model	59
3.5	Conceptual map of how the dynamic stall model is applied besides the actuator line theory. Image taken from [65]	60
3.6	Description of the different conditions experienced by the flow around a blade when dynamic stall occurs	61
3.7	Example of the different phases of dynamic stall, image taken from [64]	64
3.8	Distribution of the velocity deficit along the wake for the Jensen - Katic model	72
3.9	Velocity deficit distribution for the BPA model	73
3.10	Different values for different cases analysed, image from [10]	74
3.11	Overview of py-wake library workflow, image from [82]	76
3.12	Structure of engineering models for wind farms in py-wake, image from [82]	76

3.13	Visualization of wake's evolution moving downstream for the top-hat model	78
3.14	Distribution of the velocity deficit and the evolution of wake width for the Abkar top-hat (top) and Gaussian model (bottom)	79
3.15	Visualization of the wake's evolution moving downstream for the Gaussian model	80
4.1	Shape of the NACA 0012 symmetric profile. Data provided by http://airfoiltools.com/plotter/index?airfoil=naca0018-il	84
4.2	NACA0012 polar for the small scale case	85
4.3	A visualization of the H-rotor turbine used in [110] and for the validation, image from [110] . . .	86
4.4	Shape of the NACA 0018 symmetric profile. Data provided by http://airfoiltools.com/plotter/index?airfoil=naca0018-il	86
4.5	NACA0018 polar for the medium scale case	87
4.6	Polar used for the high Reynolds' number case	88
4.7	Schematic of the control volume used in every case and the related dimensions	89
4.8	Description of the cells in the mesh and the different refinement	90
4.9	Overview of the mesh used for the low Reynolds' number case	91
4.10	Overview of the mesh used for the medium Reynolds' number case	91
4.11	Overview of the mesh used for the high Reynolds' number case	91
4.12	Inflow condition for the small scale turbine	92
4.13	Inflow condition for the medium scale turbine	93
4.14	Inflow condition for the large scale turbine	93
4.15	Contours of mean streamwise velocity and in-plane velocity vectors at different downstream positions normalized by the incoming wind speed for wind tunnel experiments (top) and numerical simulation (bottom) for the low Re case	100
4.16	Comparison of mean streamwise velocity deficit profiles along crossflow (top) direction at mid-span and along spanwise (bottom) direction of the normalized streamwise component from [65, 110] and the ones obtained from the numerical simulation for the medium Reynolds number case	101
4.17	Comparison of mean velocity deficit profiles along crossflow (top) direction at mid-span and spanwise (bottom) direction of the normalized streamwise component from [96] and the ones obtained from the numerical simulation for the medium Reynolds number case	102
4.18	Influence of mesh variation on mean streamwise velocity deficit profiles for low Re case	103
4.19	Influence of mesh variation on mean streamwise velocity deficit profiles for medium Re case . . .	104
4.20	Influence of mesh variation on mean streamwise velocity deficit profiles for high Re case	104
4.21	Overview of the wake evolution (top) and comparison between the predictions from the wake model, field and numerical data for case 1 in Table (4.11) (bottom)	105
4.22	Overview of the wake evolution (top) and comparison between the predictions from the wake model, field and numerical data for case 2 in Table (4.11) (bottom)	106
4.23	Overview of the wake evolution (top) and comparison between the predictions from the wake model, field and numerical data for case 3 in Table (4.11) (bottom)	107
4.24	Overview of the wake evolution (top) and comparison between the predictions from the wake model and, and numerical data for case 4 in Table (4.11) (bottom)	108
4.25	Overview of the wake evolution (top) and comparison between the predictions from the wake model, field and numerical data for case 5 in Table (4.11) (bottom)	109
4.26	Overview of the wake evolution (top) and comparison between the predictions from the wake model, field and numerical data for case 6 in Table (4.11) (bottom)	110
4.27	Self-similarity study for Abkar et al. [3] case for $C_T = 0.34$ (top) and $C_T = 0.34$ (bottom) along both spanwise and crossflow direction	111
4.28	Self-similarity study for Tescione et al. [110] case along both spanwise and crossflow direction .	112
4.29	Self-similarity study for Shamsoddin et al. [97] case along both spanwise and crossflow direction for $AR = 2$ (top), $AR = 1$ (centre) and $AR = 0.25$ (bottom)	113
4.30	Comparison between the predictions from the models developed in this thesis and the ones from the original model [2] for Case 1 in Table (4.14)	114

5.1	Mean streamwise velocity contours and in-plane velocity vectors normalized with freestream value at cross section $x = 7D, 11D$ for (a,b) low Re case (c,d) medium Re case and (e,f) high Re case	116
5.2	Streamwise vorticity contours normalized with diameter and freestream speed, in-plane mean velocity vectors normalized at cross section $x = 7D, 11D$ for (a,b) low Re case (c,d) medium Re case and (e,f) high Re case	117
5.3	Profiles of mean streamwise velocity deficit normalized with maximum deficit at each location normalized with $r_{\frac{1}{2}}$ along crossflow direction at mid-span (top) and spanwise direction at wake's centre (bottom) for different downstream sections in different Re condition	118
5.4	Comparison of wake width along crossflow direction (a) and spanwise direction (b) calculated with numerical simulations in different Re conditions. Values were calculated considering wake's centre as reference and not $\frac{y}{D} = \frac{z}{D} = 0$. Data for low case are mirrored	118
5.5	Comparison of the maximum velocity deficit (top) and the mean velocity deficit (bottom) calculated along crossflow direction at mid-span by numerical simulations for different Re conditions	119
6.1	Streamwise velocity contours and in-plane normalized vectors at cross section $x = 7D, 11D$ for (a,b) low Re, I case, (c,d) high Re, I case, (e,f) low Re laminar case and (g,h) high Re laminar case	122
6.2	Comparison of the maximum velocity deficit (top), of the mean velocity deficit (centre) and the minimum normalized velocity (bottom) calculated along spanwise direction at mid-span by the numerical simulations for different turbulent conditions	123
6.3	Comparison of wake width along crossflow direction (top) and spanwise direction (bottom) calculated with numerical simulations along crossflow direction in different I conditions	124
7.1	Overview of velocity deficit and wake's expansion for low Reynolds' number case along $x - z$ plane for $y = 0$ (left) and $x - y$ plane at mid-span (right) for (a) AL + URANS simulation (b) NOJ, (c) BPA, (d) NOJ-N and (e) BPA-N wake models	128
7.2	Mean streamwise velocity contours and in-plane velocity vector normalized by the incoming wind speed at cross section $x = 10D$ for (a) AL + URANS simulation, (b) NOJ, (c) BPA, (d) NOJ-N and (e) BPA-N wake models for low Re case	129
7.3	Profiles of mean streamwise velocity deficit along crossflow direction at mid-span (top) and spanwise direction for $y = 0$ (bottom) for different downstream sections, comparison between data from different analytical models and numerical simulation in low Re conditions	130
7.4	Comparison of wake width calculated with numerical simulations and analytical models along crossflow direction at mid-span (top) and spanwise direction for $y = 0$ (bottom) in low Re conditions	131
7.5	Comparison of the maximum velocity deficit (top) and the mean velocity deficit (bottom) calculated by the numerical simulation and wake models along crossflow direction at mid-span in low Re conditions	132
7.6	Deviation of the maximum (left) and the mean velocity deficit (right) from numerical data for different wake models. The errors are based on the data evaluated along crossflow direction at mid-span in low Re conditions using the maximum values as reference for the error.	132
7.7	Overview of velocity deficit and wake's expansion for medium Reynolds' number case along $x - z$ plane for $y = 0$ (left) and $x - y$ plane at mid-span (right) for (a) AL + URANS simulation (b) NOJ, (c) BPA, (d) NOJ-N and (e) BPA-N wake models	133
7.8	Mean streamwise velocity contours and in-plane velocity vector normalized by the incoming wind speed at cross section $x = 9D$ for (a) AL + URANS simulation, (b) NOJ, (c) BPA, (d) NOJ-N and (e) BPA-N wake models for medium Re case	134
7.9	Profiles of mean streamwise velocity deficit along crossflow direction at mid-span (top) and spanwise direction for $y = 0$ (bottom) for different downstream sections, comparison between data from different analytical models and numerical simulation in medium Re condition	135
7.10	Comparison of wake width calculated with numerical simulations and analytical models along crossflow direction (top) and spanwise direction at mid-span (bottom) in medium Re conditions	136
7.11	Comparison of the maximum velocity deficit (top) and the mean velocity deficit (bottom) calculated by the numerical simulation and wake models along crossflow direction at mid-span in medium Re conditions	138

7.12	Deviation in the maximum velocity deficit (left) and in the mean velocity deficit (right) for different wake models. The errors are based on the data evaluated along crossflow direction at mid-span for medium Re case using the maximum value as reference for the error.	138
7.13	Overview of velocity deficit and wake's expansion for high Reynolds' number case along $x - z$ plane for $y = 0$ (left) and $x - y$ plane at mid-span (right) for (a) AL + URANS simulation (b) NOJ, (c) BPA, (d) NOJ-N and (e) BPA-N wake models	139
7.14	Mean streamwise velocity contours and in-plane velocity vector normalized by the incoming wind speed at cross section $x = 9D$ for (a) AL + URANS simulation, (b) NOJ, (c) BPA, (d) NOJ-N and (e) BPA-N wake models for high Re case	140
7.15	Profiles of mean streamwise velocity deficit along crossflow direction at mid-span (top) and spanwise direction for $y = 0$ (bottom) for different downstream sections, comparison between data from different analytical models and numerical simulation in high Re condition	141
7.16	Comparison of wake width calculated with numerical simulations and analytical models along crossflow direction (top) and spanwise direction (bottom) at mid-span in high Re conditions	142
7.17	Comparison of the maximum velocity deficit (top) and the mean velocity deficit (bottom) along spanwise direction at mid-span calculated by the numerical simulation and wake models in high Re conditions	143
7.18	Deviation in the maximum velocity deficit (left) and in the mean velocity deficit (right) for different wake models. The errors are based on the data evaluated along crossflow direction at mid-span for high Re using the maximum value as reference for the error.	143
7.19	Overview of velocity deficit and wake's expansion at mid-span plane according to [3] for $C_T = 0.34$ (left) and $C_T = 0.64$ (right) for (a) NOJ, (b) BPA, (c) NOJ-N and (d) BPA-N wake models	144
7.20	Mean streamwise velocity deficit profiles along crossflow direction at mid-span (top) and spanwise direction for $y = 0$ (bottom) for different downstream sections for $C_T = 0.34$, comparison between data from different analytical models and literature data from [3]	145
7.21	Mean streamwise velocity deficit profiles along crossflow direction at mid-span (top) and spanwise direction (bottom) for different downstream sections for $C_T = 0.64$, comparison between data from different analytical models and literature data from [3]	146
7.22	Evolution of the wake area along crossflow direction at mid-span (top) and spanwise direction at $y = 0$ (bottom) according to [3] for $C_T = 0.34$ (left) and $C_T = 0.64$ (right) for different wake models	147
7.23	Evolution of the maximum deficit value (top) and the mean velocity value (bottom) along spanwise direction at mid-span according to [3] for $C_T = 0.34$ (left) and $C_T = 0.64$ (right) for different wake models	149
7.24	Deviation in the maximum velocity deficit (top) and in the mean velocity deficit (bottom) compared to data from [3] for $C_T = 0.34$ (left) and $C_T = 0.64$ (right) for different wake models. The errors are based on the data evaluated along crossflow direction at mid-span using the maximum value as reference for the error.	149
7.25	Overview of velocity deficit and wake's expansion at mid-span according to [110] for (a) NOJ, (b) BPA, (c) NOJ-N and (d) BPA-N wake models	150
7.26	Profiles of mean streamwise velocity component along crossflow direction at mid-span (top) and spanwise direction (bottom) for different downstream sections, comparison between data from different analytical models and literature data from [3]	151
7.27	Comparison between values calculated by analytical wake models and literature for maximum velocity deficit (top) and the mean velocity deficit (bottom) calculated along spanwise direction at mid-span for Tescione et al. [110] case	152
7.28	Deviation in the maximum velocity deficit (left) and in the mean velocity deficit (right) compared to data from [110] for different wake models. The errors are based on the data evaluated along crossflow direction at mid-span and the maximum value as reference for the error.	152
7.29	Overview of velocity deficit and wake's expansion according to [97] for $H = 100m, AR = 2$ (left), $H = 50m, AR = 1$ (center) and $H = 12.5m, AR = 0.25$ (right) for (a) NOJ, (b) BPA, (c) NOJ-N, (d) BPA-N wake models	153
7.30	Profiles of mean velocity deficit streamwise velocity along crossflow direction at mid-span (top) and spanwise direction (bottom) for different downstream sections, comparison between data from different analytical models and literature data from [97] for case $H = 100m, AR = 2$	154

7.31	Profiles of mean streamwise velocity deficit along crossflow direction at mid-span (top) and spanwise direction (bottom) for different downstream sections, comparison between data from different analytical models and literature data from [97] for case $H = 50m, AR = 1$	154
7.32	Profiles of mean streamwise velocity deficit along crossflow direction at mid-span (top) and spanwise direction (bottom) for different downstream sections, comparison between data from different analytical models and literature data from [97] for case $H = 12.5m, AR = 0.25$	155
7.33	Wake width evaluation along crossflow direction at mid-span plane (top) and spanwise direction at $y = 0$ plane (bottom). The cases reported are in agreement with data from [97] and feature $AR = 2$ (top right) $AR = 1$ (top left) and $AR = 0.25$ (bottom) for different wake models. The errors are based on the data evaluated along spanwise direction for $y = 0$. Moreover here spanwise wake width is normalized with the diameter, since H is not constant.	156
7.34	Evolution of the maximum deficit value (top) and the mean velocity value (bottom) along the symmetry plan for $y = 0$ according to [3] for $AR = 2$ (left), $AR = 1$ (centre) and $AR = 0.25$ (right) for different wake models compared with literature data	158
7.35	Deviation in the maximum velocity deficit (top) and in the mean velocity deficit (bottom) respect with data from [97] for $AR = 2$ (left) $AR = 1$ (centre) and $AR = 0.25$ (right) for different wake models. The errors are based on the data evaluated along spanwise direction for $y = 0$ and the reference error is the maximum value.	158
A.1	Unpredictability of the oil price due to the geopolitical situation during the last century and a half	168
A.2	Percentage of electricity produced (scaled) by sources. Image from [38]	169
A.3	Visualization of the Persian windmill. From [91]	170
A.4	Dutch windmill. Image from [91]	170
A.5	(A.5a) Outwood mill, Surrey (A.5b) Jack (Black) and Jill (White) mills at Clayton, West Sussex	171
A.6	(A.6a) Brush turbine, (A.6b) and (A.6c) la Cour turbine	171
A.7	Wind turbine installed capacity all over the world during the last 40 years (A.7a) and the last 7 (A.7b). Data from World Wind Energy Association – WWEA. Online source: https://wwindea.org/world-wind-capacity-at-650-gw/	172
A.8	Denmark data: (A.8a) electricity production by sources (A.8b) GWh produced during the period January 2018 - April 2020. Source [39]	173
A.9	Each dot corresponds to a wind turbine site	174
A.10	Germany data: (A.10a) electricity production by sources (A.10b) GWh produced during the period January 2018 - April 2020. Source [39]	174
A.11	China data: (A.11a) electricity production by sources (A.11b) GWh produced during the period January 2018 - April 2020. Source [39]	175
A.12	US data: (A.12a) electricity production by sources (A.12b) GWh produced during the period January 2018 - April 2020. Source [39]	176
A.13	United Kingdom data: (A.13a) electricity production by sources (A.13b) GWh produced during the period January 2018 - April 2020. Source [39]	176
A.14	France data: (A.14a) electricity production by sources (A.14b) GWh produced during the period January 2018 - April 2020. Source [39]	177
A.15	Belgium data: (A.15a) electricity production by sources (A.15b) GWh produced during the period January 2018 - April 2020. Source [39]	177
A.16	The Netherlands data: (A.16a) electricity production by sources (A.16b) GWh produced during the period January 2018 - April 2020. Source [39]	178
A.17	Italy data: (A.17a) electricity production by sources (A.17b) GWh produced during the period January 2018 - April 2020. Source [39]	178
A.18	Canada data: (A.18a) electricity production by sources (A.18b) GWh produced during the period January 2018 - April 2020. Source [39]	179
A.19	Russia data available. Total energy supply by source in kilotonne of oil equivalent (ktoe), 1 toe = 11.63 MWh. Source from IEA (International Energy Agency) https://www.iea.org/countries/russia	179
A.20	How terrain modifications affect the wind speed profiles experienced by wind turbine, image from [44]	181
A.21	Black paint on a wind turbine blade, image from [63]	182

D.1	Comparison between the predictions from the models developed in this thesis and the ones from the original model [2] for Case 2 in Table (4.14)	215
D.2	Comparison between the predictions from the models developed in this thesis and the ones from the original model [2] for Case 3 in Table (4.14)	216
D.3	Comparison between the predictions from the models developed in this thesis and the ones from the original model [2] for Case 4 in Table (4.14)	216
D.4	Evolution of the maximum deficit value (top) and the mean velocity value (bottom) according to [3] for $AR = 2$ (left), $AR = 1$ (centre) and $AR = 0.25$ (right) for different wake models compared with literature data	217
D.5	Profiles of mean streamwise velocity deficit along crossflow direction at mid-span (top) and spanwise direction at wake's centre (bottom) for different downstream sections in different Re condition	218
D.6	Profiles of mean streamwise velocity deficit along crossflow direction at mid-span (top) and spanwise direction at wake's centre (bottom) for different downstream sections in different turbulent conditions	219

List of Tables

2.1	Summary and comparison of existing wake models for HAWT	39
2.2	Summary and comparison of existing wake models for VAWT	43
2.3	Comparison between turbulence methods	45
3.1	Coefficients used for the $k - \epsilon$ model in the current study	52
3.2	Tolerance values used during the calculations	55
3.3	Algorithm options used during the calculations	57
3.4	Coefficients for the Leishman-Beddoes models provided by [21]	66
3.5	Summary of the equations used for each method analysed	67
3.6	Values of the wake decay constant for the Jensen model	74
4.1	Cases analysed for the validation of numerical simulations	83
4.2	Properties of the small scale wind turbine	84
4.3	Values used for the dynamic stall model SH/SG for the small scale turbine	85
4.4	Properties of the turbine for the medium Reynolds' number case	86
4.5	Values used for the dynamic stall model SH/SG for the medium scale case	86
4.6	Properties of the large scale wind turbine	87
4.7	Values used for the dynamic stall model SH/SG for the large scale case	88
4.8	Description of the control volume for the numerical simulations	89
4.9	Details related to the meshes used	92
4.10	Description of the turbulent boundary conditions for medium Reynolds case	93
4.11	Validation cases field measurements data	95
4.12	Growth parameters for the NOJ model depending on the case	95
4.13	Growth parameters for the BPA-Niayifar model depending on the turbulence intensity	95
4.14	Description of the parameters used for code debug	96
4.15	Parameters used in the comparison with Abkar & Dabiri [3]	97
4.16	Parameters used in the comparison with Shamsoddin et al. [97]	97
4.17	New values for the thrust coefficients without considering tower and struts	98
4.18	Parameters used in the mesh sensitivity analysis for each numerical simulation	103
C.1	Format style for the literature data	208
C.2	Format style for input parameters	209

Nomenclature

Parameters

x	Streamwise coordinate [m]	C_T	Thrust coefficient [-]
y	Crossflow coordinate [m]	C_P	Power coefficient [-]
z	Spanwise coordinate [m]	a, a'	Induction factor [-]
V	Velocity [$\frac{m}{s}$]	TSR, λ	Tip-Speed-Ratio [-]
V_t	Velocity tangent to the blades [$\frac{m}{s}$]	σ	Solidity [-]
V_n	Velocity normal to the blades [$\frac{m}{s}$]	D_w	Wake's crossflow dimension [m]
V_{rel}	Velocity relative to the blades [$\frac{m}{s}$]	H_w	Wake's spanwise dimension [m]
V_{loc}	Local velocity [$\frac{m}{s}$]	A_w	Wake's area [m^2]
V_∞	Freestream velocity [$\frac{m}{s}$]	r	Wake radius at a generic x , radial coordinate [m]
V_h	Velocity at hub height [$\frac{m}{s}$]	r_0	Starting wake radius (NOJ) x [m]
V_a	Velocity behind the rotor [$\frac{m}{s}$]	x_a	Onset point location [m]
ΔV	Velocity deficit [$\frac{m}{s}$]	k	Turbulent kinetic energy [$\frac{m^2}{s^2}$]
$u = V_x$	Streamwise velocity component [$\frac{m}{s}$]	ϵ	Dissipation rate [$\frac{m^2}{s^3}$]
$v = V_y$	Crossflow velocity component [$\frac{m}{s}$]	ω	Specific dissipation rate [$\frac{1}{s}$]
$w = V_z$	Spanwise velocity component [$\frac{m}{s}$]	L	Turbulence reference length [m]
p	Pressure [$\frac{kg}{ms^2}$]	l	Mixing length [m]
Ω	Angular velocity [$\frac{deg}{s}$] or [$\frac{rad}{s}$]	μ	Dynamic viscosity [$\frac{kg}{ms}$]
Re	Reynolds' number [-]	ν	Kinematic viscosity [$\frac{m^2}{s}$]
Re_c	Re based on chord [-]	ρ	Air density [$\frac{kg}{m^3}$]
Re_D	Re based on diameter [-]	k^*, k_w	Wake decay constant [-]
D	Turbine's diameter [m]	ϵ	Wake starting dimension (BPA) [m]
H	Blade height [m]	σ	Standard deviation (BPA) [m]
z_h	Hub height [m]	μ_T, ν_T	Turbulent viscosity [-]
A_p	Turbine's frontal area [m^2]	I	Local turbulence intensity [-]
A_a	Area behind the rotor [m^2]	I_+	Added turbulence intensity [-]
c	Blade chord [m]	I_∞	Freestream turbulence intensity [-]
B	Blades number [-]	α	Angle of attack [deg] or [rad]
AR	Aspect ratio [-]		

θ	Azimuthal angle [<i>deg</i>] or [<i>rad</i>]	N_z	Number of elements along z [m]
θ_p	Pitching angle [<i>deg</i>] or [<i>rad</i>]	x_0	Outer cells base dimension [m]
f_i	Source term in equations [$kg \frac{m}{s}$]	f_n, f'_n	Separation point and separation point delayed [-]
C_L	Lift coefficient [-]	T_p	Time constant, delayed pressure response [-]
C_D	Drag coefficient [-]	T_f	Time constant, separation point delay [-]
C_{D_0}	Drag coefficient at $\alpha = 0$ [-]	T_v	Time constant, vortex shedding decay [-]
C_N	Normal force coefficient [-]	T_1	Time constant, vortex passage [-]
C_T	Tangential force coefficient [-]	T_α	Time constant, related to stall onset [s]
Δt	Time step [s]	τ	Temporal scale for vortex shedding [-]
Δx	Cell dimension [m]	r	Reduced pitch rate (dynamic stall) [-]
η	Kernel function [-]	B	Vortex shedding non-dimensional constant [-]
Δz	Blade element extension [m]	η	Tangential force efficiency factor (dynamic stall) [-]
Vol	Cell volume [m^3]	E_0	Constant for tangential force coefficient [-]
L_x	Domain dimension along x [m]	α_{dso}	Constant critical stall-onset angle of attack [<i>deg</i>] or [<i>rad</i>]
L_y	Domain dimension along y [m]	$\frac{r}{r_{\frac{1}{2}}}$	Half width of the wake [m]
L_z	Domain dimension along z [m]		
N_x	Number of elements along x [m]		
N_y	Number of elements along y [m]		

Abbreviations

ABL	Atmospheric Boundary Layer	URANS	Unsteady Reynolds-Averaged-Navier-Stokes
VAWT	Vertical Axis Wind turbine	LES	Large Eddy Simulations
HAWT	Horizontal Axis Wind turbine	CVP	Counter Rotating Vortex Pair
BPA	Bastankhah & Porté-Agel	AL	Actuator line
NOJ	N.O. Jensen model	AS	Actuator surface
BPA-N	BPA model with Niayifar's law	TKE	Turbulent kinetic energy
NOJ-N	NOJ model with Niayifar's law		

1

Introduction

1.1. Context analysis and problem statement

During the last decades climate change, pollution and greenhouse effect have acquired a huge relevance in modern society. The indiscriminate exploitation of natural resources, especially fossil fuels, with no regard for Earth's health has lead to a pivotal situation: will mankind be able to overcome this desperate status quo? Ice melting, rising of sea levels, extreme and violent weather events as well as ocean's pollution (and so on) have shed light on the consequences of human activities, encouraging common people as well as entire nations to take into action to save the planet as long as it is still possible. Scientists and researchers have also demonstrated that the more time passes, the more damages related to climate change increase. So it is extremely important to start facing the problem as soon as possible.

One of the most important part of this struggle lies in overthrowing fossil fuels from their top position as energy sources, in order to promote renewable approaches based on nuclear, solar or wind energy. Many of these alternatives have been took in consideration only when financial or economic crisis arose during the last century (after Yom Kippur war or Lehman Brothers bankrupt, for example). As soon as the periodic crisis had ceased, renewable energy sources were put aside and forgotten until the following crisis. For this reason, the major part of studies, tests and researches about such solutions have been conducted only during the recent years.

Focusing on wind energy, its exploitation is one of the oldest solution conceived by mankind. There are proofs that even Persians in 900 AD used a drag-driven windmill to pump water and grind grain. The reader is referred to Appendix (A) to learn more about the history of these beautiful machines and the context in which they are used today. Wind is among the most used renewable energies all over the world and, on account of that, huge amount of studies about wind turbines are conducted in order to improve their efficiency and decrease the cost of the electricity which they provide. As long as the cost decreases, more and more people will be interested in adopting wind turbines instead of traditional sources of energy (natural gasses, fossil fuels, coal and so on) that harm the planet.

In such context lies this thesis and its purpose of helping the scientific community in understanding wind turbines by improving the knowledge at disposal. In fact even if the most common wind turbines that feature a horizontal axis of rotation (for this reason called HAWT - horizontal axis wind turbines) have reached a 'plateau status', vertical axis wind turbine (VAWT) still not. Technology level for HAWT has reached a full mature condition: there are no more substantial improvements that can be done to increase their performance and the most obvious solution, the increase of the swept area, leads to logistic problems as well as expensive production processes. VAWTs instead have always been ignored along the years, in the belief that they show poor performances compared to HAWTs. However this is not true and they show many advantages (as will be discussed in detail in Chapter (2)) as well as the potential to be more efficient than HAWTs especially when wind farm are considered. In fact, turbines' rotors generate wakes which alter the inflow of downstream turbines, decreasing their performances and power extraction (associated losses usually range from 5% up to 20% [9]). Therefore turbines' location is a critical part of layout optimization during the design process. Moreover, the increased turbulence level due to the upwind turbines leads to fatigue loading of downstream rotors and decreases turbine's lifetime. On account of that, it is essential to understand wakes,

predict their directions and how they affect wind farms layout and how they depend on turbines geometrical and mechanical features. Here lies one of the advantages of VAWTs: thanks to their properties, they can be placed closely together compared to HAWTs, increasing the amount of power extracted for surface unit. However, even for VAWTs, it is necessary to pay close attention when studying the correct layout for a wind farm to maximize the power extracted from the wind. This is not an easy task since a totally accurate investigation would be unrealistic to be accomplished, because of the experimental limitations due to the size of the elements involved and the complexity of the phenomena: in real life wind farm layout can be analysed only once the entire farm is built, while wind tunnel experiments can be extremely complex if several turbines are considered (unless simplified model are used). Therefore the numerical approach is essential in modern days, especially in preliminary design steps, since computational capacity constantly rises with time thanks to higher and higher performance CPUs produced. However even the numerical approach can lead to major problems: dealing with several turbines (whose dimensions can be significant) implies using meshes with huge amount of cells (millions over millions). Moreover the aerodynamics of VAWTs is extremely complex and turbulent, with vortical structures generated by rotor's presence spacing from small to large scales. A totally accurate simulation should solve every structure at each scale: this means that the smallest cell has a dimension similar to smallest eddies. It is obvious to draw an important conclusion: direct numerical simulations for VAWTs field flow are not feasible, especially when an entire wind farm is considered. Therefore it is necessary to simplify the study, where possible, in order to elaborate sufficiently accurate predictions that allows to define the optimum location of each turbine in a wind farm. Possible solutions are LES (Large Eddy Simulations) or RANS (Reynolds Averaged Navier Stokes) equations as well as many other simplified models that will be analysed in detailed. Special attention must be given towards analytical wake models which represent the core of this thesis.

1.2. Research objective and research questions

The objective of this research is to test, verify and analyse the performance demonstrated by existing analytical wake models for VAWTs.

The main research objective can be summarized as: a detailed study and analysis of existing analytical wake models for vertical axis wind turbine with the purpose of exploring their accuracy, validity and limitations. The main objective is supported by the following side-objectives:

- **Sub-objective (a):** comparing the analytical wake models against literature data to assess their validity and performance. Investigating the influence of thrust coefficient and aspect ratio variations on models accuracy.
- **Sub-objective (b):** comparing the analytical wake models against numerical simulation data, covering Reynolds numbers from $\approx 10^5$ up to $\approx 10^7$. Investigating wake models performances and validity at different scales and ambient turbulent conditions.
- **Sub-objective (c):** studying the Reynolds effect on wake shape and velocity deficit evolution by means of numerical simulations.
- **Sub-objective (d):** qualitatively analysing ambient turbulence effect on wake recovery process

This thesis research is driven by the following research questions:

1. How is characterized the aerodynamics of a VAWTs and how does its wake develop?
 - **(a)** How is the velocity deficit affected when variation in AR and C_T are experienced?
 - **(b)** How does ambient turbulence intensity affect the wake recovery and wake's width evolution?
 - **(c)** What are the consequences of deflection on wake structure?
2. How to model the wake of a turbine keeping a low computational cost?
 - **(b)** How do wake models replicate the wake evolution and recovery for both HAWTs and VAWTs?
 - **(a)** What are the basis and the starting equations of analytical wake models for HAWTs and VAWTs?
 - **(c)** How is the accuracy of wake models influenced by the simplifications adopted?

3. How does scale and turbulent ambient intensity affect the wake evolution?
 - (a) What are the common properties observed in VAWT wakes at different Reynolds number and different scales?
 - (b) Does VAWT wake display any kind of similarity when considering different Reynolds' number?
 - (c) What are the consequences of different turbulence intensity on wake's structure and recovery?
 - (d) What is the correlation between Reynolds' number and turbulence intensity when recovery is considered?
4. Which is the range of validity of analytical wake models for VAWT?
 - (a) How do thrust coefficient and aspect ratio variations affect wake models accuracy?
 - (b) How are predictions from wake models affected by turbulence intensities ranging from low to high values?
 - (c) Can wake models replicate the recovery process correctly?
 - (d) What level of accuracy do wake models display when different scales are considered?

1.3. Methodology

In order to answer the research questions and pursue thesis objective, a series of numerical studies and comparison between literature data and results from URANS simulations supported by actuator line technique have been carried out. The latter is a simplified model which will be described afterwards and it was validated against literature and experimental data. This way has been possible to better understand how analytical wake models for VAWTs behave and which are their advantages as well as their weak points, in order to suggest possible improvements. The tests have been conducted using different parameters and scales, the latter range from small wind turbines ($D = 0.3m$), to medium wind turbines ($D = 1m$) up to utility scale wind turbines ($D = 50m$). Therefore the effect of Reynolds' number as well as scaling properties in the wake were analysed. This is a relevant target, since it could aid in understanding VAWT's aerodynamic and if the particular flow field at different scales persists with the same features. With the aim of qualitatively understanding turbulence's effect on wake evolution, a series of comparisons between flow field generated in different turbulence conditions were carried out. This aspect of the study was functional to realize the implications of wake decay constant in analytical models and so of ambient turbulence intensity. Guidelines for answering the research questions are the following ones:

1. To characterize the aerodynamics of a VAWTs:
 - (a) Analysing previous researches in the literature. Focusing on wake aspects
 - (b) Studying the effect of different parameters on wake structure
 - (c) Review of what are the most relevant aspects in the wake and its evolution
2. To model the wake with a low computational cost:
 - (a) Studying previously developed models both for HAWTs and VAWTs, learning about the state-of the art, the possible alternatives and other solutions.
 - (b) Testing existing wake models for HAWTs, observing their structure, implementation and results as well as their limitations.
 - (c) Analysing the existing wake decay constant laws, evaluating their limitations and their assumptions like the self-similarity.
 - (d) Implementing existing wake models for VAWTs, validating the code structure and relevant assumptions.
3. To provide higher fidelity data as a comparison and validation for VAWTs:
 - (a) Analysing, studying about the actuator line model supported by URANS equations. Learning about its limitation and implementation.

- (b) Testing different cases ranging from small to large scale, with different turbulence intensities.
 - (c) Validating the model by comparison against experimental and literature data.
 - (d) Testing numerical set up sensitivity to mesh size.
4. To evaluate Reynolds' number and ambient turbulence intensity effect on wake structure:
- (a) Testing different Reynolds' number case by considering different scale turbines.
 - (b) Comparing the results obtained at different scales to search for wake similarity properties.
 - (c) Testing turbines in different turbulence intensity conditions, including no-turbulence cases (laminar).
 - (d) Comparing the results in different turbulence conditions, evaluating consequences on wake structure and wake recovery.
5. To investigate validity of wake models:
- (a) Comparing the predictions against data from numerical simulations, covering cases from small to large scale turbines and from low to high turbulence intensity.
 - (b) Analysing wake models validity and accuracy when considering different scales and turbulence conditions.
 - (c) Analysing wake decay constant performance and limitations when considering low turbulence cases.
 - (d) Comparing the predictions against literature data, testing the influence of thrust coefficient and aspect ratio on wake models.
 - (b) Analysing wake models validity and accuracy when considering different thrust coefficients and aspect ratios.

1.4. Thesis outline

In this section a brief description of each chapter of the thesis is reported. The purpose is to provide an outlook and a concise overview of the work to figure out how the thesis is structured and which are the core parts. For more details, the reader is referred to the specific chapters.

- **Chapter 1, Introduction:** Introduces the global context of the climate crisis, the role of wind energy and VAWTs in this fight and the motivation for the research. The targets and objective are identified and supported by the research questions, the methodology and the thesis outline.
- **Chapter 2, Literature study:** Review of the literature with the purpose of acquiring the relevant background needed to decide the approach to the research and which are the gaps that still needs to be investigated and studied.
 - Detailed analysis and characterization of VAWTs aerodynamics at different scales, with focus on wake scale.
 - Analysis of methods for turbine modelling for both HAWTs and VAWTs. Focus on actuator methods and the actuator line.
 - Study and analysis of approaches to model the wake behaviour for HAWTs and VAWTs. Close attention was given towards analytical wake models for both the type of turbines, since they are thesis' core, with a related deep and detailed review.
- **Chapter 3, Methods:** Analysis of tools and approaches used to study the problem. Introduction of some of the main obstacles and limitations observed.
 - Introduction of the URANS equations, their implementation and how they are solved. Focus on the turbulence models, their differences and why $k - \epsilon$ was selected.
 - Derivation of the actuator line model for VAWTs supported by the description of dynamic stall model and how it is implemented. Interaction of the model with URANS equations in the flow solving operations.

- Description of sub-models for actuator line theory and their implementation.
- Derivation and deep analysis of wake models for both HAWTs and VAWT. Introduction of the expressions for the velocity deficit and the wake decay constant problem, how they were faced in the thesis and which equations were used.
- **Chapter 4, Validation:** Validation of the numerical and analytical tools at different scales and conditions, according to literature and high fidelity data.
 - Analysis of the benchmark cases used for the validation process for both numerical simulations and analytical models.
 - Validation of the numerical set up based on URANS and actuator line theory at different scales.
 - Testing of mesh sensitivity at each scale.
 - Validation of the analytical wake models for HAWTs based on the py-wake library.
 - Validation of the self-similarity hypothesis for VAWT wake using literature data.
 - Debugging procedure and code validation for VAWTs wake models.
- **Chapter 5, Reynolds' number effect analysis:**
 - Running numerical simulations based on actuator line and URANS set up with different Reynolds' number by considering different scales wind turbines.
 - Evaluating wake similarities and possible Reynolds' effect at different scales.
- **Chapter 6, Ambient turbulence effect analysis:**
 - Running numerical simulations based on actuator line and URANS set up with different ambient turbulence intensity levels and considering no-turbulence cases.
 - Evaluating effect on wake recovery and its development as well as wake's shape.
- **Chapter 7, Analytical wake models performance and validity study:** Presentation of the results and discussion of wake models accuracy and validity range. Analysis of wake properties in different conditions.
 - Comparison of wake models results against numerical simulations data at different scales and different turbulence intensities.
 - Comparison of wake models predictions against literature data featuring different thrust coefficients and aspect ratios.
 - Evaluating wake models performances and validity when operating in previous conditions, with particular attention on the limitations and how they can be overcome.
 - Evaluating wake decay constant laws accuracy, limitations and when they provide reliable results.
- **Chapter 8, Conclusions:** Reports conclusions and reflections on the work. It sums up the results, analysing them compared to the research target motivation, proposing where necessary a prospect for future studies, highlighting possible research gaps.
- **Appendix A:** Historical overview, discussion and presentation of wind turbines throughout the centuries. Detailed description of the global context, how different nations deals with wind energy and why wind turbines are among the most used sources of renewable energy.
- **Appendix B:** Detailed description and derivation of models for turbine and wake modelling for both HAWTs and VAWTs. The models presented here are the same of Chapter (2) but discussed in depth.
- **Appendix C:** Analysis, description and presentation of the Python code scripts used for wake models development to perform the calculations as well as the ones used in the validation procedure.
- **Appendix D:** Appendix that provides additional but less relevant results, especially images.

2

Literature study

2.1. Introduction to VAWTs

Vertical axis wind turbines are among mankind's most ancient creations [59] (see Appendix (A) for more details). They feature a vertical rotational axis and extract energy from the wind by converting its kinetic energy into electricity and reducing its momentum. In order to do so an alternating current induction generator is present. The surface swept by the blades is a cylinder (unlike HAWTs that can be modelled as 2D discs) and they can display various and different shapes. Here some details and some images regarding the most famous existing VAWTs and their features.

- The Magdalen Island turbine was one of the first turbines installed during the oil crisis in 1977.
- The Éole turbine is the largest VAWT ever constructed, with a power output of 3.8 MW and an height of 110 m. However, because of vibration problems experienced the rotational speed was limited to extract an output of 2 MW [91]. A representation of this turbine is reported in Figure (2.1).
- The Sandia 34m turbine is the most tested and studied design because of its C_p which is the highest among VAWTs.
- The Anew-B1 turbine is the second largest turbine if we consider both the area and the power output (1.5 MW). It is shown in Figure (2.2).

More details about the development and the state of the art of VAWTs can be found in [70].

2.1.1. VAWTs classification

Two main types of VAWTs exist:

- Savonius rotor: it is a drag-driven turbine whose blades are more similar to rounded paddles creating an S-shaped surface with high solidity. It uses the action and reaction of the stream to operate [59]. Even if it shows good self-starting properties and high power output at reduced wind speed, the efficiency is extremely poor. However at the same time Savonius rotors are extremely reliable and easy to maintain. Most of the times this concept is used for small, simple wind rotors with the task of driving pumps or mechanical equipment that request high torque at small rotation speeds.
- Darrieus rotor: it is a lift-driven turbine, more similar to common HAWTs. Blades are similar to airfoils and can show different shapes, ranging from classic H-rotors (or giromills) to Φ -shaped rotors. In every possible case they all exploit lift force component to generate torque. Blades can be connected to the tower/shaft with horizontal and vertical struts when considering H-rotor turbines, with a certain amount of parasitic drag, decreasing the overall efficiency. Moreover an increased bending moment is experienced. At the same time the swept area increases, the blades can be constructed easily and the base tower can be higher (more intense winds). With Φ shaped blades instead the performance decreases, when considering elements near the rotational axis, as well as the swept area. Such elements



Figure 2.1: Éole turbine [17]



Figure 2.2: Anew-B1 turbine [50]

can be connected too with horizontal struts. Darrieus configuration is the most common design used for VAWTs especially because of its higher performances. It presents some disadvantages, since it lacks self-starting capability at low wind speed values. To overcome this problem a small Savonius rotors is added to the tower structures to provide high startup performance.

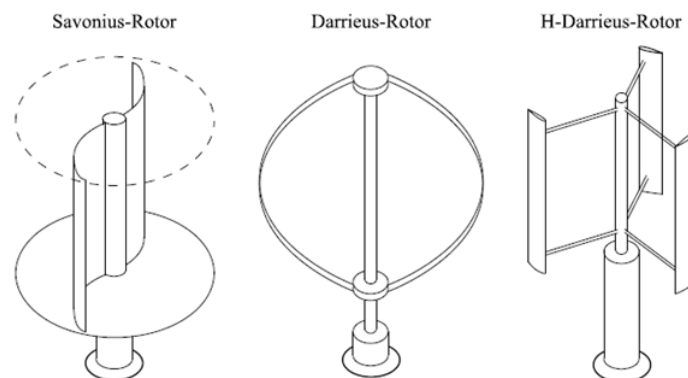


Figure 2.3: Different types of VAWTs, image from [91]

Additional details regarding the existing versions of Savonius and Darrieus rotors can be found in [70].

2.1.2. Comparison with HAWTs

VAWTs clearly show many advantages compared to HAWTs:

- They exhibit higher power densities compared to HAWTs because of their faster wake recovery and especially the possibility of increasing the swept area maintaining a reduced footprint at the same time.
- They have a lower center of gravity that allows to complete all the maintenance operations at ground level, avoiding risks and simplifying components substitution when necessary: all the heavy components can be placed near the ground, largely decreasing maintenance and installation costs that represent a huge part of the total cost. Therefore VAWTs show an economic advantage.
- Their blades can be realised easily as different sections attached to the main tower, lowering the installation and production costs.
- They are omnidirectional and do not require a yaw control mechanism because freestream velocity is always perpendicular to the rotational axis. Even this means lower costs since VAWTs do not require expensive yaw-control mechanism and can operate with the same efficiency with winds from any possible direction and in regions where rapid variations of it are experienced.

VAWTs' aerodynamics is definitely more complex than HAWTs', discouraging from adopting this solution. Furthermore, global interest unfortunately has always been focused on HAWTs in the belief that they're more efficient. This delayed the development of VAWTs for years. Field tests and modern calculations have disproved this wrong belief provided by wind tunnels experiments. At the same time HAWTs' knowledge and exploitation has reached a plateau status: the level of technology and development shows limited margins of improvements. On account of that renewed interested about VAWTs has grown during the last decade in order to better understand their features and increase the related knowledge. Another important aspect that has revitalized this concept are the remarkable performances showed in urban environment, where intense turbulence is experienced. This holds huge relevance in actual society where more and more interest in reducing pollution and global warming phenomena is growing up. VAWTs perform better than HAWTs in such conditions, especially when considering small scale and micro wind turbines (see Appendix (A)) for more details. Moreover wind farms based on VAWT show a smaller footprint because single turbines can be placed closer one another, achieving a higher power density, as mentioned before.

In fact modern wind farms with HAWTs need a relevant amount of space to separate wind turbines from near ones and avoid interferences due to harmful interactions with wakes of other turbines. Therefore power

density (power for unit of surface) decreases. Moreover, the inefficiency of the power plant has to be compensated by taller wind turbines, this way it is possible to reach higher altitudes and more intense wind. However, this leads to some additional problems, firstly the costs, but also greater visual, acoustic, radar and environmental impact. VAWTs' swept area instead can increase irrespectively of their footprints (it grows vertically) and they can potentially achieve higher power densities than the traditional horizontal-axis wind turbines. In fact, while wind farms made up of HAWTs produce 2 or 3 watts of power per square meter of land area, a farm composed by VAWTs can reach an order of magnitude greater, if the layout is correctly set up [19]. So using a larger number of VAWTs over a fixed area enables to capture a greater portion of wind energy than what could be extract with a group of HAWTs. Moreover, there is no need of using taller and taller wind turbines and is possible to reduce the complexity and cost of each one of them. A study by Dabiri [19] demonstrated that using near counter-rotating VAWTs leads to an improvement of the energy extracted (up to 11% [94]) and a decrease in the recovery length necessary (recovers to 95% of the freestream value within 6D [49]). This is possible because of constructive aerodynamic interactions that occur between adjacent turbines. VAWTs work at lower tip speed ratios (respect to HAWTs) that means also lower rotational velocity or, in other words, lower noise produced and lower environmental impact on ecological systems (like birds, see Appendix (A)) but, at the same time, lower C_p reached [42].

In order to propose a fair overview of VAWTs to the reader, it is necessary to point out some of their major disadvantages, for sake's of knowledge [32, 44]:

- They tend to stall under gusty wind condition.
- The torque generated is not steady and therefore the load driven by the turbine experiences fluctuations in power input and, consequently, in power output.
- Studies focused on dynamic analysis of VAWTs are extremely difficult because of the variability of inflow conditions experienced by the blades.
- The flow field generated by VAWTs is extremely complex and it is difficult to fully analyse and understand it.
- Lower power coefficients compared to HAWTs.
- Blades operate in the wake during their revolution experiencing load fluctuations and leading to fatigue problems and earlier failures.
- Production costs are too expensive at present days: since vertical-axis rotors rotate at a slower speed and they experience higher torques to obtain high power, they feature higher weights and their production costs are correspondingly higher.

A comparison of the power coefficient C_p achievable with HAWTs and VAWTs is reported as function of the tip speed ratio in Figure (2.4): the differences between the values are not so big as it commonly believed. Moreover, because of structural and economic considerations, large VAWTs cannot be easily designed and built. This is a weak point in the match against high-power HAWTs and a major limitation. However, considering offshore turbines, there is no need for turbines to operate at elevated heights and (as stated before) they can be placed closer together when considering wind farms.

2.1.3. Working principles and relevant parameters

As mentioned before, a VAWT is able to convert kinetic energy from the wind to electric power. In order to do so, it extracts momentum from the wind, enabling the blades to generate a certain amount of torque that makes the whole turbine rotate. The tower (or shaft) is connected to a gearbox and an electric generator that produces electricity while rotating. The latter is then distributed along the line (directly to the loads) or stored in batteries, as reported in Figure (2.5).

The turbine's rotor is identified by its radius R or its diameter D and its number of blades B . The latter are characterized by the chord length c and their length H and rotate according to the rotational velocity Ω . The velocity seen by the blades (relative velocity), as displayed in Figure (2.6), is the sum of the tangential rotational velocity, the inflow velocity and the induced velocity which is due to turbine's presence. The size of the induced velocity changes during the rotation and depends on the thrust coefficient and on how the

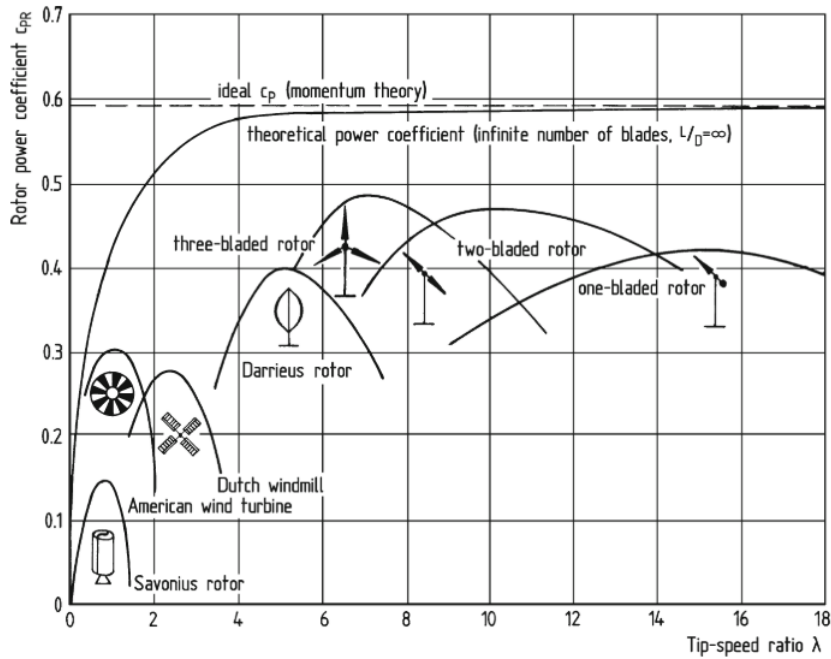


Figure 2.4: Comparison of the power coefficients for different turbines, image from [32]

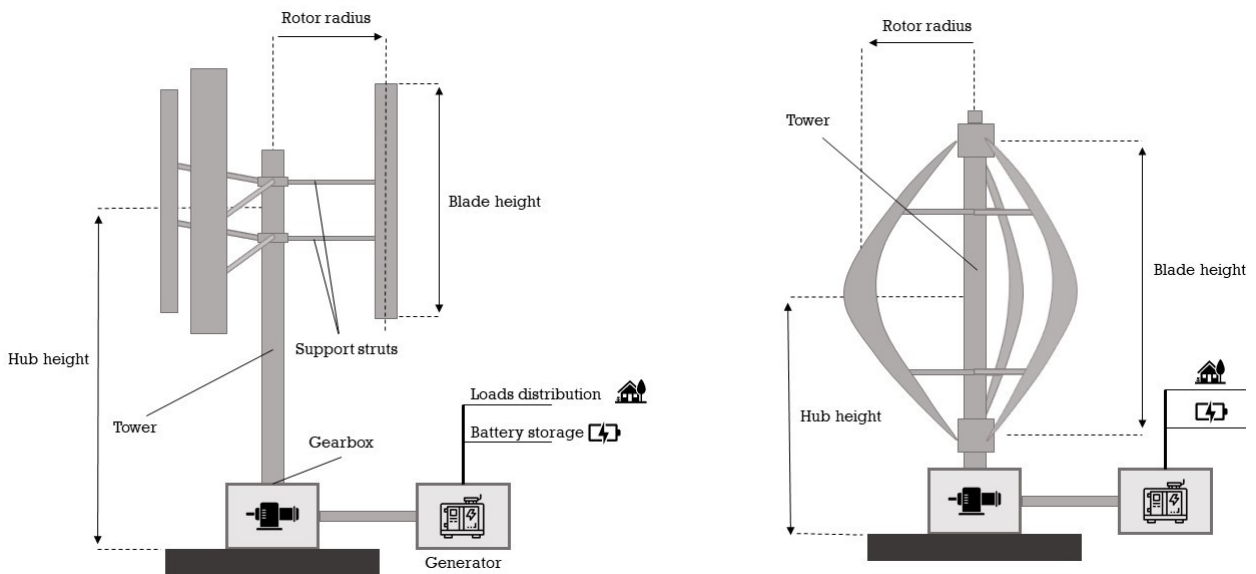


Figure 2.5: Main components of a H-VAWT (left) and a Phi-shaped (or troposkien) VAWT (right)

forces are distributed along the blades. For this reason both the angle of attack as well as the relative velocity change during the revolution.

This implies that each section cannot operate in optimal (design) conditions over the whole cycle: one of the reason why VAWTs are still considered inferior to HAWTs.

The relative velocity shows a certain angle respect to blades' chord-line. Such angle is the angle of attack α and can be related to the velocity components using the pitch angle θ_p (the angle between the airfoil chord-line and the tangent to rotating path).

$$\alpha = \tan^{-1}\left(\frac{V_n}{V_t}\right) - \theta_p \tag{2.1}$$

The azimuth angle θ is the angle between the crossflow direction and blades' location. Such angle is used

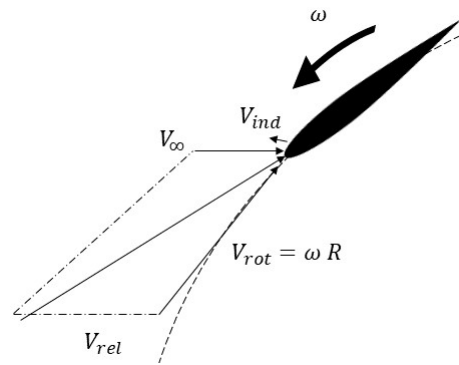


Figure 2.6: Schematic of velocity triangles in VAWTs

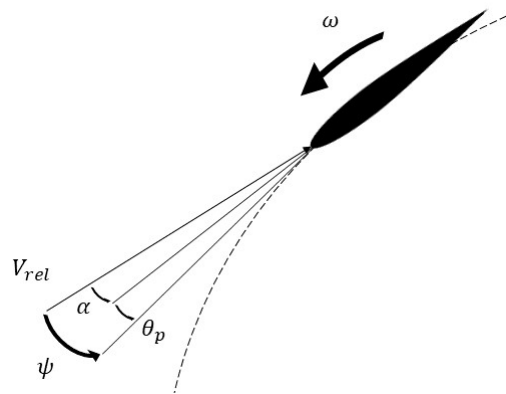
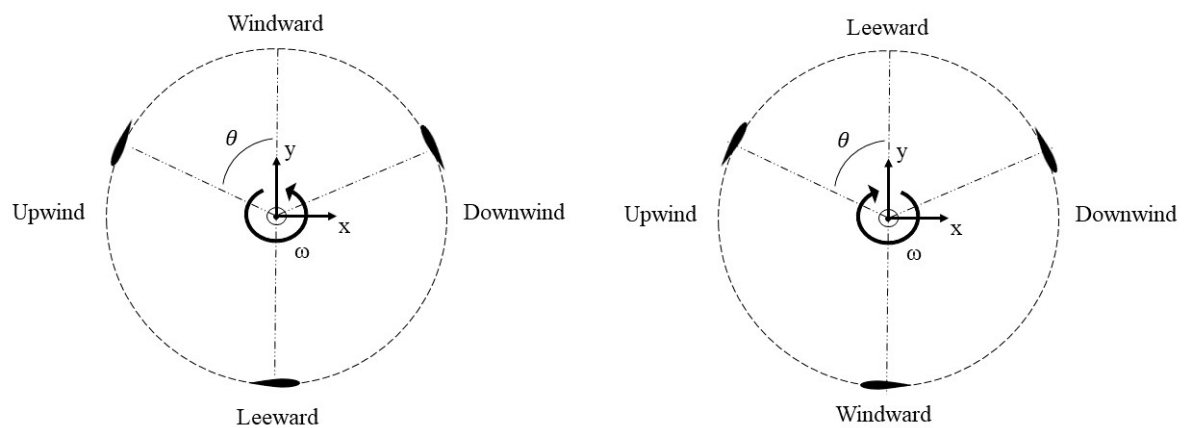


Figure 2.7: Schematic of the angles used when discussing VAWTs

to split the volume around the turbine in four main regions:

1. Upwind region, the first half of the circle described by the blades in the horizontal plane
2. Downwind region, the second half of the circle described by the blades in the horizontal plane
3. Leeward region, located on one side, here blades' rotational velocity and inflow velocity show the same direction
4. Windward region, located on one side, here blades' rotational velocity and inflow velocity show opposite direction

Figure 2.8: Denomination of the flow regions when a positive (left) and negative (right) rotational velocity Ω is observed

The range of the azimuth angle over the four regions depends on the convention used. In Figure (2.8) is reported the convention used in the current work.

The last angle to be considered is the inflow angle ψ , which is the angle between the airfoil chord-line and the tangent of the rotational path. Such angle is the sum of the pitch angle and the angle of attack.

The angle of attack changes during the revolution, achieving positive values during the upwind part of the revolution and negative in the downwind part. Similarly the velocity of the flow relative to the blades is highest at the leeward side, where rotational velocity and inflow velocity have the same direction while is lowest at the windward side for the opposite reason. Considering the forces, instead, the normal component per unit span changes during the cycle with positive values in the upwind region and negative ones in downwind region while the maximum is observed at the most upwind position. The tangential component instead aims towards rotational direction during the largest part of the cycle.

Many dimensional and non-dimensional parameters are used when describing VAWTs. It is essential to introduce them since they will be mentioned constantly in the thesis:

1. Diameter and height (D and H): the geometrical properties of the turbine, the first one describes blades' distance from the axis of rotation while the second one their elongation.
2. Thrust coefficient (C_T): non-dimensional parameter that expresses the force exerted on the turbine along streamwise direction. It is the sum of the forces experienced by the blades, the struts and the tower.

$$C_T = \frac{T}{\frac{1}{2}\rho V_\infty^2 A_p} \quad (2.2)$$

Where A_p is the area projected by the turbine $A_p = DH$, T is the thrust, V_∞ the freestream velocity and ρ the air density.

3. Power coefficient (C_P): non-dimensional parameter which expresses the power extracted from the wind by the turbine. It can be related to the tip speed ratio as shown in Figure (2.4).

$$C_P = \frac{P}{\frac{1}{2}\rho V_\infty^3 A_p} \quad (2.3)$$

Where P is the power generated.

4. Tip speed ratio (TSR): it is the ratio between the tangential velocity of the blades $V_t = \Omega R$ and the inflow velocity V_∞ .

$$\lambda = \frac{\Omega R}{V_\infty} \quad (2.4)$$

Where R is turbine's radius and Ω its rotational speed.

5. Aspect ratio (AR): a parameter that expresses the geometrical properties of the turbine. It is the ratio between blade's length and turbine's diameter. compared to HAWTs this is a brand new parameter: HAWTs display the same elongation along each direction, while VAWTs extension changes along span-wise and crossflow direction.

$$AR = \frac{H}{D} \quad (2.5)$$

6. Rotor solidity (σ): it expresses the ratio between the amount of area of the blades and the total swept area of the rotor. In other words it expresses how much of the area occupied by the rotor is really covered by the blades.

$$\sigma = \frac{Bc}{D} \quad (2.6)$$

Where B is the number of blades and c their chord length.

2.2. Aerodynamics of VAWTs

Vertical axis wind turbines are characterized by unique features especially in terms of the aerodynamics flow that surrounds these structures. The related phenomena have been analysed differently according to their typical scale. A summary of them is reported in Figure (2.9). In order to accomplish this target, the literature (papers, researches and studies of different kinds accomplished through the years: numerical, experimental and theoretical ones) was essential. Thanks to these great sources of wisdom, it was possible to characterize the aerodynamic of a VAWT universally. Even if every following aspect is relevant, close attention has been given to wake scale analysis because of the objectives of this thesis. Therefore a more detailed analysis and review about this topic was carried out.

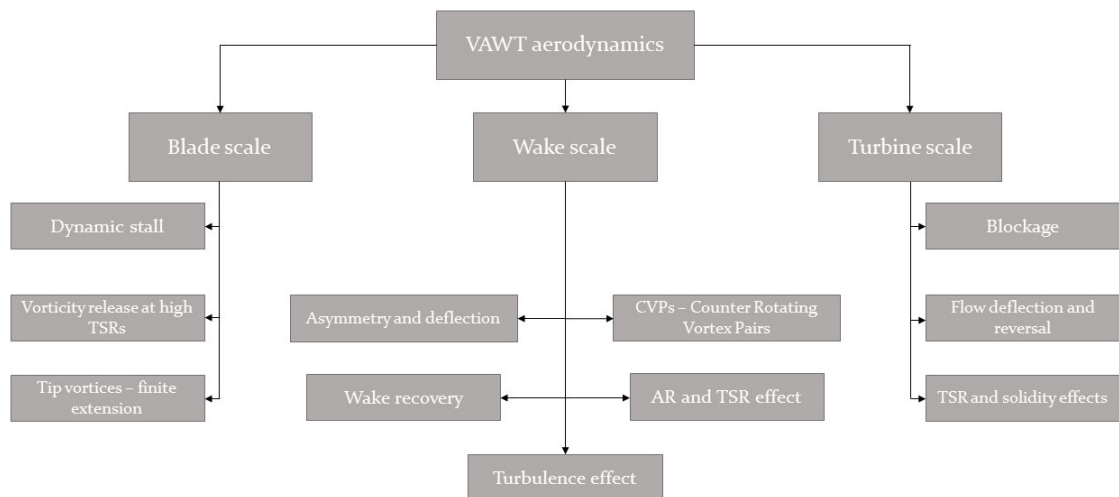


Figure 2.9: Brief recap of the main phenomena that characterize the different scales in VAWT's aerodynamics

2.2.1. Blade scale

2.2.1.1. Dynamic stall and rotational effects

Blades' aerodynamics in VAWTs are dominated by rotational effects and the consequent unsteadiness. In fact, during their revolution the blades experience a different incoming velocity which leads to periods of lifting or stalling, according to their azimuthal position. This periodical change in the relative velocity (sum of the blade rotational velocity and the local flow velocity, [34, 90]) means that blades experience a variation in the angles of attack while moving along the circular path: that's a triggering effect for the dynamic stall phenomenon. Dynamic stall is a periodical release of vorticity and vortical structures in the wake because of the blades. The structures generated move downstream according to an axial velocity, lower than free-stream velocity and related to it by a specific parameter (called β , function the solidity [24]).

Vorticity generated when the dynamic stall occurs is higher than what is seen in the static stall case and it is released from the leading edge especially because of boundary layer inversion. Once released, vortex structures travel downstream towards the trailing edge inducing a pressure wave on airfoil's surface (see [21]). Dynamic stall is commonly used as a passive method for power control in wind turbines but it leads to increased blade loads and larger oscillations, with consequent fatigue problems. Moreover, since it leads to the formation and shedding of large vortices that interact with the blades, an increased noise level is observed.

Dynamic stall is dominant in the near wake region at low TSRs but the phenomenon is not homogeneous along the whole rotation (see [86, 87, 110]):

- Retreating blades have huge relevance in the process, generating the largest and strongest structures, with highest coherence, capable of surviving far downstream than the other ones
- Advancing blades instead experience lower angles of attack, with smaller and weaker vortical structures shed

- Blades in downwind position experience a lower velocity than the free stream with a consequent increase in the effective TSR and a decrease in angles of attack. Structures generated here are weak and rapidly decay.

Because of incidence variation, separation points on the inner and outer surfaces of the blades move and a related pattern of vortical structures is generated. For the inner surface, separation mainly occurs during the upwind motion of the blades and, at low TSRs, for a wider portion of surface than what happens for higher TSRs. During the downwind motion instead, the flow is almost always attached to the blades. For the outer surface the stall is more severe during the downwind motion, and more intense for low TSRs (see [78, 86]). Considering with more attention blades' upwind motion, the vortical structures generated (which are the strongest) are shed by both the leading edges and the trailing edges of the blades according to the following sequence (see [119]):

1. The vortex created at the leading edge starts to roll up and grows during the first half of upwind motion. When it reaches a dimension similar to the chord length and when the blade starts moving towards the leeward region the vortex detaches from the blade (this happens almost after a revolution of 50° from the most upwind position) because of the growth of the trailing edge vortex.
2. After the trailing edge vortex stops growing, it is released in the wake before reaching the most leeward position
3. Both the trailing and leading edge vortices move downstream, interact each other and can potentially hit the blades (see [24]).

This process is affected by the Reynolds number: with higher values the separation is delayed, modifying the shedding frequency and the downstream transport. Consequently the blades-wake interaction and wake's vorticity distribution are modified (see [119]).

Dynamic stall phenomenon depends on TSR (as stated before) and displays relevance generally below $TSR < 4$ depending on the context (see [52]). With lower TSR, the blades experience a wider range of angles of attack (the relative velocity changes) generating shed vorticity regions larger than the ones generated under higher TSRs. Besides that, with lower TSRs blades tend to interact more with their own wakes than the ones generated by others as happens for higher TSRs (see [87]). When higher TSR values occur, blades frequency passage is higher, hence more structures are generated. In the latter case they tend to interact more with other blades' wake. This happens because the vortical structures generated are transported at a lower velocity relative to the blades (see [86]): different kind of interactions are observed depending on the differences between wake convection characteristic time and blade's rotation and so on vortices relative speed. Therefore, logically, TSR is a great watershed for the phenomenon which occurs (see [24]):

- For a single-bladed turbine (where interactions can only occur with blade's own wake):
 1. If $TSR > \beta$ interactions with previously generated wakes occur at the first half of the downwind passage.
 2. When the TSR is higher than $\frac{\beta\pi}{2}$ interactions occur with one wake at the downwind region.
 3. Interactions with two or more wake occurs along all the circular path when TSR is higher than $\frac{3\beta\pi}{2}$.
- For a n-bladed turbine:
 1. When TSR is lower than $\frac{\beta\pi}{2n}$, the blade interactions are limited to the left rear quadrant and occur with blades' own wake or the one intercepted by another blade.
 2. When TSR is lower than $\frac{\beta\pi}{2}$, the blade interacts with its own wake in the downwind region
 3. When TSR is lower than $\frac{5\beta\pi}{2n}$, the blade interacts with its own wake and the wake shed by another blade along the whole circular path
 4. When TSR is higher than $\frac{5\beta\pi}{2n}$, the blade interacts with the wakes generated by each foil along all the circular path

TSR has relevance also on the spanwise vorticity pattern along turbine's radius:

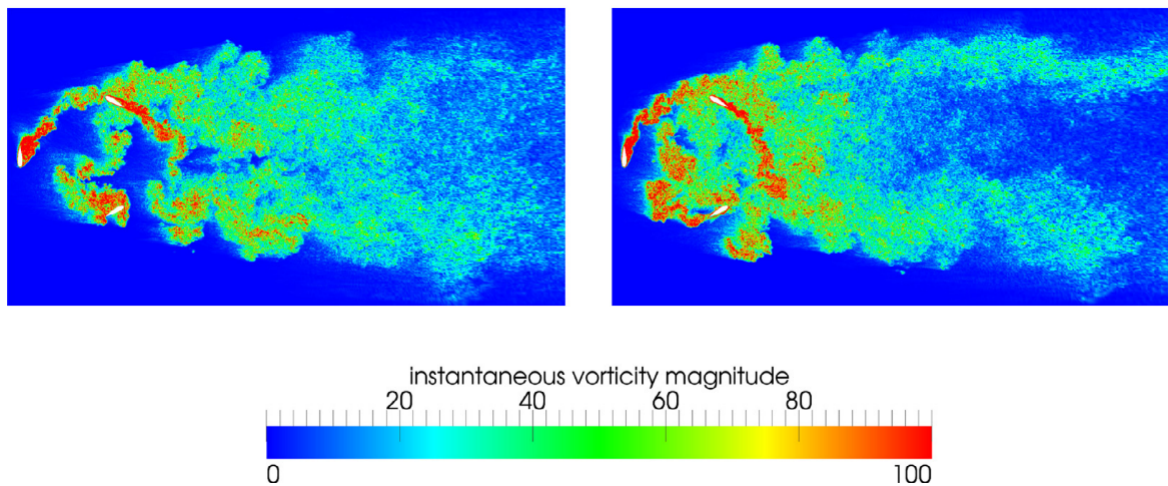


Figure 2.10: Normalized instantaneous vorticity magnitude from the study by Posa et al. [87]. The results have been obtained by a LES simulation for $TSR = 1.35$ (left) and $TSR=2.21$ (right)

- With higher TSRs: the highest values in vorticity magnitude are located at the edges of the turbine but featuring almost equal sharp peaks
- With lower TSRs: higher values are located at the edges, but with a lower magnitude and a more relevant asymmetry than previous case. At leeward side the local maximum is diffused, because of the released vortical structures, while at windward side is sharper. Moreover, high vorticity values are observed at the wake's centre.

In both cases peaks' decay when moving downstream is more intense at the edges than at the centre (see [86]).

Vortices shed by the blades when suffering dynamic stall are also responsible for peaks in wake's turbulence intensity. These peaks are higher when the environmental turbulence intensity increases, but at the same time the increase in peaks' value is less intense reaching a plateau status. Both wake's turbulence intensity as well as turbulent kinetic energy (TKE) are higher for the leeward region (strong asymmetric distribution which persist even downstream, [86]), where blades retreat and the dynamic stall has more relevance (where vortex shedding and blade-vortices interactions are experienced [62]), while it is lower for the windward region where the flow reattaches on the advancing blades (the difference in turbulence intensity peaks is approximately 15%, [68, 87]). Nevertheless, when TSR increases, regions with high TKE values become smaller, but still located at the leeward side with consequent asymmetry. Higher values of TKE are also shown for lower TSRs in the core of the wake in the near region with a rapid decay moving downstream (see [86]). As logically deducible, a variation in the environmental turbulence intensity leads to variations in the dynamic stall phenomenon. In fact, blades critical Reynolds' number varies with the turbulent intensity and consequently also the lift and drag ratio, which increases. As result, the position of the separation points changes and this can delay the onset of dynamic stall (see [4]). Last but not least, dynamic stall has huge influence on wake's development process [20, 119]. The specific steps that occur on a blade experiencing dynamic stall will be analysed in Section (3.1.2.1) when discussing how to model this phenomenon.

2.2.1.2. Vorticity release at high TSRs

Dynamic stall is not the only source of vortex shedding, since at high TSR (generally > 4), periodical changing in velocity vector as well as angles of attack (also related to blades-wakes interaction [92]) leads to a variation in airfoil's bound circulation which in turn causes a release of an equal and opposite amount of circulation in blades' wake. So even when dynamic stall has lower relevance, shed vorticity has an important role in characterizing blades' wake (see [110]). The vorticity released in the wake has sign which depends on circulation's variation: when circulation increases (moving from the windward to the upwind position), negative vorticity is released in the wake, when decreases (moving from the upwind to the leeward position) the opposite happens (see [13]). Consequently, strong vortical structures, which tend to roll up, are generated. Considering

instead the downstream part of the revolution, the circulation is almost constant and only weak structures are generated. Such structures are separated into the ones due to shed vorticity and the ones related to trailing vorticity. They are responsible, in different ways, of the induction experienced by the flow that achieves the highest values at the midspan (see [13]). Even structures released during previous revolutions are responsible for the induction experienced by the flow.

Due to rotational movement, wakes generated by the blades have a cycloidal pattern and are transported downstream, but due to their high velocity gradients and the interactions with the tower and the blades they are diffused almost instantly (wakes no longer detectable after 1.5D downstream [92, 110]). In particular, interaction of blades with their own wakes is one of the main aspects of blades' aerodynamic. In fact, it leads to vorticity concentrations that create large scale coherent structures transported downstream, similarly to the ones seen in the dynamic stall. Moreover, the interaction process is also supported by wake deformation.

2.2.1.3. Tip effects

Finite extension of the blades has to be taken into account too and the subsequent origin of large-scale tip vortices. The latter are the strongest elements of trailing vorticity and are released due to the spanwise distribution of circulation. These vortices are responsible for wake's curvature and they interact rolling up together,

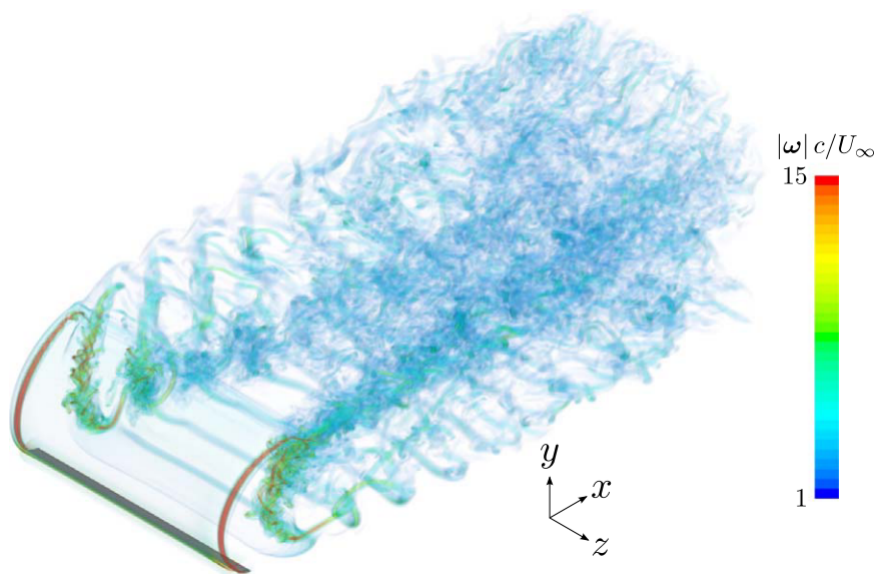


Figure 2.11: Visualization of the vorticity magnitude generated by a VAWT's blade. The tip vortices are visible near the edges of the blade. Image from [13]

moving downstream differently according to the azimuthal position of the blades: inward when the blades are located at the upwind and downwind region and outward when they are at the leeward and windward region (see [23, 110]). However, this motion distribution is not symmetric compared to the vertical axis because of the different blockage exerted by the blades remarking a further asymmetric aspect of the VAWT wake (see [23]). Considering the region where inward motion is observed, these structures are responsible for the high levels of induction, especially concerning spanwise velocity component (towards wake centre), which leads to wake contraction along the same direction (see [13]). A visualization of the tip vortices motion is shown in Figure (2.12).

Even tip vortices strength is not constant along the rotation and it is related to circulation's variation. They are stronger when released by blades at the most upwind position (highest angle of attack) while they are extremely weak at the downwind part of the revolution, where their circulation is almost constant (see [13, 23]). Turbine's parameters like the number of the blades and TSR have influence on tip-vortices intensity. Due to interactions, vortex stretching and turbulent diffusion, tip vortices are dissipated early in the wake (no more detectable from 2D downstream, [110]). One of the most relevant interactions occurs with the vortical structures shed from the blades (at wake's centre), which leads to an irregular pattern for the spanwise vortices cited before. The latter tend to breakdown (at midspan height this happens for 3.5D [13]) for these interactions because of the high level of turbulence. Considering the upper and lower blades tips, the vortices

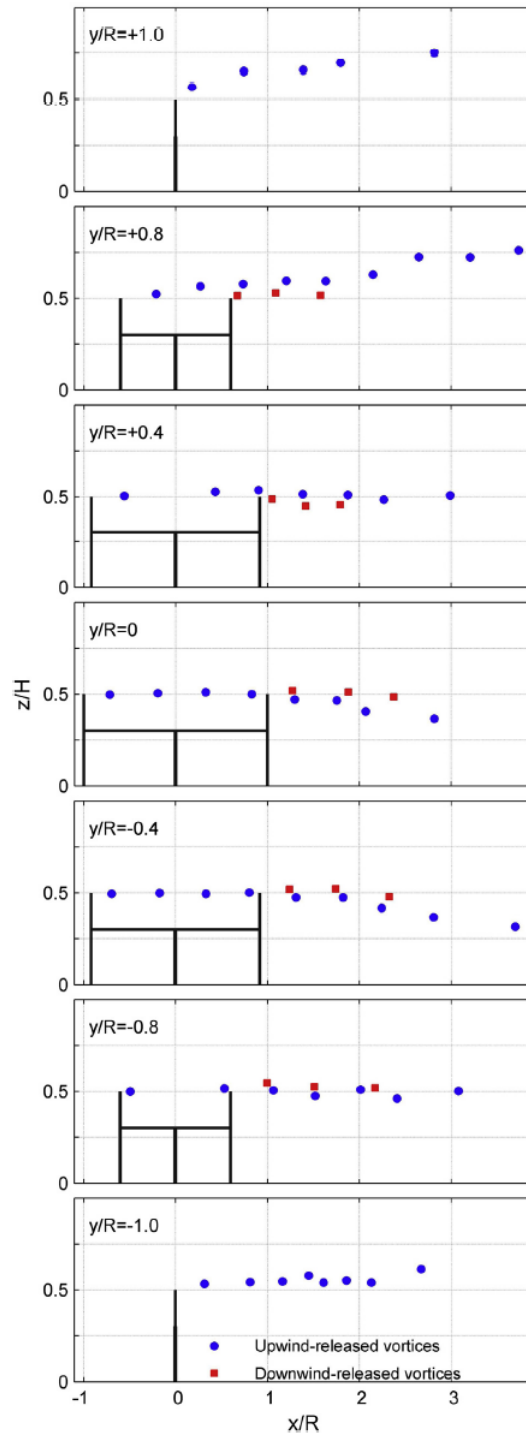


Figure 2.12: Location of the tip vortices during turbine's rotation and their different motion. The image is from [110]

generated move downstream with different velocity because of self-induction: the ones generated from the lower tips travel faster than the ones related to the upper tips. Therefore lower tip vortices interacts earlier with blades at downstream positions (see [92]). However, it's relevant to take into account that not only tip vortices but also the remaining part of trailing vorticity is released in the wake, which rolls up with the tip vortex itself creating a single greater structure. This rolled up vortex moves inboard or outboard according to the azimuthal position (see [23]).

2.2.2. Turbine scale

When approaching a turbine operating at low TSR (from 0 to 1, [18]), and high solidity (high number of blades) the blockage effect is dominant and consequently a certain amount of volume is deflected towards lateral directions while the remaining volume passes the turbine and wake regions behind the blades are also observed. With higher TSR the flow instead accelerates near the leeward region and on turbine’s top (along both streamwise and spanwise direction) and decelerates near the windward region but, in general, tends to follow the rotation of the turbine (see [18, 90]). This displays a certain relevance in deflecting the wake towards one side [88] inducing a crossflow component (see [45]), as will be discussed below. Hence there are regions where the time-averaged velocity has only a crossflow component (directed along the diameter) and regions where the flow is totally reversed and directed upwind. This occurs especially at the windward region, where the blade advances with a rotational velocity opposite to flow’s direction (see [18, 90]) and velocity’s magnitude can reach values higher than freestream’s ones because of the flow acceleration due to the blades [83]. The reversal effect is relevant at high TSRs, where the amount of volume of reversed flow is significant, even if it features equal maximum and mean velocity deficit (passing from TSR=1.25 to TSR=2.5 the reverse flow volume doubles, [90]).

After being deflected by turbine’s presence, the flow converges towards the axis (at $x = 2D$ according to [78]),

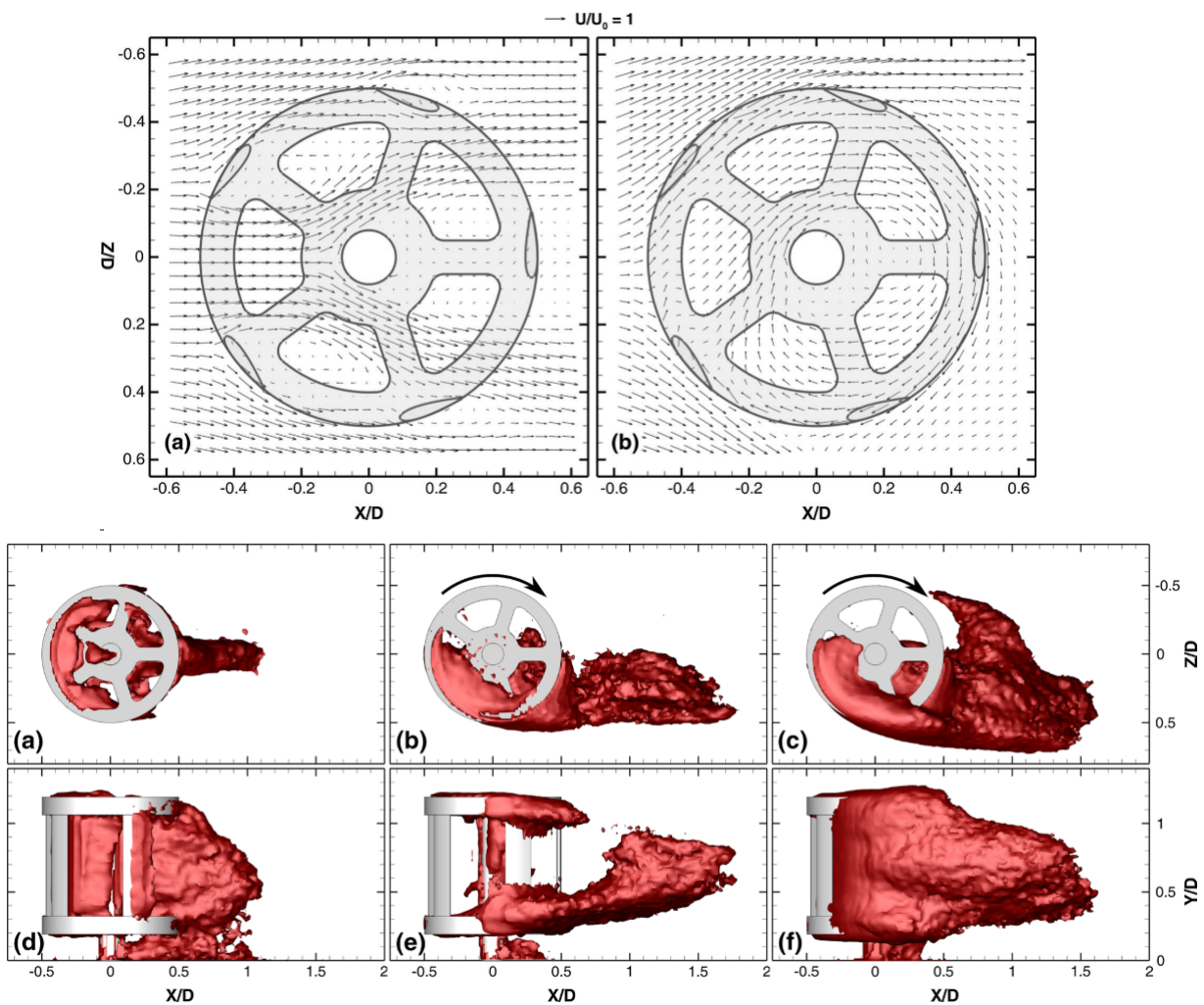


Figure 2.13: Visualization of how the TSR affects the blockage exerted on the flow (top) by a high-solidity turbine and the amount of reversed flow (bottom). Image from [90]

enhancing the wake recovery process. For a H turbine whose ends are shaped as disks, regions of high shear are created by the rotation of the disks and by both the crossflow and spanwise velocities (towards the wall) induced (see [18, 90]). Such regions, located at the top and bottom of the turbine, are zones of negative and

positive vorticity that tend to roll up creating vortices that move downstream and they generate regions of negative and positive spanwise velocity, respectively, along the wall normal direction (similar to 'S' shaped profiles, [83]) whose intensity decreases moving downstream.

Solidity has a major effect on turbines, changing their power output (with a higher solidity the power peak decreases and occurs at a lower TSR), and especially wake's asymmetry, which will be discussed in the next section. In fact the number of blades modifies the crossflow pattern because of the different acceleration experienced by the flow and its different frequency (see [34, 83]). Moreover, the deficit entity increases with higher solidity but at the same time the wake recovery will be faster. Nevertheless, the effect of this parameter is influenced by the AR used, as will be described later.

2.2.3. Wake scale

One of the most important aspects to deal with is the particular wake of VAWTs that requires a detailed universal description, based on the literature, in order to define its unique features. As well as HAWT farms, VAWT farms show the same problem of wakes interacting and interfering with the inflow of downstream turbines leading to a lower efficiency of the entire farm. In fact, a perturbed inflow condition spoils the energy extraction of a turbine and, in terms of huge wind farms, this results in wasting potential energy and money. Moreover, loads generated by the turbulent structures of the wake that interacts with a downstream turbine, lead to fatigue problems that might cause major failures or shorten the operative life of the turbine. Due to this substantial issue, it is crucial to understand VAWT's wake, how it recovers and in how much space, as well as its structures and how it develops in order to figure out the best spacing and the best wind farm layout. Even for HAWTs the situation is similar and maximizing the efficiency and the power extracted is a common goal for both the wind turbines type.

2.2.3.1. Near wake and far wake distinction

There are two main regions in a wind turbine wake: near and far wake region. Unlike HAWTs, the distinction between the two regions has not been defined for VAWTs yet. For HAWTs the near wake ends when the pressure effects related to vortices structures can be neglected (approximately from 2 to 4 diameter [28]) but there is not such a clear definition for VAWTs. By the way the main features of these zones can be outlined:

1. The **near wake region** is the area just behind the rotor which is heavily influenced by the rotor structures, the blades and their rotation as well as the vortex structures created. Kadum et al. [45] proposed an extension for this region up to $\frac{x}{D} = 2.5$. Here the maximum value of velocity deficit and strong gradients of pressure are observed. Generally, it is considered the region where the power extraction due to the turbine activity and the structures created from the dynamic stall (discussed before) are spotted. The latter shield the core of the wake from interactions with high speed flow, delaying the wake recovery (see [78]).
2. The **far wake region** where rotor geometry's effects are less evident while turbulence effects play a significant role (especially for small wind turbines, which are typically installed near to ground where buildings, trees and so on can increase freestream turbulence levels [4]). In fact, thanks to turbulence mixing the slowest layers of the wake interact with the high speed outer region and, supported by the entrainment process, the wake recovers gradually up to the freestream velocity value. Since mixing is boosted by turbulence, atmospheric turbulence has a huge role in defining the spatial length that the wake needs to fully recover. The wake recovery process has different properties for HAWTs and VAWTs: in both cases the process is not visible behind the turbine whereby expansion take the lead, but VAWTs experience stronger advection. For this reason the amount of space needed to recover up to freestream values is shorter for VAWT (see [13]).

The existence of a third region, a transitional one, has been proposed by [78] and it establishes a link between the others. Here the wake recovery process increases its intensity, while a slow decay in the deficit (but also in the turbulence activity) is observed up to the deep far wake region. An expression for the transitional region onset point is suggested by Araya et al. [6] who located this point at $x \approx 2D$ for almost every Reynolds number.

2.2.3.2. Wake's asymmetry and deflection

The wake behind the turbine expands and gradually recovers due to the entrainment process, however, even if it seems similar to a HAWT's wake [110], it is an asymmetric wake deflected towards one side (the upwind-turning side of the turbine) where it shows a stronger deficit [3]. This has been proved also with the actuator line theory [8]. The deflection, which causes a lateral expansion and a faster recovery (see [65]), is not homogeneous along the spanwise direction and decreases when moving towards the upper edge of the turbine (see [62]). The crossflow deflection is related to lateral forces resulting from the asymmetric force distribution during blades rotation and due to the difference between incoming speed and tangential velocity of the blades, whose maximum is achieved at the windward region (see [3, 88]). Therefore, the wake centre position is not located along the symmetry axis.

Since wake deflection towards windward side increases in the near region (up to 4 radii/2.5 diameters downstream, [45, 110]), it is logical that it does not occur only because of rotor action. The latter induces crossflow component in flow (with higher values near the rotor region) with rotation (see [3, 45, 65]), but deflection is still present while moving downstream. The source has to be found in:

1. The self-induction of the wake along crossflow direction is due to rotation, which propels the fluid (as stated in the previous section), and the higher blockage at the windward side which leads to lower pressure levels [65]. For these reasons and for the strong angular momentum at the downstream side, crossflow motion is generated but its intensity decreases moving downstream [83]. Also the vortical structures shed by the blades play a relevant role in flow induction, which causes deflection and asymmetry (especially in the near wake, [13]). Similarly because of turbine rotation, a spanwise velocity component is generated with positive values at leeward side and negative ones at windward side, but its presence is limited to the only region where rotational effects are relevant (up to 2.5D downstream, [45]).
2. The counter-rotating vortex pairs (CVPs), which are related to lateral force distribution and responsible for a further deflection and deformation of the wake through induced side flows (see [36]).

2.2.3.3. CVPs - Counter-rotating vortex pairs

CVPs's strength is generally higher at the windward side, where higher blockage is experienced. As well as the wake centre, they are not located along the symmetry axis, but their position depends on lateral forces distribution along blades' path. However, the latter depends on TSR and consequently also the asymmetry in the horizontal plane (see [3, 36, 97]) shows a strong dependence on TSR: with higher values, the asymmetry decreases (also the dynamic stall effect, as discussed before, which is an asymmetry source with lower relevance). Moreover, moving downstream the rotational effect has no more influence and also CVPs' effect decreases: the wake gradually becomes symmetric.

Besides that, CVPs, whose elongation is comparable to blades' length, are extremely relevant in speeding up the wake recovery (especially at the windward side) because of the entrainment of unperturbed higher velocity mean flow around the turbine, which mixed with slower fluid in the wake enables to boost the recovery process. They are also responsible for the changing in the cross-sectional shape of the wake, making it similar to a 'C'/clover-leaf/kidney, because of the flows inducted (see [36, 78]). This particular shape disappears moving further downstream. However even if the turbulence mixing shows a remarkable role in re-energizing the wake, the advection of mean flow due to CVPs is primary source of recovery. However, their intensity in both horizontal and vertical planes is not homogeneous (see [83, 89, 90]):

- The ones generated from the windward side of the wake are stronger, with higher vorticity magnitude along the streamwise direction
- CVPs' efficiency is higher in the upper part of the wake, since the mixing process in the lower part is damped by wall's presence: hence with less restrictions the wake recovers faster to unperturbed value in the upper region. The same boost in upper region of the wake has been observed also by Ouro et al. [78] and many others.

CVPs' strength and mixing capacity increases with TSR, promoting greater wake asymmetries (in the near wake) and faster recovery (see [90]), with consequently uniform distribution achieved earlier. The increase in wake deflection across the horizontal plane when the TSR increases is also reported by [18] but not related to CVPs action. Similar CVPs have been observed by Ryan et al [90] and considered as tip vortices with great

relevance (similar to the ones cited in Section (2.2.1.3)) on the blockage effect experienced by the flow, which reaches his peak just behind the rotor, and on wake recovery.

However, no study has demonstrated yet why CVPs are generated. A solution has been proposed by Bastankhah et al. [11] who related their presence with crossflow and spanwise velocities induced to satisfy continuity equation. Similarly their origin has been related to specific spatial distribution of crossflow and spanwise components generated in the wake (see [83]). Even an analytical model has been introduced by Rolin & Porté-Agel [89] to investigate the aerodynamic phenomena that lead to lateral forces exerted on the flow (related to the CVPs, as cited before). A beautiful visualization of both wake's asymmetry as well as CVPs is shown in Figure (2.14)

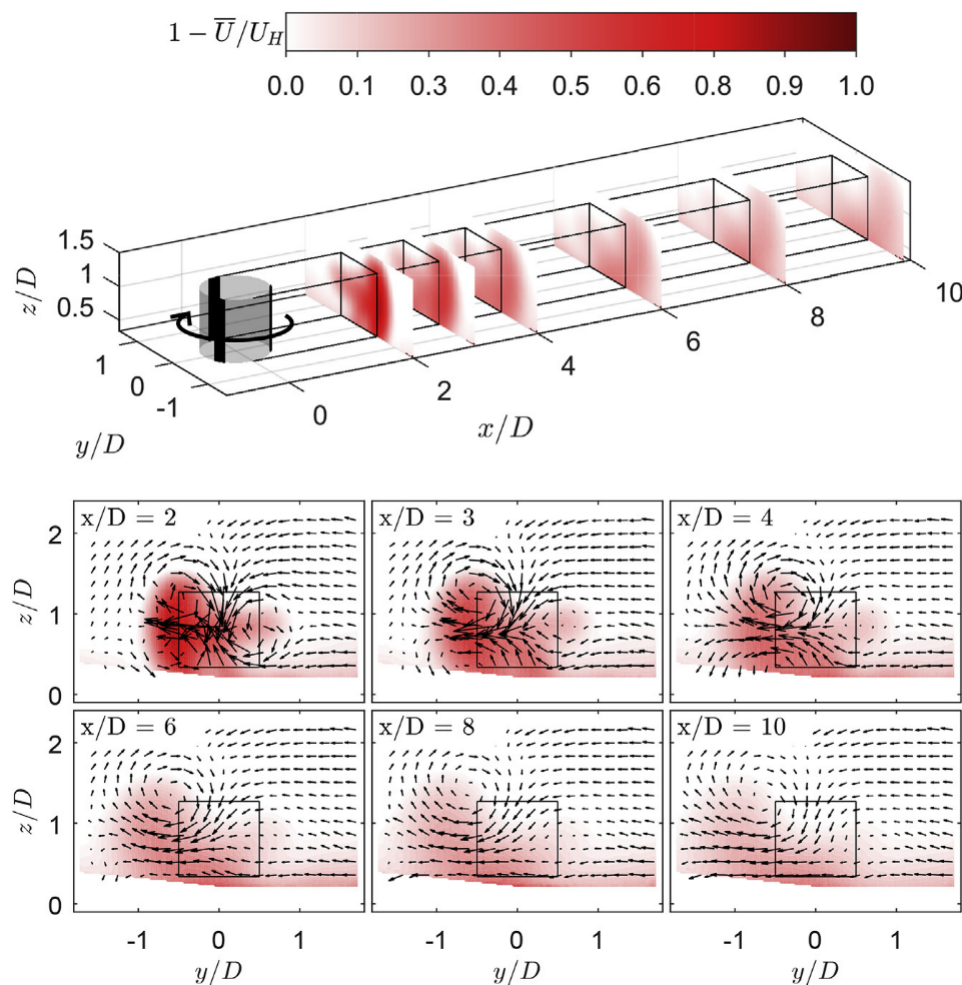


Figure 2.14: Images from [89] which allow to understand both how wake's centre is deflected moving downstream (top) as well as the CVPs generated at the edges of the turbine and how they evolve (bottom).

2.2.3.4. Aspect ratio and TSR effect on velocity deficit

The entity of the velocity drop as well as wake's extension is related to the cross-sectional area of the turbine and so to the aspect ratio. In fact at higher ARs (at a fixed diameter) the wake becomes stronger (i.e. the velocity deficit increases) because of the higher blockage and momentum extracted. Moreover it becomes larger along all the three directions and recovery length increases (see [2, 3, 97]). This is valid when considering a fixed solidity, otherwise a superposition of both effects is obtained (see [34]). In fact AR's variation has influence on solidity's effect: if the AR is not sufficiently high, wake's faster recovery triggered by high solidity values is not experienced. In such case the spanwise transport has more relevance in recovery than the cross-flow one (see [34]). A relevant fact is that the far wake region shows a shape which is almost the same even with different ARs: a circular one. This is an important results as it shows that it is incorrect to assume

that the shape of the wake in the far region is elliptical, assumption incorrectly made in several wake models for VAWTs [2, 51] as will be discussed in the related Section (2.5.1).

Besides the AR, also the tip-speed-ratio is strictly related to the momentum extracted from the turbine, in fact it is related to the thrust coefficient (see [36]) and with higher TSR values, deeper velocity deficits are experienced. At the same time, a higher TSR has a positive effect on wake recovery, 'deleting' earlier the proof of turbine's presence in the wake (see [18, 90]) because also of the stronger CVPs created.

2.2.3.5. Turbulence effect on wake's development

Wake recovery mainly occurs due to transport by means of the mean velocity field (especially along the vertical direction [13, 89]). For HAWTs instead wake recovery is mainly triggered by turbulent transport. The latter as well as the turbulent activity in general plays a role in the recovery of VAWTs' wake, even if not as significant as for HAWTs. Considering in fact the turbulence activity, it is essential in mixing the flow from faster to slower regions of the wake, enabling an earlier return to the freestream velocity value. So analysing a point at a certain distance from the rotor in the near wake region, when higher environmental turbulence intensity is observed, the velocity deficit will be lower than an opposite case (see [68]). Turbulence intensity influence decreases when lower AR are observed, however this leads to lower efficiency because of higher tip losses (see [13]).

Speaking about turbulence, another considerable aspect is how the turbulent activity (turbulent kinetic energy TKE, Reynolds stresses...) is distributed in the wake. The higher values are located both at the edges of the wake and at wake's core. At the edges of the wake strong streamwise fluctuations are observed because of the high shear and swarming of vortical structures (even the ones coming from the dynamic stall), as shown in [45, 78]. At the windward side freestream and rotational velocity are opposite [83] generating huge amounts of turbulent kinetic energy. It is critical to underline that large scale structures located here are generated by blades' interactions with their own wakes in a certain vorticity sheet, as discussed in Section (2.2.1) (see [110]). High shear means also strong gradients, therefore here are located the highest values of this variable, as well as of the Reynolds stresses, they are both related. The TKE as well as the turbulence intensity and the Reynolds stresses decrease when moving downstream. In the core of the wake instead high turbulent activity occurs because of large fluctuations in streamwise (see [62]) and spanwise velocity. The main reason of the fluctuations presence is the strong momentum gradient [88], strictly related to the boundary layer structure and justified by the vertical turbulent flux of momentum. Similar intense fluctuations are also reported by [45] for a higher solidity turbine with different sign according to the region considered. Low values of turbulence activity are observed instead where the velocity deficit is maximum, because the core is shielded by vortical structures and is unable to interact with the outer flow.

Since the target of this thesis is the analysis and review of wake models, more attention has been given towards the wake description. In this way, it has been possible to stress the main features of the VAWT wake that are supposed to be replicated by a wake model. However, since wake models are intrinsically based on approximations, not all the aspects described have the same level of relevance with a particular focus on the velocity deficit, the wake shape and how it is affected by turbulence and so on.

Sections (2.4) and (2.5.1), related to wake models analysis, are essential in understanding the limits displayed by wake models and in figuring out what a wake model is capable of replicating and what not.

2.3. Turbine modelling: from HAWT to VAWT

2.3.1. Turbine modelling for HAWTs

The state-of-the-art methods described here are used to model turbine's influence on the flow and its performances. So they're useful to model the force term in the equations used (Euler, RANS, LES and so on).

2.3.1.1. Actuator disk theory for HAWT

The actuator disk theory has been developed for propellers but it fits extremely well even with wind turbine's rotor case. On account of that it is still widely used. Introduced by Rankine, Greenhill and Froude a long time ago (1865-1889), it is based on assuming the rotor as a permeable disk that allows the flow to pass through the rotor experiencing forces due to surface presence. It is strictly related to the BEM model, since it can be used to represent the blade elements but can also be coupled with a numerical solution of the Navier-Stokes equations (such as LES or RANS, similarly to what is done with the actuator line theory that will be discussed later).

The disc's presence leads to the addition of surface forces that act on the incoming flow, replacing the rotor. Such addition can be accomplished using tabulated airfoil 2D data, for example. The latter has to be corrected to account for tip effects, similarly to what happens for the BEM theory when the factor F is introduced. Considering that airfoils subjected to temporal variations of the angle of attack experience dynamic stall, it is necessary to add a model to replicate such behaviour.

The main results obtained with this model are the wind deficit and wake losses, especially in the far wake region, where the discrepancies between reality and predictions are limited. The main problem of this technique is that the axisymmetric assumption means having a force distribution along the actuator disc where the influence of the blades is modelled as an integrated quantity in the azimuthal direction. Moreover all the complex vortical structures generated by a real rotor are neglected and (being a 1D model) all the 3D effects are neglected, or (at least) only modelled. This theory is the basis of the streamtube models and can also be coupled with the BEM theory, providing it the value of induced velocity.

2.3.1.2. Blade element momentum theory - BEM

Firstly developed by Glauert [27] the blade element momentum theory (BEM) allows to evaluate the steady loads depending on wind conditions, rotational speed and pitch angle of the blades [31]. All the geometric features of the turbine are considered during the evaluation. The control volume considered is divided into annular elements each one representing a portion of the blades. The lateral edges of the streamtubes are streamlines and so no flow passes across such surfaces. The calculation of torque and thrust is done considering each element as a 2D element.

Some assumptions are introduced with this model:

- The annular elements are totally independent: everything that happens inside each one of them, does not affect the others
- The force generated by the blades on the flow is constant for each element considered. This means assuming a rotor with infinite number of blades incorrectly. On account of that a correction proposed by Prandtl is necessary.
- The pressure distribution along the curved tubes does not contribute to axial force.

BEM methods allows to find expressions for the induction factors a and a' and force coefficients, more details on how it works are reported in Appendix (B). Moreover such type of method is extremely important and is the basis of many other models developed for both HAWTs and VAWTs (streamtube models, actuator line and surface models and so on...). It can be combined with other models capable of evaluating of induced velocity, creating a loop cycle.

2.3.1.3. Actuator surface model for HAWT

The actuator surface model is based on the 3D Navier-Stokes solver combined with body forces distributed along the blades surface. Introduced by Shen et al. for 2D and 3D cases [100, 101] it is an evolution of the actuator line model and its work flow is explained in Figure (2.15). It is based on depicting the blades using

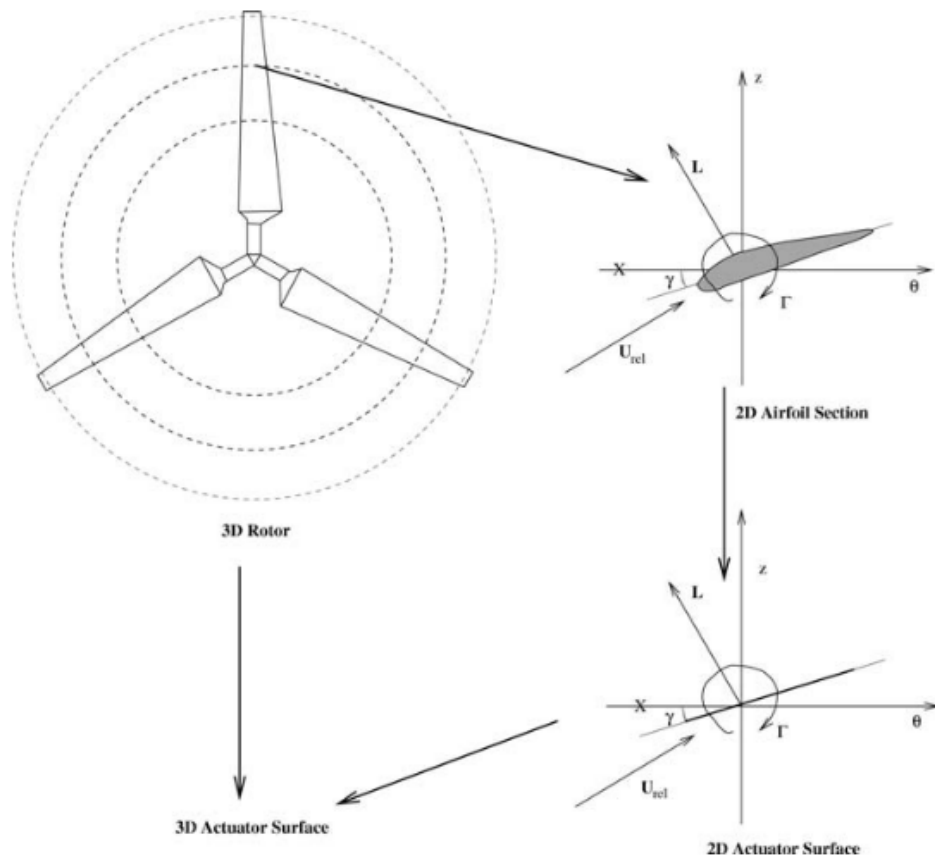


Figure 2.15: Work flow of the 3D actuator surface method. Image from [100]

several lines, recreating so an entire surface. However the approach is almost the same used for the actuator line theory in Section (2.3.1.4). The main points are:

- Induced, rotational and inflow velocities are combined to obtain the angle of attack.
- The angle of attack is used to extract the 2D force coefficients of each blade elements (the lines are divided as for the actuator line).
- Force coefficients are used to determine the forces exerted on the flow.
- Forces evaluated are added to the equations as source terms and the calculation starts again.

More details on the calculation, how it is performed and the equations used are reported in Appendix (B). The actuator surface shows better performances respect with the actuator line model because of its higher accuracy in replicating the blockage experienced by the flow due to the blades. However the computational cost rises.

2.3.1.4. Actuator line model for HAWTs

The actuator line model has been introduced by Sørensen and Shen in [104]. It is based on the blade element momentum theory and flow models built upon Navier-Stokes equations. By tracking and monitoring the blades position, which are replaced by lines and split into elements (see Figure (2.16)), it is possible to determine the distribution of the loads along the blades and so the forces exerted on the flow by using tabulated data for force coefficients. Then forces exerted on the flow are added to the equations used (Navier-Stokes, RANS, LES and so on), while induced velocity, velocity triangles and angle of attacks are calculated again and used to re-calculate the forces. So it is a loop calculation. More details on the calculation process are reported in Appendix (B). Being relatively computationally inexpensive, the actuator line is one of the most used model even if it requires multiple corrections. High accuracy is observed especially when dealing with

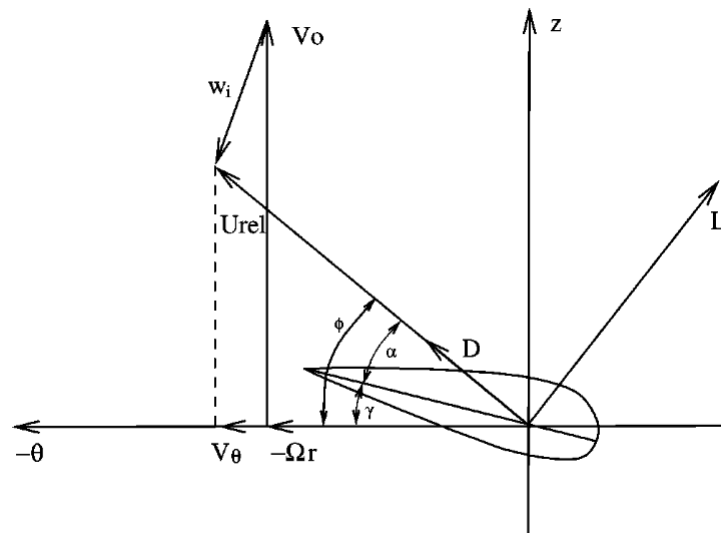


Figure 2.16: Cross-section airfoil element, image from [104]

the far wake, while some discrepancies are observed in the near wake. Another advantage lies in avoiding boundary layers, lowering the computational cost, and unlike actuator disk theory, it allows to replicate the motion of the blades which are not in a static condition. This gives a better physical representation of the wind turbine blades.

The actuator line theory is extremely important for the purpose of this study, even in its VAWT version (that will be discussed in detail in Chapter (3)). In fact it will be validated against literature data and compared with wake models predictions, in order to investigate both their accuracy and their limitations.

2.3.2. Turbine modeling for VAWTs

Similarly to what has been discussed in Section (2.3.1), here some of the state-of-the-art ways to represent VAWT's influence on the flow are reported and analysed. However not all the following methods have the same purpose: some of them are used to provide the induced velocity, while others need the inflow velocity at the blades and are used to model the source term in the equations.

2.3.2.1. Actuator disk model

The actuator disk theory for VAWTs is applied in the same way as for HAWT case described in Section (2.3.1.1). However, with reference to Newman [71], it is possible to test different conditions for the actuator disc. In fact a first study was conducted using only one disc, with its axis perpendicular to freestream flow. In order to replicate the rotational effect of the turbine, different induction factors have been used for the leeward and windward part of the turbine: this way a different drag is experienced and subsequently a torque that allows turbine's rotation. By combining continuity equation as well as Bernoulli's and momentum equations is possible to find an expression for the power coefficient C_P whose maximum achievable value is equal to Betz's limit $\frac{16}{27}$. Such limit is reached at a higher tip speed ratio compared to HAWT and for this reason, operating at lower TSRs, the power generated from a VAWT is lower. Using instead two actuator discs, the highest torque configuration is replicated: one of the disc is located at the most upwind position, the other at the most downwind one. Using the same equations as before, an expression for the C_P is introduced whose maximum value is $\frac{16}{25}$, slightly higher than the previous case. Similarly to HAWTs, this theory is valid when the far wake region is considered, where influence of the turbine and rotor decreases and all the vortical structures generated have less relevance. Moreover, comparing the results for HAWTs and VAWTs, the second ones are slightly less accurate because of the assumption of an axisymmetric wake. An aspect definitely not true for VAWTs.

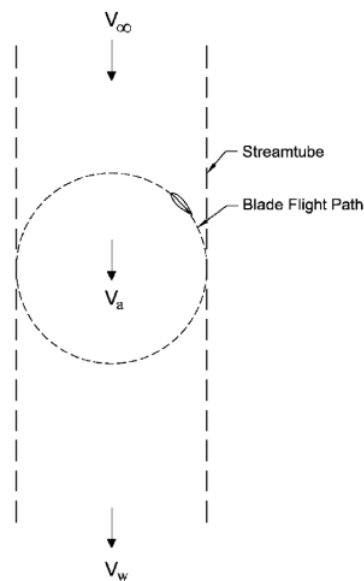


Figure 2.17: Schematic of single streamtube model from [41]

2.3.2.2. Streamtube models

Streamtube models are based on the equivalence between the forces generated on the blades and the rate of change of momentum of air along the streamtube considered. Several models have been proposed along the years, each one with different properties. By predicting the induced velocity, they can be coupled with BEM theory (on which these models are based on) to evaluate turbine's performances. However the main drawbacks with such models are their poor predictions in case of high tip speed ratios and high solidities, in other words when the momentum 1D equation is inadequate. Most important, such models do not take into account any blade's revolution or related effects, therefore relevant phenomena like the dynamic stall are not considered. Many different versions exist and can be grouped depending on the number of tubes considered and their location:

- **Single streamtube model:**

Proposed by Templin [108] for the first time. The whole turbine is enclosed within a single streamtube and the inner part of the rotor shows a constant induced velocity, similarly to what happens for the actuator disc theory. In fact turbine's presence is modelled by an actuator disc located at the centre of the streamtube with its axis perpendicular to freestream direction (check Figure (2.17)). All the major properties that affect the flow and turbine's performance characteristics such as airfoil stalling, blade solidity, rotor aspect ratio and thrust coefficient are considered in this model, but this does not occur for the wind shear effect. However, the constant induction shown by the inner part of the rotor is not realistic, since it should change with azimuthal variations of the blades. For this reason, such model shows good predictions for cases with lightly loaded wind turbine and it totally neglects flow's variation inside the rotor.

- **Multiple streamtube model:**

Here the control volume is split into several streamtubes, one besides the other but still independent. At the centre of each tube, an actuator disc is placed (see Figure (2.18)). The induced velocity is no more constant, overcoming the problem of the uniform axial induction experienced in the single streamtube models. However the induction factors are constant along each one of the tubes, so there is no difference when considering the upwind or downwind part of the revolution. Wind shear effects can also be included as well as many other effects (Reynolds number effect, flow curvature effect ...) can be added to the first versions of the models, as proposed by Wilson and Lissaman [118] and Strickland [106]. Even if improvements compared to single streamtube models are shown, the accuracy decreases when rotor loads increase because no account is given towards azimuthal induction variation.

- **Double-Multiple streamtube model:**

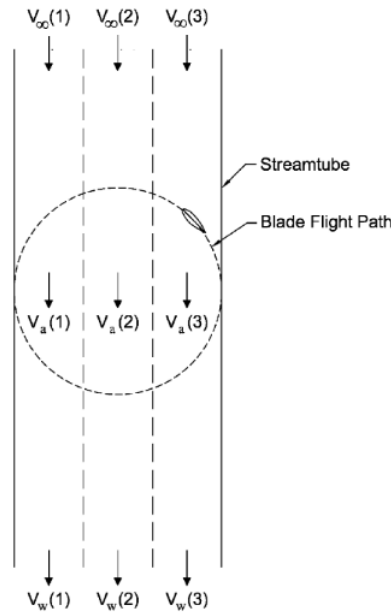


Figure 2.18: Schematic of multiple streamtube model from [41]

Introduced by Paraschivoiu [81], this model is the most common and the most used, but at the same time more complex than previous ones. It is based on a distinction in the calculation when considering the upwind and downwind part of the rotor. In order to accomplish such calculations, two actuator discs in tandem are placed in the streamtubes, one for each part and with local induction velocity assumed constant, as show in Figure (2.19). A different induced velocity is observed in the upwind and downwind region and the values are provided to the BEM model in an iterative cycle. This way

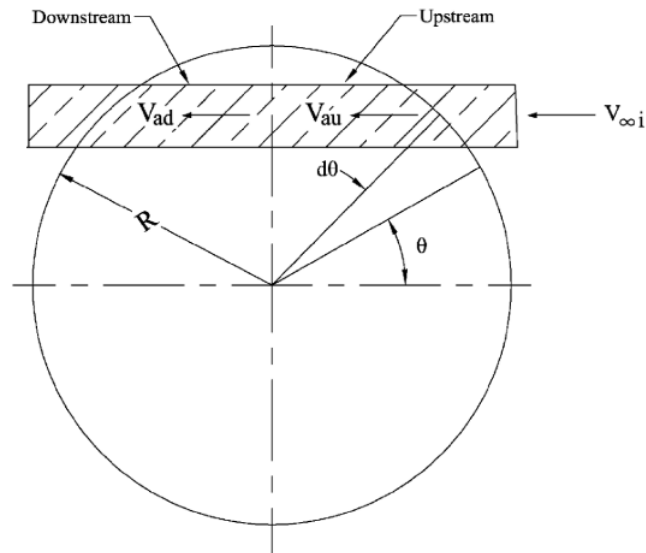


Figure 2.19: Schematic of double multiple streamtube model from [41]

is achieved a better accuracy, but the power estimated is too high compared to the experimental data, especially for high solidity turbine cases. Moreover, while the upwind part of the model influences the downwind part, the opposite is not observed and since the wake generated from the upwind actuator is assumed to be fully expanded, the second actuator sees a reduced equivalent inflow speed. Furthermore neglecting the induction along vertical direction leads to wrong predictions of the tangential forces, as reported by Ferreira [23]. Last but not least, streamtubes do not modify their sections mov-

ing downstream, they remain constant. On account of that, newer versions of the model have been proposed, improving its accuracy.

2.3.2.3. Actuator surface

Supported by LES equations, this model is similar to the one discussed in Section (2.3.1.3) from Shen et al. [100] and has been proposed by Massie et al. [62] for VAWTs for the first time. The model itself is a simple extension of the actuator line model for VAWT, since blades are replaced by lines, whose combination describes the blade surface. This way a better modelling of the dynamic stall phenomenon is possible. How the blades are modelled and the main parameters used are reported in Figure (2.20), similarly to Figure (2.21).

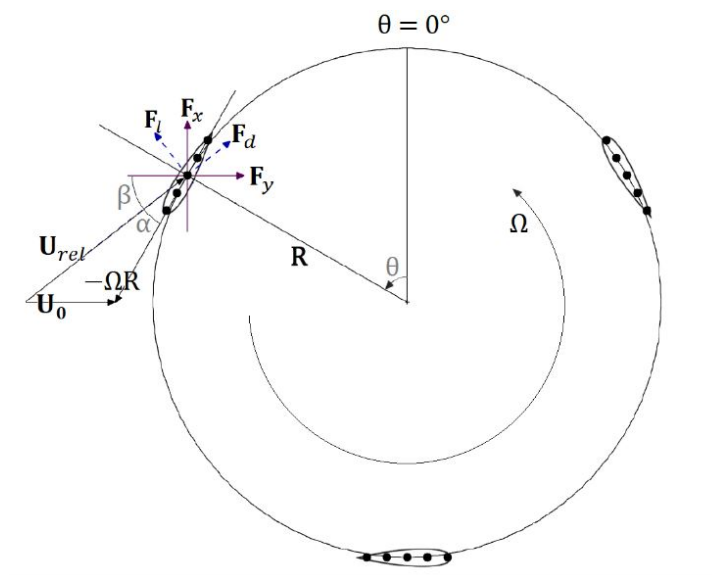


Figure 2.20: Actuator surface model blade discretization, forces and vectors, image from [62]

As for the actuator line theory, actuator surface model needs to be coupled to a set of equations (LES or RANS...) and its purpose is to evaluate lift and drag for each blade section considered. In fact the blades are divided in elements Δz along their span and each one of them applies a constant force on the flow.

$$F_l = \frac{1}{2} \rho C_l c \Delta z (\Omega R)^2 \quad (2.7)$$

$$F_d = \frac{1}{2} \rho C_d c \Delta z (\Omega R)^2 \quad (2.8)$$

The lift and drag coefficients C_l and C_d are provided by the literature [79] thanks to numerical simulations that couples LES and the immersed boundary method. Moreover, such coefficients keep into account also the corrections due to dynamic stall. Evaluating the local velocity at the blade centre of mass and summing it to the rotational velocity is possible to obtain the relative velocity and then the angle of attack. The procedure is almost the same used for the actuator line theory. Once forces are evaluated, they are added to the equation set (especially the momentum equation) and the loop used for the other cases starts also here since the induced velocity needs to be corrected.

The great advantage of this model is its ability to replicate wake asymmetry and expansion as well as the complex flows inside VAWT's perimeter with good fidelity, unlike what happens for the actuator line model. This happens because of its better ability in replicating the blockage generated by the turbine when the blades are in the upwind region of their motion. However, this better performances needs to be paid in computational resources. Moreover the model is unable to resolve the local, large-scale flow structures which occur at blade scale unless the grid is refined, but good results are provided only in the case of too fine grid resolutions, that leads to high computational cost similarly to blade-resolved simulations. This way the purpose of creating a simplified model is lost.

2.3.2.4. Actuator line model for VAWTs

Considering a VAWT, the actuator line theory can be applied similarly to what happens for a HAWT. In this case however, the lines, which identify the blades position, move along the circular path defined by turbine's rotation. Such lines are located at the quarter chord location of each element and the forces are applied at these positions. Force's components are shown in Figure 2.21, their evaluation is based on 2D force coefficients extracted from airfoils' polars similarly to the HAWTs case.

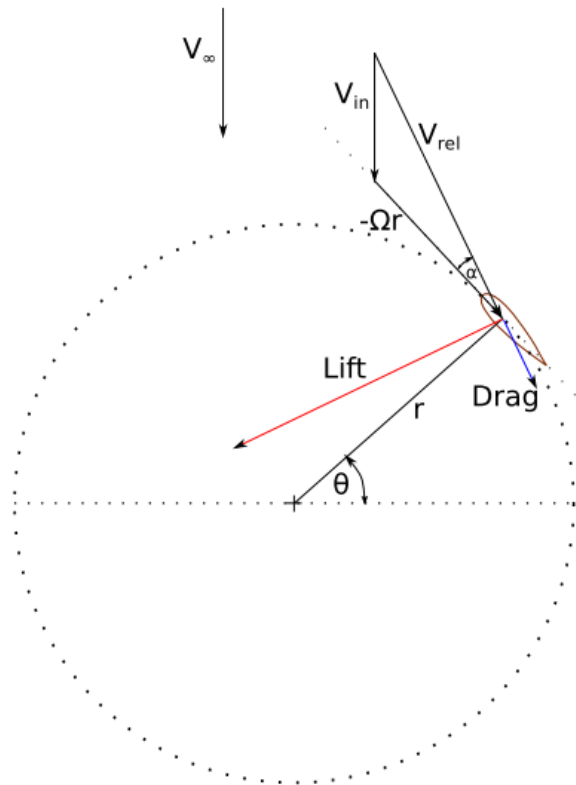


Figure 2.21: Cross-section airfoil element for a VAWT, image from [66]

Obviously, the procedure is different compared to the one adopted for HAWTs in Section (2.3.1.4) but the main steps are the same: using the angle of attack (as well as the Reynolds number) is possible to determine the lift and drag 2D coefficients experienced by each line element according to tabulated data. Then such coefficients are used to evaluate the forces exerted on the flow and consequently velocity's induction: the calculation then starts again.

The great advantage of the actuator line model for VAWT is being computationally inexpensive, even requiring some corrections (discussed in the Chapter (3)), and provides good results especially in the far wake. This makes the actuator line model a perfect tool to evaluate analytical wake model predictions. In fact, since analytical wake models show good accuracy when considering far wake region, it is obvious to think about actuator line simulations coupled with a set of equations (RANS or LES) as a validating tool. This way is also possible to have high fidelity data to understand how much accurate wake models really are. On account of that, actuator line model will be used (coupled with URANS) to pursue the targets of this thesis. More details about its structure and its implementation will be given in Chapter (3).

Returning to the actuator line features, it displays one major drawback: low accuracy is observed in the near-wake. Obviously if coupled with LES and not RANS equations, the accuracy rises as well as the computation cost, losing the advantage of a simplified model. In fact aspects such as using boundary layer in the mesh can be avoided, moreover the blades are represented as lines without the requirement of moving meshes. Having the possibility to replicate the rotation allows to give a more physical representation of turbine's blades and by considering their motion, it's possible to capture the unsteady-periodic nature of the wake in case of high accuracy methods.

2.3.2.5. Actuator cylinder

The theory introduced by Madsen [60] is based on representing the VAWT as an actuator cylinder with radial and tangential forces distributed along its cylindrical surface. This is an evolution of the actuator disc concept based on the phenomena related to VAWTs. Similarly to other models it allows to calculate the velocities induced on the flow starting from a force estimation. Most of the time it is coupled with the BEM theory in a calculation method (as seen with other models) which is an iterative process based on two main steps:

1. Using the BEM model to determine the force calculated using the velocity field extracted by the actuator cylinder method
2. Using the actuator cylinder method to calculate the flow field using the force field calculated by the BEM theory

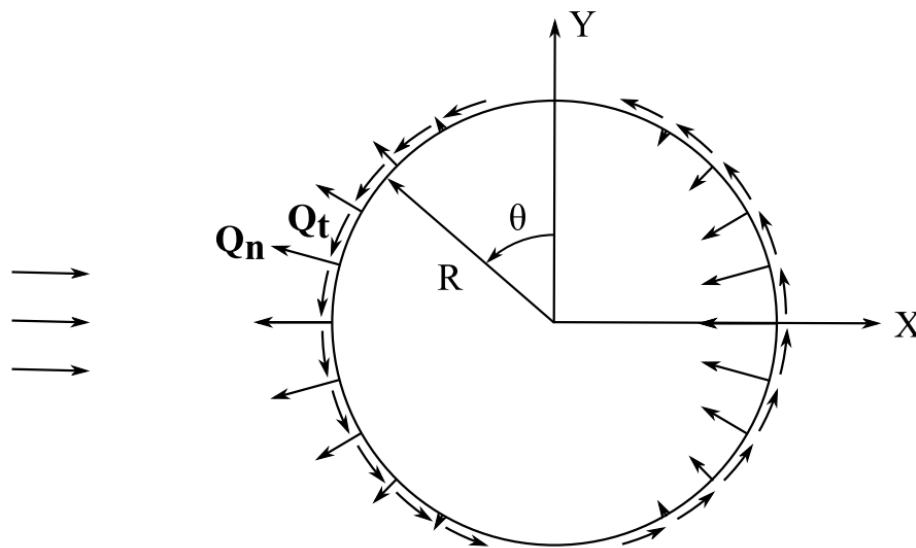


Figure 2.22: Loads distribution for radial and tangential forces along the cylinder, image from [16]

This model is more accurate than actuator disk and streamtube models because it accounts for the effect of the downwind part of the rotor on the upwind part. Moreover the modelled effect evolves at each azimuthal position because of the radial variation of tangential and radial forces. Therefore the results obtained are more accurate and can be applied also for Φ -shaped rotors. At the same time this model is unable to replicate phenomena like blade-vortex interactions as well as blade's rotation.

2.3.2.6. Blade resolved methods for VAWTs

Geometry resolved approaches are needed to achieve a correct resolution of the flow field developed at the blades. Therefore there are models that aim at replicating the interactions between vortices, blades and airfoils with the highest possible accuracy. Such phenomena are extremely complex to be modelled and for this reason when using simplified models are neglected. This way is possible to solve and analyse all the vortex structures created during blades passage, tracking their position and their evolution as well as blades interactions with the wake.

Such models are based on different approaches, but they all rely most of the time on introducing the turbine as a geometrical model inside the simulations and not using a simplified support model (actuator line, actuator surface etc...). The main solutions used are based on different equations and approaches:

- LES equations combined with immersed-boundary (IB) formulation [79, 80, 86] or other models, able to resolve the coherent structures, they are based on resolving the larger scales in the flow while small scales are parameterized and modelled using a subgrid scale model (more details are reported in Appendix (B)). The IB method is then used to simulate the solid moving geometries with high accuracy by exerting a force represented by the f_i term on a specific region of fluid nodes. For more details check

[79, 80]. In some case, IB method is substituted by actuator line or surface models to lower the computational cost. LES are computationally much more expensive than RANS but able to better describe vortices' evolution (especially if coupled with IB methods). In fact results have proved that the eddy-resolving nature of LES increases the accuracy respect with RANS models, but at higher computational cost. Therefore LES is, in theory, able to replicate wake-blades interactions when considering flows dominated by large-scale energetic vortices (like leading and trailing edge generated by dynamic stall). To compensate for the high computational cost specific LES models like the so-called 2.5D simulations have been introduced, check the one reported by Li et al. [58] for more details.

- Full Navier-Stokes equations, solved using a specific solver (for example h/p discontinuous Galerking-Fourier with sliding meshes, [24]). Extremely expensive in terms of computational resources because blades are not modelled, but directly resolved and all the scales are studied and resolved. Such approach is a DNS (direct numerical simulation), but it's out of the possibilities of modern computer both when dealing with single turbines as well as entire wind farms.

2.4. Analytical wake models for HAWT

Studying the flow field around a turbine is a task that can be accomplished with different levels of accuracy. In fact especially when speaking about wind farms, it is not simple to analyse the field generated by each turbine in an exact way: testing large number of wind turbines in a wind tunnel is quite difficult if not using simplified models (porous disks for example), while concerning the numerical aspect, computational cost can be too high.

Focusing on the latter kind of models, many of them are built with the target of simplify the calculation in order to overcome their major drawback. This leads to a lower computational cost because aspects which show less importance on the phenomenon considered are neglected. Therefore the *level of accuracy* is a watershed and depends on the approach used: there are models that neglect more aspects, with stronger assumptions, and ones with lighter assumptions that are more accurate but more 'expensive'. Depending on the level of detail required and the aspects that need to be replicated with high fidelity, it is possible to select one model or another.

Analytical wake models are a powerful tool when speaking about wind turbines. Considering wind farms with several wind turbines, defining the optimum location of each one of them is very important in order to maximize the power output. Industries and companies when designing a wind farm have to make decisions based on relatively simple analytical wake models which guarantee low computational cost. Such analytical models capture the wake region, the velocity deficit, but they don't take into account details like the blade effects, the vortical structures created and similar. Sacrificing the need for a full correct and detailed solution, wake models allow to the most important acquire information during the wind farm design process.

In order to fully understand how wake models work, how they are developed, what they neglect and which is the state of the art, a review of existing models for HAWTs has been made.

2.4.1. Jensen model

The model presented by Jensen [43] is probably the oldest wake model developed. It is still widely used due to its simplicity and low computational cost. Several updated versions of this model have been developed during the past years and one of the most famous is the one proposed by Katic et al. [47]. The original model is based on neglecting the near wake region and all the periodical and vortical structures as well as the rotation and the pressure gradient effects, in order to deal with the wake as a negative jet. Only the mass continuity equation is used and the velocity distribution is a top-hat distribution (see Figure (2.23)). The wake develops linearly moving downstream according to a specific parameter k^* . Specific details on its structure and its equations are reported in Chapter (3).

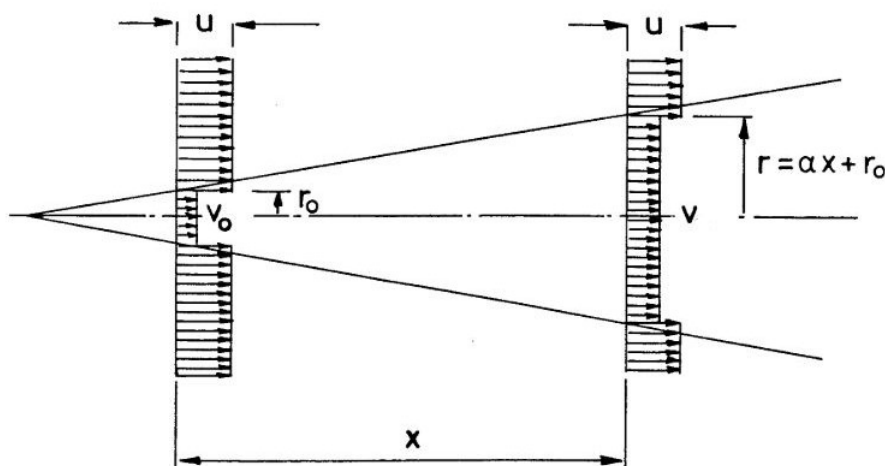


Figure 2.23: Control volume used in Jensen's model with the related symbols used in the equation: V is the speed in the wake, r is its radius, r_0 the wake radius at rotor position, V_a the velocity just behind the rotor and V_∞ the freestream speed [43]

It is necessary to take into account some problems that occur when using Jensen's model. First of all the use of the mass conservation equation only leads to a wrong expression for side flows. Secondly, even if the model predicts the maximum velocity deficit reasonably well in some regions sufficiently downstream

(far from the rotor), it underestimates the maximum velocity deficit in other regions at wake's centre and overestimates it at the edges of the wake (with subsequent problems when evaluating the power extracted from a downwind turbine in a wind farm). These discrepancies increase in the near wake and because of the top hat distribution (not realistic) and using the mass conservation only. Moreover, as reported in [46], this model is valid only from at least 3 diameters downstream of the turbine because of the assumption of totally turbulent wake. However such model is a sufficiently accurate tool when dealing with the far wake where the results are good. It also requires an extremely limited amount of input parameters (unlike more complex models), a great advantage during preliminary design process. A code version of Jensen' method structured according to [82] for HAWTs will be tested and validated against experimental, LES and RANS data. This will be the basis of the implementation of the same model for a VAWT, as will be discussed in Chapter (3).

2.4.2. Larsen model

Larsen model [53] (which features an updated version [54] with different boundary conditions) starts from assuming the flow region behind the turbine as a fully turbulent zone. This way it is possible to use Prandtl's turbulent boundary layer equations, the Navier-Stokes equations for high Reynolds numbers. The velocity distribution used is more complex than the one seen for Jensen's method in Section (2.4.1) and shows a radial dependency. So unlike the previous model, it's much more accurate and realistic, but at the same requires many constants and parameters as input values. Many of them do not show a universal value, constituting a major drawback.

In total accordance with full turbulent case equations, the wake develops non-linearly and its width is proportional to $\propto x^{\frac{1}{3}}$. Even in its expression constants and parameters appear and need to be defined. The results provided by the wake model are the perturbation components along radial and axial direction in the wake at each downstream coordinate.

More assumptions made when developing this model are the following ones:

- The far wake is assumed to start just behind the rotor with the initial wake expansion equivalent to that just after pressure recovery. By this way no account is given to the near wake region nor a specific model for this zone, where the pressure equilibrium is reached yet, is provided.
- In order to use Prandtl's equations for the boundary layer, the wake is considered as a free turbulent shear flow and it is handled like a boundary layer problem: the size of the free turbulence region in the direction perpendicular to the mean flow is negligible compared to its amount along streamwise direction.
- Prandtl's mixing layer theory is assumed to model Reynolds stresses
- Wake's width at rotor position is assumed equal to the turbine diameter

Having too many parameters to be provided, the Larsen model, even if overall performs better than Jensen's model, it is not suitable to be converted for VAWTs because many of the input required are extremely specific and their expressions are not known for VAWTs. However additional details on its equations and its implementation are provided in Appendix (B).

2.4.3. Ainslie model

This is a field/implicit model from [5], different from the other kinematic models and based on a parabolic simplification of the RANS equations to reduce the computational cost. However everything has a price, in fact this kind of models are not able to describe the near wake region, where pressure gradients are strong. Therefore model's validity starts from two diameters downstream of the turbine (where far wake onsets). By solving the RANS simplified equation using a numerical approach (which requires a discretization method, a solver and so on...) the velocity components along both radial and axial direction in the wake are calculated. This model is still used and during the years several improvements, corrections and additions have been proposed. One of them, for example, is based on using a simple Gaussian velocity distribution for the lateral velocity component along all the wake, avoiding the necessity of solving a linear equation for each downstream location even for this component and lowering the computational cost. More details on how the equations are solved and their form are reported in Appendix (B).

Even if considered as an analytical wake model Ainslie model is more similar to a simplified numerical approach, so it is expected to perform more accurately compared to Jensen and Larsen methods for example.

At the same time, since a numerical solution of the parabolic RANS equations is required, computational cost raises and it is not comparable with the one from wake models. Moreover a significant number of constants and parameters (as for Larsen method) without universal value is required: an additional drawback.

2.4.4. Frandsen model

The model from [25] is based on mass and momentum conservation. Several terms in the momentum equation are neglected, like the acceleration term, the pressure term and the gravity term as well as the shear forces. The approach used is extremely similar to Jensen and Larsen models and it merges some aspect of both of them. In fact it is based on a top-hat (constant) distribution of the velocity defect so only one component is evaluated, the axial one. At the same time self-similarity of the velocity profiles is assumed, similarly to what has been done by Larsen in Section (2.4.2). Moreover, a non-linear development for wake's width is assumed coherently with the self-similarity assumption for a classic turbulent case. More details about the related equations are reported in Appendix (B).

Since the model is theoretically valid only in the far wake region (because of the neglect of pressure term in the momentum equation) the results in the near wake are poor. At the same time it shows a good level of accuracy for the deficit value when dealing with the far wake, even if the constant distribution is definitely not realistic and could show the same problem reported in Section (2.4.1). Another advantage of this method is its low computational cost when performing the calculations. At the same time however it requires more parameter respect with the Jensen model and they must be evaluated experimentally. Talking about disadvantages, besides the ones already cited, there's a really strong assumption which needs to be discussed. In fact even if the validity of the model is limited to the far wake region where the self-similarity assumption is verified, the pressure equilibrium is assumed to be reached just behind the turbine. This way it is possible to apply the actuator disk theory to determine the velocity value, as well as the area A_a , assumed as onset values. The existence of the near wake region, where the wake expands, is consequently neglected. Moreover every rotational aspect involving the turbine has been neglected, so no effect has been modelled in what is supposed to be the near wake region part.

2.4.5. Fuga method

Model proposed by Ott et al. [75, 76] is based on pre-calculated look-up tables used to construct the velocity field behind one or several turbines and easily solve the set of RANS equations coupled. This way is possible to speed up the calculations of the velocity components along both axial and radial directions. It also requires an atmospheric boundary inflow condition since it is the most realistic condition and occurs in real wind farms. Since this model is intended to be a tool to optimize turbines' location in wind farms, it is obvious to use such condition. It is necessary to point out that this is a different wake model respect with previous one. As for the Ainslie model discussed in Section (2.4.3), Fuga method is more like a numerical model than an analytical one and even if based on the same equations of previous models (check Appendix (B) for more details), is much more complex but at the same time one of the most robust CFD based models [28]. In fact it also requires a numerical approach to solve the equation, even if the computational cost is reduced by using look-up tables.

However, being a simplified model and is based on assumptions (as stated before) and on limitations. As reported in [75] the model is unable to correctly replicate wake meandering and for this reason the wakes generated by the model are extremely straight, unlike real ones. Moreover linearized RANS only have one length scale and are not able to distinguish between large scale eddies, which are responsible for the wake meandering, and small scale eddies that allow mixing.

2.4.6. BPA model

The model for HAWT proposed by [10] is based on overcoming the limitations encountered by previous models which can be summarized as:

- The model proposed by Jensen [43] and its earlier version from Katic et al. [47] takes into account mass conservation only and not momentum conservation, with a consequent wrong expression for the side flows. Moreover the top-hat velocity distribution is not realistic.
- The model proposed by Frandsen et al.[25] neglects the existence of a certain amount of space after the turbine necessary for the static pressure to recover to the freestream value and reach the equilibrium.

On account of these limitations, the model is built starting from both mass and momentum conservation along streamwise direction. A Gaussian distribution for the velocity deficit in the wake is used since, according to previous studies, self-similarity is achieved in the far wake as for a bluff body. As consequence of this assumption, the model is valid only starting from a certain point downstream, the onset point that marks the difference between near and far wake. This way is possible to neglect the pressure term in the equations. In agreement with self-similarity assumption in a stratified inflow turbulent condition (ABL condition), the wake expands linearly. A wake decay constant (or wake expansion factor) k^* needs to be provided, but as for the other models, the value proposed is not universal and it needs to be tuned experimentally. Like other models this is a major drawback, since it depends on the case analysed.

In order to calculate the values at the onset point, the deficit predicted by the current model, whose validity range is limited to the far wake region only, is equated to the one predicted by Frandsen model which assumes a top-hat distribution and places the onset point just behind the rotor. This way we assume that the pressure has already reached the equilibrium at the rotor position, but that is not true since a certain downstream distance is necessary to recover and self-similarity is observed only from a certain downstream point on. This way the predicted values of wake width at rotor position are overestimated. Moreover the ground effect is neglected, but considering its influence the differences in terms of results are minimal. So it can be neglected without losing accuracy, as proved using imaging techniques.

Overall the model shows probably the highest accuracy among analytical wake models for the far wake, where the comparisons with data showed a good agreement. This because of the Gaussian distribution, more realistic respect with the top-hat distribution, that suits perfectly for the wake of a wind turbine that (if the vortical structures are neglected) is extremely similar to a jet flow. A detailed investigation of the structure of this model will be carried out in Chapter (3) since a version from [82] have been tested in order to be validated against experimental, LES and RANS data. This way has been possible to better understand it and prove its validity before testing it for a VAWT.

2.4.7. Updates and additions to the BPA model

Several corrections and additions have been proposed for the BPA model through the years. The current subsection will analyse some of them.

- **IEA37 [40]:** a simplified version of the BPA model which features a specific value for the growth rate k_y^* (equal to 0.0324555) and the following equation for the ε :

$$\varepsilon = \frac{1}{\sqrt{8}} \quad (2.9)$$

The expression for the velocity deficit and the one for the wake expansion become the following ones:

$$\frac{\Delta V}{V_\infty} = \begin{cases} \left(1 - \sqrt{1 - \frac{C_T}{8 \frac{\sigma_y^2}{D^2}}} \right) e^{-0.5 \left(\frac{y_i - y_g}{\sigma_y} \right)^2} & x_i - x_g > 0 \\ 0 & \text{otherwise.} \end{cases} \quad (2.10)$$

$$\sigma_y = k_y (x_i - x_g) + \frac{D}{\sqrt{8}} \quad (2.11)$$

Where $x_i - x_g$ is the distance from the rotor position along freestream direction, while $y_i - y_g$ in cross-flow direction.

- **Niyifar method [72, 73]:** which introduces a different expression for the growth rate based on turbulence intensity, This addition will be analysed in details in Chapter (3) since it will be used for both the HAWT and VAWT case.
- **Zong method [120]:** based on some significantly new expression for the wake width and for the growth rate. The wake width expression comes from [98] and is:

$$\frac{\sigma_y}{D} = 0.35 \cos(\beta) + k_w \ln \left[1 + e^{\frac{x - x_{th}}{D}} \right] \quad (2.12)$$

$$\frac{\sigma_z}{D} = 0.35 + k_w \ln \left[1 + e^{\frac{x - x_{th}}{D}} \right] \quad (2.13)$$

Where β is the yaw angle and x_{th} is the near wake length whose expression comes from [115] and is also reported in [73]. The growth rate is expressed as function of the added turbulence intensity I_+ and the environmental turbulence intensity I_∞ :

$$k_W = 0.38 (I_\infty^2 + I_+^2)^{\frac{1}{2}} + 0.004 \quad (2.14)$$

The added turbulence intensity is expressed as:

$$I_+ = 0.73 a^{0.83} I_\infty^{0.03} \left(\frac{x}{D}\right)^{-0.32} \quad (2.15)$$

Last but not least, in order to keep into account the wake expansion in the near region due to the pressure gradient, thrust coefficient is expressed as an error function:

$$C_T(x) = C_{T0} \left(1 + erf\left(\frac{x}{D}\right)\right) 0.5 \quad (2.16)$$

Where C_{T0} is the thrust coefficient at rotor's position. This way it's possible to replicate a gradual increase of the wake deficit until $x = 2D$.

2.4.8. BPA yawed model

The model proposed by (Bastankhah and Porté-Agel, 2016) for yawed HAWTs is based on steady continuity equation as well as RANS equations simplified according to an experimental/numerical budget study. This model is different from previous ones since it takes into account wake's centre deflection due to a certain yaw angle present: the yaw angle pushes the wake towards one side making it asymmetric.

The main assumptions made are:

- The pressure term is neglected in the momentum conservation along streamwise direction. The model is valid for the far wake only.
- No ground's effect
- The skew angle experienced by the wake is always small (even with high yaw angles) so it is possible to assume $\tan(\theta) \simeq \theta$ in the momentum conservation along streamwise direction.

Another relevant assumption is self-similarity for the far wake, as for BPA original model in Section (2.4.6) and the subsequent Gaussian distribution for the velocity deficit already seen. Here a Gaussian distribution is introduced also for the skew angle, which is a quantity evaluated at each downstream location. Unlike what happened with Frandsen model in Section (2.4.4), here the self-similarity is applied only in the far wake region, and the values at the onset point are calculated according to a specific approach, coherent with the assumptions. However, as far as the yaw angle experienced is limited, this assumption along vertical direction does not lead to major errors, otherwise a Gaussian distribution cannot be assumed.

Wake's width develops linearly, according to the self-similarity hypothesis under a stratified turbulent inflow condition (ABL condition), but wake decay constants are still a weak point since they need to be tuned and depends on the case considered. One last aspect that deserves to be discussed is how the onset values are provided. An original and interesting approach is proposed: it is assumed that the values up to the onset points are constant (wake width, deficit, skew angle and so on...) in order to replicate the potential core of a jet flow. In fact in this region the flow can be assumed inviscid and with constant properties. However, this is not an high fidelity representation of what happens in the near wake, but allows to calculate with sufficiently accuracy the onset values. Such approach is a good alternative respect with solutions provided by previous wake models such as the Frandsen model or the original BPA model itself.

Here some reflections and conclusions about the model analysed:

- Many assumptions have been made regarding the limited magnitude of the yaw and skew angles.
- An elliptical shape for the wake is assumed behind the rotor depending on yaw angle. This way the projected area of the turbine changes.
- Wake's centre displacement is only due to yaw angle and not because of the interactions between the rotating wake and the incoming shear flow, which is unrealistic.

- Wake's centre is assumed to be located always at hub height z_h along the vertical direction.
- As mentioned before, constant values in the potential core region up to the onset point are assumed but the real values of velocity are higher and not constant throughout the region. However the assumption is sufficiently correct to predict accurate values at least at the onset point.
- In addition to the yaw angle, the thrust coefficients and the geometrical properties of the turbine (diameter, height, hub height and so on) it requires 3 coefficients that needs to be tuned according to the case analysed and do not show a universal expression.

In the end, the BPA yawed model is one of the most accurate existing analytical wake models. Respect with top-hat models (Jensen, Frandsen and so on) it provides better values of both wake's width and velocity deficit, especially in the far wake. At the same time the idea of modelling the near wake as the core of a jet flow is a brilliant and innovative idea that overcomes the intrinsic theoretical error on which the Frandsen and BPA model are based on.

Model	Starting equations	Velocity distribution	Wake width development	Pro	Cons
Jensen [43]	Mass conservation	Top-hat	Linear	<ul style="list-style-type: none"> - Low computational cost - Easy application - Good accuracy in far wake 	<ul style="list-style-type: none"> - Not accurate - Wrong formulation - Valid after onset
Larsen [53]	Navier-Stokes for high Reynolds number	Non-constant	Non-linear ($\propto x^{\frac{1}{3}}$)	<ul style="list-style-type: none"> - Knowledge about BL equations used here - Provides two components 	<ul style="list-style-type: none"> - Valid only in far wake - Starting dimensions equal to value at the onset - Near wake neglected
Ainslie [5]	Parabolic form of RANS	Non-constant	Based on solution	<ul style="list-style-type: none"> - High accuracy - Provides 2 components - Provides corrections for non-equilibrium condition 	<ul style="list-style-type: none"> - Only for far wake - No spanwise component - Higher computational cost more complex
Frandsen [25]	Mass and 1D momentum conservation	Top-hat	Non-linear ($\propto x^{\frac{1}{2}}$)	<ul style="list-style-type: none"> - Low cost - Easy application - Good predictions in far wake 	<ul style="list-style-type: none"> - Self similarity in near wake - No radial variation - Pressure equilibrium neglected
Fuga [75]	RANS for quasi-steady case	Non-constant	Based on solution	<ul style="list-style-type: none"> - Low cost due to look-up tables - Simplified by linearization - Extremely robust 	<ul style="list-style-type: none"> - Complex - Assumption on eddy viscosity - Unable to replicate meandering (straight wakes)
BPA [10]	Mass and momentum conservation	Gaussian	Linear	<ul style="list-style-type: none"> - Based on previous models limitations - One component along 2 directions - Good accuracy in the far wake 	<ul style="list-style-type: none"> - Only for far wake - Wrong assumption for defining onset values - Wake decay constant needs to be tuned
BPA yawed [11]	Mass conservation and RANS	Gaussian	Linear	<ul style="list-style-type: none"> - Allows to describe wake's centre deflection - Good prediction of onset values - Good accuracy in far wake 	<ul style="list-style-type: none"> - Only for far wake - No account for pressure equilibrium - Constant values assumed for near wake - Wake decay constant needs tuning

Table 2.1: Summary and comparison of existing wake models for HAWT

2.5. Wake modeling for VAWTs

As mentioned in Section (2.4) there are different methods with different levels of accuracy to replicate the field flow behind a VAWTs, as for HAWTs. The purpose of this model is to introduce and calculate the induced velocity along the wake in order to provide it to models discussed in Section (2.3).

2.5.1. Analytical wake models for VAWTs

Analytical models for VAWTs are based on the same considerations made for HAWTs in Section (2.4). However since the aerodynamics of VAWTs is more complex than the one of HAWTs, mainly due to the blades rotational effects, strong assumptions and simplifications are made. Nevertheless, this is a topic not totally explored yet because VAWTs are still less diffused than HAWTs and therefore the only existing analytical wake models for VAWTs are translations of the ones for HAWTs. For example the models proposed by [2, 77, 83] are substantial translations of HAWTs wake models discussed in Sections (2.4.1), (2.4.4) and (2.4.6) [10, 25, 43]. Unfortunately, using models that are not based on VAWTs aerodynamic phenomena results in neglecting some unique aspects of this kind of turbines that could lead to wrong results when modifying some parameters like the aspect ratio or the turbine type. In other words it is extremely common that such models do not show universal validity.

2.5.1.1. Lam & Peng model

Lam and Peng [51] proposed a new wake model for H-rotor wind turbines which is similar to Jensen's model with some interesting additions. In fact it aims to replicate the asymmetry of VAWT's wake by assuming a top-hat distribution and a bi-elliptical shape to describe the wake as seen in Figure 2.24. The expression for the velocity defect is built upon mass conservation. To replicate the asymmetry, the wake develops linearly

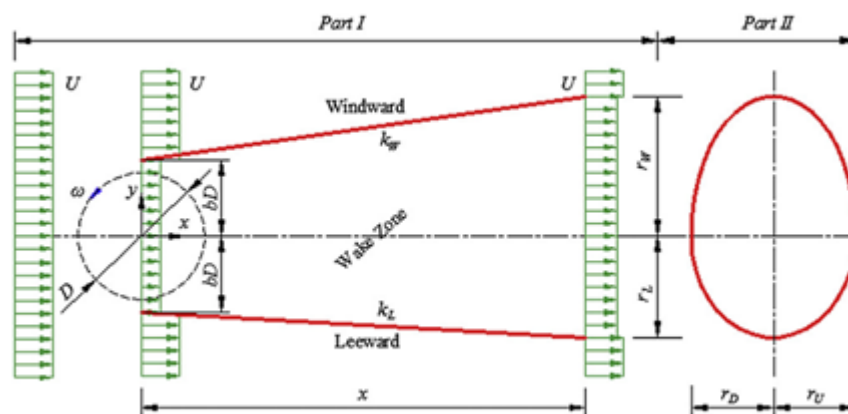


Figure 2.24: Geometry of the wake and flow field distribution in the Lam & Peng model [51]

according to 4 different coefficients (tuned with experimental data) k_W , k_D , k_U , k_L , one for each side of the wake (windward, downward, upward, leeward). One of the main assumptions states that k_U and k_D are assumed equal, so the wake maintains a top-bottom symmetric shape, while the others are different in order to replicate the left-right asymmetry, one of VAWTs' wake main features. More details about the equations used are reported in Appendix (B).

It is crucial to point out some limitations that afflict the model:

- The elliptical shape for the far wake, as demonstrated in the literature [97], is not correct since in the far wake the effect of the aspect ratio tends to disappear and the shape tends to be a circular one.
- Top-bottom symmetry is not correct if ground effect or the tower is considered.
- Using only mass conservation leads to a wrong expression for the side flows which violates the momentum equation.
- The wake shows a really strong asymmetry in the near wake region mainly due to the cross flows induced by a lateral force resulting from an asymmetric force distribution along the blades path. So as-

suming a circular-starting shaper for the wake (the edges are located at the same distances from the rotor for $x=0$) neglects the idea of replicating the asymmetry, moreover the frontal area of a VAWT is a rectangle.

- 3 different coefficients to express the wake expansion are needed and since their values are not universal, a tuning operation is needed.

Besides the disadvantages and the problems of this model is extremely simple and intuitive with a low computational cost and it showed good agreement with experimental data for the wake width and the velocity deficit predicted. It inherits all the pros of the Jensen model discussed in Section (2.4.1), but also its problems.

2.5.1.2. Abkar model

Abkar proposed two different models reported in [2] and valid for H-rotors only. One features a top-hat velocity deficit distribution and the other a Gaussian distribution. These models are a translation of Jensen [43] and BPA [10] models for HAWTs. They both assume a linear expansion of the wake according to a wake decay parameter that needs to be tuned because its value depends on the case analysed, as for the other models. The starting equations are the mass conservation for the top-hat model and the momentum equation for the Gaussian model.

It is relevant to underline that using only the mass conservation leads to a wrong expression for the side flows, since it violates the momentum conservation and the top-hat distribution is a strong limitation and not realistic. Moreover the related paper proposes the same growth rates along both vertical and spanwise directions that leads to a symmetrical shape for the wake. As far as is known, this is not true because of the presence of the struts and the tower but especially of the ground. In the same time, it is correct to assume a circular shape in the Gaussian case for the wake in far region, according to [97]. This assumption is valid only for the Gaussian model, while the top-hat assumes a rectangular shape, which is not realistic. It is also necessary to point out that the Gaussian distribution is not correct for the near wake, and the starting values at the onset point are based on the same procedure from [10] (which in turns is based on [25]), so the region with pressure gradients is neglected.

The predictions of the wake models are accurate especially in the far wake for the Gaussian distribution. However, when simulating turbines with high aspect ratios, discrepancies were observed especially concerning the profiles along spanwise direction. This occurs because the velocity defect along this direction does not show a full Gaussian distribution just behind the turbine. Moreover, using the same wake growth rates along both spanwise and crossflow directions means neglecting wake asymmetry in the near wake. Some of the limits of this model that could be improved, according to the theory, can be summarized:

- Neglecting wake asymmetry is a correct idea for the very far wake region, however a certain amount of the asymmetry needs to be taken into account also in the first part of this region because of CVPs action which is totally neglected here.
- Symmetric shape of the wake at the start means neglecting the lateral forces due to blades rotation and the subsequent asymmetry, which is one the most relevant features of VAWTs' wake. No account to rotational effects and deflection is given at all.
- It is necessary to provide the wake decay constants. This requires a tuning operation, since they depend on the case analysed.

These two models are extremely relevant for the purpose of this thesis. A numerical version of both of them has been developed and validated against numerical simulations featuring URANS equations and actuator line modelling for VAWT (according to [8, 65, 104]) as well as against literature data.

Why choosing this model, if its features different problems and inaccuracies? Among VAWTs wake models, it provides the highest accuracy and when compared to Lam & Peng model, the required inputs are less (only 1 against 3) simplifying the calculations during preliminary design studies. Moreover the assumption of a circular wake in the far wake is much more realistic than an elliptical shape and assuming different growth parameters for each side is not the best idea to replicate asymmetry, since from a certain location downstream asymmetry is no more relevant. Coupled with the top-hat model it can overcome the problem of not being valid in the near wake region. In fact the values predicted there, as well as wake's extension are much more similar to top-hat wake models predictions. This solution is also valid to overcome Gaussian's model

inaccuracy when ARs values are high. Specific details about the structure of both the model are reported in Chapter (3).

2.5.1.3. Ouro models

Ouro et al. [77] proposed two different models similar to the ones proposed by [10] and [25]. However there are several novelties respect with previous models:

- The proposed models distinguish between two length scales which express the wake expansion: one related to the diameter D_w and one related to the height H_w . The product between them returns the cross sectional area of the wake A_w for each downstream position.
- The wake evolution starts at an onset point (crucial for the Gaussian model) named x_a , where the pressure equilibrium is reached. This point is located at $x_a = 0.5D$, here the near wake region ends.
- One of the most relevant novelties of this model are the two different growth rates for the horizontal and spanwise direction (k_{wy} and k_{wz} respectively) to keep into account the different phenomena which occurs along these directions:
 1. Along the horizontal direction the main entrainment comes from the vortices generated from the blades
 2. Along the spanwise direction, shear layers (generated from tip vortices) have the most relevant role in the entrainment process

Following these assumptions, two different wake models are proposed and built upon momentum balance and RANS equations where pressure and viscous terms were neglected (details in Appendix (B)). The first model features a top-hat distribution for the velocity deficit, while the other one features a Gaussian distribution, after having assumed self-similarity. Wake's width development is not the same for both cases, for the top-hat model it is a non-linear wake development (similar to the one proposed by Frandsen [25]) while in the second case a linear development is assumed. In both cases however, it is necessary to provide the wake decay constants, and since they are assumed different along vertical and crossflow direction, 4 different constants need to be determined empirically since the expressions provided are not universal. It is also necessary to point out that in both cases the location of the onset point is always present, this means that it is impossible to use this model for the near wake region. At the same time however, values at this point are calculated with the actuator disk theory which is not so accurate, lowering the overall quality of the predictions.

As for previous ones, the limitations of these models are analysed. First of all the onset point is assumed to be located at $x_a = 0.5$. This means that up to this point the pressure gradients are not relevant, but as far as is known, there is still not a clear definition for VAWTs about where the near wake region really ends. In order to find the wake area at the onset point the actuator disk theory is used. This theory however provides a value for the area just behind the rotor and not at a distance of $0.5D$. This way the value obtained for wake's start is related to a region where pressure equilibrium has not been reached yet, similarly to assuming a core zone with constant values like what has been done by Bastankhah and Porté-Agel [11]. Moreover no account is given to the rotational effect and the deflection experienced by the wake in the near wake. So even if the asymmetry in the $x - z$ plane is replicated, no attempt to reproduce the wake asymmetry (especially in the near wake) in the $x - y$ plan has been tried. An additional problem are the 4 constants that are needed to complete the model and describe wake's development. Since the equations provided to calculate them are not universal, it's necessary to tune them with data, similarly to what is done for the other models.

However the results obtained from this model were sufficiently accurate in several conditions tested (different thrust coefficients, different TSRs ...). The only case in which the accuracy decreases is for high ARs, where the Gaussian assumption is not totally correct along vertical direction as already observed by Abkar [2].

Model	Starting equations	Velocity distribution	Wake width development	Pro	Cons
Lam & Peng [51]	Mass conservation	Top-hat	Linear	<ul style="list-style-type: none"> - Considers the asymmetry in the wake - Simple, low cost 	<ul style="list-style-type: none"> - Only for far wake - No vertical asymmetry - 2 decay constants do be tuned - Asymmetry not correct in far wake - Starting shape not correct - Bi-elliptical shape in far wake
Abkar [2]	Mass and momentum conservation	Top-hat and Gaussian	Linear	<ul style="list-style-type: none"> - Easy application and low cost (top-hat) - Good predictions in the far wake (Gaussian) - Circular shape for far wake (Gaussian) - Possible asymmetry along crossflow and spanwise direction (Gaussian) 	<ul style="list-style-type: none"> - Only for H rotors - No account for asymmetry - Rectangular shape (top-hat) - Provides only 1 component (top-hat) - Uses only mass conservation (top-hat) - Only far wake (Gaussian) - Not correct onset values - Low accuracy at high AR
Ouro [77]	RANS and momentum equation	Top-hat and Gaussian	(Top-Hat) Non Linear (Gaussian) Linear	<ul style="list-style-type: none"> - Defines onset point - Potential asymmetry along crossflow and spanwise directions - Easy and low cost - Accurate in far wake 	<ul style="list-style-type: none"> - Only for far wake - Actuator disk theory for onset values (like Frandsen) - No horizontal asymmetry - Rectangular shape for the wake (top-hat) - Wake decay constants not universal

Table 2.2: Summary and comparison of existing wake models for VAWT

2.5.2. Vortex models

Models that are a trade-off between CFD and actuator models. The first model was developed by Strickland et al. [107] and such class of models is capable of replicating wake's dynamics and the related induction effects starting from the vorticity equations (derived from the Navier-Stokes equations). This way is possible to obtain the relative velocity at the blades. Unlike other models, this is a model that has to be solved in time, so it gives an unsteady solution.

Such models are based on Helmholtz's and Kelvin's theorems. The former states that circulation is constant along a vortex line and must form a closed path, without the possibility of ending in the fluid. The second one states that the time rate of change of circulation in a closed loop must be zero. On account of that, blades can be modelled as a 2D lifting line located at the quarter chord point while wakes are modelled with series of vortex points in 2D or with vortex lattice generated by overlapped vortex rings in 3D, this leads to a specific influence on the inflow condition for the blades. However different possibilities to replicate airfoil's presence have been introduced, for example using sources and doubles in [103] or sources and vorticity distributions [111] in order to simulate the lifting surface: there is a great amount of possible solutions and different methods.

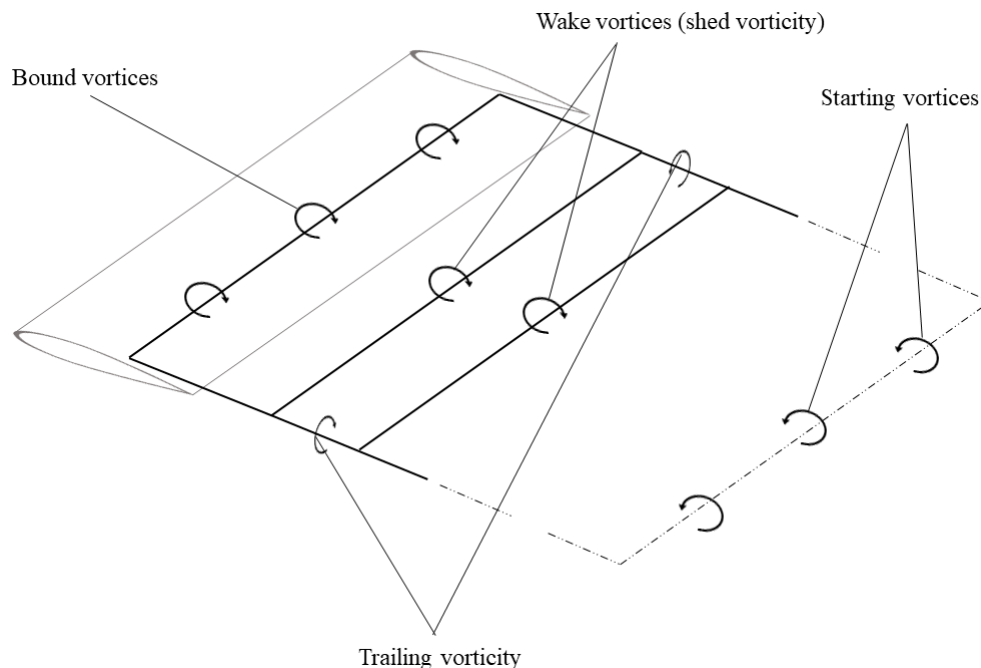


Figure 2.25: Schematic of how the blade and the vortex structures are replicated in a vortex model

Once the induced velocity has been evaluated using the Biot-Savart law (that allows to evaluate the velocity induced by a vortex filament at each possible point), it is used (with the rotational velocity) to calculate the angle of attack, essential in order to figure out the amount of lift and drag from the look-up tables. This procedure can be accomplished using the BEM theory that can be combined with the current model. Most of the times, vortex models are substituted by panels methods, which do not require the use of look-up table but instead use specific equations to determine the loads. Such models however do not keep into account viscous effects that have to be modelled with additional tools. The same happens for the dynamic stall phenomenon. Vortex and panel methods are able to replicate highly loaded rotors for high TSRs and most especially they are able to provide information regarding near wake's shape. However such models lack the ability of modelling blade-vortex interactions and the subsequent effects on lift and drag coefficients evaluated.

2.5.3. RANS models

RANS equations are based on statistical approach and a decomposition of quantities into mean values and fluctuations. By solving them it is possible to obtain only mean values but the computational cost is low compared to DNS or LES simulations. When dealing with wind turbines they can be coupled with actuator models to represent turbine's influence on the flow or the physical geometry (as a CAD file) can be introduced

in the control volume. The former solution is preferred in order to maintain a low computational cost. Another problem when dealing with RANS is that an extremely complex term is 'generated' from the non-linear inertial terms of the starting equations. This term represents the turbulence stresses and needs to be modelled. For this reason turbulence models are introduced as closure models in order to equate the number of unknowns and equations at disposal. There are many existing turbulence models, the most common ones are grouped according to the number of equations used:

1. Zero-equation models, Prandtl's mixing length model
2. One-equation models
3. Two-equation models, like the $k - \epsilon$, the $k - \omega$ and the $k - \omega$ SST model. These are the most common ones.

A brief comparison of the turbulence models is reported in Table (2.3). For more details the reader is referred

	Prandtl's mixing length	$k - \epsilon$	$k - \omega$	$k - \omega$ SST
Based on	Algebraic expression for eddy viscosity's length scale	Transport equation for k and ϵ	Transport equation for k and ω	Merging of $k - \epsilon$ and $k - \omega$ model
Pro	- Extremely simple and immediate, only requires the mixing length	- Keeps into account eddy viscosity transport - Extremely suitable for high Re cases	- Keeps into account eddy viscosity transport - Doesn't need empirical function to account for viscosity dumping effect	- Suitable for every possible condition - Best results achieved
Cons	- Mixing length has to be specified and the appropriate expression depends on the geometry of the flow - Turbulent viscosity isn't constant, it's a property transported by the flow not depending only on y	- Empirical functions without universal validity - Inaccuracy with low Reynolds' numbers - Inaccuracy with adverse pressure gradients, separation and reattachment	- Depends on the inflow conditions - μ_t and c_f are affected by inflow conditions	- Complex

Table 2.3: Comparison between turbulence methods

to Chapter (3) to learn more about the RANS which has been used. Further details can be found also in [85, 109, 112, 117], which have been the basis to understand turbulence models and deciding which was more appropriate for the current study.

Mean values are obtained when solving the RANS equations. Such approach is not the best when dealing with VAWTs: even being computationally economic, RANS are not accurate enough to capture flow separation experienced by the blades, as well as the vortices generated by dynamic stall. In the end, poor performance are shown by RANS equations in vortex modelling. However, if it is accept to neglect all the effects related to blades rotation maintaining the focus on mean quantities only (especially in far wake), this is one of the best choices, considering the computational cost-accuracy ratio. Moreover, the choice is motivated also by the fact that numerical simulations in this study are used as a comparison for analytical wake models which are reliable only in the far wake.

Several studies about VAWTs have been accomplished using RANS equations. Some of them are [14, 15, 26, 30, 35, 61, 74, 121]. The reader is referred to these papers for more details while to Chapter (3) to learn more about RANS and how they have been used in this thesis.

3

Methods

In this Chapter the approach used is presented and described in details. The first section deals with the URANS coupled with actuator line model simulation, describing with precision both the aspects with particular focus on the numerical numerical approach used in OpenFOAM [116] to solve the equations, as well as the inner structure of the actuator line model and how it is implemented, along its sub-models, in turbinesFoam library. Second section explores the analytical wake models used for both HAWTs and VAWTs, introducing the wake decay constant dilemma. A brief description of how wake models are implemented in py-wake library [82] and its structure is provided as well.

3.1. Numerical simulation of the wake of VAWTs

URANS equations have been coupled with the actuator line used to test wind turbines of different scales. This way has been possible to obtain a high fidelity model to be compared with analytical wake models. In order to perform the numerical simulations, the free-source software OpenFOAM was and especially its library turbinesFoam [7]. Both of them will be discussed in details in this section.

3.1.1. URANS equations

The numerical simulations are performed starting from a specific set of equations used to model the represent the flow field. In Chapter (2) both LES and RANS were discussed, as well as their pro and cons. On account of the cases studied, the URANS equations have been chosen. They are substantially RANS equations but with a specific addition concerning the temporal aspect of the phenomena that will be discussed afterwards. As already mentioned RANS (and also URANS) are based on a statistical approach towards the turbulence. In fact because of the random velocity fluctuations, the extreme complexity of turbulent flows as well as the impossibility of exactly computing velocity components due to the high Reynolds' number, main quantities are decomposed into mean values and fluctuations with zero mean giving birth to the Reynolds equations or Reynolds Averaged Navier Stokes equations (RANS).

The mentioned decomposition is applied to all the main quantities (pressure, velocity and so on):

$$u = \bar{u} + u' \quad (3.1)$$

$$v = \bar{v} + v' \quad (3.2)$$

$$w = \bar{w} + w' \quad (3.3)$$

$$p = \bar{p} + p' \quad (3.4)$$

Such quantities are introduced in the Reynolds averaged Navier-Stokes equations. Many of the terms can be eliminated and the resulting equations for an incompressible case are:

$$\frac{\partial \bar{u}}{\partial x} + \frac{\partial \bar{v}}{\partial y} + \frac{\partial \bar{w}}{\partial z} = \frac{\partial u'}{\partial x} + \frac{\partial v'}{\partial y} + \frac{\partial w'}{\partial z} = 0 \quad (3.5)$$

$$\rho \frac{D\bar{V}}{Dt} = \rho g - \nabla \bar{p} + \mu \nabla^2 \bar{V} - \rho \frac{\partial}{\partial x_j} \left(\overline{u'_i u'_j} \right) + \bar{f}_i = \rho g - \nabla \bar{p} + \nabla \cdot \tau_{ij} + \bar{f}_i \quad (3.6)$$

$$\tau_{ij} = \mu \left(\frac{\partial u_i}{\partial x_j} + \frac{\partial u_j}{\partial x_i} \right) - \rho \overline{u'_i u'_j} \quad (3.7)$$

In the momentum equation (3.6) the Reynolds stresses tensor $\rho \overline{u'_i u'_j}$ emerges. This is a symmetric never negligible tensor that depicts the effect of the velocity fluctuations on the mean flow and is generated by the non-linearity of the Navier-Stokes equations. More specifically, it is generated from the correlation of two velocity fluctuation components at the same point. It consists of the normal stresses along the diagonal, which do not demonstrate a relevant contribute to mean momentum's transport, and the off-diagonal components which are dominant in momentum transported by turbulent motion. This term is the source of analytic difficulties in equations' resolution since its analytic form is not known. Moreover this way many unknown quantities, related to the turbulent structures, are introduced, exceeding the number of equations at disposal. In fact tensor's components are related to both the fluid physical properties and the local flow conditions. No analytic expressions are known to solve the problem, up to now. The equations at disposal are not enough (4 equations, excluding the energy one, against 10 unknown quantities), therefore it is necessary to introduce a closure method based on additional relations or empirical models for turbulent cases. Similar models only replicate and emulate turbulence effects on the flow field, they do not provide exact results. One of the relation that can be added is the one for the turbulent kinetic energy k and its conservation:

$$k = \frac{1}{2} \left(\overline{u' u'} + \overline{v' v'} + \overline{w' w'} \right) = \frac{1}{2} \overline{u'_i u'_i} \quad (3.8)$$

$$\frac{Dk}{Dt} = - \frac{\partial}{\partial x_i} \left[\overline{u'_i \left(\frac{1}{2} u'_j u'_j + \frac{p'}{\rho} \right)} \right] - \overline{u'_i u'_j} \frac{\partial \bar{u}_j}{\partial x_i} + \frac{\partial}{\partial x_i} \left[\overline{v u'_j \left(\frac{\partial u'_i}{\partial x_j} + \frac{\partial u'_j}{\partial x_i} \right)} \right] - \overline{v} \frac{\partial u'_j}{\partial x_i} \left(\frac{\partial u'_i}{\partial x_j} + \frac{\partial u'_j}{\partial x_i} \right) \quad (3.9)$$

Turbulent kinetic energy exhibits considerable relevance when dealing with turbulent flows because it plays a major role in characterizing the flow field. However even if two equations were added, the last terms present are extremely difficult to be evaluated, therefore (as stated before) closure models are needed.

Regarding the last term in momentum equation (3.6), the turbine can be included as a geometrical model or its presence can be modelled within the volume forces term. In this thesis the actuator line plays an important part since models and provide the source term in the equations. This way is possible to maintain a low computational cost. Other terms will be solved numerically and need to be discretized according to the procedure reported in Section (3.1.1.5).

3.1.1.1. The unsteady aspect

It has been mentioned about using URANS and not RANS simulation, but they present several differences. The latter are very limited but relevant when dealing with unsteady flows. In fact turbulent flows in complex geometries often show oscillating behaviour of large coherent structures, even when considering steady state boundary condition [37, 69, 93]. One of the possible ways to numerically solve these oscillations are LES, that might be too computationally expensive (and not part of this thesis), or URANS equations, which have pro and cons. They are used when long-term periodical oscillations are observed in a turbulent flow and the flow is not statistically stationary. This is the case of the flow past a wind turbine, for example, for which URANS allows to solve frequencies and profiles of large-scale coherent structures which helps in increasing the accuracy of the calculation. In other words, URANS can resolve unsteady mean-flow large scale structures, typical of an unsteady periodical flow. How to deal with a similar unsteady flow? The difference in the approach compared to RANS is simply based on a definition. While mean quantities are time (and also spatial) averaged in RANS equations, leading to a constant mean value in time, in URANS, since the flow is unsteady, the mean value changes over time as simply visualized in Figure (3.1). In this case averaged components obtained are function of time. In order to track their evolution an ensemble average is required. In fact the properties of a random process can be evaluated using ensemble averages (mean values) at specific instants. So the main difference between RANS and URANS lies in the average function applied to the quantities. The exact definition of the ensemble average is:

$$\bar{\phi}(\vec{x}, t) = \lim_{N \rightarrow \infty} \frac{1}{N} \sum_1^N \phi(\vec{x}, t) \quad (3.10)$$

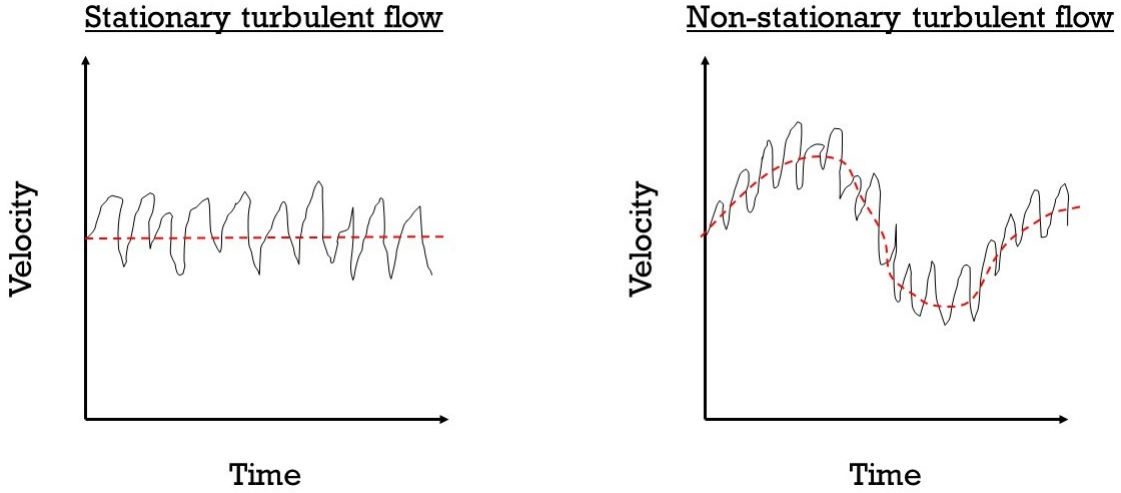


Figure 3.1: Difference in the mean value for a steady and unsteady state condition

Such operation is automatically performed by OpenFOAM itself. In simple words ensemble averaging means that if the time of sampling is long enough compared to fluctuations' time scale and sufficiently small compared with the time scale of the main phenomena in the flow, it is possible that the mean value changes in time, following the evolution of the largest scales, while the smallest are not resolved. However, increasing the accuracy of the solution means inevitably increasing the computational cost of the simulations.

3.1.1.2. Turbulence model

As mentioned before, the turbulence show great impact on the resultant flow field, the accuracy reached as well as the required computational resources and time. So it is an aspect that needs to be studied with attention, to avoid any possible numerical error. In fact there is no strict correlation between turbulence modelling, that deals with parameters that do not show a real counterpart, and real life turbulence. So it is necessary to deal with the choice of the model and the parameters used carefully .

There are many different turbulence models that can be used, more or less complex depending on the number of equations adopted. The main groups are:

1. Zero-equation models: which feature only an additional algebraic equation for the eddy-viscosity used to model turbulent stresses similarly to viscous stresses by using the gradient expressions (even if they are extremely different). For a 2D case for example (boundary layer flow):

$$\tau_t = -\rho \overline{u'v'} = \mu_t \frac{\partial \bar{u}}{\partial y} \quad (3.11)$$

μ_t is the eddy viscosity, which is not a fluid property but depends on flow conditions and geometry (the eddies). There are many expressions for this parameter, one of the most common comes from the mixing-length theory which relates every turbulent fluctuation to a length scale and a velocity gradient:

$$-\overline{u'v'} \approx (const) u'_{rms} v'_{rms} \approx (const) \left(l_1 \frac{\partial \bar{u}}{\partial y} \right) \left(l_2 \frac{\partial \bar{u}}{\partial y} \right) \quad (3.12)$$

$$\mu_t \approx \rho l^2 \left| \frac{\partial \bar{u}}{\partial y} \right| \quad (3.13)$$

Where l_1 and l_2 are the mixing lengths, which are related to eddy size. Assuming $l_1 = l_2 = l$, it is possible to provide some expressions for l depending on flow conditions:

- In sublayer:

$$l \approx y^2 = l_a \quad (3.14)$$

- In the overlap layer:

$$l \approx ky = l_b \quad (3.15)$$

- In the outer layer:

$$l \approx \text{constant} = l_{\text{outlayer}} \quad (3.16)$$

Additional relations for l in these cases are provided by the literature to keep into account how l changes moving away from the wall (Van Driest correction):

$$l_{a,b} \approx ky \left[1 - e^{\left(-\frac{y^+}{A}\right)} \right] \quad (3.17)$$

$$l_{\text{outlayer}} \approx 0.09\delta \quad (3.18)$$

Where A is a constant, δ is the boundary layer width and y^+ the viscosity units. This way is possible to take into account the viscosity dumping action on the eddies. Introducing such expressions in previous equations, the model is able to provide good accuracy in the complete velocity profile, by assuming a linear relation between Reynolds stresses and the mean rate-of-strain tensor S_{ij} . However the model is unable to compute the turbulent energy or the fluctuating components. Moreover it is an incomplete model, since the mixing length has to be specified and the appropriate expression depends on the geometry of the flow. Most importantly, the turbulent viscosity cannot be assumed constant, since it is a property which is transported by the flow and cannot depend only on y . For this reason a step forward is the introduction of transport equations for k and ε .

2. One-equation model: which introduces equations for the turbulent kinetic energy and the eddy viscosity. Introducing L as turbulence length scale or effective eddy size, a random eddy in the flow would have a velocity scale equal to $k^{\frac{1}{2}}$ and consequently the following dissipation rate:

$$\varepsilon \approx (\text{const}) \frac{k^{\frac{3}{2}}}{L} \quad (3.19)$$

Assuming, in equation (3.20) that first term at right hand side is akin to gradient diffusion (as shown in equation (3.21)), equation (3.20) becomes:

$$\bar{u} \frac{\partial k}{\partial x} + \bar{v} \frac{\partial k}{\partial y} \approx - \frac{\partial}{\partial y} \left[\overline{v' \left(\frac{1}{2} u'_i u'_i + \frac{p'}{\rho} \right)} \right] + \frac{\tau}{\rho} \frac{\partial \bar{u}}{\partial y} - \varepsilon \quad (3.20)$$

$$- \overline{v' \left(\frac{1}{2} u'_i u'_i + \frac{p'}{\rho} \right)} \approx (\text{const}) \frac{\partial k}{\partial y} \quad (3.21)$$

$$\bar{u} \frac{\partial k}{\partial x} + \bar{v} \frac{\partial k}{\partial y} \approx \left[(\text{const}) \frac{\partial k}{\partial y} \right] + v_t \left(\frac{\partial \bar{u}}{\partial y} \right)^2 - (\text{const}) \frac{k^{\frac{3}{2}}}{L} \quad (3.22)$$

Which needs to be added to previous equations as well as an additional expression for the turbulence length scale. The latter can be assumed to be the mixing length seen in the previous model. The results however are not such an improvement respect to the ones obtained from the zero-equation model.

3. Two-equation model, $K - \varepsilon$: based on equation (3.22) for the turbulent kinetic energy and an additional one for the turbulence dissipation. Using these values is possible to evaluate a length-scale, a time-scale and a quantity similar to the eddy viscosity, without the need of having an expression for the mixing-length scale.

This is one of the most commonly used and complete turbulence model and is based on the following equations:

$$\frac{Dk}{Dt} \approx \frac{\partial}{\partial x_j} \left(\frac{v_t}{\sigma_k} \frac{\partial k}{\partial x_j} \right) + v_t \frac{\partial \bar{u}_i}{\partial x_j} \left(\frac{\partial \bar{u}_i}{\partial x_j} + \frac{\partial \bar{u}_j}{\partial x_i} \right) - \varepsilon \quad (3.23)$$

$$\frac{D\varepsilon}{Dt} \approx \frac{\partial}{\partial x_j} \left(\frac{v_t}{\sigma_\varepsilon} \frac{\partial \varepsilon}{\partial x_j} \right) + C_t v_t \frac{\varepsilon}{k} \frac{\partial \bar{u}_i}{\partial x_j} \left(\frac{\partial \bar{u}_i}{\partial x_j} + \frac{\partial \bar{u}_j}{\partial x_i} \right) - C_2 \frac{\varepsilon^2}{k} \quad (3.24)$$

Where σ_k and σ_ε are effective Prandtl numbers and correlate the eddy diffusion of k and ε to the momentum eddy viscosity which is modelled as follows:

$$\sigma_k = \frac{\nu_t}{\nu_k} \quad (3.25)$$

$$\sigma_\varepsilon = \frac{\nu_t}{\nu_\varepsilon} \quad (3.26)$$

$$\nu_t \approx \frac{C_\mu k^2}{\varepsilon} \quad (3.27)$$

The empirical constants show specific values depending on the case analysed. Moreover there are some empirical equations that need to be applied to the constants and allow to keep into account viscosity's effect on k and ε when near wall region is considered. However, even if $k-\varepsilon$ model is accurate for simple flows, it can be quite inaccurate for complex flows where walls are present, mainly because of the turbulent viscosity, the ε equation but especially when adverse pressure gradients are experienced. Furthermore, the empirical functions applied to the constants are not universal, and depend on the flow considered. However the model perfectly fits high Reynolds number cases, where separation and reattachment do not occur.

4. Two-equation model, $k-\omega$: model used for inhomogeneous flows, where $\omega = \frac{\varepsilon}{k}$, the specific dissipation rate, is introduced. Based on the equation:

$$\frac{\overline{D}\omega}{\overline{D}t} = \nabla \cdot \left(\frac{\nu_t}{\sigma_\omega \nabla \omega} \right) + (C_{\varepsilon 1} - 1) \frac{P\omega}{k} - (C_{\varepsilon 2} - 1) \omega^2 + \frac{2\nu_t}{\sigma_\omega k} \nabla \omega \cdot \nabla k \quad (3.28)$$

Where $C_{\varepsilon 1}, C_{\varepsilon 2}$ are constants, $\sigma_\omega = \sigma_k = \sigma_\varepsilon$ and $P = \frac{\partial \overline{u}_i}{\partial x_j} \left(\frac{\partial \overline{u}_i}{\partial x_j} + \frac{\partial \overline{u}_j}{\partial x_i} \right)$. It differs just for the last term (in case of inhomogeneous flows) from the same equation obtained for $k-\varepsilon$ model. The equations used are the ones for k (3.23) and ν_t (3.27) and the previous one for ω , which substitutes the one for ε . This model is the second most widely used and is superior in how it deals with both the viscous near wall region as well as the effects of the pressure gradients. No empirical functions to model viscosity effects on the constants are needed. However it's less accurate when dealing with non-turbulent free stream boundaries because of its extreme sensitivity on inflow conditions: minimal changes in k_∞ leads to major changes on μ_t or ν_t and on the c_f , the friction coefficient.

5. Two-equation model, $k-\omega$ SST: is a model that couples the $k-\varepsilon$ and $k-\omega$ to overcome their limits. Since the two models when formulated differ for just one term, it is possible to introduce a function F_1 to smoothly change from one model to the other according to the region considered.

$$\frac{\overline{D}\omega}{\overline{D}t} = \nabla \cdot \left(\frac{\nu_t}{\sigma_\omega \nabla \omega} \right) + (C_{\varepsilon 1} - 1) \frac{P\omega}{k} - (C_{\varepsilon 2} - 1) \omega^2 + (1 - F_1) \frac{2\nu_t}{\sigma_\omega k} \nabla \omega \cdot \nabla k \quad (3.29)$$

When the near wall region is considered, F_1 assumes a value (1) that 'deletes' the additional term, so the $k-\omega$ model is used. Considering instead the flow outside the boundary layer, F_1 makes possible to maintain the additional term and use the $k-\varepsilon$ consequently $F_1 = 0$. The F_1 function shows a smooth transition all over the domain, so even in the border region it is possible to obtain good results. Such function displays an hyperbolic expression that depends on the distance from the wall. Moreover, a limited viscosity is considered, with a second function F_2 which aims to limit the turbulent viscosity in order to avoid unrealistic high values of μ_t due to erroneous values of wall shear stress evaluated. Obviously such model achieves the best results compared to the previous ones but is much more complex.

First models are simple but they lack in both physical content and accuracy, while newer models are more accurate but also more complex. But the choice of the turbulence model to be used is straightforward. Keeping into account their pro and cons and in which occasion is better to use one model or the other, the model chosen was the $k-\varepsilon$ model for one main reason: the only weak point of this model is its inability to perform accurate prediction in case of adverse pressure gradients, separation and reattachment which all happen in case of walls' presence. Therefore such model is inaccurate with low Reynolds' number, when such phenomena are experienced more easily. However in the cases analysed by the current thesis the problem is totally overcome because of the total absence of walls: the blades are not physically presents, they are represented

$k - \varepsilon$ coefficients used	
σ_k	1
σ_ε	1.3
C_1	1.44
C_2	1.92
C_μ	0.09

Table 3.1: Coefficients used for the $k - \varepsilon$ model in the current study

just as lines and as force sources added in the equations. For such reason the model is the most suitable for the current study and using the $k - \omega$ model which is extremely sensitive to inflow's conditions variations is pointless. Moreover the $k - \omega$ SST model is not necessary, since there is no necessity to merge the two models to overcome the limitations of the $k - \varepsilon$, which are not encountered. This allows to avoid further complexity and additional computational cost. The easiest model, based on Prandtl' mixing length is not used, because it is the least accurate and turbulence mixing needs to be modelled as best as possible, since it is a crucial aspect when considering VAWTs and especially the recovery in the wake discussed in Section (2.2.3). The coefficients used in the model for all the cases are reported in Table (3.1) and are the most up-to-date provided by Launder & Sharma [55]. Nevertheless, some attempts of using also the $k - \omega$ were carried out, with no major improvements seen in the results.

3.1.1.3. The inflow condition

It is necessary to spend a few words discussing about the boundary conditions at the inlet for the turbulent kinetic energy k and the dissipation rate ε , since the $k - \varepsilon$ model will be used. The values are set according to two different empirical equations proposed in the literature [85] as well as in OpenFOAM guide [116]. The equation for k is:

$$k = \frac{3}{2} (V_{ref} I)^2 \quad (3.30)$$

This comes from the definition of the turbulence intensity:

$$I = \frac{\sqrt{\frac{u'^2 + v'^2 + w'^2}{3}}}{V_{ref}} = \frac{\sqrt{\frac{2k}{3}}}{V_{ref}} \quad (3.31)$$

Equation (3.30) can be used only for isotropic turbulence. The dissipation rate can be expressed as:

$$\varepsilon = \frac{C_\mu k^{\frac{3}{2}}}{L} \quad (3.32)$$

Where C_μ is a constant of the model, set to 0.09 and L is a reference turbulent length.

It is crucial to underline that the values predicted by these equations are only initial estimates and the relations are not exact but only empirical. Especially regarding the turbulent kinematic energy the relation with turbulence intensity, it is not 'direct' and the k is more sensitive to the range of I used, and not the exact value. This happens because the values used do not necessarily have a physical meaning and the whole model just tries to emulate how the turbulence behaves. This leads to some problems when testing the different cases since the exact values of turbulence intensities are not used in the simulations. Another relevant aspect is that in order to realise a constant turbulence intensity all over the domain, is possible to set an extremely low ε in order to avoid turbulence dissipation and replicating as best as possible the environmental turbulence intensity.

3.1.1.4. Numerical approach

It is necessary to discuss about the numerical resolution of the equations, which, in this thesis, is based on the open-source software OpenFOAM [116], as already mentioned. It is able to solve RANS equations (as well as many other kind of equations) in an infinite amount of different possible ways. Many information as well as material about the software can be found on the web or in the guide [116], however this is not the aim of the thesis. The target of this section is to discuss about the solving process chosen in the library used. There are many possible approaches to perform numerical calculations:

- Finite differences
- Finite elements
- Finite volumes

In our case the chosen approach is the third one. This implies that the equations used are exactly the conservation equations and not a weak form of them which loses its physical meaning. Such equations are expressed in their integral forms and integrated across each cell into which the computational domain is split. The quantities that have to be computed (velocity, pressure and so on) are calculated using a specific scheme and by converting volume integrals to surface integrals. Then are distributed along each cell but it is necessary to evaluate the fluxes and the values at cells' faces. The latter step is carried out by the discretization process. Why using the finite volumes approach? There are several reasons to do it, first of all it is the best method when dealing with fluid dynamics simulations because it ensures the respect of the conservation laws which are directly resolved. Therefore the physical meaning of the problem is defended and it is easier to understand what is physically happening. Moreover, the coding version of such method is simple and saves computational time.

3.1.1.5. Discretization

Starting from a generic momentum conservation equation with ϕ as generic variable:

$$\int_{V_{ol}} \frac{\partial}{\partial t} (\rho\phi) dV_{ol} + \int_{V_{ol}} \nabla \cdot (\rho\phi \vec{V}) dV_{ol} = \int_{V_{ol}} \nabla \cdot (\Gamma \nabla \phi) dV_{ol} + \int_{V_{ol}} S_{\phi} dV_{ol} \quad (3.33)$$

Where the first is the unsteady term, the second one the convection term, the third one the diffusive term and the last one the term related to source terms that, for the current study is related to the force sources placed here by the actuator line model.

In the case studied, the equations are:

$$\int_{V_{ol}} \nabla \vec{V} dV_{ol} = 0 \quad (3.34)$$

$$\rho \int_{V_{ol}} \frac{\partial}{\partial t} (\vec{V}) dV_{ol} + \rho \int_{V_{ol}} \nabla \cdot (\vec{V} \vec{V}) dV_{ol} = \int_{V_{ol}} \nabla \cdot (\Gamma \nabla \vec{V}) dV_{ol} + \int_{V_{ol}} f dV_{ol} \quad (3.35)$$

The discretization operates on such equation in order to re-write it as a simple linear system:

$$A \vec{x} = \vec{b} \quad (3.36)$$

Where A is a matrix, \vec{x} represents the unknown variables and \vec{b} is the known term. Depending on which discretization scheme is used, A and \vec{b} change their expressions. It is necessary to provide both a **temporal scheme** to discretize time derivative and **spatial schemes** to discretize spatial derivatives and in particular gradients, divergences and laplacians.

In this thesis the discretization process used is the same for all the cases analysed but it is different according to the quantity which is considered. The temporal scheme used is the Euler scheme, which is implicit and therefore allows to 'avoid' the necessity of using a Courant number lower than one. Such scheme is a first order method used for unsteady cases and allows to discretize the time derivatives as reported in equation (3.37):

$$\frac{\partial \phi}{\partial t} = \frac{\phi - \phi_0}{\Delta t} \quad (3.37)$$

Where ϕ is a generic quantity and ϕ_0 is the same parameter at a previous time.

Spatial schemes are strictly related to interpolation schemes to compute values at cells' faces starting from the values at cells' centres. All of them are coupled with Gauss' theorem in order to convert volume integrals in surface integrals. However the discretization changes according to what term is considered:

- Gradient: the gradient which have to be discretize are for p and V . The gradient is defined as:

$$\nabla \phi = \frac{\partial}{\partial x_1} \phi \vec{i} + \frac{\partial}{\partial x_2} \phi \vec{j} + \frac{\partial}{\partial x_3} \phi \vec{k} \quad (3.38)$$

The gradient is firstly related to the divergence and than the Gauss' theorem is applied (equation (3.39)).

$$\int_V (\nabla \cdot \vec{V}) dV = \oint_S (\vec{n} \cdot \vec{V}) dS \quad (3.39)$$

In this case a linear interpolation is used in order to extrapolate faces' values. Moreover for V gradients an additional option is used: a limiter, which allows to obtain a value at cells' face that does not overcome the values of near cells that represent the limits. This way the smoothness of the distribution is ensured and does not lead to numerical errors. Using 1 as coefficient for this option, if the value at cell's face extrapolated by the tangent is higher than the one of the near cell, it is set equal to the latter.

- Divergence: divergence is defined as:

$$\nabla \cdot \vec{Q} = \frac{\partial Q_x}{\partial x} + \frac{\partial Q_y}{\partial y} + \frac{\partial Q_z}{\partial z} \quad (3.40)$$

Where \vec{Q} is a generic vector. The divergence appears especially in the convective term and it is related to surface integrals with Gauss' theorem (3.39) which represent the flux ϕ of a certain quantity across that surface. The discretization process depends on the quantity considered and it is not universal in this study:

1. $\phi(k, \varepsilon, v_T)$: first order method which features cells' faces values based on upstream velocity and its direction. This allows to understand where the 'information' are transported. It enables to assume cell values as isotropic with a value that represents the average value.
2. $\phi(V)$: a linear-upwind method is used, which is equivalent to the upwind method but with an additional correction based on velocity gradient in the cell.

For every case an additional 'bounded' option is provided, this allows to add a linear source term in the transport equations. Such term removes a component proportional to continuity error and speeds up the convergence process. Once convergence is reached, such term is removed.

- Laplacian: related to the diffusive term and discretized using the Gauss theorem (3.39). Here a linear interpolation scheme to transform coefficients from cell values to the faces is assumed as well as a surface-normal gradient scheme. The latter is extremely important and is used to express the component, normal to the face, of the gradient of values at the centres of the 2 cells that the face connects. Such calculation is based on subtracting the value at the cell centre on one side from the values in the centre of the other side and then dividing it by the distance. When the vector connecting the cells is orthogonal to the surfaces, gradient's evaluation is second order accurate but a regular mesh aligned with Cartesian coordinates is required. In current case (and in most of the cases) a correction to provide orthogonality is necessary, in order to ensure second order accuracy. Such correction is based on the angle between the cell-cell vector and the face normal vector. This is translated into a parameter ψ that ranges from 0 to 1 and here is set to 0.333, value that offers great stability.

3.1.1.6. Solver and convergence criteria

Once the matrix A and vector \vec{b} are created, it's necessary to solve the linear system. If A is a simple diagonal matrix, it is possible to invert it and calculate the solution:

$$\vec{x} = A^{-1} \vec{b} \quad (3.41)$$

However most of the times A features terms also outside of its diagonal. Therefore numerical solvers are introduced. Even here there could be many topics to discuss about, but again it is not the aim of this work. The most important thing to be remembered is that solvers allow to evaluate the solution of the system reducing as much as possible the computational cost. Solvers are coupled with smoothers in order to minimize possible numerical problems that can arise during the calculations and to avoid instability phenomena. The whole process is governed and triggered by residuals and both absolute and relative tolerance: in other terms the calculations proceed until a certain threshold is reached.

Even the solvers used for the linear systems are the same for all the cases analysed but they're different depending on the quantity considered: *GAMG* will be used for the pressure p while *smoothSolver* for the remaining quantities (V, k, ε, v_T).

Quantity	Tolerance values		Solver
	Absolute tolerance	Relative tolerance	
p	10^{-4}	0	GAMG
p_{corr}	10^{-6}	0.01	GAMG
p_{final}	10^{-6}	0	GAMG
V, k, ε, ν_T	10^{-6}	0.1	smoothSolver (Symmetric Gauss Seidel)
$(V, k, \varepsilon, \nu_T)_{final}$	–	0	smoothSolver (Symmetric Gauss Seidel)

Table 3.2: Tolerance values used during the calculations

1. *GAMG*: used for symmetric and asymmetric matrices. It is really efficient in transporting the information along the domain and is a multi-grid solver, therefore the solution is firstly evaluated in a coarse grid (provided by the used) which will then be used as a starting point when introducing a finer grid. Here the agglomeration operation is accomplished according to the option *faceAreaPair* where faces are identified and merged one to the other and the number of cells at the most coarse level is specified (here 10). A *DIC / GaussSeidel* smoother is then added to ensure that any possible 'spike' created during the solving process is smoothed-out.
2. *smoothSolver*: used for V, k, ε, ν_T , based on the symmetric Gauss-Seidel smoother.

The tolerance used depends on the values calculated by the solver during the various steps of the algorithm (which will be explained in the next section). However a summary of the value used (divided between solvers used) is reported in Table (3.2).

3.1.1.7. Solution algorithm

The equations are not solved just in one iteration but it is necessary to execute the calculations more and more times since the solver is an iterative solver that allows to close the gap to the exact solution step by step. Here the algorithm plays its role, determining the specific steps of the calculation process: it defines how the solver is applied and on which equations.

The algorithm used in *turbinesFoam* is the *pimple* algorithm which is used for incompressible cases with Newtonian fluids under transient turbulent conditions. The algorithm is a combination of two other algorithms, *piso* and *simple* algorithms:

- *PISO* algorithm: used for incompressible transient cases with turbulent flows. It features a time-explicit method and needs to satisfy a certain condition on the Courant number Co (equation (3.42)) which has to be lower than one, otherwise instability problems arise.

$$Co = \frac{V_{ref} \Delta t}{\Delta x} \quad (3.42)$$

- *SIMPLE* algorithm: used for incompressible cases with turbulence flows in a steady-state condition. There are no conditions to be satisfied regarding the Courant number.

Combining such algorithms, the problem is considered transient but the simple algorithm allows to find the steady-state solution for each time step. This way there is no need to satisfy any condition on the Courant number: in other words this is an implicit method.

The *pimple* algorithm is based on two main loops: a outer and a inner loop which is possible to analyse step by step:

1. Starting from the initial values (related to the previous time step) the velocity field is calculated using the momentum equation without considering the ∇p term.
2. The Laplacian of pressure p is evaluated as function of the velocity field and pressure's gradient at previous time step.
3. p is evaluated from the Laplacian of pressure. Then, the p value is used at step 2 and 3. The latter are repeated until a certain tolerance is reached (between the starting and final values calculated) or a certain number of iterations identified by the parameter *nNonOrthogonalCorrectors* is reached.

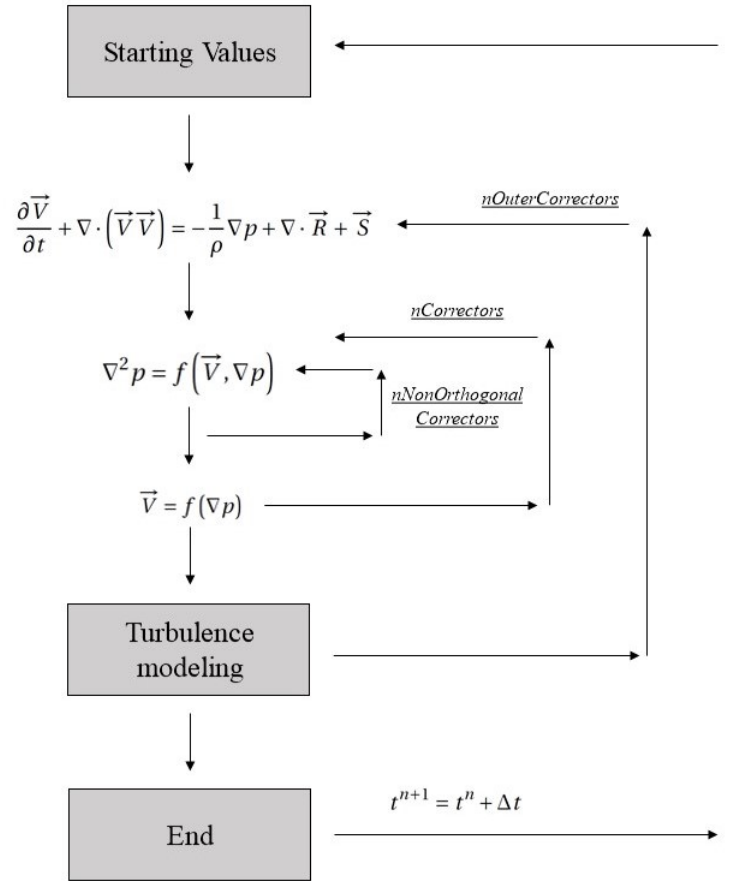


Figure 3.2: Schematic of the pimple algorithm

4. The velocity field is evaluated according to the continuity equation. This is also a verification, in order to figure out if the calculation is proceeding properly and the residuals are decreasing. The obtained value is introduced at step 2, and this new mid loop is repeated until a certain tolerance or a certain number of iterations identified by $nCorrectors$ is reached. This passage is used because at step 1 the velocity field was calculated according to the Reynolds stresses only, which are function of the velocity field itself. However before re-starting from point two is possible to move to the next step or do it only at the last iteration, depending on which value was assigned to *turbOnFinalIterOnly*
5. After the end of the 'inner loop' with the previous step, it is necessary to evaluate the turbulence effect. This can be done in two ways as stated before: just after the evaluation of the new velocity field at step 4 or at the end of the inner loop. In either cases however, the turbulence effect is modelled and evaluated, than it is introduced at step 1 in the evaluation of the velocity field closing the 'outer loop'. The iterations on the outer loop (whose ending part is defined by the turbulence evaluation) are based on a certain tolerance or a certain number of iterations defined by $nOuterCorrectors$
6. After reaching the end of the outer loop, the values calculated during the current time step are used as initial values for the next time step. So everything restarts from step 1.

A schematic representation of the calculation is reported in Figure (3.2). It is necessary to underline that every calculation can be made using a certain relaxation factor α that helps in achieving a more stable solution but slowing down the convergence speed. Such relaxation factor allows to modify the initial value for the following time step averaging the initial and final value at each time step, as shown in equation (3.43), where ϕ is a generic quantity. This way the value introduced is not a totally new one and the possible variation in the variables calculated is limited. Once all the iterations for a certain time step have been accomplished, the relaxation factor is set to 1, therefore the quantities obtained are more realistic. However it was not necessary

for this work to use a relaxation factor.

$$\phi^i = \phi^{i-1} - \alpha (\phi^{i-1} - \phi^i) \quad (3.43)$$

It is important to report that to reduce the computational cost and avoid too many iterations (keep in mind that this a simplified model) the forced requirements are not so 'tight'. Moreover, no control on the residuals and relaxation factor have been used (as mentioned). A summary of the value used is reported in Table (3.3), with reference to Figure (3.2).

Algorithm values	
Algorithm option	Value
nNonOrthogonalCorrectors	0
nCorrectors	2
nOuterCorrectors	1
turbOnFinalIterOnly	true

Table 3.3: Algorithm options used during the calculations

3.1.2. Actuator line model for VAWTs

The main target of this section is to define the actuator line model, discuss in details about how it works and how is implemented in the open-source library *turbinesFoam* for OpenFOAM. In fact such tool will be used (after being validated) to run different simulations to study VAWTs and to obtain data useful in a comparison with predictions from wake models.

Starting from equations (3.5) and (3.6) the purpose of the actuator line method, as already discussed, is to model the source force term in momentum equation. This way is possible to replicate turbine's effect on the flow by means of a loop calculation.

First of all, blades, which are replaced by lines, are split into a certain number of elements whose extension Δz can be set directly inside the code. Each one of the element will be considered 2D and will exert a constant force on the flow. Obviously the number of elements used depends on the case analysed, usually with higher Reynolds, more elements are introduced. This is the same approach of the BEM theory discussed in Chapter (2). A visual explanation of the geometry of the elements is shown in Figure (3.3). Since elements are assumed 2D, the 2D lift and drag coefficients C_l and C_d can be used to express the forces exerted on the flow. In order to evaluate them, airfoil polars are needed. They can be obtained experimentally, by testing the airfoils in wind tunnels at different angles of attack and Reynolds numbers. However, since turbines' blades experience a wide range of angle of attack (ranging from -180° to 180°) there is a shortage of similar data in the literature. Fortunately, the work from Klimas & Sheldahl [99] reports polars for different airfoil and different Reynolds' number, it has been essentials for thesis' goal. More details about the data extracted from this text are reported in Section (4.1), with particular attention on the polars used in each case analysed.

With the force coefficients at disposal, lift and drag forces per spanwise length unit can be expressed:

$$f_L = \frac{1}{2} \rho c C_L |V_{rel}|^2 \quad (3.44)$$

$$f_D = \frac{1}{2} \rho c C_D |V_{rel}|^2 \quad (3.45)$$

However, in order to evaluate the force coefficients from the tabulated data, it is necessary to provide the angle of attack. Its value is strictly related to the velocity relative to the blades, V_{rel} . It's expression is evaluated starting from the RANS solution. In fact in order to determine the angle of attack of each blade, the vectorial sum of the rotational velocity of the blade Ωr and the local inflow velocity V_{local} (lower than freestream value) is needed. Solving the RANS equations (when solving LES the procedure is the same) is possible to determine the local inflow magnitude and direction (influenced by the induced velocity) and then add it to the rotational velocity. Afterwards the force coefficients will be corrected to account for the dynamic stall, the end effects and other aspects.

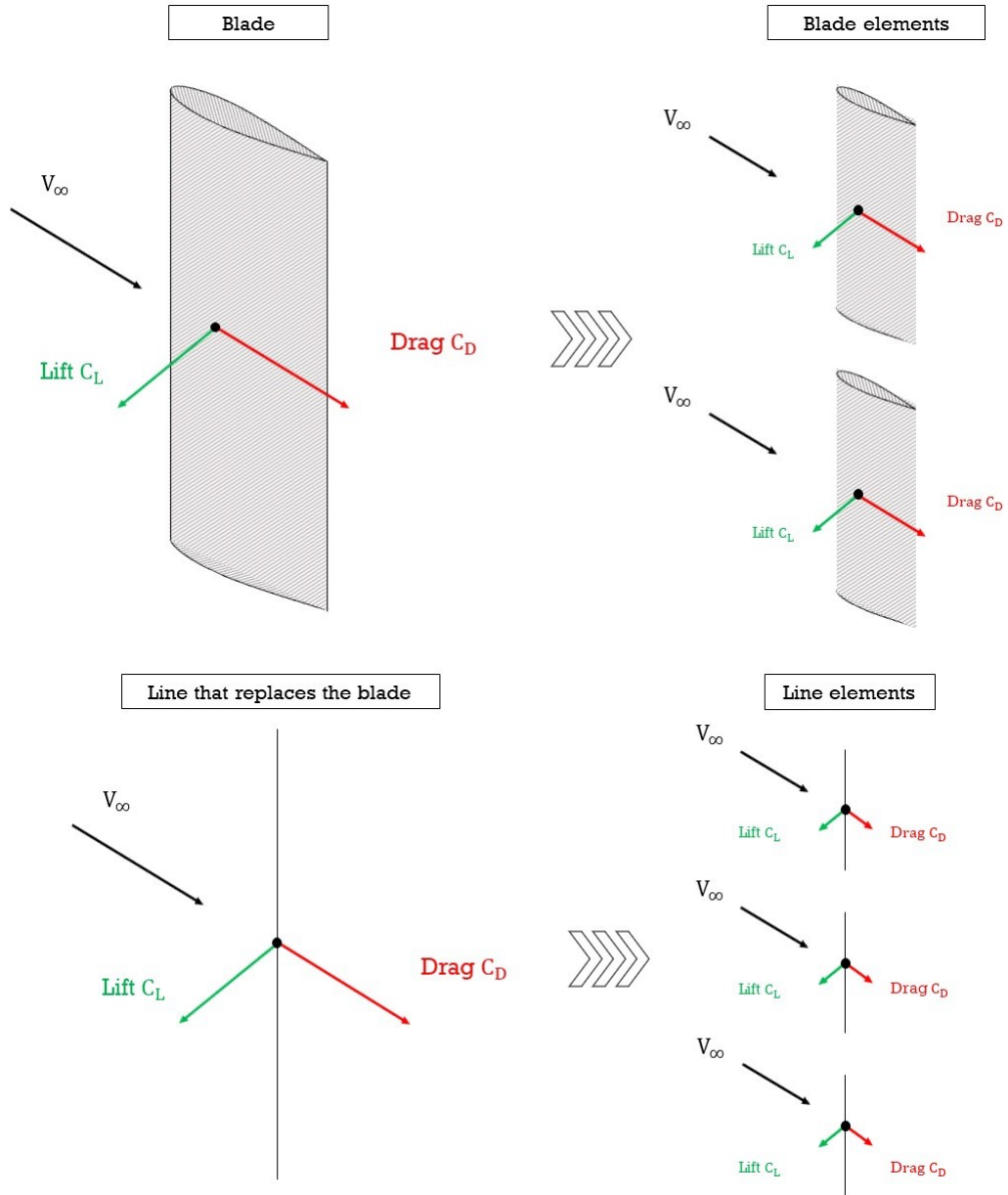


Figure 3.3: How the blades are divided into elements and how the lines are divided

However in order to solve the RANS equations and provide the local inflow velocity it is necessary to provide an initial estimation of the source term (or the angle of attack or the velocity relative to the blades). This means that the entire calculation is an iterative process, a loop, and the dual relation between RANS equations and actuator line model is based on the angle of attack, the local velocity at the blades and the source term. A schematic representation of the calculation procedure is reported in Figure (3.4). So in the last step the force term is introduced in the vectorial momentum equation (which, as stated before, can also be a LES equation according to the chosen methodology):

$$\frac{\partial \vec{V}}{\partial t} + \vec{V} \cdot \nabla \vec{V} = -\frac{1}{\rho} \nabla p + \nu \nabla^2 \vec{V} + \vec{f} \quad (3.46)$$

Body forces represented by the \vec{f} term are then modelled according to (3.44) and (3.45), for each of the line element considered and assumed constant. After being multiplied for the span length Δz , the forces for each element are summed to extract the values of tangential and normal force generated along each line-blade. Then, according to the number of blades considered, the forces over each line are summed and it is possible

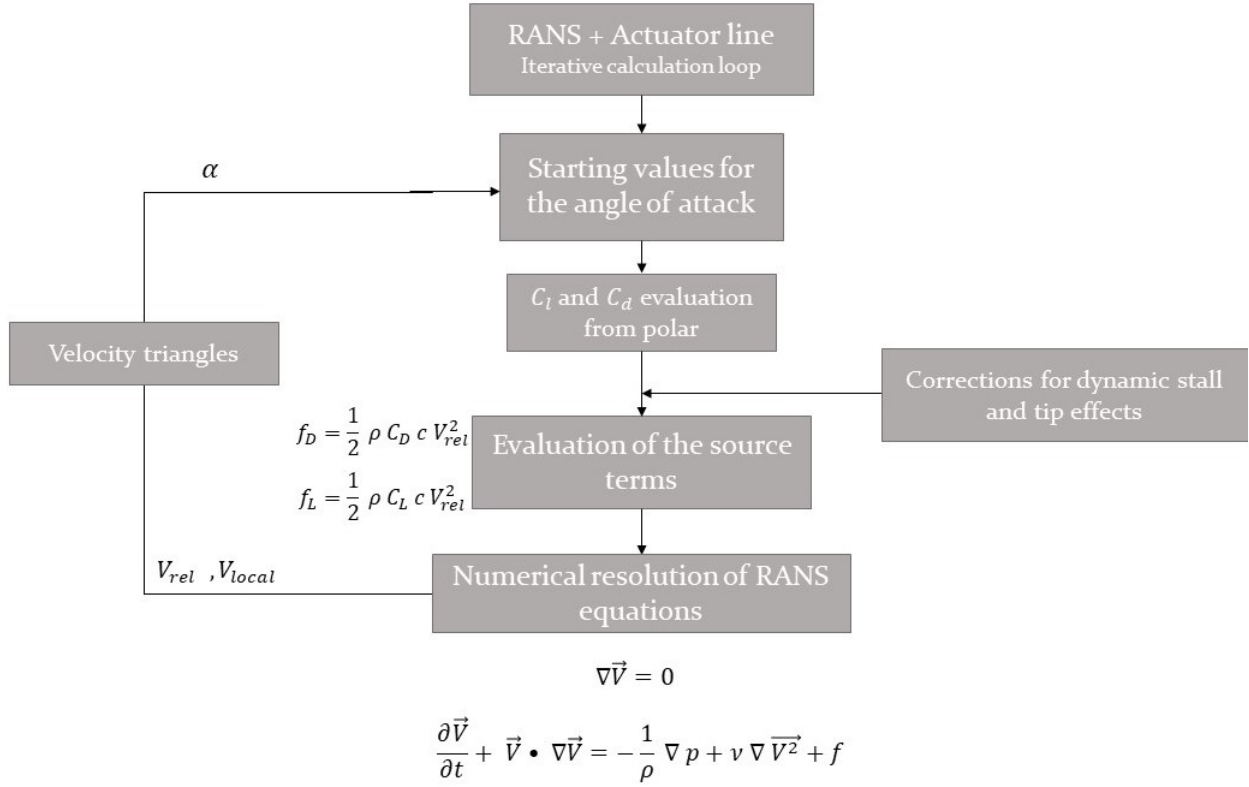


Figure 3.4: Schematic of the calculation loop when coupling RANS and actuator line model

to obtain the overall lift (or torque) and drag (or thrust) experienced by the turbine. This way is possible to perform calculations related to the power aspects of the turbine and especially about the thrust coefficient. In order to accomplish this procedure as well as studying the VAWT effect on the flow by coupling Navier-Stokes derived equations and actuator line model, the *turbinesFoam* library has been developed by Bachant et al. [7, 8, 64–67], for the open-source software OpenFOAM. This library has been used in this thesis work. It was chosen because writing a total new code is not an easy task, especially in OpenFOAM, so this was a considerable opportunity to perform the calculations without wasting too much time creating new tools or programmes, when open-source software are available.

The code follows all the steps cited before. A certain amount of space inside the control volume of the simulation is 'reserved' to the turbine. In this region the force sources are spatially located and distributed along a certain number of cells. In fact, similarly to what was discussed in Appendix (B) for HAWTs, the force evaluated is distributed smoothly along several cells of the mesh according to a Gaussian shape expressed by equation (3.47). Such gimmick is applied in order to avoid instabilities due to steep gradients.

$$\eta = \frac{1}{\varepsilon^3 \pi^{\frac{3}{2}}} e^{\left[-\left(\frac{|\vec{r}|}{\varepsilon}\right)^2\right]} \quad (3.47)$$

ε can be expressed in different ways:

- Related to the chord length:

$$\frac{c}{4} \quad (3.48)$$

- Related to the local mesh size:

$$4 \sqrt[3]{V_{cell}} \quad (3.49)$$

Where V_{cell} is the local mesh size

- Related to the momentum thickness due to the drag force presence:

$$\frac{c C_D}{2} \quad (3.50)$$

Generally, it is assumed as the higher of these three parameters:

$$\varepsilon = \max \left[\frac{c}{4}, 4 \sqrt[3]{V_{cell}}, \frac{cC_D}{2} \right] \quad (3.51)$$

In fact, a steep gradient, responsible for discontinuities in the flow, could lead to numerical problems. This way a similar dangerous possibility is avoided.

Even if it seems that the actuator line allows an easy approach to replicate VAWT's presence, it is essential to point out that many corrections and additions to the basic model are needed in order to take into account many effects that are extremely relevant in VAWT' aerodynamic and must be replicated. In fact a VAWT encounters unsteady conditions during its operative activity, because of both the angle of attack and relative velocity. Such conditions need unsteady aerodynamic models to augment the static foil characteristics, in order to capture the time resolved response of the attached flow loading and effects of flow acceleration, also known as added mass. Moreover, the angles of attack encountered by a VAWT blade will be high enough to encounter dynamic stall, whose features are described in Chapter (2). It is therefore necessary to model both unsteady attached and detached flow to obtain accurate loading predictions and improve the accuracy of the model. In conclusion each one of the main corrections used in *turbinesFoam* will be discussed and analysed. This way it is possible to have a better overview of how such aspects are replicated.

3.1.2.1. Dynamic stall model

The dynamic stall model has huge relevance in evaluating the forces acting on the line-blades during the revolution. Described in detail in Section (2.2.1) it is an unsteady phenomenon that has to be modelled correctly in order to figure out how the loads on the blades change during the revolution. In Figure (3.5) is shown a flow chart concerning how the dynamic stall model is used in the RANS + actuator line model set up and which is its role in the iterative calculation procedure. For *turbinesFoam* library [7, 66] the model is based

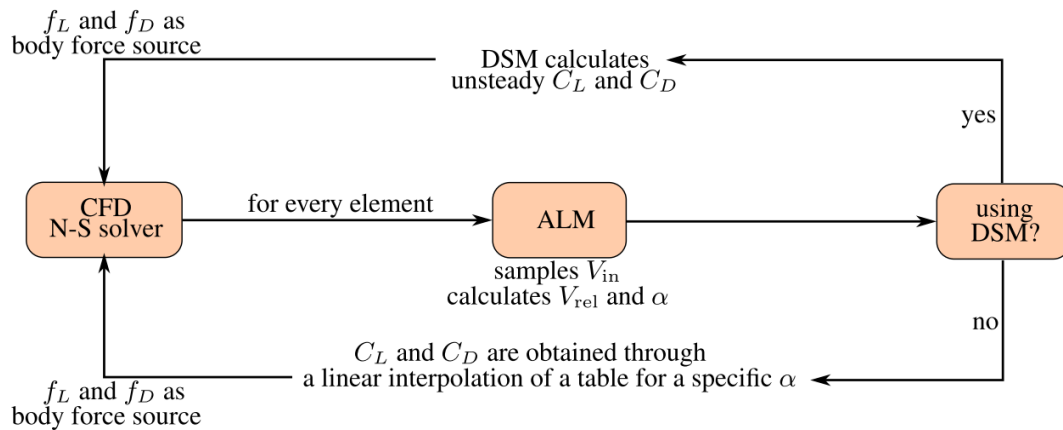


Figure 3.5: Conceptual map of how the dynamic stall model is applied besides the actuator line theory. Image taken from [65]

mainly on the Leishman-Beddoes model [56, 57] and some different versions of it with some modifications:

- Leishman-Beddoes 3G, from [12]
- Leishman-Beddoes SH or SG, from [102]

The original Leishman-Beddoes model is analysed in detail firstly, then the modifications featured by the other models will be discussed similarly to what was proposed by Dyachuk et al. [21]. The purpose of the analysis is to understand which is the best solution for this study.

3.1.2.1.1 Leishman-Beddoes model

The model is divided into 3 main parts which depend on the condition experienced by the flow on the blades. In Figure (3.6) and (3.7) a general idea of the main steps that define the different parts of the phenomenon is displayed.

Every part is implemented separately in the Leishman-Beddoes model (and also in its 'improved' versions).

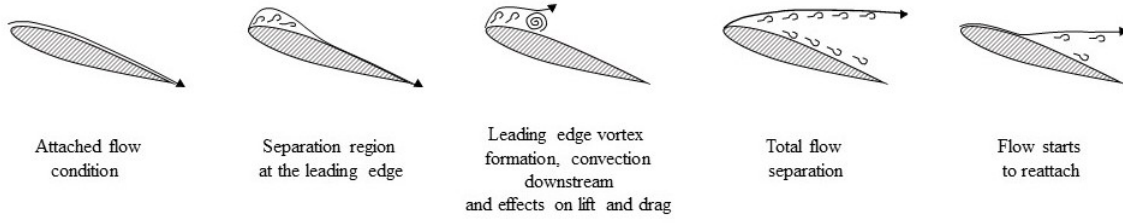


Figure 3.6: Description of the different conditions experienced by the flow around a blade when dynamic stall occurs

1. **Analysis of forces in unsteady conditions when the flow is attached:** when the flow is attached two main effects have to be considered: circulatory loads due to the time-variation of the bound-vortex and the impulsive loads due to the step variation of the angle of attack. The two effects are modelled separately.

Starting from the first one, the related normal force coefficient is expressed as:

$$C_{N_n}^C = C_{N_\alpha} \alpha_{E_n} \quad (3.52)$$

Where C_{N_α} depends on the Reynolds number and is the slope that relates the normal force coefficient C_n^C and the equivalent angle of attack α_{E_n} . The latter is obtained from the geometrical angle of attack and the deficiency functions X_n and Y_n , which are derived empirically:

$$\alpha_{E_n} = \alpha_n - X_n - Y_n \quad (3.53)$$

$$\begin{cases} X_n = X_{n-1} e^{(-b_1 \beta \Delta s)} + A_1 \Delta \alpha_n e^{\left(\frac{-b_1 \beta \Delta s}{2}\right)} \\ Y_n = Y_{n-1} e^{(-b_2 \beta \Delta s)} + A_2 \Delta \alpha_n e^{\left(\frac{-b_2 \beta \Delta s}{2}\right)} \end{cases} \quad (3.54)$$

Where $A_1 = 0.3$, $A_2 = 0.7$, $b_1 = 0.14$, $b_2 = 0.53$ while $\beta = 1 - M^2$ which presents M as Mach number. However the constants cited before may need a specific tuning depending on the case analysed. This is a first warning, since the model cannot perform accurately in every possible case. In fact the tuning of these parameters, as well as many others mentioned in the following sections, is a crucial aspect when validating the model against data.

$\Delta \alpha_n$ expresses the change occurring in α at two different time steps, n and $n - 1$. Δs is the normalized time step:

$$\Delta s = \frac{2V \Delta t}{c} \quad (3.55)$$

The second contribution that has to be considered is the one related to the impulsive loads, which features a specific empirical expression:

$$C_{N_n}^I = \frac{4K_\alpha T_I}{M} \left(\frac{\Delta \alpha_n}{\Delta t} - D_n \right) \quad (3.56)$$

With T_I the non-circulatory time constant:

$$T_I = \frac{c}{a} \quad (3.57)$$

While K_α is a constant expressed as:

$$K_\alpha = \frac{0.75}{1 - M + \pi (1 - M^2) M^2 (A_1 b_1 + A_2 b_2)} \quad (3.58)$$

D is instead the deficiency function during the response to impulsive loads:

$$D_n = D_n - 1e^{\left(-\frac{\Delta t}{k\alpha}\right)} \quad (3.59)$$

Summing the contribute from the circulatory loads and the impulsive loads, it is possible to obtain the total normal force coefficient when considering attached flow in unsteady conditions:

$$C_{N_n}^P = C_{N_n}^C + C_{N_n}^I \quad (3.60)$$

However in unsteady conditions a certain delay in the pressure response is experienced. This leads to a modification in the normal force coefficient and the angle of attack which is related to a new deficiency function, D_P . The latter depends on a time constant T_p related to the pressure response with a value extracted from the literature. However, similarly to the previous mentioned constants, it is possible to tune this value according to the conditions analysed.

$$C'_{N_n} = C_{N_n}^P - D_{P_n} \quad (3.61)$$

$$\alpha'_n = \frac{C'_{N_n}}{C_{N_\alpha}} \quad (3.62)$$

$$D_{P_n} = D_{P_{n-1}} e^{\left(-\frac{\Delta s}{T_p}\right)} + \left(C_{N_n}^P - C_{N_{n-1}}^P\right) e^{\left(-\frac{\Delta s}{2T_p}\right)} \quad (3.63)$$

2. **The definition of dynamic stall condition:** in order to figure out if the stall is occurring or not, the C'_{N_n} in equation (3.61) is compared with a critical value, C_{N_1} . When the absolute value of the first one is higher than the second one, stall onsets:

$$|C'_{N_n}| > C_{N_1} \Rightarrow \text{Stall occurs} \quad (3.64)$$

3. **The forces experienced due to the vortex shedding when the flow is separated:** two different effects have to be considered even here: separation, which occurs both at the trailing and leading edge, and the vortex shedding phenomenon. The first one is related to the dynamic delay experienced in the movement of the boundary-layer separation point and depends on the position of the latter one and the amount of dynamic lag. The position of the separation point in such unsteady condition is different from the same value but in static stall condition and is expressed using the Kirchhoff's flow approximation:

$$f'_n = \begin{cases} 1 - 0.3e^{\frac{|\alpha'_n| - \alpha_1}{S_1}} & |\alpha'_n| < \alpha_1 \\ 0.04 + 0.66 \frac{\alpha_1 - |\alpha'_n|}{S_2} & |\alpha'_n| \geq \alpha_1 \end{cases} \quad (3.65)$$

The constants S_1, S_2 and α_1 are function of the Reynolds number. However it is necessary to keep into account also the additional delay due to unsteady effects on the boundary layer, which is time dependent. This leads to a new expression for the separation point f'' obtained using a deficiency function D_f :

$$f''_n = f'_n - D_{f_n} \quad (3.66)$$

$$D_{f_n} = D_{f_{n-1}} e^{-\frac{\Delta s}{T_f}} + (f'_n - f'_{n-1}) e^{\left(\frac{\Delta s}{2T_f}\right)} \quad (3.67)$$

T_f is a time constant related to the delay of the separation point lag and is influenced by the vortex shedding phenomenon (as mentioned next).

Once the location of the dynamic separation point is obtained, it is possible to reformulate the normal force coefficient expression. Here two different terms are observed, the term related to how the separation point moves along the airfoil surface during the dynamic stall phenomena and the term related to the impulsive loads, which are still experienced:

$$C_{N_n}^f = C_{N_\alpha} \alpha_{E_n} \left(\frac{1 + \sqrt{f''_n}}{2} \right)^2 + C_{N_n}^I \quad (3.68)$$

The second aspect that has to be considered when dealing with separated flow is the vortex shedding. Considering the vortex that grows during the rotation at the leading edge, at a certain time it detaches and moves downstream inducing the so called 'vortex lift' on the surface of the airfoil. In fact its presence induces a certain amount of pressure on the remaining part of the airfoil during the convection until it passes the trailing edge. The phenomenon repeats periodically so it is necessary to take into account also the other vortices generated for the shedding. The vortex-lift effect is expressed as:

$$C_{v_n} = C_{N_n}^C \left(1 - \left(\frac{1 + \sqrt{f_n''}}{2} \right)^2 \right) \quad (3.69)$$

This effect is proportional to the normal force coefficient experienced when the flow is attached because of circulatory loads and the normal force coefficient due to the displacement of the separation point when experiencing dynamic stall. Adding it to the normal force coefficient:

$$C_{N_n}^v = C_{N_{n-1}}^v e^{\left(-\frac{\Delta s}{T_v}\right)} + (C_{v_n} - C_{v_{n-1}}) e^{\left(-\frac{\Delta s}{2T_v}\right)} \quad (3.70)$$

As mentioned before this effect only persist for a certain amount a time: once the vortex passes the trailing edge, the load experienced disappears quickly. Imaging to track the vortex position using a non-dimensional time parameter τ , when it detaches from the leading edge $\tau = 0$. When the vortex has reached the trailing edge $\tau = T_{vl}$ so the lift effect only persist for $0 < \tau < T_{vl}$ where T_{vl} is the time constant. Once the vortex has passed the trailing edge, the T_v constant decreases and the second term in equation (3.70) as well. The vortex lift effect reduces quickly.

But how to consider several vortex due to shedding? In order to replicate this effect it is assumed that vortices develop again after a certain amount of time after that the main vortex has passed the trailing edge. The amount of time considered is expressed as T_{st} so after $T_{vl} + T_{st}$, τ is set to zero and the effect repeats. Since it is all related to vortex shedding, the time constant T_{st} is obviously related to the Strouhal number which is one of the non-dimensional parameter (the other is the Reynolds number) that rules the vortex shedding phenomenon:

$$T_{st_n} = \frac{2(1 - f_n'')}{0.19} \quad (3.71)$$

It is crucial to underline that the vortex lift effect is observed only when the absolute value of the angle of attack increases, not when it decreases (in the latter case $C_{N_n}^v$).

For the separated flow, the two effects have to be considered at the same time, summing the two terms:

$$C_{N_n} = C_{N_n}^f + C_{N_n}^v \quad (3.72)$$

Concerning instead the tangential force coefficient C_T , it is expressed by Kirchhoff's relation:

$$C_T = \eta C_{N_\alpha} \alpha_E^2 \sqrt{f''} \quad (3.73)$$

η is a parameter provided by the literature and called as 'efficiency factor'. It keeps into account that the maximum value of the tangential force coefficient is not actually reached. Moreover, when separation occurs (for $f'' < 0.7$) it is possible to introduce an approximation for the relation between C_T and f'' where the first one is proportional to the latter raised to 1.5.

In order to keep into account the different flow status, some modifications to the time constants T_f and T_v are needed:

- T_f : when vortex shedding phenomenon occurs, the location of separation point at the trailing edge changes extremely fast. For this reason T_f decreases and during the vortex convection shows an halved value

$$T_f = 0.5 T_f \text{ for } 0 < \tau \leq T_{vl} \quad (3.74)$$

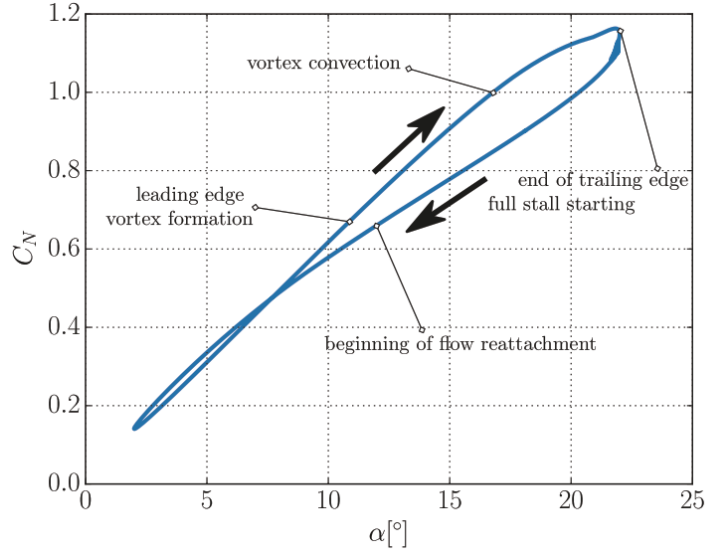


Figure 3.7: Example of the different phases of dynamic stall, image taken from [64]

The value of D_f in equation (3.67) changes accordingly and decreases, since delay is minimized. Re-attachment of flow does not occur until the vortex has passed the trailing edge, for this reason T_f quadruplicates:

$$T_f = 4T_f \text{ for } T_{vl} < \tau \leq 2T_{vl} \quad (3.75)$$

Once the flow reattaches, dynamic stall ends and T_f shows an halved value:

$$|C'_{N_n}| < C_{N_1} \Rightarrow T_f = 0.5T_f \quad (3.76)$$

- T_v : after the vortex passage vortex lift (as mentioned before) decreases significantly. In order to replicate this aspect, T_v value in equation (3.70) is halved, this way the vortex lift contribution is minimized.

$$\tau > T_{vl} \Rightarrow T_v = 0.5T_v \quad (3.77)$$

All the equations on which the model is based on are summarized in the first column of Table (3.5) while Figure (3.7) shows a typical evolution of the normal force coefficient when dynamic stall happens. Once the normal and tangential force coefficients have been evaluated it is necessary to relate their expression to lift and drag coefficients (C_L and C_D respectively).

$$C_{L_n} = C_{N_n} \cos \alpha_n + C_{T_n} \sin \alpha_n \quad (3.78)$$

$$C_{D_n} = C_{N_n} \sin \alpha_n - C_{T_n} \cos \alpha_n + C_{D_0} \quad (3.79)$$

Where C_{D_0} is the drag coefficient at zero angle of attack.

With reference to Figure (3.4), the new values of force coefficients are corrected by Leishman-Beddoes model and provided to calculate the source terms in momentum equation. One last important aspect is that, in turbinesFoam, before the dynamic stall function is launched, the static profile data for each element is interpolated linearly based on local chord Reynolds number calculated according to the detected inflow velocity at each actuator line element. The profile data properties like the stall angle, zero-lift drag coefficient, and separation point curve fit parameters are then recomputed for each time step in order to consider Reynolds' number effect on the static data.

3.1.2.1.2 Leishman-Beddoes 3G model

As mentioned before this model is an 'evolution' of the Leishman-Beddoes model. Proposed by Beddoes in [12] it features some slight modifications compared to the original model:

1. **Considering attached unsteady flow:** The expressions for the deficiency functions slightly change and a third one is added.

$$X_n = X_{n-1} e^{-\frac{\beta \Delta s}{T_1}} + A_1 (\eta_{L_n} - \eta_{L_{n-1}}) e^{-\frac{\beta \Delta s}{2T_1}} \quad (3.80)$$

$$Y_n = Y_{n-1} e^{-\frac{\beta \Delta s}{T_2}} + A_2 (\eta_{L_n} - \eta_{L_{n-1}}) e^{-\frac{\beta \Delta s}{2T_2}} \quad (3.81)$$

$$Z_n = Z_{n-1} e^{-\frac{\beta \Delta s}{T_3}} + A_3 (\eta_{L_n} - \eta_{L_{n-1}}) e^{-\frac{\beta \Delta s}{2T_3}} \quad (3.82)$$

Where the new parameter η_L is a forcing term related to the pitching motion:

$$\eta_{L_n} = \alpha_n + \frac{2}{2V} \dot{\alpha}_n \quad (3.83)$$

Moreover the expressions for normal forces when considering the case of unsteady attached flow change, this time more significantly.

$$H_n = H_{n-1} e^{-\frac{\Delta t}{T_I}} + (\lambda_{L_n} - \lambda_{L_{n-1}}) e^{-\frac{\Delta t}{2T_I}} \quad (3.84)$$

Where:

$$T_I = \frac{c}{a} \frac{1+3M}{4} \quad (3.85)$$

$$\lambda_{L_n} = \frac{\pi}{4} \left(\alpha_n + \frac{2}{4V} \dot{\alpha}_n \right) \quad (3.86)$$

The new term λ_L expresses the pitching motion around the airfoil quarter-axis. No additional corrections are made when dealing with the sum of the values or the deficiency function to replicated dynamic's lag on separation point.

2. **Dynamic stall condition:** the same condition of the original Leishman-Beddoes model in equation (3.64) is used.
3. **Considering separated flow:** here, unlike in the original model, separation occurs when $f < 0.6$, for this reason the expression for f' in equation (3.65) slightly changes.

$$f'_n = \begin{cases} 1 - 0.4e^{-\frac{|\alpha'_n| - \alpha_1}{S_1}} & |\alpha'_n| < \alpha_1 \\ 0.02 + 0.58 \frac{\alpha_1 - |\alpha'_n|}{S_2} & |\alpha'_n| \geq \alpha_1 \end{cases} \quad (3.87)$$

Concerning the vortex shedding effect instead, this phenomenon is modelled by an additional modification of the separation point (f_{3G_n}) according to the deficiency function in equation (3.67) (seen before) and the modulation parameter V_x which is a periodic function. Therefore there is no need to add the time constant T_{st} to keep into account additional vortices.

$$f_{3G_n} = f''_n - D_{f_n} V_{x_n} \quad (3.88)$$

Vortex lift ends when the angle of attack decreases and V_x is set to zero. The new separation point must assume a value from 0 to 1 in order to display a realistic physical meaning.

$$V_x = \begin{cases} \left(\sin \left(\frac{\pi \tau}{2T_{vl}} \right) \right)^{\frac{3}{2}} & 0 < \tau \leq T_{vl} \\ \left(\cos \left(\frac{\pi(\tau - T_{vl})}{T_v} \right) \right)^2 & \tau > T_{vl} \end{cases} \quad (3.89)$$

Once its expression is found, it is introduced in an equation similar to (3.68). The results is:

$$C_{N_n}^v = C_{N_a} \alpha_{E_n} \left(1 + \sqrt{f_{3G_n}} \right)^2 \quad (3.90)$$

The only required correction is for the time constant T_f , whose (similarly to the original model) value is halved after the release of the leading-edge vortex because the separation point moves quickly.

All the equations are reported in detail in the second column of Table (3.5).

3.1.2.1.3 Leishman-Beddoes SH model

The SH model is another evolution of the Leishman-Beddoes model developed by Sheng et al. [102]. It is the most recent one. The modifications observed are the following ones:

1. **Considering attached unsteady flow:** While the expressions for circulatory and impulsive loads remain the same of the 3G model, the expression for the delayed angle of attack changes, and a new deficiency function D_{α} , based on the new time constant T_{α} , related to stall onset, is introduced.

$$\alpha'_n = \alpha_n - D_{\alpha_n} \quad (3.91)$$

$$\alpha'_n = \alpha'_{n-1} e^{\left(-\frac{\Delta s}{T_{\alpha}}\right)} + (\alpha_n - \alpha_{n-1}) e^{\left(-\frac{\Delta s}{2T_{\alpha}}\right)} \quad (3.92)$$

2. **Dynamic stall condition:** The most relevant modifications are located here. The expressions for the critical angle of attack α_{cr_n} changes depending on the reduced pitch rate r_n and are based on the constant critical stall-onset angle α_{ds0} and the static stall-onset angle α_{ss} .

$$\alpha_{cr_n} = \begin{cases} \alpha_{ds0} & r_n \geq r_0 \\ \alpha_{ss} + (\alpha_{ds0} - \alpha_{ss}) \frac{r_n}{r_0} & r_n < r_0 \end{cases} \quad (3.93)$$

$$r_n = \frac{\dot{\alpha}_n c}{2V} \quad (3.94)$$

The reduced pitch rate makes distinction between a condition of dynamic stall and quasi-steady stall. So stall is met when:

$$|\alpha'_n| > \alpha_{cr_n} \Rightarrow stall \quad (3.95)$$

3. **Considering separated flow:** The normal force related to how the separation point moves shows the same expression seen for the 3G model. Considerable modifications instead are related to the vortex shedding phenomena, whose induced loads are linked to the difference between the separation point in static condition f and the one in dynamic condition f'' . The first one is expressed according to Kirchoff's equation similarly to the equation for f'_n in the 3G model.

$$f_n = \begin{cases} 1 - 0.4e^{\frac{|\alpha_n| - \alpha_1}{S_1}} & |\alpha'_n| < \alpha_1 \\ 0.02 + 0.58 \frac{\alpha_1 - |\alpha_n|}{S_2} & |\alpha_n| \geq \alpha_1 \end{cases} \quad (3.96)$$

Where V_x is expressed in the same way as for 3G model. The expression for the subsequent normal force is:

$$C_{N_n}^v = B_1 (f''_n - f_n) V_x \quad (3.97)$$

Where B_1 is a constant that needs to be provided.

4. **Tangential force coefficient:** Its expression slightly changes introducing an additional constant to keep into account possible negative values that occur in separated regime.

$$C_T = \eta C_{N_{\alpha}} \alpha_E^2 \left(\sqrt{f''} - E_0 \right) \quad (3.98)$$

Airfoil	T_{α}	α_{ss} deg	α_{ds0} deg	r_0	T_v	T_{vl}	B_1	η	E_0
NACA0012	3.90	14.95	18.73	0.01	11	8	0.75	1	0.25
NACA0015	5.78	14.67	17.81	0.01	8	5	0.50	1	0.25
NACA0018	6.22	14.68	17.46	0.01	11	5	0.50	1	0.20
NACA0021	6.30	14.33	17.91	0.01	11	9	0.50	0.975	0.15
NACA0025	6.95	13.59	17.22	0.01	4	3	0.50	0.90	0.18

Table 3.4: Coefficients for the Leishman-Beddoes models provided by [21]

	Leishman-Beddoes	Leishman-Beddoes 3G	Leishman-Beddoes SH/SG	
Attached flow	Circulatory loads evaluation	$C_{N_n}^C = C_{N_n} \alpha E_n$ $\alpha E_n = \alpha_n - X_n - Y_n$ $\begin{cases} X_n = X_{n-1} e^{(-b_n \beta \Delta s)} + A_1 \Delta \alpha_n e^{\left(\frac{-b_n \beta \Delta s}{2}\right)} \\ Y_n = Y_{n-1} e^{(-b_n \beta \Delta s)} + A_2 \Delta \alpha_n e^{\left(\frac{-b_n \beta \Delta s}{2}\right)} \end{cases}$ $\beta = 1 - M^2$ $\Delta s = \frac{2V \Delta t}{c}$	$C_{N_n}^C = C_{N_n} \alpha E_n$ $\alpha E_n = \eta_{L_n} - X_n - Y_n - Z_n$ $\begin{cases} X_n = X_{n-1} e^{\left(-\frac{\Delta s}{T_n}\right)} + A_1 (\eta_{L_n} - \eta_{L_{n-1}}) e^{\left(-\frac{\Delta s}{2T_n}\right)} \\ Y_n = Y_{n-1} e^{\left(-\frac{\Delta s}{T_n}\right)} + A_2 (\eta_{L_n} - \eta_{L_{n-1}}) e^{\left(-\frac{\Delta s}{2T_n}\right)} \\ Z_n = Z_{n-1} e^{\left(-\frac{\Delta s}{T_n}\right)} + A_3 (\eta_{L_n} - \eta_{L_{n-1}}) e^{\left(-\frac{\Delta s}{2T_n}\right)} \end{cases}$ $\beta = 1 - M^2$ $\Delta s = \frac{2V \Delta t}{c}$	$C_{N_n}^C = C_{N_n} \alpha E_n$ $\alpha E_n = \eta_{L_n} - X_n - Y_n - Z_n$ $\begin{cases} X_n = X_{n-1} e^{\left(-\frac{\Delta s}{T_n}\right)} + A_1 (\eta_{L_n} - \eta_{L_{n-1}}) e^{\left(-\frac{\Delta s}{2T_n}\right)} \\ Y_n = Y_{n-1} e^{\left(-\frac{\Delta s}{T_n}\right)} + A_2 (\eta_{L_n} - \eta_{L_{n-1}}) e^{\left(-\frac{\Delta s}{2T_n}\right)} \\ Z_n = Z_{n-1} e^{\left(-\frac{\Delta s}{T_n}\right)} + A_3 (\eta_{L_n} - \eta_{L_{n-1}}) e^{\left(-\frac{\Delta s}{2T_n}\right)} \end{cases}$ $\beta = 1 - M^2$ $\Delta s = \frac{2V \Delta t}{c}$
	Impulsive loads evaluation	$C_{N_n}^I = \frac{4k_c T_n}{M} \left(\frac{\Delta \alpha_n}{\Delta t} - D_n \right)$ $D_n = D_{n-1} e^{\left(-\frac{\Delta s}{T_n}\right)}$ $T_n = \frac{c}{a}$ $K_{imp} = \frac{0.75}{1 - M^2 + (1 - M^2)^2 X^2 (A_1 b_n + A_2 b_n)}$	$C_{N_n}^I = \frac{4}{M} H_n$ $H_n = H_{n-1} e^{\left(-\frac{\Delta s}{T_n}\right)} + (\lambda_{L_n} - \lambda_{L_{n-1}}) e^{\left(-\frac{\Delta s}{2T_n}\right)}$ $T_n = \frac{c}{a} \frac{1 + 3M}{4}$ $\lambda_{L_n} = \frac{c}{a} (\alpha_n + \frac{2}{T_n} \alpha_n)$	$C_{N_n}^I = \frac{4}{M} H_n$ $H_n = H_{n-1} e^{\left(-\frac{\Delta s}{T_n}\right)} + (\lambda_{L_n} - \lambda_{L_{n-1}}) e^{\left(-\frac{\Delta s}{2T_n}\right)}$ $T_n = \frac{c}{a} \frac{1 + 3M}{4}$ $\lambda_{L_n} = \frac{c}{a} (\alpha_n + \frac{2}{T_n} \alpha_n)$
Total value	$C_{N_n}^P = C_{N_n}^C + C_{N_n}^I$	$C_{N_n}^P = C_{N_n}^C + C_{N_n}^I$	$C_{N_n}^P = C_{N_n}^C + C_{N_n}^I$	
Total value delayed	$D_{P_n} = D_{P_{n-1}} e^{\left(-\frac{\Delta s}{T_n}\right)} + \left(C_{N_n}^P - C_{P_{n-1}}^P \right) e^{\left(-\frac{\Delta s}{T_n}\right)}$ $\alpha_n' = \frac{C_{N_n}^P}{C_{N_n}}$	$D_{P_n} = D_{P_{n-1}} e^{\left(-\frac{\Delta s}{T_n}\right)} + \left(C_{N_n}^P - C_{P_{n-1}}^P \right) e^{\left(-\frac{\Delta s}{T_n}\right)}$ $\alpha_n' = \frac{C_{N_n}^P}{C_{N_n}}$	$D_{P_n} = D_{P_{n-1}} e^{\left(-\frac{\Delta s}{T_n}\right)} + \left(C_{N_n}^P - C_{P_{n-1}}^P \right) e^{\left(-\frac{\Delta s}{T_n}\right)}$ $\alpha_n' = \alpha_n - D_{\alpha_n}$ $\alpha_n' = \alpha_n' e^{\left(-\frac{\Delta s}{T_n}\right)} + (\alpha_n - \alpha_{n-1}) e^{\left(-\frac{\Delta s}{T_n}\right)}$	
Stall condition				
	$ C_{N_n}^I > C_{N_n}$	$ C_{N_n}^I > C_{N_n}$	$\alpha \alpha_{cr} = \begin{cases} \alpha_{d50} & r_n \geq r_0 \\ \alpha_{s55} + (\alpha_{d50} - \alpha_{s55}) \frac{r_n}{r_0} & r_n < r_0 \end{cases}$ $r_n = \frac{\alpha_{cr}}{2V}$	
Separated flow	Trailing edge separation	$C_{N_n}^I = C_{N_n} \alpha E_n \left(\frac{1 + \sqrt{f_n}}{2} \right) + C_{N_n}^I$ $f_n = \begin{cases} 1 - 0.3e^{-\frac{ \alpha_n }{s_1}} & \alpha_n < \alpha_1 \\ 0.04 + 0.66 \frac{\alpha_1 - \alpha_n }{s_2} & \alpha_n \geq \alpha_1 \end{cases}$ $f_n' = f_n' - D_{f_n}$ $D_{f_n} = D_{f_{n-1}} e^{-\frac{\Delta s}{T_n}} + (f_n' - f_{n-1}') e^{\left(\frac{\Delta s}{T_n}\right)}$	$C_{N_n}^I = C_{N_n} \alpha E_n \left(\frac{1 + \sqrt{f_n}}{2} \right) + C_{N_n}^I$ $f_n = \begin{cases} 1 - 0.4e^{-\frac{ \alpha_n }{s_1}} & \alpha_n < \alpha_1 \\ 0.02 + 0.58 \frac{\alpha_1 - \alpha_n }{s_2} & \alpha_n \geq \alpha_1 \end{cases}$ $f_n' = f_n' - D_{f_n}$ $D_{f_n} = D_{f_{n-1}} e^{-\frac{\Delta s}{T_n}} + (f_n' - f_{n-1}') e^{\left(\frac{\Delta s}{T_n}\right)}$	$C_{N_n}^I = C_{N_n} \alpha E_n \left(\frac{1 + \sqrt{f_n}}{2} \right) + C_{N_n}^I$ $f_n = \begin{cases} 1 - 0.4e^{-\frac{ \alpha_n }{s_1}} & \alpha_n < \alpha_1 \\ 0.02 + 0.58 \frac{\alpha_1 - \alpha_n }{s_2} & \alpha_n \geq \alpha_1 \end{cases}$ $f_n' = f_n' - D_{f_n}$ $D_{f_n} = D_{f_{n-1}} e^{-\frac{\Delta s}{T_n}} + (f_n' - f_{n-1}') e^{\left(\frac{\Delta s}{T_n}\right)}$
	Vortex Shedding	$C_{N_n}^V = C_{N_n}^V e^{\left(-\frac{\Delta s}{T_n}\right)} + (C_{N_n}^V - C_{N_{n-1}}^V) e^{\left(-\frac{\Delta s}{T_n}\right)}$ $C_{N_n}^V = C_{N_n}^C \left(1 - \left(\frac{1 + \sqrt{f_n}}{2} \right)^2 \right)$ $T_{st} = \frac{2(1 - f_n')}{0.18}$	$C_{N_n}^V = C_{N_n} \alpha E_n (1 + \sqrt{f_{3G}})^2$ $f_{3G} = f_n' - D_{f_n} V_{3G}$ $V_3 = \begin{cases} \left(\frac{\sin\left(\frac{\pi \tau}{2T_{st}}\right)}{2T_{st}} \right)^{\frac{2}{3}} & 0 < \tau \leq T_{st} \\ \left(\frac{\cos\left(\frac{\pi(\tau - T_{st})}{2T_{st}}\right)}{2T_{st}} \right)^{\frac{2}{3}} & \tau > T_{st} \end{cases}$	$C_{N_n}^V = B_1 (f_n' - f_n) V_3$ $f_n = \begin{cases} 1 - 0.4e^{-\frac{ \alpha_n }{s_1}} & \alpha_n < \alpha_1 \\ 0.02 + 0.58 \frac{\alpha_1 - \alpha_n }{s_2} & \alpha_n \geq \alpha_1 \end{cases}$ $V_3 = \begin{cases} \left(\frac{\sin\left(\frac{\pi \tau}{2T_{st}}\right)}{2T_{st}} \right)^{\frac{2}{3}} & 0 < \tau \leq T_{st} \\ \left(\frac{\cos\left(\frac{\pi(\tau - T_{st})}{2T_{st}}\right)}{2T_{st}} \right)^{\frac{2}{3}} & \tau > T_{st} \end{cases}$
Total value	$C_{N_n} = C_{N_n}^I + C_{N_n}^V$	$C_{N_n} = C_{N_n} \alpha E_n (1 + \sqrt{f_{3G}})^2 + C_{N_n}^I$	$C_{N_n} = C_{N_n}^I + C_{N_n}^V$	
Tangential value	$C_T = \eta C_{N_n} \alpha E_n^2 \sqrt{f_n}$	$C_T = \eta C_{N_n} \alpha E_n^2 \sqrt{f_n}$	$C_T = \eta C_{N_n} \alpha E_n^2 (\sqrt{f_n} - E_0)$	

Table 3.5: Summary of the equations used for each method analysed

The detailed equations for this model are reported in the third column of Table (3.5).

In conclusion the dynamic stall model used is the same for all the three cases analysed: the Leishman-Beddoes SH/SG. Such model, used for low Mach number, was chosen because of is the newest version available and performs better than the other models in different TSRs conditions as stated in [21], matching experimental results with higher accuracy.

However the settings are not the same for every case, because even if the constants are provided with the models (check Table (3.4)), they are not universal and it is necessary to tune some of the constants depending on the conditions analysed, as stated before. Since the simulations are run at different Reynolds number there is a substantial variation in the coefficients to be used that will be discussed in Chapter (4).

3.1.2.2. Tip correction

As already discussed, drag and lift coefficients are evaluated as 2D coefficients, since line elements are considered bidimensional. However, it is necessary to consider also the end effects related to the finite extension of the blades, otherwise the problem is not realistic. As already discussed in Section (2.2.1.3), tip effects and tip vortices are a relevant aspect when dealing with VAWTs so it is necessary to model this aspect.

Since vortex lines always need to create closed loops, lift distribution due to bound vortex must drop to zero at the edges when considering blades with a finite extension. Unfortunately it is not possible to apply Glauert's correction, which is largely used for HAWTs, as reported in [8]. Therefore the only way to model the 3D effect correctly is using Prandtl's lifting line theory, as mentioned in [8, 64]. According to it, angle of attack can be expressed in equation (3.99) as function of the non-dimensional span θ .

$$\alpha(\theta) = \frac{2S}{\pi c(\theta)} \sum_1^N A_n \sin\theta + \sum_1^N n A_n \frac{\sin n\theta}{\sin\theta} + \alpha_{L=0}(\theta) \quad (3.99)$$

S is the span length, $c(\theta)$ is the chord length, N the number of elements along the foil. By turning this equation into an expression with matrices and solving it, the A_n Fourier coefficients are obtained.

$$[\alpha_m] - \alpha_{L=0} = [D_{mn}] [A_n] \quad (3.100)$$

$$D_{mn} = \left[\frac{2b}{\pi c_m} \sin n\theta_m + n \frac{\sin n\theta_m}{\sin\theta_m} \right] \quad (3.101)$$

Such coefficients are essential in order to evaluate the circulation's distribution. Since the aim is to obtain a new expression for the lift coefficient (that includes the tip effects), using Kutta-Joukowski theorem it is possible to relate the circulation and the lift force.

$$\Gamma(\theta) = 2SV_\infty \sum_{n=1}^N A_n \sin n\theta \quad (3.102)$$

$$C_L(\theta) = \frac{-\Gamma(\theta)}{\frac{1}{2}cV_\infty} \quad (3.103)$$

The correction applied to the lift coefficient evaluated using the actuator line method is expressed by normalising the spanwise lift coefficient distribution and obtaining a value in the range [0,1]. The correction coefficient is called F and is expressed as:

$$F = \frac{C_L(\theta)}{C_L(\theta)_{max}} \quad (3.104)$$

Such coefficient is multiplied to the 2D coefficient evaluated before. The great difference respect to Glauert's theory is that there's no necessity of specifying rotor parameters.

3.1.2.3. Added mass effect

Since the flow around the blades experience a certain amount of acceleration, the additional force exerted on the flow must be considered. In turbinesFoam library, referring to [8, 64], the phenomenon is modelled introducing two new coefficients to express the additional force along the chord direction and the chord normal direction for each element, as shown in equations (3.105) and (3.106). Such values need to be added to the normal and tangential force coefficients calculated by the dynamic stall model. This calculation is based on the model proposed by Strickland [107] by considering a pitching flat plate in potential flow.

The new coefficients are expressed as:

$$C_{n_{AM}} = -\frac{\pi c V_{rel,N}}{8|V_{rel}^2|} \quad (3.105)$$

$$C_{c_{AM}} = -\frac{\pi c \dot{\alpha} V_{rel,N}}{8|V_{rel}^2|} \quad (3.106)$$

Where $V_{rel,N}$ is the normal component of the relative velocity. Similarly a coefficient to express the moment respect to the chord line is introduced:

$$C_{m_{AM}} = -\frac{C_{n_{AM}}}{4} + \frac{V_{rel,N} V_{rel,T}}{8|V_{rel}^2|} \quad (3.107)$$

As before, $V_{rel,T}$ is the tangential component of relative velocity.

Introducing the angle of attack α in equations (3.105), (3.106) and (3.107), the lift and drag coefficients (that needs to be added to the ones predicted by the dynamic stall model) are obtained.

$$C_{l_{AM}} = C_{n_{AM}} \cos(\alpha) + C_{c_{AM}} \sin(\alpha) \quad (3.108)$$

$$C_{d_{AM}} = C_{n_{AM}} \sin(\alpha) - C_{c_{AM}} \cos(\alpha) \quad (3.109)$$

Once reported to the axis used for calculations of the other coefficients, the values are summed:

$$C_D = (C_d)_{2D} F = (C_{d_{AM}} + C_{d_{dyn,stall}}) F \quad (3.110)$$

$$C_L = (C_l)_{2D} F = (C_{l_{AM}} + C_{l_{dyn,stall}}) F \quad (3.111)$$

Where $C_{l_{dyn,stall}}$ and $C_{d_{dyn,stall}}$ are the values resulting when dynamic stall correction is applied to original values.

3.1.2.4. Flow curvature

Since the blades rotate, curvature effects are triggered during the movement. So it is not simple to evaluate a single angle of attack to be used in the static polars data because it will not be constant due to such effects. On account of that it is necessary to introduce a correction model. In turbinesFoam library it is based on Goude's work [29], as reported in [8, 64]. The effective angle of attack here is expressed as:

$$\alpha = \delta + \arctan \frac{|V_{local}| \cos(\theta - \beta)}{|V_{local}| \sin(\theta - \beta) + \Omega R} - \frac{\Omega x_{0r} c}{V_{ref}} - \frac{\Omega c}{4V_{ref}} \quad (3.112)$$

Here δ is the pitch angle of the blade, V_{local} the local inflow velocity, θ the azimuthal position, Ω turbine's angular velocity, R is the radius and x_{0r} is a normalized blade attachment point along the chord. V_{ref} is the reference flow velocity used to calculate the angle of attack.

Such correction is based on considering a flat plate along a circular path in potential flow whose effective angle attack α is corrected in the same way. With a 'lighter' expression:

$$\alpha = \alpha_{uncorrected} - \frac{\Omega c}{2V_{rel}} \quad (3.113)$$

Such correction leads to an offset in the angle of attack, whose magnitude increases during the first half of the revolution and decreases during the second half of the revolution.

3.1.2.5. Reynolds' number effect on the model

Reynolds' number show two different levels of influence in the model: on the polar used for dynamic stall model and on the vortex formation and especially the shedding effect. The first effect was already discussed briefly. In fact static airfoil polars are affected by Reynolds' number that determine their shape. Moreover profile data are interpolated linearly for each element based on local chord Reynolds number calculated according to the detected inflow velocity at each actuator line element. The profile data properties like the stall angle, zero-lift drag coefficient, and separation point curve fit parameters are then recomputed for each time step in order to consider Reynolds' number effect on the static data.

Considering instead the vortex shedding, as for a cylinder immersed in the flow, is controlled by two main

adimensional parameters: Reynolds' number and Strouhal number, that is related to the frequency of the phenomena. The latter is often referred to as normalized shedding frequency. However, depending on the Reynolds number used and the different ratio between inertial and viscous forces, the vortex generated show different patterns more or less regular. So the structures shed by the blades will display different shapes according to the Re used.

3.2. Analytical wake modelling

As mentioned several times, wake models are the core of this thesis. Therefore, in this section a more detailed study of some of them has been performed. First of all, HAWT wake models used will be presented, discussed and analysed in their equations and their detailed properties. Since their implementation is based on the *py wake* library [82] an short explanation of how it is implemented here will be given. These models will be discussed because, even if VAWTs are the main topic of the this thesis, wake models for such turbines are based on the ones already existing for HAWTs so at first it is necessary to prove their validity. Then the wake models used for VAWTs will be discussed and analysed in details.

3.2.1. Wake model for HAWTs

As already mentioned before, the chosen methods for HAWTs are Jensen's method (NOJ) [43], discussed in Section (2.4.1) and the BPA model (2.4.1). This choice has been made because these wake models are almost the only existing ones for both HAWTs and VAWTs. This is a undeniable proof that there is still a huge amount of study regarding VAWT waiting to be carried out, unlike HAWTs where many wake models, with different levels of accuracy, have been developed.

3.2.1.1. Jensen model for HAWTs

As discussed in Chapter (2) Jensen model is based on mass conservation only and on the assumption of a top-hat (constant) distribution at each coordinate downstream of the turbine:

$$\pi r_0^2 V_a + \pi (r^2 - r_0^2) V_\infty = \pi r^2 V \quad (3.114)$$

Such equation is applied to a control volume whose edges are defined by a point just behind the turbine and a generic point in the wake as shown in Figure (2.23). From this equation is possible to extract an expression for wake's velocity:

$$V = V_\infty \left[1 - \frac{2}{3} \left(\frac{r_0}{r_0 + k_w x} \right)^2 \right] \quad (3.115)$$

Where the following expression has been used to relate the velocity behind the turbine and the freestream (it comes from the classical theory):

$$V_a = \frac{1}{3} V_\infty \quad (3.116)$$

However this expression do not show universal validity, so it can be seen as a major simplification. In reality, the relation $V_a - V_\infty$ is function of blades' loading.

To keep into account the variation in crosswind velocity, it's possible to introduce a correction for both x and r_0 by adding a modulation factor based on cosine. A further correction is related to the ground presence which is neglected and to keep it into account the imaging technique is used: another wind turbine is placed at the negative hub respect with the first turbine. However the differences experienced in the solution are minimal and, due to the complexity of this procedure, it is avoided.

Wake develops linearly (equation (3.117)) according to a growth rate parameter, here called k_w . Such parameter is set equal to 0.1 in the original paper but it can be tuned according to experimental measurement (also the value of 0.070 is proposed). The starting value for wake's width r_0 differs from turbine's radius, since the models is valid only from 3D downstream of the turbine.

$$r = r_0 + \alpha x \quad (3.117)$$

Katic et al. [47] proposed an equation to express the velocity deficit (and not the velocity in the wake) based on the same equation by assuming a as the initial velocity deficit $1 - \frac{V_r}{V_\infty}$ and relating it to the thrust coefficient according to the actuator disk theory as follows:

$$a = \frac{(1 - \sqrt{1 - C_T})}{2} \quad (3.118)$$

Where D is turbine's diameter and k_w the linear growth rate of wake's width. Using this equation is possible to obtain the following expression for the velocity deficit:

$$\frac{\Delta V}{V_\infty} = \frac{(1 - \sqrt{1 - C_T})}{(1 + 2k_w \frac{x}{D})^2} \quad (3.119)$$

The velocity deficit is preferred to absolute velocity in the wake because it better points out how the wake is developing and how much has been recovered, especially when dealing with wind farms. A visualization of the velocity deficit expressed by Katic update is shown in Figure (3.8).

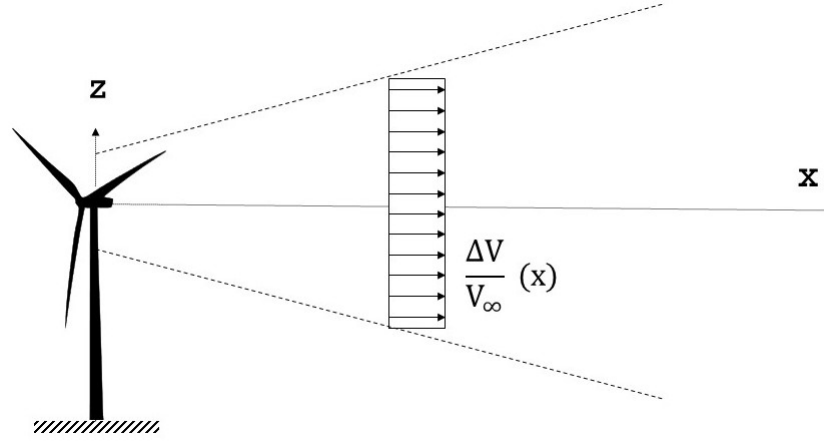


Figure 3.8: Distribution of the velocity deficit along the wake for the Jensen - Katic model

3.2.1.2. BPA model for HAWTs

The BPA model [10] is one of the most accurate analytical state-of-the-art wake models and it is based on the new assumption of using a Gaussian distribution. The starting point of this model are mass and momentum conservation where pressure (in accordance with the far-wake properties) and viscous terms are neglected. Therefore the following expression can be obtained:

$$\rho \int V (V_\infty - V) dA = T \quad (3.120)$$

Where $T = \frac{1}{2} \rho C_T A_0 V_\infty^2$ is the force experienced because of turbine's presence. As stated before, self-similarity is achieved in the far-wake region and, on account of that, it is possible to describe the normalized velocity deficit as function of the normalized radial coordinate r :

$$\frac{\Delta V}{V_\infty} = C(x) f\left(\frac{r}{\delta(x)}\right) \quad (3.121)$$

Where $C(x)$ is the maximum velocity deficit at the x position, $\delta(x)$ is wake's width at x position while f is the function which relates the two normalized variables and, as stated before, described as a Gaussian function since, according to previous studies, self-similarity is achieved in the far wake as for a bluff body. As consequence of the latter assumption, the model validity starts only from a specific point downstream $x = 2.5D - 3D$ called the onset point. A visualization of the distribution used and of the onset point is reported in Figure (3.9). Introducing the Gaussian function in the equation we obtain:

$$\frac{\Delta V}{V_\infty} = C(x) e^{-\frac{r^2}{2\sigma^2}} \quad (3.122)$$

Where σ is the standard deviation of the distribution which is related to wake's width while the shape is assumed circular. σ shows a linear development moving downstream (according to the self-similarity assumption) when considering an ABL inflow condition as discussed in Chapter (2). Assuming self-similarity for a classic turbulent wake leads instead to a non-linear development (like the one mentioned for the Larsen method in Section (2.4.2)).

$$\frac{\sigma}{D} = k^* \frac{x}{D} + \epsilon \quad (3.123)$$

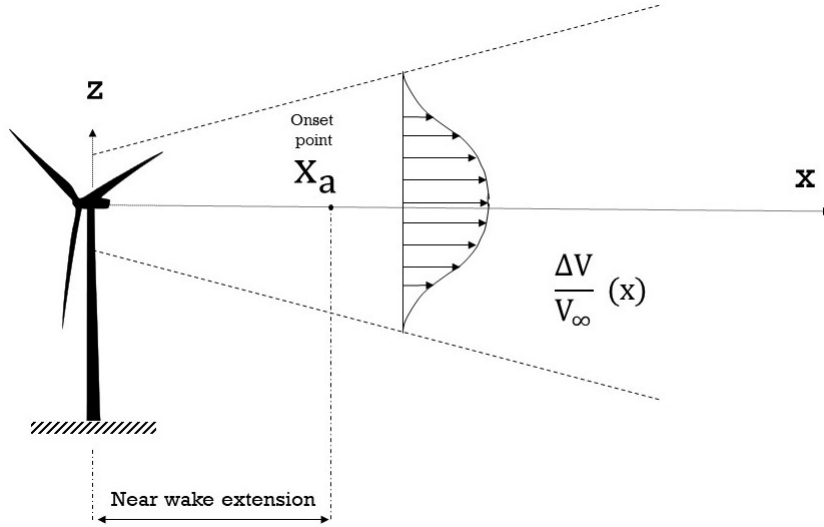


Figure 3.9: Velocity deficit distribution for the BPA model

Where k^* is the growth rate parameter (empirically derived), while ϵ is the wake width at $x = 0$. As mentioned before, the first one is a weak point of the model, since it doesn't have a universal expression or a universal value. ϵ in the original model is determined by equating the velocity deficit predicted by Frandsen et al. in [25] and the one from the current model, but this is not a correct approach observing the results of the comparison with experimental data.

Using the expression for T and (3.120), (3.122) is possible to obtain the $C(x)$ value:

$$C(x) = 1 - \sqrt{1 - \frac{C_T}{8\left(\frac{x}{D}\right)^2}} \quad (3.124)$$

With all the necessary terms at disposal, the velocity deficit can be expressed as function of the maximum velocity deficit, the geometrical properties of the turbine (the diameter and the hub height), the thrust coefficient, the coordinates, the growth rate and ϵ :

$$\frac{\Delta V}{V_\infty} = \left(1 - \sqrt{1 - \frac{C_T}{8\left(k^* \frac{x}{D} + \epsilon\right)^2}}\right) e^{-\frac{1}{2\left(k^* \frac{x}{D} + \epsilon\right)^2 \left(\frac{z-z_h}{D}\right)^2 + \left(\frac{y}{D}\right)^2}} \quad (3.125)$$

As stated before, the expression of ϵ is found equating a constant velocity deficit distribution behind the turbine and the Gaussian one predicted by the current model. From this calculation the following value is obtained:

$$\epsilon = 0.25\sqrt{\beta} \quad (3.126)$$

Where β (as for Frandsen model) comes from the actuator disk theory and relates the area swept by the turbine and the area just behind the initial expansion (where pressure has reached the equilibrium) and is function of the thrust coefficient only:

$$A_a = \beta A_0 \quad (3.127)$$

$$\beta = \frac{1}{2} \frac{1 + \sqrt{1 - C_T}}{\sqrt{1 - C_T}} \quad (3.128)$$

By comparison with LES data, a better estimation of ϵ can be provided:

$$\epsilon = 0.2\sqrt{\beta} \quad (3.129)$$

3.2.1.3. Wake decay constants

One of the main aspects to deal with is the choice of the wake decay constant, a parameter strictly related to wake width development. In analytical wake models it expresses a link between wake width and the coordinates downstream of the turbine considered. As stated before, several expressions have been proposed

in the literature as well as constant values to be assumed. Nevertheless, such equations and values are not universal, they depend on the case analysed, as stated many times. Even Bastankhah and Portè-Agel [10] already mentioned the need of a deeper understanding about how the growth rate is affected under different conditions.

The best approach to define the wake decay constant would be to perform a series of experimental tests with the same Reynolds number and finding an equation to express how this parameter changes with the turbulence intensity. In fact many studies [10, 11] stated that such parameter only depends on the turbulence intensity, which changes along the wake. So, a law depending on the local turbulence intensity, the downstream coordinate and the Reynolds' number should be provided. Otherwise the best idea is to test different expressions for the wake decay constant from the literature and search for the one used for a similar case to the one studied.

Validating the HAWTs wake models different expressions are considered to calculate the wake decay constant. For the Jensen model, the value used depends only on the location of the turbine, as reported in Table (3.6). This is an extremely simple way to express the wake decay constant and do not require any additional

Jensen model - k	
Onshore turbine	0.1
Offshore turbine	0.04

Table 3.6: Values of the wake decay constant for the Jensen model

input or tuning. At the same time it is not that accurate. A possible alternative would have been to use the values proposed by Jensen in the original paper, 0.1, as mentioned in the related paper, however this value is too high.

Concerning the BPA model instead, things are more complex. There are several values proposed in [10], as shown in Figure (3.10), and, as mentioned before, they are not the same value since they depend on the condition tested. From Figure (3.10) and the related conditions reported in [10], it is possible to conclude

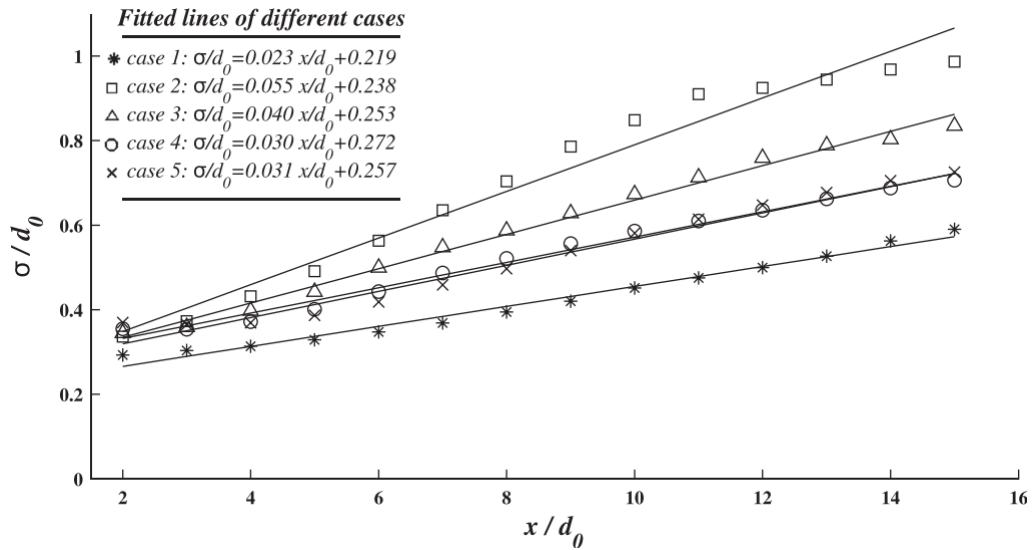


Figure 3.10: Different values for different cases analysed, image from [10]

that the effect of turbulence intensity on wake growth is related to mixing effects, which have a turbulent nature. Turbulence intensity of the incoming flow modifies this phenomenon leading to different recovery lengths. With low environmental turbulence intensity ($I_\infty < 0.07$) its influence on the wake growth parameter decreases and the turbulence added by the turbine has more relevance. Modifying the thrust coefficient C_T (with fixed turbulence intensity) it seems instead that wake's width at small downwind distances is larger for higher C_T , but moving downstream the difference remains almost constant with similar slopes.

These are important conclusion but rather than using one of the values reported by Bastankhah, searching for the most similar conditions to the ones analysed in this thesis work, the expression used is the one proposed by Niayifar et al. [72], called Niayifar's law. Such expression reported in equation (3.130) is valid only

for high turbulence cases and requires the calculation of the induction factor. Focusing on the method itself, it assumes that k^* only depends on turbulence intensity (thrust coefficients does not have any influence) and especially the local value:

$$k^* = 0.3837I + 0.003678 \quad (3.130)$$

where I is the local turbulence intensity at hub height. In fact when moving downstream the turbulence intensity changes as well as the growth rate parameter so evaluating the local turbulence intensity according to equations (3.131) and (3.132) and then using it in equation (3.130) is possible to calculate the k^* . However, after a certain amount of space, turbulence intensity remains constant and so the k^* , so theoretically it would be possible to use only one value of I , the freestream one, in order to simplify the calculation, but with major error.

$$I_+ = \sqrt{I^2 - I_\infty^2} \quad (3.131)$$

Where I_+ is the added turbulence intensity (due to the turbine presence) and I_∞ is the ambient turbulence intensity.

$$I_+ = 0.73a^{0.8325} I_\infty^{0.0325} \left(\frac{x}{D}\right)^{-0.32} \quad (3.132)$$

a is the induction factor that can be calculated with the actuator disk theory. Final remark is that, as mentioned, the expression is valid for only turbulence intensities in the following range $0.065 < I < 0.15$. In order to overcome such problems, the code version of the Niayifar's law in py-wake library [82] assumes different values depending on the turbulence intensity experienced:

- If $I > 0.15$, $k = 0.064$
- If $0.065 \leq I \leq 0.15$, $k = 0.4I + 0.004$
- If $I < 0.065$, $k = 0.0026$

This way is possible to have an expression for the wake decay that changes depending on the conditions. The great advantage of HAWTs is that there are many similar equations that, even without universal validity, provide a wide range of possible solutions and it is possible to choose the one most similar to the case currently analysed. This not happens for VAWTs that suffer a substantial shortage of studies. So deciding which wake decay constant to use is a compromise for VAWTs.

3.2.1.4. py wake

py-wake is an open source library developed in Python environment. It has been used to test the validity of wake models for HAWTs, before translating them to VAWT cases. Here in fact, several analytical wake models are already implemented and supported by optimization packages. This make py-wake a considerable tool at disposal in studying wake models performances and limitations.

In particular py-wake is a wind farm simulation tool that can perform different tasks:

1. Calculating wind farm flow fields
2. Calculating power production of wind farms
3. Calculating annual energy production of wind farms

Even being implemented in Python is extremely fast due to the vectorization used and the numerical libraries used. Still featuring different engineering models, the interface is unified for all of them, generalizing the approach to the calculation. The calculation performed is based in a series of step, reported in Figure (3.11).

Input parameters for each turbine are defined in the *Site* and *WindTurbines* modules. The first one requires as the location of the turbine, wind features (reference value and direction) and expresses the local wind condition in terms of wind speed, direction and turbulence intensity. Moreover it also evaluates the probability of each possible combination of wind speed and direction, as well as the distance along the three main coordinates between turbines (which is complex in non-flat terrain conditions). The library already provides a few predefined sites of different complexities. The second module, *WindTurbines*, requires the effective velocity as input and then calculates the power, the thrust coefficients and provides the geometrical properties of the turbine (hub-height and diameter). All the information are provided to the *WindFarmModel* module that calculates (after calling the engineering models or higher order simulations) the effective wind speed, power productions and flow maps, which are the most relevant for the purpose of this thesis.

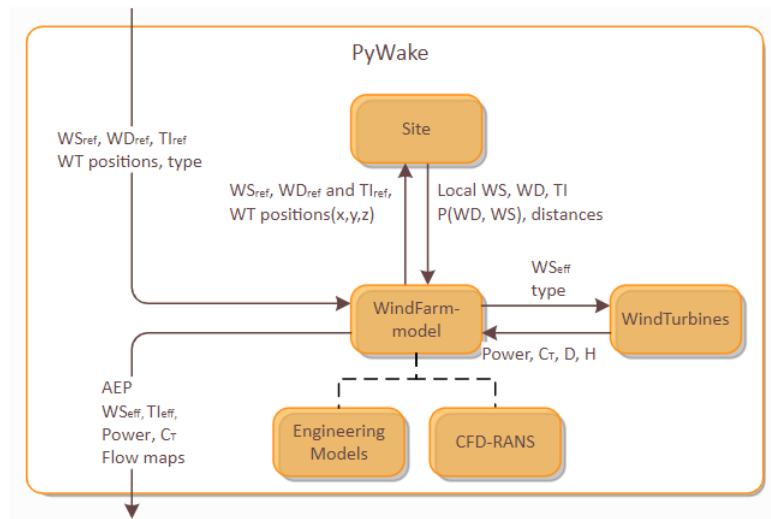


Figure 3.11: Overview of py-wake library workflow, image from [82]

Engineering wind farm models aims to select which procedure are used to replicate blockage and how it (and the wake) propagate downstream. They based on a common structure, displayed in Figure (3.12), starting from a model to evaluate wake's deficit from one turbine to another in the module *DeficitModel*. There is a *SuperpositionModel* package that defines how to superimpose the deficit generated by different turbines and a *Blockage DeficitModel* module that has the target of calculating the blockage deficit from one turbine to the other in the plant. The last three modules are *RotorAverageModel*, to consider wind speed variation over the rotor, *textitDeflectionModel* used in case of yawed turbines and *TurbulenceModel* to replicate the turbulence added from the turbine in the wake.

py-wake library features two possible classes for wind farm models:

- *Propagate-Downwind*: very fast model since it only performs a minimum of deficit calculations. It iterates over all turbines in downstream order, calculating at each iteration the effective wind speed at the current turbine as the free stream wind speed minus the sum up the deficit from upstream sources. Using this velocity as inflow value, it calculates the deficit caused by the current turbine on all downstream

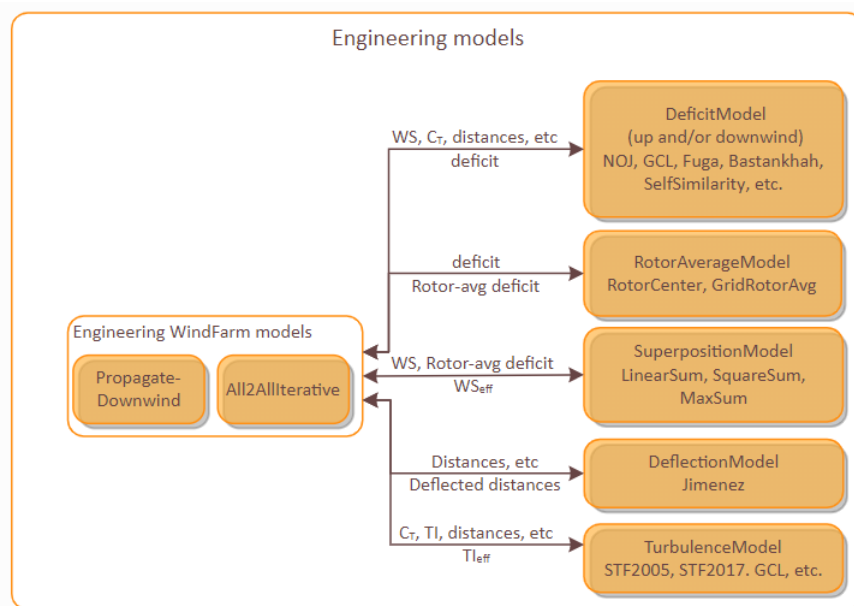


Figure 3.12: Structure of engineering models for wind farms in py-wake, image from [82]

destinations. This procedure neglects upstream blockage effects.

- *All2Alliterative*: slower than the previous but correctly replicates the blockage effect. Even in this case the model sums up the deficit from all wind turbine sources and calculates the deficit iteratively, seeking for convergence and recalculating even the velocity and thrust coefficient of upwind turbines, because of the blockage effect.

For more details about the modules used, the possible solution and everything more technically related `py-wake`, the reader is referred to [82]. However, among all the packages at disposal, the core of the library are the wake deficit models, which are several:

- NOJ model, Jensen model
- Fuga model, using look-up tables
- BPA model (only far wake)
- BPA coupled with IEA task 37 documentation [40]
- Larsen model
- BPA model coupled with Niayifar's law
- BPA model coupled with Zong update

Each one of the model is based on a specific structure that features a class function to calculate the deficit which is called in the wind farm model itself. Almost every model features a series of function in the deficit calculation that are similar most of the times. The ones most frequently observed are:

- Function to calculate the effective velocity deficit.
- Function to calculate the wake decay parameter
- Function to calculate wake's radius.
- Function to calculate deficit transport towards downstream direction.

The ones that will be validated in Chapter (4) against experimental and numerical data are the NOJ model and the BPA model coupled with Niayifar' law, in order to investigate their validity before transposing them to VAWTs case. Their implementation is based on Section (3.2.1.1) and (3.2.1.2).

3.2.2. Wake model for VAWTs

As discussed in Chapter (2) the wake model for VAWTs chosen to be implemented are the models from Abkar [2]. Here a summary of why such models (top-hat and Gaussian) have been chosen is presented:

- The range of choices of analytical wake models for VAWTs is not so wide
- Only one input parameter is required, or 2 if the asymmetry along spanwise and crossflow directions is considered
- Correct shape for the far wake (circular one)
- High accuracy in the far wake region
- Top-hat model overcomes the deficits of the Gaussian model, which is not able to replicate near wake flow field as well as high ARs conditions
- Extremely easy to be implemented

Therefore, the following sections will describe in details the wake models, their equations as well as the assumptions in detail compared to the others already cited in Chapter (2).

3.2.2.1. Top-hat model

As already stated, this model is a translation of the Jensen model [43] for HAWTs. The wake is assumed to have a rectangular shape that develops linearly along both crossflow and spanwise directions according to the following expressions:

$$H_w = H + 2k_{wz}x \quad (3.133)$$

$$D_w = D + 2k_{wy}x \quad (3.134)$$

Where H and D are the height and the diameter of the turbine while k_{wz} and k_{wy} are the growth rates of the wake for the z and y direction respectively. The shape evolution of the wake is shown in Figure (3.13). The growth rates depend on the turbulence intensity only (for an ABL inflow condition) and it is possible to

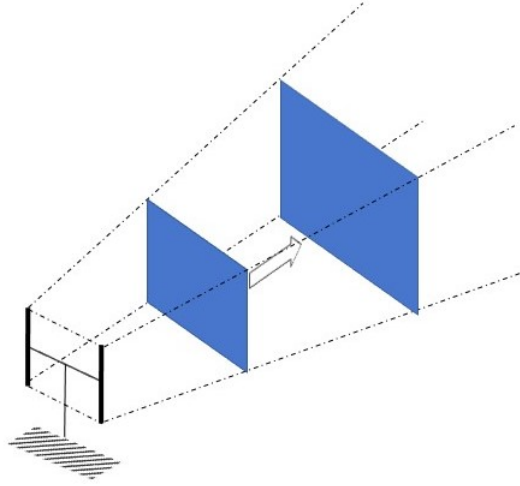


Figure 3.13: Visualization of wake's evolution moving downstream for the top-hat model

assume them equal along both crossflow and spanwise direction. An equation for k_w is proposed:

$$k_{wy} = k_{wz} = k_w = 0.4I \quad (3.135)$$

The proposed equation will be discussed in details in the following sections since the choice of the wake decay constant is a relevant topic.

Introducing a control volume whose surfaces are located at a certain downstream point in the the wake and just behind the rotor, it is possible to write the mass continuity equation (this leads to the neglect of side flows) and express the velocity deficit normalized with the freestream velocity:

$$\rho A_w V = \rho V_a A_p + \rho V_\infty (A_w - A_p) \quad (3.136)$$

A_w is the wake area at a generic downstream position and A_p is the turbine projected area ($A_p = HD$). The induction factor ' a ' which relates the velocity just behind the rotor (V_a) and the freestream velocity V_∞ is introduced and expressed according to the actuator disk theory (1D momentum theory):

$$V_a = (1 - 2a) V_\infty \quad (3.137)$$

$$a = 0.5 \left(1 - \sqrt{1 - C_T} \right) \quad (3.138)$$

So it only depends on the thrust coefficient.

Introducing equation (3.137) in (3.136), the following expression for the velocity deficit is obtained:

$$\frac{\Delta V}{V_\infty} = \frac{V_\infty - V_w}{V_\infty} = \frac{2a}{(1 + 2k_{wz} \frac{x}{H})(1 + 2k_{wy} \frac{x}{D})} \quad (3.139)$$

Such velocity deficit is a top-hat distributed velocity deficit, a constant distribution along both spanwise and vertical direction, determined according to the induction factor (and so the thrust coefficient) and the geometrical properties of the turbine.

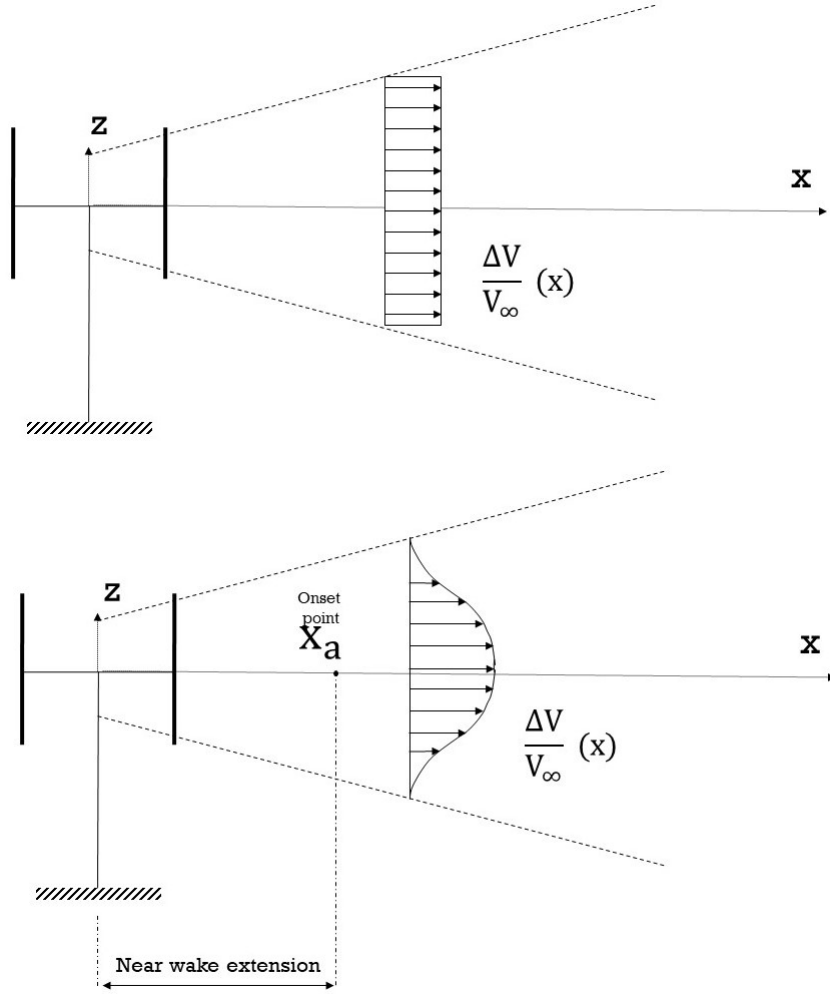


Figure 3.14: Distribution of the velocity deficit and the evolution of wake width for the Abkar top-hat (top) and Gaussian model (bottom)

3.2.2.2. Gaussian model

The Gaussian model instead is a translation of the one proposed by [10] and is based on self-similarity in the VAWT wake, which has been demonstrated several times (see for example [3]). On account of that a 2D Gaussian distribution is used for the velocity deficit, as shown in Figure (3.14).

Even in this case the wake develops linearly and its width is related to the standard deviation. Wake's shape is elliptical if different growth rate constants are assumed:

$$\sigma_z = k_z^* x + \epsilon H \quad (3.140)$$

$$\sigma_y = k_y^* x + \epsilon D \quad (3.141)$$

k_y^* and k_z^* are the growth rate, while ϵ is the width of the wake at the rotor position. The values suggested for the growth rate parameters are the same along both the crossflow and spanwise direction for the ABL inflow condition used in this study:

$$k_y^* = k_z^* = k^* = 0.35I \quad (3.142)$$

Assuming growth parameters equal means having a circular shape for the wake, as shown in Figure (3.15). The expression used for ϵ is the same of [10] and is based on equating the deficit predicted by the top-hat model at the onset point and the one predicted with the Gaussian distribution. This means that the starting values of wake deficit and wake width are the ones calculated just behind the turbine with the actuator disk theory. So no account is given towards near wake and the fact that equilibrium is not reached yet.

$$\epsilon = 0.25\sqrt{\beta} = 0.25\sqrt{\frac{1}{2} \frac{1 + \sqrt{1 - C_T}}{\sqrt{1 - C_T}}} \quad (3.143)$$

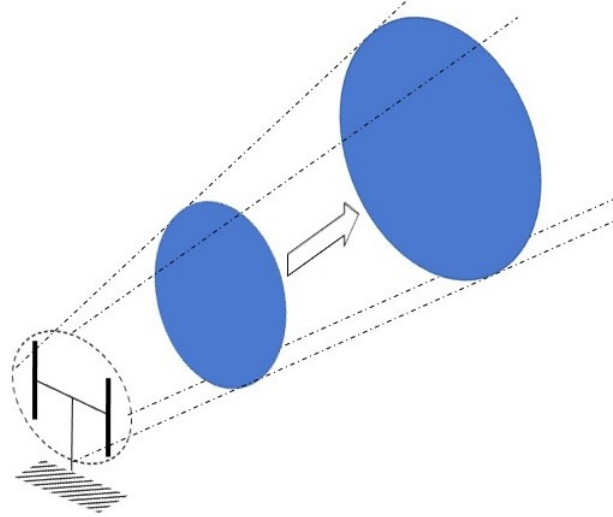


Figure 3.15: Visualization of the wake's evolution moving downstream for the Gaussian model

The expression for the velocity deficit comes from the mass and momentum balance. As for BPA model [10], the maximum value of the velocity deficit is obtained by adding the expression for the thrust coefficient and the velocity in the wake in the momentum conservation.

$$T = \frac{1}{2} \rho c A_p C_T V_\infty^2 \quad (3.144)$$

$$\frac{\Delta V}{V_\infty} = C(x) e^{-\frac{r^2}{2\sigma^2}} \Rightarrow V = V_\infty \left(1 - C(x) e^{-\frac{1}{2} \left[\left(\frac{z-z_h}{\sigma_z} \right)^2 + \left(\frac{y}{\sigma_y} \right)^2 \right]} \right) \quad (3.145)$$

Equations (3.144) and (3.145), are introduced in (3.146), which has been simplified by neglecting the pressure and viscous terms.

$$\rho \int V (V_\infty - V) dA = T \quad (3.146)$$

$$C(x) = \frac{\Delta V_{max}}{V_\infty} = 1 - \sqrt{1 - \frac{C_T}{2\pi \left(\frac{\sigma_z \sigma_y}{A_p} \right)}} \quad (3.147)$$

The resulting expression for the maximum velocity deficit allows to find an explicit expression for the velocity deficit.

$$\frac{\Delta V}{V_\infty} = \frac{\Delta V_{max}}{V_\infty} e^{-\frac{1}{2} \left[\left(\frac{z-z_h}{\sigma_z} \right)^2 + \left(\frac{y}{\sigma_y} \right)^2 \right]} = \left(1 - \sqrt{1 - \frac{C_T}{2\pi \left(\frac{\sigma_z \sigma_y}{A_p} \right)}} \right) e^{-\frac{1}{2} \left[\left(\frac{z-z_h}{\sigma_z} \right)^2 + \left(\frac{y}{\sigma_y} \right)^2 \right]} \quad (3.148)$$

Where z_h is the hub height and $A_p = DH$ is the turbine area. As for the top-hat model, this equation only needs as input the geometric properties of the turbine, the thrust coefficient and the wake decay parameter.

3.2.2.3. Wake decay constant and turbulence effect on the models

The choice of the wake decay constant is one of the major issues when dealing with analytical wake models for VAWTs. Unlike HAWTs, there is a substantial shortage of studies and analysis focused on defining equations, relations or simply constant values that express wake recovery rate. Moreover, VAWT present a flow field absolutely different from the one of a HAWT and it is not possible to simply translate the equations used for HAWT and expect an high accuracy for the results. However, since there are no alternatives, equations for HAWT wake decay constant are widely used, unless experimental tuning is possible (this implies being able to use facilities and so on).

After such preliminary considerations, the problem is discusses. The wake decay parameter or wake growth rate k_w or k^* relates wake's expansion to the downstream coordinate x , as already mentioned in Section (3.2.1.3). Considering a VAWT, it is possible to make a distinction between wake decay constant value along

the horizontal plane ($x - y$ plane) k_y^* and its value along the vertical plane ($y - z$) k_z^* since the expansion experienced along the two directions is not the same and is affected, especially in the near wake, by the geometrical properties of the turbine (the height H and the diameter D). In studies from the literature [2], these values were assumed equal, in order to replicate a circular shape in the far wake (where the wake is independent from the AR value). However, the values used for VAWTs wake models are based on experimental tuning [51] or specific laws for HAWTs [2]. The former do not meet the requirements of this thesis, moreover (as already stated several times) their expression is not universal and depends on many factors. The second case (which is extremely relevant) will be discussed afterwards, as it is one of the approach replicated in this thesis.

Before moving on, the possible approaches when defining the wake decay constant are summarized:

- Assumed constant when considering uniform inflow conditions [43]
- Tuned according to numerical/experimental studies [10, 51]
- Based on empirical laws [2, 72]

The solutions used in this thesis are now presented and analysed.

3.2.2.3.1 Niayifar's law

The first law used is the one from [72], which has been already discussed for the HAWT case in Section (3.2.1.3). The equations used are the same of before, for the sake of clarity, they have been reported also here:

$$k^* = 0.3837I + 0.003678 \quad (3.149)$$

$$I_+ = \sqrt{I_{wake}^2 - I_0^2} \quad (3.150)$$

$$I_+ = 0.73a^{0.8325}I_0^{0.0325}\left(\frac{x}{d}\right)^{-0.32} \quad (3.151)$$

The distinction for the k value/expression depending on the local turbulence intensity has been kept:

- If $I > 0.15$, $k = 0.064$
- If $0.065 \leq I \leq 0.15$, $k = 0.4I + 0.004$
- If $I < 0.065$, $k = 0.0026$

Unlike the HAWT case, this set of equations has been tested also with a different expression for the induction factor (3.152) reported in [16]. Such equation is a polynomial relationship function of the thrust coefficient and a series of constants, it also accounts for the Glauert correction when considering induction factors higher than 0.5. It is important to point out that also this equation is for HAWTs and not for VAWTs.

$$a = k_3C_T^3 + k_2C_T^2 + k_1C_T + k_0 \quad (3.152)$$

Where $k_3 = 0.0892074$, $k_2 = 0.0544955$, $k_1 = 0.251163$ and $k_0 = -0.0017077$. However, the differences compared to the classic expression from the actuator disk theory are irrelevant.

Another aspect that is important to report is that the Niayifar law was tested also using the freestream turbulence intensity only and not the local turbulence intensity. This way the dependency from the latter parameter is lost, but since after a certain amount of space I remains constant, testing the same environmental value was considered a good idea, even in order to avoid applying an equation based on the induction factor. The latter in fact is a specific parameter for HAWTs. Unfortunately the results were poor and did not meet the previous mentioned expectations. For this reason the classic approach of the method has been used.

Some conclusion about this assumption can already be drawn. This model was chosen because provides one of the few expressions for the wake decay constant that presents an explicit relation with the local turbulence intensity that, as mentioned in Section (2.2.3.5), suffers major variations moving downstream when considering the wake of a VAWT. However, this relation showed some problems because is for HAWTs that experience an ABL inflow condition and not for VAWTs in uniform inflow condition.

In the end high accuracy results when using this equation is not expected, but studying and testing it allows to make some conclusions about its performances and where it reaches the best results when compared with high fidelity data.

3.2.2.3.2 Abkar's law

Additional expressions for the wake decay constant are provided by Abkar [2] as we mentioned before. Such expressions have been reported in equation (3.135) for the top-hat model and (3.142) for the Gaussian model and are reported here for the sake of clarity:

- For the top-hat model:

$$k_{wy} = k_{wz} = k_w = 0.4I_\infty \quad (3.153)$$

- For the Gaussian model:

$$k_y^* = k_z^* = k^* = 0.35I_\infty \quad (3.154)$$

As shown, such equations has been used as function of the freestream turbulence intensity since it has been observed that its value is almost constant behind the turbine. Moreover, this way is possible to compare the results of a law based on a non-constant turbulence intensity and one based on a constant value of it. Using the freestream turbulence intensity is less accurate, since in reality the value changes, but at the same time no additional equations, which are based on HAWTs aerodynamic and not VAWTs' ones, are introduced. Such equations would increase the complexity, the input required and could potentially lead to an additional error. Abkar's laws assume the same values along both spanwise and crossflow direction, in order to replicate the circular shape of the far wake. They have been introduced for HAWTs in ABL inflow condition, so even in this case the results to be expected are not so accurate. They will be compared with the predictions obtained using the previous Niayifar law, in order to figure out which one performs better and where.

A possible idea for future researches is introducing a new expression that allows to calculate the wake decay constant as function of the Reynolds number, the downstream position and the local turbulence intensity. The target would be taking into account specific and unique phenomena of VAWTs (not seen in HAWTs) such as the tip vortices, that have huge relevance in wake recovery and consequently on the wake decay constant. This way it would be possible overcome the problems related to non-universal expression that are widely used at the moment.

4

Validation and cases analysis

Validation of results when dealing with different types of implementations is extremely important since it enables to understand possible bugs in the code but especially if any kind of algorithm or numerical problem is present. In particular, when dealing with CFD simulations, numerical issues related to the discretization, the resolution and so on can give birth to erroneous results. For this reason it is always necessary to make comparisons with data already validated from the literature or experimental data as validity 'tests' for the presented calculations.

This section deals with the validation aspect, firstly presenting the cases used for this procedure, enlisting the parameters used and then presenting the results coming from the validation itself for both numerical simulations and analytical wake models.

4.1. Benchmarks and simulations set-up

Different study cases were adopted to validate and analyse both the results from the numerical simulations as well as from analytical wake models. In the latter case, the validation was carried out against both literature data and the same numerical cases studied for the actuator line model coupled with URANS equations. In this section all the data related to such cases are reported and briefly analysed. Such data are extremely important for discussions in Section (4.2) and Chapter (7).

4.1.1. Numerical simulations cases analysed

In this section the study cases are analysed one by one. Three different cases are proposed for the comparison, one based on an experimental study and the others coming from literature studies. This way is possible to cover from low to high Reynolds numbers. The cases and the related studies are reported in Table (4.1). Therefore the purpose of this section is to:

AL + URANS simulations cases		
Case name	Source	Related paper
Low Reynolds' number	Experimental tests	Huang et al. [36]
Medium Reynolds' number	PIV measurements and LES simulations	Tescione et al. [110], Mendoza et al. [65]
High Reynolds' number	LES simulations	Shamsoddin et al. [96]

Table 4.1: Cases analysed for the validation of numerical simulations

- Understand the differences between the cases analysed and which are the requirements needed to perform the calculations for different Reynolds' numbers

- Figure out which are the settings and the conditions used for the numerical simulations in terms of mesh used, inflow condition and so on

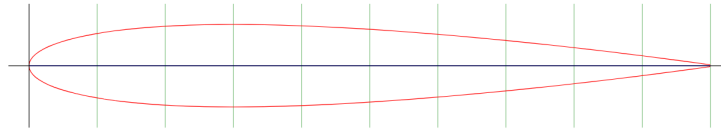


Figure 4.1: Shape of the NACA 0012 symmetric profile. Data provided by <http://airfoiltools.com/plotter/index?airfoil=naca0018-il>

4.1.1.1. Cases description

- **Small VAWT - Low Reynolds' number:**

The case reported here features a small scale wind turbine experimentally studied at the TU Delft university and realized by Huang et al. [36]. Such turbine was tested in a wind tunnel open-jet facility and studied using the robotic particle image velocimetry (PIV) technique.

The turbine is a two-bladed H-rotor VAWT with NACA0012 used for the blades with a tower and horizontal struts that connect the former to the blades. A summary of the geometric properties is reported in Table (4.2). The simulation was run for 6 seconds to replicate almost 80 revolutions of the turbine, while the time step Δt used is 0.0005 s.

Turbine properties	
Diameter	0.3 m
Height	0.3 m
Blade chord	0.003 m
Number of blades	2
Tip speed ratio λ	2.5
Rotational speed	≈ 796 rpm
Reynolds number Re_D	≈ 103000

Table 4.2: Properties of the small scale wind turbine

- **Airfoil data:** As mentioned before, the blades as well as the horizontal struts are modelled with NACA0012 airfoils, which are symmetric (reported in Figure (4.1)).

As mentioned in Section (3.1.2) the local Reynolds number is required in order to extract the values from the polar to model the force source term. In this case its value is low, as reported in equation (4.1).

$$Re_c = \frac{\rho V_\infty \lambda c}{\mu} \approx 31500 \quad (4.1)$$

Where μ is $1.7885 \cdot 10^{-5} \frac{kg}{ms}$, $\rho = 1.225 \frac{kg}{m^3}$, the TSR λ is 2.5. The NACA0012 polar is provided by [99] for $Re_c = 2 \cdot 10^4$, which is the polar based on the closest Re_c to the real value experienced. The polar obtained is reported in Figure (4.2).

- **Dynamic stall model:** As for the other cases, the dynamic stall model used is the Leishman-Beddoes SG/SH. However, in this case the model was finely tuned for two main reasons:
 - When considering a low TSR (generally lower than 4, but depends on the case considered), dynamic stall model acquires high relevance because of the increase in the angles of attack experience by the blades. This is expectable if velocity triangles are considered as already discussed in Section (2.2.1).
 - With low Reynolds' number, dynamic stall happens very severely, with effects on blade's forces distribution and highly influencing the wake if TSR and turbine's configuration are kept constant. The correct forces distribution is complex to be obtained in similar conditions. For this reason the tuning operation (which is complex and time consuming) is necessary.

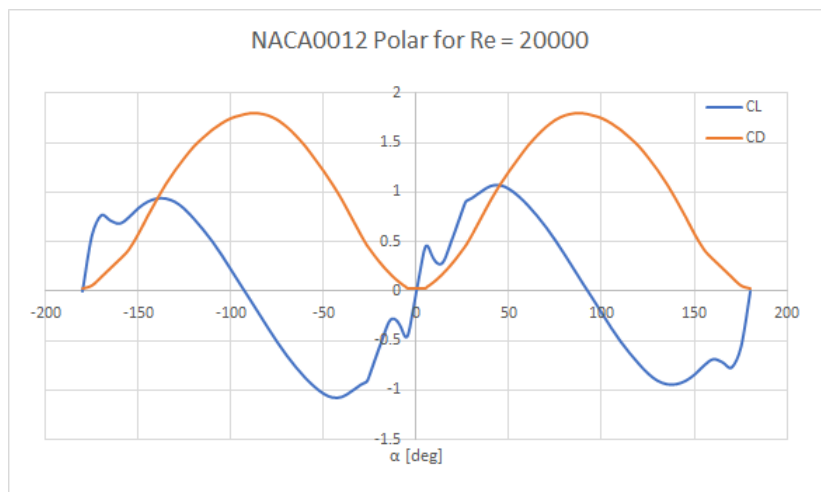


Figure 4.2: NACA0012 polar for the small scale case

Since it was a difficult tuning operation, it is possible to affirm that dynamic stall shows a major impact when low Reynolds number are observed. The coefficients introduced after the tuning operation are reported in Table (4.3), they differ from the values proposed by Dyachuk et al. [21] in Section (3.1.2.1).

Dynamic stall model coefficients	
T_p	0.5
T_f	3
T_α	3.9
$\alpha_{d.s0}$	18.73
r_0	0.01
T_v	11
T_{vl}	8
B_1	0.75
η	1
R_0	0.25

Table 4.3: Values used for the dynamic stall model SH/SG for the small scale turbine

- **Medium VAWT - Medium Reynolds' number:**

Based on the study of Tescione et al. [110] (but also used for the actuator line model validation from Mendoza et al. [65]) where a medium scale wind turbine is tested in a wind tunnel using stereoscopic particle image velocimetry (stereo PIV). The turbine is a two-bladed H-rotor VAWT with NACA0018 used for the blades. An image of the turbine used is reported in Figure (4.3), while a summary of the geometric properties is reported in Table (4.4). The attachment point between blades and struts is located at a distance of $0.4c$ from the leading edge. The struts are profiled as NACA0018, with a chord of $0.023m$, they are connected to the blades and the turbine tower and installed at a distance of $0.2m$ from the blade tips.

The simulation has been run for 6 seconds to replicate almost 45 revolutions of the turbine, while the time step Δt used is 0.002 s.

- **Airfoil data:** As stated before, the airfoil used to model the blades is NACA0018 whose shape is reported in Figure (4.4).

Blades' Reynolds number is calculated according to the tip-speed-ratio and the chord:

$$Re_c = \frac{\rho \lambda V_\infty c}{\mu} \simeq 172000 \quad (4.2)$$

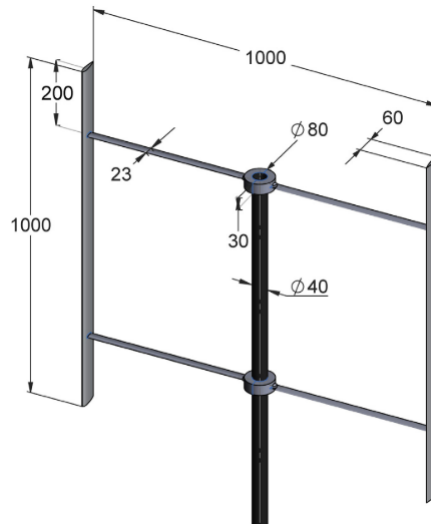


Figure 4.3: A visualization of the H-rotor turbine used in [110] and for the validation, image from [110]

Turbine properties	
Diameter	1 m
Height	1 m
Thrust coefficient	0.8
Blade chord	0.06 m
Number of blades	2
Tip speed ratio λ	4.5
Rotational speed	≈ 800 rpm
Reynolds number Re_D	≈ 637.000

Table 4.4: Properties of the turbine for the medium Reynolds' number case

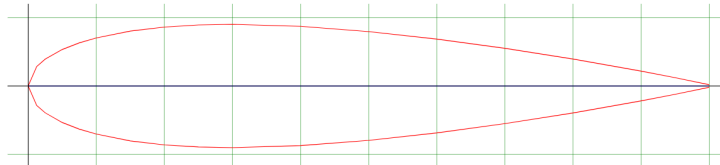


Figure 4.4: Shape of the NACA 0018 symmetric profile. Data provided by <http://airfoiltools.com/plotter/index?airfoil=naca0018-il>

Dynamic stall model coefficients	
T_p	1.5
T_f	3
T_α	3.9
α_{ds0}	18.73
r_0	0.01
T_v	11
T_{vl}	8
B_1	0.75
η	1
R_0	0.25

Table 4.5: Values used for the dynamic stall model SH/SG for the medium scale case

Where μ is $1.7885 \cdot 10^{-5} \frac{kg}{ms}$, $\rho = 1.225 \frac{kg}{m^3}$, the TSR λ is 4.5. On account of such Reynolds number, the polar used for the airfoil (essential in the application of the dynamic stall model and the actuator line theory itself) is extracted from [99]. The table selected is related to $Re_c = 2 \cdot 10^5$ which is the closest value to the current case. The polar obtained is reported in Figure (4.5).

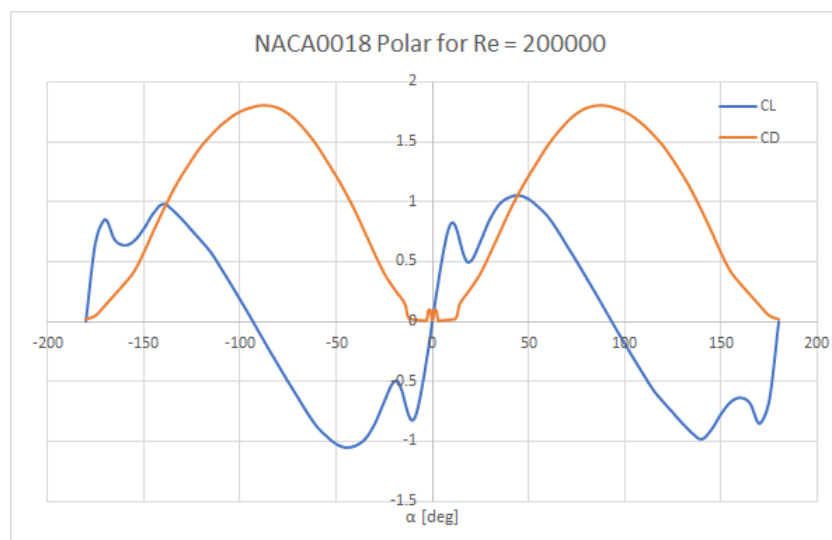


Figure 4.5: NACA0018 polar for the medium scale case

- **Dynamic stall model:** The dynamic stall model used here is the Leishman-Beddoes SH/SG model discussed in Section (3.1.2.1.3). The only remarkable aspect is what coefficients were used for it: they are reported in Table (4.5).

In this case the difference with the values suggested in [21] is limited.

- **Large scale VAWT - High Reynolds' number:**

The case of high Reynolds' number was replicated with reference to [96]. In this paper a LES framework, already validated, coupled with actuator line theory, was used to study an utility scale wind turbine. The latter is a three straight-bladed whose specifications are representative of VAWTs with a nominal capacity of 1 MW, like the so-called 'Éole' turbine in Canada that was mentioned in Chapter (2). The specifications and the geometric properties are reported in Table (4.6) while the blades are modelled as NACA0018 airfoils, like the previous test case for the medium Reynolds number.

The test was conducted using only the blades, no account has been given towards horizontal struts or the tower which are totally absent in the simulation. Even if it may seem strange testing a turbine without such additional parts, it is the convention when conducting numerical tests. The simulation

Turbine properties	
Diameter	50 m
Height	100 m
Blade chord	1.5 m
Number of blades	3
Tip speed ratio λ	4.5
Rotational speed	≈ 16.5 rpm
Reynolds number Re_D	≈ 33000000

Table 4.6: Properties of the large scale wind turbine

was run for 365 seconds to replicate almost 100 revolutions of the turbine, while the time step Δt used is 0.1 s.

- **Airfoil data:** As stated before the blades are modelled as NACA0018 airfoils, whose geometry is reported in Figure (4.4). However in this case the local Reynolds number, evaluated according to

the tangential velocity of the blades, is extremely high compared to the previous case.

$$Re_c = \frac{\rho V_\infty \lambda c}{\mu} \simeq 4500000 \quad (4.3)$$

For this reason it was not possible to use the polar from the previous case. Fortunately, it was assumed the polar provided by [99] for $Re_c = 5 * 10^6$ which represented the closest value. As for the previous cases, the polar used for this case is reported in Figure (4.6).

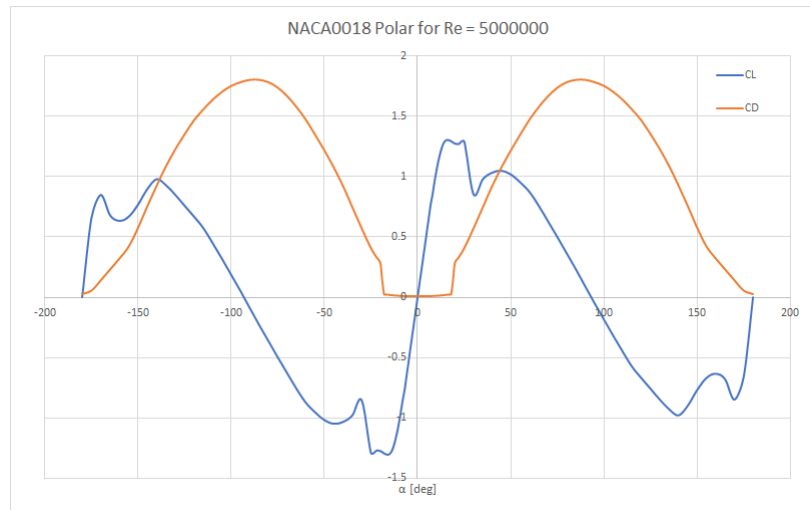


Figure 4.6: Polar used for the high Reynolds' number case

- **Dynamic stall model:** There are no particular details to be mentioned for the dynamic stall model since it displays less relevance compared to lower Reynolds cases, even because the TSR used is high (4.5).

The values used are reported in Table (4.7). Notice that they are almost equal to the ones suggested by Dyachuk et al. [21] and reported in Table (3.4).

Dynamic stall model coefficients	
T_p	1.7
T_f	3
T_α	6.22
α_{ds0}	17.46
r_0	0.01
T_v	11
T_{vl}	8
B_1	0.5
η	1
R_0	0.2

Table 4.7: Values used for the dynamic stall model SH/SG for the large scale case

4.1.1.2. Numerical set up

Here the major information about the settings used in the numerical simulations are presented and discussed. It is necessary to point out that the majority of the settings used were suggested by turbinesFoam library [7] and OpenFOAM itself. Otherwise it would have been too complex and time consuming creating all the tools to analyse and perform the calculations in order to provide a method valid for the comparisons.

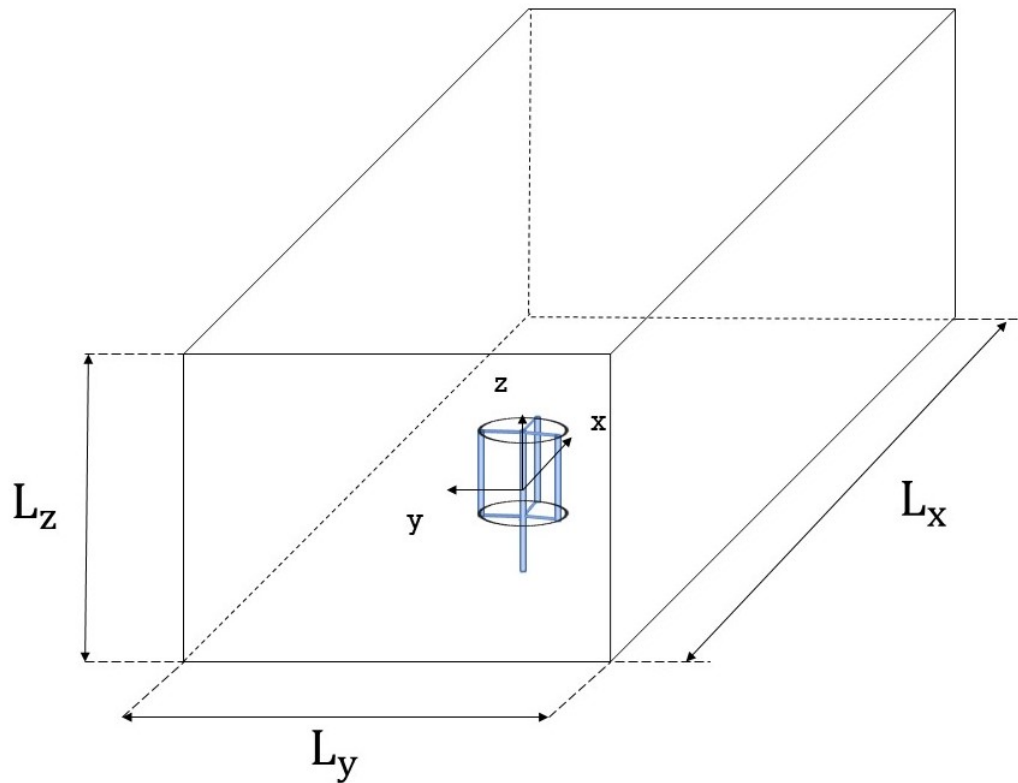


Figure 4.7: Schematic of the control volume used in every case and the related dimensions

- **Control volume and mesh:**

For each case analysed, the control volume was similar to a box (like a wind tunnel) and was characterized by 3 dimensions, one along each direction: L_x , L_y and L_z . Inside the box the blades were replaced by lines and divided into elements, acting as a force source in the domain, as discussed in Section (3.1.2). In this part of the validation, both the tower and the horizontal struts were considered (for the experimental cases). The dimensions are displayed in Figure (4.7) and reported for each different Reynolds' number case, as well as the number of blade elements (also for the struts) in Table (4.8). The choice of domain dimensions was driven by previous literature numerical studies and by the values suggested there.

AL + URANS simulations control volume details

Case name	L_x [m]	L_y [m]	L_z [m]	# Blade elements	# Tower elements	# Struts elements
Low Reynolds' number	6	2.4	2.1	20	20	6
Medium Reynolds' number	25	8	7	20	20	6
High Reynolds' number	1000	400	650	200	-	-

Table 4.8: Description of the control volume for the numerical simulations

Considering instead the mesh description, the same approach was used for all the three cases analysed, choosing cubic cells and a mesh refined by levels, where bigger cells are split into little and little portions, in order to perform a more accurate calculation. The base size of the cells was set depending on

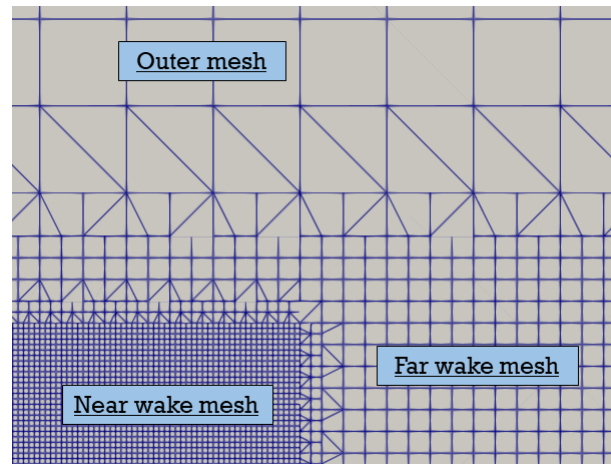


Figure 4.8: Description of the cells in the mesh and the different refinement

the number of cells used to divide each side of the box. Even if it is not a great refinement technique, it is crucial to take into account that it was necessary to reduce the computational cost.

The refinement was focused on specific regions: the far wake, the near wake and the turbine region. Generally the far wake region (near the outlet surface) presents a lower level of refinement, since gradients are much less intense, so there was no need to use too many cells, otherwise the computational cost would rapidly increase. The near wake instead features high gradients and rapid variations, so the largest number of cells was located there to capture such flows. The exact refinement region will be briefly described and introduced in the next sections, but 3 levels of refinement can be identified:

- Outer mesh, where the bigger cells are located
- Far wake mesh, where intermediate cells are located
- Near wake mesh, where the grid is finest

In some cases there was no distinction in the refinement performed in the near and far wake, so the dimensions were the same. The location of refinement regions will be discussed for each case, while the most relevant data regarding the mesh are reported in Table (4.8), with reference to Figure (4.8).

- **Mesh refinement, Low Re:** The most relevant details about the mesh are reported in Table (4.9) but an overview of the refinement is shown in Figure (4.9). The refinement was focused on a single region which covers both the near wake, turbine's position and the far wake. Such region is a box whose opposite vertices are $P_1 = (-0.6, -0.6, -0.6)$ and $P_2 = (3.6, 0.6, 0.6)$. The really far wake region instead (near the outlet surface) was not refined, since gradients are much less intense, so too many cells were not required here, otherwise the computational cost would rapidly increase. Here, as mentioned before, there was no difference between the refinement in the near and far wake: the level set is the same. In fact, since the case features a small scale turbine at low TSRs, dynamic stall displayed huge relevance.

Refining the mesh was possible to increase the accuracy and have a better overview of how the flow is affected by the dynamic stall phenomena.

- **Mesh refinement, Medium Re:** In this case, unlike the previous one, the refinement was different in the far and near wake, where gradients are much more higher and it was necessary to capture flow's quick variations. The refinement level for the near wake and turbine's region was the same, whose opposite vertices were $P_1 = (-0.75, -0.6, -0.6)$ and $P_2 = (4, 0.6, 0.6)$ while cells' size is reported in Table (4.9).

In the far wake instead gradients are much less intense, so too many cells were not required here, otherwise the computational cost would have rapidly increased. Such region was identified by a box whose opposite vertices were located at $P_3 = (-0.75, -0.75, -0.75)$ and $P_4 = (20, 0.75, 0.75)$. To better understand the location of such regions, see Figure (4.10).

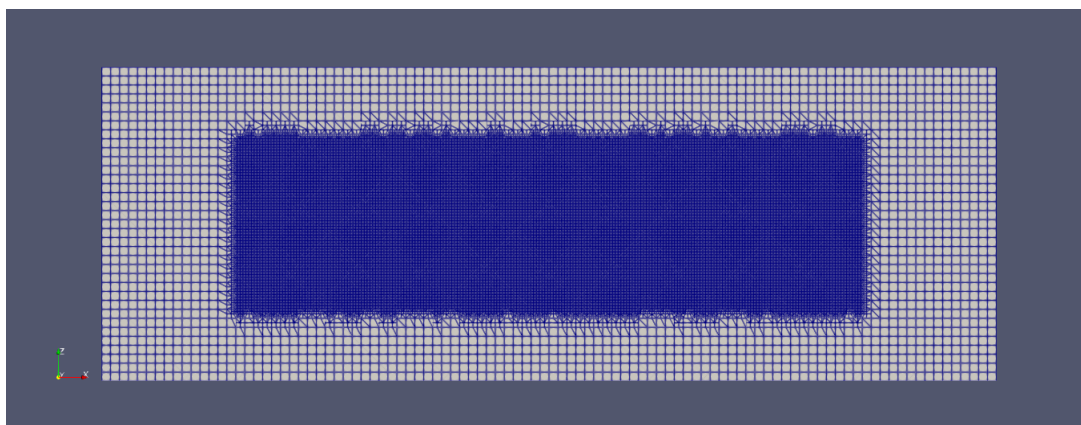


Figure 4.9: Overview of the mesh used for the low Reynolds' number case

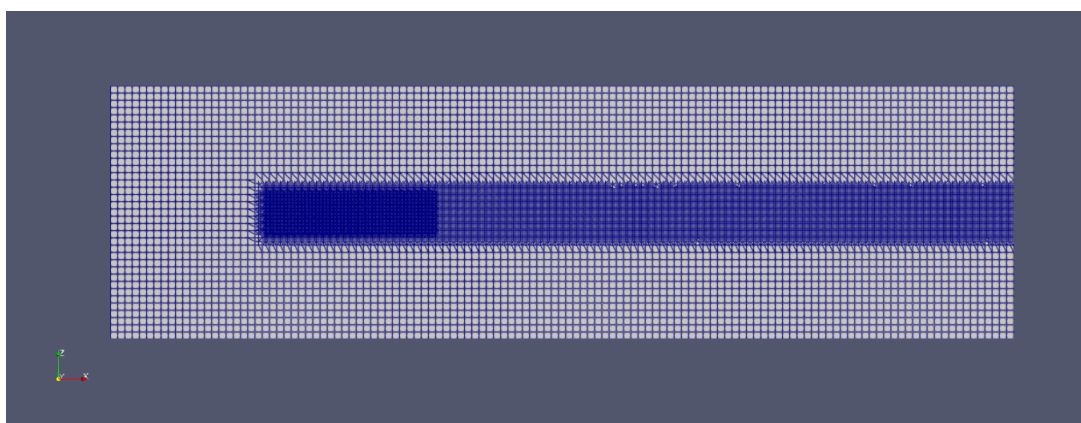


Figure 4.10: Overview of the mesh used for the medium Reynolds' number case

- **Mesh refinement, High Re:** The refinement level were different here for the far, near and turbine region. However the latter ones could be considered as a single portion of space: a box whose opposite points were $P_1 = (-100, -100, -100)$ and $P_2 = (150, 100, 200)$.

The finest grid was located in the near wake, where highest pressure gradients are present. Even the mesh in the region near the wall is refined, since in the original paper the hub of the turbine is located at a distance of $2D$ from the ground so it was necessary to refine this region.

The far wake region instead features a coarser grid and spaces from point $P_3 = (-100, -175, -100)$ to $P_4 = (800, 175, 200)$. Figure (4.11) shows the different refinement regions assumed in this case.

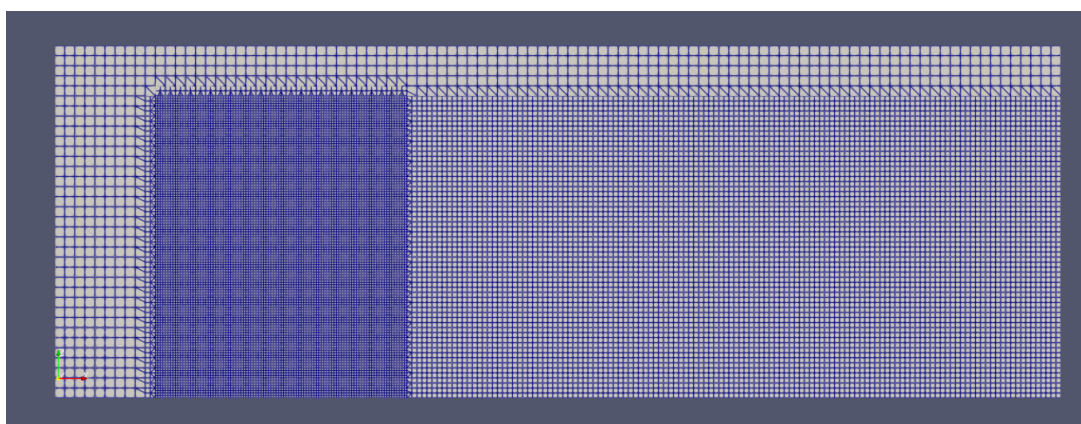


Figure 4.11: Overview of the mesh used for the high Reynolds' number case

AL + URANS simulations control volume details

Case name	N_x	N_y	N_z	# Cells	# Outer cell dimensions [m]	# Far wake cell dimension [m]	# Near wake cell dimension [m]
Low Reynolds' number	100	40	35	≈ 14 million	0.06	0.0075	0.0075
Medium Reynolds' number	125	40	35	≈ 4 million	0.2	0.05	0.0125
High Reynolds' number	100	40	35	≈ 1.8 million	10	5	2.5

Table 4.9: Details related to the meshes used

• **Inflow and boundary condition:**

- **Low Re:** The inflow condition was a uniform condition, with a velocity at the inlet equal to $5 \frac{m}{s}$ and whose profile is reported in Figure (4.12). The turbulence intensity was set to 1%, an extremely low value but coherent with a wind tunnel study. The turbulent kinetic energy and dissipation rate values were set according to the equations discussed in Section (3.1.1.3) The lateral surfaces of the domain as well as the bottom and top

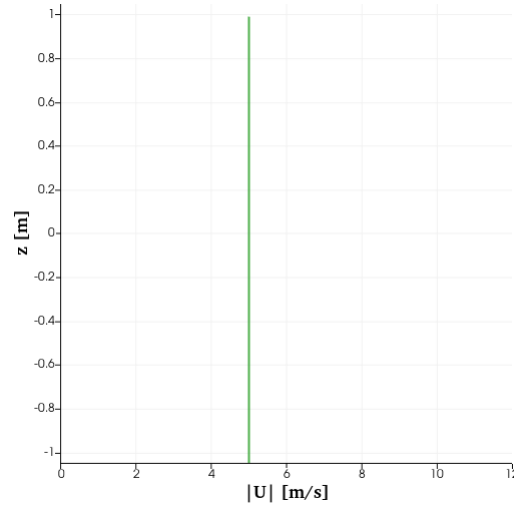


Figure 4.12: Inflow condition for the small scale turbine

wall were considered as patches, with zeroGradient condition (Neumann condition) for all the quantities calculated (V , k , ε and so on). So the noSlip condition was absent.

- **Medium Re:** The inflow condition was a simple uniform inflow condition with $9.3 \frac{m}{s}$ set as freestream value for the velocity. The slip condition at the lower and side walls was replicated setting a moving wall, with local velocity set to $1 \frac{m}{s}$ for this reason the profile obtained was not totally uniform (see image Figure (4.13)). For the top wall instead, slip condition was directly set.

The turbulence intensity was set equal to wind tunnel's maximum value, which is 0.5%, an extremely low value. The related values of turbulent kinetic energy as well as dissipation rate were evaluated according to equations reported in Section (3.1.1.3).

Unlike previous case, here side, top and bottom surfaces were considered as walls and not as patches. On account of that values on the boundaries were set according to the wall functions proposed by OpenFOAM for k , ε , ν_T . More details are reported in Table (4.10).

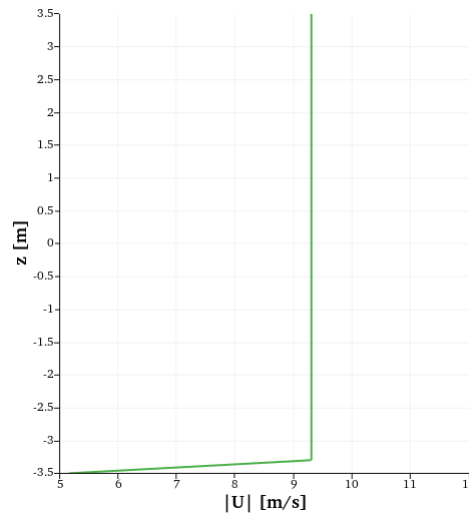


Figure 4.13: Inflow condition for the medium scale turbine

Boundary conditions for turbulence quantities

Parameter	Surface	Condition	Description
k	Top, bottom, side walls	kqRWallFunction	Neumann boundary condition
ϵ	Top, bottom, side walls	epsilonWallFunction	Weighted average of values at faces
ν_T	Top, bottom, side walls	nutkWallFunction	Calculated according to k

Table 4.10: Description of the turbulent boundary conditions for medium Reynolds case

- **High Re:** The inflow condition featured a uniform velocity profile with value $9.6 \frac{m}{s}$ that is reported in Figure (4.14). The turbulence intensity of the inflow was set at 4% since it was a high turbulence intensity case. However it is necessary to mention that the inflow condition used in the original study was an ABL inflow condition, not replicated because it was far from the objects of this thesis. Moreover the turbulence intensity used was not the one seen in the original study since the estimations for the inflow turbulence are not exact equations and they distinguish only the range of turbulence used (high, medium and low) and not slight variations. On account of that, the chosen value was a compromise and the dissipation rate was set in order to avoid the decay and replicate the constant turbulence intensity rather than satisfy the equation mentioned in (3.1.1.3).

Concerning the boundary conditions, all the surfaces (bottom, top and side) were considered

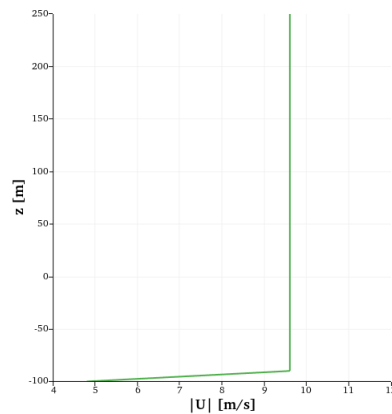


Figure 4.14: Inflow condition for the large scale turbine

as walls. However side and top walls feature a slip condition, while the bottom wall present a

noSlip condition for the velocity. The turbulence parameters instead were all based on the same functions listed for the medium Reynolds case in Table (4.10).

4.1.2. Set-up of analytical wake models for HAWTs

The models analysed in the thesis were developed based on the open source library, pywake. In order to analyse the level of accuracy and the limitations of HAWTs model, they have been validated against data coming from field measurements, LES and RANS numerical simulations, according to the procedure mentioned in the related GitLab folder [82].

The cases analysed are described in Table (4.11) and feature different parameters such as geometrical properties, inflow conditions and so on. This way the validation process was more robust, since the largest possible range of conditions were tested to check models' reliability. The numerical data used for the comparison, as reported in [82], were extracted from [114] (both LES and RANS data) and from [113] (only RANS data). The field data as well were extracted from these papers and are based on measurements of single wind turbine wakes. The models validated here are the Jensen model, called as NOJ (developed according to [43])

Site name	Downstream measurement locations	TI at z_h [%]	C_T	U at z_H [$\frac{m}{s}$]	Diameter D [m]	Height H [m]
Wieringermeer West	3.5D	8	0.63	10.7	80	80
Wieringermeer East	2.5D	6	0.63	10.9	80	80
Nibe B	2.5D, 4D, 7.5D	8	0.89	8.5	40	45
Nordtank 500	2.5D	11.2	0.7	7.45	41	36
NREL-5MW Low $TI_{h,\infty}$	-	4	0.79	8	126	90
NREL-5MW High $TI_{h,\infty}$	-	12.8	0.79	8	126	90

Table 4.11: Validation cases field measurements data

and the Gaussian model, called BPA model (developed according to [10, 72]). For the first model, the growth parameters are selected according to turbine's location, as described in Table (3.6) and in Table 4.12 for sake of clarity. In the BPA model the growth parameters are chosen according to the Niayifar law described before

Case location	Growth rate parameter
Onshore case	$k_w = 0.1$
Offshore case	$k_w = 0.04$

Table 4.12: Growth parameters for the NOJ model depending on the case

[72] depending on the turbulence intensity used, as shown in Table 4.13).

Turbulence intensity range	Growth rate parameter
$I < 0.065$	$k^* = 0.026$
$0.065 \leq I \leq 0.15$	$k^* = 0.4I + 0.004$
$I > 0.15$	$k^* = 0.064$

Table 4.13: Growth parameters for the BPA-Niayifar model depending on the turbulence intensity

4.1.3. Analytical wake models cases analysed for VAWTs

As for the numerical simulations, analytical wake models have been studied and tested in different conditions according to:

- Literature data, extracted from [3, 97, 110]. In addition to these cases, the code was debugged comparing the results with the original model from [2]
- Data from the numerical simulations discussed in the previous section

Since the cases extracted from numerical simulations have been already discussed, only few additional details will be mentioned.

4.1.3.1. Comparison with literature data - Cases analysed

Analytical wake models require several inputs:

- Diameter
- Height of the blades
- Hub height
- Turbulence intensity
- Inflow velocity
- Thrust coefficient

Such data are not always reported in literature studies, therefore not many free access studies are complete for the comparison except the ones listed before. These cases will be presented and described in this section while the results will be discussed in Chapter (7).

4.1.3.1.1 Code testing and debugging with reference to Abkar [2]

Since the analytical wake models were already proposed by Abkar [2], in order to test the validity of the code (which is reported in Appendix (C)) and speed up the debugging operations, the results were compared with the ones reported in this paper. The details of how the comparison was performed at code level are reported in Appendix (C) Section (C.2).

The cases used for this operation, which will be discussed also in Section (4.2), feature an H-rotor turbine under different conditions, reported in Table (4.14). Each one of these cases come from literature and a specific set of studies, both numerical and experimental.

Code debug cases parameters

Case	$z_h [m]$	$D [m]$	$H [m]$	λ	$c [m]$	C_T	$U_h [\frac{m}{s}]$	$I [%]$	Related paper	Typology
1	40	26	24	3.8	0.75	0.65	7	9.1	Abkar et al. [1, 3]	Numerical study
2	40	26	24	2.5	0.75	0.34	7	9.1		
3	40	26	48	3.8	0.75	0.64	7	9.1		
4	100	50	100	4.5	1.5	0.8	9.6	8.3	Shamsoddin et al. [96]	Numerical study
5	6	1.2	6.1	2.2	0.11	0.47	10.9	6.7	Hezaveh et al. [33], Kinzel et al. [48]	Numerical, experimental studies

Table 4.14: Description of the parameters used for code debug

4.1.3.1.2 Comparison with Abkar & Dabiri [3]

This paper is the LES study of a a 200 kW Darrieus-type VAWT that features an H-rotor and three straight blades, each one modelled as NACA 0018 airfoil. The model used here was previously validated against experimental data, so the results can be considered as high fidelity data for the comparison.

The geometric parameters used for this simulation are reported in Table (4.15). The real inflow condition used in this simulation is the ABL inflow condition, which cannot be replicated by the analytical wake model. Mean velocity profiles are extremely relevant for the purpose of the comparison and in this study are reported for $\frac{x}{D} = [3, 6, 9, 12, 15]$.

A final remark concerns the possibility of testing how the model performs under different C_T and consequently TSRs. This allows to verify the model in a wide range of conditions and also to observe the phenomena discussed in Section (2.2.3).

Parameters used	
Diameter D	26 m
Height H	24 m
Hub Height c	0.75 m
Velocity at hub V_h	$7.5 \frac{m}{s}$
Turbulence intensity I	10%
Tip speed ratio λ	2.5, 3.8
Thrust coefficient C_T	0.34, 0.64
Reynolds number Re_D	≈ 13500000

Table 4.15: Parameters used in the comparison with Abkar & Dabiri [3]

4.1.3.1.3 Comparison with Tescione et al. [110]

The case reported here is the same discussed for the numerical validation, so the related parameters have been already reported in Table (4.4). The only parameter to be added is the turbulence intensity, which is set to 0.5%. However the comparison here is slightly different since no wall influence is replicated.

This case was chosen since it is the only experimental study that provides all the input parameters necessary to complete wake models calculations and allows to analyse how wake models perform in the near wake and in low turbulence intensity level.

4.1.3.1.4 Comparison with Shamsoddin et al. [97]

The study from Shamsoddin et al. [97] is a set of numerical experiments featuring a LES framework previously validated. The turbine considered is a three-bladed H-rotor whose blades are NACA 0018 airfoils. Following the conventions, no tower or horizontal struts were considered. The detailed parameters used are reported in Table (4.16) As the previous case, the inflow condition is an ABL condition. The values considered

Parameters used	
Diameter D	50 m
Height H	100, 50, 12.5 m
Hub Height c	100 m
Velocity at hub V_h	$9.6 \frac{m}{s}$
Turbulence intensity I	8.3%
Tip speed ratio λ	4.5
Thrust coefficient C_T	0.8
Reynolds number Re_D	≈ 33000000

Table 4.16: Parameters used in the comparison with Shamsoddin et al. [97]

here are related to the ones at hub height, because the analytical wake models are not capable of replicating such complex inflow condition.

One final remark is that comparing different aspect ratios allows to analyse the performance of the model and its accuracy in the largest possible range of conditions. As mentioned for the previous case in this case it is possible to verify what was discussed in Section (2.2.3.4) and analyse the ability of wake models in replicating the phenomena.

4.1.3.2. Comparison with numerical simulations - Cases analysed

No particular aspects needs to be mentioned about the settings used in the comparison with numerical simulations, since the parameters are the same listed in Section (4.1.1). There is just one major thing to point out: since wake models do not consider tower's and struts' effect, they were removed from numerical simulations in order to replicate the most equal conditions. This means that the thrust coefficients used are slightly different compared to the cases used for the validation of the numerical simulations. The new values are reported for each case in Table (4.17) and were calculated thanks to the numerical simulations, according to

the procedure discussed in Section (3.1.2).

The difference between the case with and without tower and struts can be evaluated by:

$$C_{T,tot} = \frac{(C_{T,blades}0.5\rho V^2 A_p + C_{T,rod}0.5\rho V^2 A_{rod})}{0.5\rho V^2 A_p} \quad (4.4)$$

$C_{T,blades}$ is the thrust coefficient related to the blade only, $C_{T,rod}$ is the thrust coefficient related to the struts and according to the literature can be assumed equal to 1.1, A_{rod} is the area of the struts. This is an empirical relation so it is expected to not be totally correct. The value for the high Reynolds' number case used is higher than the original one because the calculation is not totally accurate, moreover, in the original literature case no tower or struts were considered.

New thrust coefficients		
Case	Old C_T	New C_T
Low Re	≈ 0.65	≈ 0.72
Medium Re	0.8	≈ 0.765
High Re	0.8	≈ 0.83

Table 4.17: New values for the thrust coefficients without considering tower and struts

4.2. Verification of the models and simulations

This section deals with the results from the validation process at different levels:

- For the numerical simulations
- For the analytical wake models from py-wake library
- For the self-similarity hypothesis in VAWT's wake
- For the debugging of code scripts developed

For each one of these cases, the results will be reported and discussed.

4.2.1. Validation of the numerical simulations

The core of the validation process lies in the numerical simulations. As mentioned before it is extremely important to analyse the results and search for possible numerical errors that appear during such tests. As mentioned in Section (4.1.1) three main cases are proposed:

- Low Reynolds number case
- Medium Reynolds number case
- High Reynolds number case

Next subsections will deal with each one of them.

4.2.1.1. Low Reynolds case validation

The validation carried out for the low Re case is different from the other ones and is based on a qualitative comparison with experimental results. The data reported are for mean streamwise velocity contours evaluated at different cross-sections in the near wake. The data are reported in Figure (4.15).

As observed, wakes reveal similar structures and shapes. Starting from $\frac{x}{D} = 0.5$, a slight displacement of the wake center is observed in the numerical simulation towards negative y . The same deflection is not observed in the experimental data until $\frac{x}{D} = 1.5$. Moving downstream, the wake tends to be more and more deflected, assuming a trapezoidal shape in both cases. The edges of the wake are smoother in the experimental case and the deficit experienced is slightly lower than numerical case but the area with the lowest values is correctly replicated by the actuator line model. Considering velocity normalized vectors, the vortices and rotational regions of the wake are qualitatively replicated and the CVPs are observed at both leeward and windward side of the wake. Strongest CVPs, which induce higher spanwise and crossflow velocity components, are located at the windward side, according to [36, 78, 83, 89, 90]. Here they promote a faster recovery thanks to the strong induction provided. Deformation of wake's shape, which tends to a clover leaf shape, is a direct consequence of side flows induced by CVPs.

Overall, the qualitative agreement shown by the numerical simulation is good, even if some small differences are observed. However it is an unexpected result (but only qualitative), since actuator line model fits more data related to far wake region.

4.2.1.2. Medium Reynolds case validation

The mean crossflow (top) and spanwise (bottom) velocity profiles of the normalized streamwise component are reported in Figure (4.16) for the medium Reynolds number case. The profiles are reported as function of y and z normalized coordinates for different sampled sections. In this case the planes sampled are focused on the near wake of the flow.

Starting from the top image, a good agreement is observed between the results obtained from numerical simulation and both the ones provided by Mendoza (which are based on the same numerical calculation tool) and the experimental ones from Tescione. The shape of the wake is perfectly replicated, especially the deflection towards positive y because of blade's rotation and the different relative velocity experienced by the blades in concordance with what was discussed in Section (2.2.3.2). However the deflection experienced is not so strong because the TSR is high (4.5) but, at the same time, Reynolds' number, that distinguishes between cases where inertial or viscous effects display more relevance, is quite low. Therefore convection is not

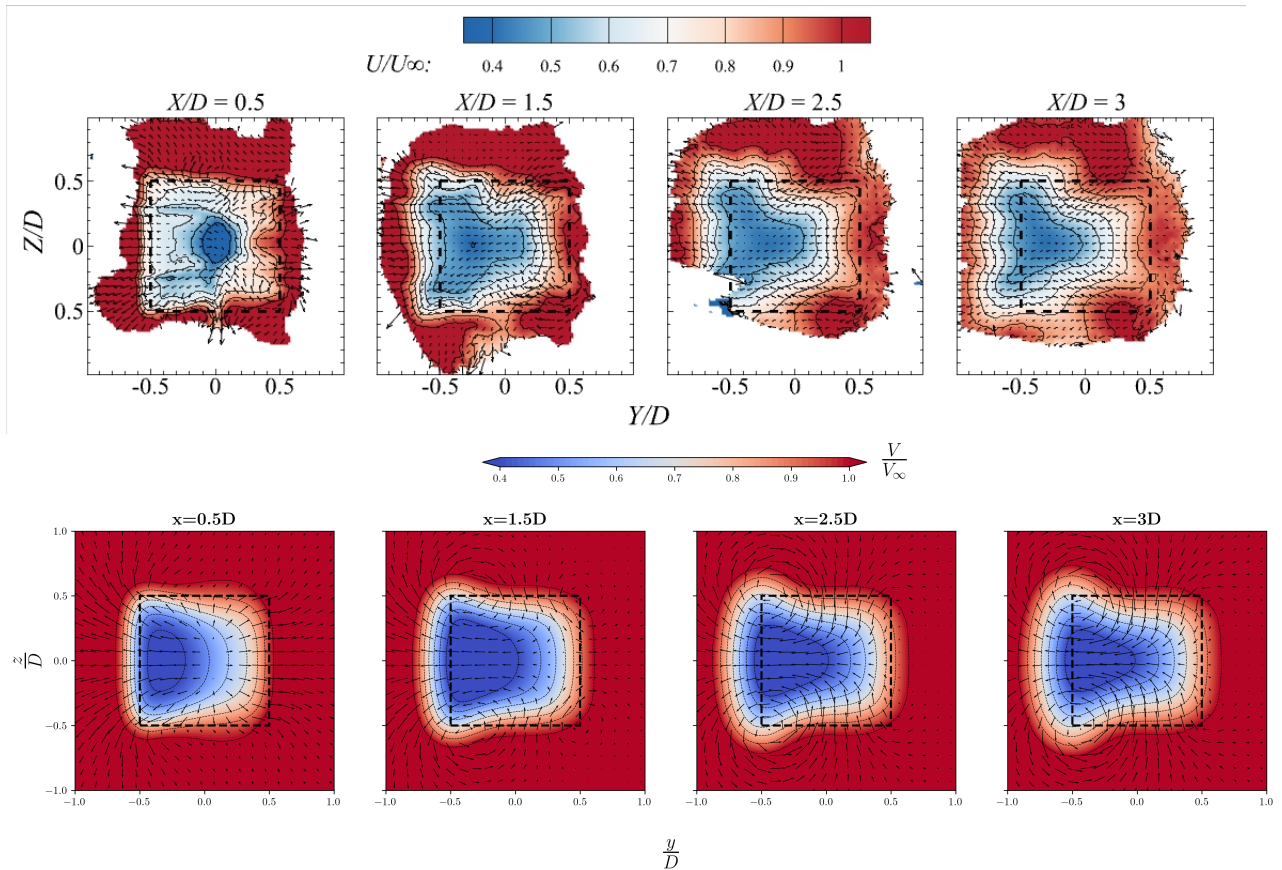


Figure 4.15: Contours of mean streamwise velocity and in-plane velocity vectors at different downstream positions normalized by the incoming wind speed for wind tunnel experiments (top) and numerical simulation (bottom) for the low Re case

strong enough to provide efficient mixing with high speed flow. Therefore a certain level of asymmetry is seen. There is a little discrepancy for $x = 2D$ where the shape calculated by Tescione shows a slightly higher degree of asymmetry respect with numerical data. At the same time current simulation provides higher maximum values of the deficit, over-predicting the thrust experienced by the turbine. However the discrepancies shown in this case are limited and negligible. Results obtained for the spanwise direction shows lower accuracy, especially when dealing with the last sampled sections ($x = 1.5D, 1.75D, 2D$). In fact the numerical simulation (as well as the one from Mendoza) fails in predicting the enhanced recovery that occurs at the top of the wake. Such recovery is experienced because of tip-vortices that allows mixing of the wake with high-speed fluid, as discussed in Section (2.2.1.3). RANS simulations are not able to replicate such action as well as the vortex structures generated by the blades' tips, therefore a higher deficit is shown in the upper part of the profile. The region near turbine's mid-span ($0 < \frac{z}{D} < 0.2$) instead displays values similar to literature data even if the recovery process is slightly overestimated.

It is possible to conclude that even if some aspects are not correctly replicated, the numerical set up featuring the actuator line and URANS equations, provides correct results, especially when considering crossflow velocity profiles of streamwise component. Such profiles are crucial in the comparison with analytical wake models since, most of the times, the profiles provided by the latter are calculated for the same spanwise coordinate. Slightly lower accuracy is observed when dealing with velocity profiles along z coordinate, here the model is unable to correctly replicate the tip vortices effect on the wake, which has a major effect on wake recovery process. However, both the shape of the wake, its evolution and the streamwise component magnitude evaluated are almost equal to the ones provide by higher accuracy results. This means that the numerical tool is correctly validated for this case, providing a reliable method for the comparison with analytical wake models in a 'medium' Reynolds' number case.

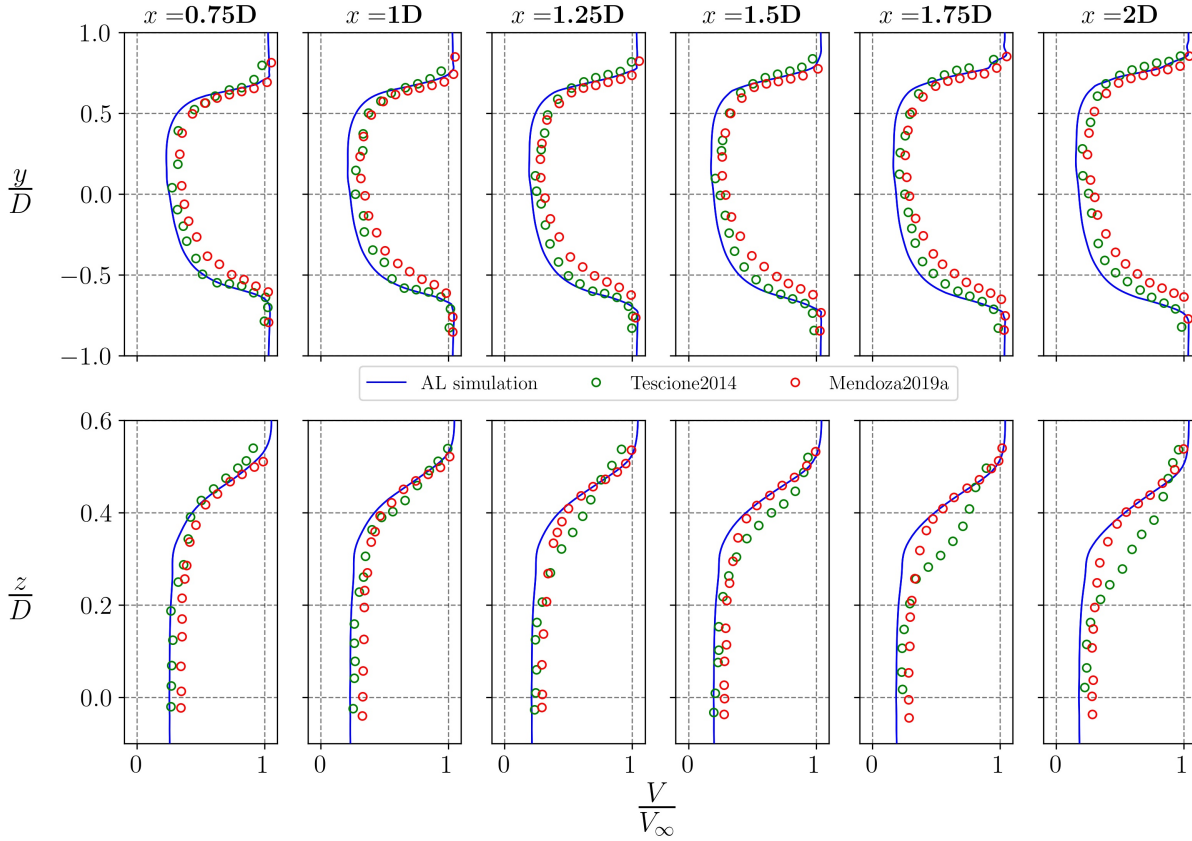


Figure 4.16: Comparison of mean streamwise velocity deficit profiles along crossflow (top) direction at mid-span and along spanwise (bottom) direction of the normalized streamwise component from [65, 110] and the ones obtained from the numerical simulation for the medium Reynolds number case

4.2.1.3. High Reynolds case validation

As for previous case, mean velocity deficit profiles of streamwise component are reported in Figure (4.17) for both crossflow (top) and spanwise direction (bottom). Before moving on, it is crucial to point out that, as already mentioned in Section (4.1.1), the inflow condition is different: Shamsoddin's [96] simulation features an ABL inflow condition, here a uniform inflow condition was assumed instead. Therefore high accuracy is not expected for the profiles along spanwise coordinate. With this basis, the results are reported and analysed.

Considering Top Figure (4.17), the mean velocity profiles along crossflow direction at mid-span show good agreement with literature data. The shape of the wake is correctly replicated in the near wake, even if for $x = 1D, 3D, 5D$ there are some discrepancies at the edges of the wake, where higher turbulence is experienced which has a huge role in promoting wake interactions with high speed flows [45, 78]. Such part of the near wake is full of vortical wake structures that RANS simulations are not able to replicate. However, the minimum velocity value calculated is almost the same of the literature data, even if some major discrepancies are observed for $x = 3D, 5D$, where the deficit recovers faster in the current studied case. Such trend is reversed starting from $x = 7D$ and the recovery shown in literature data is faster. By the way the differences are minimal, and the maximum deficit predicted by the two models is almost always the same. So for the literature case, the wake has not reached the fully-developed state yet, while this does not occur for the numerical case, showing a constant recovery. The asymmetry is observed even if extremely limited: the center of the wake is slightly shifted towards the positive y region, and this is observed also in the literature case. Considering spanwise velocity profiles in Bottom Figure (4.17), the difference in the inflow condition assumed is evident: the region above the turbine features a non constant profile, as well as the one located near the ground. However the most relevant part is the core of the wake, its shape and how it evolves. Considering the near wake region, the maximum deficit evaluated is almost equal to the literature value both in near and far wake, even if suffering the same problem observed for crossflow profiles at $x = 3D, 5D$. If the upper part of the core of

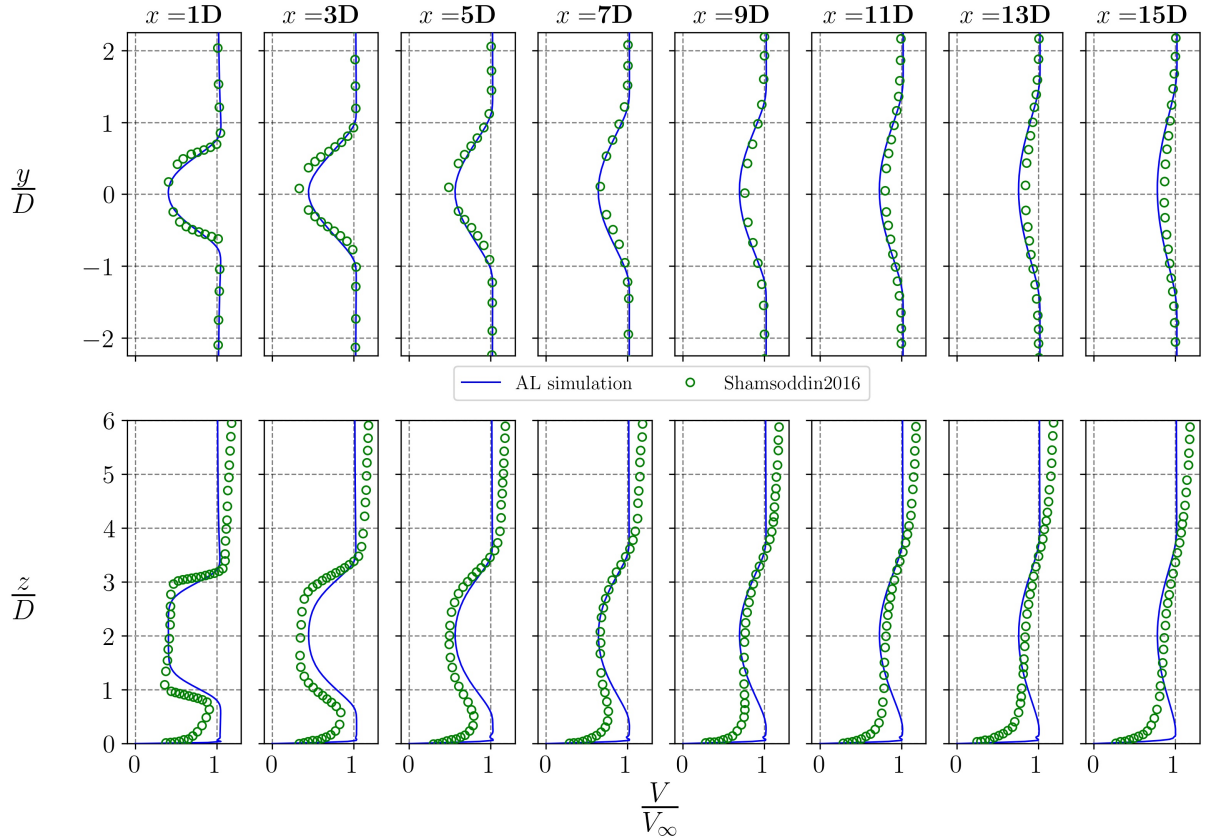


Figure 4.17: Comparison of mean velocity deficit profiles along crossflow (top) direction at mid-span and spanwise (bottom) direction of the normalized streamwise component from [96] and the ones obtained from the numerical simulation for the medium Reynolds number case

the wake only is considered, the shape is correctly replicated, but the difference in recovery observed before, occurs even here when moving from near wake to the fully developed wake and further downstream in far wake.

In conclusion, even for the high Reynolds number the numerical set up allows to correctly replicate the behaviour of higher fidelity simulations. The main difference observed are in the recovery and the discrepancy in the velocity distribution, mainly due to the inflow condition. Maximum deficit and wake's width expansion calculated show high accuracy and they will be a valuable tool in the comparison with analytical wake models.

4.2.1.4. Mesh sensitivity analysis

After the model was validated, a series of test regarding the analysis of the mesh sensitivity were run. This way was possible to evaluate eventual inaccuracies in the numerical solution obtained and to observe any possible dependency on mesh size. The starting meshes used for this analysis are the ones described in Table (4.9). The approach was based on testing 2 additional simulations for each case, one with fewer cells and one with more cells. To increase and decrease cells number, the outer cell dimension mentioned in Table (4.9) was modified and the settings used are reported in Table (4.18).

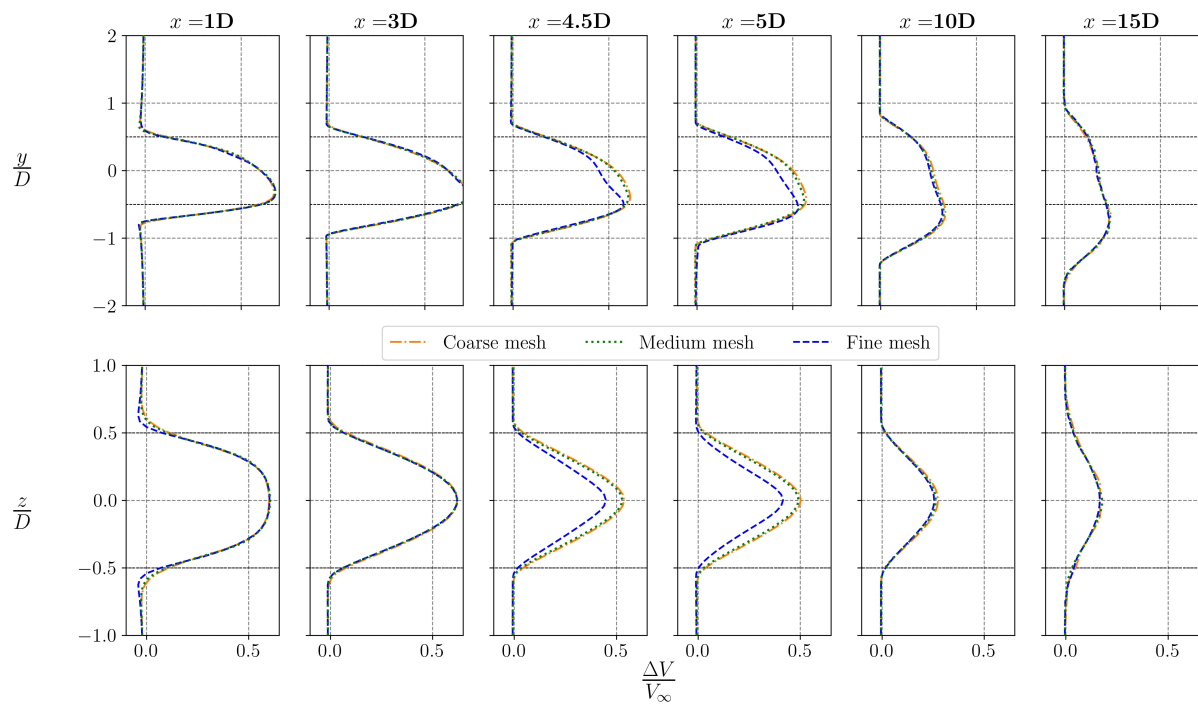
Resulting data in terms of streamwise mean velocity profiles are reported for each case in Figure (4.18), (4.19) and (4.20).

As shown, the results are totally insensitive to mesh size when considering the medium and high Re case in Figure (4.19) and (4.20), providing almost the same results. Therefore, there was no need to increase the number of cells here and the overall accuracy of the model, since the improvement in the accuracy would not have been so remarkable, but the computational time would have raised extremely fast. The same comments could be made for the low Re case in Figure (4.18), however here the differences are not so relevant but present. However it was decided to not use the high mesh resolution, since the computational time became

Mesh type	Low Re		Medium Re		High Re	
	Coarse	Fine	Coarse	Fine	Coarse	Fine
Old x_0 [m]	0.06		0.2		10	
New x_0 [m]	0.075	0.05	0.25	0.143	12.5	7.15
Old # cells	$15 \cdot 10^7$		$4 \cdot 10^7$		$1.7 \cdot 10^7$	
New # cells	$7.5 \cdot 10^7$	$25 \cdot 10^7$	$2 \cdot 10^7$	$11.5 \cdot 10^7$	$8.4 \cdot 10^6$	$14 \cdot 10^7$
Old computational time [h]	48.5		14		6	
New computational time [h]	31.20	130	13.3	68	4.5	14
CPUs used	32	48	32	32	64	32
Memory per core	$4 \frac{GB}{core}$					

Table 4.18: Parameters used in the mesh sensitivity analysis for each numerical simulation

extremely long (48 hours against 130): the amount of time requested for a single comparison was too high, while the improvement in the results were not equally different.

Figure 4.18: Influence of mesh variation on mean streamwise velocity deficit profiles for low Re case

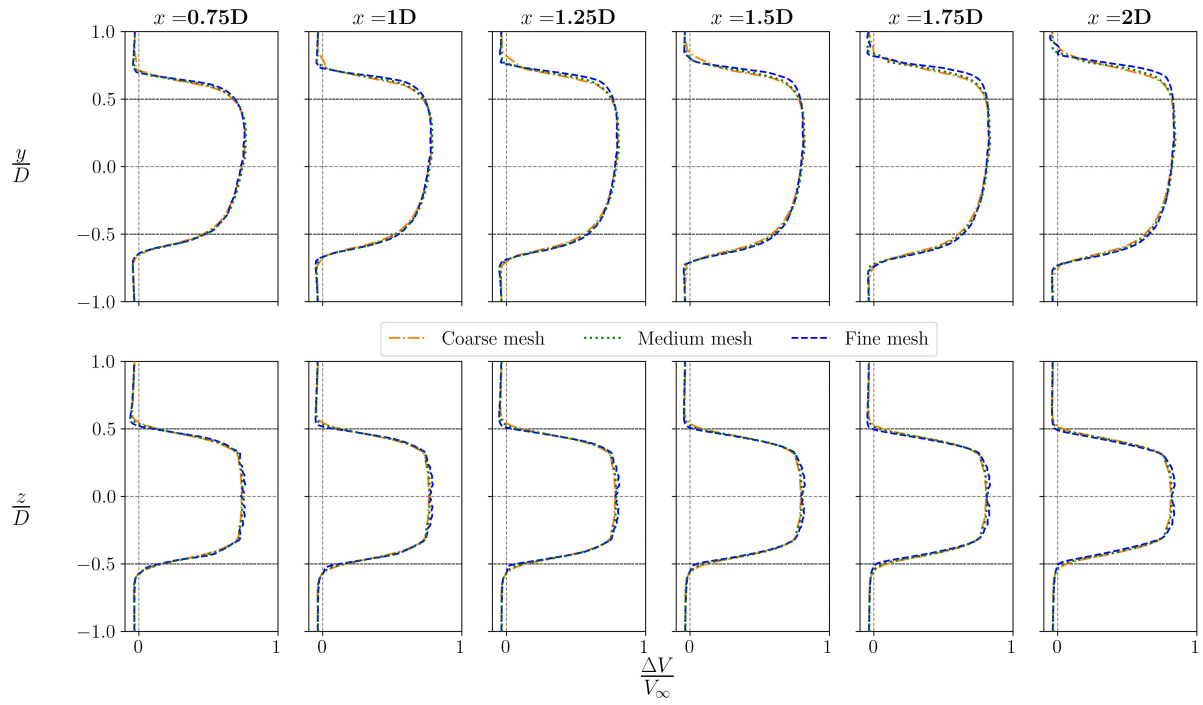


Figure 4.19: Influence of mesh variation on mean streamwise velocity deficit profiles for medium Re case

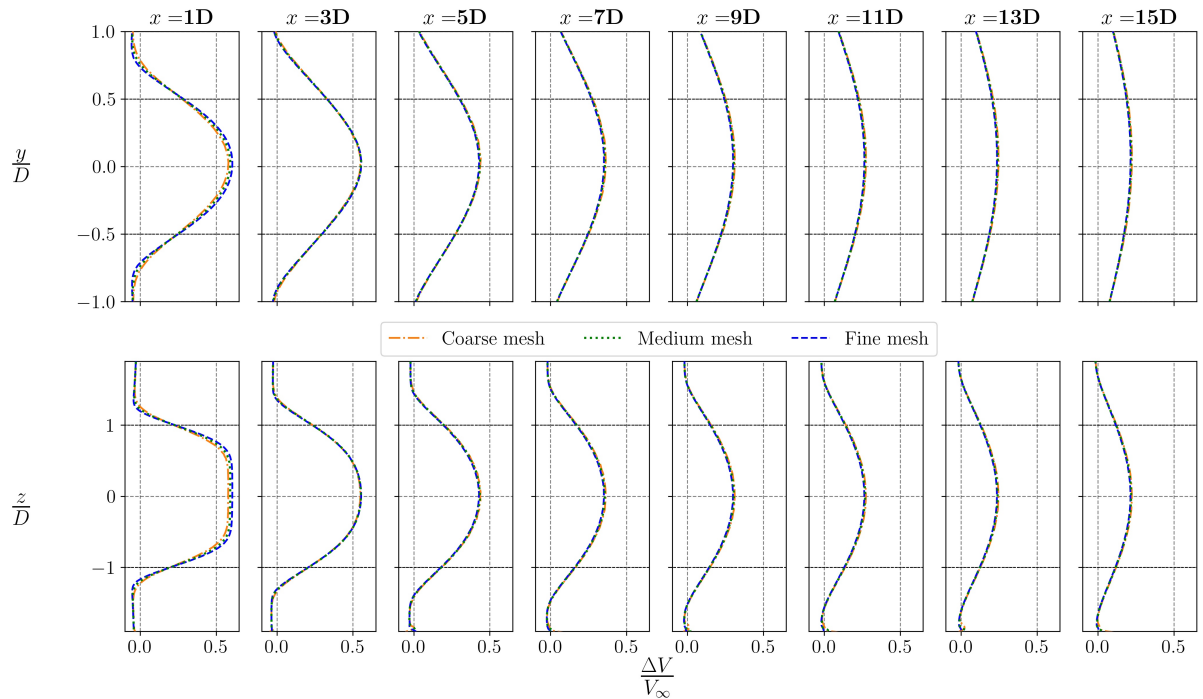


Figure 4.20: Influence of mesh variation on mean streamwise velocity deficit profiles for high Re case

4.2.2. Validation of analytical wake models for HAWTs from py-wake

In order to better understand the wake models for HAWT and how they work, numerical code versions of some of the models described before are analysed and validated in this chapter. These versions were developed in the py-wake library for Python [82] and here are validated against data from LES and RANS simulations as well as field measurements (when available) to point out possible discrepancies.

4.2.2.1. Case 1 analysis

The results obtained for the validation in the first case are reported in Figure (4.21). A good agreement is observed between data from wake models and higher fidelity data. In the near wake for $x = 2.5D$ values predicted by the top-hat model and the numerical simulations match, while Gaussian model tends to overestimate the maximum deficit. This can be observed also in the Top Figure (4.21), since no red region is displayed for the NOJ model. Such overestimation can be related to the fact that the Gaussian model is not valid for near wake region and provides only constant values there. For $x = 3.5D$ the deficit shape and the

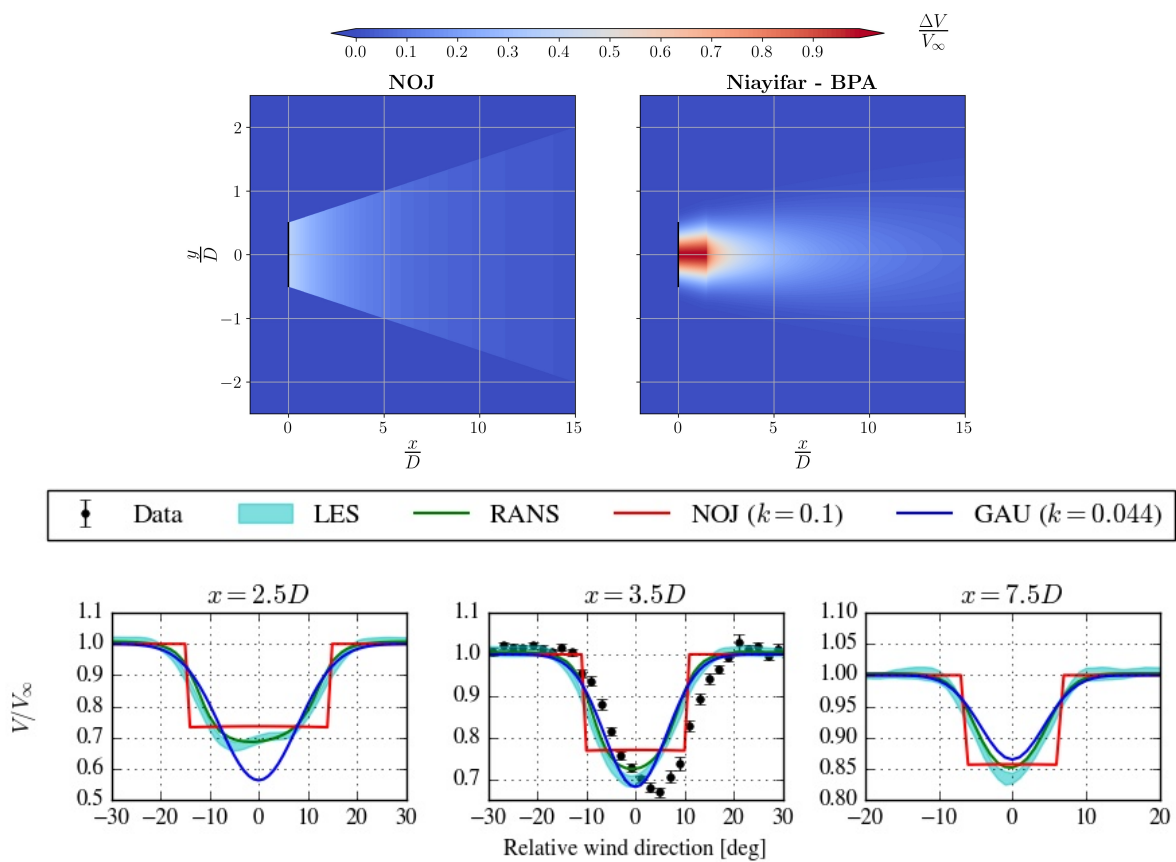


Figure 4.21: Overview of the wake evolution (top) and comparison between the predictions from the wake model, field and numerical data for case 1 in Table (4.11) (bottom)

maximum value predicted by the Gaussian model are extremely similar to the experimental value even if the latter distribution is slightly shifted. Top-hat model instead predicts a value higher than the average value of the other data. Moving further downstream the analytical results are extremely similar compared to numerical data, with all the curves collapsing to the same region even for Jensen’s model. According to Top Figure (4.21), the wake needs almost $14D$ to recover up to 90% of the freestream value when using the top-hat model while almost $15D$ when considering the Gaussian model. However at the same time the area affected by the wake evaluated with NOJ model is almost two times bigger than the one evaluated with the Gaussian one.

4.2.2.2. Case 2 analysis

In Case 2 the results (shown in Figure (4.22)) for the near wake show almost the same behaviour of Case 1, but in this case discrepancies between Gaussian model and experimental data increase while the shape remains almost the same. At the same time the values predicted by the top hat model are more similar to the numerical data but showing almost the same error of Gaussian case compared to experimental data. The Gaussian overestimation can be observed in Top Figure (4.22), where (as before) no red region is displayed. For $x = 3.5D$ the discrepancy between the deficit calculated by Gaussian model and higher fidelity models decreases. Moving further downstream at $x = 7.5D$, the wake shows a slightly higher deficit compared to previous case since a lower turbulence intensity (and consequently k) is experienced compared to Case 1. Therefore the values displayed in top Figure (4.22) are more 'blue' than the ones in Top Figure (4.21). The difference is not too visible because the higher velocity value influences the results as well. At the same time all the curves are observed to collapse to the same region in the far wake. So even in this case, the values

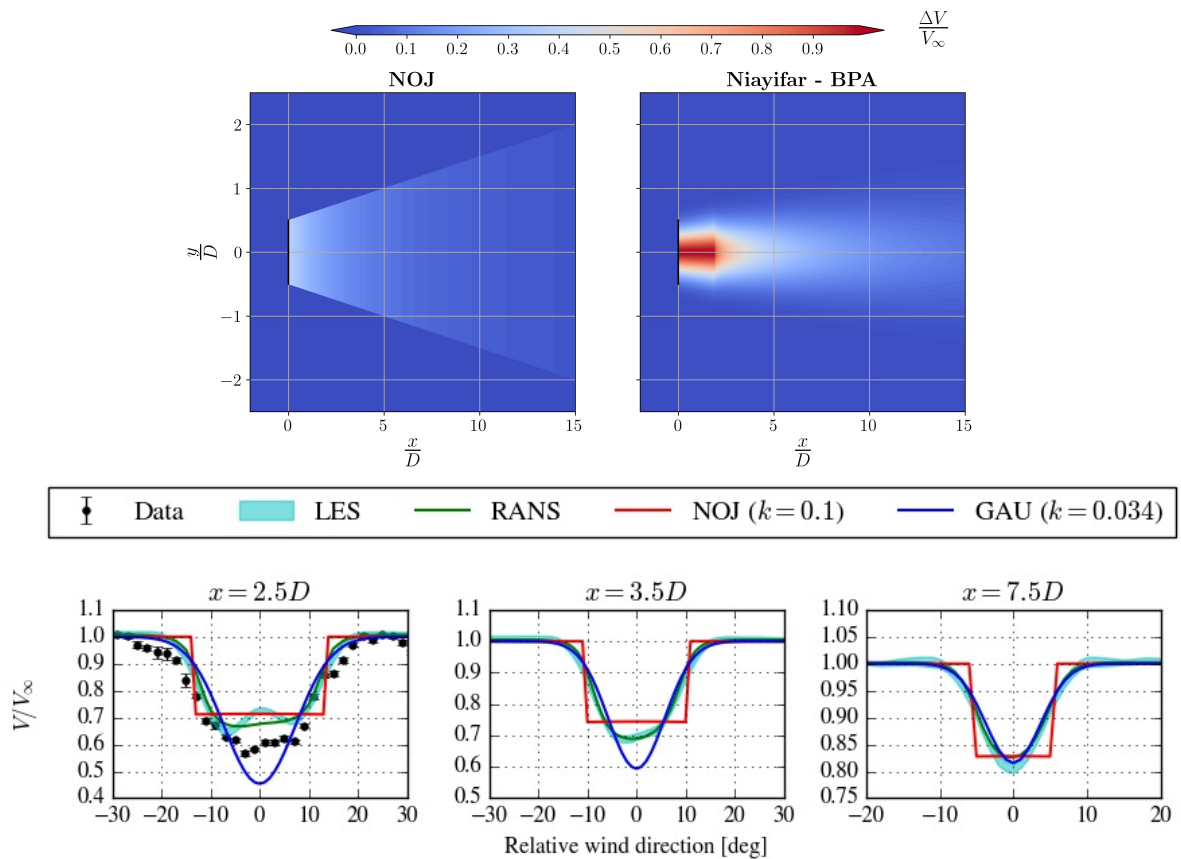


Figure 4.22: Overview of the wake evolution (top) and comparison between the predictions from the wake model, field and numerical data for case 2 in Table (4.11) (bottom)

predicted by wake models are extremely reliable for the far wake region. Moreover, the area affected by wake for the NOJ model is wider than for Gaussian model, while the recovery process experienced is similar..

4.2.2.3. Case 3 analysis

The case shown in Figure (4.23) is the only one that features experimental data for each downstream coordinate analysed. The agreement demonstrated between predictions from wake models and experimental/numerical data is extremely high for both the maximum values evaluated as well as the shape of the distributions. The Gaussian model especially shows almost the same behaviour of the experimental data even for $x = 4D$, where NOJ overestimates the values. The same occurs when considering $x = 7.5D$. However, starting from the near wake for $x = 2.5D$, in this case the Gaussian model does not overestimate the values experienced and the top-hat model shows high deficit values (this is the first time that a red region is displayed for this model). This can be related to the high thrust coefficient (0.89) compared to previous cases. On account

of that the deficit experienced is more intense and in the near wake the overall values are higher than Case 2. At the same time the constant near wake region for the Gaussian model is not as extended as previous cases, therefore downstream length necessary for the wake to fully develop is reduced. Moving downstream

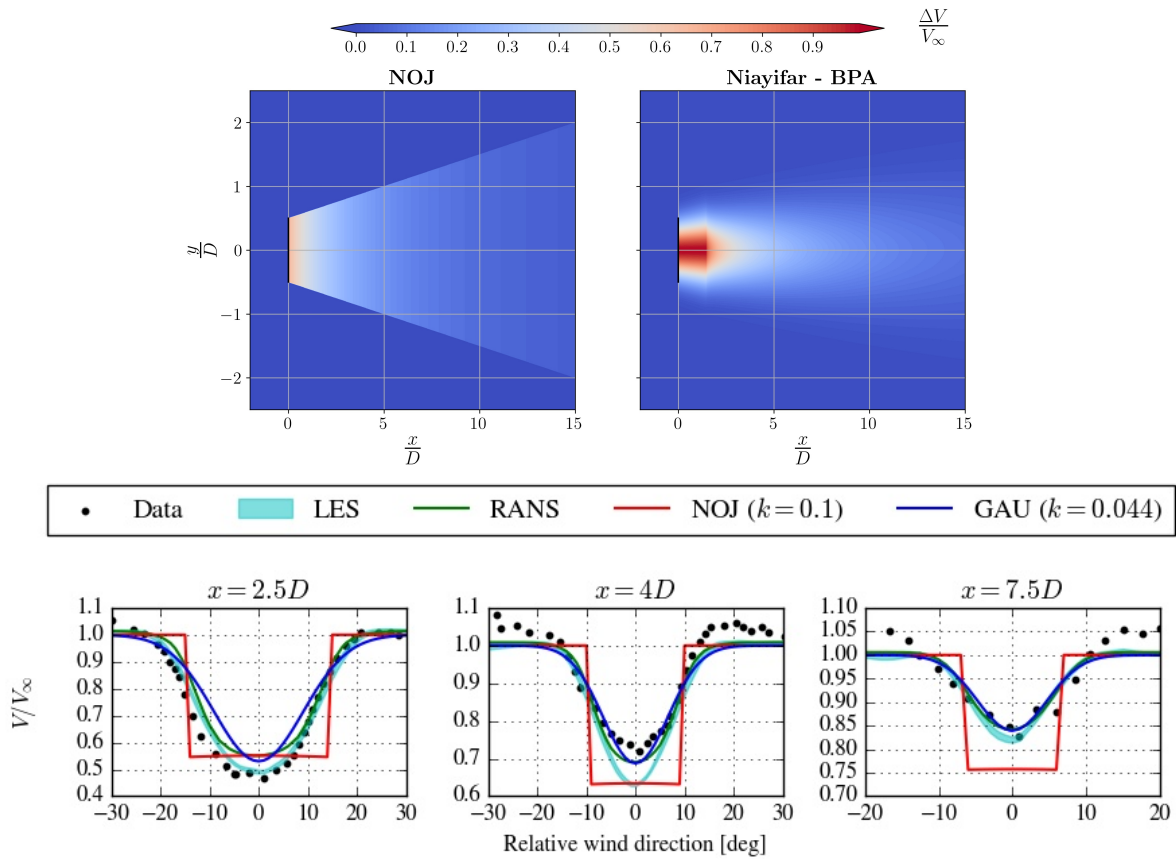


Figure 4.23: Overview of the wake evolution (top) and comparison between the predictions from the wake model, field and numerical data for case 3 in Table (4.11) (bottom)

at $x = 4D$ top-hat model accuracy degrades, with maximum values predicted that differ from experimental data for less than 0.1. Here as for $x = 7.5D$ results from Gaussian model tend to behave as experimental data. Top-hat model in the far wake does not provide correct data, with an error of almost 10% compared to experimental data. This can be related to its inability to correctly model the recovery process when dealing with high-thrust cases. Wake's width evolution reported in Top Figure (4.23) is almost the same experienced and seen in previous case with the only difference that at $x = 15D$ the wake calculated by NOJ model has not totally recovered yet.

4.2.2.4. Case 4 analysis

Case 4 reported in Figure (4.24) reveals a good agreement for $x = 2D$ between experimental data and Gaussian predictions in terms of both maximum deficit and distribution's shape. Higher discrepancies are experienced with top-hat model instead. Moving downstream at $x = 5D$ experimental data show a relevant drop in the maximum deficit evaluated which is not replicated by any of the models. This way the situation overturns and both top-hat and Gaussian overestimate the correct values. Such predictions show almost the same maximum values and a higher agreement with numerical than experimental ones. Moving downstream the maximum deficit predicted by Gaussian model is lower than both numerical and top-hat values. As for Case 3, the latter method shows some problems and inaccuracies in replicating wake's recovery, even if the deficit shown in top Figure (4.24) at $x = 15D$ is almost the same with the same differences in wake's width observed in previous cases.

The consequences of high turbulence intensity can be seen in the far wake: unlike previous cases (1, 2 and 3), the wake recovers more quickly, but it even starts from a lower deficit value since the thrust coefficient is

lower than case 2. Such turbulence intensity, strictly related to a high wake decay constant, testifies the 0.9

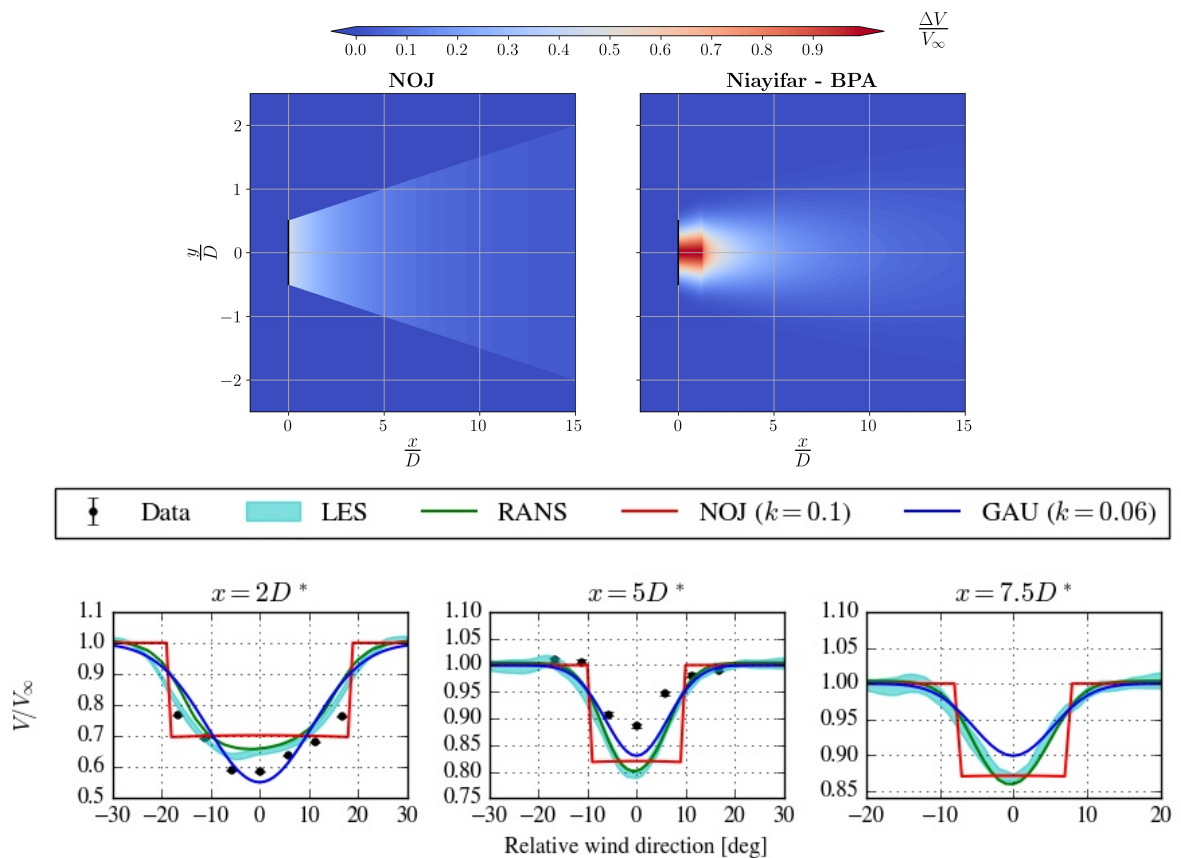


Figure 4.24: Overview of the wake evolution (top) and comparison between the predictions from the wake model and, and numerical data for case 4 in Table (4.11) (bottom)

value shown for Gaussian distribution in the far wake, because, as stated before in fact, top-hat model does not correctly replicate wake recovery unlike Gaussian model. At the same time, a high k value leads to a faster development of the wake. In fact in top Figure (4.24) the red region is extremely limited.

4.2.2.5. Case 5 analysis

In Case 5 reported in Figure (4.25), no experimental data are available unfortunately. In this case a huge discrepancy between the value calculated by the numerical simulations, the top-hat model and the Gaussian one is shown in the near wake for $x = 2.5D$. Such condition is related to the low wake decay parameter used and so to low turbulence intensity values. In fact the red region that, as mentioned before, depicts a constant deficit area, is extremely wide, covering almost the first 5 diameters downstream. For such reason the maximum deficit predicted by the Gaussian model is extremely high. Such constant region is introduced when the term inside root square in equations (3.125) provides values lower than one, this way is possible to avoid imaginary numbers. At the same time, the term inside the square root is substituted by 0, leading to a constant value responsible for this region. Moving downstream at $x = 5D$ the situation gets better and the same values are predicted by top-hat model and numerical simulations. Gaussian model still overestimates the correct values, but the discrepancy has decreased from 0.4 to less than 0.1. At $x = 7.5D$ values from wake models provide the same maximum deficit, slightly higher than the one from numerical simulations. In this case wake's width evaluated by the top-hat model is extremely similar to the one calculated with the Gaussian model and the results of the numerical simulations. In this case, with low turbulence intensity, top-hat model is able to replicate a faster wake recovery compared to Gaussian model. In fact, with reference to Top Figure (4.25), the velocity has recovered to more than 90% at $x = 15D$ for the Jensen model, while for the BPA is still recovering.

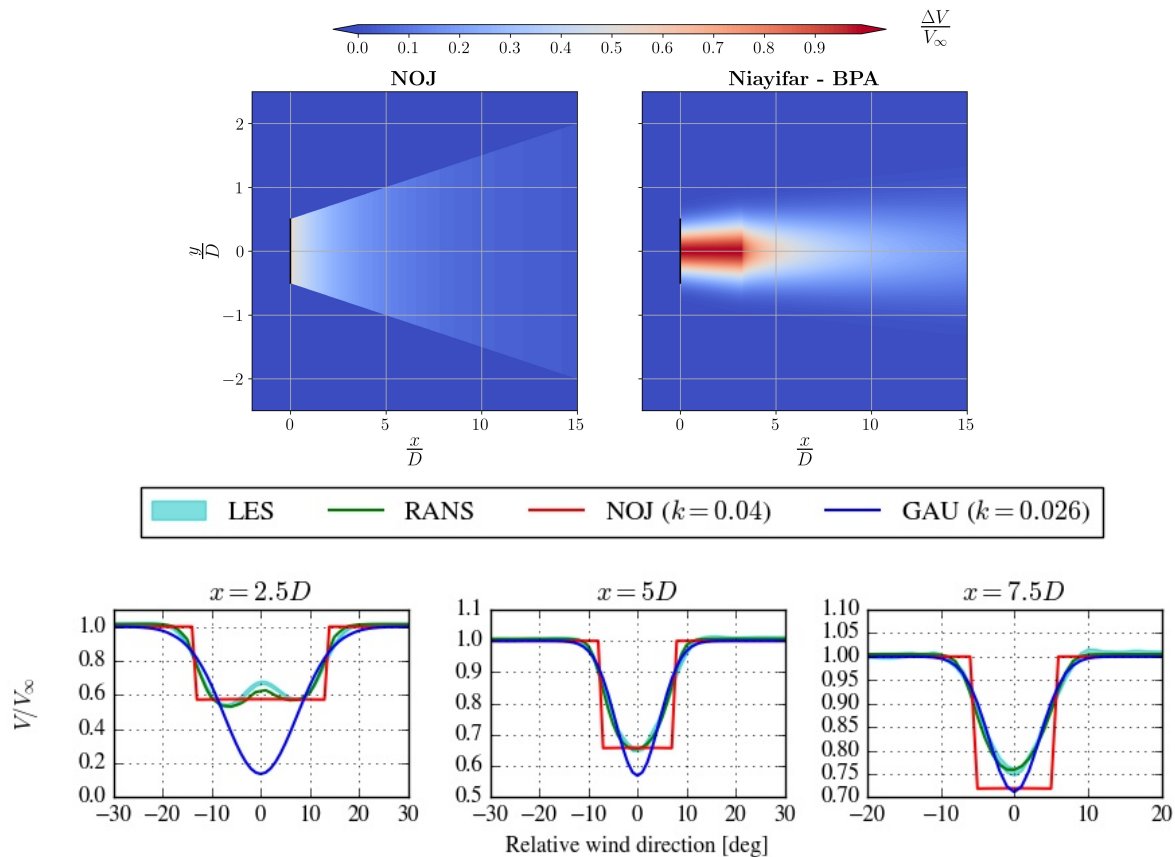


Figure 4.25: Overview of the wake evolution (top) and comparison between the predictions from the wake model, field and numerical data for case 5 in Table (4.11) (bottom)

4.2.2.6. Case 6 analysis

Case 6 reported in Figure (4.26) differs from the previous one for the turbulence intensity used. Here I is higher and therefore the predictions of the Gaussian model are much better in the near wake at $x = 2.5D$ because of the much higher wake decay constant elaborated. Moving downstream to $x = 5D$ as well as $x = 7.5D$ wake models results show a good agreement with numerical data with higher fidelity to LES data for the Gaussian model. Even in this case, with high turbulence intensity, top-hat model seems to struggle in replicating wake recovery and providing a maximum deficit value too high compared to other cases but similar to RANS data.

Another relevant aspect is the recovery length: at $x = 7.5D$ the BPA model has already recovered to 90% of the freestream value, unlike NOJ model. This is observed because turbulence intensity has increased and unlike previous case where the deficit was still at 30%, here turbulence activity enhances wake recovery, since it is one of the major actors in allowing wake recovery for HAWTs.

4.2.2.7. General reflections

In conclusion the level of accuracy displayed by analytical wake models is high especially when dealing with far wake region since the error made here was small or totally negligible in all the cases analysed. It was something expected, since they are applied especially for such regions but this testify what was discussed in Chapter (2) when speaking about the limitations of tools like the ones validated here. So wake models *really* display high quality predictions of the maximum deficit value and wake's width for the far wake at a low computational cost. Moreover the good agreement shown testifies the correct implementation in the py-wake library.

However, some problems for the near wake region are observed. The Gaussian model is extremely unreliable when dealing with near wake since it is valid from the onset point (which is located between $x = 2D$ and $x = 3D$, as discussed in Chapter (2) and (3)). Such region extends when the turbulence intensity (and there-

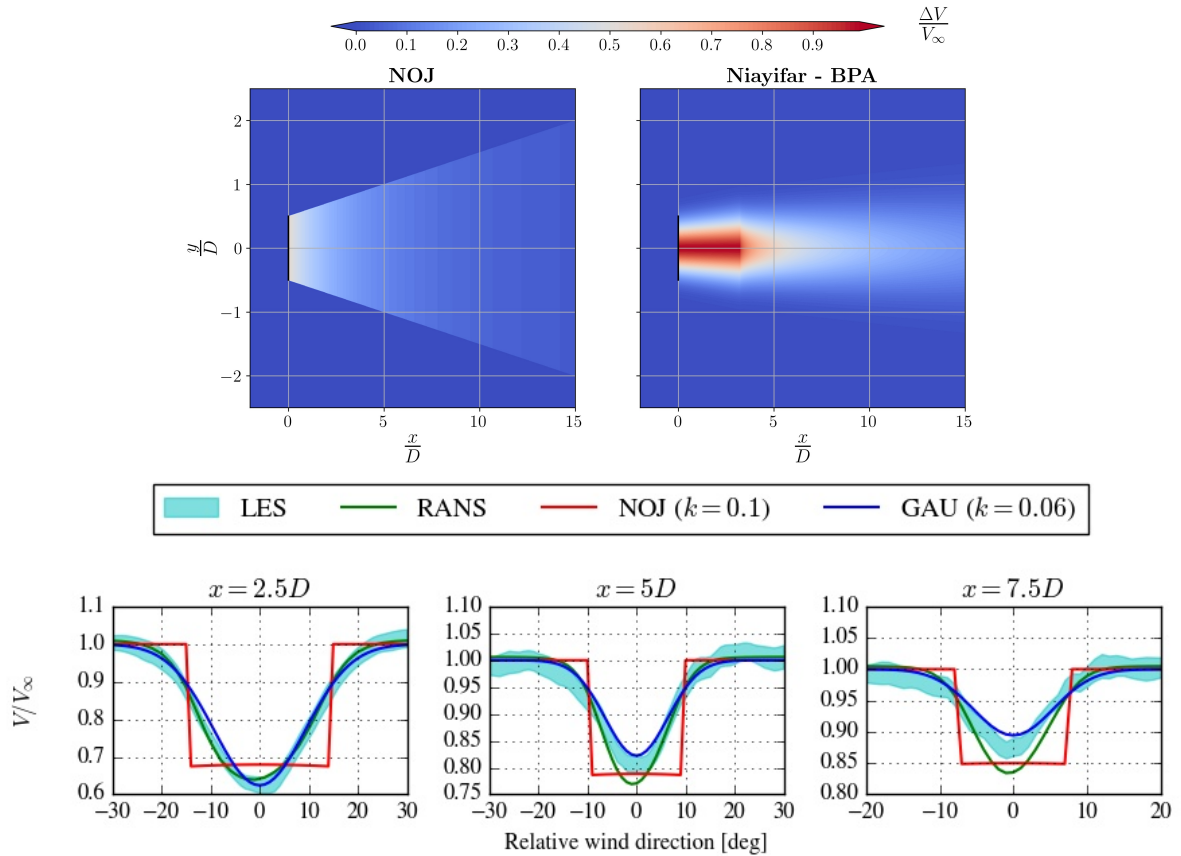


Figure 4.26: Overview of the wake evolution (top) and comparison between the predictions from the wake model, field and numerical data for case 6 in Table (4.11) (bottom)

fore wake decay constant) decrease, so the predictions from BPA model show lower accuracy. This happens probably because no model is used to replicate the turbulence activity and the vortex structures which hold major relevance in the near wake. When higher turbulence intensity is experienced, the extension of such region (the so-called 'red-region') decreases with a consequent improvement in the accuracy. For Jensen model instead the situation is reversed: when low turbulence intensity is observed, predictions in the near wake are more accurate than BPA's ones with a good level of agreement reached in the far wake region. At the same time however, when high thrust coefficients are experienced top-hat model struggles in correctly replicating wake recovery process even if a high value of turbulence intensity is experienced.

In both cases (high and low turbulence intensity) the predictions for the far wake region are extremely reliable and they fit both numerical and field data for the Gaussian model especially. This occurs because the far wake region shows a wake evolution which is not affected by the turbulence activity or the rotational effects of the blades, therefore no modelling of such aspects here is needed. Moreover modifications on main parameters do not lead to major discrepancies and was observed that wake models have great ranges of validity, especially for the far wake region: even modifying the thrust coefficient, the diameter or the freestream velocity, the predictions are sufficiently accurate for a wake model. In the end, the statement reported in the introduction of Section (2.4) is confirmed: even if they display limitations for the sake of low computational cost, wake models for HAWT are able to predict with good fidelity the most relevant aspects of a wind turbine which are essential during the design process of wind farms.

4.2.3. Verification of self-similarity hypothesis for VAWT far wake

The BPA model features a Gaussian distribution for the velocity deficit. As mentioned in Chapter (3), this assumption is related to the self-similarity property of velocity deficit in far wake region. This typical trend is observed only after a certain point downstream of the turbine and was studied by means of experimental and numerical simulations. In order to verify this hypothesis, literature data were plotted according to a

specific normalization procedure, which will be discussed also in Section (??) when studying Reynolds' number effect. Parameters used are maximum deficit experienced that normalizes the generic deficit, and the half wake width: the radius value related to a deficit experienced equal to half of the maximum value. If the curves collapse into a single Gaussian for different downstream section, then self-similarity is observed and the hypothesis is confirmed. In this research, values used for the verification are the ones extracted from the literature for the cases described in previous Section (4.1.3).

Starting for Abkar [3] case, data are reported in Figure (4.27). At lower C_T self-similarity is observed along both y and z direction. However it is necessary to mention that for $x = 3D$, the distribution along crossflow direction is slightly shifted towards positive value. This is something expected, since self-similarity hypothesis is valid only in far wake. At the same time, values for $x = 3D$ along spanwise direction feature a slight deviation compared to values at sections further downstream. Considering higher C_T , curves collapse better along y direction, even when considering the nearest position ($x = 3D$). The same is not observed along z direction, since the portion of the curves located at positive $\frac{r}{r_{1/2}}$ seems to be more and more translated towards positive values, however the difference is minimal and was already spotted by Bastankhah et al. [10] and could be related to possible errors in data extraction, since it is difficult to capture the finest difference in a Gaussian distribution in far wake.

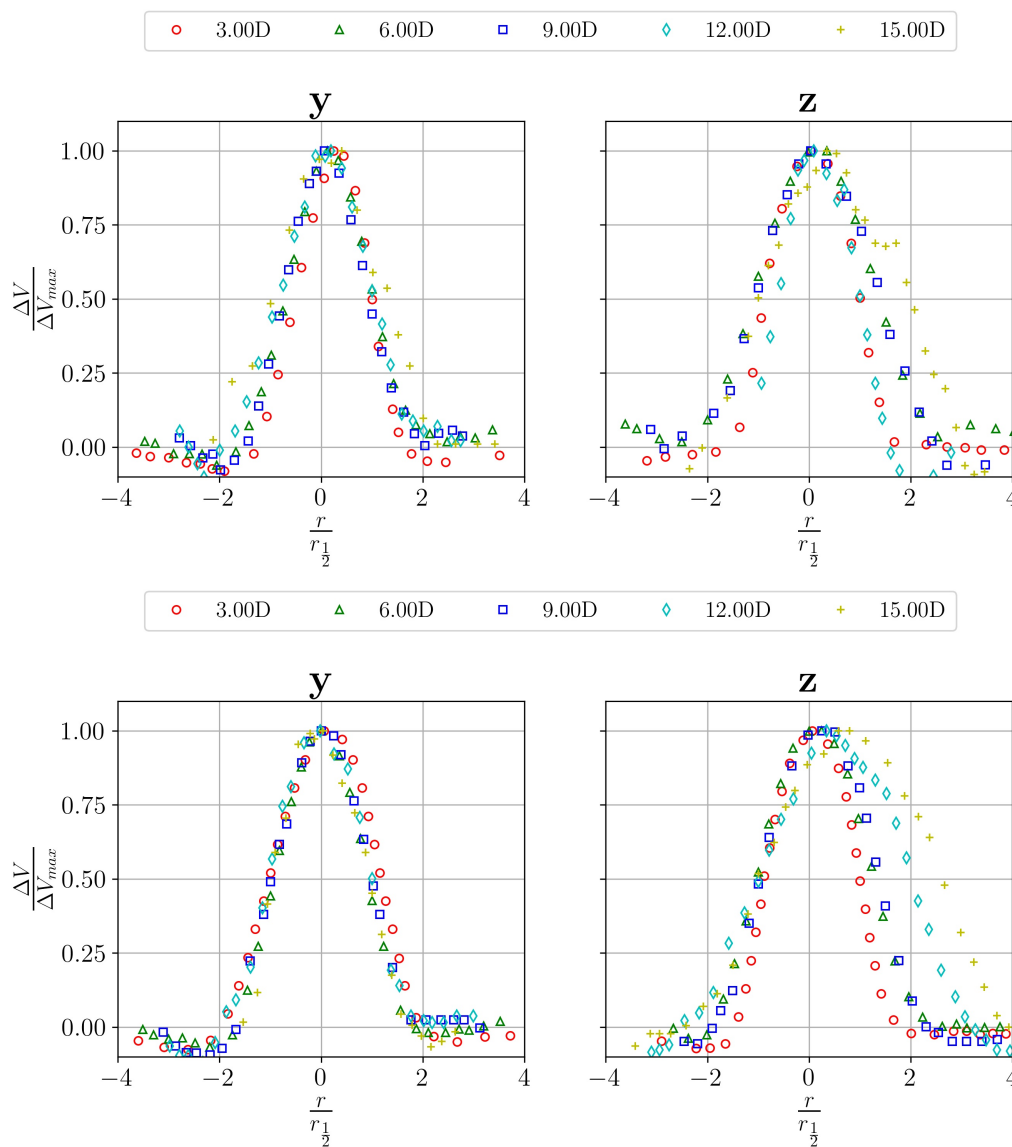


Figure 4.27: Self-similarity study for Abkar et al. [3] case for $C_T = 0.34$ (top) and $C_T = 0.34$ (bottom) along both spanwise and crossflow direction

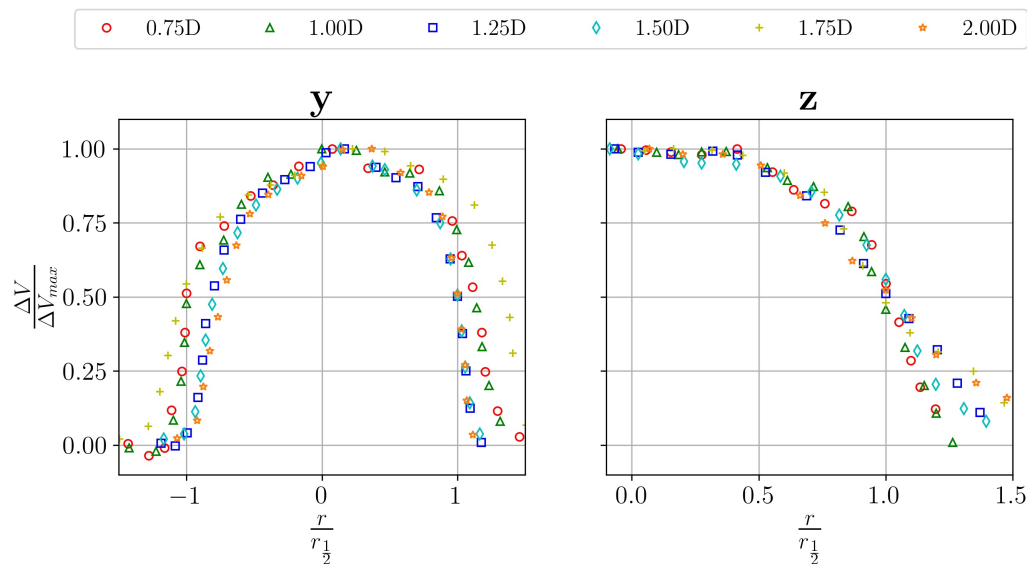


Figure 4.28: Self-similarity study for Tescione et al. [110] case along both spanwise and crossflow direction

Considering now the case reported by Tescione et al. [110] in Figure (4.28) the situation observed is extremely similar. Considering results along crossflow direction, curves tend to overlap and display a certain displacement towards positive $\frac{r}{r_{1/2}}$, as observed before because of wake deflection. Therefore the distribution is not exactly symmetric since near wake is considered, but the curve collapse into one another. With reference to spanwise direction instead, data show less disagreement, showing a compact distribution for the all region examined, excluding wake's edge.

The case from Shamsoddin et al [97] is analysed with reference to Figure (4.29). Starting from $AR = 2$ case, self-similarity is evident along crossflow direction, with the only values at $x = 1D, 3D$ that display a minimal deviation. Considering instead values along spanwise direction, they tend to collapse but the trend observed at the edges is not symmetric and reveals a certain deviation at different x . Moreover it seems that the shape at the nearest x is more similar to a rectangular shape, then becoming more similar to a Gaussian moving downstream. The positive $\frac{r}{r_{1/2}}$ region displays instead constant values, with a flat trend. This behaviour is probably related to the AR effect, however even in this case, self-similarity is clear.

At lower $AR (= 1, 0.25)$, the self-similarity along crossflow direction shows the same features observed in previous cases with intense overlapping near wake's centre, and more deviation near the edges. However, the latter aspect, that is displayed by values for $x = 1D$, is damped at $AR = 0.25$ where differences are spotted only at positive $\frac{r}{r_{1/2}}$ region because of wake's deflection. Profiles along z direction display a similar trend, with the flat region observed for $AR = 2$ that is smoothed at lower AR .

Overall, even if some differences related to wake's deflection, C_T and AR effects are observed, self-similarity property is satisfied for VAWTs' wakes, even if not perfectly. However, as testified in [10, 11] the observed level of disagreement can be tolerated.

4.2.4. Validation of the code structure for VAWT wake models

In order to evaluate the performance of the code scripts for the VAWTs wake models and debugging them, a comparison with the original version from Abkar [2] was carried out, as already mentioned. The code scripts are reported in Appendix (C) while the cases analysed are reported in Section (4.1.3.1). For sake of concise, only one of the four cases is reported here in Figure (4.30). The remaining results are reported in Appendix (D). The reader is referred to that appendix to witness the code reliability in different cases.

As shown in Figure (4.30), the code provides the same results obtained by Abkar from the original model no matter the parameters used for both NOJ and BPA model for VAWTs. On account of that the implemented versions of the wake models for VAWTs is valid, free from potential bugs and provides correct implementation of the analytical models. However, only one law for the wake decay constant was tested, the one provided

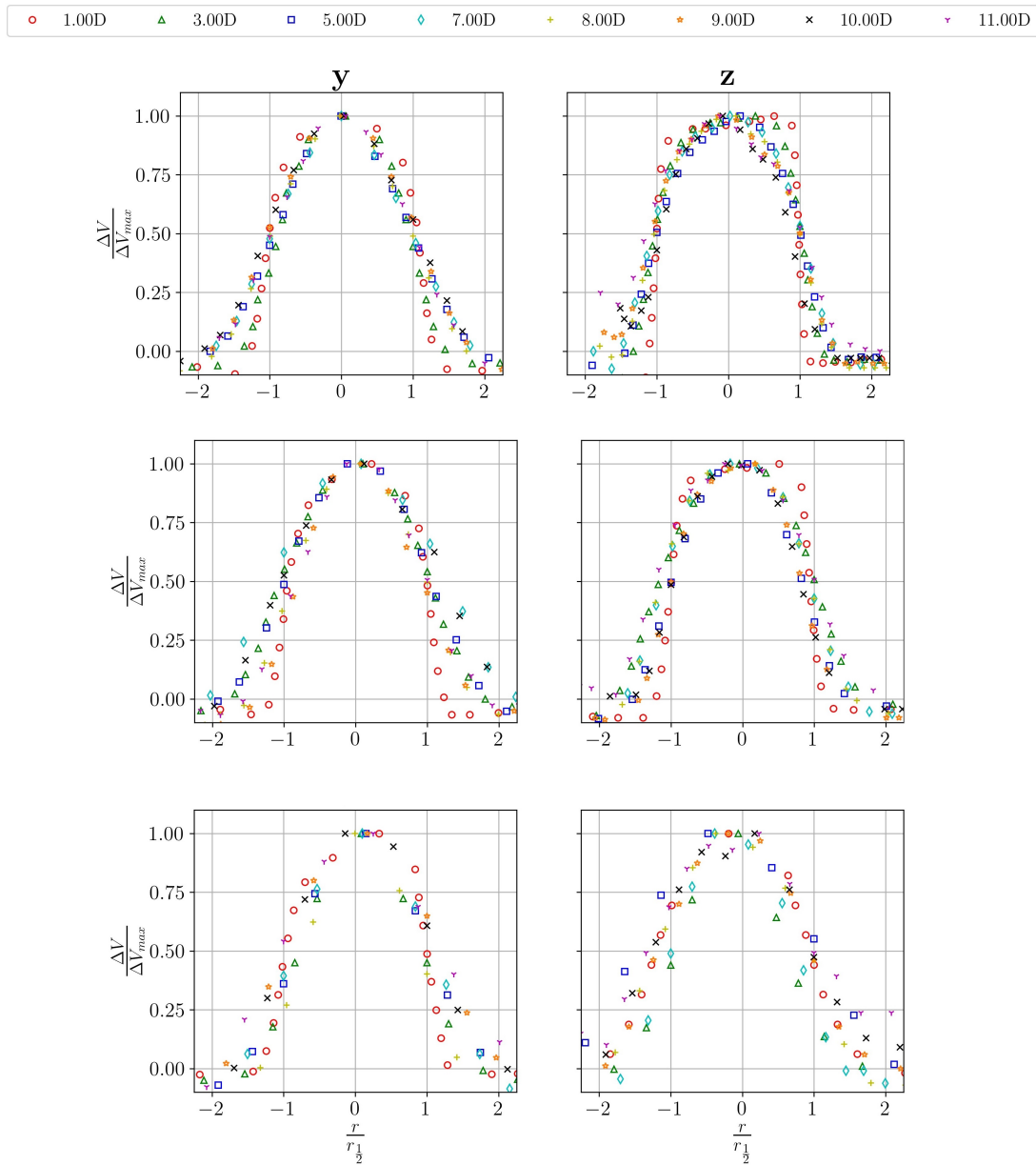


Figure 4.29: Self-similarity study for Shamsoddin et al. [97] case along both spanwise and crossflow direction for $AR = 2$ (top), $AR = 1$ (centre) and $AR = 0.25$ (bottom)

by Abkar and discussed in Section (3.2.2.3). Nevertheless, Niayifar's law was implemented according to the already-validate library `py-wake`, without any bug or error experienced.

The debugging operation was crucial in finding out some errors and bugs in the code scripts, which could have led to erroneous and wrong results.

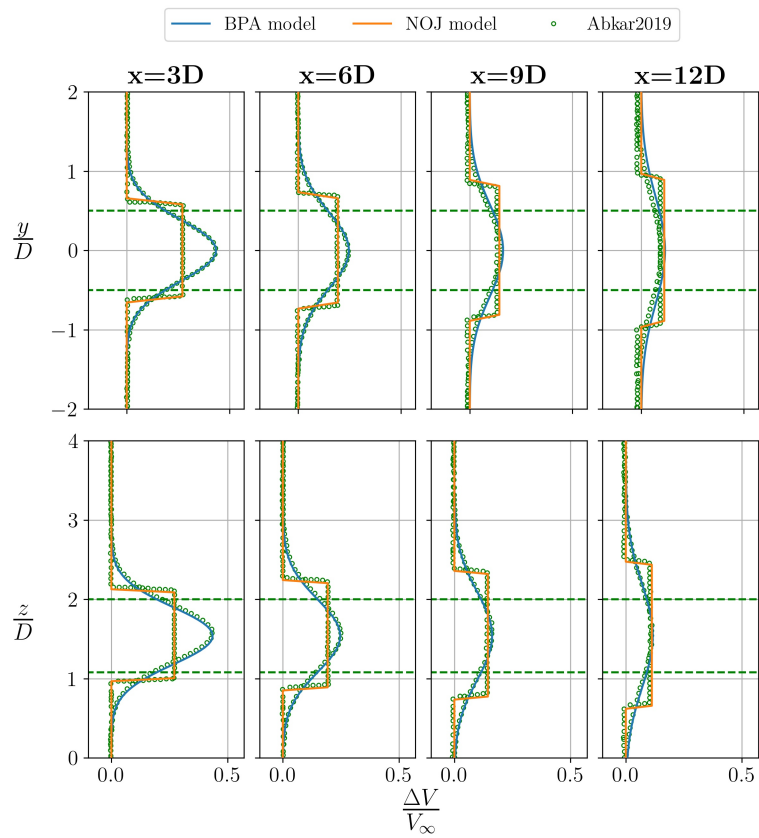


Figure 4.30: Comparison between the predictions from the models developed in this thesis and the ones from the original model [2] for Case 1 in Table (4.14)

5

The Reynolds' number effect on VAWT wake

In order to figure out if wake's features are actually replicated at different scales with the same properties, a study on Reynolds' number effect based on the numerical simulations was conducted. The purpose is to understand if wake models could potentially provide reliable results ranging from small scale turbines to large scale turbines. This occurs in case wake's features are independent on Reynolds' number. In other words it would be possible to apply wake models independently on the scale considered.

5.1. Wake similarity under different Reynolds numbers

A first overview of how the wake is characterized at different Re is reported in Figure (5.1), where mean velocity contours and normalized in-plane vectors are reported for two different downstream coordinate. When considering the low and medium Re case, the asymmetry experienced by the wake is evident. The features related to the latter have been already discussed before, but the similarities for low and medium case are evident. For the latter, CVPs action has already mixed wake's core and the vertical extension of the wake is limited. The large scale case CVPs are still present but weak compared to the other cases. It seems that higher Re values tend to minimize CVPs' influence on the wake, being dissipated earlier [110]. At the same time, focusing on the centre part of the wake for low and medium case, the differences with the higher case are not so noticeable: all the three cases display almost a circular shape for wake's centre. At first look, it seems that when experiencing deflection in low Reynolds' number, the wake maintains a certain circular shape. Therefore, even at different scales, turbine's wake seems to show similar properties and the same overall structure even if the deflection leads to strange shapes, but only apparently, since the core of the wake remains intact. Moreover even the velocity magnitude shown is extremely similar, especially when considering $x = 11D$ section.

Additional information about the CVPs structure for the different cases can be provided by Figure (5.2) where streamwise vorticity contours are reported. As displayed, the vortices pattern is similar for all the three cases. Qualitatively speaking, it seems that the intensity of CVPs at high Re has dropped, unlike the other two cases especially the medium ones. In the latter case, higher absolute values than low Re case are observed, but it could be related to TSR influence according to what was discussed in Chapter (2) and observed in previous cases analysed. Being vortical structures, inertial effect may have significant results in their structure and dissipation.

Since it would be unfair to compare the velocity profiles at $\frac{y}{D} = 0$ because of the deflection experienced by the wake, the profiles along y were extracted considering the effective wake centre, which is translated. Such profiles are reported in Appendix (D). In fact in order to identify possible Reynolds' effect it is necessary to assume a specific set of normalization parameters: the maximum velocity value ΔV_{max} and the radius at which the deficit displayed is half the maximum value $r_{\frac{1}{2}}$. Such normalization is commonly used when testing Re effects in jet-flows and is suggested also in [10, 11]. Crossflow profiles are reported for $z = 0$, while spanwise

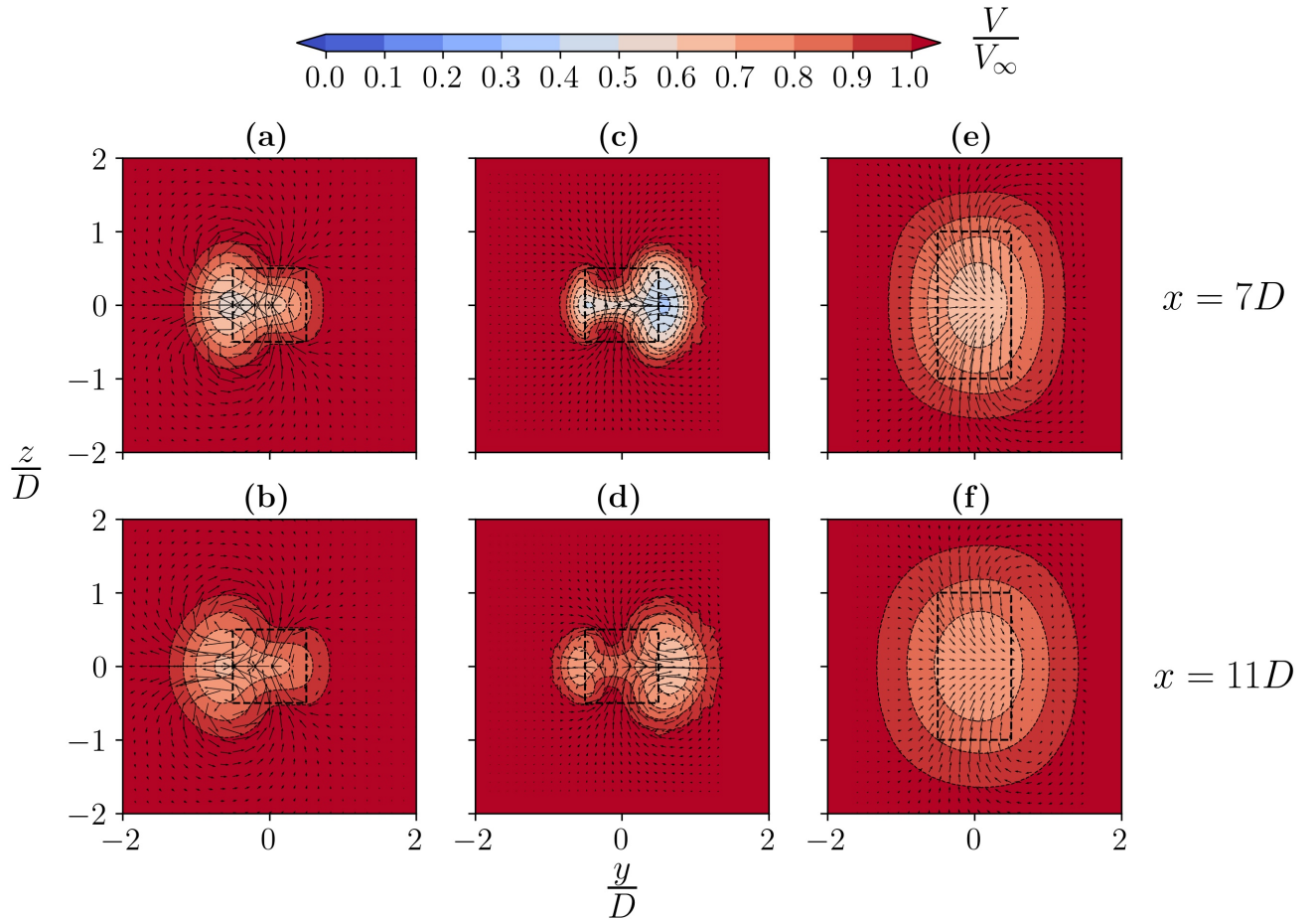


Figure 5.1: Mean streamwise velocity contours and in-plane velocity vectors normalized with freestream value at cross section $x = 7D, 11D$ for (a,b) low Re case (c,d) medium Re case and (e,f) high Re case

profiles are considered along the y identified by wake's centre. This is an important aspect, since for the low and medium case the wake is deflected. Moreover, $r_{\frac{1}{2}}$ was evaluated moving from wake's centre towards the nearest edge of the wake, otherwise the comparison would have not been fair. Results for small case were also mirrored, since the turbine rotates clockwise in that case, unlike the others. Using these parameters to normalize the deficit and coordinate values at each section, the Reynolds number effect was investigated.

With reference to Figure (5.3), velocity profiles with the new normalization are displayed. Considering crossflow profiles at first it seems that Reynolds effect is experienced. However, as observed in Figure (5.1) the region of the wake which is not affected by CVPs' action (region with positive $\frac{r}{r_{\frac{1}{2}}}$ values) shows collapsed curves. Considering instead the region with negative values, wake in low and medium Re cases is strongly skewed compared to the high Re case. Therefore, as already theorized, wake displays the same structure at different Re where no CVPs' action is observed. The remaining part of the wake instead displays a certain degree of skewness depending on deflection intensity.

This is a relevant result, since allows to use wake models with a certain confidence even when wake deformation is experienced, being aware that a certain portion of the wake is correctly replicated at least, providing even the maximum deficit value. Moreover, if deflection does not occur, the wake displays the same shape at different Re .

Considering profiles along spanwise direction, where no deflection is experienced, the absence of Reynolds' number effect is more evident than considering crossflow profiles only. Here curves tend to collapse instantly, displaying the same shape and trend along the whole domain.

Wake width evolution provides useful information for the current study. With reference to the Top Figure (5.4), wake's width evolution features different trend depending on the case analysed. For low and medium

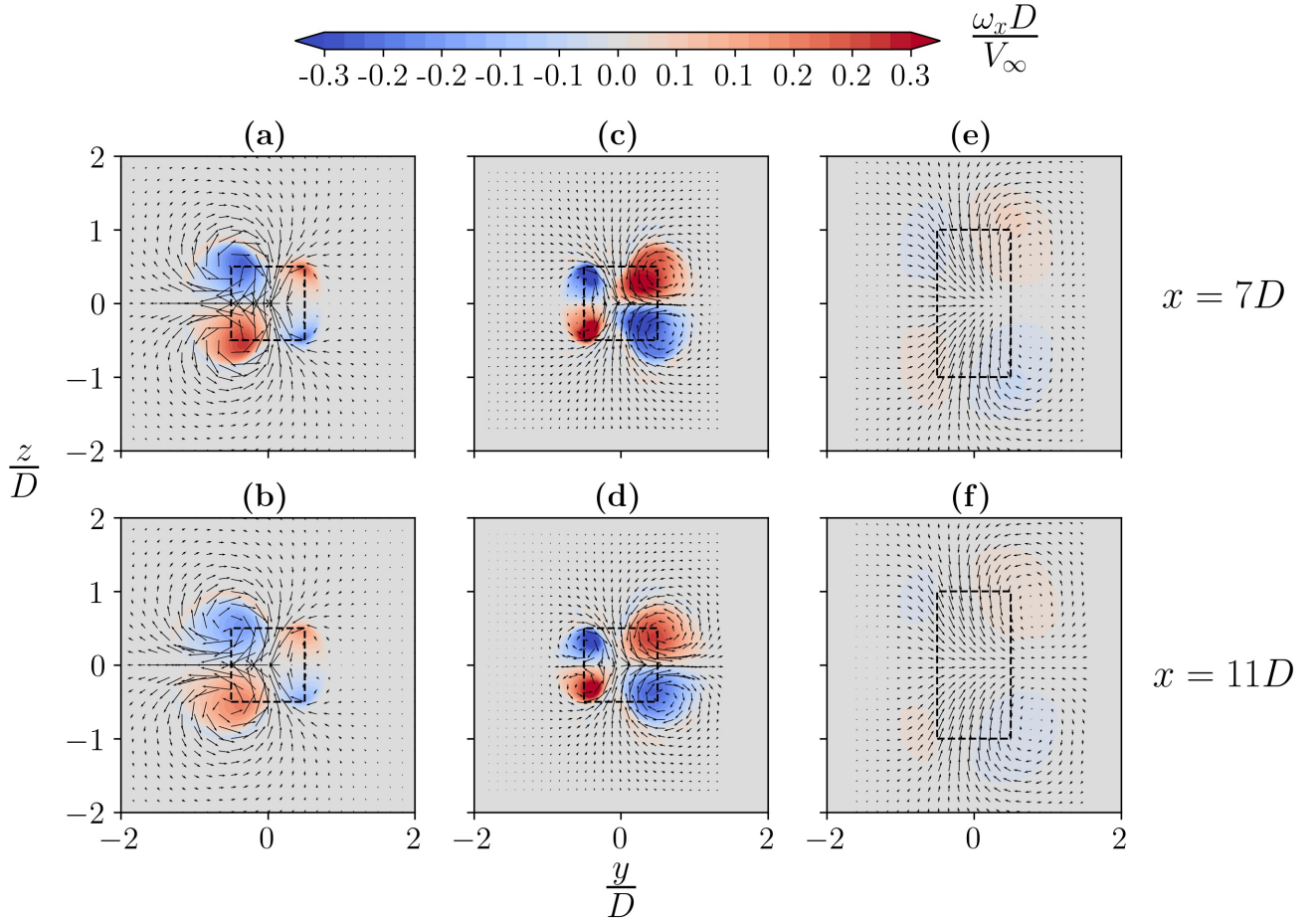


Figure 5.2: Streamwise vorticity contours normalized with diameter and freestream speed, in-plane mean velocity vectors normalized at cross section $x = 7D, 11D$ for (a,b) low Re case (c,d) medium Re case and (e,f) high Re case

Re the trend observed is similar: wakes tend to expand and the centre moves towards windward region, because of the side flows induced by CVPs that stretch the wake. At the same time, the expansion observed at windward side is limited, being at straight contact with high velocity fluid with the major part of the deficit concentrated on the other portion of the wake. Compared to wake's evolution displayed by high Re case, it seems that values for the deflected case are simply translated and display a different slope and limited expansion along crossflow direction.

Considering the spanwise direction instead as in Figure (5.3), the Reynolds' effect is not observed since values tend to overlap one another, proving that excluding deflection effect, at all the scales studied properties observed are the same.

Some more evidences are presented by maximum and mean deficit values along the wake and reported in Figure (5.5). Considering the maximum values, the same trend is observed: a region where wake recovery is triggered follows one another where wake develops reaching the overall maximum deficit. Such deficit apparently increases when considering lower Re values but all the data tends to the same asymptotic behaviour. It seems that decreasing Re the values are shifted to the top-left, highlighting more and more the region where the deficit increase. This makes sense, since the near wake region becomes more and more limited. In fact the high Re case does not display the region where deficit increases observed for previous case, probably it is located between $x = 0$ and $x = 1D$, confirming previous hypothesis.

Mean values in Bottom Figure (5.5) show the same trend of maximum deficit value with no particular differences or remarkable aspects.

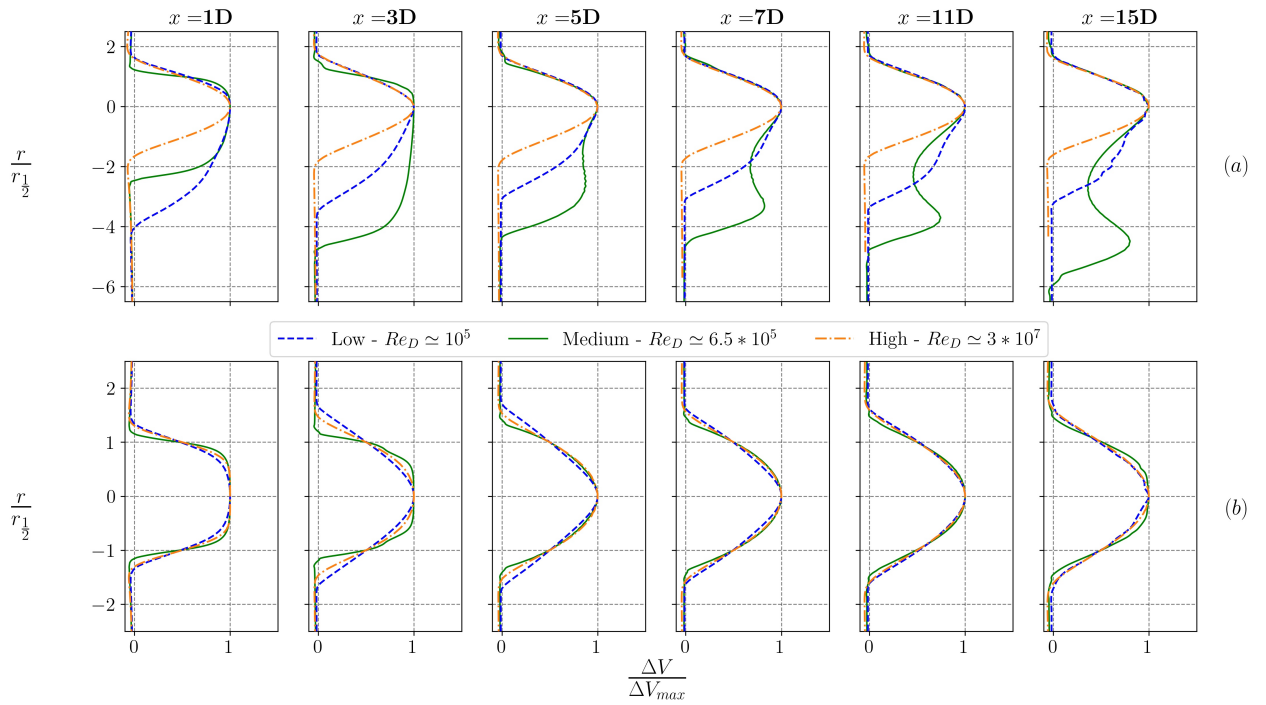


Figure 5.3: Profiles of mean streamwise velocity deficit normalized with maximum deficit at each location normalized with $r_{\frac{1}{2}}$ along crossflow direction at mid-span (top) and spanwise direction at wake's centre (bottom) for different downstream sections in different Re condition

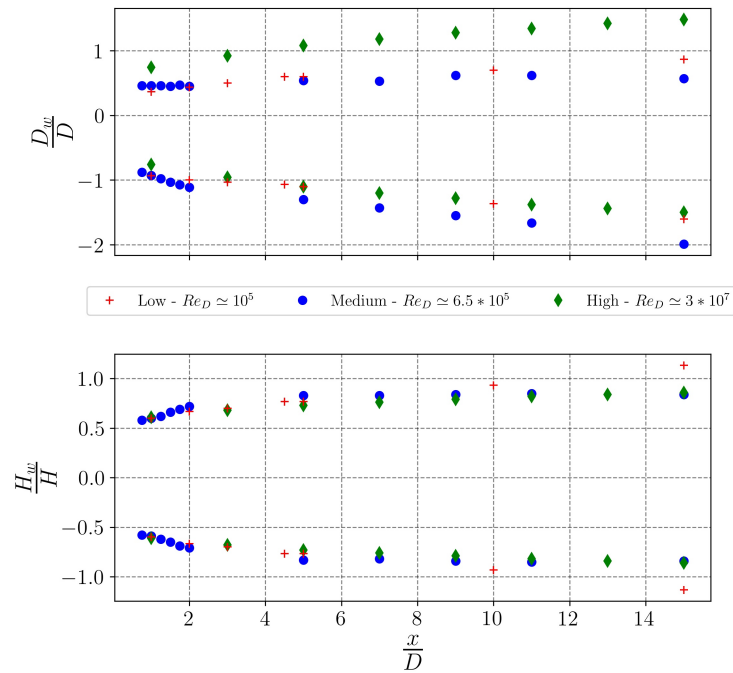


Figure 5.4: Comparison of wake width along crossflow direction (a) and spanwise direction (b) calculated with numerical simulations in different Re conditions. Values were calculated considering wake's centre as reference and not $\frac{y}{D} = \frac{z}{D} = 0$. Data for low case are mirrored

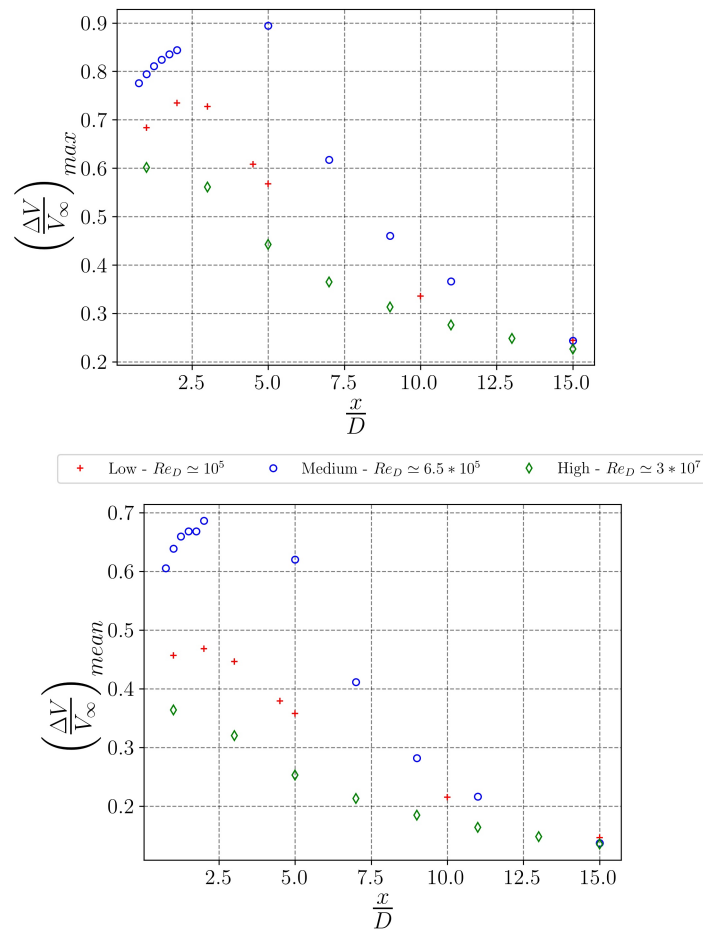


Figure 5.5: Comparison of the maximum velocity deficit (top) and the mean velocity deficit (bottom) calculated along crossflow direction at mid-span by numerical simulations for different Re conditions

5.2. Conclusions

After the analysis and the comparison between different Re , it is possible to conclude that similarity can be observed in the wake at different Reynolds' numbers. As shown, wake centre, even if shifted, displays almost the same shape at all different scales. Moreover, comparing velocity profiles with adequate scaling parameters showed that the portion of the wake where CVPs advection is not experienced do not change structure and neither shape at different Re . The remaining part of the wake, which displays deflection does not demonstrate the same behaviour, with a subsequent degree of skewness in the distribution. This leads to the conclusion that if wake deflection was not experienced, all the shapes would have been absolutely the same displaying similarity along the wake. This hypothesis is corroborated by other aspects here listed:

- Profiles in Figure (5.3) along spanwise direction display a total independence on Re .
- Wake width evolution along spanwise direction in Figure (5.4) displays the same trend for each Re case with values overlapping at each downstream section. The same is not observed for wake's crossflow width, but seems to be simply translated.
- The evolution of maximum and mean deficit value is the same, but translated. Probably introducing the correct scaling parameters the curves would overlap.

The partial absence of Reynolds' effect leads to important consequences. Displaying the same behaviour for a portion of the wake that contains the maximum deficit at every different Re means that wake models would be able to replicate at least the maximum deficit with considerable accuracy when considering both small and large scale wind turbine. Therefore, even if afflicted by several limitations that cannot be neglected, they can still be considered reliable even in conditions non totally valid for their application.

6

The turbulence effect

Another relevant aspect that needs to be analysed is the turbulence effect on wake's evolution and especially on wake recovery. In Chapter (2) Section (2.2.3.5) was largely discuss how the environmental turbulence affects the wake and its ability to enhance wake recovery process thanks to the mixing phenomena [68]. In this section, a qualitative study about the turbulence effect on the wake was carried out. The purpose it to acquire a qualitative knowledge about how turbulence intensity variation affects wake recovery at different scales, in order to be potentially replicated in analytical wake models.

6.1. Ambient turbulence effect on wake recovery

The starting points are the numerical simulations already analysed and some new ones based on the same parameters but in a laminar case, evaluated turning off the $k - \varepsilon$ model. This way four main cases can be analysed and compared: one based on low turbulence intensity and low Reynolds' number (case introduced in Section (4.1.1) and analysed in Section (7.1.2)), one on high turbulence intensity and high Reynolds' number (check Section (4.1.1) and (7.1.3)) and the same but without using a turbulence model, assuming laminar regime.

Unfortunately, because of the high deformation displayed by the wake in laminar cases, it is not possible to identify a specific relevant velocity profile. Therefore this qualitative analysis will be based only on the evaluation of deficit map, maximum deficit, averaged deficit value and minimum velocity. In Appendix (D) however, the velocity profiles for $\frac{z}{D} = 0$ are reported, in case the reader is interested in evaluating their structure.

With reference to Figure (6.1) that reports the cross-sections obtained at two different downstream locations for the four cases analysed, shapes revealed by the wake are extremely different one another. Each wake displays unique features. Differences between the first two cases could be related to the fact that lower turbulence intensity means lower mixing activity that (as reported in Chapter (2)) leads to a slower recovery. The wake may require longer downstream distances to recover up to the freestream value. Moreover, as shown here, structures like the CVPs vortices that should be dissipated early in the wake are still present, deforming wake's shape. In fact, since the mixing process is extremely weak or even inhibited, CVPs are not merged with the outer part of the wake. With high turbulence intensity instead, it seems that for the second case wake is not deformed and at the same time provides a lower deficit value at wake's centre. Considering now the low Re laminar case, the shape assumed is probably due to viscous effects that play the biggest role in slowly dissipating the wake but at the same time vortices are still present (check the cross-section (f) in Figure (6.1)). However the shape of the wake is too much deformed and it is not easy to determine what exactly happens, even qualitatively. More specific information can be provided by the last case, where the shape observed is extremely similar to the one from case 2, especially for $x = 7D$. Here the velocity deficit is still extremely high, even if it seems to undergo a slow decrease. Vortical structures are spotted as well but it seems that they do not lead to a major distortion of the wake area as observed before.

Another possible consequence of low turbulence is that wake shows lower expansion and a reduced area. This consideration is probably correct, keeping in mind that wake decay constant used in wake models are

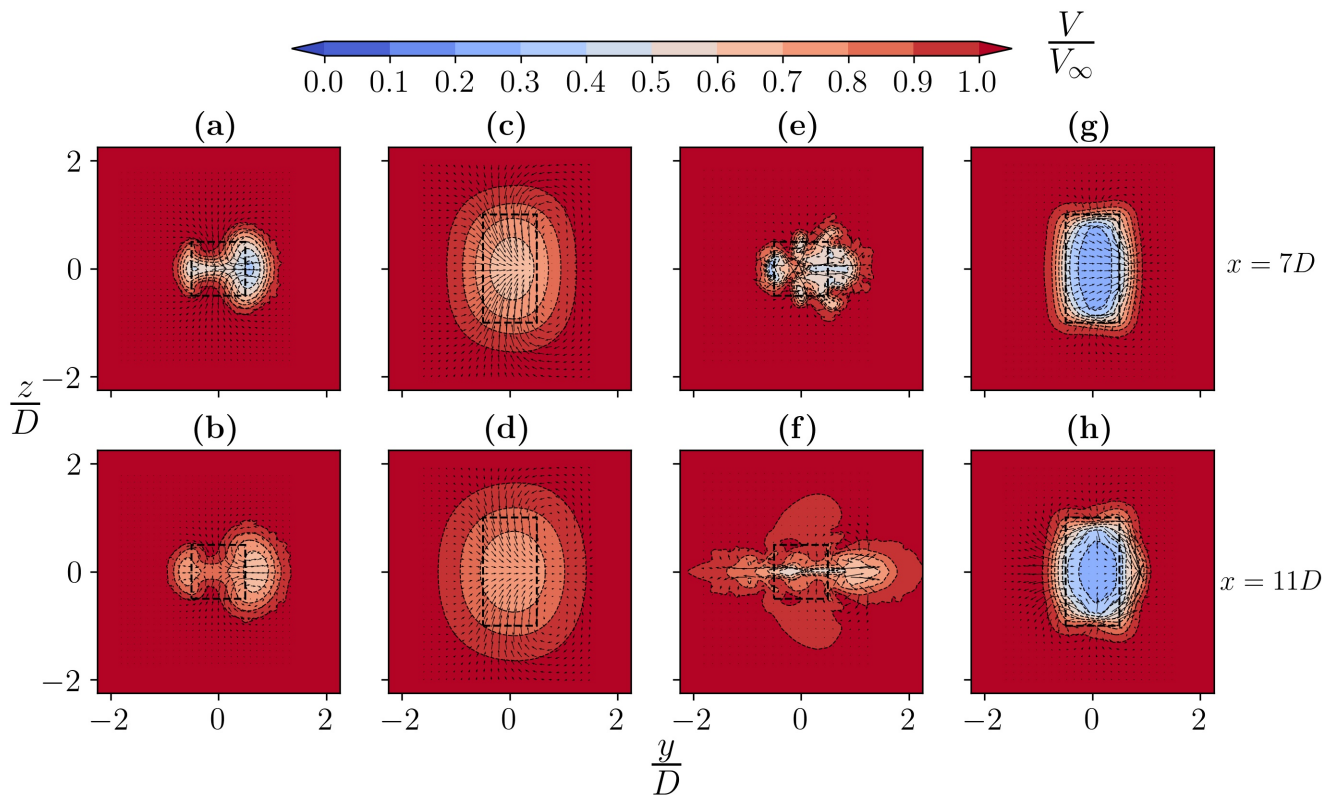


Figure 6.1: Streamwise velocity contours and in-plane normalized vectors at cross section $x = 7D, 11D$ for (a,b) low Re, I case, (c,d) high Re, I case, (e,f) low Re laminar case and (g,h) high Re laminar case

related to turbulence intensity and with higher values wake (in analytical wake models) expands faster. However it is critical to remember that this is only a qualitative discussion, since also Reynolds' effect plays an important role.

Some more reflections can be made analysing different parameters related to the velocity at mid-span and how they evolve. Starting from Top Figure (6.2) three possible behaviours are spotted:

- Initial development of the wake: the deficit increases in the first downstream region and then the wake slowly recovers. Such behaviour is observed for the low Re, I cases both in turbulence and laminar condition. It was already observed when considering cases analysed in the current section.
- Wake already developed from the start: the recovery process starts immediately behind the turbine. Such behaviour is observed in the high Re, I case
- Stationary condition of the wake, with constant deficit value displayed. Observed for the high Re laminar case where recovery seems to be extremely slow.

It is possible to propose some explanations regarding the three options mentioned. Concerning the first group, the turbulent case displays a faster recovery as already mentioned. The combination of no-turbulence and low Reynolds number allows viscous effects to be particularly strong. This is probably the reason of the recovery displayed here, something not expected. Otherwise another possibility could be related to the only action of vortices and CVPs that may still be present because of the low Reynolds number. The high Reynolds number case (second behaviour) displays a fast recovery probably due to the high turbulence used, the trend is similar to the one experienced by the first group. Regarding the last case, here an opposite condition compared to the first one is observed: probably wake is unable to recovery by means of viscous effects only because of the extremely high Re experienced. Inertial effects are dominant and the wake probably evolves far and far downstream before being dissipated.

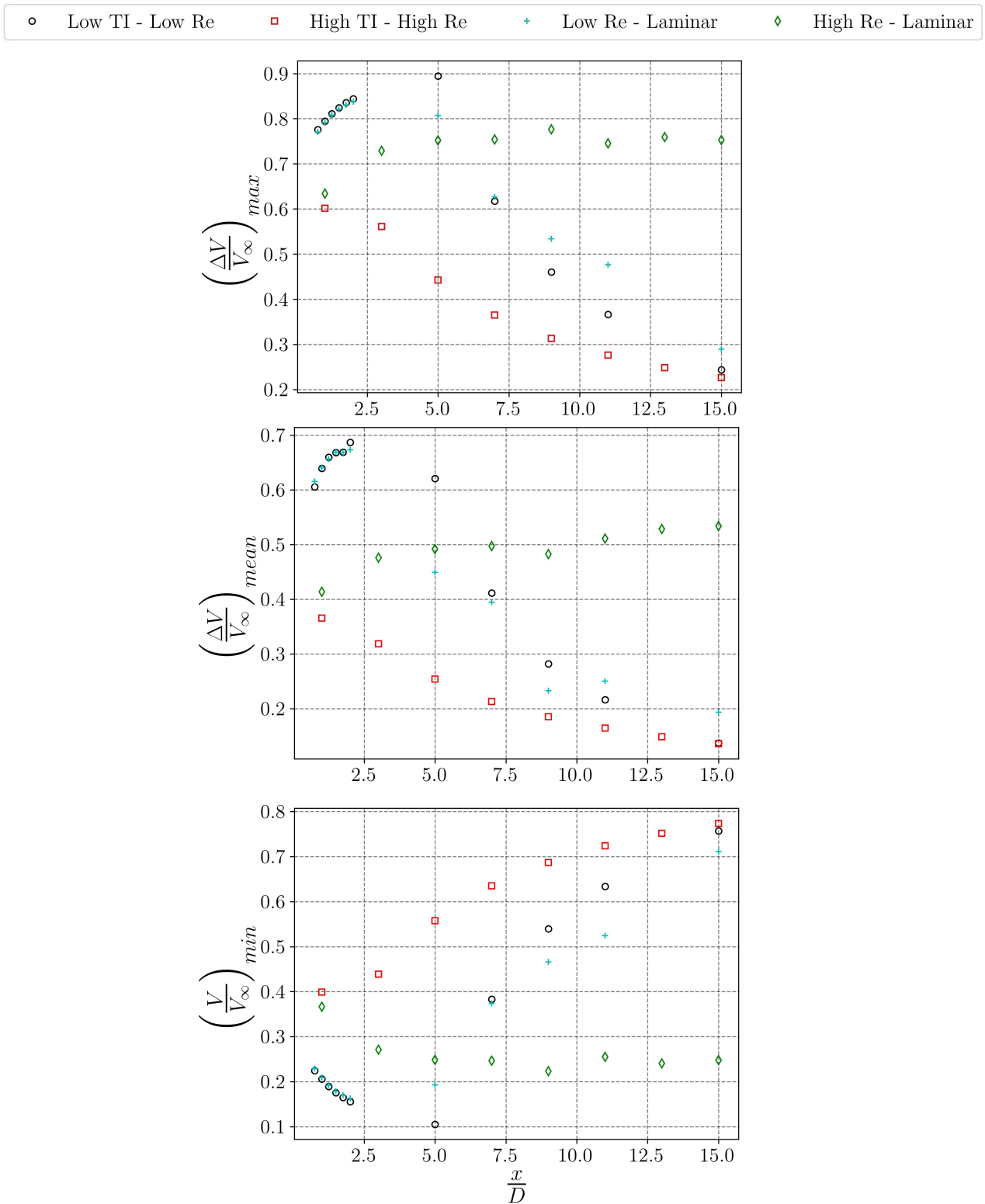


Figure 6.2: Comparison of the maximum velocity deficit (top), of the mean velocity deficit (centre) and the minimum normalized velocity (bottom) calculated along spanwise direction at mid-span by the numerical simulations for different turbulent conditions

The same trend is observed also when considering the average value and the minimum velocity value of the wake in Figure (6.2). From the bottom figure (but also from previous ones) the slope of the curves may be related to the different recovery experienced. Providing an equation that relates the deficit evolution down-

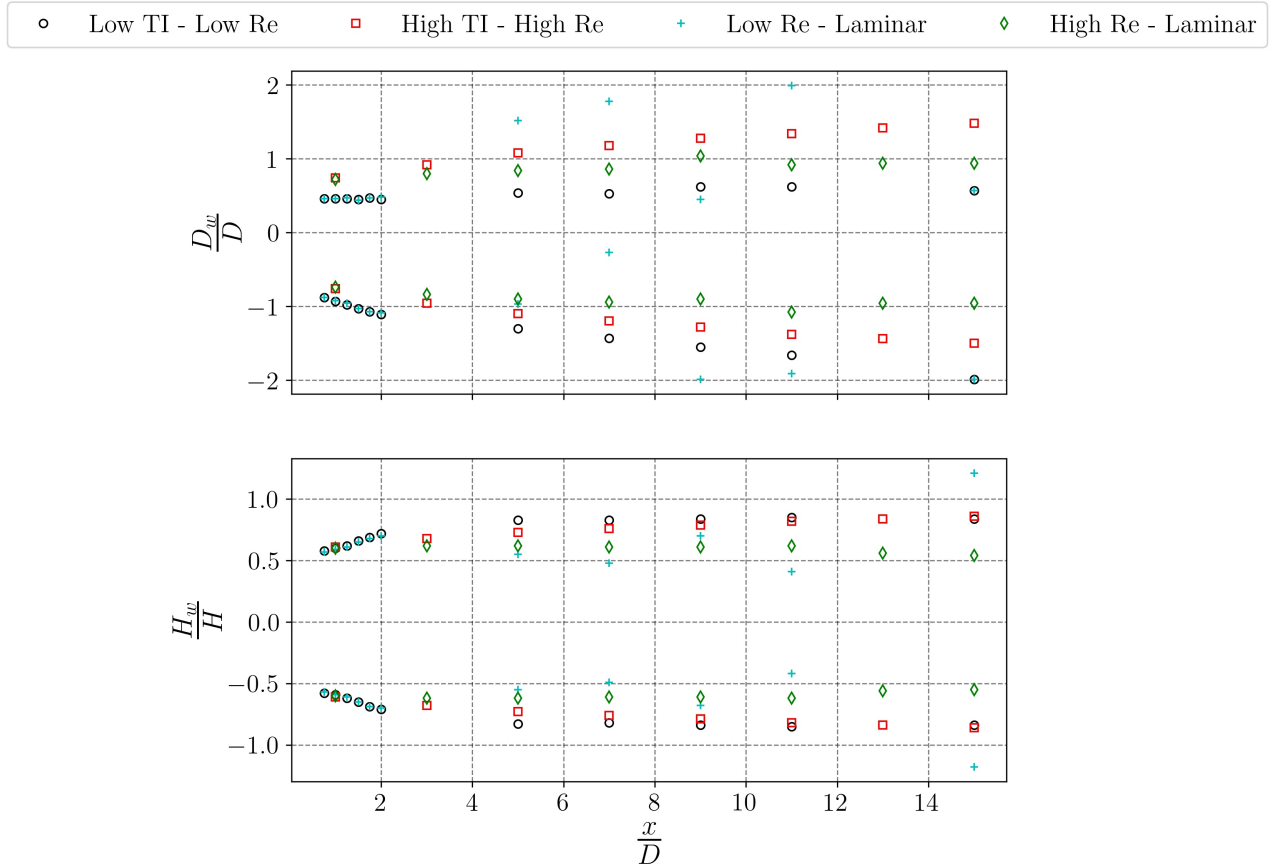


Figure 6.3: Comparison of wake width along crossflow direction (top) and spanwise direction (bottom) calculated with numerical simulations along crossflow direction in different I conditions

stream and the turbulence intensity could be the target of future researches.

The last step of the analysis is based on the comparison of wake widths, reported in Figure (6.3). Wake's extension along spanwise direction was evaluated considering the location of the maximum deficit, in order to make a more fair comparison and 'avoid' the spurious effect due to the deflection. According to what is shown in Top Figure (6.3), wake width increases when I effect is present. For the low I case, the expansion is limited and mainly observed at leeward side, since due to CVPs action the wake is stretched. For high I case instead a the wake expands symmetrically as already seen.

The trend displayed by small scale laminar case is unpredictable: the wake seems to be dominated by vortices action. The latter seem to push the wake from one side to the other. For the large scale laminar case instead, wake does not expand nor decay: it remains constant.

Considering instead spanwise direction, it seems that turbulence effect on the expansion is limited but constant for not laminar cases, with almost the same trend. In this case values from small scale in laminar condition tends to follow better the more predictable trend. Moreover seem to display a symmetric development compared to mid-span plane. The high Re laminar case displays the same behaviour observed along crossflow direction, without experiencing any expansion.

6.2. Conclusions

Drawing some conclusions about the turbulence effect on the wake is not an easy task and it is only possible to provide a few qualitative statement:

- Wake's shape is strongly affected by the turbulence intensity, but it depends also on the Reynolds' number. The two effects need to be considered connected since at low Re in no turbulence conditions, wake

is still able to mainly because of CVPs and especially viscous action, while at high Re in no turbulence conditions the dominance of inertial effect does not enable recovery. So an additional aspect acquires importance: viscous effects.

- It seems that CVPs are strong when lower I conditions are experienced and persist further downstream but showing a different impact on wake's structure: while for low Re they seem to play a considerable role in deforming wake shape's and ensure recovery, at high Re they are dissipated because of inertial effects.
- In high Re and I case, the wake tends to recover faster to freestream values with the minimum velocity that displays a higher slope, and so a faster variation.

7

The range of validity of existing wake models

In this Chapter are reported and discussed all the results obtained from the comparisons between analytical results and higher fidelity data. The first Section analyses the comparison with numerical simulations while the second Section deals with the analysis of how predictions from wake models behave compared to literature data when fixed and variable parameters are used.

For the sake of concise, the following nomenclature for the four different wake models is assumed:

1. **NOJ**: For the Jensen top-hat model based on [43] coupled with Abkar's law for the wake decay constant [2]
2. **BPA**: For the Gaussian model based on [3, 10] coupled with Abkar's law for the wake decay constant [2].
3. **NOJ-N**: For the Jensen top-hat model based on [43] coupled with Niayifar's law for the wake decay constant [72].
4. **BPA-N**: For the Gaussian model based on [3, 10] coupled with Niayifar's law for the wake decay constant [72].

7.1. Comparison against numerical simulations

In this section results from analytical wake models will be compared against actuator line numerical simulations. The three cases introduced in Section (4.1) will be analysed one by one. The final comments can be found at the end of the Chapter.

7.1.1. Comparison for low Re case

Starting from the low Reynolds number case, an overview of the flow field generated by the wake is reported in Figure (7.1). As shown, there are considerable discrepancies between the results from numerical simulation and wake models along both spanwise and crossflow direction. None of the models is able to correctly replicate the smoothly-distributed deficit experienced in the near wake region as well as wake's expansion along spanwise direction. The latter is observed up to a certain downstream region ($x \approx 5$), but then starts to decrease slowly and the wake-affected area becomes more and more limited. Along crossflow direction wake expands constantly and is clearly deflected towards one side (negative y) where the maximum deficit value is located, as discussed in Section (2.2.3.2) [8, 88, 90]. Top-hat models provide a relatively accurate shape and extension of the wake along crossflow direction, but they show poor accuracy in evaluating the velocity deficit and its distribution. BPA model shows its limits, providing a vast constant deficit region. The reasons of such behaviour are small case turbine and low turbulence intensity. In fact the extremely low turbulence intensity results in a negative value in the square root in equation (3.147). On account of that, according to the code reported in Appendix (C), the terms is substituted by 0. Such constant term persist moving downstream, so no variations are experienced. Only in the far far wake, the higher values of wake's width allows the term

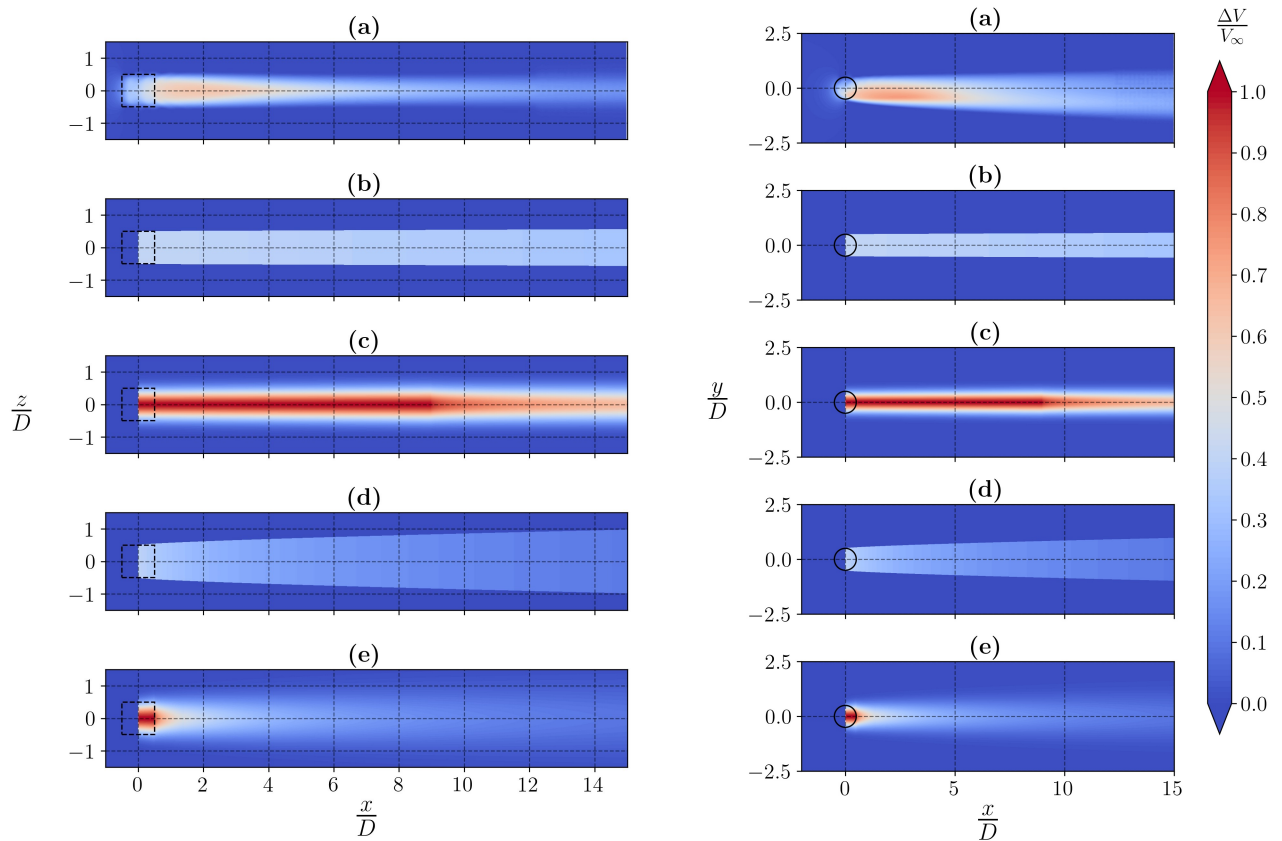


Figure 7.1: Overview of velocity deficit and wake's expansion for low Reynolds' number case along $x-z$ plane for $y=0$ (left) and $x-y$ plane at mid-span (right) for (a) AL + URANS simulation (b) NOJ, (c) BPA, (d) NOJ-N and (e) BPA-N wake models

to be higher than one. At the same time, it is possible to observe the subsequent 'red-region', whose extension is remarkable. NOJ-N model provides the most similar maximum deficit distribution to AL simulation among wake models for both spanwise and crossflow direction. However, even in this case the models can be considered only qualitatively good, since wake is dissipated too quickly.

Considering the cross sections of velocity contours reported in Figure (7.2) for $x=10D$ based on the actuator line simulation and analytical wake models, some additional qualitative details can be observed. First of all, the deflection experienced by the wake towards windward side is clearly observed. Wake's centre moves towards negative y and the shape is deformed by CVPs action (see Section (2.2.3.3)) [36, 78] resembling a kidney or a clover-leaf. CVPs' presence is revealed by velocity vectors, with stronger vortices at windward side, where the wake is shielded from outer flow, delaying its recovery. Wake models are not able to predict wake deflection, providing a 'stationary' wake shape. Moreover, as observed in Figure (7.1), most of the models do not replicate with sufficient accuracy the velocity deficit, except for the NOJ model that provides a value similar to the one observed at the center of the kidney-shaped wake. BPA model still experiences the onset point problem, while BPA-N model overestimate the wake recovery and underpredicts wake extension. NOJ-N model results in a wake dimension qualitatively similar to the one provided by AL simulation. A more detailed review of the real accuracy of wake models can be made only analysing the mean velocity profiles.

Before moving on to the next analysis it is necessary to point out a relevant assumption. Mean velocity profiles are reported and analysed at $\frac{z}{D} = 0$ and $\frac{y}{D} = 0$ for crossflow and spanwise direction respectively. A different comparison would have featured the profiles considering wake centre displacement in numerical simulation. This would have allowed to compare the effective maximum deficit experienced by the wake, but it could be considered unfair, since the purpose of the thesis is to study the limitations of wake models. This way in fact it would have not been possible to observe wake deflection that wake models are not able to replicate, since they consider maximum deficit always located at $\frac{z}{D} = 0$ and $\frac{y}{D} = 0$.

The mean velocity profiles in Figure (7.3) lead to several conclusions regarding wake models accuracy.

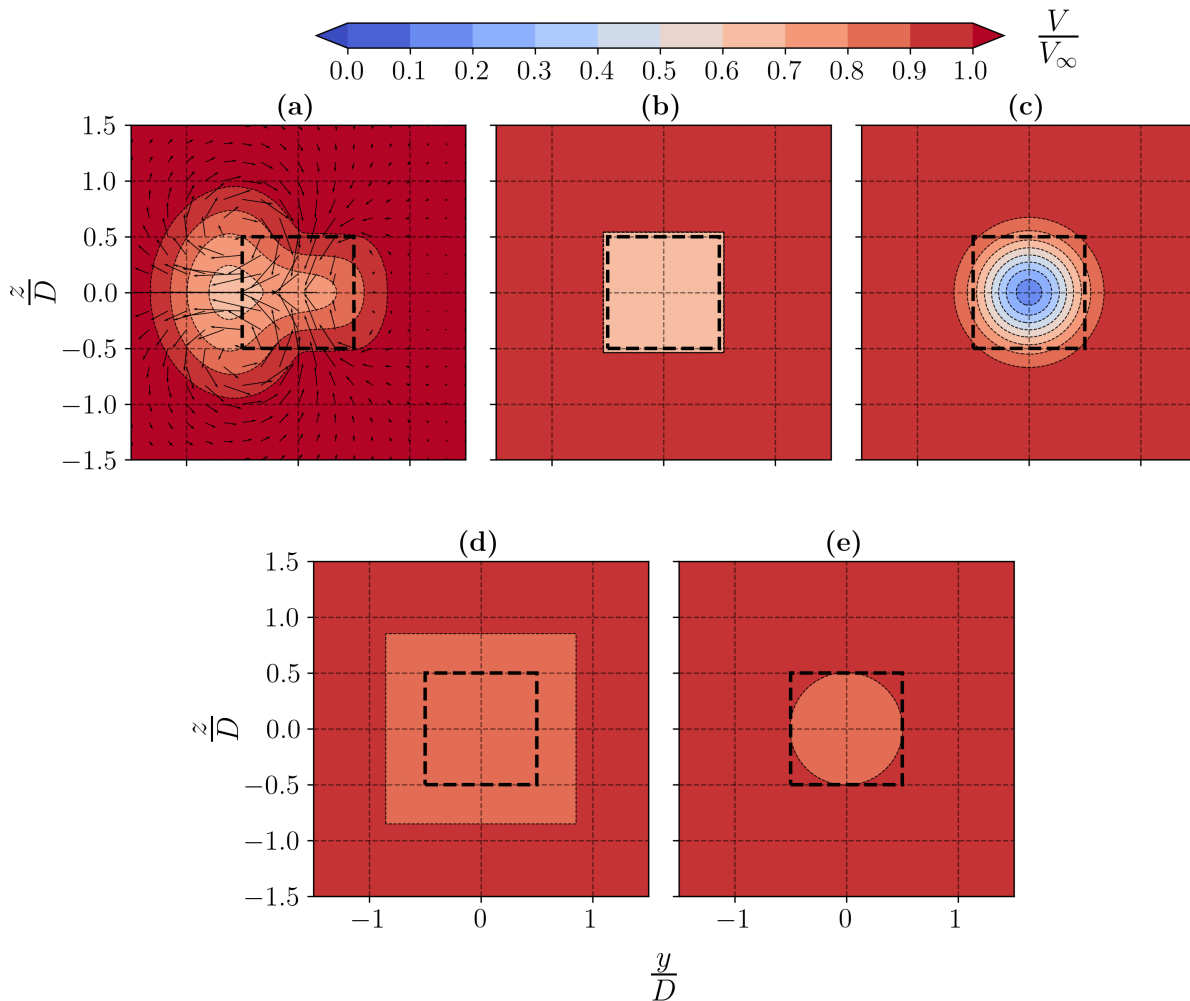


Figure 7.2: Mean streamwise velocity contours and in-plane velocity vector normalized by the incoming wind speed at cross section $x = 10D$ for (a) AL + URANS simulation, (b) NOJ, (c) BPA, (d) NOJ-N and (e) BPA-N wake models for low Re case

Starting from Top Figure (7.3), the deflection experienced by the wake is observed clearly along crossflow direction, revealing one of the major drawbacks and limitations of VAWTs wake models. In fact they cannot replicate wake asymmetry, that even being a phenomenon typically observed in the near wake, in cases like the one presented here persists even up to the far wake. A similar behaviour is justified by the low TSR and Reynolds' number. The former is known to be responsible for higher deflection in the wake, as discussed in Section (2.2.3.4) [3, 36, 97], strongly affecting wake's shape. A low Reynolds' number means weak inertial effects, enabling vortical structures to persist up to the far wake without being dissipated.

The comparison can be discussed for each wake model singularly:

- NOJ model provides lower values in the near wake while moving downstream the discrepancy compared to numerical data decreases. The highest level of agreement is reached at $x = 10D$ but from that point on, values provided are higher than the correct ones. In conclusion the model overestimates wake recovery in the first part of the wake and overestimates in the second.
- BPA model suffers the 'onset-point' problem for a vast portion of the wake as already seen in Figure (7.1). It overestimates the deficit value, which is considered constant up to the onset point. The delay in reaching such fictional point is due to low turbulence intensity. After $x = 5D$ the model passes the onset point, but the deficit values predicted are still far from the numerical ones.
- NOJ-N underestimates the correct values along almost the whole domain considered. Moving towards downstream direction, the discrepancy diminishes as observed for $x = 15D$.

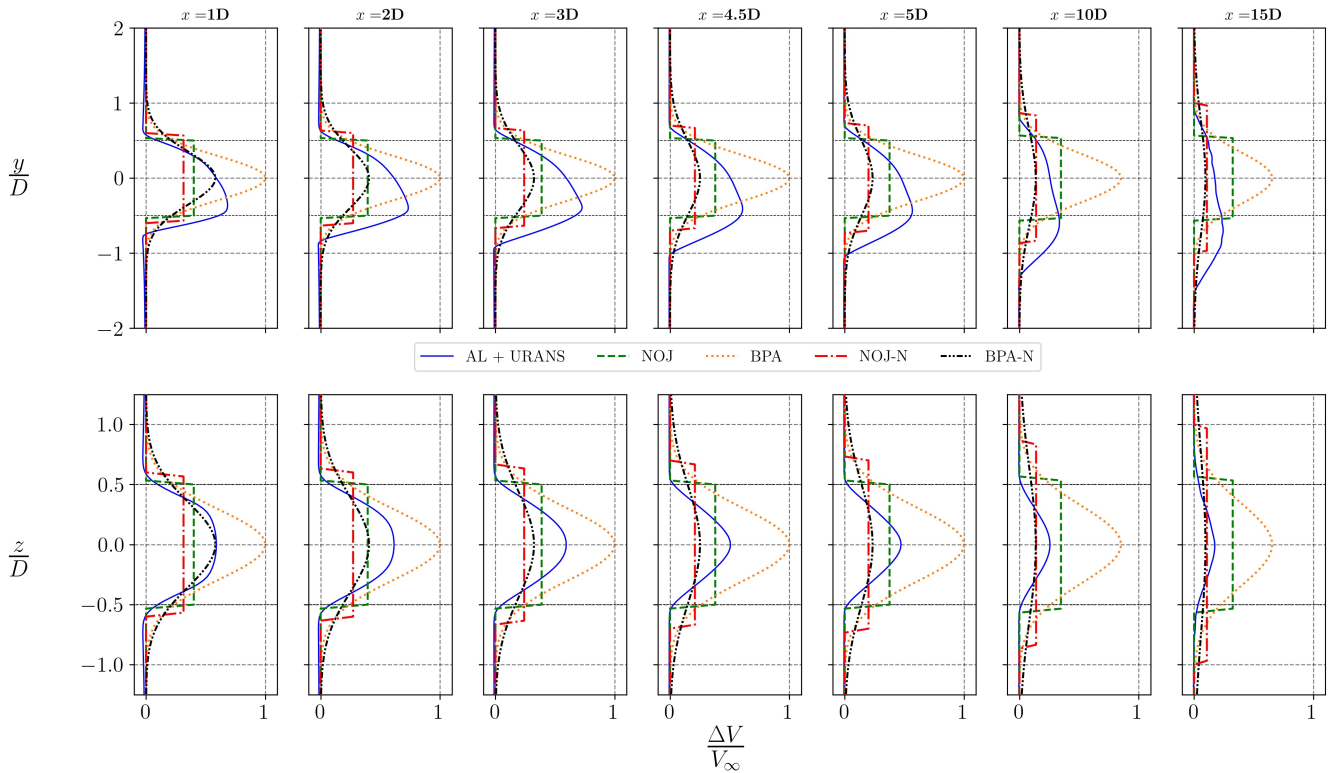


Figure 7.3: Profiles of mean streamwise velocity deficit along crossflow direction at mid-span (top) and spanwise direction for $y = 0$ (bottom) for different downstream sections, comparison between data from different analytical models and numerical simulation in low Re conditions

- BPA-N model suffers the fate of the previous model, underestimating the correct values along the whole domain. At the same time, the disagreement shown reduces moving downstream.

Discrepancies related to wake's width coming from numerical simulation and analytical wake models will be discussed afterwards.

No particular deflection or effects related to turbine's spanwise extension are observed in Bottom Figure (7.3). It is crucial to shed light on a relevant aspect observed: according to numerical data, the wake does not expand along the vertical plane crossing the center of the VAWT, but shrinks. A possible explanation of such behaviour will be discussed when dealing with the medium Re case in the next section, but it is possible to inform the reader that is a phenomenon related to wake's deflection and deformation.

Since no deflection is experienced along spanwise direction, models are more capable of replicating wake's features. In the near wake, BPA-N model provides values similar to numerical ones. The same level of agreement will be observed in Section (7.2.2) for the medium Re case. At $x = 2D, 3D, 4.5D$ the accuracy demonstrated by this model drops, since it overestimates wake recovery rate as for crossflow profiles. Further downstream at $x = 10D$ and $15D$, discrepancy shown slowly decays, providing good agreement with numerical data. Similarly, NOJ-N model reveals the same trend which provides almost equal results of BPA-N in the near wake, but showing stronger inaccuracy in the near wake. Model based on Abkar's law reveal almost the same trend observed along crossflow direction, without specific changes.

The comparison of wake widths calculated by numerical simulations and wake models aims to investigate wake expansion and the portion of area affected by the velocity deficit at a certain downstream coordinate. Additional information, fundamental when deciding the layout of turbines in a wind farm are provided this way. With reference to Figure (7.4), the extension of the wake along both crossflow and spanwise direction for $\frac{z}{D} = 0$ and $\frac{y}{D} = 0$ respectively, is revealed. Starting from y direction in Top Figure (7.4), the deflection

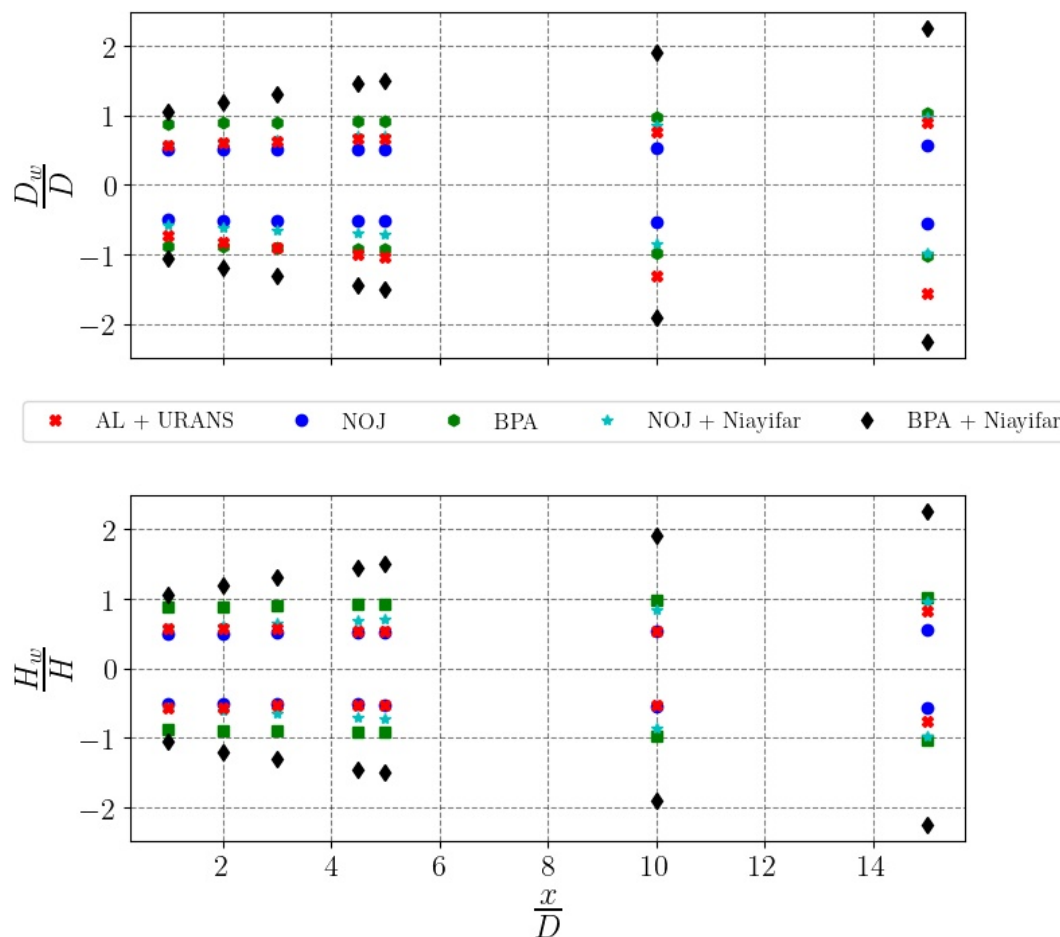


Figure 7.4: Comparison of wake width calculated with numerical simulations and analytical models along crossflow direction at mid-span (top) and spanwise direction for $y = 0$ (bottom) in low Re conditions

experienced in the numerical case seen in Figure (7.2) and (7.3) is clearly observed. The wake expands towards negative y as seen before, but displaying a linear development as assumed in Section (3.2.2) [2, 10, 11]. None of the wake models is capable of replicating a similar evolution, characterized by a different wake decay parameter k^*, k_w for the two sides of the wake. At the same time, the agreement shown when considering crossflow direction and in particular leeward side (where no deflection is experienced) is considerable. The slope and the values observed for BPA and both top hat models is not so far from the ones displayed by numerical data. Even if, considering Figure (7.3) wake's widths calculated by wake models seemed to be totally different compared to values from numerical simulation, the current comparison revealed a good agreement in terms of absolute value.

Similarly, wake's widths comparison along spanwise direction shows even more agreement between numerical and analytical results. As for crossflow direction, BPA and both top-hat models similar to numerical ones due to the fact that no deflection is experienced. At the same time, a substantial difference is observed for the slope: in the numerical case, the wake shrinks and not expand, so a negative slope is observed.

Lastly, maximum velocity deficit values at each downstream section analysed are compared. A premise is necessary even in this case. Since it would be unfair to consider top-hat models in the evaluation of the maximum, a second analysis, based on the mean value was carried. The results are reported in Figure (7.5). The reader is now referred to Top Figure (7.5) and the deviation bars in Left Figure (7.6). The deviation was calculated as the difference between the maximum/mean velocity deficit elaborated by the wake model considered and the literature/numerical value. After subtracting them, the result was then normalized using the maximum mean deficit value or the maximum maximum deficit for the case analysed. A considerable discrepancy is observed between the values calculated by BPA model and the ones from AL simulation. The

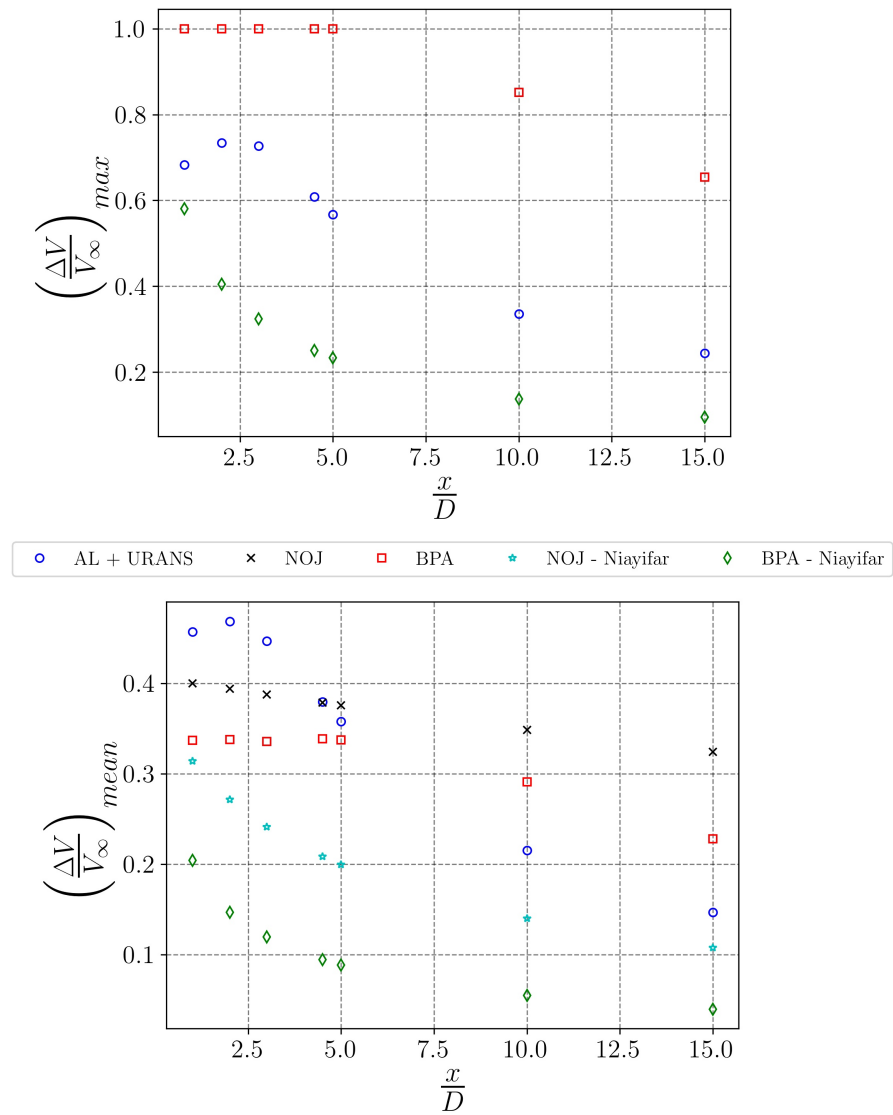


Figure 7.5: Comparison of the maximum velocity deficit (top) and the mean velocity deficit (bottom) calculated by the numerical simulation and wake models along crossflow direction at mid-span in low Re conditions

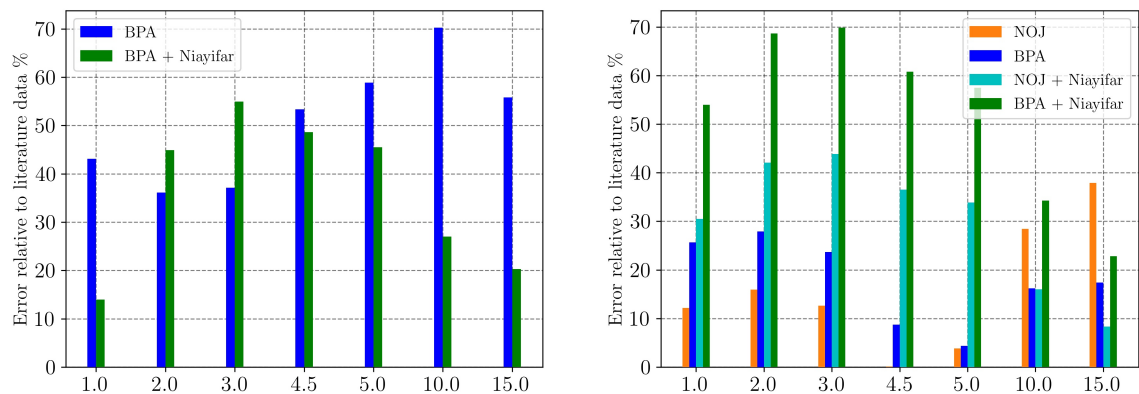


Figure 7.6: Deviation of the maximum (left) and the mean velocity deficit (right) from numerical data for different wake models. The errors are based on the data evaluated along crossflow direction at mid-span in low Re conditions using the maximum values as reference for the error.

deviation ranges from 40% to 70%, ensuring the unreliability of the model in low turbulence and Reynolds' number case. BPA-N model provides a certain level of agreement especially in the very near and far wake ($x = 1D, x = 15D$) where the deviation is below 20%. However, in the remaining wake region BPA-N model displays an average deviation of 40%.

Overall, Gaussian models performs poorly in the calculation of the maximum deficit for the low Re case. The inaccuracy shown here is related to the problems largely discuss before (self similarity not satisfied, low Re and I , inability to replicate the wake recovery, constant region for BPA model...). This is an unobjectionable statement of their limitations.

Observing mean values in Bottom Figure(7.5) and Right Figure (7.6), additional details can be mentioned. NOJ and BPA model reveal a considerable agreement with numerical data with a decreasing deviation observed until $x = 5D$. Up to this downstream location, the discrepancy shown is limited below 15% and 25% for NOJ and BPA model respectively. When then moving further downstream ($x = 10D, 15D$) the error increases, displaying a rapid variation. NOJ-N model, reveals instead an increasing deviation trend up to 45% for $x = 3D$ and then a considerable decrease with less than 10% deviation at $x = 15D$. BPA-N model shows the poorest performances, with deviations up to 70%.

Overall NOJ and BPA model can be considered more reliable in the region up to $x = 5D$. Then, since they tend to underestimate recovery rate, the error tends to increase. NOJ-N model was already observed to provide accurate results in far wake region, as observed in Figure (7.3) so it could be coupled with models based on Abkar's law to provide reliable estimations of mean values. An additional relevant aspect observed in both Top and Bottom Figure (7.5) is that according to numerical data, the wake develops at a first stage, reaching the maximum deficit for $\frac{x}{D} = 2$ and then the deficit starts to decrease slowly. This way it is possible to distinguish between what can be called near and far wake. None of wake models is able to model such evolution.

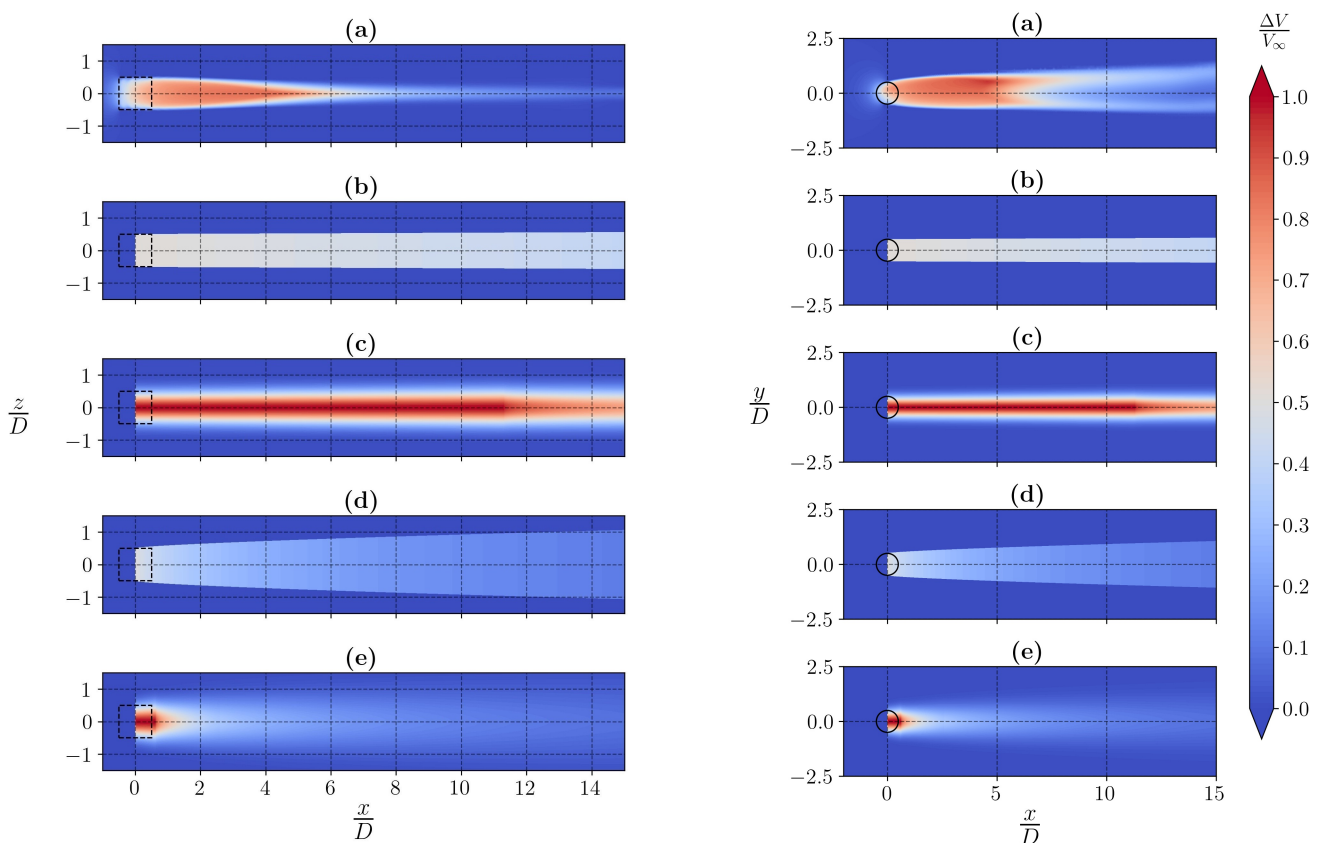


Figure 7.7: Overview of velocity deficit and wake's expansion for medium Reynolds' number case along $x - z$ plane for $y = 0$ (left) and $x - y$ plane at mid-span (right) for (a) AL + URANS simulation (b) NOJ, (c) BPA, (d) NOJ-N and (e) BPA-N wake models

7.1.2. Comparison for medium Re case

The comparison for the medium Reynolds' number case is based on the parameters listed in Table (4.4) and (4.17). Considering Figure (7.7) an overview of the flow field can be presented. Starting from Left Figure (7.7), a deficit higher than low Reynolds' number case is observed. This can be related to the higher TSR experienced, as discussed in Section (2.2.3.4) [18, 36, 90], that leads to higher momentum extraction. So the 'red-region' is extended and more intense. As for the low Re case, the wake tends to shrink along spanwise direction and not to expand. This behaviour can be related to the fact that maximum deficit is not located at $\frac{y}{D} = 0$ but because of CVPs action is shifted towards windward region: as observed in Section (2.2.3.3) high TSRs means both weaker asymmetry and stronger CVPs. The latter however promote deflection because of the side flows induced so the net resultant effect needs to be considered [36, 78, 90]. Advection and mixing due to CVPs lead to stronger wake recovery at wake's core, while the edges of the wake are shielded by outer flow, surviving far downstream. For this reason, because maximum deficit is not located at $\frac{y}{D} = 0$, wake shrinks along spanwise direction.

Considering the crossflow direction in Right Figure (7.7) the asymmetry shown by the wake is clearly weaker than previous case, but still largely present because of the small scale and low I . Moving downstream the previous statement is even more clear: the edges of the wake persist up to $x = 15D$ with a limited deficit, while wake's core has almost totally recovered.

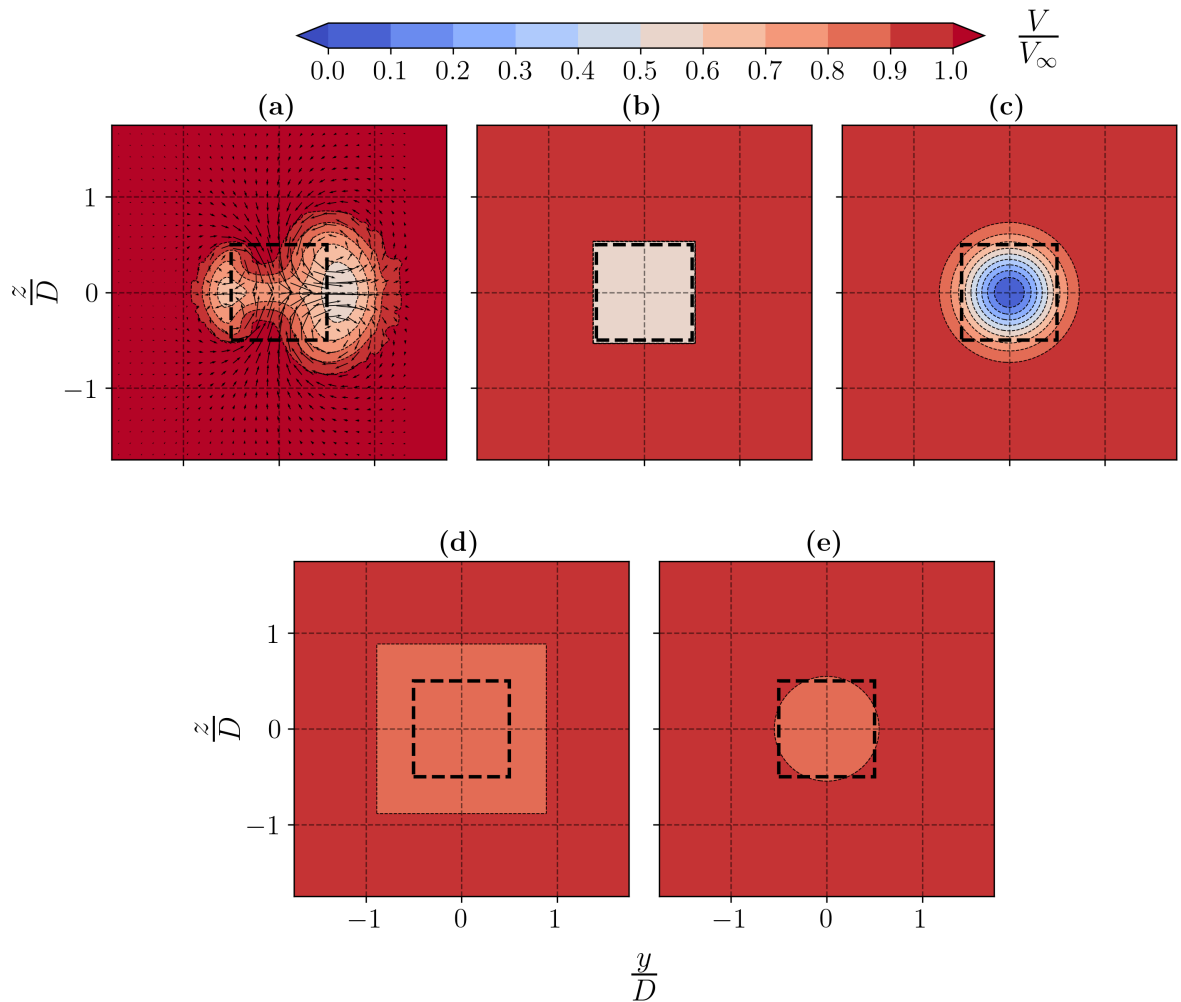


Figure 7.8: Mean streamwise velocity contours and in-plane velocity vector normalized by the incoming wind speed at cross section $x = 9D$ for (a) AL + URANS simulation, (b) NOJ, (c) BPA, (d) NOJ-N and (e) BPA-N wake models for medium Re case

At a first look results from analytical wake models cannot be considered accurate along both directions.

As for low Re case, the BPA model passes the onset point late in the wake, because of the low turbulence intensity experienced. Therefore is only able to model a wide region that features a constant deficit value. BPA-N model overpredicts the recovery rate dissipating too early the wake along both crossflow and spanwise directions, as already seen before. Top-hat models are able to replicate wake's width evolution along crossflow direction qualitatively well. Especially NOJ-N seems the only model to provide results similar to numerical ones in the far wake.

Investigating the mean streamwise velocity contours reported in Figure (7.8), the influence of the CVPs discussed before is evident. Being stronger at windward side it promotes strong advection fluxes that mix the wake enabling a faster recovery at wake's centre. For this reason the wake at $\frac{y}{D} = 0$ tends to shrink. At the same time, these strong vortices shift wake's centre which is shielded and persist moving downstream. In high I and Re conditions, CVPs are dissipated earlier but for the special conditions of current case, this does not occur (as for low Re case).

Analytical models are not able to replicate a similar phenomena, neither its influence on wake recovery through advection. Therefore wake's shape remains the same and expands vertically, something that is observed only in the shielded region. However, at the same time, the deflection experienced means that (as for previous case) the velocity profiles reported for $\frac{y}{D} = 0$ at the symmetry plan are not located at real wake's centre position. So the profiles do not consider the effective velocity profiles along wake's center but velocity profiles along a geometric symmetry plan. For a more detailed review it is necessary to consider velocity profiles, in order to fully understand also the consequences of deflection.

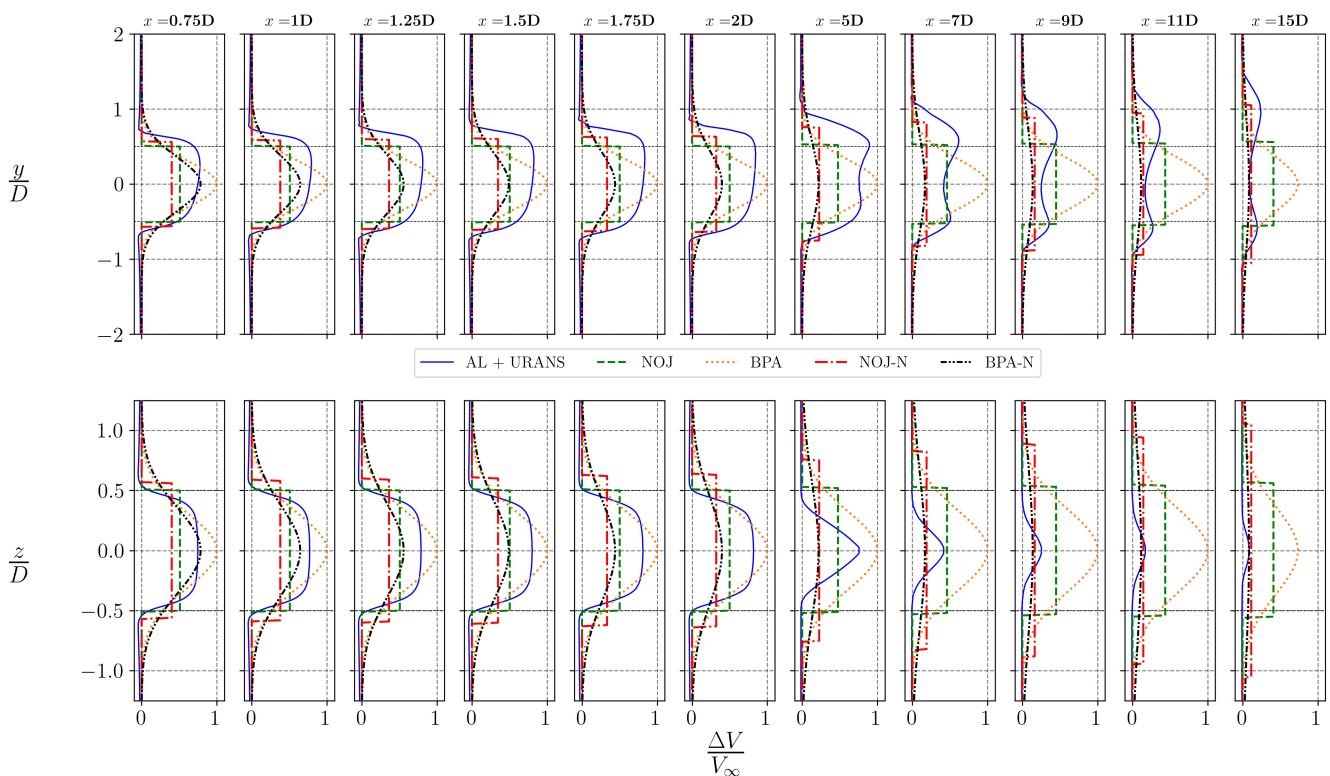


Figure 7.9: Profiles of mean streamwise velocity deficit along crossflow direction at mid-span (top) and spanwise direction for $y = 0$ (bottom) for different downstream sections, comparison between data from different analytical models and numerical simulation in medium Re condition

The focus is now on velocity profiles in Top Figure (7.9). Before reviewing wake models performances, it is important to notice in the near wake from $x = 0.75D$ to $x = 2D$ the wake expansion depicted by numerical data. The shape is the same at each section but it is developing, the maximum deficit increases and the

recovery process has not started yet. A similar delay is experienced because of the reduced environmental turbulence intensity which is overwhelmed by wake's expansion. A slight but significant asymmetry is observed at these sections, but not as strong as the low Reynolds case reported in Figure (7.3). Moving downstream, wake's shape seems to be deformed by CVPs action, with wake centre apparently shrunk and with two different peaks that resemble a bimodal distribution. The reality, as already mentioned, is that wake's center is no more located at $\frac{y}{D} = 0$ but is shifted towards positive y . This behaviour is related to low turbulence and low Reynolds number experienced that makes possible for the wake to be deformed by vortices and to evolve undisturbed up to the far wake without observing merging phenomena at wake's edges where CVPs remain intact and are not dissipated. At the same time wake centre shows a faster recovery, thanks to the flow averted by vortices and allowing wake shrinking along spanwise direction. This was a predictable behavior after observing the wake's shape reported in Figure (7.8) and especially the vortices, as we saw in Figure (7.3). Consequently, the velocity profiles reported in Bottom Figure (7.9) are not obtained considering the wake's centre position and subsequently the wake observed does not expand in the far wake, but tends to shrink. With reference to Top Figure (7.9), as expectable, wake models struggle in replicating with high fidelity numerical data in similar conditions. Their inability to replicate asymmetry (and its consequences) was already assessed in previous case, but it is a limitation that must not be disregarded. In fact it could be considered the core of the differences between the wake of a HAWT and the one of a VAWT. The most accurate values are provided by BPA-N model for $x = 0.75D$ but its level of accuracy quickly drops moving downstream, since wake recovery is overestimated. As for low Re case, the values obtained for the far wake from $x = 11D$ are similar to values at wake's core in the numerical case. The same trend was already observed in the low Re case. However, the agreement observed is due to wake deflection only, otherwise, numerical data would be higher. BPA model suffers the onset-point problem even here, not being valid here since it is still considered near wake region by the model itself. As for the previous case, this behaviour is related to the low I and Re values. Even if the value predicted by BPA model can be considered similar to the correct one in the near wake, they do not have any physical meaning. NOJ model largely underestimates the deficit value, from $x = 0.75D$ to $x = 7D$.

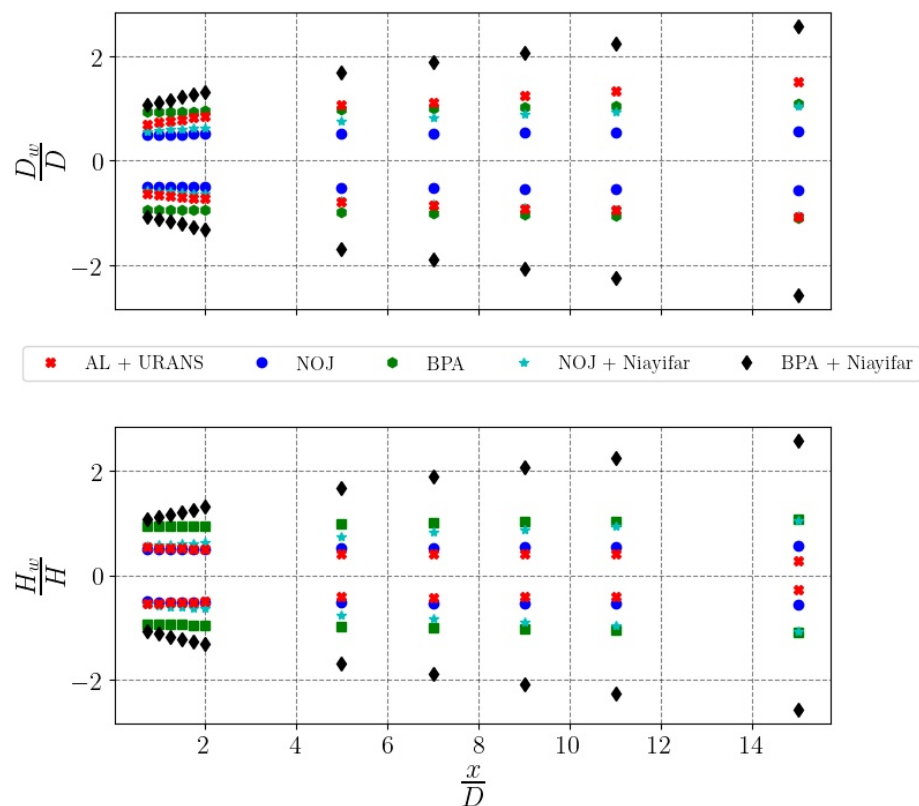


Figure 7.10: Comparison of wake width calculated with numerical simulations and analytical models along crossflow direction (top) and spanwise direction at mid-span (bottom) in medium Re conditions

At these locations, NOJ model provides almost the same maximum deficit, but with erroneous predictions in the far wake. Probably, without wake deflection the values would have been extremely similar. However this is an aspect that can be studied afterwards using mean values. NOJ-N model, overestimates the wake decay up to $x = 9D$, from that point on it provides good agreement with numerical data and almost the same maximum value. However, the warning mentioned before for BPA-N model has relevance even here. The accuracy observed along spanwise direction changes drastically when the effects of massive wake's deflection are triggered (from $x = 5D$ on). No relevant difference are observed compared to spanwise profiles. Even here BPA-N model provides good results at $x = 0.75D$ and then far downstream. The same previous fate waits for the NOJ-N model, that displays good agreement only in the far wake, thanks to the augmented recovery due to CVPs advection. Models based on Abkar's law display poor agreement with numerical data. This could be related to their slower recovery rate compared to models based on Niayifar's law, which feature a specific equation for k^* , k_w even in low turbulence cases. But as far as observed, it cannot be considered reliable.

The asymmetric expansion of the wake along crossflow direction can be observed also in Top Figure (7.10), where $\frac{D_w}{D}$ shows higher values at windward side. Even if the shape of the wake resulting from numerical simulation is totally different compared to results from wake models, the total area covered is similar to the one calculated by NOJ, BPA, and NOJ-N wake models. This is valid also when considering the wake at leeward side, with more accuracy shown by wake models since weaker deflection is experienced here. Moreover, even in this case, wake's expansion can be considered linear if the region spacing from $x = 0.75D$ to $x = 2D$ is not considered. Here it displays a non-linear development.

Wake's extensions along spanwise direction in Bottom Figure (7.10) reveals the decrease in numerical values experienced due to wake shrinking. All the models are not capable of replicating wake contraction, therefore they provide different trends as well as absolute values. However in the near wake, top-hat models reveal good agreement in terms of absolute value predicted, while the only NOJ model is still reliable in the far wake, with limited deviation. Even if the slope is negative, the wake stills develops linearly.

In order to make a more fair comparison, in Figure (7.11) the maximum velocity deficit as well as the mean velocity deficit along crossflow direction at mid-span are reported. This way, even if the wake centre is deflected towards windward side, it is still possible to compare the velocity value there with the ones provided by wake models.

As shown in Top Figure (7.11) and Left Figure (7.12) low agreement is observed in the maximum velocity deficit with an average deviation of 30-40% when considering Gaussian models. The differences are mainly due to wake models inability in replicating the recovery in such low Reynolds' number condition properly. A certain portion of downstream length is spotted. Here the wake is still evolving and has not reached the maximum value yet, located at $x = 5D$, in agreement to what was observed in Figure (7.9). After $x = 5D$, wake starts to recovery. The trend observed with a first region of development and a second one where the wake recovers, cannot be replicated by wake models, as already seen in the low Re case. They can model wake recovery only.

The mean value extracted from numerical simulation shown in Bottom Figure (7.11) follows the same trend of increase-decrease but with the maximum mean value achieved earlier, at $x = 2.5D$. Such difference can be explained by the fact that the wake starts to assume a deformed shape, with the maximum value related to the peak at windward side, while the core of the wake starts to shrink, decreasing the mean value. With reference to the error bars in Right Figure (7.12), a considerable deviation is observed for all the models in the region from $x = 0.75D$ to $x = 5D$. The average value spaces from 40 to 60% with peaks of 80%. NOJ model is the only model that shows a relative limited deviation, always below 25%. The trend is reversed in the far wake: NOJ-N and BPA-N models show a constant decrease in the deviation, while NOJ model reaches values up to 40%. Also the deviation observed for the BPA model is limited.

However data need to be evaluated in a context: model based on Niayifar's law overestimate the recovery rate. The agreement demonstrated with numerical data do not have to mislead the reader, since it is mainly related to the augmented recovery due to CVPs. Otherwise the accuracy displayed would have been much different.

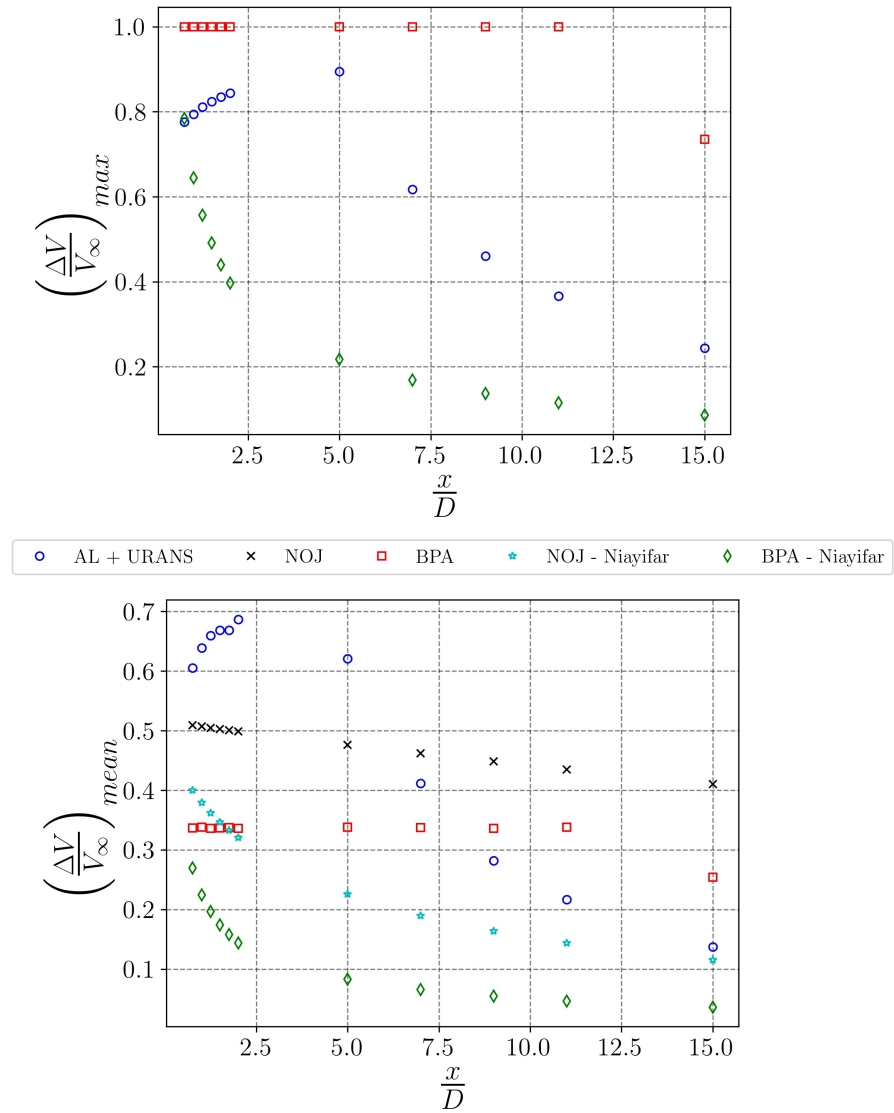


Figure 7.11: Comparison of the maximum velocity deficit (top) and the mean velocity deficit (bottom) calculated by the numerical simulation and wake models along crossflow direction at mid-span in medium Re conditions

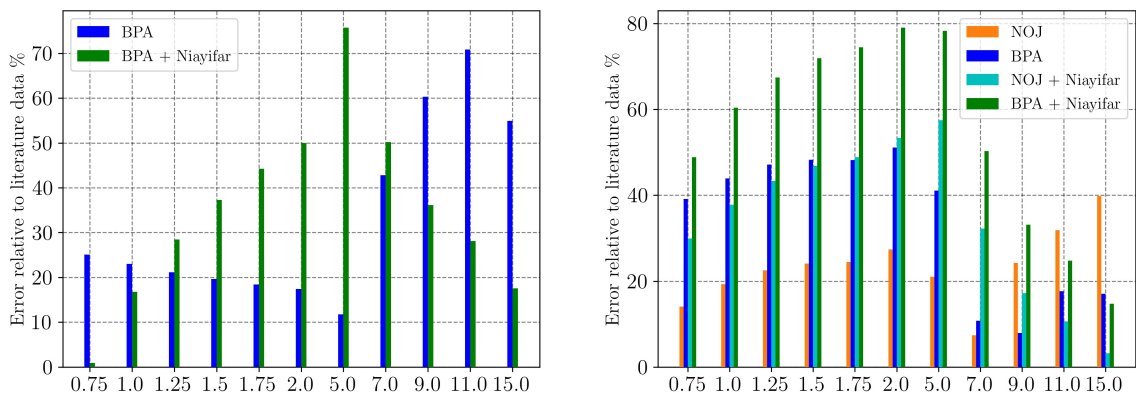


Figure 7.12: Deviation in the maximum velocity deficit (left) and in the mean velocity deficit (right) for different wake models. The errors are based on the data evaluated along crossflow direction at mid-span for medium Re case using the maximum value as reference for the error.

7.1.3. Comparison for high Re case

The last case analysed is the high Reynolds number case, tested according to the parameters reported in Table (4.6) and (4.17). Starting the analysis with the overview in Figure (7.13), a considerable improvement compared to previous cases is observed. Here, since a large scale turbine is considered, as well as high turbulence intensity, wake models are able to work in their optimum conditions.

Considering the deficit map along $x-z$ plan in Left Figure (7.13), wake does not display the shrinking effect observed before and constantly expands towards downstream region. The dimensions reached are far wider than previous case and this could be related to AR's effect. As discussed in Section (2.2.3.4), higher ARs means wider wakes along spanwise direction [2, 3, 97]. With reference to Right Figure (7.13) no lateral displacement of wake's centre is observed because of the high TSR, Re and I experienced. In fact the lateral force exerted by the blades is less intense [36], leading to weaker deflection. At the same time, inertial forces are stronger, dissipating all the vortical structures generated by the blades quickly. Therefore, even if present, CVPs would be weak and not able to allow mixing effect. I , even if displays lower relevance than advection [13, 89], plays a significant role in wake recovery. The higher its value, the faster deficit decreases [68].

In this case, wake models display a qualitative excellent agreement with numerical data, replicating wake's main features (width and deficit) reasonably well. Only the BPA-N model seems to overestimate the recovery, even in this case, but, overall, a considerable agreement is observed. A conclusion can be already drawn: analytical models display a considerable improvement compared to previous cases.

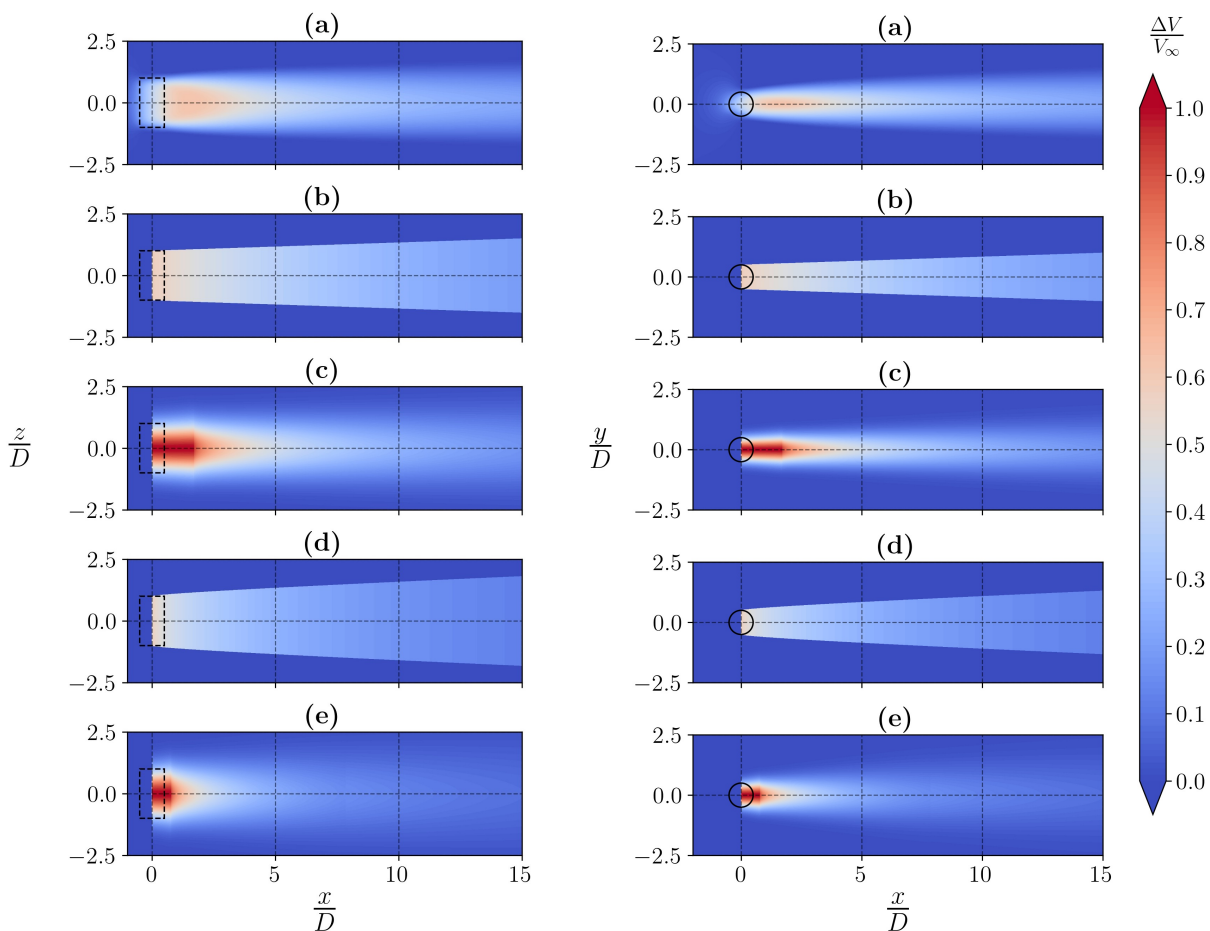


Figure 7.13: Overview of velocity deficit and wake's expansion for high Reynolds' number case along $x-z$ plane for $y=0$ (left) and $x-y$ plane at mid-span (right) for (a) AL + URANS simulation (b) NOJ, (c) BPA, (d) NOJ-N and (e) BPA-N wake models

Figure (7.14) reveals for the first time a significant agreement between both the shape as well as the velocity values predicted by models and numerical simulations. The actuator line model supported by URANS still points out the presence of CVPs that, unlike previous cases are extremely weak (the scale used is the same for

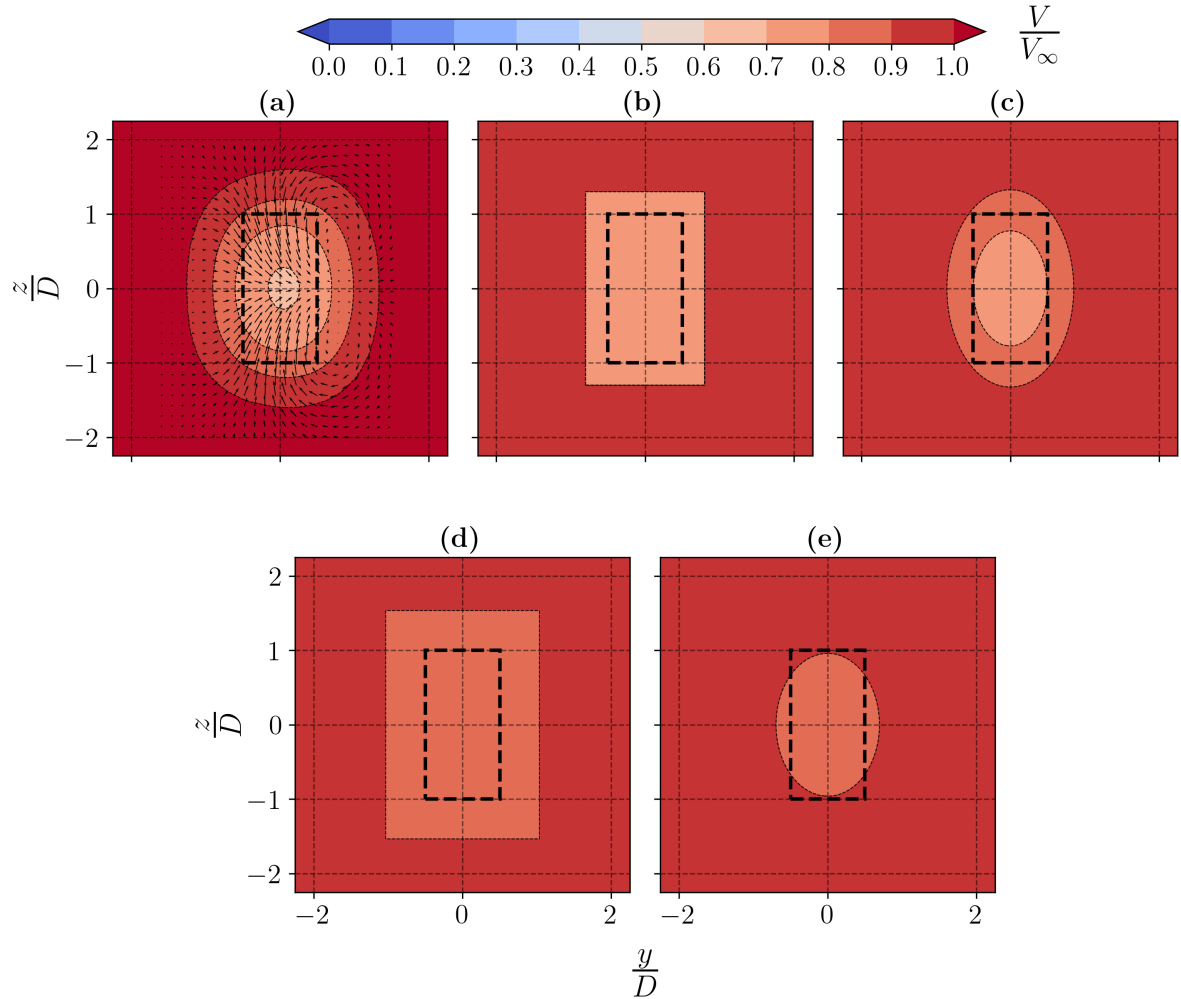


Figure 7.14: Mean streamwise velocity contours and in-plane velocity vector normalized by the incoming wind speed at cross section $x = 9D$ for (a) AL + URANS simulation, (b) NOJ, (c) BPA, (d) NOJ-N and (e) BPA-N wake models for high Re case

all the three cases analysed up to now). Another relevant result is that the wake can be considered symmetric, with a circular shape not affected by the AR in the far wake, as already mentioned in [97]. Top-hat models provide a good results in term of wake width and deficit calculated, while BPA-N aw is the only model to display poor accuracy in wake's width estimation. The standard BPA model displays why it is considered the most accurate, demonstrating excellent agreement with numerical data. Mean streamwise velocity profiles will now be considered and studied.

With reference to Figure (7.15), mean streamwise velocity profiles are considered. Starting from the Top Figure (7.15) no deflection is demonstrated by numerical data, with the maximum deficit located just at $\frac{y}{D}, \frac{z}{D} = 0$. The only relevant aspect is observed in Bottom Figure (7.15) the trapezoidal shape along span-wise direction for $x = 1D$, resulting from the AR effect [97].

Concerning the results from wake models, a considerable level of agreement between numerical and analytical results is displayed. Starting from the Top Figure (7.15) at $x = 1D$, discrepancies are observed for the BPA model because of the usual onset point problem. However the wake's shape from numerical simulation is extremely similar to the Gaussian one. Moving downstream the discrepancies decrease more and more and starting from $x = 5D$, BPA model totally overlaps the numerical values. The accuracy remains almost the same even further downstream, even if the BPA slightly underpredicts the maximum deficit. As for previous cases, BPA-N model displays good agreement with numerical data in the near wake. However, moving downstream the accuracy dramatically decreases, revealing the main problem of Niayifar's law: it tends to over-predict the recovery rate. NOJ model provides value extremely similar to numerical ones along all the wake portion

investigated, providing a level of accuracy that could be compared with BPA model if the maximum deficit would be considered. Moving downstream, from $x = 3D$ high level agreement between BPA model and AL plus URANS data is observed. NOJ-N model outperforms BPA-N, providing values slightly higher.

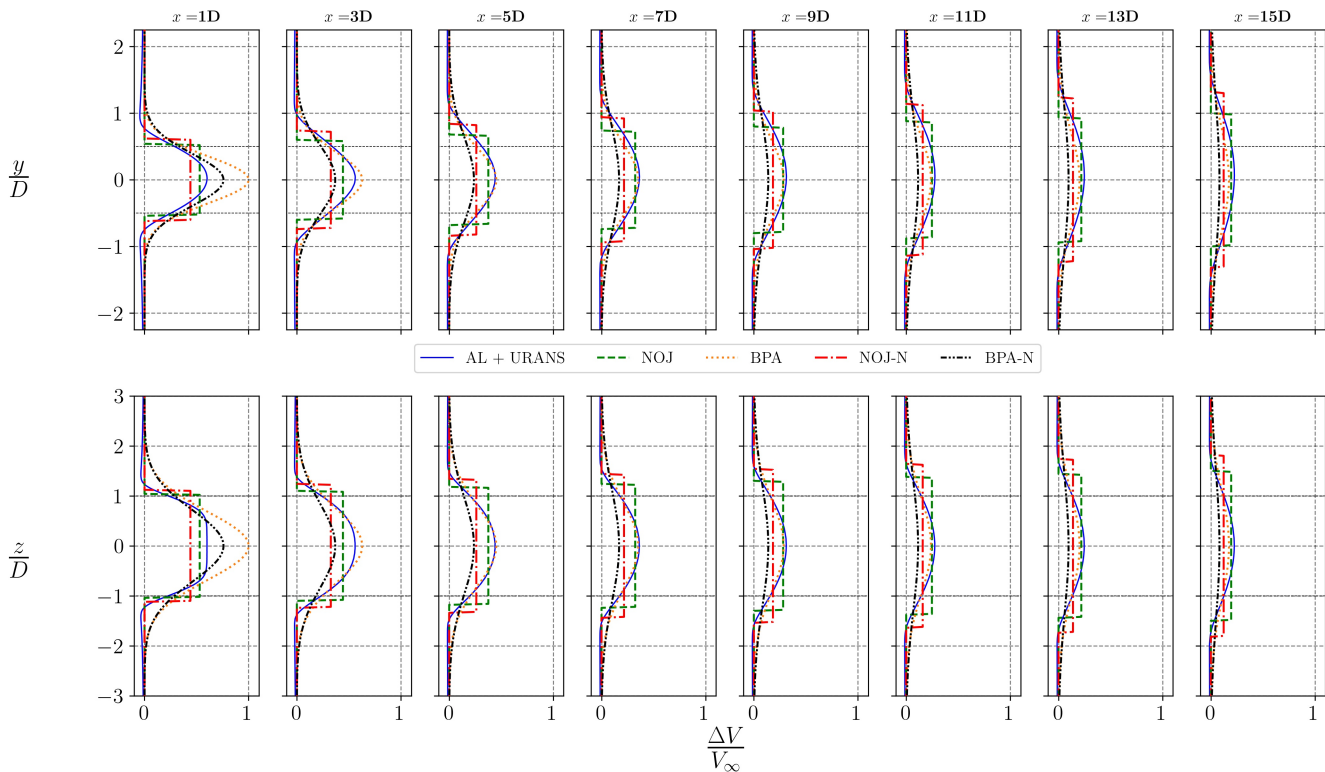


Figure 7.15: Profiles of mean streamwise velocity deficit along crossflow direction at mid-span (top) and spanwise direction for $y = 0$ (bottom) for different downstream sections, comparison between data from different analytical models and numerical simulation in high Re condition

Profiles of mean streamwise velocity deficit along spanwise direction reported in Bottom Figure (7.15) display almost the same trend observed along crossflow direction, but with some additional features. Considering the near wake at $x = 1D$, blades length leads to a rectangular shape for the wake, as mentioned before. This is caused by the AR value (equal to 2), similarly to what will be observed when comparing the predictions with literature data in Section (7.2.3). The effect experienced here is, by the way, not as strong and intense as will be observed afterwards. This may be related to the high Reynolds number used and the strong advection that tends to eliminate similar influences.

As already observed BPA model provides the highest accuracy among wake models, followed by the NOJ model. The latter however provides a wake shape for $x = 1D$ more similar to the real rectangular one. The same behaviour is displayed by NOJ-N model, while BPA-N suffers the same problems seen along crossflow direction.

With reference to Top Figure (7.16), wake's width along the horizontal plan constantly increases as pointed out by the data. Excluding the BPA-N model which tends to overestimate the amount of area covered by the deficit, BPA, NOJ and NOJ-N models all provides values similar to numerical data, especially the two latter. Even in this case, according to numerical data, the wake expands linearly as assumed in Chapter (3), slowly expanding. The same behaviour is observed at both leeward and windward side, since no deflection is experienced.

With reference to Bottom Figure (7.16) the same trend is observed along the vertical plan. In this case BPA model largely overestimates wake expansion, while top-hat models show considerable agreement (and even

overlapping) with numerical data. So in high Reynolds' and turbulence conditions, top-hat models are more reliable when it comes to evaluating wake's extension. In this case however, the reason could also be related to the higher AR introduced.

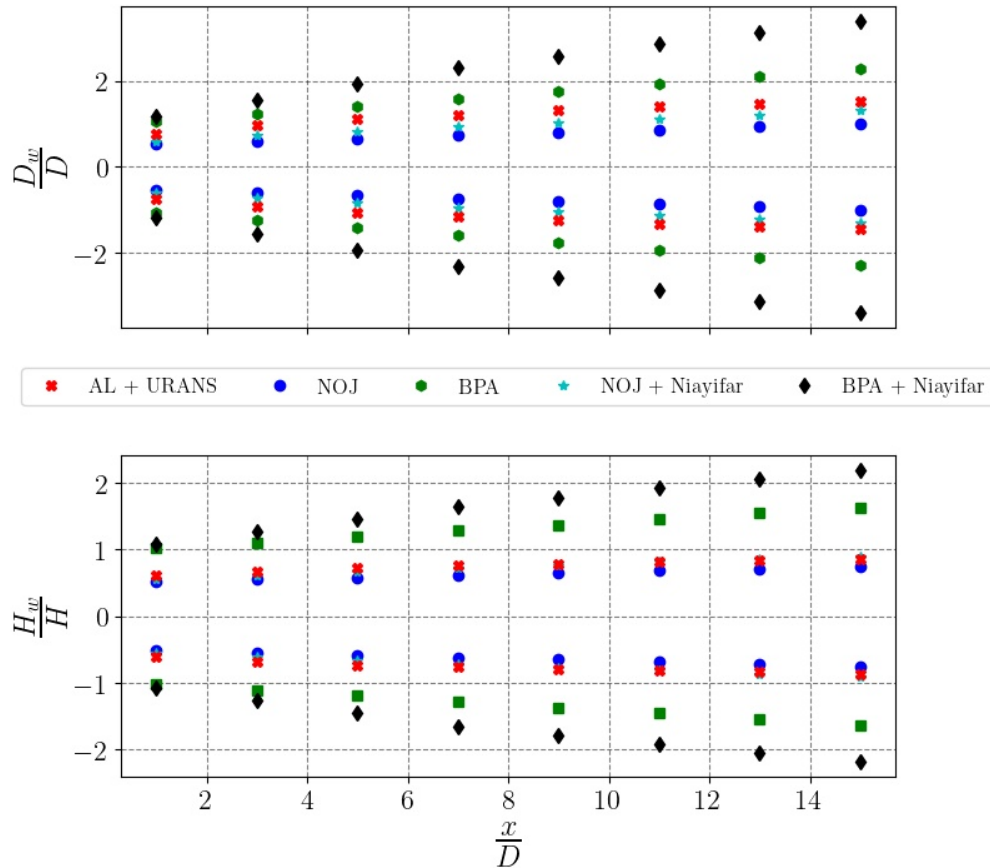


Figure 7.16: Comparison of wake width calculated with numerical simulations and analytical models along crossflow direction (top) and spanwise direction (bottom) at mid-span in high Re conditions

Observing Figure (7.17) and (7.18) additional reflections about models accuracy can be discussed. Starting from maximum deficit value the agreement shown by BPA model is considerable. The deviation, if the first value for $x = 1D$ is excluded, is always lower than 10%, reaching even a minimum of 2% for $x = 5D$. The same is not observed for the BPA-N model, that display an averaged 25% deviation. It seems that the three curves tend to a common value moving towards far wake and the values for BPA-N are shifted compared to the others. When it comes to evaluate the deficit value averaged along the whole wake, unexpectedly the NOJ-N high accuracy, with a averaged deviation (excluding the first section) of less than 5%. All the other models instead provide considerable discrepancies and deviation, but the error decreases moving far and far downstream.

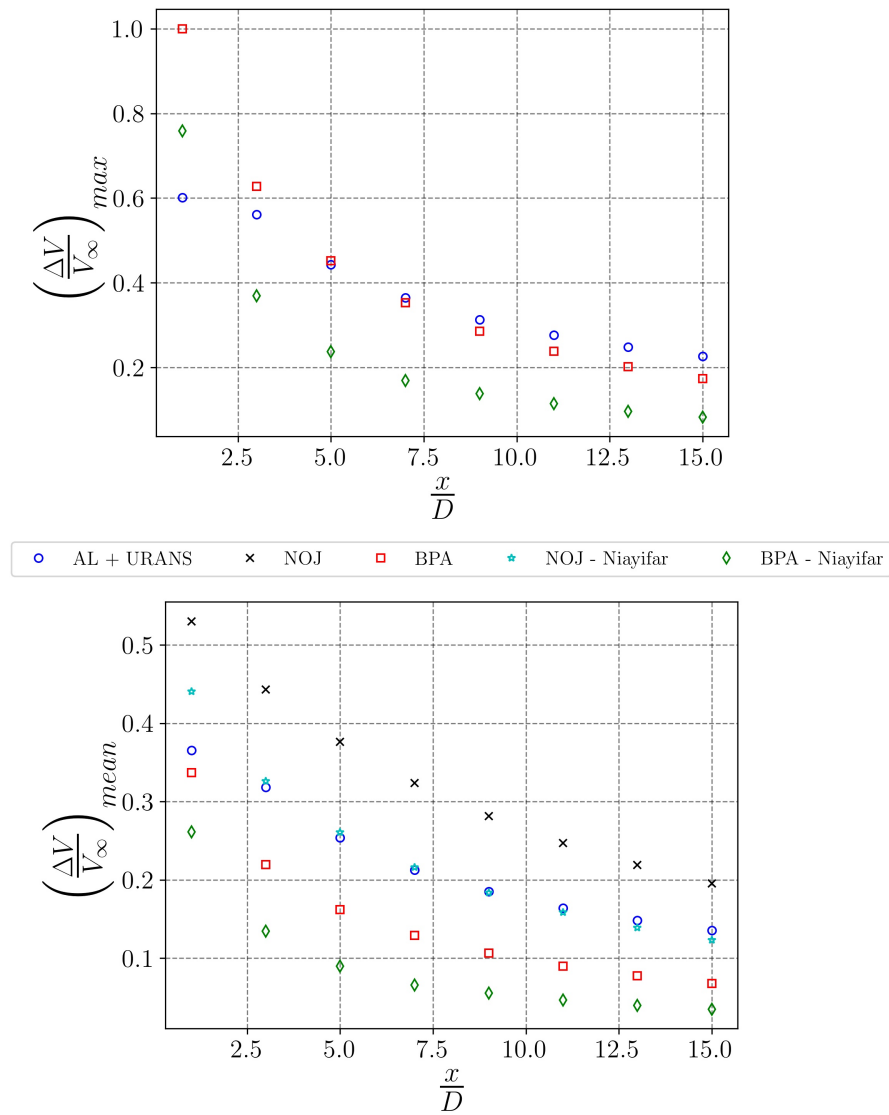


Figure 7.17: Comparison of the maximum velocity deficit (top) and the mean velocity deficit (bottom) along spanwise direction at mid-span calculated by the numerical simulation and wake models in high Re conditions

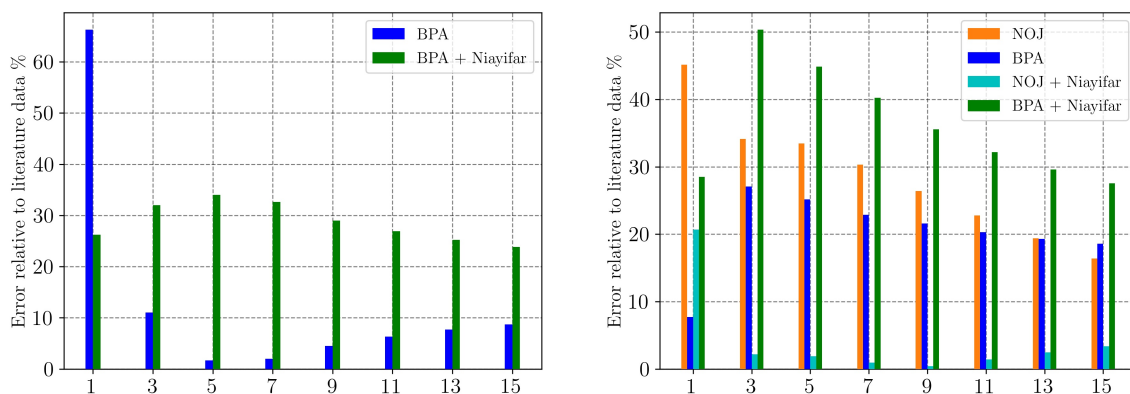


Figure 7.18: Deviation in the maximum velocity deficit (left) and in the mean velocity deficit (right) for different wake models. The errors are based on the data evaluated along crossflow direction at mid-span for high Re using the maximum value as reference for the error.

7.2. Comparison against literature data

As mentioned before in Chapter (4) the comparison is carried out for 3 different literature cases. Each one of them will be discussed separately.

7.2.1. Comparison with Abkar & Dabiri [3] - Thrust coefficient effects

The values used for this simulation are reported in Table (4.15). In this case how the effects of thrust coefficient variations influence the validity of wake models is analysed.

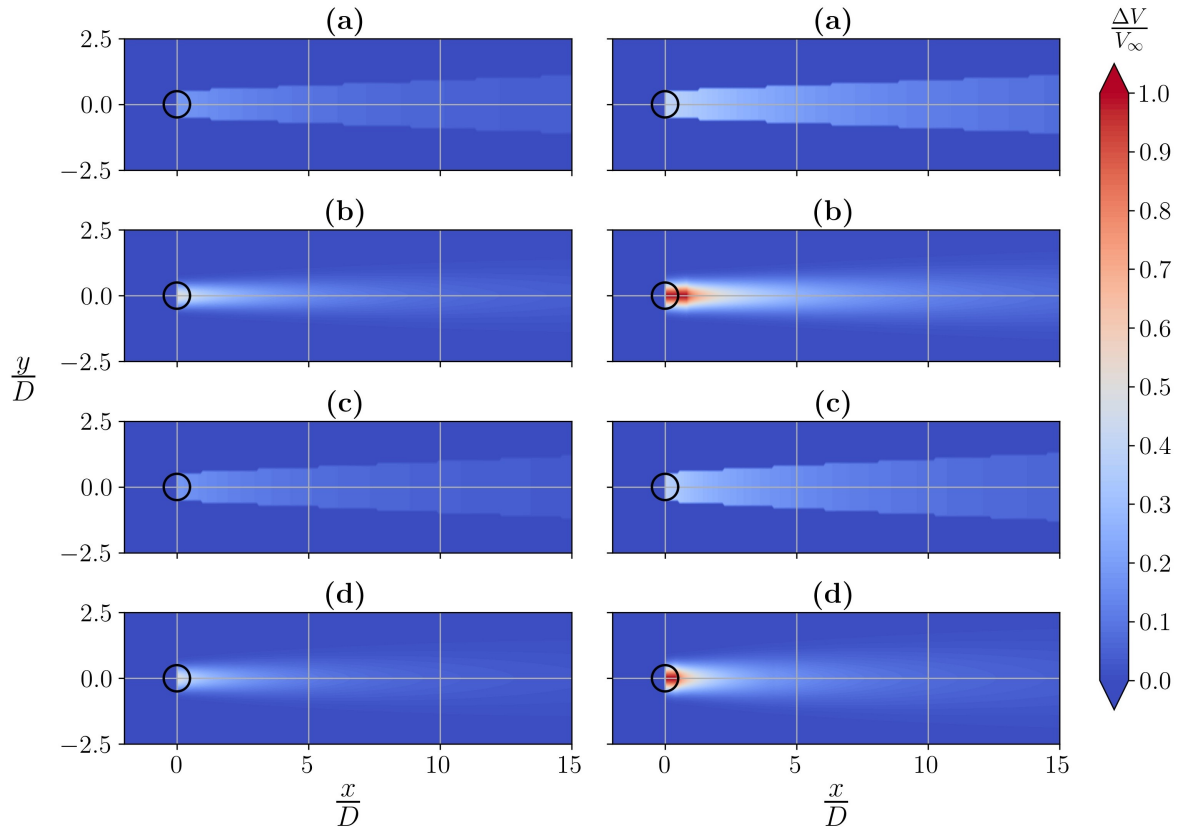


Figure 7.19: Overview of velocity deficit and wake's expansion at mid-span plane according to [3] for $C_T = 0.34$ (left) and $C_T = 0.64$ (right) for (a) NOJ, (b) BPA, (c) NOJ-N and (d) BPA-N wake models

An overview of how the wake develops in the two cases is reported in Figure (7.19). With reference to $C_T = 0.34$ case, the wake expands moving downstream and recovers up to the freestream value. The latter is reached at different locations depending on the model considered. Considering case $C_T = 0.64$, the deficit observed is higher (a certain amount of 'red regions' are observed in this case). Consequently the wake needs more space to recover up to the freestream value. In fact considering both NOJ and BPA models, if the thrust coefficient increases the deficit predicted by equation (3.139) and (3.148) increases because the numerator raises. On account of that the deficit is higher but at the same time thrust coefficient demonstrate zero influence on wake recovery as already seen in Section (3.2.1.3) and (3.2.2.3) [10, 11]. Therefore wake needs a wider space to recover. In fact for $C_T = 0.64$, the wake has not recovered totally yet in some cases. The zero influence displayed by thrust coefficient on wake's recovery is something not totally accurate, since experiencing higher thrust coefficients most of the times means higher TSRs that enhance CVPs' strength and their ability to improve wake's recovery, as mentioned in Chapter (2).

The recovery process obviously changes depending on the law used for the growth rate parameter. As observed in the first set of comparisons, Niayifar's law leads to lower values of recovery length with the wake that dissipate earlier the velocity deficit. This behaviour is observed for both NOJ-N and BPA-N model). At the same time the BPA-N distinguishes local turbulence intensity value, modifying subsequently the k^* . This

allows BPA-N model to overcome the problem observed for BPA model, limiting the size of the constant region where the model is not valid. However to analyse accurately the differences between the models, a comparison of velocity mean profiles is needed.

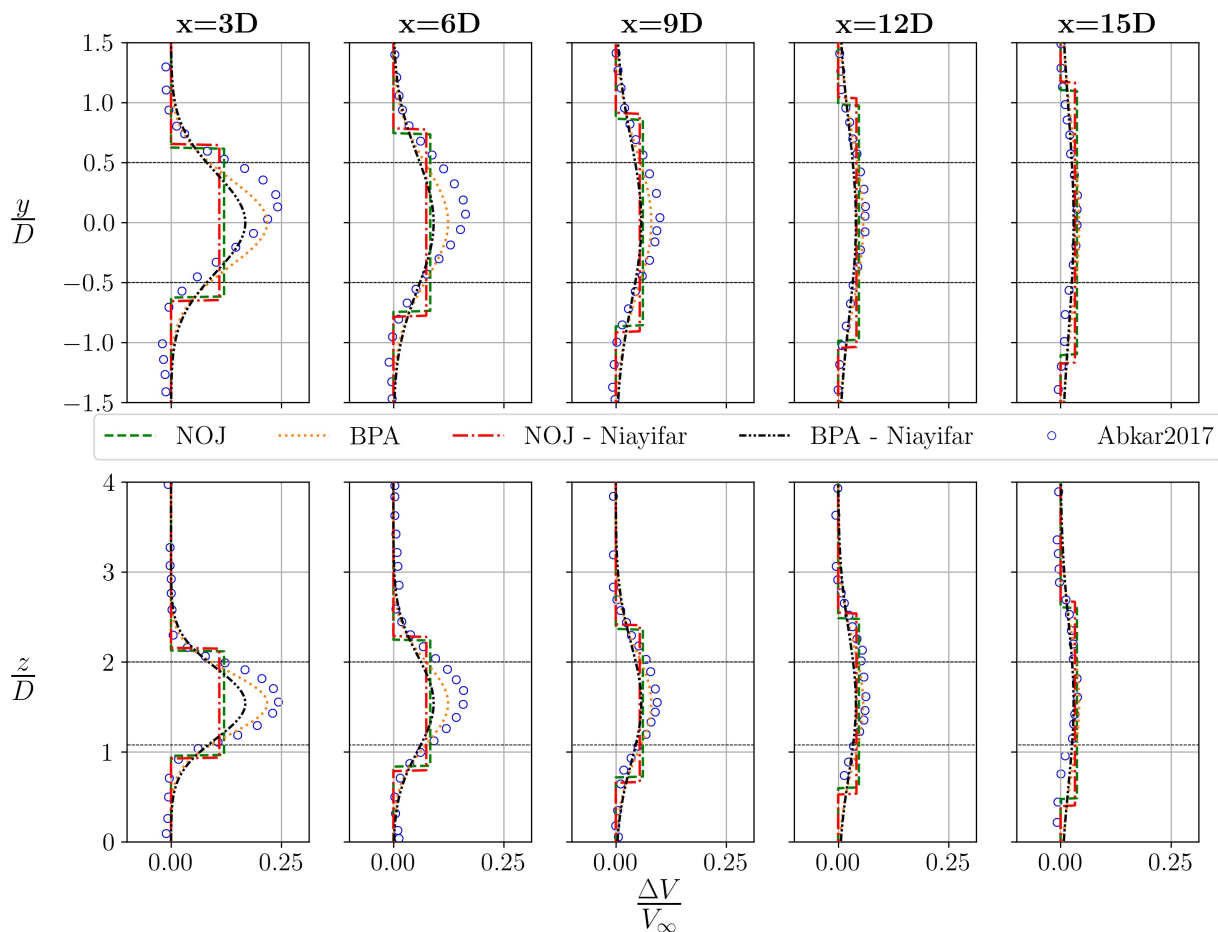


Figure 7.20: Mean streamwise velocity deficit profiles along crossflow direction at mid-span (top) and spanwise direction for $y = 0$ (bottom) for different downstream sections for $C_T = 0.34$, comparison between data from different analytical models and literature data from [3]

Considering the mean velocity profiles in Figure (7.20) some more accurate conclusions can be discussed. The velocity profiles along crossflow coordinate y reported in Top Figure (7.20) show different agreement with literature data depending on wake's region considered. For example for the largest discrepancies are at $x = 3D$ and $x = 6D$. Here wake models are not able to replicate wake's deflection towards positive y . At the same time real wake's width is overestimated at negative y : compared to analytical results the wake is shifted towards positive y , but displaying a slightly different shape.

BPA model performs provides the lowest deviation at $x = 3D$. A non-unitary value is observed for this model since the onset point has been already passed and the model has already entered the far wake region. Moving downstream towards the far wake ($x = 9D, 12D, 15D$) the accuracy displayed increase not only for BPA model but for all wake models: all the curves tend to collapse one another, providing almost the same results for maximum velocity deficit. better than the top-hat ones in predicting the maximum deficit, especially the ones that features Abkar's law for the wake decay constant. As mentioned before BPA-N model overestimates wake recovery, so the deficit decreases faster, but in the far wake the discrepancy is limited, as observed for the comparison with numerical simulations. The overall results in the far wake are not perfect since a minimal difference is observed at the edges of the wake in the far wake, but the accuracy displayed is considerable. Considering now the Bottom Figure (7.20) and the profiles along spanwise coordinate $\frac{z}{D}$, the level of agree-

ment shown in the near wake is higher: no deflection is experienced along this direction, so the shape predicted fits better numerical data than what was observed in previous case. However, the differences at the edges of the wake persist. They could be justified by two different aspects:

1. Turbulence activity is more intense at wake's edges [45, 78, 86] and especially at windward region, justifying the asymmetric shape along both crossflow and spanwise direction.
2. The inflow condition is a stratified boundary layer condition in the literature case. Therefore the inflow velocity is not uniform and the values at higher and lower $\frac{z}{D}$ are respectively higher and lower than mid-span's value.

BPA model displays from $x = 3D$ a significant agreement with literature data for both maximum deficit as well as wake's shape. Moving downstream data from the two cases still match, but from $x = 12D$ the overestimation provided by BPA model for the lower half of the spanwise domain is observed.

BPA-N model shows almost the same trend observed before with an overestimation of wake's width at $x = 3D$ coupled with the inability to replicate the slower recovery rate observed for literature data. As usual, the data provided in the far wake are in total agreement with literature ones. The same previous trend is observed for top-hat models.

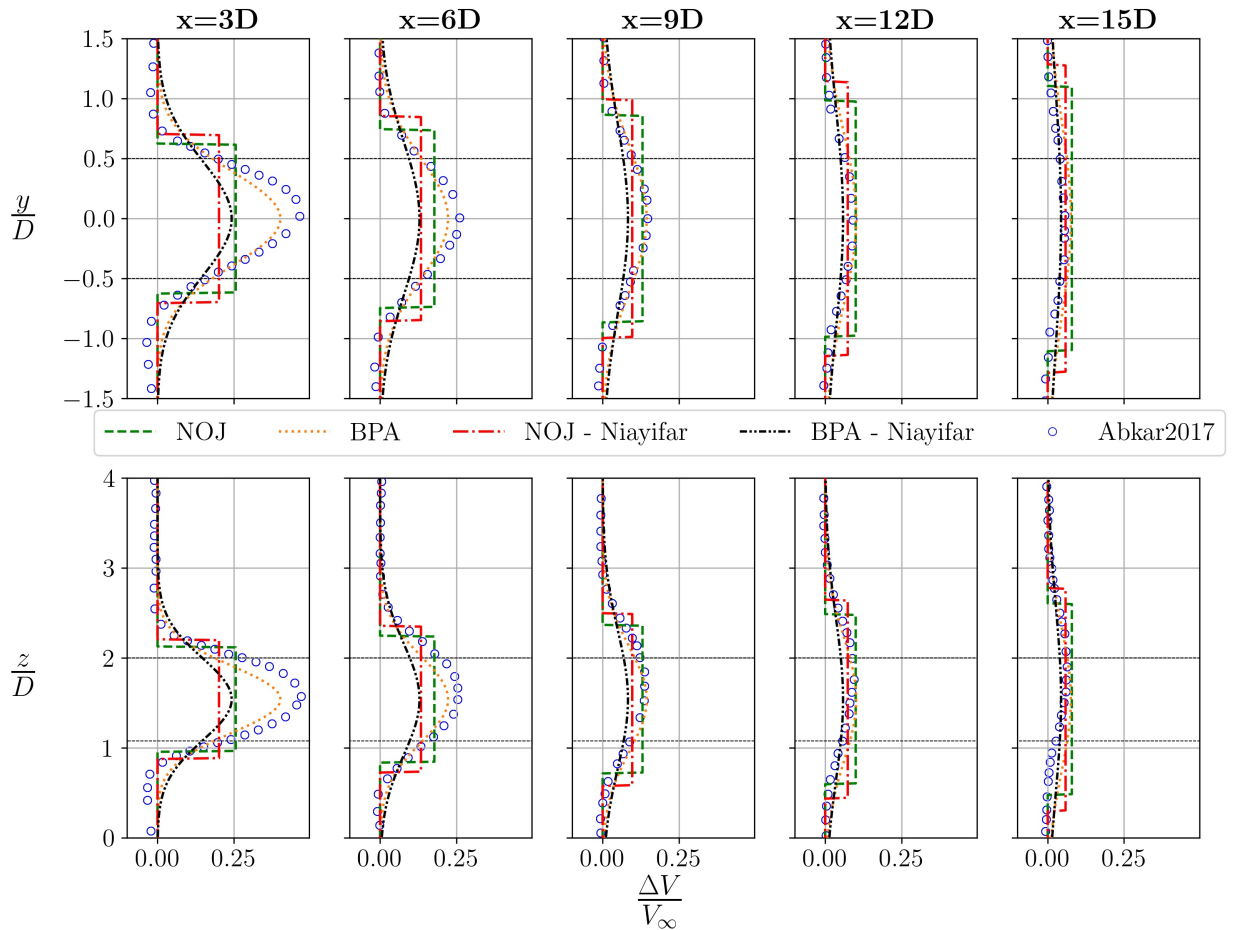


Figure 7.21: Mean streamwise velocity deficit profiles along crossflow direction at mid-span (top) and spanwise direction (bottom) for different downstream sections for $C_T = 0.64$, comparison between data from different analytical models and literature data from [3]

Overall the accuracy displayed along spanwise direction is considerable. Curves tend to collapse showing high level of agreement with literature data in the far wake. The latter however are slightly shifted towards higher z , so the maximum deficit is not located exactly at the mid-span, something observed when studying

wake's features in Chapter (2) but also related to the ABL inflow condition that analytical model cannot replicate.

Considering now the higher thrust coefficient case $C_T = 0.64$ reported in Figure (7.21), higher deficit are observed, in agreement with [18, 36, 90]. The deflection experienced by the wake is minimal compared to previous case because of higher TSR. This leads to considerable agreement with literature data since wake models for VAWTs are not able to replicate wake's asymmetry, as already mentioned when analysing the comparison with numerical simulations.

Starting from crossflow profiles in Top Figure (7.21), even in this case BPA models provides high accurate estimations along the whole domain. For $x = 12D$ and $x = 15D$ the values provided are slightly higher. This confirms that the recovery expressed by Abkar's law is more reliable than Niayifar's one, but its accuracy degrades when far wake is considered. The reason of this behaviour could be related to the fact that turbulence intensity in the wake is higher than ambient one. Therefore, since Abkar's law takes into consideration the freestream ambient turbulence only, it is unable to replicate the increased turbulence intensity. Subsequently the deficit recovers slowly. The problem experienced by Abkar's law coupled with the limitations of Niayifar's law shed light on the inability of existing relations for the wake decay constant.

As hinted, BPA-N model shows the usual limitations observed and already discussed in the cases.

NOJ model can challenge BPA model for the best level of accuracy demonstrated, especially in the region ranging from $6D$ to $15D$, even if the same underestimation of wake recovery is observed. NOJ-N displays the same trend of BPA-N model, but it shows the best agreement in the far wake, matching the maximum deficit value for $x = 15D$.

Wake's extension evaluated along crossflow direction suffers the same 'problems' at the edges seen for the previous case, showing no influence of thrust coefficient on this aspect. Overall wake models provide accurate results, even in this case curves tend to collapse, showing high agreement with literature data. At the same time, the model can be considered more valid than previous case since, without wake's deflection along crossflow direction, they are able to replicate wake's shape even in the near wake.

The trend observed along crossflow direction in Bottom Figure (7.21) is almost the same observed along spanwise direction. No deflection is experienced in the near wake, but (as happened for the previous case) far wake profiles show a certain degree of translation towards higher $\frac{z}{D}$, related to the ABL inflow condition.

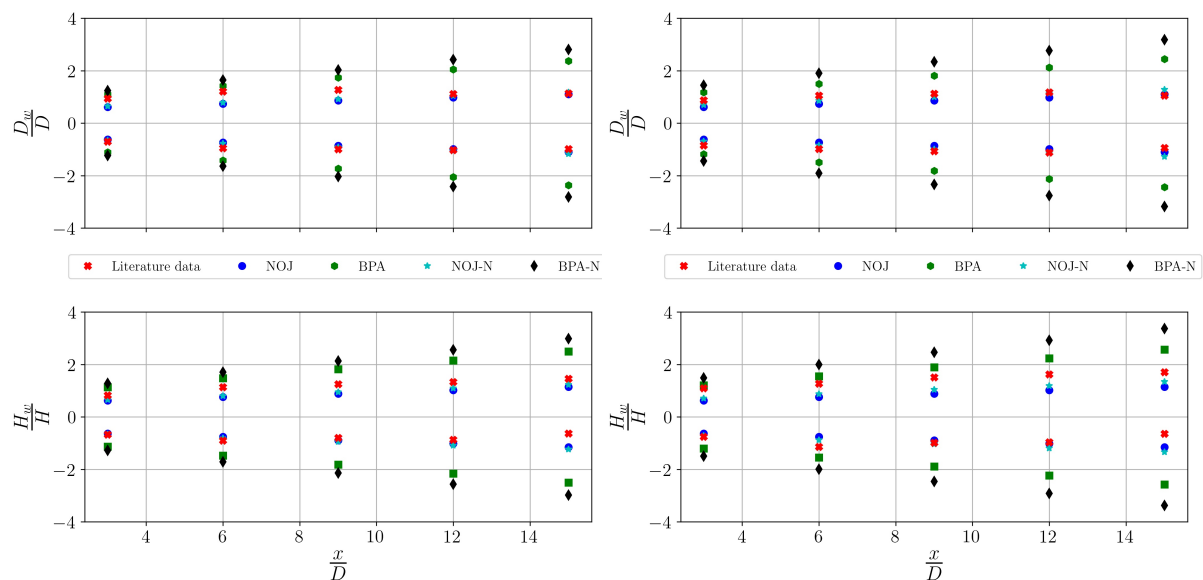


Figure 7.22: Evolution of the wake area along crossflow direction at mid-span (top) and spanwise direction at $y = 0$ (bottom) according to [3] for $C_T = 0.34$ (left) and $C_T = 0.64$ (right) for different wake models

Some additional details can be provided observing Figure (7.22) where wake's width evolution is reported. For the lower C_T case, the highest accuracy is displayed by top-hat models whose predictions overlap numerical data when predicting wake width along crossflow direction. The overlapping is observed along the entire

domain. Gaussian models display lower accuracy instead, overestimating the value in the far wake, but providing correct values in the near wake. Considering instead higher C_T , discrepancies with previous case are minimal and the same trend is observed. However Gaussian models tend to increase the value predicted when considering higher C_T , increasing their deviation from literature data. The same trend is observed along the spanwise dimension of the wake area, but no additional details are observed.

Considering the maximum deficit and the average velocity deficit along the wake in Figure (7.23) and the error bars in Figure (7.24) it is possible to compare in a more fair way literature data and wake models predictions. Starting from considering the maximum deficit reported in Top Figure (7.23) for both C_T , literature data trend is correctly replicated, especially in the far wake where BPA model displays a less than 5% deviation. Overall the accuracy shown by this model is high, considering the values obtained in Section (7.1.1) and (7.1.2). However it is crucial to point out also the significant difference between the literature data and the mean value elaborated by the BPA model at $x = 3D$. This happens because even if the onset point has been passed, the self-similarity hypothesis is not totally correct and the results obtained are affected by error. This is something that will be observed periodically in the current Chapter, pointing out the limitation of the BPA model which is considered the most accurate one. BPA-N model instead provides higher deviation values, ranging from 30 to 4% in the far wake where, as already mentioned, it matched numerical results.

In the higher C_T case displayed in Top Left Figure (7.23) and (7.24), the deviation for BPA model further decreases, with an average value lower than 5%. Also BPA-N model provides more accurate values, leading to the conclusion that the more C_T (and so TSR) raises, the more accuracy of wake models increases.

Considering mean values instead the situation is slightly different: overall the deviation experienced is below 20%, but increases with higher C_T contrary to what was observed for the maximum velocity deficit. BPA model outperforms the other wake models both at higher and lower C_T . However for the latter case, the deviation displayed is higher.

NOJ model instead shows the highest average deviation at both C_T (13.8% and 18.8%). Its counterpart, the NOJ-N model, provides better results with average deviation of 11% and 10%. The same results when comparing the two top-hat models will be observed in many of the following cases analysed, leading to some important conclusions about the NOJ and NOJ-N models.

BPA-N model can be displays large deviations up to $x = 6D$ but in a decreasing trend. Therefore when reaching the far wake region, the averaged deviation is nearly 8% for both lower and higher C_T case. This testifies the accuracy provided by this model when far wake is considered.

Overall the trend observed in Figure (7.23) is almost the same for all the models analysed. The curves seem to be just translated vertically.

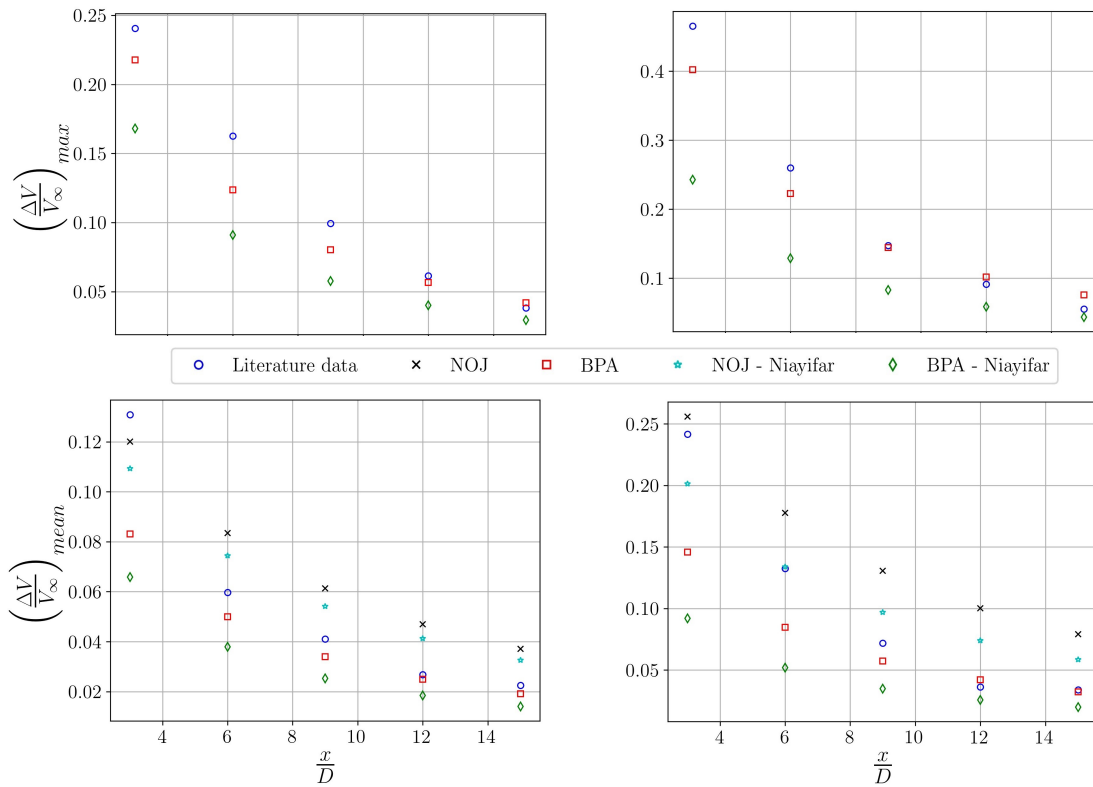


Figure 7.23: Evolution of the maximum deficit value (top) and the mean velocity value (bottom) along spanwise direction at mid-span according to [3] for $C_T = 0.34$ (left) and $C_T = 0.64$ (right) for different wake models

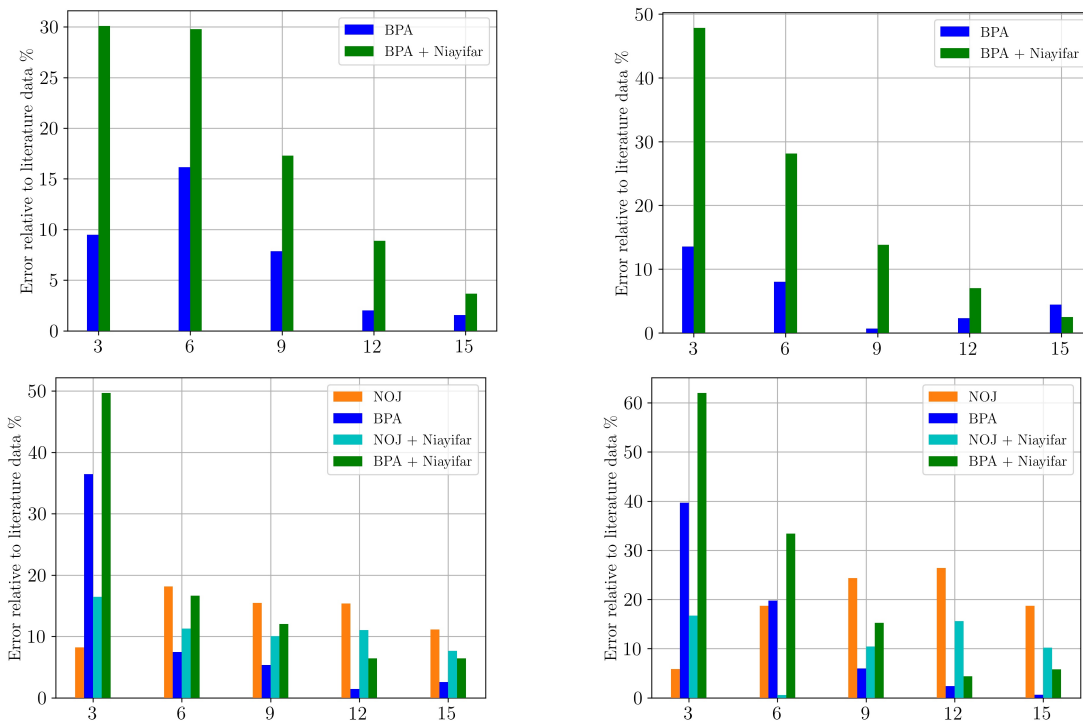


Figure 7.24: Deviation in the maximum velocity deficit (top) and in the mean velocity deficit (bottom) compared to data from [3] for $C_T = 0.34$ (left) and $C_T = 0.64$ (right) for different wake models. The errors are based on the data evaluated along crossflow direction at mid-span using the maximum value as reference for the error.

7.2.2. Comparison with Tescione et al. [110] - Low turbulence intensity effect

The comparison with the experimental study from Tescione et al. [110] allows to understand more about how wake models perform in the near wake and especially in low turbulence intensity conditions. With reference to the data reported in Table (4.15) and turbulence intensity set to 0.5% the analysis starts with focus on Figure (7.25). The results obtained using Abkar's law are extremely different with respect with the ones from

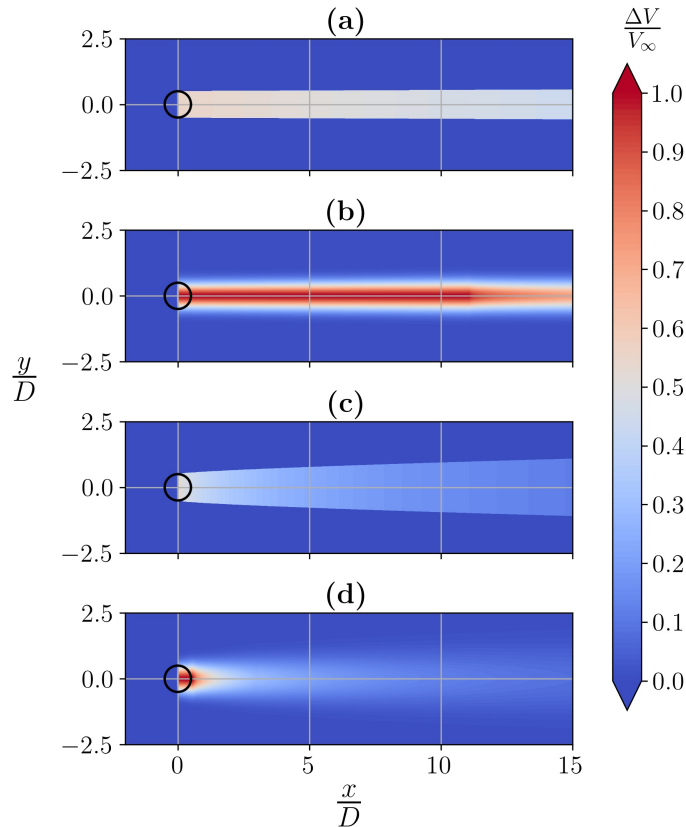


Figure 7.25: Overview of velocity deficit and wake's expansion at mid-span according to [110] for (a) NOJ, (b) BPA, (c) NOJ-N and (d) BPA-N wake models

Niyifar's law. They elaborate deficit much higher than the ones provided by NOJ-N and BPA-N models. Moreover a so-called red region is observed for BPA model, featuring a relevant extension. The reason of a similar development are the same discussed in Section (7.1.1) and (7.1.2) and are related to the onset-point problem. The low turbulence intensity has a relevant effect on the wake's width: the expansion experienced by the wake is extremely limited, with Case (a) and (b) that show almost the same dimensions for wakes. The latter display a straight expansion, without any sign of expansion along crossflow direction. The reason why predictions show so low accuracy lies behind the equations used for the wake decay constant in this case: such equations are valid only in high turbulent environment, something not experienced in this case.

Considering the results obtained with Niyifar's law, previous problem is not observed since the wake decay constant changes depending on the local turbulence intensity and does not show only a specific value, constant along the whole domain. The expansion for these models is described properly by the equation for k^* , k_w , even if it is not as strong as for Abkar's case [3]. At the same time, the high values of deficit (red-region) are limited to the extremely near wake and the downstream distance necessary for the recovery is shorter for case (d) than for (c): as already observed the BPA-N features a more intense recovery, while NOJ-N provides more realistic results. More considerations and specific details can be provided discussing about the velocity profiles.

The reader is now referred to Figure (7.26) where mean velocity profiles along both y and z direction are reported. As obvious, the whole comparison is focused on the near wake only, a region where wake models are not reliable. Starting from Top Figure Figure (7.26) the first relevant thing observed is that none of the

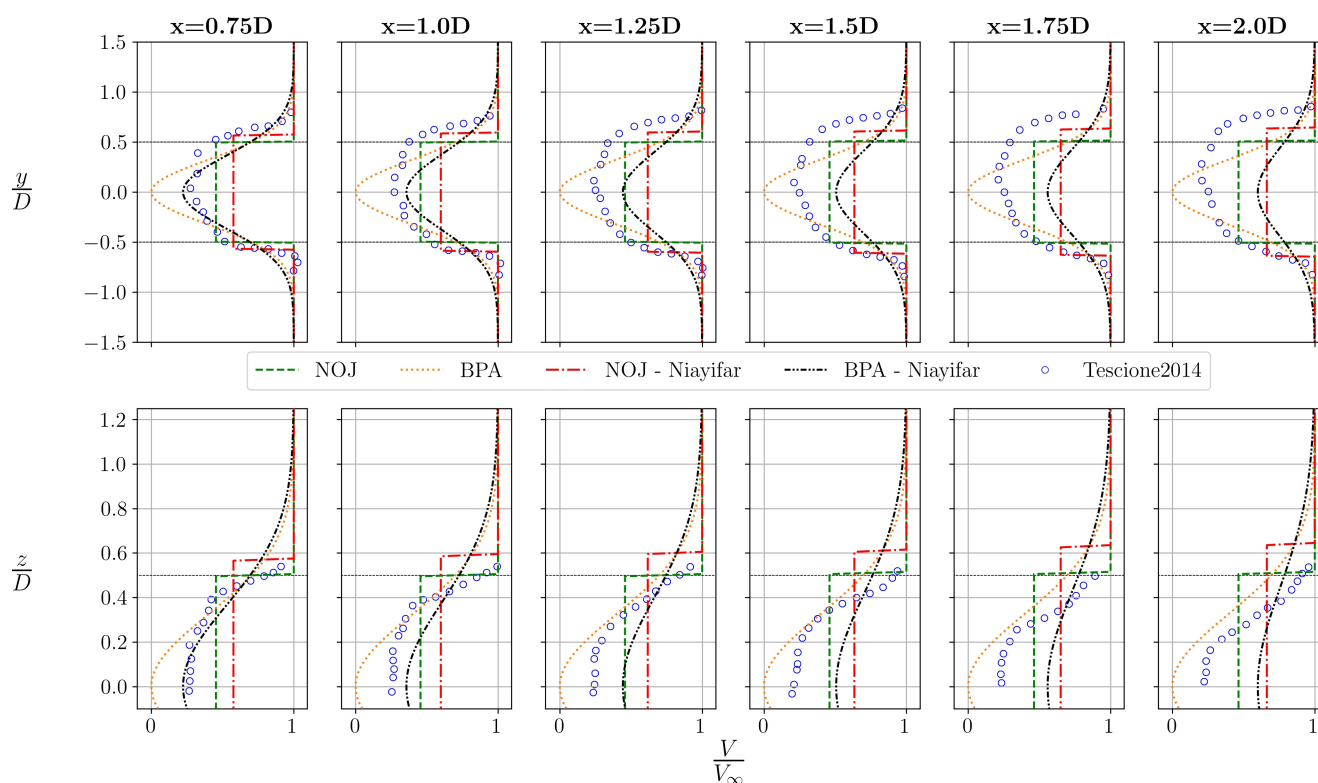


Figure 7.26: Profiles of mean streamwise velocity component along crossflow direction at mid-span (top) and spanwise direction (bottom) for different downstream sections, comparison between data from different analytical models and literature data from [3]

wake models used is capable of replicating the deflection experienced by the wake, as already seen. As consequence of the onset-point problem, BPA model provides the same results along the entire domain, overestimating the maximum deficit experienced but at the same time it provides the highest agreement with numerical data.

BPA-N provides instead reliable values at $x = 0.75D$ and $x = 1D$, but in the range from $x = 1D$ to $x = 2D$ the deficit is almost halved. The same fate is observed for NOJ-N model, which at least seems to provide a correct wake width. Probably, a specific tuning of the values in the far wake would overcome the problem.

The performances shown by NOJ model can be located between the previous models cited: it provides values higher than the ones from models based on Niayifar's law from $x = 1.25D$ but at the same time, lower than the ones from BPA model. As the NOJ-N, it is capable of replicating almost the same wake's shape. Such agreement however decreases moving further downstream.

However the global accuracy displayed is extremely poor and even wake's width is apparently affect by high error with the a substantial underestimation. But the latter aspect has been already investigated in Section (7.1.2) in Figure (7.10).

Moving to the profiles along spanwise direction in Bottom Figure (7.26), the following statement can be summarized:

- BPA-N model provides good agreement for $x = 0.75D, x = 1D$, while its accuracy decreases moving downstream.
- BPA model overestimates the values for all the sections analysed
- Top-hat models result in profiles whose shape visually the most resemble literature data

Since this case has been already analysed in Section (7.1.2), the reader is referred to Figure (7.10) to learn more about the wake width predictions. The image and the considerations were not reported here because it would have been redundant since the considerations would have been exactly the same, but only focused on

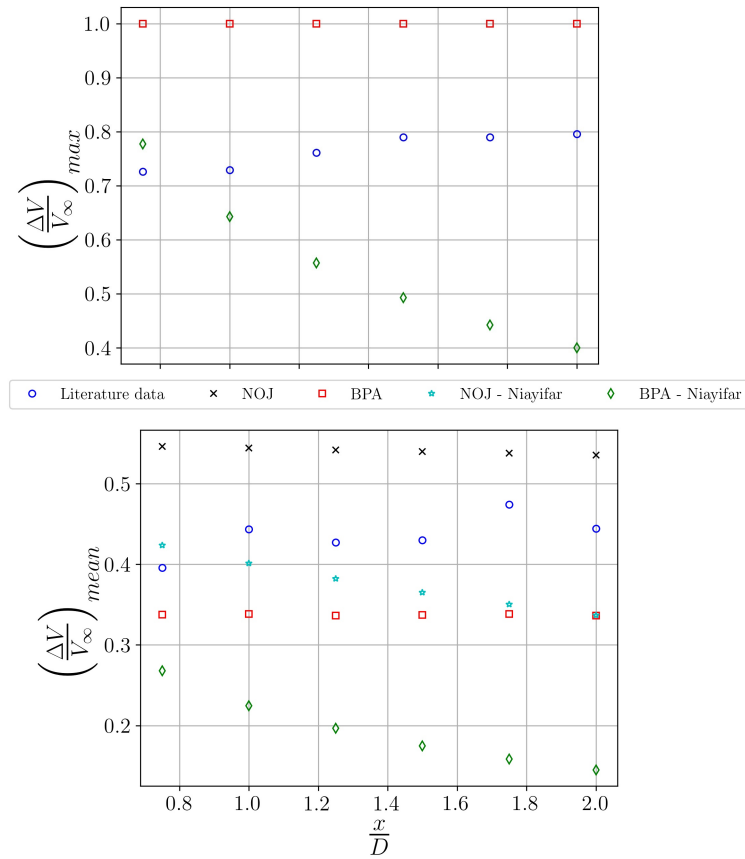


Figure 7.27: Comparison between values calculated by analytical wake models and literature for maximum velocity deficit (top) and the mean velocity deficit (bottom) calculated along spanwise direction at mid-span for Tescione et al. [110] case

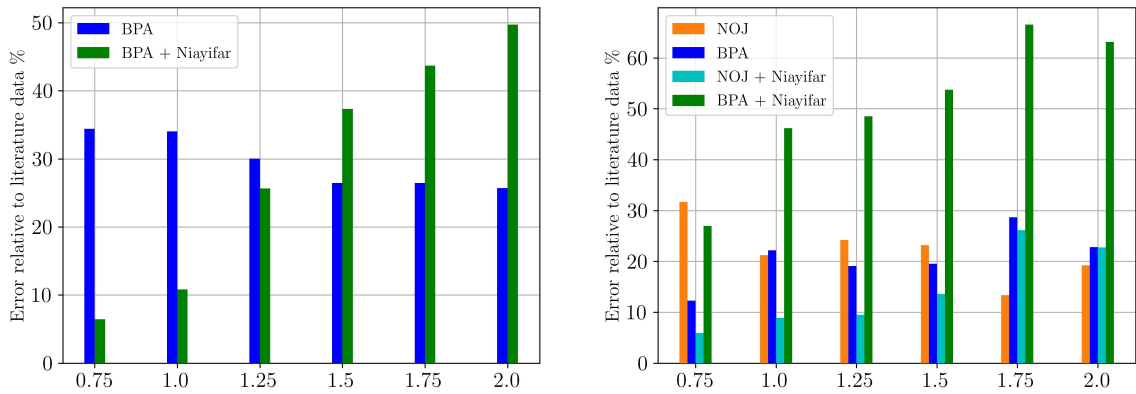


Figure 7.28: Deviation in the maximum velocity deficit (left) and in the mean velocity deficit (right) compared to data from [110] for different wake models. The errors are based on the data evaluated along crossflow direction at mid-span and the maximum value as reference for the error.

the near wake region.

As for the other cases, the investigation of how the maximum velocity deficit as well as the mean deficit value is discussed. With reference to Top Figure (7.27) and (7.28), its possible to assess one of great weaknesses of analytical wake model: replicating the near wake and the wake development. BPA and BPA-N models show an average deviation of 29% when evaluating the maximum deficit. The trend showed by BPA-N model anticipate an even higher error moving further downstream.

Concerning the mean deficit value in Bottom Figure (7.27) and Right Figure (7.28), the same problem ob-

served before is experienced: for the literature data, the mean value increases because of wake development. In the other cases the mean deficit decreases or remains constant since the turbulence intensity is extremely low and but at the same time is the only feature that can model the effective recovery experienced by the wake. The overall average deviation is 13% higher than Abkar's case. However it is necessary to point out that excluding values from BPA-N model, the average deviation drops from 27% to 17%. In some cases, NOJ-N model shows a deviation of less than 10%, as a statement of its high quality in predicting the mean value in the wake.

7.2.3. Comparison with Shamsoddin et al. [97] - Aspect ratio effect

The parameters used in the last comparison are reported in Table (4.16). Since 3 different ARs are used, its effects on wake models predictions will be analysed. With reference to the overview in Figure (7.29), it is observed that when the AR decreases, so does the velocity deficit as well as wake's extension along streamwise and crossflow direction, in agreement to what was discussed in Section (2.2.3.4) [2, 3, 97]. Therefore wake models are capable of replicating such behaviour, since geometrical properties directly affect both wake's width and velocity deficit calculated.

In order to provide more details related to how different wake models behave when AR changes, mean velocity profiles are analysed. Starting from the highest AR case reported in Figure (7.30) a high level of agreement

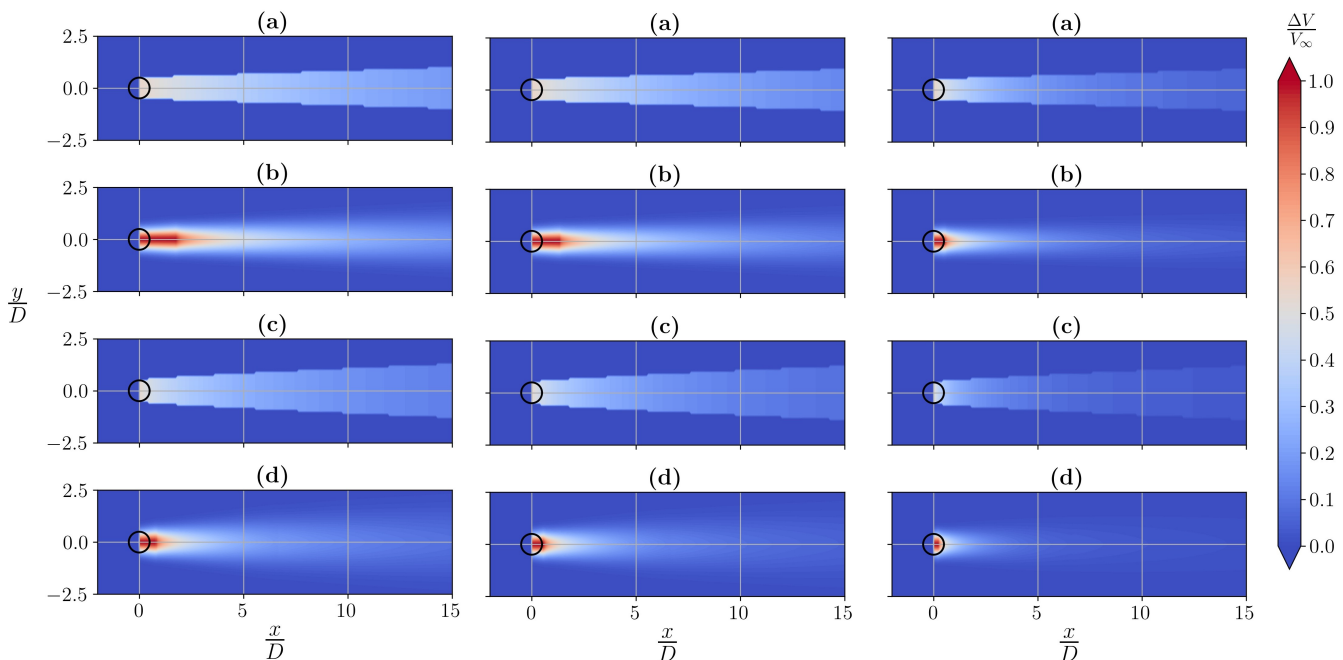


Figure 7.29: Overview of velocity deficit and wake's expansion according to [97] for $H = 100m$, $AR = 2$ (left), $H = 50m$, $AR = 1$ (center) and $H = 12.5m$, $AR = 0.25$ (right) for (a) NOJ, (b) BPA, (c) NOJ-N, (d) BPA-N wake models

is reached with literature data. With reference to Top Figure (7.30), the first section analysed at $x = 1D$ is not correctly replicated by Gaussian models, they both overestimate the maximum and wake's width experienced (BPA model has not passed the onset point yet). At the same time however the shape replicated is similar to the one from literature data. Moving further downstream, from $x = 3D$ BPA predictions fit the high fidelity data with a considerable level of accuracy along the entire domain. It achieves the best accuracy among models tested, especially in the far wake ($x = 7D, 8D, 9D, 10D, 11D$). BPA-N model instead displays the common behaviour observed for the other cases, with recovery rate overestimation.

Top-hat models in the near wake show limited discrepancies compared to literature data, but while differences increase for NOJ-N moving downstream, they decrease for NOJ model, whose accuracy can challenge BPA method. Considering instead Bottom Figure (7.30), the effect of the aspect ratio is observed. At $x = 1D$ the wake resembles the rectangular shape of turbine's frontal area. Therefore top-hat models, especially NOJ, are capable of perfectly replicating wake's shape, unlike Gaussian models. Moving downstream aspect ratio's

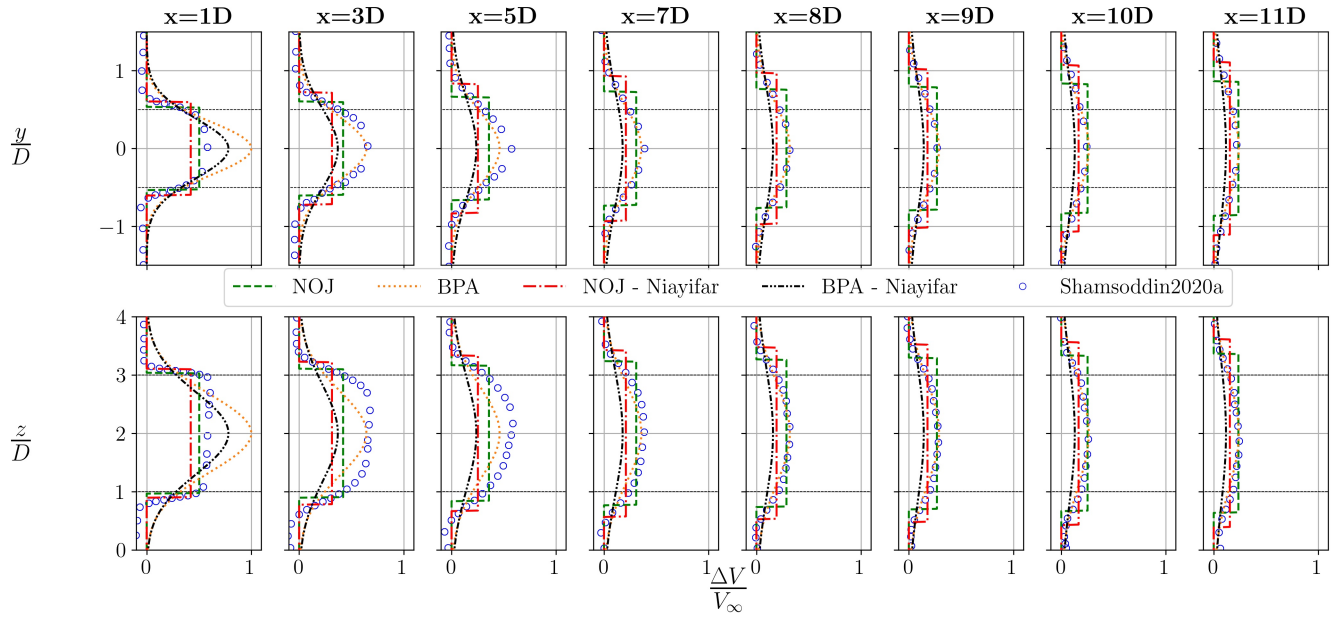


Figure 7.30: Profiles of mean velocity deficit streamwise velocity along crossflow direction at mid-span (top) and spanwise direction (bottom) for different downstream sections, comparison between data from different analytical models and literature data from [97] for case $H = 100m$, $AR = 2$

influence decreases and at $x = 7D$ BPA model provides almost the same values from the literature. In previous sections $x = 3D, 5D$ the wake is 'evolving' towards the typical Gaussian shape always observed in the far wake region. Therefore AR's effect decays from a certain downstream position. Moving further downstream no significant changes are observed except the agreement on maximum deficit provided by BPA and NOJ models.

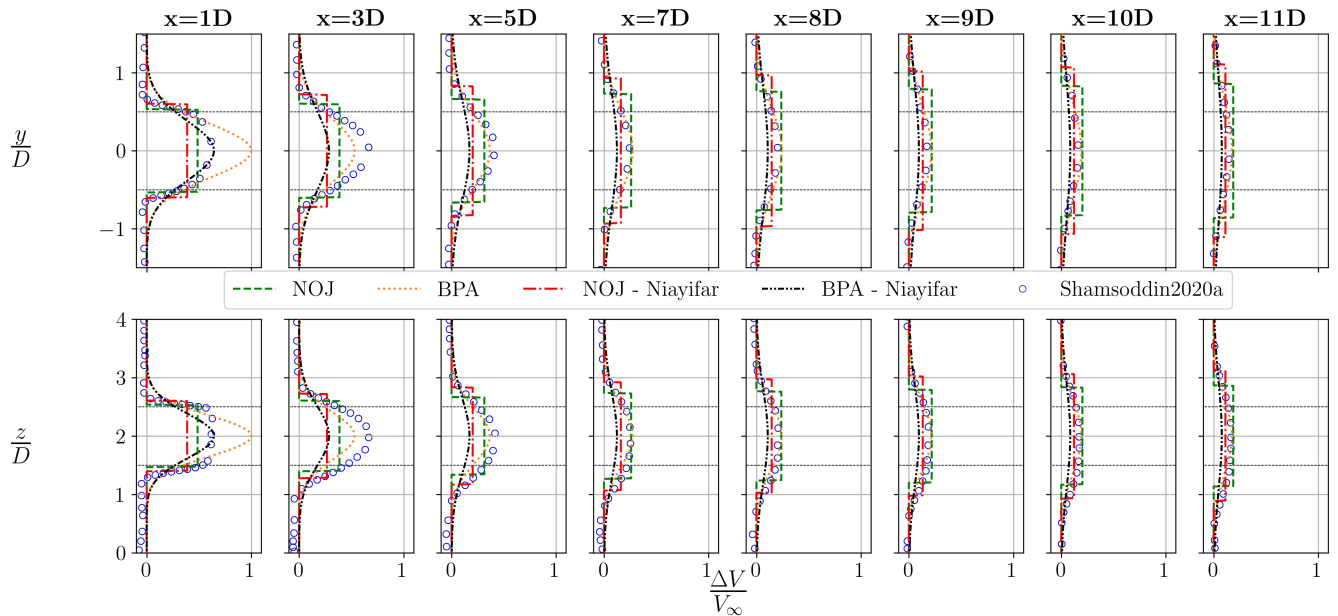


Figure 7.31: Profiles of mean streamwise velocity deficit along crossflow direction at mid-span (top) and spanwise direction (bottom) for different downstream sections, comparison between data from different analytical models and literature data from [97] for case $H = 50m$, $AR = 1$

Even along this direction, models based on Niayifar's law are not reliable both in near and far wake, suffering the problems discussed before.

Considering now $AR = 1$ in Figure (7.31), high accuracy is observed even in this case. With reference to Top Figure (7.31), BPA-N law provides good estimation of both wake's width and maximum deficit, overlapping literature data. Such behaviour was already observed in Figure (7.26) where it was the only model showing good results for the near wake. However, moving downstream its accuracy degrades quickly, just to display a considerable agreement in the far wake, where curves tend to collapse as observed in Figure (7.26) and (7.15).

The most accurate model is the BPA, that shows a perfect agreement with literature data starting from $x = 5D$ on. Top-hat model NOJ provides almost the same level of accuracy observed in the higher AR case, especially for the far wake. Overall models based on Niayifar's law (except what mentioned before) underestimate the velocity deficit and demonstrate lower accuracy than models based on Abkar's law. In this case the discrepancy with literature data in far wake is lower than what was shown in previous case. Bottom figure shows more details about the AR's influence.

compared to Figure (7.30) the rectangular shape of the near wake is less marked. It is more like a middle-way between a rectangular and Gaussian shape, so AR's influence is decreased. Even if not being a total rectangular shape, NOJ model with Abkar's law provides the best accuracy, especially in terms of wake's width, even if it underestimates the maximum deficit. The same trend of previous case is then observed: BPA achieves the best accuracy, perfectly fitting the data while NOJ model provides almost the same maximum deficit. As before, wake model's based on Niayifar's law show low agreement with literature data up to the far wake.

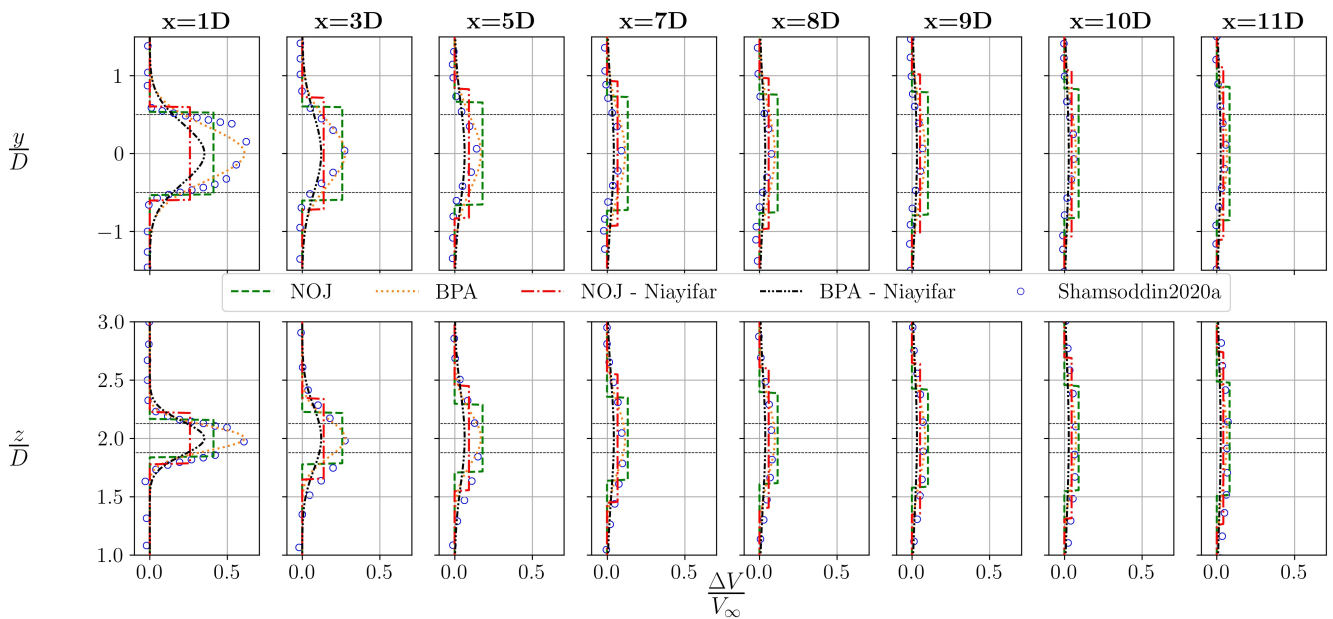


Figure 7.32: Profiles of mean streamwise velocity deficit along crossflow direction at mid-span (top) and spanwise direction (bottom) for different downstream sections, comparison between data from different analytical models and literature data from [97] for case $H = 12.5m, AR = 0.25$

With reference to Figure (7.32) the lower AR case is analysed. Considering crossflow profiles, BPA model provides high accuracy from section $x = 1D$. This happens because the turbine considered is small and at high turbulence intensity levels, so the onset point is located early in the wake. BPA provides the best accuracy also moving downstream, while NOJ model tends to slightly overestimate the maximum deficit in far wake. In this case models based on Niayifar's law are definitely inaccurate in the near wake, providing low values respect with literature data. At the same time, the high recovery rate leads to underestimated values. This could be related to the fact that the deficit is limited because of turbine's limited dimensions and the high recovery rate tends to quickly dissipate any trace of turbine's presence. A slightly deflection of wake's centre is observed in both spanwise and crossflow profiles, something that wake model cannot replicate and

that may be related to the higher extension of the turbine along crossflow direction.

Considering spanwise profiles in Bottom Figure (7.32) AR 's influence is no more observed even in near wake at $x = 1D$: BPA model matches perfectly literature data from here on, even if some slight disagreement because of the deflection is observed. Such deflection could be related to the action of tip-vortices discussed in Section (2.2.1.3). Other models show the same behaviour observed for profiles along crossflow direction: all of them provide almost the same results for the far wake, showing a good level of agreement with literature data.

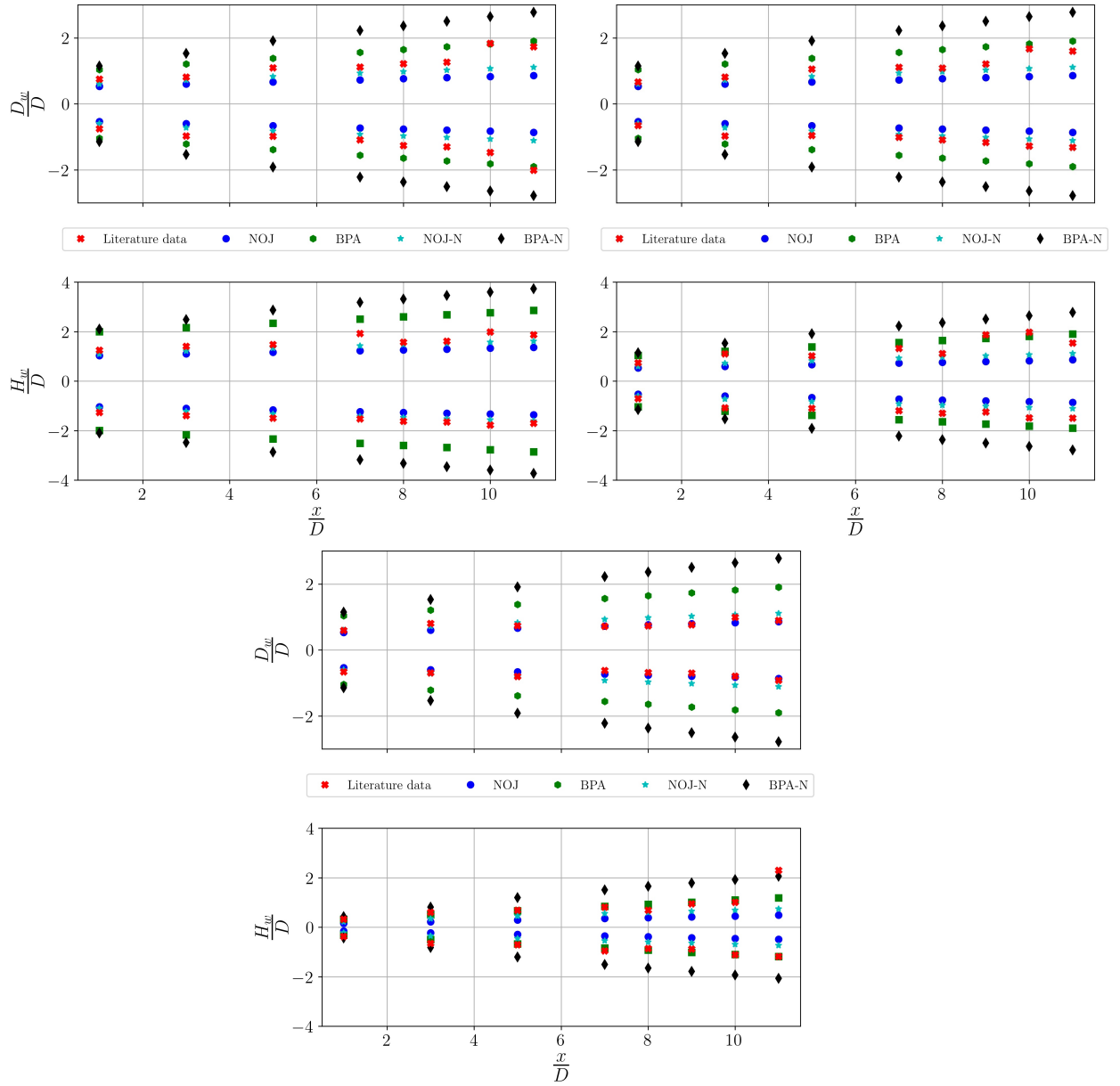


Figure 7.33: Wake width evaluation along crossflow direction at mid-span plane (top) and spanwise direction at $y = 0$ plane (bottom).

The cases reported are in agreement with data from [97] and feature $AR = 2$ (top right) $AR = 1$ (top left) and $AR = 0.25$ (bottom) for different wake models. The errors are based on the data evaluated along spanwise direction for $y = 0$. Moreover here spanwise wake width is normalized with the diameter, since H is not constant.

Considering Figure (7.33), wake width is now analysed. compared to higher AR case, it seems that having a higher agreement leads to a higher expansion of the wake, especially along crossflow direction. For $AR = 0.25$ in fact the expansion is limited, with half the values reached for the highest case. Such behaviour was already discussed in Section (2.2.3.4) [2, 3, 97] and here is confirmed.

Wake models behaviour is not the same for all the cases: with higher AR values tend to increase one another the separation along spanwise direction, while with lower values the difference is limited. The same trend is not observed along crossflow direction instead.

Concerning the accuracy of the values predicted, NOJ and NOP-N models are the most accurate, providing almost the same trend of literature data in every AR condition and along both spanwise and crossflow direction. BPA and BPA-N models instead are less accurate, especially along crossflow direction. In the latter case, no significant variation are displayed when modifying the AR . For the spanwise direction instead, the more AR is low, the more higher the accuracy observed for these two models is.

As for the previous cases, it is important to study the maximum and mean deficit values. With reference to Figure (7.34) and Figure (7.35) maximum and mean values are considered along spanwise direction and not at mid span since the target is studying AR effect on wake models. The reader is referred to Appendix (D) to check how maximum and mean deficit along crossflow direction evolve moving downstream.

With reference to the highest AR case, the maximum velocity deficit predicted by the BPA model displays high accuracy from $x = 3D$ on, overlapping with literature data in the far wake region. Excluding the first value, where onset point has not been passed yet, the average deviation displayed is less than 5%. BPA-N model instead, underestimates literature data, showing a deviation that ranges from 20 to 53%. The situation is similar for $AR = 1$ case. BPA deviation decreases by moving downstream while BPA model based on Niayifar's law instead under predicts the literature values. With decreasing AR , almost the same trend is observed and average deviations are 6% and 21% for BPA and BPA-N model respectively. In the lowest AR case reported in top left Figure (7.34), even at $x = 1D$ literature data and wake models values are totally overlapped for BPA model, while BPA-N model display higher agreement with literature data. In this case the average deviation are respectively less than 3% and 15%.

Considering the mean values in bottom Figure (7.34) the situation slightly changes. For $AR = 2$ case the region of wake development is observed up to $x = 3D$, then the wake starts to recovery. As already observed however, this is a trend not replicable by existing wake models. Observing all the three cases, it seems that for high AR wake models do not correctly replicate the exact mean value with the only BPA and NOJ-N models able to provide qualitative values in the far wake, with a deviation lower than 10%. The situation improves when AR decreases, since the two models cited before provide results closer to the literature ones. In particular, NOJ-N models display an excellent deviation lower than 9% considering the entire domain, even the near wake. For the lowest AR , wake models results match even better literature data. However NOJ and BPA-N models still feature considerable deviations, unlike BPA and NOJ-N which display an average deviation of 25% lower. However, BPA-N displays good agreement in the far wake at least: from $x = 8D$ the deviation is constantly less than 10%.

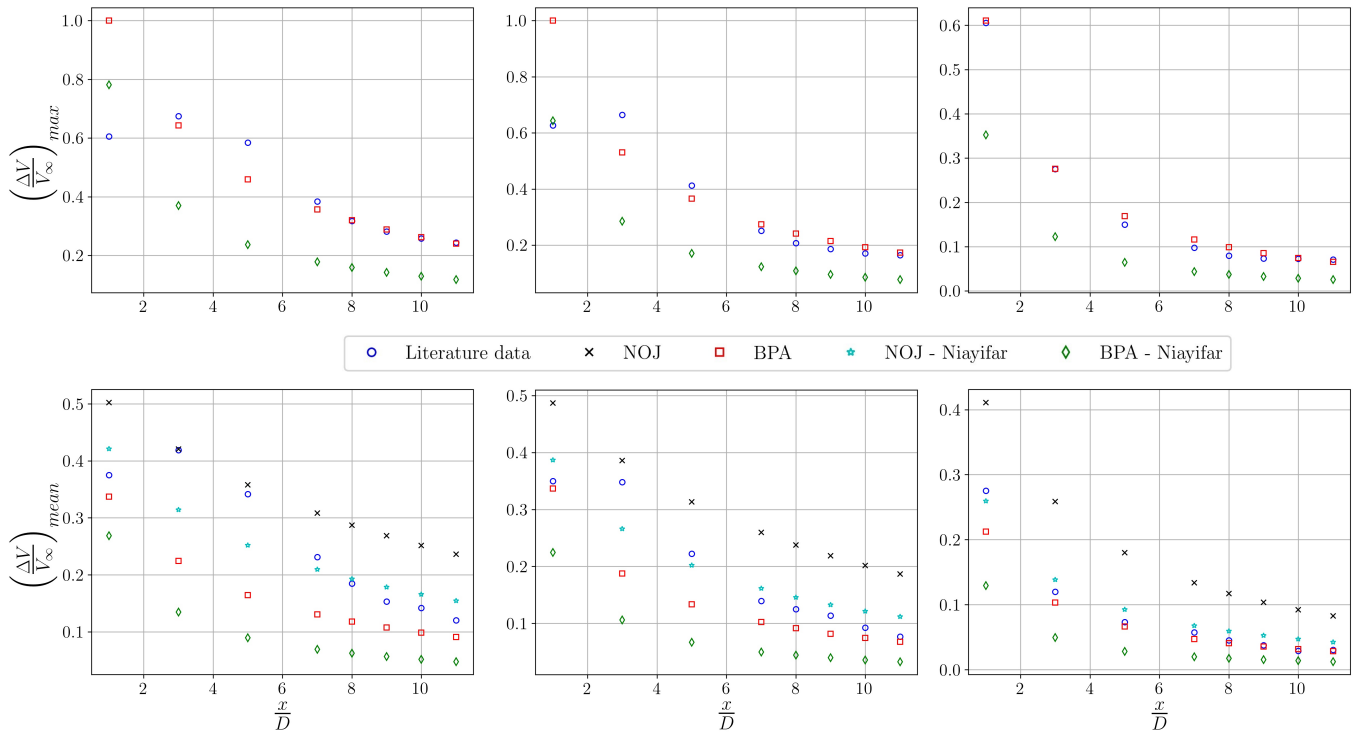


Figure 7.34: Evolution of the maximum deficit value (top) and the mean velocity value (bottom) along the symmetry plan for $\gamma = 0$ according to [3] for $AR = 2$ (left), $AR = 1$ (centre) and $AR = 0.25$ (right) for different wake models compared with literature data

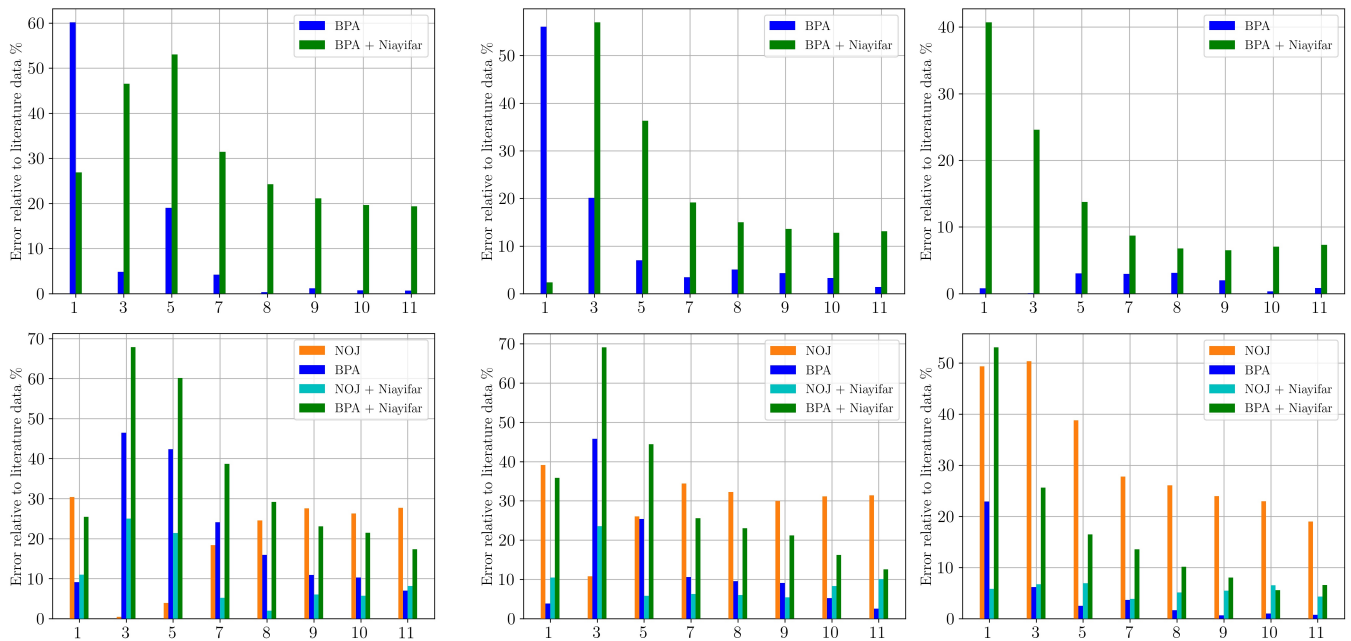


Figure 7.35: Deviation in the maximum velocity deficit (top) and in the mean velocity deficit (bottom) respect with data from [97] for $AR = 2$ (left) $AR = 1$ (centre) and $AR = 0.25$ (right) for different wake models. The errors are based on the data evaluated along spanwise direction for $\gamma = 0$ and the reference error is the maximum value.

7.3. Conclusions of the chapter

In this chapter analytical wake models are tested under a wide range of conditions, featuring different AR and C_T , spacing from low to high turbulence intensities, from small to large scale turbines. After the investigation of all previous cases, the main findings and major conclusions are listed as follows:

- The level of accuracy demonstrated by wake models drops when low turbulence intensities (0.5-1%) and Reynolds' number are experienced ($10^5 - 3.2 \cdot 10^7$). In similar cases, wakes tend to be deflected even at high TSR (4.5) easily. However it is logical to expect that the predictions made in a case of high TSR (where deflection is weaker) would more probably reveal a considerable level of accuracy. Analytical wake models, that do not consider wake's centre displacement, provides an erroneous location for the maximum velocity deficit and the deficit area. So one of the main drawbacks of wake models for VAWT is unveiled: their inability to replicate wake deflection and to not keep into account that the deficit calculated along the vertical plane is no more the maximum deficit. However, after a certain downstream position deflection becomes weak depending on the combination of I and Re . At high I mixing effects allow an earlier dissipation of the wake, as observed in Chapter (6), while inertial forces are dominant at high Re , leading to the dissipation of the vortical structures (and especially CVPs). Therefore in similar conditions, wake deflection is not experienced and wake models are able to replicate wake's evolution correctly, even in the near wake as seen for case (7.1.3), (7.2.1) and (7.2.3). In the opposite cases, wake deflection persist from near region up to far wake, without being dissipated in the control volume examined (7.1.1), (7.1.2) and (7.2.2).
- Focusing on the near wake, none of the wake models is able to replicate the development and the evolution of the near wake with high accuracy in each case analysed. Here are observed most of the consequences related to rotor's effect, which cannot be predicted by wake models, loosing in accuracy. The extension of this is not constant and depends on the case analysed. Commonly, at high turbulence intensity levels, large scales and high Reynolds number, the near wake extension is extremely limited. In the opposite case, near wake persists downstream and the expansion becomes dominant in the near wake and the deficit increases up to a certain downstream location, before showing a constant decrease. This was observed in (7.1.1), (7.1.2) and (7.2.2). Such region of wake development, where the increase in the maximum velocity deficit is observed and the wake expands is observed because turbulence intensity is too low and subsequently wake expansion is dominant and the deficit raises. Wake models cannot replicate a similar trend, since they are built upon equations for wake decay but do not consider that the wake can still develops and reach higher deficits. Wake models can only predict the recovery and not the 'evolution' that leads to higher deficit. Moreover, in Re and I low conditions, the extension of such region is wider than what could be observed in an opposite case, since such parameters 'help' in damping the expansion effect of the wake in this region. Therefore with high Re and I can be applied earlier downstream.
- BPA model interacts differently with the near wake region compared to other models. In fact when low turbulence intensity is observed BPA, provides erroneous results based on the fact that the region investigate is still considered by the model as dominated by pressure-gradients. In fact the only way recovery is replicated is by turbulence action through wake decay constant. If the latter is limited because of low turbulence levels, recovery is not replicated, the wake does not expand and the deficit remains constant. This leads to a constant value for a wide portion of the wake, something not correct and neither realistic since, as observed in Section (7.1.1), (7.1.2) and (7.2.2), since it persists for too long distances, being to provide correct results (compared to other models) since the onset point is reached late in the wake. At the same time it is the most similar evolution compared to a wake that is developing in the near wake.
- Low accuracy at low I can also be related to the fact that wake models analysed are translations of existing models for HAWTs. Such turbines are most of the time large scale turbines, therefore it would be logic to conclude that the use of VAWT wake models is recommended for large scales, and not small ones like in this case. However, even if in a similar case, NOJ-N models is able to replicate qualitatively wake's expansion and the mean value provided displays a limited deviation.
- Considering wake's width evolution, NOJ and NOJ-N models demonstrated an excellent accuracy in the results, especially when analysing portions of the wake where no deflection was experienced. They

were the only models (especially NOJ-N) able to provide a good estimation of wake's width even in low I and Re conditions and either when deflection was experienced. This, coupled with the fact that NOJ-N model displayed great capacities in predicting mean values, allows to have at least an idea of deficit's mean value and its extension.

- The linear wake development hypothesized in Chapter (3) is verified in almost all the conditions studied, as well as the assumption of a circular shape for the velocity deficit when considering the far wake region.
- The relevant deterioration of wake's models predictions observed in the near wake is not general and depends on the wake model used and what is analysed. Overall the most accurate models can be considered BPA and NOJ-N, especially the last one is able to perform much better than its counterpart NOJ. BPA and NOJ-N models provide correct estimations for the far wake and the all domain respectively.
- Evolution of the deficit along streamwise direction displays different features depending on the equation for the wake recovery used.
 - Abkar's law provides a valid recovery rate up to the far wake region. After that, however, it tends to underestimate the decrease in the deficit. This may be related to the fact that it considers the freestream turbulence intensity value only, not considering the local rise in VAWT' wake. Moreover, when low turbulence cases are considered results provided by the model display poor accuracy.
 - Niayifar's law instead overestimates wake recovery rate, providing values in the wake and lower than literature ones in the far wake. Such agreement can be related the fact that Niayifar's law takes into consideration the local turbulence intensity. However it is still unknown the accuracy of the law further downstream and its performance depends on the model considered: it displays more awful effects on BPA-N than NOJ-N, probably because the error increases when applied to the Gaussian expression. Additionally, it seems that when used in high ambient turbulence conditions, the accuracy in the near wake is no more observed. Probability it is related to the fact that by that point wake has already recovered a significant portion of the deficit. Therefore in similar cases it only demonstrate a considerable agreement in the far wake. It is important to understand that this behaviour is observed for the BPA-N only, and not for NOJ-N.

Therefore, wake decay constants used are a major limitation, since they do not take into account the real development of local turbulence intensity in the wake and are introduced for HAWTs, not VAWTs, whose wake properties are different especially considering its relation with turbulence. Moreover, even if theorized for HAWTs, they only suit high turbulence cases and not valid for low I condition. This in an additional reason of their poor accuracy.

- BPA-N wake model shows the highest level of agreement with experimental data, but only in the very near wake. Moving downstream its well-known overestimation of recovery rate leads to too optimistic values in the far wake and huge deviations in maximum and mean deficit values. However, if the mean velocity deficit only is considered, NOJ-N model law seem to be the most accurate in replicating numerical simulation predictions in the far wake. However, this does not have to mislead the reader, since wake decay constant calculated with the related expression leads to a overestimation of the recovery rate. The discrepancy could have been the highest if advection due to CVPs was not experienced.
- When high Reynolds' numbers are experienced (and so large scale turbines are considered), wake models show high accuracy when evaluating the maximum deficit and wake's width. In the opposite case, while wake's width estimations remain accurate (but only for top-hat models), maximum deficits are affected by considerable deviation. Therefore it is advised to use the values averaged over wake's extension.

After comparing wake model results and literature data from [3] the findings about wake models behaviour when variations in thrust coefficients are experienced can be discussed. First of all, higher C_T (and so higher TSR) leads to higher agreement between reality and predictions since the deflection (something that wake models cannot replicate) is weaker. A global high-level accuracy is observed among wake models. Accuracy experienced was observed to be affected by the thrust coefficient in the following terms:

- Maximum velocity deficit predicted by Gaussian models is insensitive to thrust coefficient variation, holding almost the same average deviation (maximum difference observed 3%).
- Mean values calculated by Gaussian models are higher in the near wake at higher C_T but the trend and the asymptotic values reached are almost the same.
- NOJ model provides a mean value whose deviation increases at higher C_T by 5%
- NOJ-N model, displays almost the same deviation for both cases (0.5% difference)

Overall however the local accuracy in the near wake increases when C_T raises (if BPA-N model is not considered). In particular the lower accuracy displayed by the BPA model can be also related to the fact that only sections after the onset point are analysed: since the comparison starts from $x = 3D$, wake is already full developed and such model shows high accuracy. The early overcoming of onset point is strictly related to the high turbulence intensity used. However if the real near wake would have been considered, BPA model accuracy would have dropped compared to other models. Another relevant aspect is that top-hat models tends to overestimate the mean deficit value in the far wake at higher thrust coefficients. Since this parameter does not affect wake recovery that only depends on turbulence intensity, the overestimation may be related to a too fast recovery experienced when higher deficits are observed: it is not totally correct that wake recovery is not affected by thrust coefficient. Moreover, higher thrust coefficient tends to increase the differences between models predictions but maintaining the same trend: it seems that curves of maximum and average velocity deficit are translated vertically.

Analysing the effect of the AR on wake models predictions some important conclusions can be mentioned:

- AR influence is lower at higher Re , apparently
- Wake models are capable of replicating the variations in the velocity deficit as well as wake's expansion experienced when AR changes.
- AR effect is limited to the near wake region, leading to a rectangular shape. No influence is shown on the far wake. The assumption of a circular shape [97] for the wake is so justified if the target is to model the far wake correctly.
- Top-hat model is recommended when considering near wake under high AR since it is capable of better replicating wake's shape. Moving downstream the wake develops and assumes a Gaussian shape which is perfectly replicated by BPA model. However when AR is lower, Gaussian shape is earlier assumed by the wake.
- Models based on Niayifar's law only provide good estimates for the far wake when low AR are experienced. This can be related to the fact that such law has not been tested for a VAWT but for a HAWT which considers one geometrical parameter only and not two.
- NOJ and BPA-N model reveal lower accuracy in maximum and mean deficit value predictions than BPA and NOJ-N models. BPA-N's deviation decreases when lower AR are considered, especially in the far wake. The trend demonstrated by NOJ model instead is opposite: with higher AR it displays reduced deviation, especially in the near wake where its distribution perfectly replicates the one observed in literature data. However when AR decreases or far wake sections are considered, the accuracy decrease, since the shape displayed by literature data tends to a Gaussian one.
- BPA and NOJ-N model outperforms all the other models, providing accurate values of maximum and mean velocity deficit in every AR condition experienced.

8

Final remarks

8.1. Conclusions

In this thesis the performances, reliability and range of validity of analytical wake models for Vertical Axis Wind Turbines (VAWTs) were analysed and evaluated with a set of comparison against high fidelity numerical and literature data. It was found out that analytical wake models for VAWTs display a considerable accuracy in different cases. The distinction between the levels of accuracy experienced was strongly affected by turbine's scale, Reynolds' number and turbulence intensity.

With the support of a numerical conducted about wake similarity at different scales, it was found out that a portion of the wake shows the same shape for every Reynolds number. Such region of the wake is the one not affected by deflection and CVPs advection that enhances wake mixing, allowing the core of the wake to recover faster. The non-similar portion of the wake, is affected by deflection and deformation, caused by possible different aspects. The Re -independent region displays a shape and a normalized deficit value which is comparable at different Re conditions, so this important result is not only a qualitative but also a quantitative one. Normalized velocity profiles testified this behaviour, which was never studied or observed before. Moreover, excluding the deflection experienced, which can be related to TSR , I or the scale itself, even the related portion of the wake would have probably displayed similarity.

The consequences of this result are remarkable: since a portion of the wake that presents deflection displays the same width and maximum deficit of a non deflected case. This way wake models could be potentially used to overcome the problem of wake's centre displacement, being able to provide a correct velocity deficit and a portion of wake's width. However the process is not straightforward, since wake models are not always sufficiently accurate, as mentioned before. The main conclusion observed can be summarized as:

- Models are not reliable when considering near wake region. In fact, as discussed in Chapter (2), rotor effects, pressure gradients and vortical structures play an important role in defining wake structures and properties in the near wake. Such properties are neglected when developing wake models, which are not expected to replicate correctly the wake evolution in this region. Moreover, wake extension and development, with increasing deficit, is not replicable by wake models which can only model the constant decay and recovery.
- When low turbulence intensity conditions are experienced, wake models are not reliable the equations for wake decay constants are conceived for HAWTs that experience high turbulence levels. Consequently, even when considering VAWTs, results obtained for high I are sufficiently accurate but not at low I . The discrepancies observed depend on the model used, but overall, none of the ones used was able to replicate the correct wake recovery in each possible condition. This is one of the greatest limitations of analytical models for VAWTs and in order to learn more about how turbulence intensity affect the wake and especially its recovery, a numerical comparison of turbines in different turbulence conditions was carried out. It featured 4 different cases, one at low I and low Re , one at high I and high Re and the same cases but in a no-turbulence condition. The qualitative results allowed to understand that turbulence effect on wake recovery is strictly related to Re , therefore the two needs to be

coupled. This way was possible to shed light on turbulence effect and on how it should be replicated when considering wake decay constants.

- Wake models do not consider the deflection experienced. Therefore the values predicted by models do not consider the real wake centre, but only the geometric centre of the turbine located at $y = z = 0$. Even if, as mentioned previously, wake displays similarity at different scales, it would be important to predict wake displacement and the deflection, in order to optimize the layout of a VAWT farm.
- Analysis of AR effect on wake models predictions testified that wake models are capable of replicating the variations in the velocity deficit as well as wake's expansion experienced when AR changes especially in the far wake since AR effect is limited to the near wake region, leading to a rectangular shape. Top-hat model was recommended when considering near wake under high AR because of its ability in replicating wake's shape. Moving downstream the wake develops and assumes a Gaussian shape which is perfectly replicated by BPA model. However when AR is lower, Gaussian shape is earlier assumed by the wake. Models based on Niayifar's law only provide good estimates for the far wake when low AR are experienced, but their performance are strictly related to the issues with the wake decay constant equation used that was mentioned before.
- Similarly, wake models behaviour when variations in thrust coefficients are experienced can be discussed. At higher C_T (and so higher TSR) higher agreement between reality and predictions is observed, since the deflection is weaker and a global high-level accuracy is observed among wake models.

However, not all the models perform in the same way and some of them provides more or less accurate results depending on the case analysed, but the trend mentioned concern the whole set of wake models. For example the Gaussian model supported by Abkar's law showed the best agreement with a deviation from high fidelity data for the maximum velocity deficit ranging from less than 1 % up to 8% when different C_T and AR were tested. Using instead Niayifar's law the difference increases up to 30% in the far wake. When the near wake was considered, the error for the Gaussian models increased up to 60% if Abkar's law is considered and up to 55% when using Niayifar's one. In similar cases averaged velocities calculated showed slightly better agreement with high fidelity data. A peak in the difference between maximum deficit calculated by Gaussian models was observed ranging from 50% to 40% in low turbulence intensity conditions when considering the near and far wake respectively. Top-hat models instead showed better agreement in extreme conditions, when high aspect ratios and low turbulence intensities are experienced, showing 40% deviation less than Gaussian models in the near wake for the average velocity deficit. The agreement showed by top-hat models with high fidelity data in the far wake region was found to depend on the law used for the wake decay constant when considering the velocity deficit, but independent when considering wake's width, that they were able to replicate in almost every condition. Overall the one based on Niayifar law displayed better results, providing 12% average deviation less in both high and low turbulent conditions.

It is possible to conclude that even being affected by a certain degree of accuracy due to their strong assumptions and simplifications, analytical wake models for VAWTs are a powerful tool that, supported by a low computational cost, allow to extract the main quantities observed in a VAWTs wake. However, they still suffer a considerable level of inaccuracy due to the assumptions and simplifications. Similar limitations could be overcome by improving the complexity and the potential of such models, considering a series of aspects that up to now have never been analysed in detail and modelled. Such aspects are the deflection of the wake, the wake decay constant dilemma and the development of the deficit in the near wake. By modelling them keeping into account VAWTs and not HAWTs aerodynamics, it would be possible to reach a even higher level of accuracy for analytical wake models that would be precious during the optimization of a wind farm layout.

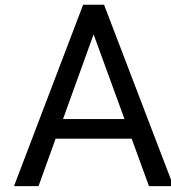
8.2. Model improvements

In order to overcome the actual limitations and problems observed in analytical wake models the following improvements aimed to extend their validity range and their accuracy are proposed:

- In low TSR and Reynolds' number conditions, the wake experiences deflection, something that existing VAWTs wake models cannot replicate. It would be a significant improvement to introduce a way to model wake's centre displacement with the aim of improving overall models' potential. This way it

would be possible to predict not only the deficit wake's width, but also its location with subsequent advantages in optimizing the layout and power extraction from VAWTs wind farm. A possible approach for this research gap could be provided by existing wake models for yawed turbine [11], where the lateral force exerted on the flow because of turbine's yaw angle pushes wake's centre towards one side and the displacement is quantified using momentum equation along crossflow direction. Similar models could be a starting point to consider asymmetry.

- To overcome the limitations of wake decay constant laws when used in low turbulence conditions, it is necessary to introduce equations that keeps into account the exact features of VAWTs' wake, and not based on HAWTs. As already seen, the turbulence pattern behind a VAWTs is complex and unique. Therefore an equation based on it, and not on HAWTs, is necessary even because mixing process are more intense and different from the ones of a HAWTs and consequentially, the wake recovers earlier. This way it would be possible to overcome one of the model main limitations caused by shortage of equations for VAWTs and to correctly replicate the recovery experienced. The latter is extremely relevant when considering how close wind turbines can be placed in a wind farm.
- Another aspect worth to be investigated is the possibility of introducing a different wake decay parameter for the windward side, where deflection is observed. Such equation should be function of the TSR, to keep into account the effective deflection, the downstream coordinate and the local turbulence intensity. However, as for the previous point, this would be a quite complex task that would require experimental studies.
- Modelling of the wake development in the near wake could be introduced by assuming two different laws for the velocity deficit: one for the region where the wake recovers, and one for the region where the deficit increases. How much the deficit increases would be defined by a specific law that keeps into also turbulence intensity. An additional equation would be required to express the extension of this region. Even this would not be an easy task.



General knowledge about wind energy

A.1. Origins and overview

A.1.1. Global context's influence

In today's world fossil fuels are, for almost every nation, one of the bases of industrial production. In fact oil and gasses are the main sources to sustain the production of electricity which has infinity applications, spacing from lights in the streets to the heating machines in our houses and therefore is essential for everyday life. Another reason why this source is so spread across the Earth is its low-cost comparing to other resources. However, this source of power (which has even led to several wars in the past century) brings along several important issues. First of all, there's a finite quantity of these fuels and its indiscriminate abuse will leave humanity without them. But where is this power source located? There are several sites spread throughout the world and the countries which hold these zones are free to choose the selling price most of the time. Nations that lack these natural sources are so forced to pay huge amounts of money to afford it, accepting the blackmailing of the oil-producing countries that most of the times are hostile toward Western nations. Its price could even be unpredictable according to the historical situation (see Figure (A.1)) one relevant example is the oil crisis in 1979 as well as the financial crisis in 2008. Similar events underline the unreliability of this resource and push to other solutions. Last but not least, the major boost to avoid the use of fossil fuels is the climate change. In fact temperatures raising, ice caps that melt, the highest levels of CO₂ emission and consequently the greenhouse effect actually are the main reasons why alternative and renewable sources of power have experienced an incredible interest during the latest years. All these aspects can be consider as a trigger for the study and development of new solutions that exploit the sun, wind, waves and so on to produce electricity without harming the planet and the coming generations.

A.1.2. Renewable resources and wind turbines

We mentioned 'other solutions' but which ones are we referring to exactly? At the moment, the most diffused are strictly related to the technology available and its quality as well as the efficiency, the economic cost and the possibility of commercialising these solutions. The most common are:

- Solar cells
- Wind turbines
- Hydroelectric power, hydro turbines and tidal wave turbines
- Biofuel sources
- Geothermal technology
- Nuclear reactors
- Coal-fired power generation

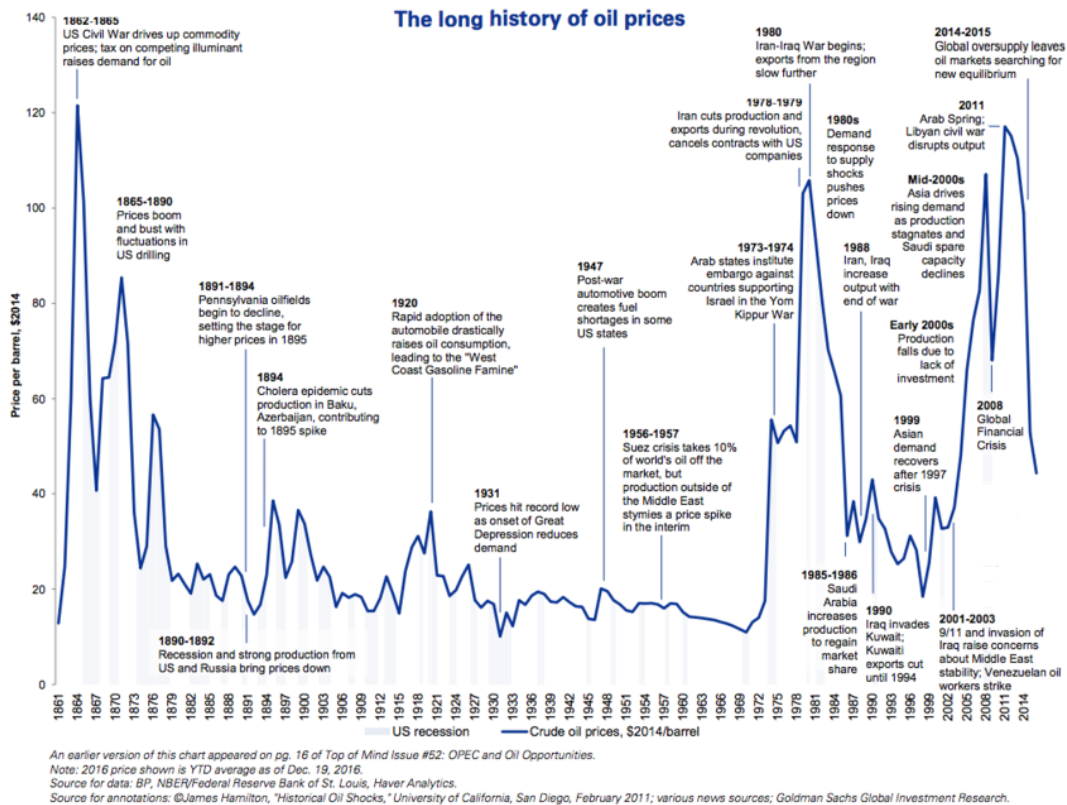


Figure A.1: Unpredictability of the oil price due to the geopolitical situation during the last century and a half

At the moment, their usage is not equal. For example nuclear power generation has the problem of potential radiation that could harm people and the environment as well as the huge cost and initial investment. Coal-fired power generating sources, instead, produce polluting gasses and do not overcome the most relevant problem cited before. Hydro turbines need water reservoirs to have a constant water pressure while tidal wave turbines have to be located in specific oceanic locations to work efficiently. Geothermal and hydrothermal plants instead require low and high temperature underground regions to harness energy sources while biofuel sources, such as biodiesel, need huge supplies of raw material, not easily available. For many people, the environmental-friendly aspect of some of these solutions is not enough to justify the necessity of changing the industrial methods used for years until now. So what is that mostly pushes such ideas? Money obviously: unlike cars and houses, there's no luxury in electricity. We do not have class A electricity or class B electricity (excluding from the discussion the different voltage and frequency levels), so no one really cares about its origin, but all care about its cost. The main requirements are its dependably availability and cheapness and so the choice between these solutions is already done. The two cleanest and most cost-effective forms of renewable energy come from the Sun and the wind. In fact they offer electrical energy at low costs, the related plants have high reliability and they provide energy without releasing any polluting gasses in contrast with other solutions cited before (coal fired thermal or nuclear plants) but with less complexity and investments. In this thesis the main focus will be the wind and in general wind turbines. Solar cells in fact are able to reach an unlimited output, but they cannot operate during night-time and in clouded regions, issues that wind turbines do not suffer and, for this reason, wind is considered at the moment the most attractive renewable energy source. In fact during almost the last 50 years, wind energy has become the main answer to the problems cited before: the rated power increased from 100 kW in the early 1980s up to 100 MW and even more today, the size of the turbines increased from a rotor diameter of 30 m up to 150 m and aerodynamic research improved efficiency of these machines. The fast development in the field is no more carried out on an experimental small-scale, but at industrial levels with bigger and bigger plants constructed and a fully mature technology. The constant growth of wind turbine (estimated around 30% for year) and especially its technology will lead to a further energy cost decrease (especially thanks to lower operational and mainte-

Global generation shares from coal and low-carbon sources, 1971-2020

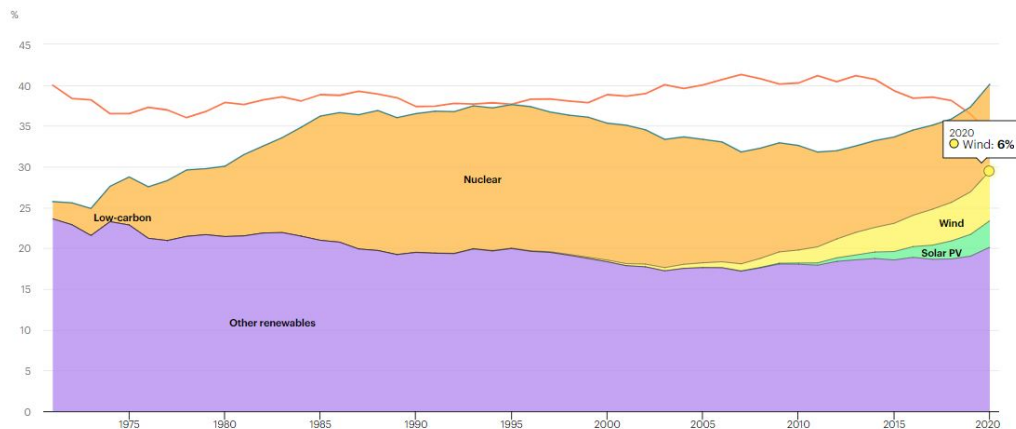


Figure A.2: Percentage of electricity produced (scaled) by sources. Image from [38]

nance costs) in future years even if at the moment it's already the cheapest electricity source. According to [91] "approximately 40 GW of wind power production capacity, equivalent to 80 Billion US \$ in investment, are added to the worldwide energy portfolio annually". Which are the main advantages? The following points can answer this question:

- The cost-efficiency: the amount of electricity generated is huge (ranges from 50 to 500 MW and even more), taking advantage of an unlimited source of power (i.e. the wind) and the investments are not comparable to other solutions
- Reliability: the technologies used are extremely matured and there's no need for frequent maintenance operations stopping the production nor the employment of operational workers like happens for coal-fired plants or nuclear plants
- Home-dimension: modern wind turbines can be used for individual houses, especially for the ones located in isolated locations, where electrical grids would not be easy to set. In this case families save a huge amount of money, avoiding bills and helping the fight against climate change and global warming. In the same way, these machines can be used to provide energy to commercial or office building and the installation is reversible
- No generation of harmful gasses (unlike other solutions), so it's an environmental-friendly solution
- Wide range of solutions and different output capacities according to the situation: we have small wind turbines more suitable for single houses energy production, wind turbines that take advantage of a specific wind direction or not, offshore or onshore configuration and so on. The wide range of solutions make them extremely useful for almost every possible situation spacing from residential to commercial or industrial requirements

Studies performed in 2010 by Jha et al. [44] predicted that by 2020 the wind turbine technology would have provided the 10% of world's electricity. Even if we haven't reached such level (especially because of the SARS-COV-2 pandemic), according to the 2020 annual report of the International Energy Agency – IEA [38] the percentage amounts to 6% (see Figure A.2). So the forecasts are pretty comforting for the next years.

How do wind turbines work, briefly? Wind turbines' working principle is based on the conversion of wind kinetic energy into mechanical power that permits blades movement and the running of an electrical generator: the energy flow is reversed compared to an electrical fan. Moreover, several aspects are refined in order to maximize the energy extracted from the wind (i.e. blade tapering, pitch control and so on). The possible usages of the power generated are extremely diversified, some of them are the following:

- Pumping water
- Driving AC induction motors to produce electricity

- Desalinating seawater (especially in coastal areas that lack fresh water)
- Crop irrigation
- Food production (grinding grain, like old windmills)

A.1.3. Historical references

There are ancient proofs of wind energy exploitation along history, some even dated 5000 BCE that testimony its usage to propel boats as well as powering furnaces through monsoon winds in 300 BCE by the Sinhalese in Sri Lanka. Major evidences of wind energy usage have been found also in Chinese and Persians by 200 BCE: the first ones used wind machines for water pumping while the second ones to grinding grains, both activities accomplished in the same manner even in the modern era. Another relevant historical proof comes again from Persia, with the famous *Persian windmill* or *Panemone Windmill* in Figure A.3 firstly described around AD 900: it's a drag-driven windmill with a vertical axis (we would call it a Savonius rotor today). In

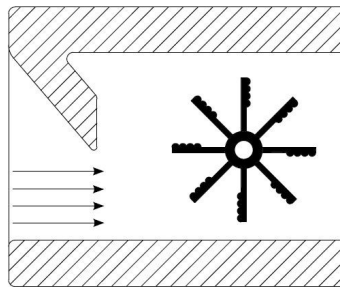


Figure A.3: Visualization of the Persian windmill. From [91]

Europe the usage of windmills started in the early part of 12th century especially in the north-western Europe. One of the most famous is certainly the Dutch windmill in Figure A.4. Here we can see that the axis changed from vertical to horizontal, exploiting the lift and not the drag effect generated by the flow. This was a huge technological development. This concept survived for several centuries and at its peak, over 100000 of them

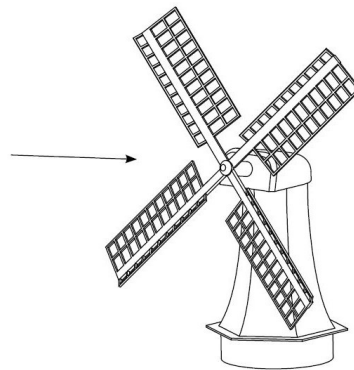


Figure A.4: Dutch windmill. Image from [91]

where located across Europe and not only in Netherlands, where, of the 10000 windmills in use around 1850, 1000 are still standing and have become also tourist sites (data from [105]). The oldest windmill that still operates is located in Britain at Outwood, Surrey and was built in 1665 (Figure A.5a). The Jack and Jill mills (1821 and 1866) located in Clayton, Sussex (Figure A.5b) are also extremely famous also thanks to a cinema appearance in the movie *The Black Windmill*. All the three were designed for corn grinding.

However these machines had several problems: they had to be manually controlled with relevant maintenance and continuous need of replacement of specific components. We can conclude that their efficiency was poor. First windmills designed to produce electricity firstly appeared during 18th century and we have several evidences:



Figure A.5: (A.5a) Outwood mill, Surrey (A.5b) Jack (Black) and Jill (White) mills at Clayton, West Sussex

- In the United States the *Brush turbine* was developed, a horizontal axis wind turbine (HAWT) in 1883 (Figure A.6a)
- In 1887 in Scotland the first vertical axis wind turbine (VAWT) to produce electricity was designed, the so-called *Blyth turbine* (Figure A.6b).
- In Denmark, always in 1887, we have the *la Cour turbine*, a HAWT (Figure A.6c).

A huge development of large windmill turbines followed in Netherlands by the 1890.

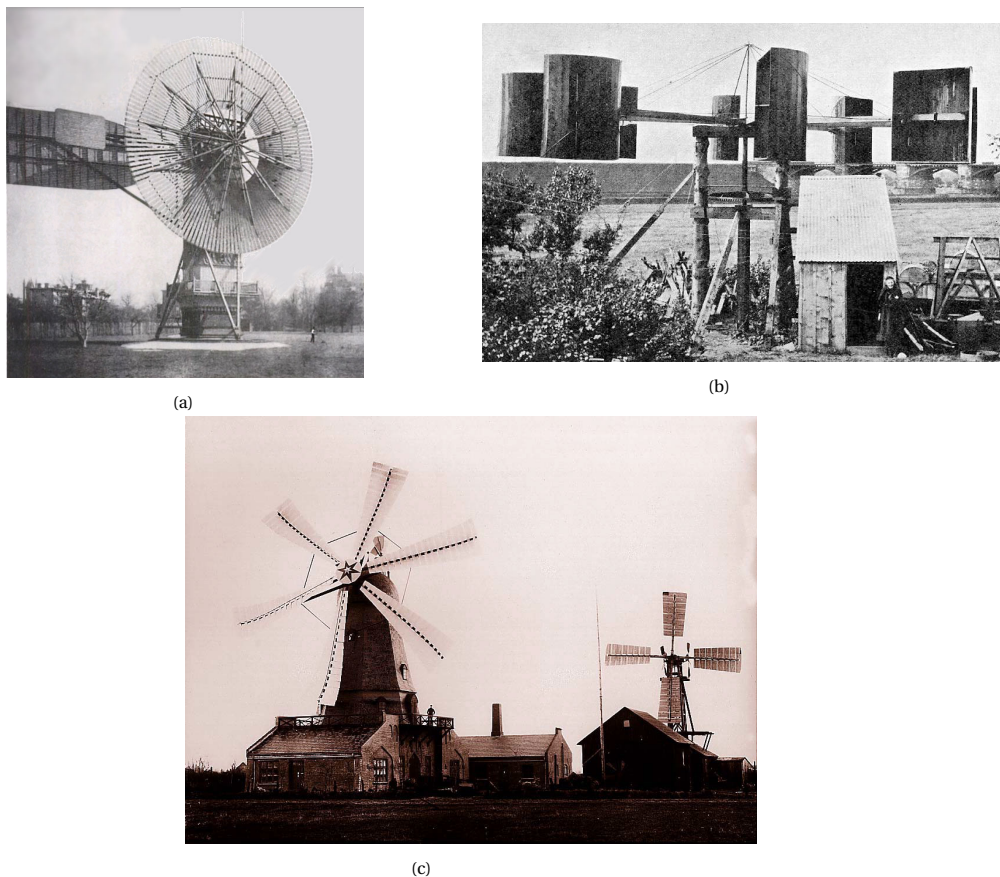


Figure A.6: (A.6a) Brush turbine, (A.6b) and (A.6c) la Cour turbine

During 1900-1940, larger and more efficient wind turbines were built, increasing the electric power output (> 100 kW but < 1 MW), over several countries (Germany, Russia and U.S.). During this century turbines were

firstly designed as power generation units and no longer as water pumping or milling applications. With the assistance from Marshall Plane in US during the post war and some minor developments were accomplished:

- The first high-capacity wind turbines were manufactured by General Electric in the US and by Mitsubishi in Japan,
- Thanks to Marshall Plan and post war funding, a 200 kW three bladed turbine was installed on the island of Gedser, in Denmark (1956-1957). This turbine is still nowadays considered as the starting point for modern wind turbine design development.

However, these were only small steps since the fall of oil prices after World War II reduced the interest in wind energy. The major push came from the oil price uncertainty during the 1970 decade due to the Yom Kippur War and the 1979 oil crisis. During this period, we have seen unprecedented developments, with several issues concerning rotor blade technologies studied and fixed introducing newer and newer solutions. Steel and aluminium rotors were studied and discarded, since the first one was too heavy and the second one suffered major fatigue problems. Wood as well, light and extremely resistant to bending effect, was tested and its moisture stabilisation weak point was solved using wood-epoxy to construct both small and large wind turbines. Later on, the fibreglass polyester, glass composite and so on were introduced and so on, now superseded by modern materials.

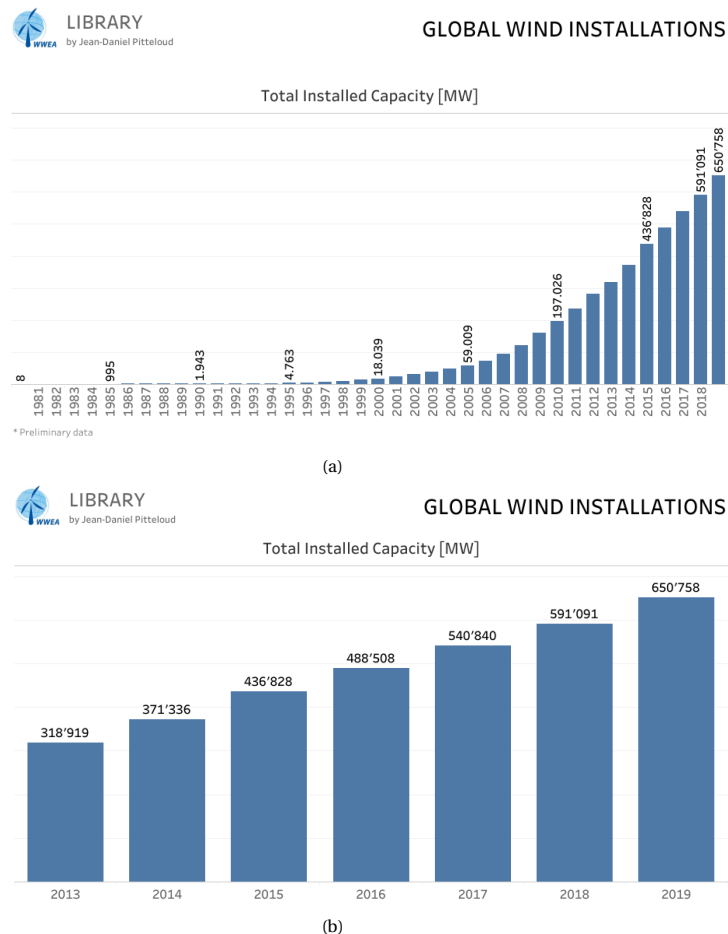


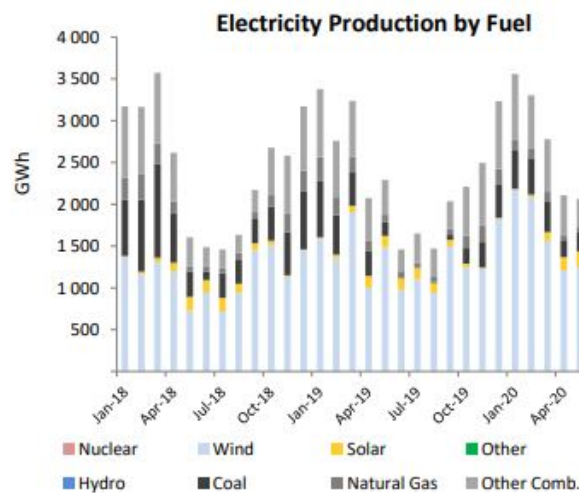
Figure A.7: Wind turbine installed capacity all over the world during the last 40 years (A.7a) and the last 7 (A.7b). Data from World Wind Energy Association – WWEA. Online source: <https://wwindea.org/world-wind-capacity-at-650-gw/>

The seventies and eighties were the years of design development and evolutions: VAWTs vs HAWTs, two-bladed vs three-bladed, upwind rotor or downwind rotor, geared vs direct drive configurations and so on. Many times the reliability of this prototypes was extremely poor and we witnessed failure after failure (due to erroneous designs or manufacturing), with machines that even operated for only a small bunch of hours before catastrophically stopping, but always contributing in gaining knowledge in wind energy field. Among

these mistaken prototypes, the Danish Gedser turbine was one that did not suffer such problems nor needed frequent maintenance and for this reason it became the forerunner of modern wind turbines. Denmark in fact, during 1970s and 1980s, had distinguished for its development in wind technology due to the public pressure of developing renewable energy sources due to the lack of natural local ones, but avoiding nuclear solutions. Other nations contributed to wind electrical power generation expansion during those years, especially Germany and United States (General Electric investigated several transversal aspects which would have essential in the following years), but a general increased interest is also attributed to the increase in demand for and consumption of energy because of the rise of world population and the development of emerging nations (China, India and Brasil). For example in California during 1980s a series of investments and tax credits helped the wind energy market, with the installation of wind turbines for 1700 MW of wind capacity, even if many of the machine used where erroneously designed and suffered failures. This contributed to the creation of a poor image for the wind industry. However this investments plan contributed to European export increase, developing and testing newer and newer technologies that would have redeemed the project in the following years. Considering the growth of the recent years, especially in terms of MWs installed in the planet (see Figure A.7a and A.7b), it is expected that wind energy power generation will continue its growth, spreading more and more across the world and becoming the main alternative to oil and fuels as source of power but at a lower coast.

	2019	
	GWh	share
CONVENTIONAL THERMAL	11 164	39.5%
Coal	2 983	10.5%
Oil	218	0.8%
Natural Gas	1 702	6.0%
Combustible Renewables	5 550	19.6%
Other Combustibles	711	2.5%
Nuclear	-	-
Hydro	16	0.1%
Wind	16 150	57.1%
Solar	963	3.4%
Geothermal	-	-
Other Renewables	-	-
Non-Specified	-	-
RENEWABLES	22 679	80.2%
NON-RENEWABLES	5 614	19.8%
TOTAL NET PRODUCTION	28 293	
+ Imports	15 982	
- Exports	10 171	
= ELECTRICITY SUPPLIED	34 105	
- Used for pumped storage	-	
- T&D Losses	2 042	
= ELECTRICITY CONSUMED	32 063	

(a)



(b)

Figure A.8: Denmark data: (A.8a) electricity production by sources (A.8b) GWh produced during the period January 2018 - April 2020. Source [39]

A.1.4. Wind turbines' usage across the world

Several countries are more and more interested in using wind turbines especially to produce energy at a lower cost and avoid the necessity of buying fuel fossils from other countries. On account of that let's proceed with an analysis focused on where wind turbines are most spread and used across the world in order to understand which nations in the modern society are more interested in the development of this renewable energy source.

Denmark

Denmark has been a pioneer in wind turbines development during the last fifty years: trying to reach independence from fuel fossils, several large wind farms were built especially offshore. Recently, some projects aimed to upgrade the turbines in the farms with newer ones which could improve the energy extracted as well as the efficiency, exploiting recent technologies: at the same time, old machines are dismantled and sold to other countries. According to the current data, more than 40% of electrical energy is generated using wind turbines and the government prepared measures to stimulate wind turbines installations also on private properties like offices, houses and similar. The goal is to definitely reach the energetic autonomy without

using others power sources except for wind turbines and other renewables. At the moment, Denmark obtains at least 45% of electrical energy from wind farms, therefore is able to provide electricity at a lower cost and avoiding greenhouse effect as well as the production of polluting gasses. Some data related to the percentage of electricity produced by sources in Denmark are reported in Figure A.8a and A.8b.

To have a better idea about the importance of wind turbines and wind energy in Denmark, Figure A.9 is a map that shows the location of almost each wind turbine in the nation.

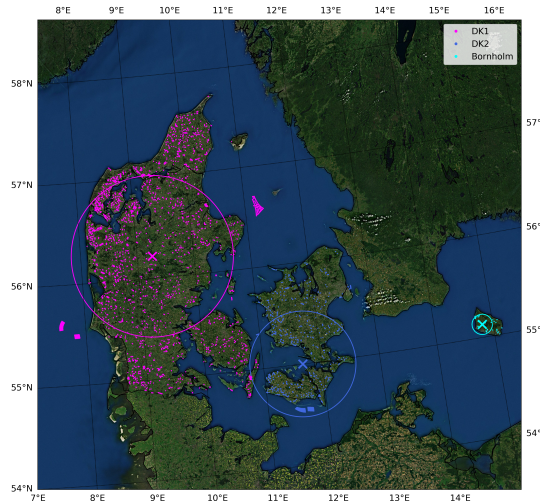


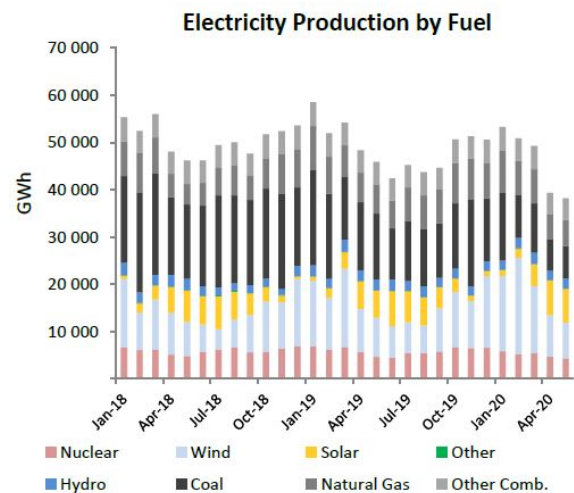
Figure A.9: Each dot corresponds to a wind turbine site

Germany

Germany is one of the most advanced country in the world in the development of wind turbine technology and represents the world's largest market for wind energy. Especially during the twentieth century's second part, we've observed a constant increase in turbines' capacity installed here, starting from 10 kW plants (1936) up to even 3 MW in the last years, with towers exceeding 140 m in height.

	2019	
	GWh	share
CONVENTIONAL THERMAL	318 151	54.2%
Coal	172 439	29.4%
Oil	4 725	0.8%
Natural Gas	87 812	15.0%
Combustible Renewables	46 897	8.0%
Other Combustibles	6 277	1.1%
Nuclear	70 983	12.1%
Hydro	25 901	4.4%
Wind	123 606	21.0%
Solar	47 517	8.1%
Geothermal	170	0.0%
Other Renewables	-	-
Non-Specified	992	0.2%
RENEWABLES	244 092	41.6%
NON-RENEWABLES	343 228	58.4%
TOTAL NET PRODUCTION	587 320	
+ Imports	40 123	
- Exports	72 792	
= ELECTRICITY SUPPLIED	554 651	
- Used for pumped storage	8 178	
- T&D Losses	26 548	
= ELECTRICITY CONSUMED	519 925	

(a)



(b)

Figure A.10: Germany data: (A.10a) electricity production by sources (A.10b) GWh produced during the period January 2018 - April 2020. Source [39]

However, interest in offshore sites has increased since the number of optimum sites on land has decreased; favourite offshore sites are in the North Sea and the Baltic Sea, due to their optimal wind energy levels, that are constant throughout the year, and the lower environmental impact. In 2010 the goal was to

reach a wind power capacity of at least 15000 MW by 2020, but the expectations have been far exceeded since the actual capacity amounts to 25000 MW and more than 21000 wind turbines installed, with an expected growth rate of 2000 MW addition each year; by 2030 a similar capacity (20000-25000 MW) is expected to be extracted from offshore sites only, with at the same time a repowering of onshore sites with newer technologies.

China

China increased its interest in wind energy during the last thirty years with the installation of several wind turbines in the Gobi Desert, an optimal location due to the high winds speed present throughout the year. Another site which has grabbed China's interest, is the Tibet region, where open lands with high wind speed are extremely suitable for wind turbines installation. Most of these turbines are connected to utility power grid systems to continuously provide electrical energy to population and since China's population counts for 1.4 billion it's absolutely relevant to assure the minimal cost and high reliability.

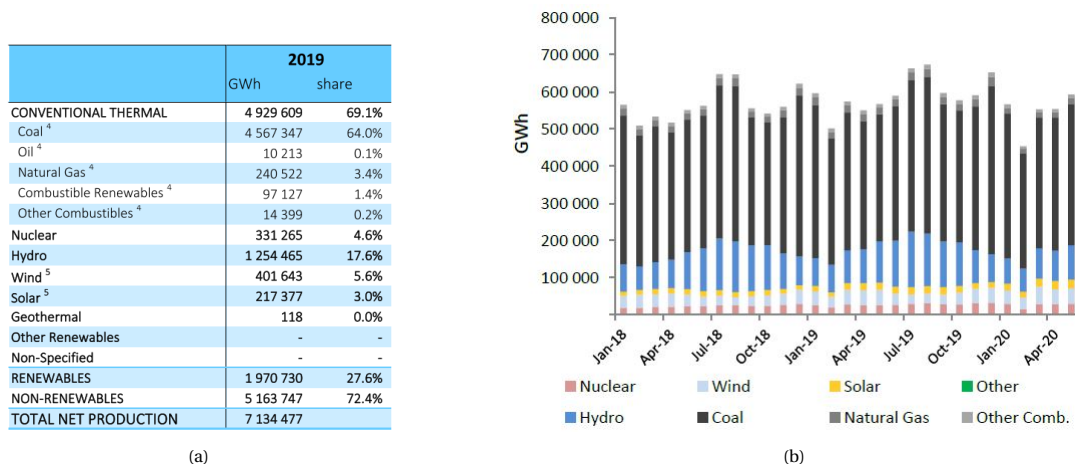


Figure A.11: China data: (A.11a) electricity production by sources (A.11b) GWh produced during the period January 2018 - April 2020. Source [39]

United States of America

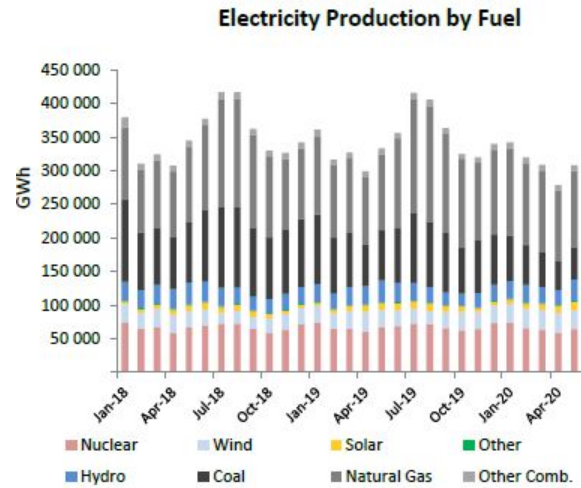
United States is the world's greatest consumer of electricity, however the higher amount of it comes from non-renewable sources like coal, natural gasses and similar. Only the 0.15% comes from wind turbines but this technology is experiencing a rapid growth rate, since many states want to avoid high costs fossil fuels and produce energy at a lower cost. Most of the turbines in US are located near coastal regions both western (California, Oregon, Washington...) and eastern (Vermont, Maine, Massachusetts...). Alongside these primary plants, there are many others spread across the country:

- Coastal regions of Alaska are extremely suitable for wind energy extraction due to the strong wind present throughout the year
- In several flat rural lands, like Montana, Kansas, Oklahoma, Texas, North and Sud Dakota wind turbines operate at minimal cost with different operational goals
- In high-speed regions like North Carolina, New York, Connecticut, wind turbines are used for residential applications. In fact, several US companies are specialized in small scale wind turbines (from 10 to 100 kW) to meet citizens demands. But as we know, wind turbines can provide energy even in isolated or less densely inhabited regions, that's why even citizens Montana, Wyoming and Appalachian Mountains states are interested in these products.

The capacity has increased up to several MW during the last years (more than 5) as well as the overall capacity with counted for 18000 MW at the end of 2005 and more than 25000 MW at the end of 2008. However, due to the amount of energy production in US, wind farms would cover near 750000 square miles in order to meet the total electricity requirements for this Nation. That would mean the area of Florida, Texas,

	2019	
	GWh	share
CONVENTIONAL THERMAL	2 641 607	63.5%
Coal	997 975	24.0%
Oil	33 903	0.8%
Natural Gas	1 540 929	37.0%
Combustible Renewables	59 007	1.4%
Other Combustibles	9 793	0.2%
Nuclear	809 070	19.4%
Hydro	294 530	7.1%
Wind	300 089	7.2%
Solar	96 195	2.3%
Geothermal	15 492	0.4%
Other Renewables	-	-
Non-Specified	4 497	0.1%
RENEWABLES	765 312	18.4%
NON-RENEWABLES	3 396 166	81.6%
TOTAL NET PRODUCTION	4 161 478	
+ Imports	59 052	
- Exports	20 008	
= ELECTRICITY SUPPLIED	4 200 523	
- Used for pumped storage	26 033	
- T&D Losses	224 697	
= ELECTRICITY CONSUMED	3 949 792	

(a)



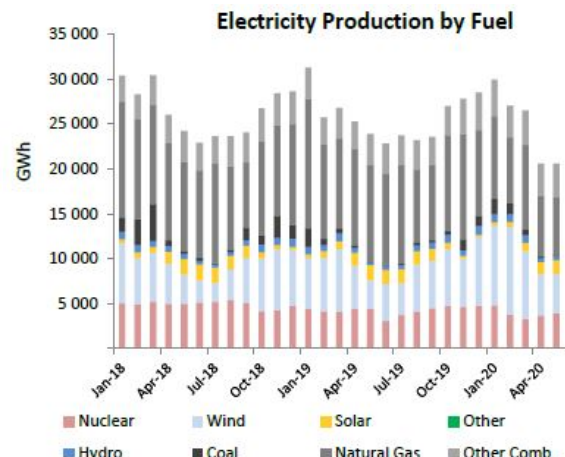
(b)

Figure A.12: US data: (A.12a) electricity production by sources (A.12b) GWh produced during the period January 2018 - April 2020. Source [39]

Montana and California combined. However the expectation is to supply the 20% of the total electricity of the country with wind turbines by 2030 especially because there are several interesting sites where turbine's installation could lead to great results and high production in contrast with the actual near 10% of total electricity produced. Absolutely thrilling is what happen in the small-town Rock Port, Missouri, that has become the first city in US to meet all the energetical requirements by using only wind turbines, even if the population amounts to only 1300 inhabitants.

	2019	
	GWh	share
CONVENTIONAL THERMAL	174 277	56.3%
Coal	7 326	2.4%
Oil	991	0.3%
Natural Gas	126 155	40.7%
Combustible Renewables	34 813	11.2%
Other Combustibles	4 992	1.6%
Nuclear	51 032	16.5%
Hydro	7 576	2.4%
Wind	64 134	20.7%
Solar	12 677	4.1%
Geothermal	-	-
Other Renewables	13	0.0%
Non-Specified	-	-
RENEWABLES	119 213	38.5%
NON-RENEWABLES	190 496	61.5%
TOTAL NET PRODUCTION	309 709	
+ Imports	24 556	
- Exports	3 385	
= ELECTRICITY SUPPLIED	330 880	
- Used for pumped storage	2 360	
- T&D Losses	26 070	
= ELECTRICITY CONSUMED	302 449	

(a)



(b)

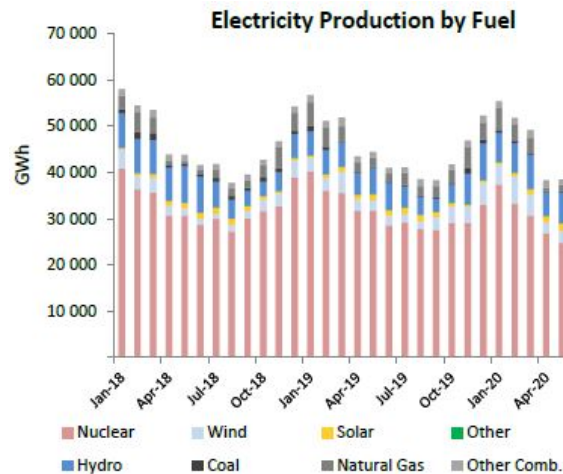
Figure A.13: United Kingdom data: (A.13a) electricity production by sources (A.13b) GWh produced during the period January 2018 - April 2020. Source [39]

United Kingdom

U.K. has been one the pioneer states for wind energy development, especially during 20th century's second half, with a particular attention in wind farms located in coastal regions. In fact there are several powerful offshore sites blessed with strong winds, where wind farms have been constructed (Scotland and England's western coastal regions as well as English Channel). Several projects have constantly been proposed during the years, with the goal of realizing plants with high power ratings like the one near Llanbrynmair in Powys,

	2019	
	GWh	share
CONVENTIONAL THERMAL	58 888	10.8%
Coal	6 101	1.1%
Oil	6 133	1.1%
Natural Gas	36 078	6.6%
Combustible Renewables	8 188	1.5%
Other Combustibles	2 388	0.4%
Nuclear	379 870	69.4%
Hydro	61 376	11.2%
Wind	34 648	6.3%
Solar	11 357	2.1%
Geothermal ⁴	117	0.0%
Other Renewables	474	0.1%
Non-Specified	659	0.1%
RENEWABLES	116 159	21.2%
NON-RENEWABLES	431 229	78.8%
TOTAL NET PRODUCTION	547 388	
+ Imports	15 593	
- Exports	73 352	
= ELECTRICITY SUPPLIED	489 629	
- Used for pumped storage	6 327	
- T&D Losses	39 849	
= ELECTRICITY CONSUMED	443 452	

(a)



(b)

Figure A.14: France data: (A.14a) electricity production by sources (A.14b) GWh produced during the period January 2018 - April 2020. Source [39]

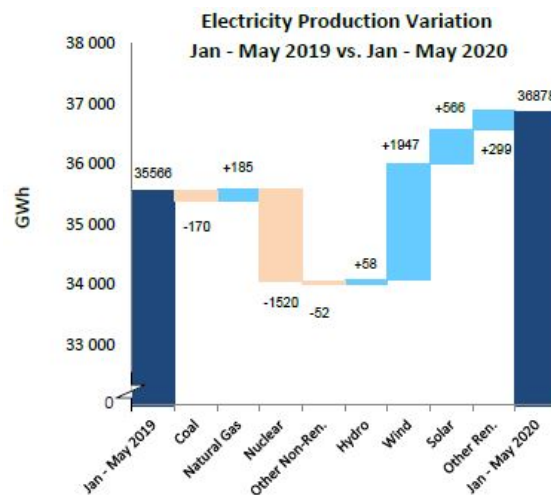
Wales, that generates about 400 MW using the newest technologies in wind turbines field.

France

Atlantic French region, as well as the northern coastal regions are extremely suited for wind farms. Here the interest in wind energy has always been high, with the development of high-power output turbines since the beginning, in order to demonstrate a valuable alternative to foreign oil. Especially 1973 oil crisis has given an additional push to this field. Even if slowly, France is adding more and more wind turbines in specific locations where stronger winds are present.

	2019	
	GWh	share
CONVENTIONAL THERMAL	33 507	37.4%
Coal	2 434	2.7%
Oil	26	0.0%
Natural Gas	24 729	27.6%
Combustible Renewables	4 987	5.6%
Other Combustibles	1 332	1.5%
Nuclear	41 359	46.1%
Hydro	1 147	1.3%
Wind	9 369	10.4%
Solar	3 919	4.4%
Geothermal	-	-
Other Renewables	-	-
Non-Specified	408	0.5%
RENEWABLES	19 421	21.6%
NON-RENEWABLES	70 288	78.4%
TOTAL NET PRODUCTION	89 709	
+ Imports	12 735	
- Exports	14 589	
= ELECTRICITY SUPPLIED	87 855	
- Used for pumped storage	1 162	
- T&D Losses	4 472	
= ELECTRICITY CONSUMED	82 220	

(a)



(b)

Figure A.15: Belgium data: (A.15a) electricity production by sources (A.15b) GWh produced during the period January 2018 - April 2020. Source [39]

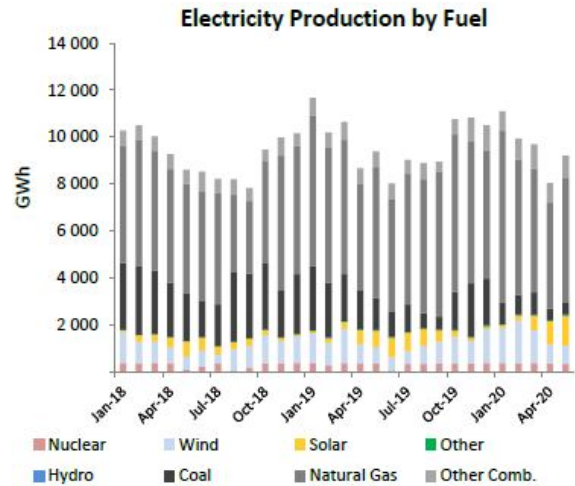
Belgium and The Netherlands

Thanks to high winds during the whole year, both coastal regions of Belgium and The Netherlands are ideal location for wind turbines installation. During the last seventy years, many wind turbines spacing from small

scale turbines to utility scale wind turbines where installed. In The Netherlands, particular interest has been given towards small scale ones, for residential applications.

	2019	
	GWh	share
CONVENTIONAL THERMAL	96 489	82.1%
Coal	19 274	16.4%
Oil	1 353	1.2%
Natural Gas	68 634	58.4%
Combustible Renewables	5 413	4.6%
Other Combustibles	1 815	1.5%
Nuclear	3 749	3.2%
Hydro	74	0.1%
Wind	11 508	9.8%
Solar	5 159	4.4%
Geothermal	-	-
Other Renewables	-	-
Non-Specified	547	0.5%
RENEWABLES	22 155	18.9%
NON-RENEWABLES	95 371	81.1%
TOTAL NET PRODUCTION	117 526	
+ Imports	20 403	
- Exports	19 548	
= ELECTRICITY SUPPLIED	118 381	
- Used for pumped storage	-	
- T&D Losses ⁴	5 731	
= ELECTRICITY CONSUMED	112 650	

(a)



(b)

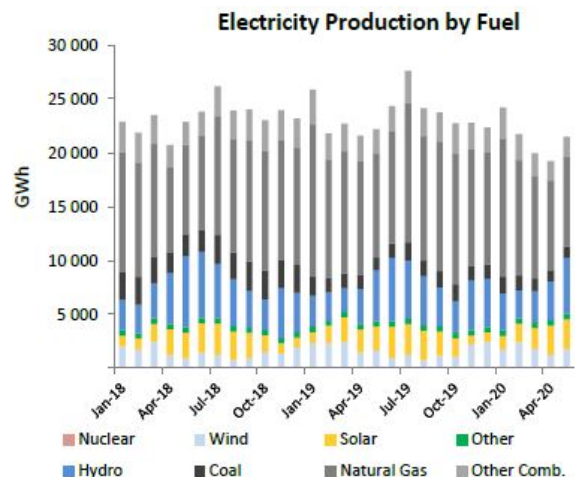
Figure A.16: The Netherlands data: (A.16a) electricity production by sources (A.16b) GWh produced during the period January 2018 - April 2020. Source [39]

Italy

Even with several coastal regions that could suit turbine’s installation requirement, Italy is not considered an ideal location for large wind farms due to the fact a large part of the population is concentrated in coastal regions. Moreover, during the last part of the 20th century, the technology has not achieved a substantial development due to the availability of cheap oil from Libya that led to a substantial indifference towards wind energy. A little push has been given by oil crisis in 1973 and the consequential installation of low capacity wind turbines.

	2019	
	GWh	share
CONVENTIONAL THERMAL	185 146	65.7%
Coal ⁵	17 134	6.1%
Oil ⁵	10 381	3.7%
Natural Gas ⁵	136 990	48.6%
Combustible Renewables ⁵	18 269	6.5%
Other Combustibles ⁵	2 373	0.8%
Nuclear	-	-
Hydro	46 955	16.7%
Wind	20 054	7.1%
Solar	23 313	8.3%
Geothermal	5 658	2.0%
Other Renewables	-	-
Non-Specified	612	0.2%
RENEWABLES	114 249	40.6%
NON-RENEWABLES	167 490	59.4%
TOTAL NET PRODUCTION	281 738	
+ Imports	43 980	
- Exports	5 817	
= ELECTRICITY SUPPLIED	319 901	
- Used for pumped storage	2 412	
- T&D Losses ⁴	18 578	
= ELECTRICITY CONSUMED	298 911	

(a)



(b)

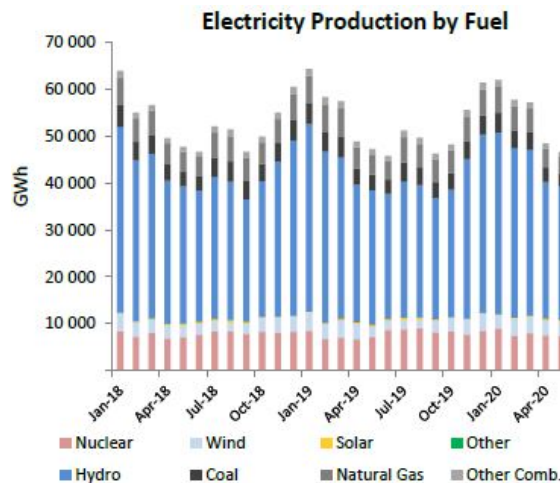
Figure A.17: Italy data: (A.17a) electricity production by sources (A.17b) GWh produced during the period January 2018 - April 2020. Source [39]

Canada

As for United States, the most relevant sites for wind turbines installation are the coastal regions, both the western and the eastern one as well with a few more located in northern Canada. These are optimal sites due to the high wind speed present, however the last ones are less exploited due to the difficulties related to the extreme environment. Moreover, here wind energy has not experienced a interest similar to other nations (Denmark, Germany. . .), in fact wind turbines were installed only in the late 20th century with low capacity and that's why only 0.1% of electrical production comes from wind turbines in Canada. However, during the last years an increasing interest has developed in wind turbines for residential applications.

	2019	
	GWh	share
CONVENTIONAL THERMAL	123 037	19.4%
Coal ⁴	45 570	7.2%
Oil ⁴	5 760	0.9%
Natural Gas ⁴	61 569	9.7%
Combustible Renewables ⁴	10 051	1.6%
Other Combustibles ⁴	88	0.0%
Nuclear	95 461	15.0%
Hydro	378 127	59.6%
Wind	33 840	5.3%
Solar	4 175	0.7%
Geothermal	-	-
Other Renewables	1	0.0%
Non-Specified	169	0.0%
RENEWABLES	426 194	67.1%
NON-RENEWABLES	208 617	32.9%
TOTAL NET PRODUCTION	634 811	
+ Imports	13 369	
- Exports	60 376	
= ELECTRICITY SUPPLIED	587 804	
- Used for pumped storage ⁴	210	
- T&D Losses ⁴	34 606	
= ELECTRICITY CONSUMED	552 988	

(a)



(b)

Figure A.18: Canada data: (A.18a) electricity production by sources (A.18b) GWh produced during the period January 2018 - April 2020. Source [39]

Russia

The first wind turbines were installed in the Soviet Union in 1931. However the infinite amount of fuel fossils, coal, oil and similar has always overshadowed the necessity of developing alternative power sources. The data at disposal are limited, but according to published reports, wind turbines are mainly located in northern and southern regions, with capacity up to 5 MW. By the way, the main source for electricity production remains oil.

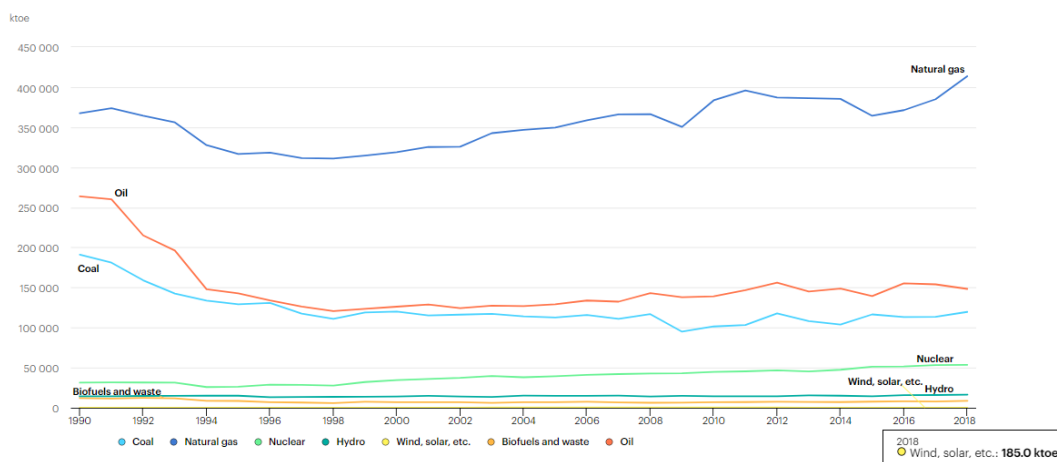


Figure A.19: Russia data available. Total energy supply by source in kilotonne of oil equivalent (ktoe), 1 toe = 11.63 MWh. Source from IEA (International Energy Agency) <https://www.iea.org/countries/russia>.

A.1.5. All that glitters ain't gold: disadvantages and environmental issues

Despite all the benefits cited, wind turbines have some major problems and disadvantages that need to be taken into account. The main issues are the following ones:

1. Installation, maintenance and costs
2. Noise pollution
3. Harmful interactions with fauna
4. Interferences with radio signals

Each one of these aspect is discussed separately.

A.1.5.1. Installation, maintenance and costs

One of the most difficult aspects when dealing with wind turbines is the definition of the installation site. This decision is affected by several aspects (even the others cited in the previous list) and is a critical one: first of all both the topographical and meteorological condition have to be taken into account. Studying both these aspects means additional costs, as well as necessity of more time to accomplish the related studies. The topographical aspects have huge relevance because of the shear exerted from the terrain on the flow. This reduces the intensity of wind speed near the surface and so the power extracted by a turbine located here. For this reason is extremely important to reach the higher layers of this region, because the wind speed increases and so the power extracted. The shear depends on the surface properties, so the range of possible conditions is extremely large: trees, buildings, desert regions, they all affect the flow in different ways. A possible solution to adapt the site to the installation is modifying the terrain both to increase the wind intensity experienced by the turbine and maximize the power extraction as reported in Figure A.20

Obviously such operations have a relevant cost and cannot always be carried on so easily for example in regions with rocky terrain, near the coasts or in regions with high hydro geological risk. Data related to meteorological conditions needs to be collected over a certain amount of time in order to understand the intensity of the wind at that location. This way is possible to understand the main wind direction which is relevant when considering turbines without yawing possibilities or wind farms. Moreover, this way is possible to figure out the achievable wind speed in the selected region: installing a wind turbine in low-wind region is not a wise choice. About a wind farm even the interaction between wind turbines has to be considered since it leads to fatigue problems and structural issues of the wind turbine. Installation and components production is (obviously) not the same for each turbine type: modern high-power wind turbines have higher costs for example. Furthermore wind turbines for urban applications, do not cost as much as the ones for wind farms. Wind speed is not even constant during the day and there are periods of time when the electricity generated is not sufficient to satisfy the demand: back-up solutions are needed as well as systems which regulate the power output of the turbine. Even this means additional costs. Moreover, maintenance operations are a relevant problem especially for horizontal axis wind turbine, where the main components are located at the top of the tower: this means working at high heights in a dangerous location (because of the mechanic components). For such operations highly qualified technicians are needed in order to solve issues or failures and to replace components. This means intensive and special training for the technicians as well as high salaries: higher costs for the company that runs the turbine or the wind farm considered. In general the cost needed for a wind turbine installation depends on several factors, like the ones cited before (maintenance, sites study, preliminary analysis, components production...) but also the design process, the tests needed and so on. Will the turbine be capable of generating enough kilowatts of electricity to justify the initial investment? A preliminary study of the costs as well as the potential electricity generated is needed as well: this is a important step of the process. Even if it's a difficult task, this way is possible to determine the economic feasibility of the project.

A.1.5.2. Noise pollution

Noise generated by wind turbines is one the greatest problems of this machines especially when dealing with old turbines. Moreover the more turbines are higher the more power is extracted and noise increases. The decibel levels reached can also produce physical pain, depending on blades' pitching especially. However the sources of noise are all the components of the turbines which are passed by the wind but their contribute

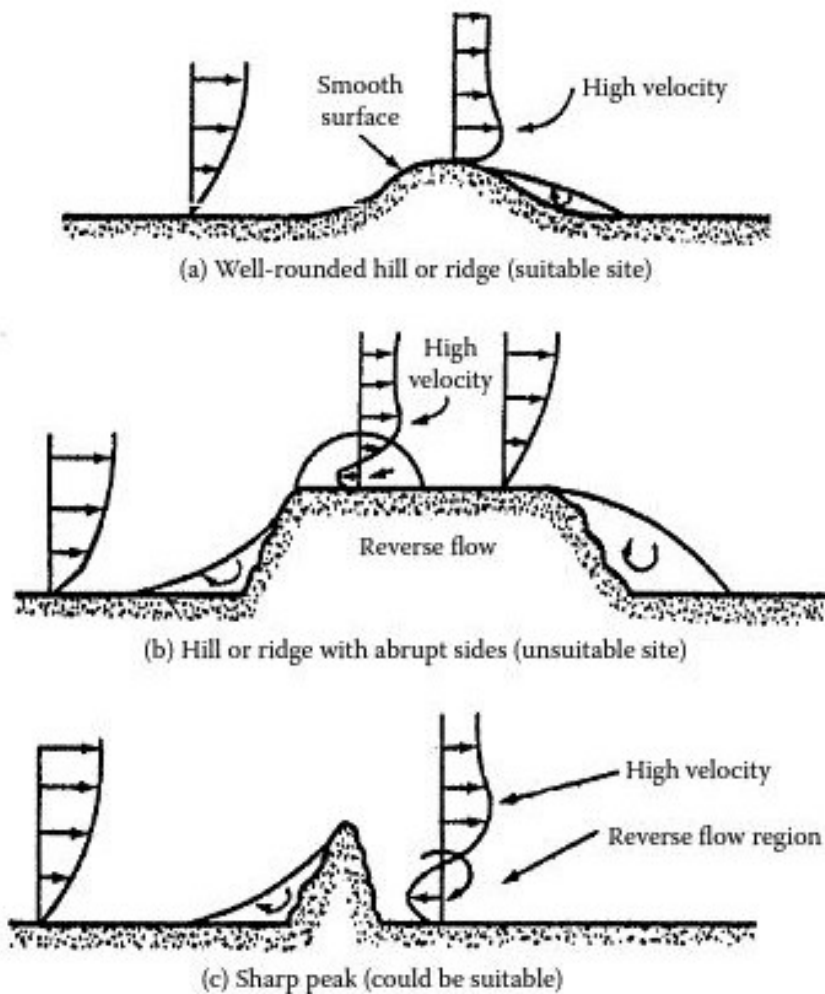


Figure A.20: How terrain modifications affect the wind speed profiles experienced by wind turbine, image from [44]

depends on their shape and their characteristic pitch. For example a two-bladed turbine will have a different noise pattern respect the one generated by a three-bladed turbine. Also the time duration over which turbine noise can be heard has to be considered. Usually cities or countries have specific regulations regarding this aspect so when deciding the installation site, this is an aspect to reckon with. However noise from wind turbines needs to be considered in a context: background noise has often the power to 'mask' the noise produced by wind turbines because it reaches higher dB. This is an aspect that has to be exploited when considering an installation site, but a more relevant target would be to reduce instead the total noise for residents near a wind turbine's site. Unfortunately predicting the dB levels near wind turbines is not easy because of the unpredictable conditions. However some methods has been proposed during the last years, like the one in [44]. A possible solution is selecting the installation sites away from cities or residential areas, this is one of the reason that has led to the creation of offshore sites. Other solutions are based on aeroacoustic studies of wind turbines in order to identify the main sources of noise and propose structural additions or modifications of these parts to reduce the dB levels. This is a solution similar to what has been done with planes' nacelles.

A.1.5.3. Harmful interactions with fauna

Wind turbines represent a relevant danger for birds flying at low altitudes as well as a substantial disturbance of the ecology near wind turbine's site. So when deciding the installation site it's extremely relevant to analyse the local fauna and avoid places where birds nest especially when they are endangered species. A recent study by the Norwegian Institute for Nature Research [63] proposed an innovative solution to avoid birds' death when moving through wind turbines. It is based on painting with black varnish part of one of the blades (as seen in Figure A.21. This way the annual fatality rate was significantly reduced at the turbines with

a painted blade by over 70% unlike what happens for wind turbines without blades painted. However this solution is not totally validated yet and it may lead to problems related to bird's migration.



Figure A.21: Black paint on a wind turbine blade, image from [63]

Moreover, especially when considering wind turbines located in rural areas, residents are not so keen on the installation of them because they are considered harmful for the nature responsible of spoiling the visual appearance of rural locations.

A.1.5.4. Interferences with radio signals

Wind turbines produce adverse effects on electronic radio and television signals. This is true especially for turbines with metallic rotor blades which are the oldest. Modern wind turbines are mainly made of wood, plastic and especially fibreglass. Electronic interferences have been experienced in the past especially in regions where radio signals were weak (remote regions), however with modern satellites and radio stations, the harmful influence of wind turbines on signals receiving has substantially disappeared.

B

Derivation and deep analysis of turbine models and wake models

In this appendix more details about methods briefly described in Chapter (2) are given in order to realize a compilation of all the existing models.

B.1. Turbine modeling for HAWTs

B.1.1. Blade element momentum theory - BEM

As discussed before, BEM is the basis for many existing models (actuator line, actuator surface and so on). It is based on equating the momentum balance along freestream direction and the predictions of the flow around the blades. This way is possible to find expressions for the induction factors a and a' . Then a loop calculation starts in order to evaluate the normal and tangential force coefficients for each of the annular elements considered when dividing the blades in sections.

The loop calculation is the basis of this model and can be summarized in the following points:

1. a and a' are set to the initial value of 0
2. evaluation of the flow angle ϕ knowing the freestream speed V_∞ and the rotational velocity:

$$\tan \phi = \frac{(1 - a) V_\infty}{(1 + a') \Omega r} \quad (\text{B.1})$$

3. evaluation of the correction factor F due to the finite number of blades:

$$F = \frac{2}{\pi} \frac{1}{\cos(e^{-f})} \quad (\text{B.2})$$

$$f = \frac{B}{2} \frac{R - r}{r \sin \phi} \quad (\text{B.3})$$

4. evaluation of the angle of attack by keeping into account the flow angle ϕ and the θ_p :

$$\alpha = \phi - \theta_p \quad (\text{B.4})$$

5. evaluation of the C_l and C_d from tables by knowing α
6. evaluation of the normal and tangential force coefficients C_n and C_t

$$C_n = C_l \cos \phi + C_d \sin \phi \quad (\text{B.5})$$

$$C_t = C_l \sin \phi - C_d \cos \phi \quad (\text{B.6})$$

7. evaluation of the induction factors (where $a_c \approx 0.2$):

$$\begin{cases} a = \frac{1}{\frac{4F \sin^2 \phi}{\sigma C_n} + 1} & a < a_c \\ a = \frac{1}{2} \left[2 + K(1 - 2a_c) - \sqrt{(K(1 - 2a_c) + 2)^2 + 4(Ka_c^2 - 1)} \right] & a > a_c \end{cases} \quad (\text{B.7})$$

$$a' = \frac{1}{\frac{4F \sin \phi \cos \phi}{\sigma C_t} - 1} \quad (\text{B.8})$$

8. depending on the difference between the induction factor evaluated at point 1 and 7, the loops starts again from point two or the calculation ends

9. summing the values obtained for each annular element is possible to evaluate the general force exerted on the flow

As stated before this model can be coupled with other models that provide the induction factors.

B.1.2. Actuator line model for HAWTs

The model is based on the assumption that blades are represented by lines which are divided in a certain number of elements, whose cross-section is reported in Figure 2.16. The generic element is located at radius r and V_t is the tangential velocity, while V_n is the normal velocity. Using these parameters is possible to introduce the local velocity relative to the rotating blade:

$$V_{rel} = (V_t - \Omega r, V_n) \quad (\text{B.9})$$

Introducing the pitch angle θ_p and the angle between V_{rel} and the rotor plane, ϕ , the two-dimensional force is:

$$f_{2D} = \frac{dF}{dr} = \frac{1}{2} \rho V_{rel}^2 c (C_L e_L + C_D e_D) \quad (\text{B.10})$$

e_D and e_L are the unit vectors in the directions of lift and drag, c is the chord, C_L and C_D are the lift and drag coefficient respectively which depend on the Reynolds' number and the angle of attack. They are determined using the tabulated data cited before, which are derived by wind tunnel tests or numerical 2D test (they are then corrected to account for 3D effects). To extract the value of the forces it is necessary to provide to the tables the angle of attack experienced by each element. In its calculation also the induced velocity displays a role: it is provided by the numerical calculation (or any other possible way) and contributes in the angle of attack calculation. Once the correct expression for the forces acting on the blades is obtained, it is introduced in the governing equations and everything starts again, since the induced velocity needs to be evaluated again. Most of the times a *regularization kernel* η is applied to the force values obtained. Its expression is described as:

$$\eta_\varepsilon(r) = \frac{1}{\varepsilon^3 \pi^{\frac{3}{2}}} e^{-\left(\frac{r}{\varepsilon}\right)^2} \quad (\text{B.11})$$

Where ε is a constant that can be expressed in different ways. The distance between the initial force points on the rotor and the measured point is expressed as r . In reality, η_ε is useful to distribute the loading on more mesh points and not just one. This way is possible to avoid the presence of step gradients in the mesh and smooth the calculation, in order to overcome potential numerical problems.

B.1.3. Actuator surface model for HAWTs

Based for example on the following set of equations for an incompressible case (most common case for wind turbines):

$$\nabla \cdot \vec{V} = 0 \quad (\text{B.12})$$

$$\rho \left(\frac{\partial \vec{V}}{\partial t} + (\vec{V} \cdot \nabla) \vec{V} \right) = -\nabla p + \mu \nabla^2 \vec{V} + \vec{f} \quad (\text{B.13})$$

Where \vec{V} is the velocity vector, p is the pressure, ρ the density and f the body forces that have to be modelled, the purpose of such model is to determine f value and introduce it into such equations (as for actuator line

model). The forces at each section are obtained using tabulated 2D lift and drag coefficients C_L and C_D which are then corrected to take into account 3D effects. Besides tabulated data it is also possible to use empirical expressions based on constants function of angles of attack and airfoil thickness provided by the literature, for more details check [100, 101].

$$\vec{f}_{2D} = \frac{1}{2} \rho V_{rel}^2 c (C_L \vec{e}_L + C_D \vec{e}_D) F_{dist} \quad (B.14)$$

F_{dist} is the distribution of pressure force along the chord of the blade, while \vec{e}_L and \vec{e}_D are the coordinate vectors for the forces to be projected along. So unlike actuator line theory, the forces are distributed non just along one line but several lines that create a surface, replicating the blockage experienced by the flow.

The relative velocity is computed by considering the induced velocity (evaluated with Biot Savart's law, or any other method that can provide it (as the actuator disk theory) and the local velocity, extracted from the simulation.

Once the relative velocities as well as the angles of attack are determined using velocity triangles, the forces are distributed according to a regularization function, the same reported in equation (B.11) for the actuator line theory, in order to avoid the same possible numerical problems.

B.2. Turbine modeling for VAWTs

B.2.1. Actuator cylinder

The starting point of the method is the introduction of the distributed body forces, distinguished in normal Q_n and tangential Q_t loading component. Each one of their expressions consider the number of blades and a non-dimensionalising parameter (the dynamic pressure) in equation (B.15) and (B.16). A visualization of the distribution is reported in Figure (2.22).

$$Q_n(\theta) = \frac{BF_n(\theta)}{2\pi R \rho V_\infty^2} \quad (B.15)$$

$$Q_t(\theta) = -\frac{BF_t(\theta)}{2\pi R \rho V_\infty^2} \quad (B.16)$$

Where F_t and F_n are the tangential and normal force, depending on the azimuthal angle. Introducing the turbine into the flow a certain amount of perturbations are created. Such perturbations are used to describe turbine's presence and relate the pressure jump and the velocity field. They are expressed as additional linear velocity components.

$$u = (1 + u'_x) V_\infty \quad (B.17)$$

$$v = (1 + v'_y) V_\infty \quad (B.18)$$

Where u'_x and v'_y are the perturbations. With the previous assumptions, it is possible to introduce the Euler equations (inviscid) which are used for a 2D steady and incompressible case. Then, the velocity expressions from equation (B.17) are added.

$$\frac{du'_x}{dx} + \frac{dv'_y}{dy} = 0 \quad (B.19)$$

$$\frac{du'_x}{dx} + u'_x \frac{du'_x}{dx} + v'_y \frac{du'_x}{dy} = -\frac{dp}{dx} \frac{1}{\rho V_\infty^2} + f_x \frac{1}{\rho V_\infty^2} \quad (B.20)$$

$$\frac{dv'_y}{dx} + u'_x \frac{dv'_y}{dx} + v'_y \frac{dv'_y}{dy} = -\frac{dp}{dy} \frac{1}{\rho V_\infty^2} + f_y \frac{1}{\rho V_\infty^2} \quad (B.21)$$

Where f_x and f_y are the volume force vector components. The second and third terms in both the last two equations are induced or second order forces g that can be neglected or not. Writing the equations as a Poisson type equation and solving it, equations (B.22) and (B.23) are obtained.

$$u'_x = u'_x(f) + u'_x(g) = -p(f) \frac{1}{\rho V_\infty^2} + \frac{1}{\rho V_\infty^2} \int_{-\infty}^X f_x dx' - p(g) \frac{1}{\rho V_\infty^2} + \frac{1}{\rho V_\infty^2} \int_{-\infty}^X g_x dx' \quad (B.22)$$

$$v'_y = v'_y(f) v'_y(g) = \frac{1}{\rho V_\infty^2} \int_{-\infty}^X \frac{\partial}{\partial y} p(f) dx' + \frac{1}{\rho V_\infty^2} \int_{-\infty}^X f_y dx' - \frac{1}{\rho V_\infty^2} \int_{-\infty}^X \frac{\partial}{\partial y} p(g) dx' + \frac{1}{\rho V_\infty^2} \int_{-\infty}^X g_y dx' \quad (\text{B.23})$$

Here the solution can be split into a part related to the prescribed forces f and a second one related to the induced forces g . Depending on which terms are considered, it is possible to have a linear or non-linear solution. For sake of brevity, only the equations for the linear solution are reported here, the others can be found in [60].

$$\begin{aligned} u'_x = & -\frac{1}{2\pi} \int_0^{2\pi} Q_n(\theta) \frac{-(x + \sin(\theta)) \sin(\theta) + (y - \cos(\theta)) \cos(\theta)}{(x + \sin(\theta))^2 + (y - \cos(\theta))^2} d\theta \\ & -\frac{1}{2\pi} \int_0^{2\pi} Q_t(\theta) \frac{-(x + \sin(\theta)) \cos(\theta) - (y - \cos(\theta)) \sin(\theta)}{(x + \sin(\theta))^2 + (y - \cos(\theta))^2} d\theta \\ & - (Q_n(\arccos(y)))^* + (Q_n(-\arccos(y)))^{**} \\ & - \left(Q_t(\arccos(y)) \frac{y}{\sqrt{1-y^2}} \right)^* - \left(Q_t(-\arccos(y)) \frac{y}{\sqrt{1-y^2}} \right)^{**} \end{aligned} \quad (\text{B.24})$$

The terms which are marked with * have to be calculated only when considering the flow in the inner part of the cylinder, while both the * as well as the ** have to be considered.

$$\begin{aligned} v'_y = & -\frac{1}{2\pi} \int_0^{2\pi} Q_n(\theta) \frac{-(x + \sin(\theta)) \cos(\theta) - (y - \cos(\theta)) \sin(\theta)}{(x + \sin(\theta))^2 + (y - \cos(\theta))^2} d\theta \\ & -\frac{1}{2\pi} \int_0^{2\pi} Q_t(\theta) \frac{(x + \sin(\theta)) \sin(\theta) - (y - \cos(\theta)) \cos(\theta)}{(x + \sin(\theta))^2 + (y - \cos(\theta))^2} d\theta \end{aligned} \quad (\text{B.25})$$

The model could be improved by adding an additional second order term for the viscous forces. Moreover it would be possible to simply add a correction to account for the non-linear part of the solution, more details are reported in [16].

In order to apply the model, the VAWT is divided into a certain number of cylindrical elements along its span-wise direction. The forces will be evaluated for each of the element and then summed. The latter procedure is achieved using the BEM theory that provides the expressions for Q_n and Q_t . Starting from these values the induced velocity is calculated and the calculation proceeds iteratively.

B.3. Wake modelling for HAWTs

Details about the implementation, derivation and the equations used by analytical wake models as well as models that provides the induced velocity to BEM models or similar, are provided in this section of the Appendix.

B.3.1. Analytical wake models for HAWTs

B.3.1.1. Larsen model

Developed according to [53], was described in Chapter (2). It is based on Navier-Stokes equations for high Reynolds' numbers. By solving them (with some assumptions) it is possible to find an expression for each wake perturbation component (considering only the first order wake model proposed) along radial r and axial direction x :

$$V_x = u = -\frac{V_\infty}{9} (c_w F x^{-2})^{\frac{1}{3}} \left[r^{\frac{3}{2}} (3c_1^2 c_w F x)^{-\frac{1}{2}} - \left(\frac{35}{2\pi} \right)^{\frac{3}{10}} (3c_1^2)^{-\frac{1}{5}} \right]^2 \quad (\text{B.26})$$

$$V_r = v = \frac{V_\infty}{3} (c_w F)^{\frac{1}{3}} x^{-\frac{5}{3}} r \left[r^{\frac{3}{2}} (3c_1^2 c_w F x)^{-\frac{1}{2}} - \left(\frac{35}{2\pi} \right)^{\frac{3}{10}} (3c_1^2)^{-\frac{1}{5}} \right]^2 \quad (\text{B.27})$$

Where V_∞ is the freestream speed, F is the rotor area, r is the radial coordinate, c_w is turbine's drag coefficient (the C_T), and c_1 is a constant determined using experimental data. The usage of the cylindrical coordinates

for the boundary layer is allowed by the neglect of wind shear. Moreover the flow is assumed incompressible, stationary and axisymmetric and the pressure term is neglected: validity's range of the model is restricted to the far wake region only, where the pressure has already reached the equilibrium. The control volume surrounds the turbine and the rotor is located at a certain downstream position x_0 which has to be determined, as well as the value for c_1 , calibrating the model. Wake width instead shows a non-linear development and is assumed as proportional to x_n and can be expressed as:

$$r_0 = \left(\frac{35}{2\pi}\right)^{\frac{1}{5}} (3c_1^2)^{-\frac{1}{5}} (c_w F x)^{\frac{1}{3}} \quad (\text{B.28})$$

Thus, unlike many other models, the wake development is non-linear and is based on the assumption that the velocities in sections perpendicular to streamwise direction are mechanically and geometrically similar. x_0 , location of the rotor and the constant c_1 are expressed as:

$$x_0 = \left[\left(\frac{D}{2\alpha_1}\right)^{-3} \left(\frac{\beta_1}{V_\infty - U_m}\right)^{\frac{3}{4}} - 1 \right]^{-1} \Delta x \quad (\text{B.29})$$

$$c_1 = \left(\frac{D}{2\alpha_1}\right)^{\frac{5}{2}} x_0^{-\frac{5}{6}} \quad (\text{B.30})$$

Easier expressions for the current model are introduced from [84]:

$$\frac{\Delta V}{V_\infty} = \frac{\Delta V_c}{V_\infty} \left[1 - \left(2\frac{r}{\delta}\right)^{\frac{3}{2}} \right]^2 \quad (\text{B.31})$$

This expression is valid only for $r \leq \frac{\delta}{2}$. ΔV_c is the velocity deficit at the center-line, expressed as:

$$\Delta V_c = \frac{35}{9} \frac{1}{2} \frac{C_T}{(\delta D)^2} \quad (\text{B.32})$$

$\frac{\delta}{D}$ is the normalized wake width, expressed as:

$$\frac{\delta}{D} = \sqrt[3]{\left(\frac{\delta_{eff}}{D}\right)^3 + \frac{k}{D^2} x} \quad (\text{B.33})$$

Where δ_{eff} is the effective rotor diameter, the wake width after that pressure recovery has occurred. k^* is the wake decay constant.

$$\frac{\delta_{eff}}{D} = \sqrt{\frac{1 + \sqrt{1 - C_T}}{2\sqrt{1 - C_T}}} \quad (\text{B.34})$$

$$k = \frac{1}{9.5} \left(\left(\frac{\delta_{9.5}}{D}\right)^3 - \left(\frac{\delta_{eff}}{D}\right)^3 \right) \quad (\text{B.35})$$

$\delta_{9.5}$ is the wake width at $x = 9.5D$ and it is related to the turbulence intensity. The expression for the latter depends on the fact that the ground presence is considered or not. If the ground is not considered:

$$\frac{\delta_{9.5,ng}}{D} = \begin{cases} 2.16 & \text{for } I_\infty \leq 0.05 \\ 2.16 + 43.4 (I_\infty - 0.05) & \text{for } I_\infty > 0.05 \end{cases} \quad (\text{B.36})$$

If the ground is considered:

$$\frac{\delta_{9.5}}{D} = \begin{cases} \frac{\delta_{9.5,ng}}{D} & \text{for } \delta_{9.5,ng} \leq \frac{z_h}{2} \\ \frac{z_h}{D} + \frac{1}{2} \delta_{9.5,ng} D & \text{for } \delta_{9.5,ng} > \frac{z_h}{2} \end{cases} \quad (\text{B.37})$$

B.3.1.2. Ainslie model

As previously discussed in Chapter (2), this model is build upon simplified parabolic RANS equations with the neglect of the pressure terms as well as viscous terms. This makes the model valid only in the far wake region (starting from two diameters downstream), where strong pressure gradients are not present. The wake is considered axisymmetric, stationary, fully turbulent and spanwise component is set to zero, since vortical effects are not relevant in the far wake region.

Even if considered as a wake model in literature, it is more similar to a particular numerical approach, with its exclusive features. In fact it allows to calculate each velocity component (streamwise and radial) by numerically solving the RANS equations mentioned before and reported in (B.38).

$$u \frac{\partial u}{\partial x} + v \frac{\partial u}{\partial r} = -\frac{1}{r} \frac{\partial r u' v'}{\partial r} \quad (\text{B.38})$$

To solve such equation a numerical approach is necessary. Moreover Reynolds stresses are modelled via eddy viscosity ε_T , proportional to the velocity defect and wake's width but also function of the ambient turbulence through the constant K_M :

$$\varepsilon = F [k_1 b (V_\infty - V_c) + K_M] \quad (\text{B.39})$$

A filter function F is introduced in order to keep into account the non-equilibrium nature of the region up to $x = 5.5D$ whose expression is:

$$F = \begin{cases} 0.65 + \left[\frac{x-4.5}{23.32} \right]^{\frac{1}{3}} & x < 5.5D \\ 1 & x > 5.5D \end{cases} \quad (\text{B.40})$$

Both k_1 (property of the shear layer) and K_M are constants determined according to empirical expressions, V_∞ is the freestream value, b is the wake's width and V_c is the velocity at wake's centre. Moreover, other initial parameters are determined according to empirical expressions and the initial velocity defect is modelled with a Gaussian distribution (see [5]).

However assuming a stationary flow field is not realistic when a turbine operating in atmospheric boundary layer is considered, as suggested in the paper. In fact wake meandering has to be taken into account when considering unstable conditions and a possible correction for the velocity deficit when considering turbulence effect was proposed:

$$\hat{d} = d_0 \left[1 + 7.12 \left(\sigma_\theta \frac{x}{b} \right)^2 \right]^{-\frac{1}{2}} \quad (\text{B.41})$$

Wake meandering leads to the displacement of the measurement point across a generic wake's profile. So the value of wake deficit seen by a fixed observer \hat{d} will be lower than the one seen in stationary condition d_0 . σ_θ is the standard deviation of wind direction fluctuations while b is wake's width.

Obviously, in order to solve the equations, a discretization method as well as a solver needs to be provided.

B.3.1.3. Frandsen model

As mentioned in Chapter (2) Frandsen model features a fistful of equations only, so it is extremely simple to be implemented. It is based on mass and momentum conservation applied to a cylindrical control volume that surrounds the turbine with a constant cross-sectional area equal to the wake area and with the horizontal axis parallel to the mean wind vector. As already said, several terms in the momentum equation are neglected, like the acceleration term, the pressure term and the gravity term as well as the shear forces acting on cylinder's surface. Self-similarity is assumed, even for the near wake region where this simplification is not totally correct. However related error shows lower impact on the results obtained. A constant distribution for the velocity deficit (here called rectangular distribution) is assumed, dependent on the downstream position only and not the radial one. The expression obtained for the velocity in the wake is:

$$\frac{V}{V_\infty} = \frac{1}{2} \pm \frac{1}{2} \sqrt{1 - 2 \frac{A_0}{A_w} C_T} \quad (\text{B.42})$$

With – or + depending on the induction factor a :

- for $a \leq 0.5$, the + solution is used
- for $a > 0.5$, the - solution is used

A_0 is instead the area at the rotor position and A_w the wake's area. A non-linear development is introduced for the wake, coherently to the self-similarity assumption in a classic turbulent environment:

$$D_w = \left(\beta + \alpha \frac{x}{D} \right)^{\frac{1}{2}} D \quad (\text{B.43})$$

Where α is a constant tuned experimentally and β is expressed as (from actuator disk theory):

$$A_a = \beta A_0 \quad (\text{B.44})$$

which is a parameter that relates the area at the onset point and the area at the rotor. D_w is instead the diameter of the wake at a certain x coordinate, while D is turbine's diameter. α is one of the major limitations of the model, since it doesn't show a universal value and changes according to the case analysed.

B.3.1.4. Fuga method

As discussed in Chapter (2) this model is unique and extremely different respect with traditional analytical wake models. It is build upon RANS equations for a quasi-steady case:

$$\frac{\partial u_j}{\partial x_j} = 0 \quad (\text{B.45})$$

$$u_j \frac{\partial u_i}{\partial x_j} = \frac{\partial \tau_{ij}}{\partial x_j} - \frac{\partial p}{\partial x_i} + f_i + \nu \nabla^2 u_i \quad (\text{B.46})$$

Where $f_i = \frac{F_i}{\rho}$ is the bulk force/forcing term, which is modelled using the actuator disk model applied to a layered control volume:

$$f_1 = -\frac{1}{2} C_T V_\infty^2 \delta(x - x_h) \Theta \left(R^2 - (y - y_h)^2 - (z - z_h)^2 \right) \quad (\text{B.47})$$

Where δ is the Dirac function while Θ a step function. Buoyancy forces as well as Coriolis force have been neglected. Moreover, the Reynolds stress tensor τ_{ij} is modelled using the eddy viscosity ν_τ , which is much higher than the kinematic viscosity ν . For this reason the viscous term can be neglected as well.

$$\tau_{ij} = \nu_\tau \left(\frac{\partial u_i}{\partial x_j} + \frac{\partial u_j}{\partial x_i} \right) + \frac{1}{3} \delta_{ij} \tau_{kk} \quad (\text{B.48})$$

The proposed expression for ν_τ are different according to the closure method adopted. In [75] are proposed three different closure methods, however only the simplest one, based on the expression (B.49), achieves the better results.

$$\nu_\tau = k u_* z \quad (\text{B.49})$$

The equations will be then linearized to obtain a simplified numerical solution that coupled with look-up tables reduces by a lot the computational cost. Moreover, an additional simplification based on using a mixed-spectral formulation to split the problem into couples of ODEs is introduced. However, in order to solve such equations, a numerical solver and a discretization has to be adopted, similarly to what happens with the Ainslie method in Section (2.4.3).

B.3.1.5. BPA yawed model

Discussed in Chapter (2) this is an innovative model since it deals with the deflection experienced by the wake flow encounters a yawed turbine. As stated before it is based on steady continuity equation and RANS equations (also in their integral form), simplified according to a numerical budget study. Besides the assumptions already mentioned there are some additional ones when analysing the equations. They can be summarised as:

- The convective terms are more relevant in the near wake region, while in the far wake region the flow is dominated by shear stress terms. It then asymptotes to the wake of a non-yawed turbine.
- Turbulent stress terms are modelled according to the Prandtl's theory introducing the eddy viscosity. This assumptions has significant effect only on the momentum conservation along streamwise direction.

- Wake deflection is strictly related to the skew angle θ which is experienced by the wake along the y axis (spanwise direction) due to the lateral force that induces side flows.
- The term $\frac{\partial^2 \bar{v}'}{\partial y^2}$ is bigger than the other terms and is balanced by the pressure gradient term in the momentum conservation along crossflow direction. This is extremely similar to what happens for 2D boundary layer equations.

On account of these assumptions the equations used are:

- The continuity equation:

$$\frac{\partial \bar{u}}{\partial x} + \frac{\partial \bar{v}}{\partial y} + \frac{\partial \bar{w}}{\partial z} = 0 \quad (\text{B.50})$$

- The momentum conservation along streamwise direction:

$$\frac{\partial \bar{u}}{\partial x} \approx \frac{\nu_T}{\bar{u}} \frac{\partial^2 \bar{u}}{\partial y^2} - \theta \frac{\partial \bar{u}}{\partial y} \quad (\text{B.51})$$

- The momentum conservation along crossflow (or spanwise) direction:

$$-\frac{1}{\rho} \frac{d\bar{p}}{dy} = \frac{\partial^2 \bar{v}'}{\partial y^2} \quad (\text{B.52})$$

where θ is the skew angle of the wake while the variables \bar{u} , \bar{v} and \bar{w} are the ensemble averaged streamwise, crossflow and spanwise velocity components. While the integral simplified form of the previous equations is:

$$\frac{d}{dx} \int_{-\infty}^{\infty} \int_{-\infty}^{\infty} [\bar{u}(\bar{u}_{\infty} - \bar{u})] dy dz \approx 0 \quad (\text{B.53})$$

$$\frac{d}{dx} \int_{-\infty}^{\infty} \int_{-\infty}^{\infty} \bar{u}^2 \theta dy dz \approx 0 \quad (\text{B.54})$$

For equation (B.53) the mean incoming velocity has been assumed only depending on the z coordinate (related to the vertical direction) and the pressure terms have been neglected even here as well as ground's presence. Moreover for equation (B.54) the shear stress term is extremely small with respect the advection term and so is neglected. The equation (B.53) expresses that the streamwise momentum deficit flow rate is conserved and independent of the downwind position while equation (B.54) expresses that the flow rate of spanwise momentum is conserved independently of the downstream position.

In order to solve the equations, self-similarity for the wake is assumed starting from a certain point, called onset point, as stated before. Therefore a Gaussian distribution for both the wake velocity and the skew angle is introduced:

$$\frac{\Delta \bar{V}}{\Delta \bar{V}_c} = e^{-0.5 \left(\frac{y^*}{\sigma_y} \right)^2} \quad (\text{B.55})$$

$$\frac{\theta}{\theta_m} = e^{-0.5 \left(\frac{y^*}{\sigma_y} + 1 \right)^2} \quad (\text{B.56})$$

Where $\Delta \bar{V}_c$ is the maximum velocity deficit, while θ_m is the maximum skew angle for each downstream position. It is crucial to underline that the self-similarity assumption has been already studied in the literature (see [10]) and here is validated by comparing the data for different downstream position and proving that the velocity profiles collapse onto a single curve (except for the edges, but the assumption is acceptable). Moreover only if the yaw angles are limited, the assumption of a Gaussian distribution along the vertical direction is satisfied. However high yaw angles ($\gamma = 30^\circ$) are not reached because of the power losses experienced which cannot be recovered by wake deflection.

The previous equations can be written also as:

$$\frac{\bar{V}(x, y, z)}{\bar{V}_{\infty}} = 1 - C e^{-\frac{(y-\delta)^2}{2\sigma_y^2}} e^{-\frac{(z-z_h)^2}{2\sigma_z^2}} \quad (\text{B.57})$$

$$\frac{\theta(x, y, z)}{\theta_m} = e^{-\frac{(y-\delta+\sigma_y)^2}{2\sigma_y^2}} e^{-\frac{(z-z_h)^2}{2\sigma_z^2}} \quad (\text{B.58})$$

where z_h is the hub height, while δ is wake's centre displacement along y direction.

Now, according to equations (B.57) and (B.58) it is necessary to provide an expression for σ , which represents the standard deviation (and so it is related to wake's width), along both spanwise and vertical direction. A linear wake development is chosen in accordance with the literature (see [10]): in case of turbulent inflow conditions (in this case due to the atmospheric boundary layer condition) the wake experiences a similar width expansion, moreover the wake has an elliptical shape whose dimensions are related to the yaw angle γ experienced in the following way:

$$\frac{\sigma_y}{D} = k_y^* \frac{(x - x_0)}{D} + \frac{\cos(\gamma)}{\sqrt{8}} \quad (\text{B.59})$$

$$\frac{\sigma_z}{D} = k_z^* \frac{(x - x_0)}{D} + \frac{1}{\sqrt{8}} \quad (\text{B.60})$$

where k_y^* and k_z^* are the growth rates while x_0 is the onset point cited before. In other terms the onset point is the point from where the current model and the self-similarity hypothesis are valid. Up to this point the values of wake deflection as well as velocity deficit are assumed constant similarly to what happens in the potential core region of jet flows, as discussed in the other chapter. These values are used as initial values to describe the far wake region, where self-similarity hypothesis is satisfied. By introducing the onset values, substituting the equations (B.57), (B.58) in (B.53) and (B.54), it is possible to obtain explicit expressions for the velocity deficit and the wake displacement (related to the skew angle) along y axis:

$$\frac{\Delta \bar{V}}{\bar{V}_\infty} = \left(1 - \sqrt{1 - \frac{C_T \cos(\gamma)}{8 \left(\frac{\sigma_y \sigma_z}{D^2} \right)}} \right) e^{-\frac{(y-\delta)^2}{2\sigma_y^2}} e^{-\frac{(z-z_h)^2}{2\sigma_z^2}} \quad (\text{B.61})$$

$$\frac{\delta}{D} = \theta_{c0} \frac{x_0}{d} + \frac{\theta_{c0}}{14.7} \sqrt{\frac{\cos(\gamma)}{k_y k_z C_T}} \left(2.9 + 1.3 \sqrt{1 - C_T} - C_T \right) \ln \left[\frac{(1.6 + \sqrt{C_T}) \left(1.6 \sqrt{\frac{8\sigma_z \sigma_y}{D^2 \cos(\gamma)}} - \sqrt{C_T} \right)}{(1.6 - \sqrt{C_T}) \left(1.6 \sqrt{\frac{8\sigma_z \sigma_y}{D^2 \cos(\gamma)}} + \sqrt{C_T} \right)} \right] \quad (\text{B.62})$$

Where θ_{c0} is the wake skew angle at the rotor position and is expressed as:

$$\theta_{c0} = \frac{0.3\gamma}{\cos(\gamma)} \left(1 - \sqrt{1 - C_T \cos(\gamma)} \right) \quad (\text{B.63})$$

The only remaining parameter is the onset point x_0 which is found according to a theory whose purpose is to find the extension of the potential core for jet flows:

$$\frac{x_0}{D} = \frac{\cos(\gamma) (1 + \sqrt{1 - C_T})}{\sqrt{2} (\alpha^* I + \beta^* (1 - \sqrt{1 - C_T}))} \quad (\text{B.64})$$

Where α^* and β^* are coefficient tuned with experimental data with values 2.32 and 0.154 respectively, however their expression is not universal and they are additional parameters that need to be provided to the model, a disadvantage.

B.4. Wake modelling for VAWTs

B.4.1. Analytical wake models for VAWTs

B.4.1.1. Lam & Peng model

The Lam & Peng model discussed in Chapter (2) is based on the assumptions already discussed as well as a specific definition for the starting location of the wake edges: they are located at the mid span ($z = \frac{H}{2}$) along the spanwise direction and at $y = \pm bD$ along cross-flow direction. ' b ' is a dimensionless parameter that, multiplied to D, expresses the point along the spanwise direction where the wake starts. In fact because of the blades rotation, the edges of the wake start at a distance higher than the half diameter along crossflow direction, as seen in Figure 2.24. According to these assumptions, wake development can be described as:

- Horizontal direction ($z = 0$):

$$\begin{cases} r_W = k_W \frac{x}{D} + b \\ r_L = -k_L \frac{x}{D} - b \end{cases} \quad (\text{B.65})$$

- Spanwise direction ($y = 0$):

$$\begin{cases} r_U = k_U \frac{x}{D} + \frac{1}{2}\eta \\ r_D = -k_D \frac{x}{D} - \frac{1}{2}\eta \end{cases} \quad (\text{B.66})$$

Where r_W , r_D , r_U , r_L are the minor and major axis of each ellipses, η is the aspect ratio $\frac{H}{D}$ where H is the height of the rotor and D its width (diameter). Their values have been discussed in Chapter (2).

The model is built upon mass conservation equation (with dimensionless coordinates) that allows to obtain the following expression:

$$\rho\pi \frac{H}{2D} b V_0 + \rho \frac{1}{2} \pi \left[\|r_W r_U\| + \|r_L r_D\| - \frac{H}{D} b \right] V_\infty = \rho \frac{1}{2} \pi (\|r_W r_U\| + \|r_L r_D\|) V \quad (\text{B.67})$$

where ρ is the air density, V_0 denotes the wake velocity at $x = 0$ and V_∞ is the freestream velocity.

Starting from the equation (B.67) an expression for velocity and normalized (with freestream value V_∞) velocity in the wake is obtain:

$$V = \frac{(\|r_W r_U\| + \|r_L r_D\|) V_\infty - (V_\infty - V_0) \frac{H}{D} b}{\|r_W r_U\| + \|r_L r_D\|} \quad (\text{B.68})$$

$$V' = 1 - \frac{2b\eta V_\Delta}{((k_W + k_L) \frac{x}{D} + 2b) (2k_U \frac{x}{D} + \eta)} \quad (\text{B.69})$$

Where V_Δ is the velocity deficit at $x=0$.

B.4.1.2. Ouro models

The Ouro models discussed in Chapter (2) is one of the most innovative analytical wake models even if largely based on HAWTs wake models yet. As mentioned previously, both the proposed models are based on a specific expression for momentum conservation obtained by the RANS equation along the streamwise direction:

$$\frac{\partial u(V_\infty - u)}{\partial x} + \frac{\partial v(V_\infty - u)}{\partial y} + \frac{\partial w(V_\infty - u)}{\partial z} = \frac{\partial u' u'}{\partial x} + \frac{\partial u' v'}{\partial y} + \frac{\partial u' w'}{\partial z} \quad (\text{B.70})$$

Where the variables with the apex are the fluctuations. Pressure and viscous terms are neglected in combination with previous assumptions.

$$\rho \int_{-\infty}^{\infty} (u(V_\infty - u)) dA = T \quad (\text{B.71})$$

Where T is the force exerted by the obstacle in the control volume and u the velocity in the wake. Starting from (B.70) it is possible to obtain the (B.71) by integrating the first one across a control volume that embeds the turbine and neglecting the shear stresses when considering a position sufficiently far from wake's centre. Moreover, the variation of turbulence stresses along the streamwise direction is negligible compared to the variation of the convective term.

Starting from the simplified equations, the two models are analysed separately:

1. **Top-hat model:** As mentioned before, this model is extremely similar to the one introduced by Frandsen et al. [25]. Here the wake develops non-linearly from the onset point according to the following expressions:

$$D_w = D \left(\beta + k_{wy} \frac{x - x_a}{D} \right)^{\frac{1}{2}} \quad (\text{B.72})$$

$$H_w = H \left(\beta + k_{wz} \frac{x - x_a}{H} \right)^{\frac{1}{2}} \quad (\text{B.73})$$

D is turbine's diameter, H is the turbine's height. β relates the turbine's area A_0 and the wake area at the onset point A_a according to the actuator disk theory:

$$\beta = \frac{A_a}{A_0} = \frac{1 - a}{1 - 2a} = \frac{1}{2} \frac{1 + \sqrt{1 - C_T}}{\sqrt{1 - C_T}} \quad (\text{B.74})$$

Where the following relations between the velocity at the onset point, freestream speed and induction factor are introduced:

$$V_a = V_0 (1 - 2a) \quad (\text{B.75})$$

$$a = \frac{1}{2} \left(1 - \sqrt{1 - C_T} \right) \quad (\text{B.76})$$

By applying the momentum balance to a control volume that surrounds the whole turbine and combining it with the previous relations, the following expression for the velocity deficit can be found:

$$\frac{\Delta V}{V_\infty} = \frac{1}{2} \left(1 - \sqrt{1 - \frac{2C_T}{\left(\beta + k_{wy} \frac{x-x_a}{D} \right)^{\frac{1}{2}} \left(\beta + k_{wz} \frac{x-x_a}{H} \right)^{\frac{1}{2}}}} \right) \quad (\text{B.77})$$

k_{wy} and k_{wz} can be expressed as $2I$ with I turbulence intensity. However it is recommended to use different values to express the non-symmetric wake development of the wake along y and z direction since tip vortices along spanwise direction and dynamic-stall vortices along the horizontal feature different properties.

2. **Gaussian model:** Using self-similarity, in accordance with literature studies [3] is possible to assume a Gaussian distribution for the velocity deficit as function of the local scales of velocity and length:

$$\frac{\Delta V}{V_\infty} = \frac{V_\infty - V}{V_\infty} = \frac{\Delta V_{max}}{V_\infty} f \left(-\frac{1}{2} \frac{r^2}{\sigma^2} \right) = C(x) f \left(-\frac{1}{2} \frac{r^2}{\sigma^2} \right) \quad (\text{B.78})$$

$\frac{r}{\sigma}$ is the distance from the wake's centre normalized with the wake width, which is assumed related to the standard deviation of the distribution. This is the length scale. The ratio $C(x) = \frac{\Delta V_{max}}{V_\infty}$ is instead the velocity scale. Adopting a Gaussian distribution (which is more realistic than the top-hat, as stated before) that accounts for both the height and the diameter of the turbine, the function ' f ' becomes an exponential:

$$V_w = V_\infty \left(1 - C(x) e^{\left(-\frac{y^2}{2\sigma_y^2} - \frac{z^2}{2\sigma_z^2} \right)} \right) \quad (\text{B.79})$$

Where σ_y and σ_z are the standard deviations of the Gaussian distributions, one for each direction to express two velocity deficit profiles ($\Delta V(y)$ and $\Delta V(z)$). They are respectively related to the diameter D and the height H of the turbine. Moreover they are related to wake's widths along the y and z directions. Their expressions are the following one:

$$\frac{\sigma_y}{D} = k_y^* \frac{x - x_a}{D} + \epsilon_y \quad (\text{B.80})$$

$$\frac{\sigma_z}{H} = k_z^* \frac{x - x_a}{H} + \epsilon_z \quad (\text{B.81})$$

So the wake development is linear. ϵ_y and ϵ_z express the wake width at the starting point, and these values are determined by equating the velocity deficit predicted by this model with the one predicted from the top-hat model for $x = x_a$ similarly to what has been done in [25][10]. This way the following expression is obtained:

$$\epsilon_z \epsilon_y = \frac{\beta}{4\pi} \quad (\text{B.82})$$

Assuming that at the onset point the normalised wake width is equal along both directions ($\epsilon_y = \epsilon_z$), the following expression is obtained:

$$\epsilon_y = \epsilon_z = \frac{1}{\sqrt{4\pi}} \sqrt{\beta} \quad (\text{B.83})$$

The obtained value is slightly higher (+12%) than the one proposed by Abkar [2].

k_y^* and k_z^* are the growth rates and can be estimated as function of the turbulence intensity as $0.35I$. However it is recommended to use different values to replicate the asymmetry in the wake evolution. Introducing the equation (B.79) in (B.71) and using (B.84) for the thrust (where C_T is the thrust coefficient), it is possible to determine $C(x)$ and an explicit expression for the velocity deficit:

$$T = \frac{1}{2} C_T \rho A_0 U_0^2 \quad (\text{B.84})$$

$$\frac{\Delta V}{V_\infty} = \left(1 - \sqrt{1 - \frac{C_T D H}{2\pi \sigma_y \sigma_z}} \right) e^{\left(-\frac{y^2}{2\sigma_y^2} - \frac{z^2}{2\sigma_z^2} \right)} \quad (\text{B.85})$$

B.4.2. Blade resolved methods for VAWTs - LES equations

Generally speaking the LES equations are basically the filtered Navier-Stokes equations, which for an incompressible case are:

$$\frac{\partial \widetilde{V}_i}{\partial x_i} = 0 \quad (\text{B.86})$$

$$\frac{\partial \widetilde{V}_i}{\partial t} + \frac{\partial \widetilde{V}_i \partial \widetilde{V}_j}{\partial x_j} = -\frac{\partial \widetilde{p}}{\partial x_i} - \frac{\partial \tau_{ij}}{\partial x_j} + \frac{1}{Re} \frac{\partial^2 \widetilde{V}_i}{\partial x_j \partial x_j} + f_i \quad (\text{B.87})$$

Operator $\langle \sim \rangle$ is for the filtered quantities. The filter is used to distinguish between small and large scale. f_i is the forcing term, Re the Reynolds' number based on reference velocity and length scales. τ_{ij} is the subgrid scale (SGS) tensor which needs to be modelled but the expressions proposed in the literature are several and extremely different.

For example, in the work from Shamsoddin & Porté-Agel [95] two closure methods for SGS stresses are used:

1. Smagorinsky model: one of the most common closure models, based on the following expression:

$$\tau_{ij} - \frac{1}{3} \delta_{ij} \tau_{kk} = -2 (C_s \widetilde{\Delta})^2 |\widetilde{S}| \widetilde{S}_{ij} \quad (\text{B.88})$$

where C_s is the Smagorinsky coefficients, while the other parameters are the same mentioned for the previous model.

2. Modulated Gradient Model (MGM): an alternative to eddy-viscosity closure models. Here the SGS tensor is modelled as:

$$\tau_{ij} = 2k_{sgs} \left(\frac{\widetilde{G}_{ij}}{\widetilde{G}_{kk}} \right) \quad (\text{B.89})$$

Additional equations for the SGS kinetic energy k_{sgs} as well as other terms are needed. For more details check [95].

Another possible model is the one reported in [22, 86]:

$$\tau_{ij} - \frac{1}{3} \tau_{kk} = -2\nu_t \widetilde{S}_{ij} \quad (\text{B.90})$$

ν_t is the eddy-viscosity (essential also for RANS simulations), τ_{kk} the trace of the SGS tensor and \widetilde{S}_{ij} the resolved strain rate tensor:

$$\widetilde{S}_{ij} = \frac{1}{2} \left(\frac{\partial \widetilde{V}_i}{\partial x_j} + \frac{\partial \widetilde{V}_j}{\partial x_i} \right) \quad (\text{B.91})$$

ν_t is strictly related to the filter used. One of its possible expression is reported in equation (B.92) and features the local filter size Δ as well as the second-order structure function of the resolved velocity field. Such parameter, reported in equation (B.93) is based on a spatial average in the region surrounding the point of coordinates \vec{x} over a sphere of radius Δ .

$$\nu_t = 0.0014 C_k^{-1.5} \Delta \sqrt{F_2^{(3)}} \quad (\text{B.92})$$

$$F_2^{(3)} = \left\langle \left[\overrightarrow{\widetilde{V}_i(x+r)} - \overrightarrow{\widetilde{V}_i(x)} \right]^2 \right\rangle_{|\vec{r}|=\Delta} \quad (\text{B.93})$$

In other cases, like the one reported in [79, 80], a Wall-Adapting Local Eddy-viscosity SGS model can be used, where the modelling of the tensor takes already into account the SGS viscosity near the walls. In this case however a special mesh that tracks the grid cells where solid parts are present is used, increasing the computational cost.

Once the SGS tensor is modelled the IB method is then used to simulate the solid moving geometries with high accuracy by exerting a force represented by the f_i term on a specific region of fluid nodes. For more details check [79, 80]. The force term can also be modelled using the actuator line or actuator surface theory to achieve a lower computational cost but with lower accuracy.

However the computational cost is extremely high, for this reason some alternative-LES model have been proposed, such as the 2.5D simulations where only a portion of the blades along spanwise direction is modelled instead of setting up a complete 3D CFD model. An alternative instead is simplifying blade's modelling by support of the actuator line or actuator surface theory [95], as stated before.

C

Wake models code scripts analysis

In this Appendix the Python code developed for wake models is reported, explained and analysed in details. Two main sections deals with two different aspects of the implementation:

1. First Section reports the version of the code that can be used universally, for any possible case
2. Second Section reports how the validation process against literature data extracted from specific paper can be conducted. It gives also hints and suggestion regarding how to potentially compare the predictions with additional literature or experimental data.

C.1. Wake models scripts structure

As discussed in detail in Chapter (2) and (3), the wake models implemented are based on the work of Abkar [2] and of Niayifar et al. [72] (for what concerns the wake decay constant expression). However even if the code deals with two different models, one based on top-hat distribution and the other on Gaussian distribution, a similar approach in the development has been chosen. This way has been possible to:

- Testing the same structure with some minor changes, to test its robustness.
- Simplifying the comprehension of the implementation process for the reader.
- Generalizing as many passages as possible in order to create a 'universal approach' in case other wake models could be introduced.
- Avoid wasting time, starting from a common basis and an approach clearly defined.

The analysis of the code will be split in several part in order to simplify the discussion according to the output generated by the code itself. So, on one side we have the script where the input values are set, models' functions are called and the final images are created, we will refer to it as output script. On the other side we have the scripts where wake models are implemented in different ways, according to what is required. However, since the code to extract the output is the same for both models, it will be discussed at once.

C.1.1. Input definition

In order to do start the calculations, the first part of the code defines the input parameters (here the ones from Case 1 reported in [2], as examples). The approach is the same, no matter which function is called or which model.

```
1 import numpy as np
2 import matplotlib
3 import matplotlib.pyplot as plt
4 from matplotlib import cm
5 from matplotlib import rc
```

```

6 from matplotlib.colors import ListedColormap
7 from matplotlib.patches import Rectangle
8 from BPA_VAWT import BPA_VAWT
9 from NOJ_VAWT import NOJ_VAWT
10 import pandas as pd
11
12 plt.rcParams.update({
13     "text.usetex": True,
14     "font.size": 16,
15     "font.family": "serif",
16     "font.sans-serif": []})
17
18 #Input parameters
19 xD = np.array([3, 6, 9, 12]) # specific downwind distances normalized respect to D
20 WS_ilk = np.array([7]) # wind speed at source turbine
21 D_src_il = np.array([26]) # diameter of source turbine
22 H_src_il = np.array([24]) # height of the source turbine
23 h_il = np.array([40]) # source turbine hub height
24 ct_ilk = np.array([0.65]) # thrust coefficient
25 TI_ilk = np.array([0.091])
26
27 #Domain definition
28 x = np.linspace(-0.75*D_src_il, D_src_il*12, 200) #downstream distance
29 y = np.linspace(-200, 200, 200) # cross wind distance (both horizontal and vertical)
30 z = np.linspace(0, 200, 200) # cross wind distance (both horizontal and vertical)

```

The input parameters used are:

- The model used, which will be analysed later
- The non-dimensional axial coordinate xD
- The crossflow coordinate y [m]
- The spanwise coordinate z [m]
- The freestream velocity WS_{ilk} [$\frac{m}{s}$]
- Turbine's diameter $D_{src_{il}}$ [m]
- Turbine's height $H_{src_{il}}$ [m]
- Turbine's hub height h_{il} [m]
- Turbine's thrust coefficient ct_{ilk}
- Ambient turbulence intensity TI_{ilk}

Such parameters as well as the domain used, can be modified according to the case to be tested. Once the input are set, it's possible to move to the next stage. The libraries used in Python are reported too at the start of the script.

C.1.2. 2D Arrays calculation

Half of the calculation has been called *2D calculation* because of the use of only 2D arrays to plot velocity profiles as well as deficit maps along horizontal planes.

C.1.2.1. Velocity deficit profiles along spanwise and crossflow direction

This part of the output allows to determine the velocity deficit profiles along the spanwise z and crossflow y direction for each of the downstream coordinates considered x (in dimensional or non-dimensional form). Once the input parameters are set, it's possible to call the function considered in nearly the same way for both models. For the BPA model the procedure is:

```

1 #Evaluation of deficit profiles along y and z directions for specific x/D values for
  the BPA_VAWT method
2 plot_deficit_map(BPA_VAWT(), xD, y, z, WS_ilk, D_src_ilk, H_src_ilk, h_ilk, ct_ilk, TI_ilk
  )

```

While for the NOJ model:

```

1 #Evaluation of deficit profiles along y and z directions for specific x/D values for
  the NOJ_VAWT method
2 plot_deficit_map(NOJ_VAWT(), xD, y, z, WS_ilk, D_src_ilk, H_src_ilk, h_ilk, ct_ilk, TI_ilk
  )

```

The *plot-deficit-map* function called aims to call the wake model's functions and preparing the output images.

```

1 def plot_deficit_map(model, xD, y, z, WS_ilk, D_src_ilk, H_src_ilk, h_ilk, ct_ilk, TI_ilk)
  :
2   deficit_Y_xD, deficit_Z_xD, width_y_xD, width_z_xD = model.deficit_profile_XD(xD, y
  , z, WS_ilk, D_src_ilk, H_src_ilk, h_ilk, ct_ilk, TI_ilk) #deficit profiles
  calculation
3   fig, ax = plt.subplots(2, len(xD), sharey='row', sharex='row', figsize=(9, 9),
  gridspec_kw={'hspace': 0.5, 'wspace': 0.9})
4   if model.getName() == 'NOJ_VAWT': #titles subplots settings
5     fig.suptitle(r"\textbf{Deficit profiles for Jensen method for VAWTs}", fontsize
  =18)
6   else: #titles subplots settings
7     fig.suptitle(r"\textbf{Deficit profiles for BPA method for VAWTs}", fontsize
  =18)
8   for i in range(len(xD)):
9     ax[0,i].plot(deficit_Y_xD[:,i],y/D_src_ilk,label='_nolegend_',zorder=4) #deficit
  plotting along Y direction, normalized
10    ax[0,i].grid(True)
11    ax[0,i].set_xlim([-0.189, max(deficit_Y_xD[:,0])+0.1])
12    ax[0,i].set_ylim([-2, 2])
13    ax[0,i].set_xlabel(r'$\Delta U/U_0$')
14    ax[0,i].set_ylabel(r'Y/D')
15    ax[0,i].set_title(r"\textbf{x=} " + r'\textbf{'}'.format(xD[i]) + r"\textbf{D}",
  fontsize=16 )
16    ax[0,i].plot(np.linspace(-0.2,1,50),np.full((50),0.5), color='green', linestyle
  ='dashed', label='_nolegend_') #turbine's projection plot
17    ax[0,i].plot(np.linspace(-0.2,1,50),np.full((50),-0.5), color='green',
  linestyle='dashed', label='_nolegend_') #turbine's projection plot
18    for i in range(len(xD)):
19      t1=ax[1,i].plot(deficit_Z_xD[i,:],z/D_src_ilk, zorder=4) #deficit plotting
  along Z direction, normalized
20      ax[1,i].grid(True)
21      ax[1,i].set_xlim([-0.1, max(deficit_Z_xD[0,:])+0.1])
22      ax[1,i].set_ylim([0, 4])
23      ax[1,i].set_xlabel(r'$\Delta U/U_0$')
24      ax[1,i].set_ylabel(r'Z/D')
25      ax[1,i].set_title(r"\textbf{x=} " + r'\textbf{'}'.format(xD[i]) + r"\textbf{D}",
  fontsize=16)
26      ax[1,i].plot(np.linspace(-0.2,1,50),np.full((50),(h_ilk-(0.5)*H_src_ilk)/D_src_ilk
  ), color='green', linestyle='dashed', label='_nolegend_') #turbine's projection
27      ax[1,i].plot(np.linspace(-0.2,1,50),np.full((50),(h_ilk+(0.5)*H_src_ilk)/D_src_ilk
  ), color='green', linestyle='dashed', label='_nolegend_') #turbine's projection
28    fig.legend(t1,(r'\textbf{'}'.format(model.getName())), loc='center', bbox_to_anchor
  =(0.1, 0, 0.8225, 0.955),fontsize=12) # plot settings

```

This part of the output script firstly calls model's function to provide the non-dimensional velocity deficits as well as wake's dimensions along two main directions. Such values are calculated for every x/D coordinate provided as input so the results are 2D arrays. After setting some options for the plots, the deficit profiles are plotted for each x/D coordinate with a *for* loop along both y and z directions. The last plots are used to define turbine's edges and have a better idea of how the flow field develops respect with the turbine.

C.1.2.2. Deficit map along streamwise and crossflow direction

The models' functions used to calculate the velocity profiles are the same used to plot the deficit map along horizontal planes. Therefore before moving on and discussing the scripts related to wake models, here is reported a second function of the output script. It allows to plot the deficit map seen along a horizontal plane located at turbine's hub. The purpose of this function is to provide a better overview of the whole flow field behind the turbine, how it develops and how it recovers to free-stream values.

Such function is called as:

```

1 #Deficit map along the horizontal plane at z=zt (hub height) evaluation for BPA_VAWT
  method
2 plot_deficit_map_xy(BPA_VAWT(), x, y, z, WS_ilk, D_src_il, H_src_il, h_il, ct_ilk,
  TI_ilk)
3 #Deficit map along the horizontal plane at z=zt (hub height) evaluation for NOJ_VAWT
  method
4 plot_deficit_map_xy(NOJ_VAWT(), x, y, z, WS_ilk, D_src_il, H_src_il, h_il, ct_ilk,
  TI_ilk)

```

The function is defined by the following lines of code:

```

1 def plot_deficit_map_xy(model, x, y, z, WS_ilk, D_src_il, H_src_il, h_il, ct_ilk,
  TI_ilk):
2     deficit_Y_xD, deficit_Z_xD, width_y_xD, width_z_xD = model.deficit_profile_XD(x/
  D_src_il, y, z, WS_ilk, D_src_il, H_src_il, h_il, ct_ilk, TI_ilk) #map deficit
  evaluation
3     cmap_test = np.r_[[1, 1, 1, 1], [1, 1, 1, 1]], cm.Blues(np.linspace(0, 1, 128))] #
  ensure zero deficit is white
4     cmap=ListedColormap(cmap_test)
5     levels = np.linspace(0, 1, 110)
6     t = np.linspace(0,2*np.pi,65) #turbine's top circular projection
7     x_r = D_src_il/2 * np.cos(t)
8     y_r = D_src_il / 2 * np.sin(t)
9     fig = plt.contourf( x/D_src_il, y/D_src_il, deficit_Y_xD, levels=levels, cmap=cmap)
10    if model.getName() == 'NOJ_VAWT': #title setting
11        plt.title(r'\textbf{Deficit xy map for Jensen method for VAWTs}', fontsize=18,
  y=1.1)
12    else:
13        plt.title(r'\textbf{Deficit xy map for BPA method for VAWTs}', fontsize=18, y
  =1.1)
14    plt.plot(x_r/D_src_il,y_r/D_src_il, color = 'black') #circle plotting
15    plt.grid(True) #plotting settings
16    colorbar_range = np.linspace(0, 1, 11)
17    plt.colorbar(fig, label=r'\Delta U/U_0$', ticks=colorbar_range, format='%.1f')
18    plt.ylabel(r"Crosswind distance [y/D]", x=0.9)
19    plt.xlabel(r"Downwind distance [x/D]", y=0.9)
20    plt.axis('equal')
21    filename2 = 'Deficit_map_xy_' + model.getName() + '.jpeg' #figure saving
22    plt.savefig(filename2,bbox_inches = "tight")

```

As for the function described before, the model is called to calculate the non-dimensional velocity deficit and wake's widths. However this time is calculated for the entire domain length x and not only some specific coordinates xD . This way more points are calculated and an entire map can be plotted. The top-view projection of the turbine (a circle) is plotted as well, to figure out instantly where the turbine is located

Now the wake models' code splits up depending on which model is used. However the differences are limited, as stated before.

C.1.2.3. NOJ wake model code for 2D calculation

The calculation performed by the NOJ wake model can be divided into two main steps:

1. Evaluation of the wake decay constant

2. Evaluation of the velocity deficit

The first step can be accomplished in several ways (this is one of the main topics of the thesis). However only one option can be provided in the calculation, therefore the other possibilities has to be commented during the script launch. Just to clearly present the code, here both the options are uncommented.

```

1 import numpy as np
2
3 class NOJ_VAWT:
4     """Implemented according to
5     Abkar, M. (2019). Theoretical modeling
6     of vertical-axis wind turbine
7     wakes. Energies, 12(1), 10.
8
9     Parameters:
10    Environmental Turbulence intensity TI_ilk
11    Thrust coefficient ct_ilk
12    Axial normalized coordinate (streamwise direction) xD
13    Crossflow coordinate y [m]
14    Spanwise coordinate z [m]
15    Wake decay constant k_ilk = kw_ilk
16    Freestream velocity WS = WS_ilk [m/s]
17    Diameter D_src_il [m]
18    Height H_src_il [m]
19    Hub height h_il [m]
20    """
21
22    def getName(self): #Definition of model's name
23        return self.__class__.__name__
24
25    def kw_ilk(self, TI_ilk,ct_ilk,xD): #Calculation of wake decay constant 1
26        """Implemented according to
27        Abkar, M. (2019). Theoretical modeling
28        of vertical-axis wind turbine
29        wakes. Energies, 12(1), 10.
30        """
31        k=0.4*TI_ilk #Tuning based on Abkar2019 for ABL inflow condition
32        return k
33
34    def kw_ilk(self, TI_ilk,ct_ilk,xD): #Calculation of wake decay constant 2
35        '''Implemented according to
36        Niayifar, A., \& Porte-Agel, F. (2015, June).
37        A new analytical model for wind farm power prediction.
38        In Journal of physics: conference series
39        (Vol. 625, No. 1, p. 012039). IOP Publishing.
40        '''
41        k3 = 0.0892074 #Literature coefficients
42        k2 = 0.0544955
43        k1 = 0.251163
44        k0 = -0.0017077
45        ind = k3 * ct_ilk**3 + k2*ct_ilk**2 +k1*ct_ilk +k0 #Induction factor 1
46        #ind = 0.5*(1-np.sqrt(1-ct_ilk)) #Induction factor 2
47        I_add=0.73*ind**(0.8325)*TI_ilk**(0.0325)*(xD)**(-0.32) #added turbulence
48        intensity
49        I_tot=np.sqrt(I_add**2 + TI_ilk**2) #Total turbulence intensity
50        if abs(I_tot) < 0.065:
51            k_ilk=0.0026
52        elif abs(I_tot) <= 0.15 and abs(I_tot) >= 0.065:
53            a=[0.38, 4e-3] #Niayifar coefficients (literature)
54            k_ilk = a[0]*I_tot+a[1] #Empirical relation for k
55        elif abs(I_tot) > 0.15:
56            k_ilk=0.064
57        return k_ilk

```

After introducing the code and which are the parameters used the two possible choices to model the wake decay constant are reported. They have been discussed both in Chapter (2) and (3). The first one is based on the expression from [2] used for the ABL inflow condition, while the second one is based on [72] and on

evaluating the added turbulence intensity in the wake using empirical equations. Such equations need the induction factor that can be expressed according to the actuator disk theory (here reported as second commented option) or the empirical polynomial expression from [16]. The expression used depends on the local turbulence intensity value. The function to evaluate k is called by the main part of the script, the second step, which performs the real calculations.

```

1  # Evaluation of deficit profiles along z and y for each xD
2  def deficit_profile_XD(self, xD, y, z, WS_ilk, D_src_il, H_src_il, h_il, ct_ilk,
3  TI_ilk):
4      WS = WS_ilk
5      term_numerator_ijlk = (1 - np.sqrt(1 - ct_ilk))
6      #Wake dimensions initialization
7      H_w = np.zeros(len(xD)) #Spanwise dimension
8      D_w = np.zeros(len(xD)) #Crossflow dimension
9      #Initialization of the velocity deficit along two directions
10     deficit_ijlk_y=np.zeros((len(y),len(xD))) #Crossflow
11     deficit_ijlk_z=np.zeros((len(xD),len(z))) #Spanwise
12     for k in range(len(xD)): #Deficit profile evaluation for each xD coordinate
13         if xD[k]>0: #To exclude points in front of the turbine
14             #wake dimension evolution for each x
15             H_w[k] = H_src_il + 2 * (self.kw_ilk(TI_ilk,ct_ilk,xD[k])) * xD[k] *
16             D_src_il
17             D_w[k] = D_src_il + 2 * (self.kw_ilk(TI_ilk,ct_ilk,xD[k])) * xD[k] *
18             D_src_il
19             #Evaluation of deficit area
20             effective_deficit_area_y = (abs(y)<=D_w[k]/2)
21             effective_deficit_area_z = ( z <= H_w[k]/2 + h_il) * (z >= h_il - H_w[k]
22             ]/2 )
23             #Deficit evaluation (location outside the wake area are set to zero)
24             deficit_ijlk_y[:, k] = WS * (term_numerator_ijlk) / ((H_w[k] / H_src_il
25             )*(D_w[k] / D_src_il))*(effective_deficit_area_y)
26             deficit_ijlk_z[k, :] = WS * (term_numerator_ijlk) / ((H_w[k] / H_src_il
27             ) * (D_w[k] / D_src_il)) * (effective_deficit_area_z)
28
29     return deficit_ijlk_y/WS, deficit_ijlk_z/WS, D_w, H_w

```

This is the core of the NOJ model developed and one of the most important part of the thesis. It's also the function called directly by the output script functions described in Section (C.1.2.1) and (C.1.2.2).

Firstly the code allocate the initial values (all zeros) for the deficit as well as wake's dimensions, depending on the length of the xD array provided (remember, it can represent a fistful of coordinates or the entire length of the domain along streamwise direction. Then, the calculation starts for the only xD coordinate downstream of the turbine. Wake dimensions are evaluate firstly and at the same time the effective wake is considered. By this way only a certain part of the y array is considered as part of the wake and introducing the Boolean mask in the deficit calculation, the constant value is assigned to the effective part only. Otherwise the deficit would have been assigned to the whole y array, since there's no dependence on y in the deficit equation The same is done for spanwise direction and then the values are normalized with freestream velocity and provided back to the output script functions.

C.1.2.4. BPA wake model code for 2D calculation

As for NOJ model, we have the same process for the evaluation of the wake decay constant and then the calculation of the deficit itself.

The first part of the code presents the parameters used in the calculation. The only difference with NOJ model is that here the decay constant is called only k and not k_w .

```

1  import numpy as np
2  import math
3
4  class BPA_VAWT:
5      """Implemented according to
6      Abkar, M. (2019). Theoretical modeling

```

```

7   of vertical-axis wind turbine
8   wakes. Energies, 12(1), 10.
9
10  Parameters:
11  Environmental Turbulence intensity TI_ilk
12  Thrust coefficient ct_ilk
13  Axial normalized coordinate (streamwise direction) xD
14  Crossflow coordinate y [m]
15  Spanwise coordinate z [m]
16  Wake decay constant k_ilk = kw_ilk
17  Freestream velocity WS = WS_ilk [m/s]
18  Diameter D_src_il [m]
19  Height H_src_il [m]
20  Hub height h_il [m]
21  """
22
23  def getName(self): #Definition of model's name
24      return self.__class__.__name__
25
26  def k_ilk(self, TI_ilk,ct_ilk,xD): #Calculation of wake decay constant 1
27      """Implemented according to
28      Abkar, M. (2019). Theoretical modeling
29      of vertical-axis wind turbine
30      wakes. Energies, 12(1), 10.
31      """
32      k = 0.35 * TI_ilk #Tuning based on Abkar2019 for ABL inflow condition
33      return k
34
35  def k_ilk(self, TI_ilk,ct_ilk,xD):
36      """Implemented according to
37      Niayifar, A., \& Porte-Agel, F. (2015, June).
38      A new analytical model for wind farm power prediction.
39      In Journal of physics: conference series
40      (Vol. 625, No. 1, p. 012039). IOP Publishing.
41      """
42      k3 = 0.0892074
43      k2 = 0.0544955
44      k1 = 0.251163
45      k0 = -0.0017077
46      #ind = k3 * ct_ilk**3 + k2*ct_ilk**2 +k1*ct_ilk +k0 #Induction factor 1
47      ind = 0.5*(1-np.sqrt(1-ct_ilk)) #Induction factor 2
48      I_add=0.73*ind**(0.8325)*TI_ilk**(0.0325)*(xD)**(-0.32) #added turbulence
intensity
49      I_tot=np.sqrt(I_add**2 + TI_ilk**2) #Total turbulence intensity
50      if abs(I_tot) < 0.065:
51          k_ilk=0.0026
52      elif abs(I_tot) <= 0.15 and abs(I_tot) >= 0.065:
53          a=[0.38, 4e-3] #Niayifar coefficients (literature)
54          k_ilk = a[0]*I_tot+a[1] #Empirical relation for k
55      elif abs(I_tot) > 0.15:
56          k_ilk=0.064
57      return k_ilk

```

The main differences with NOJ model are limited to the deficit calculation reported in the second part.

```

1   # Evaluation of deficit profiles along z and y for each xD
2   def deficit_profile_XD(self, xD, y, z, WS_ilk, D_src_il, H_src_il, h_il, ct_ilk,
TI_ilk):
3       WS = WS_ilk
4       sqrt1ct_ilk = np.sqrt(1 - ct_ilk)
5       beta_ilk = 0.5 * (1 + sqrt1ct_ilk)/sqrt1ct_ilk #Parameter related to actuator
disk theory
6       #Array's initialization
7       sigma_y_ijlk_xD=np.zeros(len(xD)) #standard deviation y
8       sigma_z_ijlk_xD=np.zeros(len(xD)) #standard deviation z
9       radical_ijlk=np.zeros(len(xD))
10      deficit_centre_ijlk=np.zeros(len(xD)) #deficit at wake's centre
11      deficit_y_ijlk_xD=np.zeros((len(y),len(xD))) #deficit along y direction

```

```

12     deficit_z_ijklxD=np.zeros((len(xD),len(z))) # deficit along z direction
13     exponent_y_ijkl=np.zeros((len(y),len(xD))) #exponent values crossflow
14     exponent_z_ijkl=np.zeros((len(xD), len(z))) #exponent values spanwise
15     for k in range(len(xD)): #Deficit profile evaluation for each xD coordinate
16         if xD[k]>0: #only points after the turbine
17             #wake standard deviation evaluation for each x
18             sigma_y_ijklxD[k]=(self.k_ilk(TI_ilk,ct_ilk,xD[k]) * xD[k] * D_src_il
19 + 0.25 * np.sqrt(beta_ilk) * D_src_il)
20             sigma_z_ijklxD[k] = (self.k_ilk(TI_ilk,ct_ilk,xD[k]) * xD[k] *
21 D_src_il + 0.25 * np.sqrt(beta_ilk) * H_src_il)
22             radical_ijkl[k]= np.maximum(0,(1. - ct_ilk / (2 * math.pi *
23 sigma_z_ijklxD[k] * sigma_y_ijklxD[k] / (D_src_il * H_src_il)))) #Avoid negatives
24             #maximum deficit evaluation (for each x/D)
25             deficit_centre_ijkl[k]= WS * (1. - np.sqrt(radical_ijkl[k]))
26             #evaluation of exponent's values
27             exponent_y_ijkl[:,k] = -0.5*(((y)/(sigma_y_ijklxD[k]))**2)
28             exponent_z_ijkl[k,:] = -0.5*(((z-h_il)/(sigma_z_ijklxD[k]))**2)
29             #definition of the deficit along y and z direction
30             deficit_y_ijklxD[:,k] = deficit_centre_ijkl[k]*np.exp(exponent_y_ijkl
31 [:,k])
32             deficit_z_ijklxD[k,:] = deficit_centre_ijkl[k]*np.exp(exponent_z_ijkl[
33 k,:])
34
35     return deficit_y_ijklxD/WS, deficit_z_ijklxD/WS, 6*sigma_y_ijklxD, 6*
36     sigma_z_ijklxD

```

After the evaluation of the constants related to the actuator disk theory, deficit values and standard deviation σ arrays are allocated (with zero as initial values).

Then the calculation process starts and σ along both direction is calculated using the expressions already seen and the wake decay constant for each streamwise coordinate considered. The $radical_{ijkl}$ parameter, which appeared in equation (3.148), is the maximum between two alternatives:

1. Zero
2. The effective value resulting from the expression

Why? Because it's necessary to keep into account that such parameter is inserted in a square root and we can only have positive values. So, a choice is made in order to provide a number without imaginary part, this could be a major risk especially in the near wake, were the model loses theoretical validity, possibly leading to absurd values.

Then the deficit is calculated according to the expressions reported in [2]. The function returns the deficit along both directions and 6 times the standard deviation. This happens because the standard deviation cannot represent the total width of the wake area and universally, it is assumed that the 99.7% of a Gaussian distribution are contained between a distance spacing from $+3\sigma$ and -3σ considered by the top of the distribution.

C.1.3. 3D Arrays calculation

As stated before, the second part of the codes deals with creating more complex images and outputs (always based on what have been experienced reading the literature) to analyse wake models results. The inputs used are the same as for the 2D Array analysis (C.1.2), as well as the Python libraries.

C.1.3.1. Deficit map along streamwise and crossflow direction

As mentioned before, the purpose of this output function is to report the data along vertical planes parallel to the axis of rotation sampling the wake of the turbine similarly to what can be is with PIV techniques in wind tunnels. This way is possible to have a great idea of how the velocity deficit evolves and how much area does it affect.

The function is called in a similar way as previous ones:

```

1 #Deficit maps along vertical planes at different x/D values, for BPA_VAWT method

```

```

2 plot_deficit_map_zy(BPA_VAWT(), xD, y, z, WS_ilk, D_src_il, H_src_il, h_il, ct_ilk,
  TI_ilk)
3 #Deficit maps along vertical planes at different x/D values, for NOJ_VAWT method
4 plot_deficit_map_zy(NOJ_VAWT(), xD, y, z, WS_ilk, D_src_il, H_src_il, h_il, ct_ilk,
  TI_ilk)

```

As can be seen, the input parameters used are always the same, it's only a matter of how they're used. The code part of this post-processing function it's almost the same as for the others:

- The calculation is performed by calling functions inside wake models scripts
- The data are arranged and plotted in specific ways

Therefore, the code used is:

```

1 def plot_deficit_map_zy(model, xD, y, z, WS_ilk, D_src_il, H_src_il, h_il, ct_ilk,
  TI_ilk):
2   Y,Z = np.meshgrid(y,z) #creating a grid
3   deficit_zy, sigma_y_xD, sigma_z_xD =model.deficit_map_zy(xD, y, z, WS_ilk, D_src_il
  , H_src_il, h_il, ct_ilk, TI_ilk) #evaluation of the deficit map
4   fig, ax = plt.subplots(1, len(xD), sharex=True, figsize=(16, 3), gridspec_kw={'
  hspace': 0.1, 'wspace': 0.65})
5   if model.getName() == 'NOJ_VAWT': #title settings
6     fig.suptitle(r'\textbf{Deficit yz map for Jensen method for VAWTs}', fontsize
  =18, y=1.3)
7   else:
8     fig.suptitle(r'\textbf{Deficit yz map for BPA method for VAWTs}', fontsize=18,
  y=1.3)
9   for k in range(len(xD)):
10    cmap_test = np.r_[[1, 1, 1, 1], [1, 1, 1, 1]], cm.Blues(np.linspace(0, 1, 128)
  )] # ensure zero deficit is white
11    cmap = ListedColormap(cmap_test)
12    levels = np.linspace(0, 1, 110)
13    c=ax[k].contourf(Y / D_src_il, Z / D_src_il, deficit_zy[k, :, :], levels=levels
  , cmap=cmap)
14    ax[k].grid(True, zorder=1)
15    ax[k].add_patch(Rectangle((-0.5, (h_il-(0.5)*H_src_il)/D_src_il), D_src_il/
  D_src_il, H_src_il/D_src_il, edgecolor='k', facecolor="none", zorder=10))
16    ax[k].set_ylabel(r"Spanwise distance [z/D]")
17    ax[k].set_xlabel(r"Crosswind distance [y/D]")
18    colorbar_range=np.linspace(0,1,11)
19    ax[k].set_xlim([-1.5, 1.5])
20    ax[k].set_ylim([0, (h_il+H_src_il*0.5)/D_src_il + 1])
21    ax[k].set_title(r'\textbf{x=}' + r'\textbf{y}'.format(xD[k]) + r'\textbf{D}"',
  fontsize=16)
22    cbaxes = fig.add_axes([0.3, 1.15, 0.4, 0.02])
23    plt.colorbar(c, orientation="horizontal", label=r"$\Delta U/U_0$", ticks=
  colorbar_range, format='%1f', cax=cbaxes)
24    filename3 = 'Deficit_map_zy_' + model.getName() + '.jpeg'
25    fig.savefig(filename3, bbox_inches = "tight")

```

However in this case there's a major difference: deficit are calculated as 3D arrays where the first index refers to the axial coordinate, while the others are for crossflow and spanwise components. The whole domain along the latter directions is divided in a grid by using the *meshgrid* function of *numpy* (a library for Python coding). This way it's like if vertical planes are represented by matrices. On account of that, new coordinates *Y* and *Z* are provided to the second function of the wake models scripts.

Similarly to the 2D case, the approach is different for the two models and the discussion splits up.

C.1.3.2. NOJ wake model code for 3D calculation

The initial part of the code, the libraries and the wake decay constant evaluation, is the same as for the 2D case. For sake's of concise, such part is not reported.

The remaining part of the code is:

```

1 # Evaluation of deficit map along z and y
2 def deficit_map_zy(self, xD, y, z, Y, Z, WS_ilk, D_src_il, H_src_il, h_il, ct_ilk,
  TI_ilk):
3     WS = WS_ilk
4     term_numerator_ijlk = (1 - np.sqrt(1 - ct_ilk))
5     #wake dimensions initialization
6     H_w = np.zeros(len(xD))
7     D_w = np.zeros(len(xD))
8     #initialization of the wake deficit, here is a 3D array with y and z are both
  matrix resulting from meshgrid
9     deficit_tot=np.zeros((len(xD),len(y),len(z)))
10    for k in range(len(xD)):
11        #wake evolution
12        H_w[k] = H_src_il + 2 * (self.kw_ilk(TI_ilk,ct_ilk,xD[k])) * xD[k] *
  D_src_il
13        D_w[k] = D_src_il + 2 * (self.kw_ilk(TI_ilk,ct_ilk,xD[k])) * xD[k] *
  D_src_il
14        #Exclusion of the area where the wake is not present
15        effective_deficit_area_y = (abs(y) <= D_w[k] / 2)
16        effective_deficit_area_z = (z <= H_w[k] / 2 + h_il) * (z >= h_il - H_w[k] /
  2)
17        effective_grid_y, effective_grid_z = np.meshgrid(effective_deficit_area_y,
  effective_deficit_area_z)
18        effective_grid= effective_grid_z*effective_grid_y #Boolean grid which
  identifies the effective wake area along the whole domain
19        #Total deficit calculation
20        deficit_tot[k, :, :] = WS * (term_numerator_ijlk) / ((H_w[k] / H_src_il) *
  (D_w[k] / D_src_il)) * (effective_grid) #deficit calculation, only for the
  effective wake area
21
22    return deficit_tot/WS, D_w, H_w

```

The first differences are observed when deficit values are allocated: this time we have a 3D array for the deficit whose dimensions are $length(xD) \cdot length(y) \cdot length(z)$. This time in fact, since the number of planes sampled is limited, there's no need to provide the entire domain's dimension along streamwise direction. Second main difference is that in order to apply the Boolean mask to limit the deficit area, a grid is created for such purpose.

It's also relevant that the original grid generated with X and Y is not used here. This happens because the equations used do not depend on such coordinates, so there's no need to use them. At the same time, they're introduced as input in order to make the code as much generalized as possible. In fact X and Y are used for the BPA model.

Once the calculation is accomplished it provides the velocity deficit as a 3D array to the output function.

C.1.3.3. BPA wake model code for 3D calculation

The approach is extremely similar to the one used for the 2D case as well as the one used by the NOJ method for the 3D case.

Input and libraries used are the same, also here the difference lies in the deficit's calculation:

```

1 # Evaluation of deficit map along z and y
2 def deficit_map_zy(self, xD, y, z, Y, Z, WS_ilk, D_src_il, H_src_il, h_il, ct_ilk,
  TI_ilk):
3     WS = WS_ilk
4     sqrt1ct_ilk = np.sqrt(1 - ct_ilk)
5     beta_ilk = 0.5 * (1 + sqrt1ct_ilk)/sqrt1ct_ilk
6     #Array's initialization
7     sigma_y_ijlk_xD=np.zeros(len(xD)) #standard deviation y
8     sigma_z_ijlk_xD=np.zeros(len(xD)) #standard deviation z
9     deficit_zy_ijlk_xD=np.zeros((len(xD),len(y),len(z))) #deficit inzialization (3
  D array)
10    for k in range(len(xD)):
11        #Wake standard deviation evolution
12        sigma_y_ijlk_xD[k] = (self.k_ilk(TI_ilk,ct_ilk,xD[k])) * xD[k] * D_src_il +
  0.25 * np.sqrt(beta_ilk) * D_src_il

```

```

13     sigma_z_ijkl_xD[k] = (self.k_ilk(TI_ilk,ct_ilk,xD[k]) * xD[k] * D_src_ilk +
14     0.25 * np.sqrt(beta_ilk) * H_src_ilk)
15     radical_ijkl = np.maximum(0, (1. - ct_ilk / (2 * math.pi * sigma_z_ijkl_xD[
16     k] * sigma_y_ijkl_xD[k]/ (D_src_ilk * H_src_ilk))))
17     #deficit a the centre evaluation
18     deficit_centre_ijkl = WS * (1. - np.sqrt(radical_ijkl))
19     #Exponents evaluation
20     exponent_zy_ijkl = -0.5 * (((Z - h_ilk) / (sigma_z_ijkl_xD[k])) ** 2)+(((Y)
21     / (sigma_y_ijkl_xD[k])) ** 2))
22     #Deficit evaluation for each XD resulting in a matrix for each coordinate
23     deficit_zy_ijkl_xD[k,:,:] = deficit_centre_ijkl * np.exp(exponent_zy_ijkl)
24
25     return deficit_zy_ijkl_xD/WS, 6*sigma_y_ijkl_xD, 6*sigma_z_ijkl_xD

```

As for the NOJ case the deficit is calculated as a 3D array but this time the new coordinates generated by the meshgrid operation Y and Z are used because the equations for the deficit depend on both the spanwise and crossflow direction. As before, the standard deviation is multiplied by 6 to consider all Gaussian distribution's extension.

C.1.3.4. Comparison of the wake models

By only adding a *for* cycle to the output function described in Section (C.1.2.1) in order to consider the wake models one at the time, it's possible to plot compare the results generated by the two models.

```

1 def plot_comparison(model1, model2, xD, y, z, WS_ilk, D_src_ilk, H_src_ilk, h_ilk, ct_ilk,
2     TI_ilk): #comparison between models
3     wakemodels=[model1, model2]
4     fig, ax = plt.subplots(2, len(xD), sharey='row', sharex='row', figsize=(9, 9),
5     gridspec_kw={'hspace': 0.5, 'wspace': 0.9}) #creating subplots
6     fig.suptitle(r"\textbf{Comparison between Jensen and BPA methods for VAWTs}",
7     fontsize=18, weight="bold")
8     for model in wakemodels:
9         deficit_Y_xD, deficit_Z_xD, sigma_y_xD, sigma_z_xD = model.deficit_profile_XD(
10         xD, y, z, WS_ilk, D_src_ilk, H_src_ilk, h_ilk, ct_ilk, TI_ilk) #evaluation of the
11         deficit for each model
12         for i in range(len(xD)):
13             ax[0,i].plot(deficit_Y_xD[:,i],y/D_src_ilk) #plot of the deficit along y
14             axis
15             ax[0,i].grid(True) #plotting settings
16             ax[0,i].set_xlim([-0.1882352, max(deficit_Y_xD[:,0])+0.1])
17             ax[0,i].set_ylim([-2, 2])
18             ax[0,i].set_xlabel(r'$\Delta U/U_0$')
19             ax[0,i].set_ylabel(r'Y/D')
20             ax[0,i].set_title(r"\textbf{x="} + r'\textbf{'.format(xD[i]) + r"\textbf{D
21             }", fontsize=16)
22             ax[0,i].plot(np.linspace(-0.2,1,50),np.full((50),0.5), color='green',
23             linestyle='dashed', label='_nolegend_') #turbine's projection
24             ax[0,i].plot(np.linspace(-0.2,1,50),np.full((50),-0.5), color='green',
25             linestyle='dashed', label='_nolegend_') #turbine's projection
26             for i in range(len(xD)):
27                 if model.getName() == 'NOJ_VAWT':
28                     t1=ax[1,i].plot(deficit_Z_xD[i,:],z/D_src_ilk) #plot of the deficit
29                     along z axis
30                 else:
31                     t2 =ax[1,i].plot(deficit_Z_xD[i, :], z / D_src_ilk)
32             ax[1,i].grid(True) #plotting settings
33             ax[1,i].set_xlim([-0.1, max(deficit_Z_xD[0,:])+0.1])
34             ax[1,i].set_ylim([0, 4])
35             ax[1,i].set_xlabel(r'$\Delta U/U_0$')
36             ax[1,i].set_ylabel(r'Z/D')
37             ax[1,i].set_title(r"\textbf{x="} + r'\textbf{'.format(xD[i]) + r"\textbf{D
38             }", fontsize=16)
39             ax[1,i].plot(np.linspace(-0.2,1,50),np.full((50),(h_ilk-(0.5)*H_src_ilk)/
40             D_src_ilk), color='green', linestyle='dashed', label='_nolegend_') #turbine's
41             projection
42             ax[1,i].plot(np.linspace(-0.2,1,50),np.full((50),(h_ilk+(0.5)*H_src_ilk)/
43             D_src_ilk), color='green', linestyle='dashed', label='_nolegend_') #turbine's

```

```

30 projection
   fig.legend(t1 + t2, (r"NOJ", r"BPA"),loc='center', bbox_to_anchor=(0.1, 0, 0.8225,
31 filename1 = 'Deficit_profile_comparison' + '.jpeg' #figure saving
32 plt.savefig(filename1)

```

C.2. Wake models scripts validation against literature data

In order to test the validity of the code scripts developed, a detailed comparison with literature data has been accomplished. The purpose of this section is to describe how this validation have been accomplished, both to testify the work as well as to provide the basis in case of future development or additional comparison with other data.

The validation process is divided into two main parts, as well as the code used to accomplish the validation:

- A part whose aim is to test if the code was set up correctly by comparing the results with the ones obtained by Abkar in [2].
- A second part that compares the predictions of the wake models with literature data (from experimental or numerical studies). The results of such comparisons are reported in Chapter (7) while an analysis of the literature cases considered is reported in Chapter (3).

Here instead is reported the code used and the related approach, in order to simplify possible future studies and the continuation of the current one.

One last detail is that the code for the wake models NOJ and BPA is the same from Section (C.1) so for the sake's of brevity, it's not reported again.

C.2.1. Validation of the code structure

As mentioned before, the first step is the analysis of the code set up or, in other terms, a check of its behaviour, a debug operation. This had allowed to find some errors related to wake's width as well as many others.

Since the wake models implemented are the same version of the ones proposed by Abkar [2], a direct comparison with the predictions obtained in this paper are made. In order to do so has been necessary to extract the literature data and organizing them into 4 Excel files, divided according to the method used (BPA or NOJ) and one for each coordinate (y and z). Moreover since the cases analysed by Abkar are 4, each Excel file has 4 different sheets, one for each case. The parameters used for each case are reported in Chapter (3). Regarding the Excel files, their structure must be the one reported in Table (C.1), in order to avoid compatibility problems with the code: The code reads even the input parameters from a .csv file, which must have a specific

y profiles or z profiles					
$\frac{x}{D} = k_1$		$\frac{x}{D} = k_2$		$\frac{x}{D} = k_3$	
$\left(\frac{\Delta V}{V_\infty}\right)_{\frac{x}{D}=k_{1,1}}$	$(y)_{\frac{x}{D}=k_{1,1}}$ OR $(z)_{\frac{x}{D}=k_{1,1}}$	$\left(\frac{\Delta V}{V_\infty}\right)_{\frac{x}{D}=k_{2,1}}$	$(y)_{\frac{x}{D}=k_{2,1}}$ OR $(z)_{\frac{x}{D}=k_{2,1}}$	$\left(\frac{\Delta V}{V_\infty}\right)_{\frac{x}{D}=k_{3,1}}$	$(y)_{\frac{x}{D}=k_{3,1}}$ OR $(z)_{\frac{x}{D}=k_{3,1}}$
$\left(\frac{\Delta V}{V_\infty}\right)_{\frac{x}{D}=k_{1,2}}$	$(y)_{\frac{x}{D}=k_{1,2}}$ OR $(z)_{\frac{x}{D}=k_{1,2}}$	$\left(\frac{\Delta V}{V_\infty}\right)_{\frac{x}{D}=k_{2,2}}$	$(y)_{\frac{x}{D}=k_{2,2}}$ OR $(z)_{\frac{x}{D}=k_{2,2}}$	$\left(\frac{\Delta V}{V_\infty}\right)_{\frac{x}{D}=k_{3,2}}$	$(y)_{\frac{x}{D}=k_{3,2}}$ OR $(z)_{\frac{x}{D}=k_{3,2}}$
$\left(\frac{\Delta V}{V_\infty}\right)_{\frac{x}{D}=k_{1,3}}$	$(y)_{\frac{x}{D}=k_{1,3}}$ OR $(z)_{\frac{x}{D}=k_{1,3}}$	$\left(\frac{\Delta V}{V_\infty}\right)_{\frac{x}{D}=k_{2,3}}$	$(y)_{\frac{x}{D}=k_{2,3}}$ OR $(z)_{\frac{x}{D}=k_{2,3}}$	$\left(\frac{\Delta V}{V_\infty}\right)_{\frac{x}{D}=k_{3,3}}$	$(y)_{\frac{x}{D}=k_{3,3}}$ OR $(z)_{\frac{x}{D}=k_{3,3}}$
...

Table C.1: Format style for the literature data

structure, reported in Table (C.2). Once all the files are ready, it's possible to start analysing the code. The first part of the code reports the libraries used and the input reading operations.

Input parameters				
Legend	Case 1	Case 2	Case 3	Case 4
D [m]	26	26	26	50
H [m]	24	24	48	100
z_h [m]	40	40	40	100
C_T	0.65	0.34	0.64	0.8
TI	0.091	0.091	0.091	0.083
W_S [$\frac{m}{s}$]	7	7	7	9.6

Table C.2: Format style for input parameters

```

1 import numpy as np
2 import matplotlib.pyplot as plt
3 from BPA_VAWT import BPA_VAWT
4 from NOJ_VAWT import NOJ_VAWT
5 import pandas as pd
6
7 plt.rcParams.update({
8     "text.usetex": True,
9     "font.size": 16,
10    "font.family": "serif",
11    "font.sans-serif": []})
12 DataPath="C:\\\" #Generic folder that contains the external data
13
14 #Code validation against original version
15 #Input parameters from .csv file
16 data_input=pd.read_csv('Input.csv', header=1, names=['Legend', 'Case_1', 'Case_2', '
17    Case_3', 'Case_4'],sep=';')
18 data_input=data_input.drop(['Legend'], axis=1)
19 case=input('Insert the case number (from 1 to 4): ') #choosing the case by keyboard
20 input
21 case_input = data_input['Case_' + case] #case input used to select the sheet
22 new_case_input=case_input.to_numpy() #conversion of the dataframe to an array
23 if int(case) != 4:
24     xD = np.array([3, 6, 9, 12]) # specific downwind distances normalized respect to D
25     for Abkar2019 case
26 else:
27     xD = np.array([3, 5, 7, 11])
28 #Saving inputs
29 ws = new_case_input[-1]
30 D = new_case_input[0]
31 H = new_case_input[1]
32 z_h = new_case_input[2]
33 Ct = new_case_input[3]
34 TI =new_case_input[4]
35 #Domain
36 x = np.linspace(-0.75*D, D*12, 200) #downstream distance
37 y = np.linspace(-200, 200, 200) # cross wind distance (both horizontal and vertical)
38 z = np.linspace(0, 200, 200) # cross wind distance (both horizontal and vertical)
39 #Trasformation of the input in arrays
40 WS_ilk = np.array([ws]) # wind speed at turbine
41 D_src_il = np.array([D]) # diameter of turbine
42 H_src_il = np.array([H]) # height of the turbine
43 h_il = np.array([z_h]) # urbine hub height
44 ct_ilk = np.array([Ct]) # thrust coefficient
45 TI_ilk = np.array([TI])

```

The input parameters are chosen depending on the case selected. As mentioned the possible cases are 4 and the user selects one of them. Such input is essential to make the code understanding which values we want to simulate. Once the .csv file is read, we have the input parameters that are instantly transformed into arrays and the domain is defined.

With the parameters at disposal, the output function is called as:

```

1 #Evaluation of deficit profiles along y and z directions for specific x/D values for
  the BPA_VAWT method against Abkar2019 values
2 plot_deficit_map(BPA_VAWT(), xD, y, z, WS_ilk, D_src_ilk, H_src_ilk, h_ilk, ct_ilk, TI_ilk
  , case)
3 filename1b= 'Deficit_profiles_BPA_VAWT' + '.jpeg'
4 plt.savefig(filename1b)
5 #Evaluation of deficit profiles along y and z directions for specific x/D values for
  the NOJ_VAWT method against Abkar2019 values
6 #plot_deficit_map(NOJ_VAWT(), xD, y, z, WS_ilk, D_src_ilk, H_src_ilk, h_ilk, ct_ilk,
  TI_ilk, case)
7 filename1c= 'Deficit_profiles_NOJ_VAWT' + '.jpeg'
8 plt.savefig(filename1c)

```

Using almost the same version of the code as the one reported in Section (C.1.2.1) it's possible to compare the velocity profiles calculated along spanwise and crossflow directions with the ones from [2].

```

1 def plot_deficit_map(model, xD, y, z, WS_ilk, D_src_ilk, H_src_ilk, h_ilk, ct_ilk, TI_ilk,
  case):
2     deficit_Y_xD, deficit_Z_xD, sigma_y_xD, sigma_z_xD = model.deficit_profile_XD(xD,
3     y, z, WS_ilk, D_src_ilk, H_src_ilk, h_ilk, ct_ilk, TI_ilk) #deficit profiles calculation
4     fig, ax = plt.subplots(2, len(xD), sharey='row', sharex='row', figsize=(9, 9),
5     gridspec_kw={'hspace': 0.5, 'wspace': 0.9})
6     if model.getName() == 'NOJ_VAWT': #titles settings and importing values from Abkar'
7     s paper
8         fig.suptitle(r"\textbf{Deficit profiles for Jensen method for VAWTs, Case }" +
9         r'\textbf{'.format(str(case)), fontsize=18)
10        abk_comp_z = pd.read_excel('Akbar_z_NOJ_VAWT.xlsx', sheet_name='Case_' + str(
11        case), header=2, na_values='nan', names=['x_' + str(xD[0]), 'z_' + str(xD[0]), 'x_
12        ' + str(xD[1]), 'z_' + str(xD[1]), 'x_' + str(xD[2]), 'z_' + str(xD[2]), 'x_' + str
13        (xD[3]), 'z_' + str(xD[3])])
14        abk_comp_y = pd.read_excel('Akbar_y_NOJ_VAWT.xlsx', sheet_name='Case_' + str(
15        case), header=2, na_values='nan', names=['x_' + str(xD[0]), 'z_' + str(xD[0]), 'x_
16        ' + str(xD[1]), 'z_' + str(xD[1]), 'x_' + str(xD[2]), 'z_' + str(xD[2]), 'x_' + str
17        (xD[3]), 'z_' + str(xD[3])])
18    else: #titles settings and importing values from Abkar's paper
19        fig.suptitle(r"\textbf{Deficit profiles for BPA method for VAWTs, Case }" + r'\
20        \textbf{'.format(str(case)), fontsize=18)
21        abk_comp_z = pd.read_excel('Akbar_z_BPA_VAWT.xlsx', sheet_name='Case_' + str(
22        case), header=2, na_values='nan', names=['x_' + str(xD[0]), 'z_' + str(xD[0]), 'x_
23        ' + str(xD[1]), 'z_' + str(xD[1]), 'x_' + str(xD[2]), 'z_' + str(xD[2]), 'x_' + str
24        (xD[3]), 'z_' + str(xD[3])])
25        abk_comp_y = pd.read_excel('Akbar_y_BPA_VAWT.xlsx', sheet_name='Case_' + str(
26        case), header=2, na_values='nan', names=['x_' + str(xD[0]), 'z_' + str(xD[0]), 'x_
27        ' + str(xD[1]), 'z_' + str(xD[1]), 'x_' + str(xD[2]), 'z_' + str(xD[2]), 'x_' + str
28        (xD[3]), 'z_' + str(xD[3])])
29
30    for i in range(len(xD)):
31        current_abk_comp_coordinate_y = abk_comp_y['z_' + str(xD[i])] #importing values
32        from Abkar along y
33        current_abk_comp_coordinate_y = current_abk_comp_coordinate_y.dropna().to_numpy
34        () #conversion to array
35        current_abk_comp_speed_y = abk_comp_y['x_' + str(xD[i])] #reading a specific
36        column
37        current_abk_comp_speed_y = current_abk_comp_speed_y.dropna().to_numpy() #
38        removing data nan
39        ax[0,i].plot(deficit_Y_xD[:,i],y/D_src_ilk,label='_nolegend_',zorder=4) #deficit
40        plotting along Y direction, normalized
41        ax[0, i].plot(current_abk_comp_speed_y, current_abk_comp_coordinate_y, 'o',
42        linewidth=1, markersize=5, markerfacecolor='none', markeredgewidth=1, label='
43        _nolegend_')
44        ax[0,i].grid(True)
45        ax[0,i].set_xlim([-0.1882352, max(deficit_Y_xD[:,0])+0.1])
46        ax[0,i].set_ylim([-2, 2])
47        ax[0,i].set_xlabel(r'$\Delta U/U_0$')
48        ax[0,i].set_ylabel(r'$Y/D$')
49        ax[0,i].set_title(r"\textbf{x=} + r'\textbf{'.format(xD[i]) + r"\textbf{D}",
50        fontsize=16 )
51        ax[0,i].plot(np.linspace(-0.2,1,50),np.full((50),0.5), color='green', linestyle

```

```

28 = 'dashed', label='_nolegend_') #turbine's projection
    ax[0,i].plot(np.linspace(-0.2,1,50),np.full((50),-0.5), color='green',
29 linestyle='dashed', label='_nolegend_') #turbine's projection
    for i in range(len(xD)):
30         current_abk_comp_coordinate_z = abk_comp_z['z_' + str(xD[i])] #same as before,
        but for z axis
31         current_abk_comp_coordinate_z = current_abk_comp_coordinate_z.dropna().to_numpy
        ()
32         current_abk_comp_speed_z = abk_comp_z['x_' + str(xD[i])]
33         current_abk_comp_speed_z = current_abk_comp_speed_z.dropna().to_numpy()
34         t1=ax[1,i].plot(deficit_Z_xD[i,:],z/D_src_il, zorder=4) #deficit plotting
        along Z direction, normalized
35         t2=ax[1, i].plot(current_abk_comp_speed_z, current_abk_comp_coordinate_z, 'o',
        linewidth=1, markersize=5,markerfacecolor='none', markeredgewidth=1)
36         ax[1,i].grid(True)
37         ax[1,i].set_xlim([-0.1, max(deficit_Z_xD[0,:])+0.1])
38         ax[1,i].set_ylim([0, 4])
39         ax[1,i].set_xlabel(r'$\Delta U/U_0$')
40         ax[1,i].set_ylabel(r'$Z/D$')
41         ax[1,i].set_title(r"\textbf{x=}" + r'\textbf{ }'.format(xD[i]) + r"\textbf{D}",
        fontsize=16)
42         ax[1,i].plot(np.linspace(-0.2,1,50),np.full((50),(h_il-(0.5)*H_src_il)/D_src_il
        ), color='green', linestyle='dashed', label='_nolegend_') #turbine's projection
43         ax[1,i].plot(np.linspace(-0.2,1,50),np.full((50),(h_il+(0.5)*H_src_il)/D_src_il
        ), color='green', linestyle='dashed', label='_nolegend_') #turbine's projection
44
45 fig.legend(t1 + t2,(r"Current study", r"Abkar2019"), loc='center', bbox_to_anchor
        =(0.1, 0, 0.8225, 0.955),fontsize=12) # plotting settings

```

The main difference with the code provided by Section (C.1.2.1) is the extraction of the values from the Excel files cited before and their plotting in comparison with the calculated data. The files are read just once, but for each xD value, the code searches in the data-frame for the correct columns to be read.

C.2.2. Validation against literature data

The second part of the validation is based on the comparison with data coming from specific literature papers [3, 97, 110]. Even in this case it's necessary to provide the Excel files according to the structure presented in Section (C.2.1). Once the file are provided the related function is called as:

```

1 #Comparison with literature data
2 literature=input('Enter literature paper keyword to compare with: ')
3 plot_literature_comparison(NOJ_VAWT(),BPA_VAWT(),literature)

```

So the data are compared with the ones coming from specific papers identified by the related keyword. In our case the keyword are:

- Tescione2014
- Abkar2017
- Shamsoddin2020a

Each one of them can be passed as an input by keyword. Now we analyse function's structure splitting it into parts. The first part deals with input parameters and how they're read.

```

1 #Comparison of wake models results with literature data
2 def plot_literature_comparison(model1, model2, literature):
3     #Reading the input parameters to run the simulation
4     if literature == 'Abkar2017' or literature=='Shamsoddin2020a':
5         literature_input=pd.read_excel(DataPath + literature + '_y.xlsx', sheet_name='
        Input', names=['H', 'D', 'U', 'I', 'zh', 'Ct'])
6         literature_input=literature_input.to_numpy().flatten()
7         ws = literature_input[2]

```

```

8     D = literature_input[1]
9     H = literature_input[0]
10    z_h = literature_input[4]
11    Ct = literature_input[-1]
12    TI = literature_input[3]
13    elif literature == 'Tescione2014':
14        literature_input = pd.read_excel(DataPath + literature + '_input.xlsx', names
=[ 'H', 'D', 'U', 'I', 'zh', 'Ct' ])
15        literature_input = literature_input.to_numpy().flatten()
16        ws = literature_input[2]
17        D = literature_input[1]
18        H = literature_input[0]
19        z_h = literature_input[4]
20        Ct = literature_input[-1]
21        TI = literature_input[3]
22    y = np.linspace(-10*D, 10*D, 200) # cross wind distance (both horizontal and
vertical)
23    z = np.linspace(-10*D, 10*D, 200)

```

The input reading process is the same for the Abkar2017 and the Shamsoddin2020a. This happens because the data extracted from this paper feature different cases, as reported in Chapter (3). In the first case we have different thrust coefficients, therefore the Excel file shows different sheets that depends on the C_T chosen. In the second case, different aspect ratios have been tested. According to the input chosen and reported in the first sheet of the Excel file related to data along y, different data are read. The structure of the input sheet is extremely simple and can be deduced by observing line 4. The parameters extracted are converted in a way wake models can understand. Regarding the Tescione2014 case instead, the process is similar but the input parameters are reported in a separated file.

Now that the input values have been extracted it's time to extract also the data.

```

1    #Acquisition of the Excel data from the files
2    if literature == 'Abkar2017':
3        xD = pd.read_excel(DataPath + literature + '_y.xlsx', sheet_name='xD', rows=1)
        .dropna(axis='columns').to_numpy().flatten()
4        lit_data_y = pd.read_excel(DataPath + literature + '_y.xlsx', sheet_name='CT_'
+ str(Ct), header=1, na_values='nan')
5        lit_data_y_names=list(lit_data_y.columns)
6        lit_data_z = pd.read_excel(DataPath + literature + '_z.xlsx', sheet_name='CT_'
+ str(Ct), header=1, na_values='nan')
7        lit_data_z_names=list(lit_data_z.columns)
8    elif literature == 'Shamsoddin2020a':
9        xD = pd.read_excel(DataPath + literature + '_y.xlsx', sheet_name='xD', rows=1)
        .dropna(axis='columns').to_numpy().flatten()
10       lit_data_y = pd.read_excel(DataPath + literature + '_y.xlsx', sheet_name='H_' +
str(int(H)), header=1, na_values='nan')
11       lit_data_y_names=list(lit_data_y.columns)
12       lit_data_z = pd.read_excel(DataPath + literature + '_z.xlsx', sheet_name='H_' +
str(int(H)), header=1, na_values='nan')
13       lit_data_z_names=list(lit_data_z.columns)
14    elif literature == 'Tescione2014':
15       xD = pd.read_excel(DataPath + literature + '_input.xlsx', sheet_name='xD', rows
=1).dropna(axis='columns').to_numpy().flatten()
16       lit_data_y = pd.read_excel(DataPath + literature + '_y.xlsx', header=1,
na_values='nan')
17       lit_data_y_names=list(lit_data_y.columns)
18       lit_data_z = pd.read_excel(DataPath + literature + '_z.xlsx', header=1,
na_values='nan')
19       lit_data_z_names=list(lit_data_z.columns)

```

Data are extracted by reading the Excel files, according to the specific cases used. Also the xD coordinates are extracted from a separated sheet in the file. The process is not the same for all the possible cases because of the differences discussed because. On account of that it's impossible to create a universal code for the validation process. Now the core of the calculation starts:

```

1  wakemodels=[model1, model2] #Definition of an array of wake models
2  if literature == 'Abkar2017':
3      fig, ax = plt.subplots(2, len(xD), sharey='row', sharex='row', figsize=(12, 9),
4                          gridspec_kw={'hspace': 0.4, 'wspace': 0.6})
5      fig.suptitle(r"\textbf{Predictions comparison with data from }" + r"\textbf{
6      {{{}}}' .format(literature) + r"\textbf{{{ $C_T = $ }}}" + r"\textbf{{{}}}' .format(
7          str(Ct)),
8          fontsize=18)
9      elif literature == 'Shamsoddin2020a':
10         fig, ax = plt.subplots(2, len(xD), sharey='row', sharex='row', figsize=(16, 7),
11                             gridspec_kw={'hspace': 0.4, 'wspace': 0.6})
12         fig.suptitle(r"\textbf{Predictions comparison with data from }" + r"\textbf{
13         {{{}}}' .format(
14             literature) + r"\textbf{{{ AR = }}}" + r"\textbf{{{}}}' .format(str((H/D))),
15             fontsize=18)
16         elif literature == 'Tescione2014':
17             fig, ax = plt.subplots(2, len(xD), sharey='row', sharex='row', figsize=(16, 9),
18                                 gridspec_kw={'hspace': 0.4, 'wspace': 0.4})
19             fig.suptitle(r"\textbf{Predictions comparison with data from }" + r"\textbf{
20             {{{}}}' .format(
21                 literature), fontsize=18)
22         for model in wakemodels:
23             deficit_Y_xD, deficit_Z_xD, width_y_xD, width_z_xD = model.deficit_profile_XD(
24                 xD, y, z, ws, D, H, z_h, Ct, TI) # evaluation of the deficit for each model
25             if literature == 'Tescione2014':
26                 deficit_Y_xD=1-deficit_Y_xD
27                 deficit_Z_xD = 1 - deficit_Z_xD
28             for i in range(len(xD)):
29                 current_lit_comp_coordinate_y = lit_data_y[lit_data_y_names[2*i + 1]] #
30                 importing values from Abkar along y
31                 current_lit_comp_coordinate_y = current_lit_comp_coordinate_y.dropna().
32                 to_numpy() #conversion to array
33                 current_lit_comp_speed_y = lit_data_y[lit_data_y_names[2*i]] #reading a
34                 specific column
35                 current_lit_comp_speed_y = current_lit_comp_speed_y.dropna().to_numpy() #
36                 removing data nan
37                 ax[0, i].plot(deficit_Y_xD[:, i], y / D, label='_nolegend_',
38                             zorder=4) # deficit plotting along Y direction, normalized
39                 ax[0, i].plot(current_lit_comp_speed_y, current_lit_comp_coordinate_y, 'o',
40                             linewidth=1, markersize=5,
41                             markerfacecolor='none', markeredgewidth=1, label='_nolegend_'
42                 )
43                 ax[0, i].grid(True)
44                 ax[0, i].set_xlim([-0.2, max(deficit_Y_xD[:, 0]) + 0.15])
45                 ax[0, i].set_ylim([-1.5, 1.5])
46
47                 ax[0, 0].set_ylabel(r'Y/D')
48                 ax[0, i].set_title(r"\textbf{x=} + r"\textbf{{{}}}' .format(xD[i]) + r"\
49                 textbf{D}", fontsize=16)
50                 ax[0, i].plot(np.linspace(-10, 10, 50), np.full((50), 0.5), color='black',
51                             linestyle='dashed',
52                             label='_nolegend_' ) # turbine's projection
53                 ax[0, i].plot(np.linspace(-10, 10, 50), np.full((50), -0.5), color='black',
54                             linestyle='dashed',
55                             label='_nolegend_' ) # turbine's projection
56             for i in range(len(xD)):
57                 current_lit_comp_coordinate_z = lit_data_z[lit_data_z_names[2*i+1]] #
58                 importing values from Abkar along y
59                 current_lit_comp_coordinate_z = current_lit_comp_coordinate_z.dropna().
60                 to_numpy() #conversion to array
61                 current_lit_comp_speed_z = lit_data_z[lit_data_z_names[2*i]] #reading a
62                 specific column
63                 current_lit_comp_speed_z = current_lit_comp_speed_z.dropna().to_numpy() #
64                 removing data nan
65                 if model.getName() == 'NOJ_VAWT':
66                     t1=ax[1, i].plot(deficit_Z_xD[i, :], z / D) # deficit plotting along Y
67                     direction, normalized
68                 else:
69                     t2 =ax[1, i].plot(deficit_Z_xD[i, :], z / D)
70                     t3=ax[1, i].plot(current_lit_comp_speed_z, current_lit_comp_coordinate_z, '
71                     o', linewidth=1, markersize=5,

```

```

52         markerfacecolor='none', markeredgewidth=1, label='_nolegend_'
53     )
54     ax[1, i].grid(True)
55     ax[1, i].set_xlim([-0.2, max(deficit_Z_xD[0, :] + 0.15)])
56     ax[1, i].set_ylim([-0.1, 1])
57     ax[1, i].set_xlabel(r'$\frac{\Delta U}{U_0}$')
58     ax[1, 0].set_ylabel(r'Z/D')
59     ax[1, i].plot(np.linspace(-10, 10, 50), np.full((50), (z_h - (0.5) * H) / D
60 ), color='black',
61                 linestyle='dashed', label='_nolegend_') # turbine's
62     projection
63     ax[1, i].plot(np.linspace(-10, 10, 50), np.full((50), (z_h + (0.5) * H) / D
64 ), color='black',
65                 linestyle='dashed', label='_nolegend_') # turbine's
66     projection
67     fig.legend(t1 + t2 + t3, (r"NOJ", r"BPA", literature), loc='center', ncol=3,
68                bbox_to_anchor=(0.01, -0.015, 1, 1)) # plotting settings
69     filename1 = 'Deficit_profile_lit_comparison' + '.jpeg' #figure saving
70     plt.savefig(filename1)

```

First of all, the deficit is calculated using each wake model in a *for* cycle. Since in Tescione's paper [110] the data express the velocity in the wake and not the deficit, a small algebraic operation is needed. Then the calculated data are plotted against literature data and the comparison is finally completed.

D

Additional data and results collection

This appendix is a collection of all the data and results 'created' in this thesis work that can be considered 'additional', reported here because they can be considered not essential for the purpose of the work. At the same time they contribute to underline work's quality and entity providing many additional details that reveal the depth of the work done.

D.1. Debugging and verification of code scripts

As mentioned in Section (4.2.4) here are reported the comparison between the predictions from the code scripts developed and from the original work by Abkar [2] for the remain cases reported in Table (4.14). As

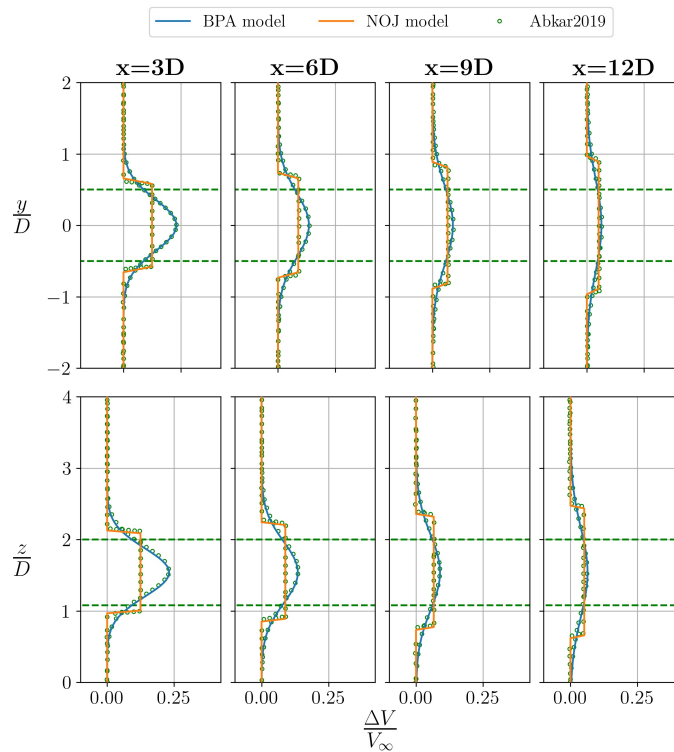


Figure D.1: Comparison between the predictions from the models developed in this thesis and the ones from the original model [2] for Case 2 in Table (4.14)

it's possible to see, even changing the parameters (AR , C_T , I and so on), the code provides exact the same results of Abkar, so it is possible to conclude that the code implementation is valid, free from bugs, and the

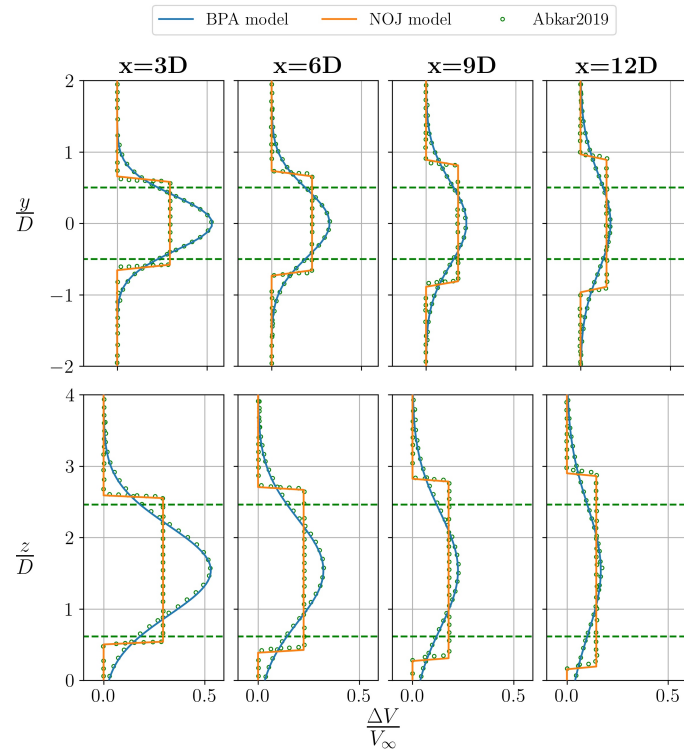


Figure D.2: Comparison between the predictions from the models developed in this thesis and the ones from the original model [2] for Case 3 in Table (4.14)

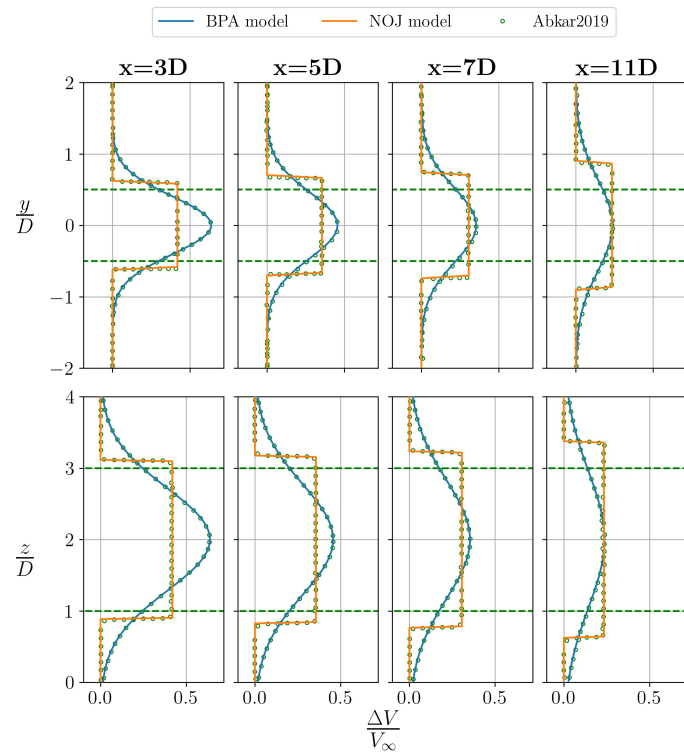


Figure D.3: Comparison between the predictions from the models developed in this thesis and the ones from the original model [2] for Case 4 in Table (4.14)

calculation process is theoretically correct. It necessary to mention that this model is based on the wake decay law provided by Abkar [2] itself, the Niayifar law has not been tested here but the implementation is the same used in py-wake library.

D.2. Maximum and mean velocity deficit along crossflow direction in Shamsoddin et al. [97]

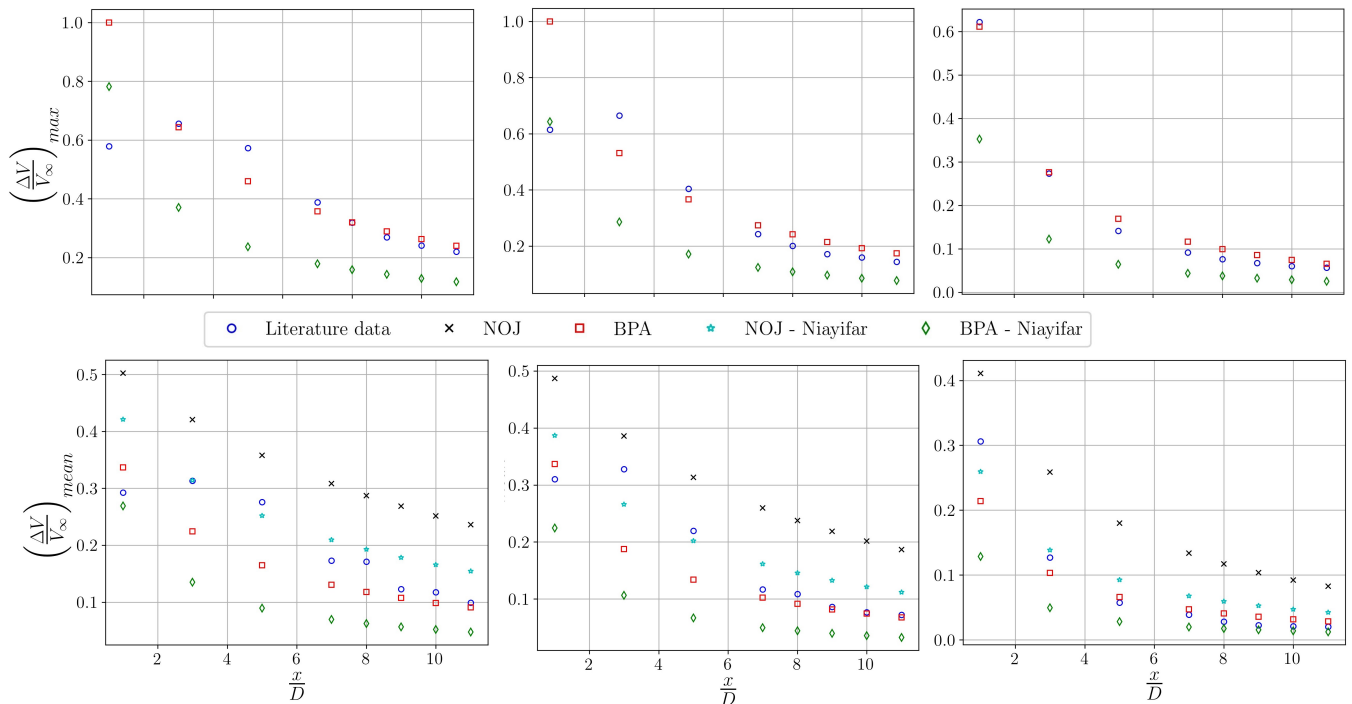


Figure D.4: Evolution of the maximum deficit value (top) and the mean velocity value (bottom) according to [3] for $AR = 2$ (left), $AR = 1$ (centre) and $AR = 0.25$ (right) for different wake models compared with literature data

D.3. Velocity profiles in the Reynolds' number effect analysis

As mentioned in Chapter (7) here the velocity profiles when considering the symmetry plan are reported in Figure (D.5).

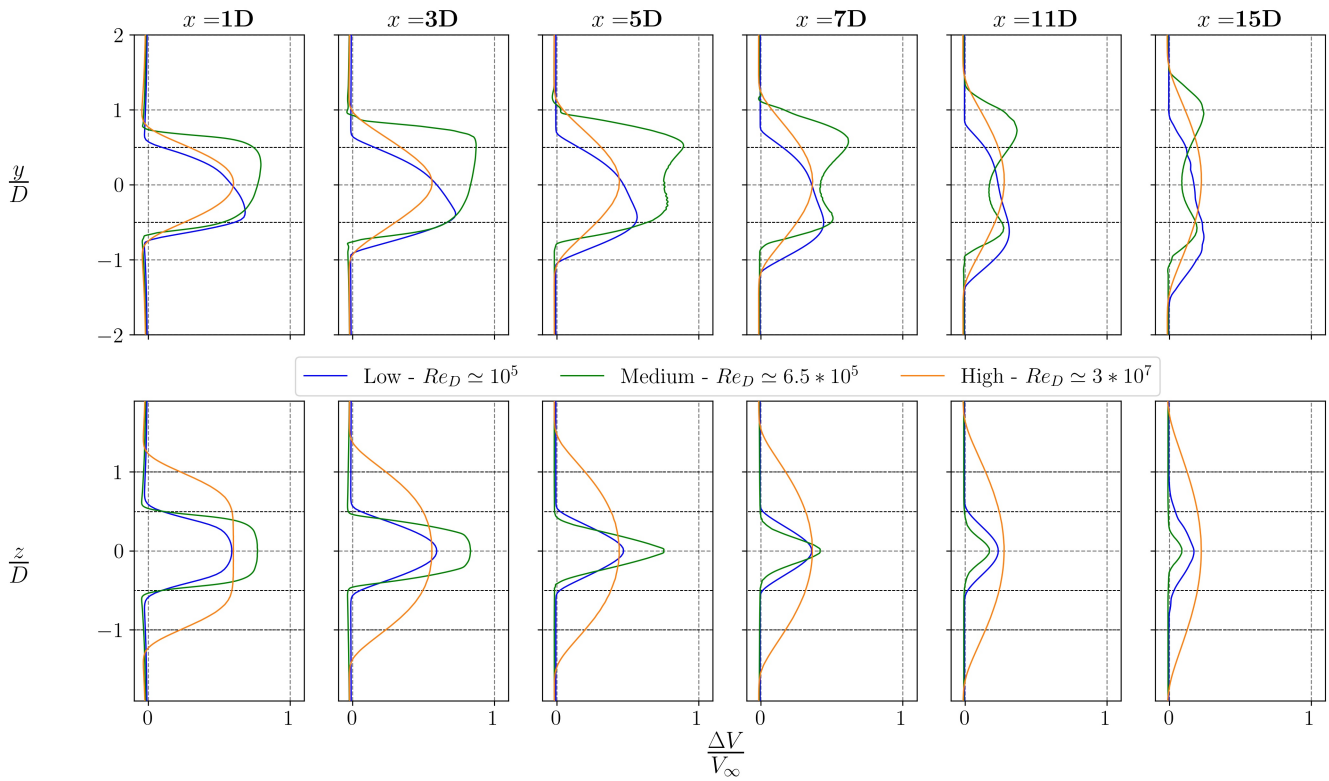


Figure D.5: Profiles of mean streamwise velocity deficit along crossflow direction at mid-span (top) and spanwise direction at wake's centre (bottom) for different downstream sections in different Re condition

D.4. Velocity profiles in different turbulent conditions

As mentioned in Chapter (7), the profiles do not provide additional information since the wake is extremely deformed in the laminar cases and it is impossible to evaluate only one relevant velocity profile. The ones evaluated for $\frac{z}{D} = 0$ are reported in Figure (D.6) and consider the horizontal plane at mid-span.

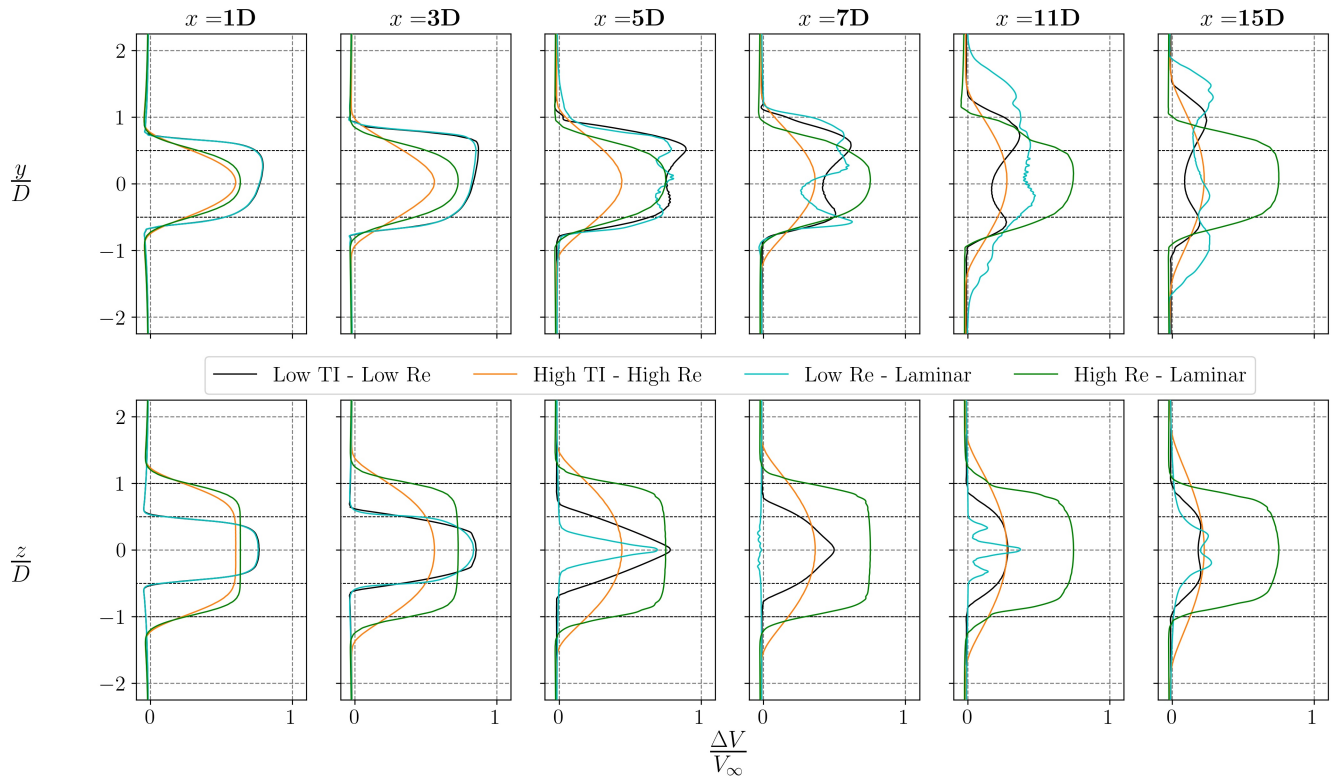


Figure D.6: Profiles of mean streamwise velocity deficit along crossflow direction at mid-span (top) and spanwise direction at wake's centre (bottom) for different downstream sections in different turbulent conditions

Bibliography

- [1] M. Abkar. Impact of Subgrid-Scale Modeling in Actuator-Line Based Large-Eddy Simulation of Vertical-Axis Wind Turbine Wakes, 2018.
- [2] M. Abkar. Theoretical modeling of vertical-axis wind turbine wakes. *Energies*, 12(1):10, 2019.
- [3] M. Abkar and J. O. Dabiri. Self-similarity and flow characteristics of vertical-axis wind turbine wakes: an LES study. *Journal of Turbulence*, 2017.
- [4] M. Ahmadi-Baloutaki, R. Carriveau, and D. S. Ting. Performance of a vertical axis wind turbine in grid generated turbulence. *Sustainable Energy Technologies and Assessments*, 2015.
- [5] J. F. Ainslie. Calculating the flowfield in the wake of wind turbines. *Journal of Wind Engineering and Industrial Aerodynamics*, 1988.
- [6] D. B. Araya, T. Colonius, and J. O. Dabiri. Transition to bluff-body dynamics in the wake of vertical-axis wind turbines. *Journal of Fluid Mechanics*, 2017.
- [7] P. Bachant, A. Goude, Daa-mec, and M. Wosnik. turbinesFoam/turbinesFoam: v0.1.1. nov 2019.
- [8] P. Bachant, A. Goude, and M. Wosnik. Actuator line modeling of vertical-axis turbines. 2018.
- [9] R. J. Barthelmie, S. T. Frandsen, M. N. Nielsen, S. C. Pryor, P. E. Rethore, and H. E. Jørgensen. Modelling and measurements of power losses and turbulence intensity in wind turbine wakes at middelgrunden offshore wind farm. *Wind Energy*, 10(6):517–528, 2007.
- [10] M. Bastankhah and F. Porté-Agel. A new analytical model for wind-turbine wakes. *Renewable Energy*, 2014.
- [11] M. Bastankhah and F. Porté-Agel. Experimental and theoretical study of wind turbine wakes in yawed conditions. *Journal of Fluid Mechanics*, 806:506–541, nov 2016.
- [12] T. S. Beddoes. A third generation model for unsteady aerodynamics and dynamic stall. *Westland Helicopter Limited, RP-908*, 1993.
- [13] M. Boudreau and G. Dumas. Comparison of the wake recovery of the axial-flow and cross-flow turbine concepts. *Journal of Wind Engineering and Industrial Aerodynamics*, 2017.
- [14] J. Bremseth and K. Duraisamy. Computational analysis of vertical axis wind turbine arrays. *Theoretical and Computational Fluid Dynamics*, 30(5):387–401, 2016.
- [15] A.-J. Buchner, M. W. Lohry, L. Martinelli, J. Soria, and A. J. Smits. Dynamic stall in vertical axis wind turbines: Comparing experiments and computations. *Journal of Wind Engineering and Industrial Aerodynamics*, 146:163–171, 2015.
- [16] Z. Cheng, H. A. Madsen, Z. Gao, and T. Moan. Aerodynamic modeling of offshore vertical axis wind turbines using the actuator cylinder method. 2016.
- [17] ChristianT. Vertical axis wind turbine, https://commons.wikimedia.org/wiki/File:Éole_à_Cap-Chat_en_2010.JPG, 2010.
- [18] A. E. Craig, J. O. Dabiri, and J. R. Koseff. Low order physical models of vertical axis wind turbines. *Journal of Renewable and Sustainable Energy*, 9(1):1–17, 2017.
- [19] J. O. Dabiri. Potential order-of-magnitude enhancement of wind farm power density via counter-rotating vertical-axis wind turbine arrays. *Journal of Renewable and Sustainable Energy*, 3, 2011.

- [20] D. De Tavernier. *Aerodynamic advances in vertical axis wind turbine*. 2021.
- [21] E. Dyachuk, A. Goude, and H. Bernhoff. Dynamic Stall Modeling for the Conditions of Vertical Axis Wind Turbines. *AIAA Journal*, 52(1):72–81, dec 2013.
- [22] M. Elkhoury, T. Kiwata, and E. Aoun. Experimental and numerical investigation of a three-dimensional vertical-axis wind turbine with variable-pitch. *Journal of Wind Engineering and Industrial Aerodynamics*, 139:111–123, 2015.
- [23] C. Ferreira, C. Hofemann, K. Dixon, G. Van Kuik, and G. Van Bussel. 3D wake dynamics of the VAWT: Experimental and numerical investigation. In *48th AIAA Aerospace Sciences Meeting Including the New Horizons Forum and Aerospace Exposition*, 2010.
- [24] E. Ferrer and R. H. Willden. Blade-wake interactions in cross-flow turbines. *International Journal of Marine Energy*, 2015.
- [25] S. Frandsen, R. Barthelmie, S. Pryor, O. Rathmann, S. Larsen, J. Højstrup, and M. Thøgersen. Analytical modelling of wind speed deficit in large offshore wind farms. In *Wind Energy*, 2006.
- [26] S. Giorgetti, G. Pellegrini, and S. Zanforlin. CFD Investigation on the Aerodynamic Interferences between Medium-solidity Darrieus Vertical Axis Wind Turbines. *Energy Procedia*, 81:227–239, 2015.
- [27] H. Glauert. Airplane Propellers. In *Aerodynamic Theory*, pages 169–360. Springer Berlin Heidelberg, 1935.
- [28] T. Göçmen, P. V. D. Laan, P. E. Réthoré, A. P. Diaz, G. C. Larsen, and S. Ott. Wind turbine wake models developed at the technical university of Denmark: A review. *Renewable and Sustainable Energy Reviews*, 60:752–769, 2016.
- [29] A. Goude. Fluid mechanics of vertical axis turbines: Simulations and model development, 2012.
- [30] K. Hamada, T. Smith, N. Durrani, N. Qin, and R. Howell. Unsteady flow simulation and dynamic stall around vertical axis wind turbine blades. In *46th AIAA Aerospace Sciences Meeting and Exhibit*, page 1319, 2008.
- [31] M. Hansen. *Aerodynamics of wind turbines*. Routledge, 2015.
- [32] E. Hau. *Wind turbines: fundamentals, technologies, application, economics*. Springer Science & Business Media, 2013.
- [33] S. H. Hezaveh, E. Bou-Zeid, J. Dabiri, M. Kinzel, G. Cortina, and L. Martinelli. Increasing the Power Production of Vertical-Axis Wind-Turbine Farms Using Synergistic Clustering. *Boundary-Layer Meteorology*, 169(2):275–296, 2018.
- [34] S. H. Hezaveh, E. Bou-Zeid, M. W. Lohry, and L. Martinelli. Simulation and wake analysis of a single vertical axis wind turbine. *Wind Energy*, 2017.
- [35] R. Howell, N. Qin, J. Edwards, and N. Durrani. Wind tunnel and numerical study of a small vertical axis wind turbine. *Renewable Energy*, 35(2):412–422, 2010.
- [36] M. Huang, C. Ferreira, A. Sciacchitano, and F. Scarano. Experimental Comparison of the Wake of a Vertical Axis Wind Turbine and Planar Actuator Surfaces. *Journal of Physics: Conference Series*, 1618(5), 2020.
- [37] G. Iaccarino, A. Ooi, P. A. Durbin, and M. Behnia. Reynolds averaged simulation of unsteady separated flow. *International Journal of Heat and Fluid Flow*, 24(2):147–156, 2003.
- [38] IEA. Global Energy Review 2020. Technical report, Paris, 2020.
- [39] IEA and OECD. Monthly Electricity Statistics. Technical report, 2021.
- [40] IEA37. Wake Model Description for Optimization Only Case Study. *System engineering in Wind Energy*, pages 2–3, 2019.

- [41] M. Islam, D. S.-K. Ting, and A. Fartaj. Aerodynamic models for Darrieus-type straight-bladed vertical axis wind turbines. *Renewable and Sustainable Energy Reviews*, 12(4):1087–1109, 2008.
- [42] P. Jamieson. *Innovation in Wind Turbine Design*. 2011.
- [43] N. O. Jensen. A note on wind generator interaction. *Risø-M-2411 Risø National Laboratory Roskilde*, 2411:1–16, 1983.
- [44] A. R. Jha. *Wind turbine technology*. 2010.
- [45] H. Kadum, S. Friedman, E. H. Camp, and R. B. Cal. Development and scaling of a vertical axis wind turbine wake. *Journal of Wind Engineering and Industrial Aerodynamics*, 2018.
- [46] J. K. Kaldellis, P. Triantafyllou, and P. Stinis. Critical evaluation of Wind Turbines' analytical wake models. *Renewable and Sustainable Energy Reviews*, 144:110991, 2021.
- [47] I. Katic, J. Højstrup, and N. Jensen. A Simple Model for Cluster. *EWEC'86. Proceedings*, 1:407–410, 1987.
- [48] M. Kinzel, D. B. Araya, and J. O. Dabiri. Turbulence in vertical axis wind turbine canopies. *Physics of Fluids*, 27(11):115102, 2015.
- [49] M. Kinzel, Q. Mulligan, and J. O. Dabiri. Energy exchange in an array of vertical-axis wind turbines. *Journal of Turbulence*, 13:1–13, 2012.
- [50] P. Kumar, K. Sivalingam, T.-C. Lim, S. Ramakrishna, and W. He. Review on the Evolution of Darrieus Vertical Axis Wind Turbine: Large Wind Turbines. *Clean Technologies*, 1:205–223, aug 2019.
- [51] H. F. Lam and H. Y. Peng. Development of a wake model for Darrieus-type straight-bladed vertical axis wind turbines and its application to micro-siting problems. *Renewable Energy*, 2017.
- [52] A. Laneville and P. Vittecoq. Dynamic stall: The case of the vertical axis wind turbine. *Journal of Solar Energy Engineering, Transactions of the ASME*, 1986.
- [53] G. Larsen. A Simple Wake Calculation Procedure. *Risø-M*, No. 2760:58, 1988.
- [54] G. C. Larsen. A simple stationary semi-analytical wake model. *Denmark. Forskningscenter Risoe. Risoe-R*, 2009.
- [55] B. Launder and B. I. Sharma. Application of the energy-dissipation model of flow near a spinning disc. *Lett. Heat Mass Transfer*, pages 131–138, jan 1974.
- [56] J. Leishman and T. Beddoes. A Semi-Empirical Model for Dynamic Stall. *Journal of The American Helicopter Society*, 34:3–17, 1989.
- [57] J. G. Leishman and T. S. Beddoes. A Generalised Model for Airfoil Unsteady Aerodynamic Behaviour and Dynamic Stall Using Indicial Method, 1986.
- [58] C. Li, S. Zhu, Y.-I. Xu, and Y. Xiao. 2.5D large eddy simulation of vertical axis wind turbine in consideration of high angle of attack flow. *Renewable Energy*, 51:317–330, 2013.
- [59] V. Lyatkher. *Wind Power: Turbine Design, Selection, and Optimization*. Hoboken John Wiley & Sons, Inc., Hoboken, 2013.
- [60] H. Madsen. *The Actuator Cylinder - A Flow Model for Vertical Axis Wind Turbines*. PhD thesis, jan 1982.
- [61] T. Maitre, E. Amet, and C. Pellone. Modeling of the flow in a Darrieus water turbine: Wall grid refinement analysis and comparison with experiments. *Renewable Energy*, 51:497–512, mar 2013.
- [62] L. Massie, P. Ouro, T. Stoesser, and Q. Luo. An actuator surface model to simulate vertical axis turbines. *Energies*, 2019.
- [63] R. May, T. Nygård, U. Falkdalen, J. Åström, Ø. Hamre, and B. G. Stokke. Paint it black: Efficacy of increased wind turbine rotor blade visibility to reduce avian fatalities. *Ecology and Evolution*, 10(16):8927–8935, aug 2020.

- [64] V. Mendoza. Aerodynamic Studies of Vertical Axis Wind Turbines using the Actuator Line Model, 2018.
- [65] V. Mendoza, P. Bachant, C. Ferreira, and A. Goude. Near-wake flow simulation of a vertical axis turbine using an actuator line model. *Wind Energy*, 2019.
- [66] V. Mendoza, P. Bachant, M. Wosnik, and A. Goude. Validation of an Actuator Line Model Coupled to a Dynamic Stall Model for Pitching Motions Characteristic to Vertical Axis Turbines. In *Journal of Physics: Conference Series*, 2016.
- [67] V. Mendoza and A. Goude. Validation of Actuator Line and Vortex Models using Normal Forces Measurements of a Straight-Bladed Vertical Axis Wind Turbine. *Energies*, 2020.
- [68] A. C. Molina, T. Massai, F. Balduzzi, A. Bianchini, G. Ferrara, T. De Troyer, and G. Bartoli. Combined experimental and numerical study on the near wake of a Darrieus VAWT under turbulent flows. In *Journal of Physics: Conference Series*, 2018.
- [69] V. D. Narasimhamurthy. *Unsteady-RANS simulation of turbulent trailing-edge flow*. Citeseer, 2004.
- [70] V. Nelson. *Innovative Wind Turbines: An Illustrated Guidebook*. CRC Press, 2019.
- [71] B. G. Newman. Actuator-disc theory for vertical-axis wind turbines. *Journal of Wind Engineering and Industrial Aerodynamics*, 1983.
- [72] A. Niayifar and F. Porté-Agel. A new analytical model for wind farm power prediction. *Journal of Physics: Conference Series*, 625(1), 2015.
- [73] A. Niayifar and F. Porté-Agel. Analytical modeling of wind farms: A new approach for power prediction. *Energies*, 2016.
- [74] A. Orlandi, M. Collu, S. Zanforlin, and A. Shires. 3D URANS analysis of a vertical axis wind turbine in skewed flows. *Journal of Wind Engineering and Industrial Aerodynamics*, 147:77–84, 2015.
- [75] S. Ott, J. Berg, and M. Nielsen. Linearised CFD Models for Wakes, 2011.
- [76] S. Ott and M. Nielsen. Developments of the offshore wind turbine wake model Fuga. *E-0046 Report*, 2014.
- [77] P. Ouro and M. Lazennec. *Analytical models for the asymmetric wake of vertical axis wind turbines*. 2020.
- [78] P. Ouro, S. Runge, Q. Luo, and T. Stoesser. Three-dimensionality of the wake recovery behind a vertical axis turbine. *Renewable Energy*, 133:1066–1077, 2019.
- [79] P. Ouro and T. Stoesser. An immersed boundary-based large-eddy simulation approach to predict the performance of vertical axis tidal turbines. *Computers and Fluids*, 152:74–87, jul 2017.
- [80] P. Ouro and T. Stoesser. Wake Generated Downstream of a Vertical Axis Tidal Turbine. In *12th European Wave and Tidal Energy Conference (EWTEC)*, 2017.
- [81] I. Paraschivoiu. Double-multiple streamtube model for Darrieus in turbines. 1981.
- [82] M. M. Pedersen, P. van der Laan, M. Friis-Møller, J. Rinker, and P.-E. Réthoré. DTUWindEnergy/PyWake: PyWake, 2019.
- [83] H. Y. Peng, H. F. Lam, and C. F. Lee. Investigation into the wake aerodynamics of a five-straight-bladed vertical axis wind turbine by wind tunnel tests. *Journal of Wind Engineering and Industrial Aerodynamics*, 155:23–35, aug 2016.
- [84] J. T. G. Pierik, J. W. M. Dekker, H. Braam, B. H. Bulder, D. Winkelaar, G. C. Larsen, E. Morfiadakis, P. Chaviaropoulos, A. Derrick, and J. P. Molly. European wind turbine standards II (EWTS-II) , 1999.
- [85] S. B. Pope. *Turbulent Flows*. Cambridge University Press, Cambridge, 2000.

- [86] A. Posa and E. Balaras. Large Eddy Simulation of an isolated vertical axis wind turbine. *Journal of Wind Engineering and Industrial Aerodynamics*, 2018.
- [87] A. Posa, C. M. Parker, M. C. Leftwich, and E. Balaras. Wake structure of a single vertical axis wind turbine. *International Journal of Heat and Fluid Flow*, 2016.
- [88] V. Rolin and F. Porté-Agel. Wind-tunnel study of the wake behind a vertical axis wind turbine in a boundary layer flow using stereoscopic particle image velocimetry. In *Journal of Physics: Conference Series*, 2015.
- [89] V. F. Rolin and F. Porté-Agel. Experimental investigation of vertical-axis wind-turbine wakes in boundary layer flow. *Renewable Energy*, 118:1–13, 2018.
- [90] K. J. Ryan, F. Coletti, C. J. Elkins, J. O. Dabiri, and J. K. Eaton. Three-dimensional flow field around and downstream of a subscale model rotating vertical axis wind turbine. *Experiments in Fluids*, 57(3):38, 2016.
- [91] A. Schaffarczyk. *Introduction to Wind Turbine Aerodynamics*. jan 2020.
- [92] F. Scheurich, T. M. Fletcher, and R. E. Brown. Simulating the aerodynamic performance and wake dynamics of a vertical-axis wind turbine. *Wind Energy*, 2011.
- [93] R. Schwarze and F. Obermeier. Performance and limitations of the unsteady RANS approach. In *PAMM: Proceedings in Applied Mathematics and Mechanics*, volume 6, pages 543–544. Wiley Online Library, 2006.
- [94] M. Shaheen and S. Abdallah. Development of efficient vertical axis wind turbine clustered farms. *Renewable and Sustainable Energy Reviews*, 63(May 2018):237–244, 2016.
- [95] S. Shamsoddin and F. Porté-Agel. Large eddy simulation of vertical axis wind turbine wakes. *Energies*, 2014.
- [96] S. Shamsoddin and F. Porté-Agel. A Large-Eddy Simulation Study of Vertical Axis Wind Turbine Wakes in the Atmospheric Boundary Layer, 2016.
- [97] S. Shamsoddin and F. Porté-Agel. Effect of aspect ratio on vertical-axis wind turbine wakes. *Journal of Fluid Mechanics*, 889:R11–R112, 2020.
- [98] C. R. Shapiro, D. F. Gayme, and C. Meneveau. Modelling yawed wind turbine wakes: A lifting line approach. *Journal of Fluid Mechanics*, 841:R11–R112, apr 2018.
- [99] R. E. Sheldahl and P. Klimas. Aerodynamic Characteristics of Seven Symmetrical Airfoil Sections Through 180-Degree Angle of Attack for Use in Aerodynamic Analysis of Vertical Axis Wind Turbines. 1981.
- [100] W. Z. Shen, J. N. Sørensen, and J. H. Zhang. Actuator surface model for wind turbine flow computations. In *Proceedings of European Wind Energy Conference and Exhibition*, volume 7, 2007.
- [101] W. Z. Shen, J. H. Zhang, and J. N. Sørensen. The Actuator Surface Model: A New Navier–Stokes Based Model for Rotor Computations. *Journal of Solar Energy Engineering*, 131(1), jan 2009.
- [102] W. Sheng, R. A. M. Galbraith, and F. N. Coton. A Modified Dynamic Stall Model for Low Mach Numbers. *Journal of Solar Energy Engineering*, 130(3), jul 2008.
- [103] L. Shi, V. A. Riziotis, S. G. Voutsinas, and J. Wang. A consistent vortex model for the aerodynamic analysis of vertical axis wind turbines. *Journal of Wind Engineering and Industrial Aerodynamics*, 135:57–69, 2014.
- [104] J. N. Sørensen and W. Z. Shen. Numerical modeling of wind turbine wakes. *Journal of Fluids Engineering, Transactions of the ASME*, 2002.
- [105] F. Stokhuyzen. *Molens: de nieuwe Stokhuyzen*. Waanders, 2007.

- [106] J. H. Strickland. A performance prediction model for the Darrieus turbine. 1976.
- [107] J. H. Strickland, B. T. Webster, and T. Nguyen. A vortex model of the Darrieus turbine: an analytical and experimental study. 1979.
- [108] R. J. Templin. Aerodynamic performance theory for the nrc vertical-axis wind turbine. 1974.
- [109] H. Tennekes and J. Lumley. *A First Course in Turbulence*. 1973.
- [110] G. Tescione, D. Ragni, C. He, C. J. Simão Ferreira, and G. J. van Bussel. Near wake flow analysis of a vertical axis wind turbine by stereoscopic particle image velocimetry. *Renewable Energy*, 2014.
- [111] G. Tescione, C. J. Simão Ferreira, and G. J. van Bussel. Analysis of a free vortex wake model for the study of the rotor and near wake flow of a vertical axis wind turbine. *Renewable Energy*, 2016.
- [112] D. J. Tritton. *Physical fluid dynamics*. Springer Science & Business Media, 2012.
- [113] M. P. Van Der Laan, N. N. Sørensen, P. E. Réthoré, J. Mann, M. C. Kelly, N. Troldborg, K. S. Hansen, and J. P. Murcia. The k- ϵ -fP model applied to wind farms. *Wind Energy*, 18(12):2065–2084, dec 2015.
- [114] M. P. Van Der Laan, N. N. Srensen, P. E. Réthoré, J. Mann, M. C. Kelly, N. Troldborg, J. G. Schepers, and E. Macheaux. An improved k- ϵ model applied to a wind turbine wake in atmospheric turbulence. *Wind Energy*, 18(5):889–907, may 2015.
- [115] P. E. J. Vermeulen. An experimental analysis of wind turbine wakes. In *3rd International Symposium on Wind Energy Systems*, pages 431–450, AA(Centrale Organisatie voor Toegepast-Natuurwetenschappelijk Onderzoek, Apeldoorn, Netherlands), jan 1980.
- [116] H. G. Weller, G. Tabor, H. Jasak, and C. Fureby. OpenFOAM 4.1, www.openfoam.org, 2017.
- [117] F. M. White. *Viscous Fluid Flow*. 2006.
- [118] R. E. Wilson and P. B. Lissaman. *Applied aerodynamics of wind power machines*. 1974.
- [119] A. Zanon, P. Giannattasio, and C. J. Simão Ferreira. Wake modelling of a VAWT in dynamic stall: Impact on the prediction of flow and induction fields. *Wind Energy*, 2015.
- [120] H. Zong and F. Porté-Agel. A momentum-conserving wake superposition method for wind farm power prediction. *Journal of Fluid Mechanics*, 2020.
- [121] W. Zuo, X. Wang, and S. Kang. Numerical simulations on the wake effect of H-type vertical axis wind turbines. *Energy*, 106:691–700, 2016.